Transactions of the ASME®

Technical Editor, **LEWIS T. WHEELER**

Department of Mechanical Engineering,
University of Houston,
Houston, TX 77204-4792

APPLIED MECHANICS DIVISION

Chairman, **A. NEEDLEMAN**
Secretary, **S. KYRIAKIDES**
Associate Technical Editors,
J. R. BARBER (2000)
R. C. BENSON (2000)
M. M. CARROLL (2000)
W. J. DRUGAN (2000)
A. A. FERRI (2000)
J. W. JU (2001)
V. K. KINRA (2002)
D. KOURIS (2002)
S. KYRIAKIDES (2000)
A. K. MAL (2001)
B. MORAN (2002)
A. NEEDLEMAN (2001)
M. ORTIZ (2001)
N. C. PERKINS (2002)
M.-J. PINDERA (2000)
K. T. RAMESH (2000)
K. RAVI-CHANDAR (2002)
D. A. SIGINER (2000)

BOARD ON COMMUNICATIONS

Chairman and Vice-President
R. K. SHAH

OFFICERS OF THE ASME
President, **R. E. NICKELL**
Executive Director, **D. L. BELDEN**
Treasurer, **J. A. MASON**

PUBLISHING STAFF
Managing Director, Engineering
CHARLES W. BEARDSLEY
Director, Technical Publishing
PHILIP DI VIETRO
Managing Editor, Technical Publishing
CYNTHIA B. CLARK
Managing Editor, Transactions
CORNELIA MONAHAN
Production Coordinator
JUDITH SIERANT
Production Assistant
MARISOL ANDINO

Transactions of the ASME, Journal of Applied Mechanics (ISSN 0021-8936) is published quarterly (Mar., June, Sept., Dec.) for $250.00 per year by The American Society of Mechanical Engineers, Three Park Avenue, New York, NY 10016.

Periodicals postage paid at New York, NY and additional mailing office. POSTMASTER: Send address changes to Transactions of the ASME, Journal of Applied Mechanics, c/o THE AMERICAN SOCIETY OF MECHANICAL ENGINEERS, 22 Law Drive, Box 2300, Fairfield, NJ 07007-2300.

CHANGES OF ADDRESS must be received at Society headquarters seven weeks before they are to be effective. Please send old label and new address. **PRICES:** To members, $40.00; to nonmembers, $250.00; single issue, $100.00. Add $40.00 (airmail $60.00) for postage to countries outside the United States and Canada.

STATEMENT from By-Laws. The Society shall not be responsible for statements or opinions advanced in papers or . . . printed in its publications (B7.1, Para. 3), **COPYRIGHT © 1999** by The American Society of Mechanical Engineers. For authorization to photocopy material for internal or personal use under those circumstances not falling within the fair use provisions of the Copyright Act, contact the Copyright Clearance Center (CCC), 222 Rosewood Drive, Danvers, MA 01923, tel: 978-750-8400, www.copyright.com. Request for special permission or bulk copying should be addressed to Reprints/Permission Department. **INDEXED** by Applied Mechanics Reviews and Engineering Information, Inc. Canadian Goods & Services Tax Registration #126148048.

Journal of Applied Mechanics

Published Quarterly by The American Society of Mechanical Engineers

VOLUME 66 • NUMBER 4 • DECEMBER 1999

837 **In Memory of A. E. Green**

TECHNICAL PAPERS

839 **On the Imperfectly Bonded Spherical Inclusion Problem**
Z. Zhong and S. A. Meguid

847 **An Analysis of Intersonic Crack Growth Under Shear Loading**
A. Needleman

858 **Consistent Hashin-Shtrikman Bounds on the Effective Properties of Periodic Composite Materials**
P. Bisegna and R. Luciano

867 **Singular Solutions in Second-Order Elasticity**
M. M. Carroll and F. J. Rooney

872 **An Approach to Characterize Nonlinear Viscoelastic Material Behavior Using Dynamic Mechanical Tests and Analyses**
H. J. Golden, T. W. Strganac, and R. A. Schapery

879 **On the Dynamic Growth of a Spherical Inclusion With Dilatational Transformation Strain in Infinite Elastic Domain**
B. Wang, Q. Sun, and Z. Xiao

885 **Application of Finite-Part Integrals to Planar Interfacial Fracture Problems in Three-Dimensional Bimaterials**
M.-C. Chen, N.-A. Noda, and R.-J. Tang

891 **Lateral Thermal Buckling of Pipelines on the Sea Bed**
D. J. Miles and C. R. Calladine

898 **A Strip Element Method for Analyzing Wave Scattering by a Crack in an Immersed Composite Laminate**
G. R. Liu, Z. C. Xi, K. Y. Lam, and H. M. Shang

904 **Analysis of Thin-Walled Closed Beams With General Quadrilateral Cross Sections**
J. H. Kim and Y. Y. Kim

913 **An Energy Method for Analyzing Magnetoelastic Buckling and Bending of Ferromagnetic Plates in Static Magnetic Fields**
W. Yang, H. Pan, D. Zheng, and Q. Cai

918 **Effective Constitutive Properties of Linear Elastic Cellular Solids With Randomly Oriented Cells**
Z. Dimitrovová

926 **The Onset of Tear Propagation at Slits in Stressed Uncoated Plain Weave Fabrics**
T. A. Godfrey and J. N. Rossettos

934 **Microstructural Stress Tensor of Granular Assemblies With Volume Forces**
K. Bagi

937 **On the Equilibrium Conditions of Nonstationary Mechanical Systems**
M. Kazic and R. Bulatovic

940 **Representation of Stokes Flow Through a Planar Contraction by Papkovich-Fadle Eigenfunctions**
M. A. Rogerson and Y. L. Yeow

(Contents continued on Outside back cover)

This journal is printed on acid-free paper, which exceeds the ANSI Z39.48-1992 specification for permanence of paper and library materials. ♾™
♻ 85% recycled content, including 10% post-consumer fibers.

Downloaded 04 May 2010 to 171.66.16.52. Redistribution subject to ASME license or copyright; see http://www.asme.org/terms/Terms_Use.cfm

CONTENTS (CONTINUED)

945 **Impulsive Squeezing With Suction and Injection**
E. A. Hamza

952 **A Thermodynamic Approach to Nonlocal Plasticity and Related Variational Principles**
G. Borino, P. Fuschi, and C. Polizzotto

964 **The Nonlinear Gaussian Spectrum of Log-Normal Stochastic Processes and Variables**
R. Ghanem

974 **An Exact Periodic Solution of a Hydromagnetic Flow of an Oldroyd Fluid in a Channel**
R. N. Ray, A. Samad, and T. K. Chaudhury

978 **Integration Scheme for Elastic Deformation and Stresses**
S. L. Lee and C. R. Ou

986 **Dynamics of Serial Multibody Systems Using the Decoupled Natural Orthogonal Complement Matrices**
S. K. Saha

997 **Response Bounds for Linear Damped Systems**
B. Hu and P. Eberhard

1004 **Transverse Normal Stress Effects in Multilayered Plates**
E. Carrera

BRIEF NOTES

Applying the Lagrange Method to Solve Problems of Control Constraints **1013**
A. Rosen

Steady-State Deflection of a Circular Plate Rotating Near Its Critical Speed **1015**
Jen-San Chen

Maximizing the Natural Frequencies and Transverse Stiffness of Centrally Clamped, Circular Disks by Thickening the Clamped Part of the Disk **1017**
A. A. Renshaw

Magnetohydrodynamic Squeeze Film Characteristics Between Parallel Circular Plates Containing a Single Central Air Bubble in the Inertial Flow Regime **1021**
R. Usha and P. Vimala

Generation (or Degeneration) of a Separation Bubble in a Liquid-Filled Cylinder Through Spin-Up (or Spin-Down) Process **1023**
S. Bhattacharyya and A. Pal

A Condition of the Existence of a Conductive Liquid Meniscus in an External Electric Field **1026**
A. F. Spivak and Y. A. Dzenis

1028 An Approximate Analytic Solution of the One-Dimensional Foil Bearing Problem
A. A. Renshaw

1032 The Nonlinear Sloshing of Liquid in Tank With Pitching
L. Yin, B. Wang, X. Ma, and J. Zou

1034 A Generalization of Cattaneo-Mindlin for Thin Strips
J. Jäger

1037 Interfacial Debonding of an Elliptical Inhomogeneity in Piezoelectric Solids
W. Deng and S. A. Meguid

1040 A Numerical Study on the Free Vibration of Symmetric Cross-Ply Laminated Cylindrical Helical Springs
V. Yıldırım

1043 Application of Laser Ultrasonics to Develop Dispersion Curves for Elastic Plates
C. Eisenhardt, L. J. Jacobs, and J. Qu

DISCUSSION

1046 **Dynamic Buckling and Post-buckling of Imperfect Cylindrical Shells Under Mechanical and Thermal Loads, Based on the Three-Dimensional Theory of Elasticity, by M. Shairyat and M. R. Eslami—Discussion by R. L. Citerley**

1048 **Tangential Loading of General Three-Dimensional Contacts, by M. Ciavarella—Discussion by J. Jäger**

ERRATA

963 **Some Problems of a Rigid Elliptical Disk-Inclusion Bonded Inside a Transversely Isotropic Space, Part I, by M. Rahman**

ANNOUNCEMENTS AND SPECIAL NOTICES

1051 Worldwide Mechanics Meeting List

1054 Special Announcement From the Technical Editor

1055 Announcement—New Reference Format

1056 Information for Authors

1057 1999 Author Index

Downloaded 04 May 2010 to 171.66.16.52. Redistribution subject to ASME license or copyright; see http://www.asme.org/terms/Terms_Use.cfm



A. E. Green

(From a photograph by I. N. Sneddon)

Albert Edward Green died on August 12, 1999 at the age of 86. He was born in London, England, and studied mathematics at Cambridge University, being awarded a First Class Honors degree in Mathematics in 1934, and a Ph.D. degree in 1937 for research carried out under the direction of Sir Geoffrey Taylor. Among his other teachers in applied mathematics and theoretical mechanics were S. Goldstein, W. R. Dean and L. A. Pars. From 1936 to 1939 he held a Research Fellowship in Jesus College (of Cambridge University). It was at the end of his nine-year stay at Cambridge that he married Gwendoline May Rudston who survives him.

A. E. Green's first teaching position was a Lectureship at Durham University in 1939. In 1948 he was appointed Professor of Applied Mathematics at King's College, Newcastle-upon-Tyne, which was then part of Durham University. During the twenty years he spent at King's College, which became the University of Newcastle-upon-Tyne in 1963, he served as Co-Chairman of the Mathematics Department for the first ten years, as Chairman for the last ten years, and was Dean of the Science Faculty during 1959-62. He left Newcastle-upon-Tyne in 1968 to become the Sedleian Professor of Natural Philosophy at Oxford University. (Another outstanding elastician, A. E. H. Love, held the chair for 41 years from 1899.) He served as Chairman of the Mathematical Institute at Oxford, 1974-76. Green gave lectures throughout Europe and the United States on numerous occasions, and he was a Visiting Professor at Brown University and at the University of California, Berkeley.

This bare recital of the main elements of Professor Green's career provides only a small indication of the wealth and importance of his contributions to theoretical and applied mechanics. His rare coupling of physical insight with sophistication in mathematical techniques is evident in close to 200 publications describing original and significant research in a broad range of topics in the mechanics of solids and fluids. His papers on linear elasticity alone place him among the most outstanding workers in theoretical mechanics. Yet he also wrote highly original articles on fluid mechanics, on nonlinear elasticity, and on the mechanics of linear and non-linear continua in general, and these important contributions were made despite time-consuming administrative duties. His two books, *Theoretical Elasticity* written with W. Zerna and *Large Elastic Deformations* written with the late J. E. Adkins, remain standard reference texts. Over the years, he also gave valuable service to the editorial boards of several journals and he supervised the work of many doctoral and post-doctoral students.

He was elected a Fellow of the Royal Society (London) in 1958. Other honors awarded him include the Smith's Prize of Cambridge University in 1936, an Sc.D. from Cambridge in 1942, honorary doctorates from the Universities of Durham (1970), Glasgow (1975), and the National

Downloaded 04 May 2010 to 171.66.16.27. Redistribution subject to ASME license or copyright; see http://www.asme.org/terms/Terms_Use.cfm

University of Ireland (1977). He received the Timoshenko Medal from the American Society of Mechanical Engineers in 1974 and the von Kármán Medal from the American Society of Civil Engineers in 1983. Collections of original papers were published in his honor in a special issue of the *Journal of Elasticity* (Vol. 5, 173-400, 1975) and in the November 1992 issue of the *Quarterly Journal of Mechanics and Applied Mathematics.* Oxford University Press republished the latter in 1994 as the book *Nonlinear Elasticity and Theoretical Mechanics,* which contains a list of his publications up to 1994.

His enthusiasm for research affected those fortunate enough to work with him. His manner was always friendly, warmhearted, unpretentious, and open with everyone he met. It is typical of his modesty that in his acceptance speech for the Timoshenko Medal he said "On looking back over the history of science one realizes that most of us can only hope to place one small brick - if that - in the edifice - and even that may get knocked out by following generations." He enjoyed gardening and walking, and was an accomplished organist. A favorite pastime of his was to play piano duets with his wife Gwen.

R. T. Shield

Downloaded 04 May 2010 to 171.66.16.27. Redistribution subject to ASME license or copyright; see http://www.asme.org/terms/Terms_Use.cfm

On the Imperfectly Bonded Spherical Inclusion Problem

Z. Zhong[1]

S. A. Meguid
Mem. ASME

Engineering Mechanics and Design Laboratory,
Department of Mechanical and Industrial Engineering,
University of Toronto,
Toronto, Ontario M5S 3G8,
Canada

An exact solution is developed for the problem of a spherical inclusion with an imperfectly bonded interface. The inclusion is assumed to have a uniform eigenstrain and a different elastic modulus tensor from that of the matrix. The displacement discontinuity at the interface is considered and a linear interfacial condition, which assumes that the displacement jump is proportional to the interfacial traction, is adopted. The elastic field induced by the uniform eigenstrain given in the imperfectly bonded inclusion is decomposed into three parts. The first part is prescribed by a uniform eigenstrain in a perfectly bonded spherical inclusion. The second part is formulated in terms of an equivalent nonuniform eigenstrain distributed over a perfectly bonded spherical inclusion which models the material mismatch between the inclusion and the matrix, while the third part is obtained in terms of an imaginary Somigliana dislocation field which models the interfacial sliding and normal separation. The exact form of the equivalent nonuniform eigenstrain and the imaginary Somigliana dislocation are fully determined using the equivalent inclusion method and the associated interfacial condition. The elastic fields are then obtained explicitly by means of the superposition principle. The resulting solution is then used to evaluate the average Eshelby tensor and the elastic strain energy.

1 Introduction

Eshelby's solution (Eshelby, 1957) for an ellipsoidal inclusion with a perfect bonded interface has played an important role in the subsequent development of micromechanics of materials; as evidenced by the books of Mura (1987) and Nemat-Nasser and Hori (1993). However, the condition of perfect bonding at the interface between the inclusion and the matrix is often inadequate in modeling the physical reality and the mechanical behavior of the interface. Typical examples include the debonding of fibers in composites and the grain boundary sliding in polycrystalline solids.

Indeed, a number of attempts have been devoted to the imperfectly bonded inclusion problem; see, for example, the work of Ghahremani (1980), Mura and Furuhashi (1984), Mura et al. (1985), Benveniste (1985), Jasiuk et al. (1987), Shibata et al. (1990), Hashin (1991), Qu (1993), Huang (1995) and Gao (1995). Among these studies, the interface was modeled as a spring layer with vanishing thickness and an assumption was made that the normal and tangential interfacial displacement discontinuities are proportional to the normal and shear tractions at the interface.

In our previous paper (Zhong and Meguid, 1996), we obtained a solution for the uniform eigenstrain problem of a spherical inclusion with a spring-type imperfectly bonded interface using the Green's function approach. The inclusion, however, is assumed to have the same elastic moduli as those of the matrix. In the present paper, we consider the more general case that of imperfectly bonded inclusion problem in which the inclusion and the matrix have different elastic moduli.

This article is divided into five main sections. Following this brief introduction, we state the problem and provide a description of the basic equations. In Section 3, we decompose the problem into three subproblems. In Section 4, we provide a solution to the different subproblems and superimpose them to obtain the total solution. In Section 5, we analyze and discuss the results. Finally, in Section 6, we conclude the paper.

2 Problem Formulation

Consider a spherical inclusion Ω embedded in an infinitely extended elastic matrix $D - \Omega$. The inclusion has elastic moduli, C^*_{ijkl}, different from those of the matrix, C_{ijkl}. The interface between the inclusion and the matrix is assumed to be imperfectly bonded, which can be modeled by a linear interfacial condition. A uniform eigenstrain ϵ^*_{ij} is prescribed only in the inclusion and vanishes in the matrix. A coordinate system, with its origin located at the center of the spherical inclusion is introduced, as depicted in Fig. 1.

The governing equations for the above problem are

$$\sigma_{ij,j} = 0 \quad \text{in} \quad D \tag{1}$$

$$\sigma_{ij} = C^*_{ijkl}(\epsilon_{kl} - \epsilon^*_{kl}) \quad \text{in} \quad \Omega \tag{2}$$

$$\sigma_{ij} = C_{ijkl}\epsilon_{kl} \quad \text{in} \quad D - \Omega \tag{3}$$

$$\epsilon_{ij} = (u_{i,j} + u_{j,i})/2 \quad \text{in} \quad D \tag{4}$$

where u_i, ϵ_{ij}, and σ_{ij} are displacements, strains, and stresses, respectively, and the repeated indices imply summation.

If we employ the spring-type interfacial model, the interfacial condition can be written as

$$[\sigma_{ij}]n_j = 0 \quad \text{on} \quad \partial\Omega \tag{5}$$

$$[u_i] = R_{ij}T_j \quad \text{on} \quad \partial\Omega \tag{6}$$

where $[\,\cdot\,]$ = (out) − (in), n_i is the outward unit normal on the interface and $T_i = \sigma_{ij}n_j$ represents the interfacial traction. Equations (5) and (6) imply that the interfacial traction remains continuous, while the displacement experience a jump across the interface which is assumed to be proportional to the interfacial traction. The second-order tensor R_{ij} represents the compliance of the interface (spring layer), which is symmetric and positive definite. If we consider the case of elastic isotropy, R_{ij} can then be written in a special form, such that

$$R_{ij} = \alpha\delta_{ij} + (\beta - \alpha)n_in_j \tag{7}$$

[1] On sabbatical leave from the Department of Engineering Mechanics and Technology, Tongji University, Shanghai 200092, P. R. China.

Contributed by the Applied Mechanics Division of THE AMERICAN SOCIETY OF MECHANICAL ENGINEERS for publication in the ASME JOURNAL OF APPLIED MECHANICS.

Discussion on the paper should be addressed to the Technical Editor, Professor Lewis T. Wheeler, Department of Mechanical Engineering, University of Houston, Houston, TX 77204-4792, and will be accepted until four months after final publication of the paper itself in the ASME JOURNAL OF APPLIED MECHANICS.

Manuscript received by the ASME Applied Mechanics Division, Aug. 12, 1996; final revision, May 4, 1999. Associate Technical Editor: J. L. Bassani.

 Copyright © 1999 by ASME

Downloaded 04 May 2010 to 171.66.16.27. Redistribution subject to ASME license or copyright; see http://www.asme.org/terms/Terms_Use.cfm

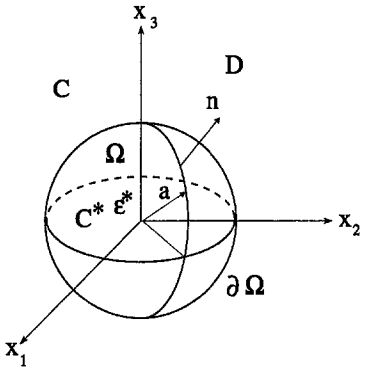


Fig. 1 A schematic of the spherical inclusion problem

where δ_{ik} is the Kronecker δ. α and β, which are positive constants, denote the respective compliance in the tangential and the normal directions of the interface. In this case, Eq. (6) can be rewritten as

$$[u_j](\delta_{ij} - n_i n_j) = \alpha \sigma_{kj} n_j (\delta_{ik} - n_i n_k) \tag{8}$$

$$[u_j] n_i n_j = \beta \sigma_{kj} n_k n_j n_i. \tag{9}$$

It can be seen from the above that α and β characterize the interfacial behavior. For example, the case where $\alpha = 0$ and $\beta = 0$ corresponds to a perfectly bonded interface, while for the case $\beta = 0$ and $\alpha \neq 0$, only interfacial sliding takes place with normal contact remaining intact. Furthermore, the case where $\beta = 0$ and $\alpha \to \infty$ represents the free sliding interface. This linear interfacial condition, corresponds, in essence, to modeling the imperfectly bonded interface by a linear spring-layer of vanishing thickness (see Hashin, 1991).

The solution of Eqs. (1)–(6) with a vanishing remote loading condition completely determines the uniform eigenstrain problem of an inclusion with a linear imperfectly bonded interface. Appendix A shows that the solution is unique.

3 Decomposition of the Problem

Using the equivalent inclusion method (see Eshelby, 1957; Mura, 1987), the material mismatch between the inclusion and the matrix can be modeled by an equivalent eigenstrain (see Fig. 2(*a*)). The equivalent equation can be expressed as

$$\sigma_{ij} = C^*_{ijkl}(u_{k,l} - \epsilon^*_{kl}) = C_{ijkl}(u_{k,l} - \epsilon^*_{kl} - \epsilon^{**}_{kl}) \quad \text{in} \quad \Omega \tag{10}$$

where ϵ^*_{ij} is the real uniform eigenstrain prescribed in the inclusion, while ϵ^{**}_{ij} denotes the equivalent (imaginary) eigenstrain defined only in the inclusion. In contrast to the perfectly bonded case, neither the equivalent eigenstrain nor the stress is uniform inside the imperfectly bonded inclusion. Therefore, Eshelby's solution is *not* valid for the imperfectly bonded inclusion problem.

The uniform eigenstrain problem of an imperfectly bonded spherical inclusion (original problem) can be further decomposed into three subproblems (see Fig. 2(*b*)). These subproblems are solved separately and then superimposed to provide the general solution of the original problem.

In subproblem I, a uniform eigenstrain ϵ^*_{ij} is prescribed inside a perfectly bonded inclusion Ω in an infinite and homogeneous medium D with a vanishing remote boundary condition. The inclusion Ω and the matrix $D - \Omega$ have the same elastic modulus tensor C_{ijkl}. This subproblem can be described by the well-known Eshelby's solution, which has the following general form for the displacement u^I_i, the strain ϵ^I_{ij} and the stress σ^I_{ij}, such that

$$u^I_i(\mathbf{x}) = -\int_{V_\Omega} C_{mnkl}\epsilon^*_{kl}(\mathbf{x}')G_{im,n}(\mathbf{x} - \mathbf{x}')dV' \tag{11}$$

$$\epsilon^I_{ij}(\mathbf{x}) = -\tfrac{1}{2}\int_{V_\Omega} C_{mnkl}\epsilon^*_{kl}(\mathbf{x}')[G_{im,nj}(\mathbf{x} - \mathbf{x}') + G_{jm,ni}(\mathbf{x} - \mathbf{x}')]dV' \tag{12}$$

$$\sigma^I_{ij}(\mathbf{x}) = -C_{ijmn}\left[\int_{V_\Omega} C_{pqkl}\epsilon^*_{kl}(\mathbf{x}')G_{mp,qn}(\mathbf{x} - \mathbf{x}')dV' + \epsilon^*_{mn}(\mathbf{x})\right] \tag{13}$$

where $dV' = dx'_1dx'_2dx'_3$, and $G_{ij}(\mathbf{x})$ is the Green's function of elasticity for infinite medium.

In subproblem II, an equivalent (imaginary) nonuniform eigenstrain ϵ^{**}_{ij} is given inside a perfectly bonded inclusion Ω in an infinite and homogeneous medium D with a vanishing boundary condition at infinity. The inclusion has the same elastic modulus tensor C_{ijkl} as that of the matrix $D - \Omega$. In this case, the displacement u^{II}_i, the strain ϵ^{II}_{ij}, and the stress σ^{II}_{ij} can be written as

$$u^{II}_i(\mathbf{x}) = -\int_{V_\Omega} C_{mnkl}\epsilon^{**}_{kl}(\mathbf{x}')G_{im,n}(\mathbf{x} - \mathbf{x}')dV' \tag{14}$$

$$\epsilon^{II}_{ij}(\mathbf{x}) = -\tfrac{1}{2}\int_{V_\Omega} C_{mnkl}\epsilon^{**}_{kl}(\mathbf{x}')[G_{im,nj}(\mathbf{x} - \mathbf{x}') + G_{jm,ni}(\mathbf{x} - \mathbf{x}')]dV' \tag{15}$$

$$\sigma^{II}_{ij}(\mathbf{x}) = -C_{ijmn}\left[\int_{V_\Omega} C_{pqkl}\epsilon^{**}_{kl}(\mathbf{x}')G_{mp,qn}(\mathbf{x} - \mathbf{x}')dV' + \epsilon^*_{mn}(\mathbf{x})\right]. \tag{16}$$

In subproblem III, an imaginary Somigliana dislocation is introduced to model the interfacial sliding and normal separation at the interface, whose Burger's vector is defined as

$$b_i = -[u_i]. \tag{17}$$

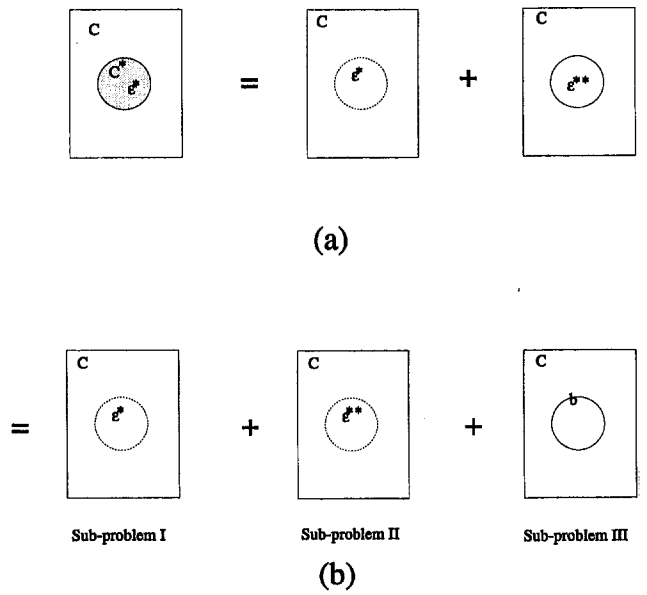


Fig. 2 Decomposition of the problem: (*a*) a schematic of the general equivalent inclusion method for an imperfectly bonded inhomogeneity and (*b*) the three different subproblems examined

Downloaded 04 May 2010 to 171.66.16.27. Redistribution subject to ASME license or copyright; see http://www.asme.org/terms/Terms_Use.cfm

This dislocation field is given by the Volterra's solution, i.e.,

$$u_i^{III}(\mathbf{x}) = \int_{\partial\Omega} C_{mnkl} b_l(\mathbf{x}') n_k(\mathbf{x}') G_{im,n}(\mathbf{x} - \mathbf{x}') dS'. \quad (18)$$

Following Asaro (1975), b_n is extended to the interior of Ω and as a result (18) can be expressed in another form using Gauss' theorem,

$$u_i^{III}(\mathbf{x}) = -\int_{V_\Omega} C_{mnkl} \epsilon_{kl}^{***}(\mathbf{x}') G_{im,n}(\mathbf{x} - \mathbf{x}') dV' + b_i(\mathbf{x}) \quad (19)$$

with

$$\epsilon_{kl}^{***} = -(b_{k,l} + b_{l,k})/2. \quad (20)$$

The corresponding strain and stress are

$$\epsilon_{ij}^{III}(\mathbf{x}) = -\tfrac{1}{2}\int_{V_\Omega} C_{mnkl}\epsilon_{kl}^{***}(\mathbf{x}')[G_{im,nj}(\mathbf{x} - \mathbf{x}') + G_{jm,ni}(\mathbf{x} - \mathbf{x}')]dV' - \epsilon_{ij}^{***}(\mathbf{x}) \quad (21)$$

$$\sigma_{ij}^{III} = -C_{ijmn}\left[\int_{V_\Omega} C_{pqkl}\epsilon_{kl}^{***}(\mathbf{x}')G_{mp,qn}(\mathbf{x} - \mathbf{x}')dV' + \epsilon_{mn}^{***}(\mathbf{x})\right]. \quad (22)$$

Therefore, the solution of the original problem can be expressed as the sum of the three subproblems I, II, and III, such that

$$u_i = u_i^I + u_i^{II} + u_i^{III} \quad (23)$$

$$\epsilon_{ij} = \epsilon_{ij}^I + \epsilon_{ij}^{II} + \epsilon_{ij}^{III} \quad (24)$$

$$\sigma_{ij} = \sigma_{ij}^I + \sigma_{ij}^{II} + \sigma_{ij}^{III}. \quad (25)$$

The interfacial traction continuity condition (5) is automatically satisfied, whereas the equivalent nonuniform eigenstrain ϵ_{ij}^{**} for subproblem II and the Burger's vector b_i for subproblem III need to be determined by the equivalent equation (10) and the interfacial condition (6), which is the key to solving the problem.

4 Solution

In the previous section, we formulated the problem in terms of three subproblems. In the present section, we use these subproblems to provide an exact solution to the imperfectly bonded inclusion problem.

4.1 Solution of Subproblem I. In this case, a uniform eigenstrain ϵ_{ij}^* is prescribed inside a perfectly bonded spherical inclusion Ω in an infinite and homogeneous medium D with a vanishing remote boundary condition. The inclusion and the matrix are isotropic and have the same shear moduli μ and Poisson's ratios ν. The solution of this subproblem can be deduced from Eshelby's solution (Eshelby, 1957) for the ellipsoidal inclusion problem. For example, the stress inside the inclusion can be obtained as

$$\sigma_{ij}^I = -\frac{2\mu}{45(1-\nu)}[10(1+\nu)\epsilon_{il}^*\delta_{lj} + 3(7-5\nu)e_{ij}^*] \quad (26)$$

where e_{ij}^* is the deviatoric part of ϵ_{ij}^*.

4.2 Solution of Subproblem II. A nonuniform eigenstrain ϵ_{ij}^{**} is given inside a perfectly bonded spherical inclusion Ω in an infinite and homogeneous medium D with a vanishing remote boundary condition. The inclusion and the matrix are isotropic and have the same shear moduli μ and Poisson's ratios ν. Asaro and Barnett (1975) have studied the nonuniform eigenstrain problem of a perfectly bonded ellipsoidal inclusion. In this section, the elastic solution for this subproblem will be explicitly obtained using the following assumed form of ϵ_{ij}^{**}:

$$\epsilon_{ij}^{**} = a^2 k\delta_{ij} + a^2 P_{ij} + Q_{il}x_l x_j + Q_{jl}x_l x_i + M_{kl}x_k x_l \delta_{ij} + N_{ij}|\mathbf{x}|^2 \quad (27)$$

where $|\mathbf{x}| = (x_i x_i)^{1/2}$, a is the radius of the spherical inclusion, k is a scalar and P_{ij}, Q_{ij}, M_{ij}, and N_{ij} are symmetric deviatoric tensors with the requirement that $P_{ll} = Q_{ll} = M_{ll} = N_{ll} = 0$.

For isotropic materials, the elastic modulus tensor C_{ijkl} can be written as

$$C_{ijkl} = \frac{2\mu\nu}{1-2\nu}\delta_{ij}\delta_{kl} + \mu(\delta_{ik}\delta_{jl} + \delta_{il}\delta_{jk}). \quad (28)$$

Green's function for infinite and isotropic medium is given by

$$G_{ij}(\mathbf{x} - \mathbf{x}') = \frac{\delta_{ij}}{4\pi\mu|\mathbf{x} - \mathbf{x}'|} - \frac{1}{16\pi\mu(1-\nu)}\frac{\partial^2}{\partial x_i \partial x_j}|\mathbf{x} - \mathbf{x}'|. \quad (29)$$

Substituting (28) and (29) into (14), we have

$$u_i^{II} = \frac{1}{8\pi(1-\nu)}[\psi_{kl,kli}^{II} - 2\nu\phi_{il,i}^{II} - 4(1-\nu)\phi_{il,l}^{II}] \quad (30)$$

with

$$\phi_{ij}^{II} = \int_{V_\Omega} \frac{\epsilon_{ij}^{**}(\mathbf{x}')dV'}{|\mathbf{x} - \mathbf{x}'|} \quad (31)$$

$$\psi_{ij}^{II} = \int_{V_\Omega} \epsilon_{ij}^{**}(\mathbf{x}')|\mathbf{x} - \mathbf{x}'|dV'. \quad (32)$$

The corresponding stress fields are calculated by $\sigma_{ij}^{II} = C_{ijkl}(u_{k,l}^{II} - \epsilon_{kl}^{**})$. Using (27)–(30), we obtain the stress inside the inclusion as follows:

$$\begin{aligned}\sigma_{ij}^{II} = &-\frac{4\mu(1+\nu)}{3(1-\nu)}a^2 k_1\delta_{ij} \\ &- 2\mu a^2\left[\frac{(7-5\nu)}{15(1-\nu)}(P_{ij} + Q_{ij}) + \frac{(1+\nu)}{5(1-\nu)}M_{ij}\right] \\ &+ 2\mu\left[\frac{2(1-7\nu)}{35(1-\nu)}Q_{mn} - \frac{6(1+\nu)}{7(1-\nu)}M_{mn}\right. \\ &\left. - \frac{2(1-7\nu)}{35(1-\nu)}N_{mn}\right]x_m x_n\delta_{ij} + 2\mu\left[\frac{(23-21\nu)}{35(1-\nu)}Q_{ij}\right. \\ &\left. + \frac{(1+\nu)}{7(1-\nu)}M_{ij} - \frac{(23-21\nu)}{35(1-\nu)}N_{ij}\right]|\mathbf{x}|^2 \\ &- 2\mu\left[\frac{2(5-7\nu)}{35(1-\nu)}(Q_{jm} - N_{jm}) - \frac{2(1+\nu)}{7(1-\nu)}M_{jm}\right]x_m x_i \\ &- 2\mu\left[\frac{2(5-7\nu)}{35(1-\nu)}(Q_{im} - N_{im}) - \frac{2(1+\nu)}{7(1-\nu)}M_{im}\right]x_m x_j \end{aligned} \quad (33)$$

for point $\mathbf{x}$ inside Ω. The stress in the matrix is given in Appendix B.

4.3 Solution of Subproblem III. In this subproblem, an imaginary Somigliana dislocation is introduced to model the in-

Downloaded 04 May 2010 to 171.66.16.27. Redistribution subject to ASME license or copyright; see http://www.asme.org/terms/Terms_Use.cfm

terfacial sliding and normal separation at the interface of the inclusion, whose Burger's vector b_i is assumed to take the form

$$b_i = a^2\lambda x_i + a^2 A_{ij}x_j + B_{kl}x_k x_l x_i \tag{34}$$

where a is the radius of the spherical inclusion, λ is a scalar, A_{ij} and B_{ij} are symmetric deviatoric tensors, with the requirement that $A_{ll} = B_{ll} = 0$. The solution of this subproblem has been obtained by Zhong and Meguid (1996), from which the stress in the inclusion can be written as

$$\sigma_{ij}^{III} = \frac{4\mu(1+\nu)}{3(1-\nu)} a^2\lambda\delta_{ij} + \frac{2\mu(7-5\nu)}{15(1-\nu)} a^2 A_{ij} + \frac{24\mu\nu}{5(1-\nu)} B_{kl}x_k x_l \delta_{ij} - \frac{4\mu}{35(1-\nu)} \times \left[2(7-4\nu)B_{ij}|x|^2 + 12\nu B_{il}x_l x_j + 12\nu B_{jl}x_l x_i - 2(7-10\nu)B_{kl}x_k x_l \delta_{ij} - \frac{7}{3}(5-\nu)a^2 B_{ij} \right] \tag{35}$$

for point **x** inside Ω. The stress in the matrix is given in Appendix C.

4.4 Superposition of Subproblems. Although the solutions of subproblems I, II, and III have been given in the previous subsections, the coefficients k, λ, P_{ij}, Q_{ij}, M_{ij}, N_{ij}, A_{ij}, and B_{ij} are still unknown. In this section, we will determine these coefficients.

Equation (10) can be rewritten as

$$\epsilon_{ij}^{**} = (D_{ijkl}^* - D_{ijkl})(\sigma_{kl}^I + \sigma_{kl}^{II} + \sigma_{kl}^{III}) \quad \text{in} \quad \Omega \tag{36}$$

where D_{ijkl}^* and D_{ijkl} are the respective inverses of C_{ijkl}^* and C_{ijkl}, i.e., the respective elastic compliance tensors of the inclusion and the matrix materials. Substituting (26), (27), (33), and (35) into Eq. (36) and interfacial conditions (8) and (9), we deduce that

$$k = \frac{k_0}{3}\left(\frac{\epsilon_{ll}^*}{a^2}\right) \quad \lambda = \frac{\lambda_0}{3}\left(\frac{\epsilon_{ll}^*}{a^2}\right)$$

$$A_{ij} = A_0\left(\frac{e_{ij}^*}{a^2}\right) \quad B_{ij} = B_0\left(\frac{e_{ij}^*}{a^2}\right) \quad P_{ij} = P_0\left(\frac{e_{ij}^*}{a^2}\right)$$

$$Q_{ij} = Q_0\left(\frac{e_{ij}^*}{a^2}\right) \quad M_{ij} = M_0\left(\frac{e_{ij}^*}{a^2}\right) \quad N_{ij} = N_0\left(\frac{e_{ij}^*}{a^2}\right)$$

where e_{ij}^* is the deviatoric part of the real uniform eigenstrain ϵ_{ij}^*, k_0, and λ_0 are determined from the following set of equations:

$$g_{11}k_0 + g_{12}\lambda_0 = -g_{11} - 1 \tag{37}$$

$$g_{21}k_0 + g_{22}\lambda_0 = -g_{21} \tag{38}$$

while A_0, B_0, P_0, Q_0, M_0, and N_0 are determined from the following set of equations:

$$h_{11}P_0 + h_{12}Q_0 + h_{13}M_0 + h_{15}A_0 + h_{16}B_0 = -h_{11} + 1 \tag{39}$$

$$h_{22}Q_0 + h_{23}M_0 + h_{24}N_0 + h_{26}B_0 = 0 \tag{40}$$

$$h_{32}Q_0 + h_{33}M_0 + h_{34}N_0 + h_{36}B_0 = 0 \tag{41}$$

$$h_{42}Q_0 + h_{43}M_0 + h_{44}N_0 + h_{46}B_0 = 0 \tag{42}$$

$$h_{51}P_0 + h_{52}Q_0 + h_{53}M_0 + h_{54}N_0 + h_{55}A_0 + h_{56}B_0 = -h_{51} \tag{43}$$

$$h_{61}P_0 + h_{62}Q_0 + h_{63}M_0 + h_{64}N_0 + h_{65}A_0 + h_{66}B_0 = -h_{61}. \tag{44}$$

The coefficients g_{ij} $(i, j = 1, 2)$ and h_{ij} $(i, j = 1, \ldots, 6)$, which are given in Appendix D, are dependent on the respective shear moduli μ^* and μ and Poisson's ratios ν^* and ν of the inclusion and the matrix as well as the interfacial compliances α and β. Therefore, k_0 and λ_0 can be obtained by solving Eqs. (37) and (38), while P_0, Q_0, M_0, N_0, A_0, and B_0 can be obtained by solving Eqs. (39)–(44). Once these coefficients are solved, the equivalent eigenstrain ϵ_{ij}^{**} and the Burger's vector of the equivalent Somigliana dislocation b_i can be easily established through (27) and (34). Accordingly, the elastic field of the original problem is completely and uniquely determined by superimposing the respective solutions of subproblems I, II, and III.

In addition to the uniqueness of the solution (see Appendix A), the assumed forms of the equivalent eigenstrain and the Burger's vector (27) and (34) satisfy all the equations and the interfacial conditions. It is then reasonable to conclude that the assumed form of the eigenstrain and the Burger's vector is exact.

4.5 Average Eshelby Tensor. In many cases, however, we only need to calculate the average strain or average stress in the inclusion in order to predict the average properties of the material.

The average strain $\bar{\epsilon}_{ij}$ and the average stress $\bar{\sigma}_{ij}$ in the inclusion can be defined as

$$\bar{\epsilon}_{ij} = \frac{1}{V_\Omega}\int_{V_\Omega} \epsilon_{ij}dV \quad \bar{\sigma}_{ij} = \frac{1}{V_\Omega}\int_{V_\Omega} \sigma_{ij}dV \tag{45}$$

where V_Ω is the volume of the inclusion Ω. Substituting (24) and (25) into (45), we obtain

$$\bar{\epsilon}_{ij} = \bar{S}_{ijkl}\epsilon_{kl}^* \tag{46}$$

$$\bar{\sigma}_{ij} = C_{ijmn}^*(\bar{S}_{mnkl} - I_{mnkl})\epsilon_{kl}^* \tag{47}$$

where I_{mnkl} is the fourth-order identity tensor and $\bar{S}_{ijkl}$ can be defined as being the average Eshelby tensor whose role in imperfectly bonded inclusion problems is equivalent to that of the Eshelby tensor in perfectly bonded inclusion problems. The average Eshelby tensor is obtained as

$$\bar{S}_{ijkl} = S_{ijmn}^E(I_{mnkl} + H_{mnkl}) + (S_{ijmn}^E - I_{ijmn})F_{mnkl} \tag{48}$$

where S_{ijkl}^E is the Eshelby tensor (Eshelby, 1957) for a perfectly bonded inclusion, while the fourth-order tensors H_{ijkl} and F_{ijkl} are established by the following relations:

$$\bar{\epsilon}_{ij}^{**} = H_{ijkl}\epsilon_{kl}^* \tag{49}$$

$$\bar{\epsilon}_{ij}^{***} = F_{ijkl}\epsilon_{kl}^* \tag{50}$$

where $\bar{\epsilon}_{ij}^{**}$ and $\bar{\epsilon}_{ij}^{***}$ are the average value of ϵ_{ij}^{**} and ϵ_{ij}^{***} in the inclusion. When the inclusion is perfectly bonded with the matrix we have $\bar{S}_{ijkl} = S_{ijkl}^E$. Accordingly, the second and third terms in (48) represent the contribution due to the imperfectly bonded interface and the material mismatch between the inclusion and the matrix.

For isotropic materials, H_{ijkl} and F_{ijkl} are determined using (27) and (34) as follows:

$$H_{ijkl} = \tfrac{1}{3}k_0\delta_{ij}\delta_{kl} + \tfrac{1}{2}(P_0 + \tfrac{2}{5}Q_0 + \tfrac{3}{5}N_0)(\delta_{ik}\delta_{jl} + \delta_{il}\delta_{jk} - \tfrac{2}{3}\delta_{ij}\delta_{kl}) \tag{51}$$

$$F_{ijkl} = -\tfrac{1}{3}\lambda_0\delta_{ij}\delta_{kl} - \tfrac{1}{2}(A_0 + \tfrac{2}{5}B_0)(\delta_{ik}\delta_{jl} + \delta_{il}\delta_{jk} - \tfrac{2}{3}\delta_{ij}\delta_{kl}). \tag{52}$$

Therefore, the average Eshelby tensor can be derived as

$$\bar{S}_{ijkl} = \frac{S_1}{3}\delta_{ij}\delta_{kl} + \frac{S_2}{2}\left(\delta_{ik}\delta_{jl} + \delta_{il}\delta_{jk} - \frac{2}{3}\delta_{ij}\delta_{kl}\right) \tag{53}$$

where

Downloaded 04 May 2010 to 171.66.16.27. Redistribution subject to ASME license or copyright; see http://www.asme.org/terms/Terms_Use.cfm

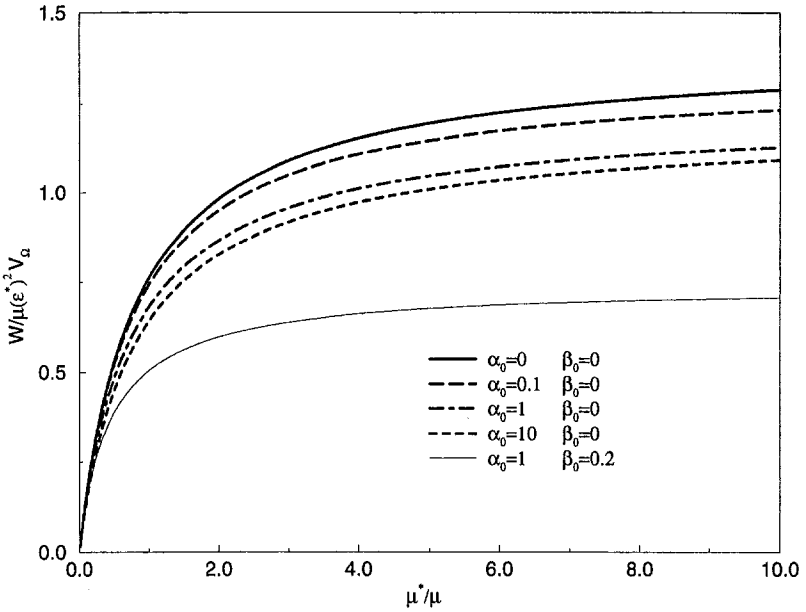


Fig. 3 Variation of the normalized elastic strain energy $W/\mu(\epsilon^*)^2V_\Omega$ versus shear moduli ratio μ^*/μ, when the eigenstrain ϵ_{ij}^* has only one nonzero component, $\epsilon_{11}^* = \epsilon^* \neq 0$, under different interfacial compliances α_0 and β_0

$$S_1 = \alpha^E(k_0 + 1) - (\alpha^E - 1)\lambda_0 \tag{54}$$

$$S_2 = \beta^E(1 + P_0 + \tfrac{2}{5}Q_0 + \tfrac{3}{5}N_0) - (\beta^E - 1)(A_0 + \tfrac{2}{5}B_0) \tag{55}$$

with

$$\alpha^E = \frac{1 + \nu}{3(1 - \nu)} \quad \beta^E = \frac{2(4 - 5\nu)}{15(1 - \nu)}.$$

In this case, $\bar{S}_{ijkl}$ is a fourth-order isotropic tensor with Voigt symmetry ($\bar{S}_{ijkl} = \bar{S}_{jikl} = \bar{S}_{ijlk} = \bar{S}_{klij}$).

4.6 Elastic Strain Energy. Let us now examine the elastic strain energy stored in body D which contains an imperfectly bonded inclusion Ω with a different elastic modulus tensor from that of the matrix. The total elastic strain energy W is shown to be

$$W = -\tfrac{1}{2}\int_{V_\Omega} \sigma_{ij}\epsilon_{ij}^* dV. \tag{56}$$

When ϵ_{ij}^* is uniform inside Ω, W can be simplified to

$$W = -\tfrac{1}{2}V_\Omega \bar{\sigma}_{ij}\epsilon_{ij}^* \tag{57}$$

where $\bar{\sigma}_{ij}$ is the average stress in the inclusion and V_Ω is the volume of Ω. Considering (47), we have

$$W = -\tfrac{1}{2}V_\Omega C_{ijkl}^*(\bar{S}_{klmn} - I_{klmn})\epsilon_{ij}^*\epsilon_{mn}^* \tag{58}$$

where C_{ijkl}^* is the elastic modulus tensor of the inclusion and $\bar{S}_{ijkl}$ is the average Eshelby tensor defined by Eq. (48).

5 Discussion

Consider the case where $\alpha = \beta = 0$ which leads to $\lambda_0 = A_0 = B_0 = 0$, which is equivalent to $b_i = 0$. This implies that there exists no displacement discontinuity at the inclusion-matrix interface. In this case, our solution is reduced to Eshelby's solution for a perfectly bonded spherical inhomogeneity with a uniform eigenstrain.

When the inclusion and the matrix have the same elastic constants ($\mu^* = \mu$ and $\nu^* = \nu$), it can be shown that $k_{ij} = P_{ij} = Q_{ij} = M_{ij} = N_{ij} = 0$, which leads to $\epsilon_{ij}^{**} = 0$ and the present solution is identical to our earlier results (Zhong and Meguid, 1996).

As reported by Ghahremani (1980), Mura et al. (1985), and Hashin (1991), the stress inside the imperfectly bonded inclusion is nonuniform. This is confirmed by the present solution. In fact, our solution indicates that the stress inside the inclusion is nonuniform, except for two special cases, as described below.

The first case is when $e_{ij}^* = 0$ and $\epsilon_{ll}^* \neq 0$, which means that the real eigenstrain has only the bulk component. In this case, one observes that $P_{ij} = Q_{ij} = M_{ij} = N_{ij} = A_{ij} = B_{ij} = 0$ and

$$\epsilon_{ij}^{**} = a^2 k\delta_{ij} \tag{59}$$

$$b_i = a^2\lambda x_i \tag{60}$$

which leads to a uniform stress field inside the inclusion. This result also indicates that the bulk component of the eigenstrain only causes a normal separation (without a sliding) of the interface.

The second case is when $\alpha = \beta$. In this case, one can show that $Q_{ij} = M_{ij} = N_{ij} = B_{ij} = 0$ and

$$\epsilon_{ij}^{**} = a^2 k\delta_{ij} + a^2 P_{ij} \tag{61}$$

$$b_i = a^2\lambda x_i + a^2 A_{ij}x_j \tag{62}$$

which leads to a uniform stress distribution inside the inclusion.

Figure 3 shows the variation of the normalized elastic strain energy $W/\mu(\epsilon^*)^2V_\Omega$ with shear moduli ratio μ^*/μ, when the eigenstrain ϵ_{ij}^* has only one nonzero component, $\epsilon_{11}^* = \epsilon^* \neq 0$, under different interfacial compliances α_0 and β_0. The results indicate that the elastic strain energy increases with increasing shear moduli ratio μ^*/μ. The results also show that the imperfectly bonded interface releases the elastic strain energy, which decreases with the increase of interfacial compliances α or β. For the case where sliding is accompanied by comparable normal separation ($\beta_0 \neq 0$), the elastic strain energy decreases considerably in comparison with the pure sliding case ($\beta = 0$).

6 Concluding Remarks

An *exact* solution is obtained for the elastic field of a spherical inclusion with an imperfectly bonded interface under remote uniform loading. The imperfectly bonded interface is modeled by a

Downloaded 04 May 2010 to 171.66.16.27. Redistribution subject to ASME license or copyright; see http://www.asme.org/terms/Terms_Use.cfm

linear spring-layer of vanishing thickness with both the tangential and the normal displacement discontinuities being considered. The elastic field induced by the uniform eigenstrain given in the imperfectly bonded inclusion is decomposed into three parts: The first part is attributed to the uniform eigenstrain prescribed in a perfectly bonded spherical inclusion; the second is formulated in terms of an equivalent nonuniform eigenstrain distributed over a perfectly bonded spherical inclusion which models the material mismatch between the inclusion and the matrix; and the third is obtained in terms of an imaginary Somigliana dislocation field which models the interfacial sliding and normal separation. The exact form of the equivalent nonuniform eigenstrain and the imaginary Somigliana dislocation are fully determined using the equivalent inclusion method and the associated interfacial conditions. The elastic fields are then obtained explicitly by means of the superposition principle. The resulting solution is then used to evaluate the average Eshelby tensor and the elastic strain energy.

Acknowledgments

This work was supported by the Natural Sciences and Engineering Research Council of Canada (NSERC), Ontario Centre for Materials Research (OCMR), and ALCOA Foundation of the USA. Partial support of Dr. Z. Zhong has also been provided by the National Natural Science Foundation of China.

References

Asaro, R. J., and Barnett, D. M., 1975, "The Non-uniform Transformation Strain Problem for an Anisotropic Ellipsoidal Inclusion," *J. Mech. Phys. Solids,* Vol. 23, pp. 77–83.

Benveniste, Y., 1985, "The Effect Mechanical Behavior of Composite Materials with Imperfect Contact between the Constituents," *Mechanics of Materials,* Vol. 4, pp. 197–208.

Eshelby, J. D., 1957, "The Determination of the Elastic Field of an Ellipsoidal Inclusion and Related Problems," *Proc. Roy. Soc., London,* Vol. A241, pp. 376–396.

Gao, Z., 1995, "A Circular Inclusion With Imperfect Interface: Eshelby's Tensor and Related Problems," ASME JOURNAL OF APPLIED MECHANICS, Vol. 62, pp. 860–866.

Ghahremani, F., 1980, "Effect of Grain Boundary Sliding on Anelasticity of Polycrystals," *Int. J. Solids Struc.,* Vol. 16, pp. 825–845.

Hashin, Z., 1991, "The Spherical Inclusion With Imperfect Interface," ASME JOURNAL OF APPLIED MECHANICS, Vol. 58, pp. 444–449.

Huang, J. H., 1995, "Elastic Fields in Polycrystalline or Composite Materials With Slip Inclusion," *Int. J. Engng. Sci.,* Vol. 33, pp. 1303–1313.

Jasiuk, I., Tsuchida, E., and Mura, T., 1987, "The Sliding Inclusion under Shear," *Int. J. Solids Struc.,* Vol. 23, pp. 1373–1385.

Mura, T., and Furuhashi, R., 1984, "The Elastic Inclusion with a Sliding Interface," ASME JOURNAL OF APPLIED MECHANICS, Vol. 51, pp. 308–310.

Mura, T., Jasiuk, I., and Tsuchida, B., 1985, "The Stress Field of a Sliding Inclusion," *Int. J. Solids Struc.,* Vol. 21, pp. 1165–1179.

Mura, T., 1987, *Micromechanics of Defects in Solids,* 2nd Rev. Ed., Martinus Nijhoff, Dordrecht, The Netherlands.

Nemat-Nasser, S., and Hori, M., 1993, *Micromechanics: Overall Properties of Heterogeneous Materials,* North-Holland, Amsterdam.

Qu, J., 1993, "The Effect of Slightly Weakened Interfaces on the Overall Elastic Properties of Composite Materials," *Mechanics of Materials,* Vol. 14, pp. 269–281.

Shibata, S., Jasiuk, I., Mori, T., and Mura, T., 1990, "Successive Iteration Method Applied to Composites Containing Sliding Inclusions: Effective Modulus and Anelasticity," *Mechanics of Materials,* Vol. 9, pp. 229–243.

Zhong, Z., and Meguid, S. A., 1996, "On the Eigenstrain Problem of a Spherical Inclusion with an Imperfectly Bonded Interface," ASME JOURNAL OF APPLIED MECHANICS, Vol. 63, pp. 877–883.

APPENDIX A

Proof of Uniqueness of Solution

Assume that there are two solutions for displacements u_i^1 and u_i^2, with σ_{ij}^1 and σ_{ij}^2 being the corresponding stresses. Assuming that $\Delta u_i = u_i^1 - u_i^2$ and $\Delta\sigma_{ij} = \sigma_{ij}^1 - \sigma_{ij}^2$, then

$$\Delta\sigma_{ij,j} = 0 \quad \text{in} \quad D \tag{A1}$$

$$\Delta\sigma_{ij} = C_{ijkl}^{*}\Delta u_{k,l} \quad \text{in} \quad \Omega \tag{A2}$$

$$\Delta\sigma_{ij} = C_{ijkl}\Delta u_{k,l} \quad \text{in} \quad D - \Omega \tag{A3}$$

$$[\Delta\sigma_{ij}]n_j = 0 \quad \text{on} \quad \partial\Omega \tag{A4}$$

$$[\Delta u_i] = R_{ij}(\Delta T_k) \quad \text{on} \quad \partial\Omega \tag{A5}$$

and $\Delta u_i = 0$ at infinity. Let us introduce a positive quantity such that

$$I = \int_{\Omega} \Delta\sigma_{ij}\Delta u_{i,j}dV + \int_{D-\Omega} \Delta\sigma_{ij}\Delta u_{i,j}dV \geq 0. \tag{A6}$$

If I is transformed using Gauss' theorem to surface integrals, we can show that

$$I = -\int_{\partial\Omega} R_{ij}(\Delta T_i)(\Delta T_j)dS \leq 0, \tag{A7}$$

since R_{ij} is a positive definite symmetric tensor. Combining (A6) and (A7), we have $I = 0$, and conclude that $\sigma_{ij}^1 = \sigma_{ij}^2$. Moreover, if the impotent terms related to the rigid-body translation and rotation are excluded, we also have $u_i^1 = u_i^2$.

APPENDIX B

The Displacement and Stress Fields in the Matrix for Subproblem II

$$\begin{aligned} u_i^{II} = {} & \frac{1+\nu}{3(1-\nu)}ka^5\frac{x_i}{|\mathbf{x}|^3} + \frac{a^5}{3(1-\nu)}\left[\frac{1-2\nu}{|\mathbf{x}|^3} + \frac{3a^2}{5|\mathbf{x}|^5}\right]P_{il}x_l \\ & + \frac{a^5}{2(1-\nu)}\left(\frac{1}{|\mathbf{x}|^5} - \frac{a^2}{|\mathbf{x}|^7}\right)P_{kl}x_kx_lx_i \\ & + \frac{2a^5}{5(1-\nu)}\left[\frac{1-2\nu}{3|\mathbf{x}|^3} + \frac{a^2}{7|\mathbf{x}|^5}\right]Q_{il}x_l \\ & + \frac{a^5}{1-\nu}\left(\frac{1}{5|\mathbf{x}|^5} - \frac{a^2}{7|\mathbf{x}|^7}\right)Q_{kl}x_kx_lx_i \\ & - \frac{2(1+\nu)a^7}{35(1-\nu)|\mathbf{x}|^5}M_{il}x_l + \frac{(1+\nu)a^7}{7(1-\nu)|\mathbf{x}|^7}M_{kl}x_kx_lx_i \\ & + \frac{a^5}{1-\nu}\left[\frac{1-2\nu}{5|\mathbf{x}|^3} + \frac{a^2}{7|\mathbf{x}|^5}\right]N_{il}x_l \\ & + \frac{a^5}{2(1-\nu)}\left(\frac{3}{5|\mathbf{x}|^5} - \frac{5a^2}{7|\mathbf{x}|^7}\right)N_{kl}x_kx_lx_i \end{aligned} \tag{B1}$$

$$\begin{aligned} \sigma_{ij}^{II} = {} & \frac{2\mu(1+\nu)}{3(1-\nu)}ka^5\left(\frac{\delta_{ij}}{|\mathbf{x}|^3} - \frac{3x_ix_j}{|\mathbf{x}|^5}\right) \\ & + \frac{2\mu a^5}{3(1-\nu)}\left[\frac{1-2\nu}{|\mathbf{x}|^3} + \frac{3a^2}{5|\mathbf{x}|^5}\right]P_{ij} \\ & + \frac{4\mu a^5}{5(1-\nu)}\left[\frac{1-2\nu}{3|\mathbf{x}|^3} + \frac{3a^2}{7|\mathbf{x}|^5}\right]Q_{ij} \\ & - \frac{4\mu(1+\nu)a^7}{35(1-\nu)|\mathbf{x}|^5}M_{ij} + \frac{2\mu a^5}{1-\nu}\left[\frac{1-2\nu}{5|\mathbf{x}|^3} + \frac{3a^2}{7|\mathbf{x}|^5}\right]N_{ij} \\ & + \frac{\mu a^5}{1-\nu}\left[\frac{1-2\nu}{|\mathbf{x}|^5} - \frac{a^2}{|\mathbf{x}|^7}\right]P_{kl}x_kx_l\delta_{ij} \\ & - \frac{\mu a^5}{1-\nu}\left[\frac{5}{|\mathbf{x}|^7} - \frac{7a^2}{|\mathbf{x}|^9}\right]P_{kl}x_kx_lx_ix_j \\ & + \frac{2\mu a^5}{1-\nu}\left[\frac{1-2\nu}{5|\mathbf{x}|^5} - \frac{a^2}{7|\mathbf{x}|^7}\right]Q_{kl}x_kx_l\delta_{ij} \\ & - \frac{2\mu a^5}{1-\nu}\left[\frac{1}{|\mathbf{x}|^7} - \frac{a^2}{|\mathbf{x}|^9}\right]Q_{kl}x_kx_lx_ix_j \\ & + \frac{2\mu(1+\nu)a^7}{7(1-\nu)|\mathbf{x}|^7}M_{kl}x_kx_l\delta_{ij} - \frac{2\mu(1+\nu)a^7}{(1-\nu)|\mathbf{x}|^9}M_{kl}x_kx_lx_ix_j \end{aligned}$$

Downloaded 04 May 2010 to 171.66.16.27. Redistribution subject to ASME license or copyright; see http://www.asme.org/terms/Terms_Use.cfm

$$+\frac{\mu a^5}{1-\nu}\left[\frac{3(1-2\nu)}{5|\mathbf{x}|^5}-\frac{5a^2}{7|\mathbf{x}|^7}\right]N_{kl}x_kx_l\delta_{ij}$$

$$-\frac{\mu a^5}{1-\nu}\left[\frac{3}{|\mathbf{x}|^7}-\frac{5a^2}{|\mathbf{x}|^9}\right]N_{kl}x_kx_lx_ix_j$$

$$+\frac{2\mu a^5}{1-\nu}\left(\frac{\nu}{|\mathbf{x}|^5}-\frac{a^2}{|\mathbf{x}|^7}\right)(P_{il}x_lx_j+P_{jl}x_lx_i)$$

$$+\frac{4\mu a^5}{1-\nu}\left(\frac{\nu}{5|\mathbf{x}|^5}-\frac{a^2}{7|\mathbf{x}|^7}\right)(Q_{il}x_lx_j+Q_{jl}x_lx_i)$$

$$+\frac{4\mu(1+\nu)a^7}{7(1-\nu)|\mathbf{x}|^7}(M_{il}x_lx_j+M_{jl}x_lx_i)$$

$$+\frac{2\mu a^5}{1-\nu}\left(\frac{3\nu}{5|\mathbf{x}|^5}-\frac{5a^2}{7|\mathbf{x}|^7}\right)(N_{il}x_lx_j+N_{jl}x_lx_i) \quad \text{(B2)}$$

for point $\mathbf{x}$ outside Ω.

APPENDIX C

The Displacement and Stress Fields in the Matrix for Subproblem III

$$u_i^{III}=-\frac{(1+\nu)a^5}{3(1-\nu)}\lambda x_i\frac{1}{|\mathbf{x}|^3}$$

$$+\frac{a^5}{6(1-\nu)}\left[3a^2A_{kl}x_kx_lx_i\frac{1}{|\mathbf{x}|^7}-3A_{kl}x_kx_lx_i\frac{1}{|\mathbf{x}|^5}\right.$$

$$\left.-\frac{6a^2}{5}A_{il}x_l\frac{1}{|\mathbf{x}|^5}-2(1-2\nu)A_{il}x_l\frac{1}{|\mathbf{x}|^3}\right]$$

$$-\frac{a^5}{30(1-\nu)}\left[\frac{30\nu a^2}{7}B_{kl}x_kx_lx_i\frac{1}{|\mathbf{x}|^7}+6B_{kl}x_kx_lx_i\frac{1}{|\mathbf{x}|^5}\right.$$

$$\left.-\frac{12\nu a^2}{7}B_{il}x_l\frac{1}{|\mathbf{x}|^5}+4(1-2\nu)B_{il}x_l\frac{1}{|\mathbf{x}|^3}\right] \quad \text{(C1)}$$

$$\sigma_{ij}^{III}=-\frac{2\mu(1+\nu)a^5}{3(1-\nu)}\lambda\left(\frac{\delta_{ij}}{|\mathbf{x}|^3}-\frac{3x_ix_j}{|\mathbf{x}|^5}\right)$$

$$+\frac{\mu a^7}{1-\nu}\left[A_{kl}\frac{x_kx_l}{|\mathbf{x}|^7}\delta_{ij}+(A_{il}x_lx_j+A_{jl}x_lx_i)\frac{1}{|\mathbf{x}|^7}\right.$$

$$\left.-7A_{kl}\frac{x_kx_lx_ix_j}{|\mathbf{x}|^9}\right]-\frac{\mu a^5}{1-\nu}\left[(1-2\nu)A_{kl}\frac{x_kx_l}{|\mathbf{x}|^5}\delta_{ij}\right.$$

$$\left.+(A_{il}x_lx_j+A_{jl}x_lx_i)\frac{1}{|\mathbf{x}|^5}-5A_{kl}\frac{x_kx_lx_ix_j}{|\mathbf{x}|^7}\right]$$

$$-\frac{2\mu a^7}{5(1-\nu)}\left[A_{ij}\frac{1}{|\mathbf{x}|^5}-\frac{5}{2}(A_{il}x_lx_j+A_{jl}x_lx_i)\frac{1}{|\mathbf{x}|^7}\right]$$

$$-\frac{2\mu(1-2\nu)a^5}{3(1-\nu)}\left[A_{ij}\frac{1}{|\mathbf{x}|^3}-\frac{3}{2}(A_{il}x_lx_j+A_{jl}x_lx_i)\frac{1}{|\mathbf{x}|^5}\right]$$

$$-\frac{2\mu\nu a^7}{7(1-\nu)}\left[B_{kl}\frac{x_kx_l}{|\mathbf{x}|^7}\delta_{ij}+(B_{il}x_lx_j+B_{jl}x_lx_i)\frac{1}{|\mathbf{x}|^7}\right.$$

$$\left.-7B_{kl}\frac{x_kx_lx_ix_j}{|\mathbf{x}|^9}\right]-\frac{2\mu a^5}{5(1-\nu)}\left[(1-2\nu)B_{kl}\frac{x_kx_l}{|\mathbf{x}|^5}\delta_{ij}\right.$$

$$\left.+(B_{il}x_lx_j+B_{jl}x_lx_i)\frac{1}{|\mathbf{x}|^5}-5B_{kl}\frac{x_kx_lx_ix_j}{|\mathbf{x}|^7}\right]$$

$$+\frac{4\mu\nu a^7}{35(1-\nu)}\left[B_{ij}\frac{1}{|\mathbf{x}|^5}-\frac{5}{2}(B_{il}x_lx_j+B_{jl}x_lx_i)\frac{1}{|\mathbf{x}|^7}\right]$$

$$-\frac{4\mu(1-2\nu)a^5}{15(1-\nu)}\left[B_{ij}\frac{1}{|\mathbf{x}|^3}\right.$$

$$\left.-\frac{3}{2}(B_{il}x_lx_j+B_{jl}x_lx_i)\frac{1}{|\mathbf{x}|^5}\right] \quad \text{(C2)}$$

for point $\mathbf{x}$ outside Ω.

APPENDIX D

Expressions for Coefficients of Eqs. (37)–(44)

$$g_{11}=-\frac{2(1+\nu)}{3(1-\nu)}(\rho_1-3\rho_2)-1$$

$$g_{12}=\frac{2(1+\nu)}{3(1-\nu)}(\rho_1-3\rho_2)$$

$$g_{21}=\frac{2(1+\nu)}{3(1-\nu)}$$

$$g_{22}=-\frac{2(1+\nu)}{3(1-\nu)}-\frac{1}{2\beta_0}$$

$$h_{11}=\frac{(7-5\nu)}{15(1-\nu)}\rho_1+1$$

$$h_{12}=-h_{15}=\frac{(7-5\nu)}{15(1-\nu)}\rho_1$$

$$h_{13}=\frac{(1+\nu)}{5(1-\nu)}\rho_1$$

$$h_{16}=-\frac{2(5-\nu)}{15(1-\nu)}\rho_1$$

$$h_{22}=\frac{2(5-7\nu)}{35(1-\nu)}\rho_1+1$$

$$h_{23}=-\frac{2(1+\nu)}{7(1-\nu)}\rho_1$$

$$h_{24}=-\frac{2(5-7\nu)}{35(1-\nu)}\rho_1$$

$$h_{26}=\frac{24\nu}{35(1-\nu)}\rho_1$$

$$h_{32}=-h_{34}=\frac{2(1-7\nu)}{35(1-\nu)}\rho_1+\frac{2(1+\nu)}{5(1-\nu)}\rho_2$$

$$h_{33}=-\frac{6(1+\nu)}{7(1-\nu)}\rho_1+\frac{2(1+\nu)}{1-\nu}\rho_2-1$$

$$h_{36}=\frac{4(7+11\nu)}{35(1-\nu)}\rho_1-\frac{12(1+\nu)}{5(1-\nu)}\rho_2$$

$$h_{42}=\frac{(23-21\nu)}{35(1-\nu)}\rho_1$$

$$h_{43}=\frac{(1+\nu)}{7(1-\nu)}\rho_1$$

$$h_{44}=-\frac{(23-21\nu)}{35(1-\nu)}\rho_1-1$$

Downloaded 04 May 2010 to 171.66.16.27. Redistribution subject to ASME license or copyright; see http://www.asme.org/terms/Terms_Use.cfm

$$h_{46} = -\frac{4(7-4\nu)}{35(1-\nu)}\rho_1$$

$$h_{51} = h_{61} = \frac{7-5\nu}{15(1-\nu)}$$

$$h_{52} = \frac{2(17-7\nu)}{105(1-\nu)}$$

$$h_{53} = \frac{12(1+\nu)}{35(1-\nu)}$$

$$h_{54} = \frac{5-7\nu}{35(1-\nu)}$$

$$h_{55} = -\frac{7-5\nu}{15(1-\nu)} - \frac{1}{2\beta_0}$$

$$h_{56} = -\frac{2(35+11\nu)}{105(1-\nu)} - \frac{1}{2\beta_0}$$

$$h_{62} = \frac{2(5-7\nu)}{105(1-\nu)}$$

$$h_{63} = -\frac{8(1+\nu)}{35(1-\nu)}$$

$$h_{64} = \frac{13-7\nu}{35(1-\nu)}$$

$$h_{65} = -\frac{7-5\nu}{15(1-\nu)} - \frac{1}{2\alpha_0}$$

$$h_{66} = \frac{2(7+19\nu)}{105(1-\nu)}$$

with

$$\alpha_0 = \frac{\alpha\mu}{a}$$

$$\beta_0 = \frac{\beta\mu}{a}$$

$$\rho_1 = \frac{\mu}{\mu^*} - 1$$

$$\rho_2 = \frac{\mu\nu^*}{\mu^*(1+\nu^*)} - \frac{\nu}{1+\nu}.$$

Downloaded 04 May 2010 to 171.66.16.27. Redistribution subject to ASME license or copyright; see http://www.asme.org/terms/Terms_Use.cfm

An Analysis of Intersonic Crack Growth Under Shear Loading

A. Needleman
Division of Engineering,
Brown University,
Providence, RI 02912
Fellow ASME

Crack growth in a homogeneous elastic solid under impact shear loading conditions is analyzed numerically, with the crack constrained to grow along a weak plane directly ahead of the initial crack tip. The configuration analyzed is a plane-strain model of that used in the experiments of Rosakis et al. (1999). A cohesive surface constitutive relation is specified along the weak plane that relates the tractions and displacement jumps across it and that allows for the creation of new free surface. The resistance to crack initiation and the crack speed history are predicted without invoking any additional failure criterion. The effect of cohesive strength and impact pulse time on the response is explored. In a certain parameter regime, the calculations reproduce, at least qualitatively, the type of crack speed histories seen in the experiments. For other parameter values, an abrupt transition from crack growth at the Rayleigh wave speed to a value above $\sqrt{2}$ times the shear wave speed is seen. This transition involves microcrack nucleation ahead of the main crack. At intersonic crack speeds, shock-like gradients in the near-tip stress field are found as seen in the experiments.

1 Introduction

A fundamental question in dynamic fracture mechanics concerns the limit on attainable crack speeds. For remotely loaded cracks in homogeneous elastic solids, the energy flux into the crack tip vanishes as the crack speed increases to the Rayleigh wave speed of the material (see Freund, 1998). However, under tensile (mode I) loading conditions crack speeds rarely attain half the Rayleigh wave speed, with crack branching and attempted crack branching playing a major role in limiting the crack speed (see, e.g., Ravi-Chandar and Knauss (1984), Xu and Needleman (1994), and Sharon and Fineberg (1996, 1999)).

On the other hand, along bimaterial interfaces where any in-plane loading inherently results in mixed mode I and mode II (shear) conditions near the crack tip, intersonic crack speeds can be reached, where by intersonic is meant crack speeds between relevant shear wave and dilational wave speeds. For example, interface crack speeds that exceed the smaller of the two Rayleigh wave speeds have been observed in experiments, e.g., Liu et al. (1993), Lambros and Rosakis (1995), Singh and Shukla (1996) and Singh et al. (1997) and in numerical simulations, Xu and Needleman (1996) and Needleman and Rosakis (1999). Liu et al. (1995) obtained asymptotic crack-tip fields for an elastic-rigid bimaterial interface that predicted the existence of a shear "shock wave" discontinuity, that radiates from the crack tip and moves with it when the crack-tip speed exceeds the smaller shear wave speed. Evidence for shock-like gradients were seen in experiments (Singh and Shukla (1996) and Singh et al. (1997)) and numerical simulations (Xu and Needleman, 1996).

There have also been indications that intersonic crack speeds can be reached in homogeneous elastic solids under mode II loading conditions. Andrews (1976) carried out a numerical analysis of a dynamically propagating shear crack with a slip weakening cohesive zone ahead of the crack tip that gave rise to a terminal crack speed that was either less than the Rayleigh wave speed or somewhat greater than $\sqrt{2}c_s$, where c_s is the shear wave speed. The mechanism for attaining intersonic crack growth involved nucleation of a secondary zone of slip ahead of the main crack. The same transition mechanism was found by Abraham and Gao (1999) in their molecular dynamics calculations of mode II crack growth. Intersonic slip propagation was also seen in the computations of Johnson (1990).

Andrews (1976) emphasized that a spread out rupture front was necessary for achieving intersonic shear crack growth; a point rupture zone, as in classical fracture mechanics, would not allow for intersonic crack growth. Analytical investigations, for example by Burridge et al. (1979) and Broberg (1989, 1994), have also indicated that crack speeds above the material's shear wave speed should be possible under mode II loading conditions. In particular, Burridge et al. (1979) considered the stability of a mode II crack in an elastic solid with a slip weakening cohesive relation like that used in the numerical calculations of Andrews (1976). Burridge et al. (1979) considered possible crack speeds less than the dilational wave speed c_d and found that crack speeds less than the Rayleigh wave speed and crack speeds between $\sqrt{2}c_s$ and c_d were stable in that the applied load needs to increase with increasing crack speed. For values of the crack speed between c_s and $\sqrt{2}c_s$, crack growth was unstable in that a decreasing load would be associated with an increase in crack speed. Indirect experimental observation of an intersonic shear rupture in a crustal earthquake has been reported by Archuleta (1982). Nevertheless, direct experimental evidence for intersonic crack growth in homogeneous elastic solids subject to remote loading was lacking until the work of Rosakis et al. (1999).

Rosakis et al. (1999) introduced a weak plane directly ahead of a notch tip by bonding two pieces of Homalite together and the specimen was subject to mode II type loading. Thus, while the material properties are homogeneous, there is a well-defined fracture plane so that straight ahead crack growth occurs. The crack-tip speeds were determined and, using dynamic photoelasticity, the crack-tip stress field was observed. Crack speeds between $\sqrt{2}c_s$ and c_d were seen. The photoelastic fringe patterns were consistent with near-tip shock-like gradients.

In this investigation, a plane-strain model of the configuration used in the experiments of Rosakis et al. (1999) is analyzed using the cohesive surface decohesion formulation in Needleman (1987) and Xu and Needleman (1994). Within this framework, the continuum is characterized by two constitutive relations; one that relates stress and deformation in the bulk material, the other that relates the traction and displacement jump across a cohesive surface. The parameters characterizing

Contributed by the Applied Mechanics Division of THE AMERICAN SOCIETY OF MECHANICAL ENGINEERS for publication in the ASME JOURNAL OF APPLIED MECHANICS.
Discussion on the paper should be addressed to the Technical Editor, Professor Lewis T. Wheeler, Department of Mechanical Engineering, University of Houston, Houston, TX 77204-4792, and will be accepted until four months after final publication of the paper itself in the ASME JOURNAL OF APPLIED MECHANICS.
Manuscript received by the ASME Applied Mechanics Division, July 19, 1999; final revision, Aug. 9, 1999. Associate Technical Editor: L. T. Wheeler.

 Copyright © 1999 by ASME

Downloaded 04 May 2010 to 171.66.16.27. Redistribution subject to ASME license or copyright; see http://www.asme.org/terms/Terms_Use.cfm

the cohesive surface separation law include a strength and the work of separation per unit area so that a characteristic length enters the formulation. These constitutive relations together with appropriate balance laws and initial and boundary conditions completely specify the initial boundary value problem. Crack initiation and the crack speed history are natural outcomes of the analysis without any additional assumptions concerning crack initiation or crack growth criteria.

2 Formulation and Numerical Method

The same formulation and numerical solution procedure as in Needleman and Rosakis (1999) is used; only the location and duration of the impact loading differ here. A finite strain Lagrangian formulation is used, with the initial undeformed configuration taken as reference, so that all field quantities are considered to be functions of convected coordinates, y^i, which serve as particle labels, and time t. The principle of virtual work is written as

$$\int_V \mathbf{S} : \delta\mathbf{E} dV - \int_{S_{\text{int}}} \mathbf{T} \cdot \delta\boldsymbol{\Delta} dS = \int_{S_{\text{ext}}} \mathbf{T} \cdot \delta\mathbf{u} dS - \int_V \rho \frac{\partial^2 \mathbf{u}}{\partial t^2} \cdot \delta\mathbf{u} dV \quad (1)$$

where $\mathbf{S}$ is the second Piola-Kirchhoff stress tensor, $\mathbf{u}$ is the displacement vector, $\boldsymbol{\Delta}$ is the displacement jump across the cohesive surface, $\mathbf{A} : \mathbf{B}$ denotes $A^{ij}B_{ji}$, and V, S_{ext} and S_{int} are the volume, external surface area and internal cohesive surface area, respectively, of the body in the reference configuration. The density of the material in the reference configuration is ρ, $\mathbf{T}$ is the traction vector and the Lagrangian strain, $\mathbf{E}$, is given by

$$\mathbf{E} = \tfrac{1}{2}(\mathbf{F}^T \cdot \mathbf{F} - \mathbf{I}), \quad \mathbf{F} = \frac{\partial \mathbf{u}}{\partial \mathbf{x}} + \mathbf{I} \quad (2)$$

with $\mathbf{I}$ the identity tensor and $\mathbf{x}$ denoting the position vector of a material point in the reference configuration.

Computations are carried out for the edge-cracked bimaterial specimen shown in Fig. 1, which is based on the experimental configuration used in Rosakis et al. (1999). One difference between the experimental configuration and that analyzed here is that in the experiments there was an initial notch, rather than a sharp crack. In the experiments, the initial notch opening prevents contact between opposite faces. In the computations, the opposite sides of the initial crack remain traction free, so that contact, if it occurs, has no effect on the subsequent response. However, crack initiation does depend on whether there is an initial notch or an initial crack. The specimen has height $L = 300$ mm, width $w = 125$ mm and a crack of length $a_i = 25$ mm (see Fig. 1). Plane-strain conditions are assumed and a Cartesian coordinate system is used as reference, with the y^1–y^2 plane as the plane of deformation. The origin of the coordinate system is at the initial crack tip.

At $t = 0$, the body is stress free and at rest. A normal velocity is prescribed on the edge $y^1 = -a_i$, along the interval $-b \le y^2 \le 0$, with $b = 50$ mm, and with the shear traction taken to vanish there. The remaining external surfaces of the specimen are traction free. Hence, the boundary conditions are

$$T^1 = 0, \quad T^2 = 0 \quad \text{on } y^2 = 0 \text{ and } y^1 < 0 \quad (3)$$

$$T^1 = 0, \quad T^2 = 0 \quad \text{on } y^2 = \pm L/2, \; y^1 = -a_i \quad (4)$$

$$T^1 = 0, \quad T^2 = 0$$

$$\text{on } y^1 = -a_i \text{ where } y^2 > 0 \text{ or } y^2 < -b \quad (5)$$

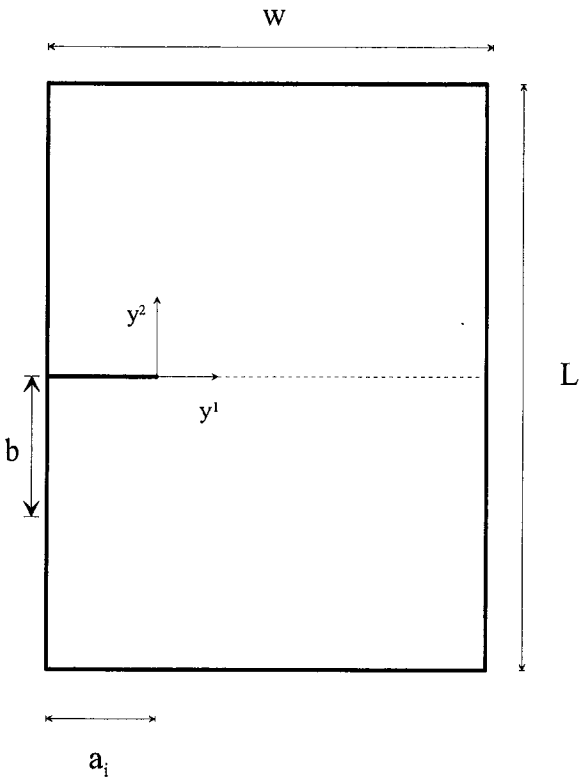


Fig. 1 Geometry of the specimen

$$u^1 = -\int V(t) dt, \quad T^2 = 0$$

$$\text{on } y^1 = -a_i \text{ and } -b \le y^2 \le 0 \quad (6)$$

where in (6)

$$V(t) = \begin{cases} V_1 t/t_r, & \text{for } 0 \le t < t_r; \\ V_1, & \text{for } t_r \le t \le t_p \\ V_1[1 - (t - t_p)/t_s], & \text{for } t_p < t < (t_p + t_s) \\ 0, & \text{for } t \ge (t_p + t_s). \end{cases} \quad (7)$$

Here, t_r is the rise time, t_p is the pulse time, and t_s is the step down time. In the calculations $V_1 = 26$ m/s and t_r and t_s are taken to be 0.1 μs. The pulse time is varied.

The continuum is characterized by two constitutive relations; a volumetric constitutive law that relates stress and strain, and a cohesive surface constitutive relation between the tractions and displacement jumps across a single cohesive surfaces that lies along the line $y^2 = 0$ in front of the initial crack.

The volumetric constitutive law for each material is taken to be that for an isotropic hyperelastic solid so that

$$\mathbf{S} = \frac{\partial W}{\partial \mathbf{E}}, \quad W = \tfrac{1}{2}\mathbf{E} : \mathbf{L} : \mathbf{E} \quad (8)$$

Here, W is the strain energy density and $\mathbf{L}$ is the tensor of isotropic elastic moduli with two elastic constants, Young's modulus E and Poisson's ratio ν. Although a finite strain formulation is used, the strains remain small enough nearly everywhere for the linear elastic idealization to be appropriate. The material parameters are taken to be representative of Homalite as given in Rosakis et al. (1999), so that $E = 5.3$ GPa, $\nu = 0.35$, and $\rho = 0.001246$ MPa/(m/s)^2.

Downloaded 04 May 2010 to 171.66.16.27. Redistribution subject to ASME license or copyright; see http://www.asme.org/terms/Terms_Use.cfm

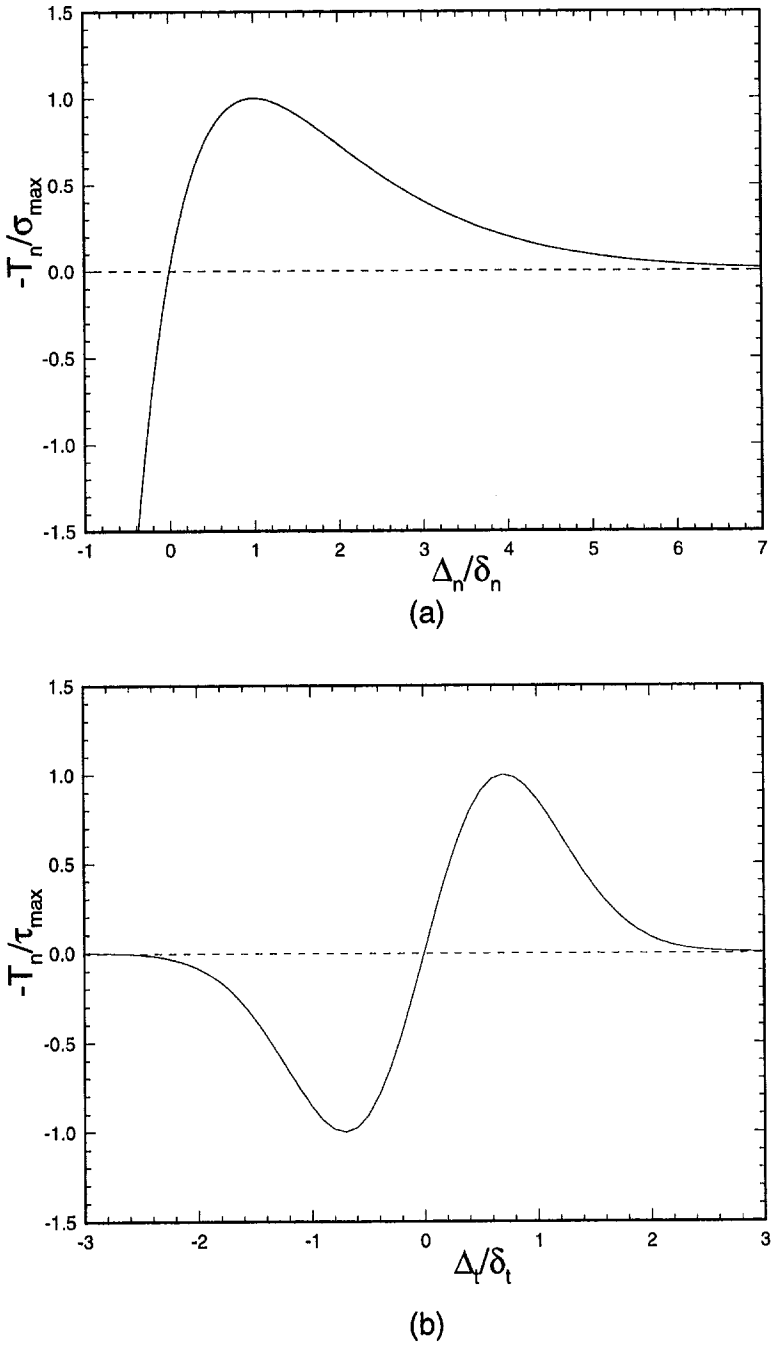


Fig. 2 (*a*) **Normal traction, T_n, across the cohesive surface as a function of Δ_n with $\Delta_t \equiv 0$.** (*b*) **Shear traction, T_t, across the cohesive surface as a function of Δ_t for $\Delta_n \equiv 0$.**

The speeds of dilatational, shear, and Rayleigh surface waves are given by (see, e.g., Freund, 1998)

$$c_d = \sqrt{\frac{E(1-\nu)}{\rho(1+\nu)(1-2\nu)}}, \quad c_s = \sqrt{\frac{E}{2\rho(1+\nu)}}, \quad c_R = c_s \frac{0.862 + 1.14\nu}{1+\nu}. \tag{9}$$

For Homalite, $c_d = 2613$ m/s, $c_s = 1255$ m/s, and $c_R = 1172$ m/s.

The cohesive surface constitutive relation used is that of Xu and Needleman (1993), which allows for tangential, as well as normal, decohesion. The normal and shear tractions are given by

$$T_n = -\frac{\phi_n}{\delta_n}\exp\left(-\frac{\Delta_n}{\delta_n}\right)\left\{\frac{\Delta_n}{\delta_n}\exp\left(-\frac{\Delta_t^2}{\delta_t^2}\right) + \frac{1-q}{r-1}\left[1-\exp\left(-\frac{\Delta_t^2}{\delta_t^2}\right)\right]\left[r-\frac{\Delta_n}{\delta_n}\right]\right\} \tag{10}$$

$$T_t = -\frac{\phi_n}{\delta_n}\left(2\frac{\delta_n}{\delta_t}\right)\frac{\Delta_t}{\delta_t}\left\{q+\left(\frac{r-q}{r-1}\right)\frac{\Delta_n}{\delta_n}\right\} \times \exp\left(-\frac{\Delta_n}{\delta_n}\right)\exp\left(-\frac{\Delta_t^2}{\delta_t^2}\right) \tag{11}$$

where $\Delta_n = \mathbf{n}\cdot\boldsymbol{\Delta}$, $\Delta_t = \mathbf{t}\cdot\boldsymbol{\Delta}$, $T_n = \mathbf{n}\cdot\mathbf{T}$ and $T_t = \mathbf{t}\cdot\mathbf{T}$ with $\mathbf{n}$ and $\mathbf{t}$ as the normal and tangent, respectively, to the surface at a

Downloaded 04 May 2010 to 171.66.16.27. Redistribution subject to ASME license or copyright; see http://www.asme.org/terms/Terms_Use.cfm

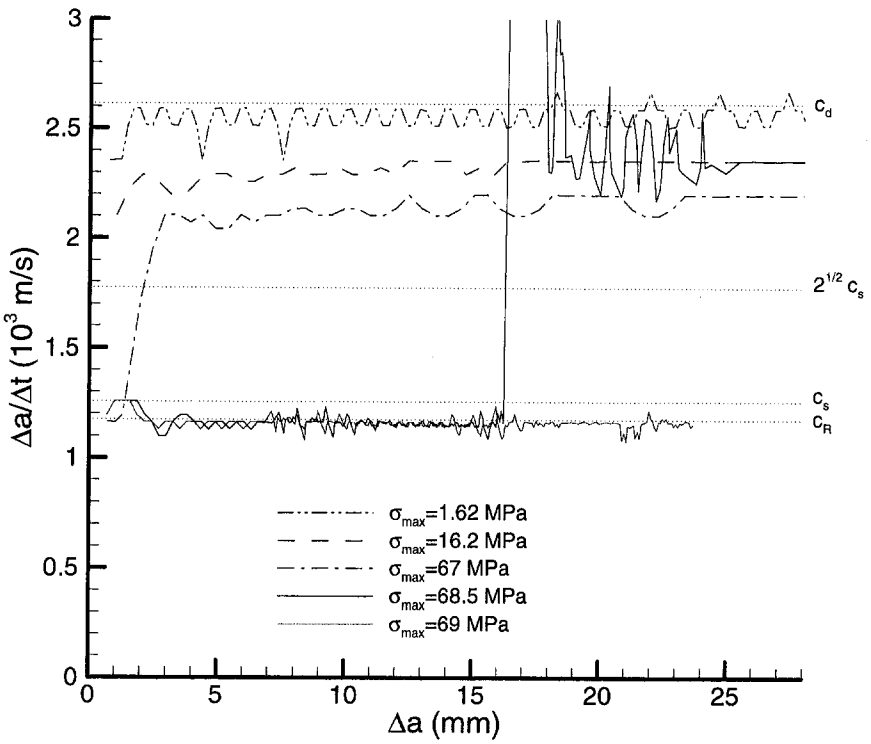


Fig. 3 Curves of crack speed, $\Delta a/\Delta t$ versus crack length, Δa, showing the effect of cohesive strength on the crack growth history. $\tau_{max} = \sigma_{max}$, $\delta_n = 0.4$ μm, $q = 0.9986$ and the pulse time $t_p = \infty$.

given point in the reference configuration. Also, $q = \phi_t/\phi_n$ and $r = \Delta_n^*/\delta_n$, where Δ_n^* is the value of Δ_n after complete shear separation with normal traction $T_n = 0$. The normal work of separation, ϕ_n, and the shear work of separation, ϕ_t, can be written as

$$\phi_n = e\sigma_{max}\delta_n \quad \phi_t = \sqrt{\frac{e}{2}}\,\tau_{max}\delta_t. \tag{12}$$

Here, $e = \exp(1)$, σ_{max} and τ_{max} are the cohesive surface normal strength and tangential strength, respectively, and δ_n and δ_t are corresponding characteristic lengths. The tractions in (10) and (11) are derived from a potential and the sign convention is that restoring tractions are positive.

The normal traction across the surface, T_n, as a function of Δ_n with $\Delta_t \equiv 0$ is shown in Fig. 2(*a*). The maximum value of $-T_n$ is σ_{max} and occurs when $\Delta_n = \delta_n$. The variation of shear traction T_t with Δ_t when $\Delta_n \equiv 0$ is shown in Fig. 2(*b*). The maximum value of $|T_t| = \tau_{max}$ is attained when $|\Delta_t| = \sqrt{2}\delta_t/2$.

The finite element discretization is based on linear displacement triangular elements that are arranged in a "crossed-triangle" quadrilateral pattern. The mesh used, which is the same as in Needleman and Rosakis (1999), has 61,312 quadrilateral elements and 247,424 degrees-of-freedom, with a uniform region in front of the initial crack of 400 × 8 rectangular quadrilateral elements. Each rectangle in the uniform region is 75 μm × 100 μm, and the mesh spacing is gradually increased in size out to the boundary. The equations of motion that result from substituting the finite element discretization into (1) are integrated numerically by an explicit integration procedure, the Newmark β-method with $\beta = 0$, Belytschko et al. (1976). A lumped mass matrix is used instead of the consistent mass matrix, since this has been found preferable for explicit time integration procedures, from the point of view of accuracy as well as computational efficiency (Krieg and Key, 1973).

3 Numerical Results

The weak plane is characterized by $\delta_n = 0.4$ μm and $r = 0$ in (10) and (11). Also, in all cases $\sigma_{max} = \tau_{max}$. The bond strength, $\sigma_{max} = \tau_{max}$, and the pulse time, t_p, are varied. In addition, two values of δ_t are used. In some calculations, δ_t is specified to be 0.9314 μm, giving $q = \phi_t/\phi_n = 0.9986$. In other calculations, the value of δ_t is computed so that $q = 1$ to machine precision. In many cases, this small difference is negligible, but in some cases it does make a noticeable difference in the results.

The main effect of the impact loading is a wave carrying a compressive stress S^{11} that reaches the crack tip at $t = 9.57$ μs. This wave reaches the free surface $y^1 = w = 125$ mm at $t = 47.9$ μs. The computations are terminated somewhat before the crack has grown to the end of the uniform mesh region. In all calculations here this occurs at or before $t = 37$ μs. Since the loading wave has not even reached the rear surface, the computations obviously terminate before any reflected wave from the rear surface reaches the crack tip. This contrasts, with the situation modeled in Needleman and Rosakis (1999), where waves reflected from the opposite surface can play a significant role in the crack growth history.

Figure 3 shows the crack speed, $\Delta a/\Delta t$, as a function of the amount of crack growth, Δa, for various values of the cohesive strength $\sigma_{max} = \tau_{max}$. With $\sigma_{max} = \tau_{max} = 69$ MPa, the work of separation is 75.0 J/m^2 and the work of separation scales linearly with σ_{max}. The first step in computing $\Delta a/\Delta t$ is to record the crack location, which is defined by the position of the furthest node from the initial crack tip ($y^1 = 0$) where Δ_t is greater than or equal to $5\delta_t$. This gives Δa at various times and the crack speed is computed from this data by successive five point least squares linear fits; i.e., through points 1 to 5, points 2 to 6, etc. The crack speed is plotted against Δa rather than against time t, because that is the way the experimental results are presented in Rosakis et al. (1999).

In Fig. 3, $q = 0.9986$ and t_p is such that $V(t) = V_1$ for all $t > t_r$, which will be denoted as $t_p = \infty$. For a cohesive strength of 69 MPa, the crack propagates at the Rayleigh wave speed. When the

Downloaded 04 May 2010 to 171.66.16.27. Redistribution subject to ASME license or copyright; see http://www.asme.org/terms/Terms_Use.cfm

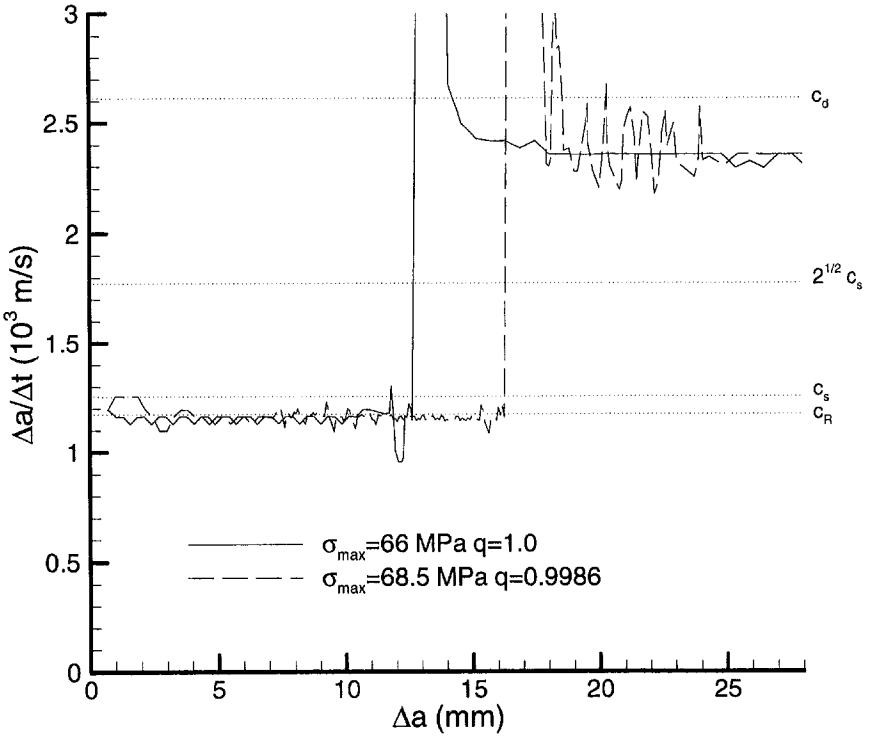


Fig. 4 Curves of crack speed, $\Delta a/\Delta t$ versus crack length, Δa for two sets of parameters where a transition occurs from crack growth at the Rayleigh wave speed to intersonic crack growth. $\tau_{max} = \sigma_{max}$, $\delta_n = 0.4$ μm and the pulse time $t_p = \infty$.

cohesive strength is reduced to 67 MPa, the crack quickly accelerates to an intersonic speed. Decreasing the cohesive strength further results in a crack speed that increases somewhat with decreasing cohesive strength and for a cohesive strength of 1.62 MPa, the crack speed is only slightly less than c_d. The crack growth history with $\sigma_{max} = \tau_{max} = 68.5$ MPa shows a transition case. The crack propagates for a while at the Rayleigh wave speed c_R. Then there is an abrupt transition during which the crack speed appears to exceed c_d. This, of course, does not actually occur. What happens is that a microcrack nucleates ahead of the main

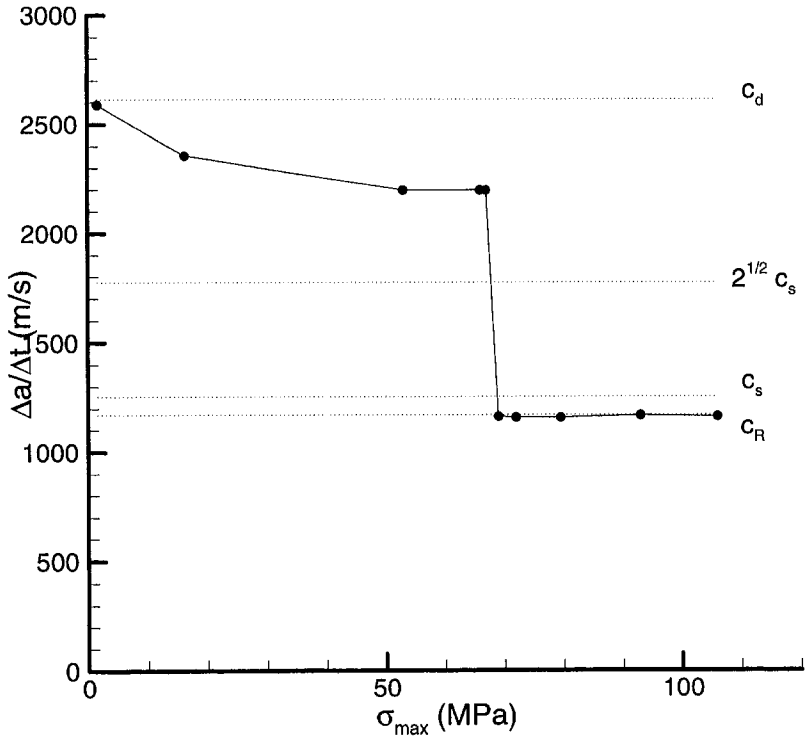


Fig. 5 Nominal crack speed versus cohesive strength. $\tau_{max} = \sigma_{max}$, $\delta_n = 0.4$ μm, $q = 0.9986$ and the pulse time $t_p = \infty$.

Downloaded 04 May 2010 to 171.66.16.27. Redistribution subject to ASME license or copyright; see http://www.asme.org/terms/Terms_Use.cfm

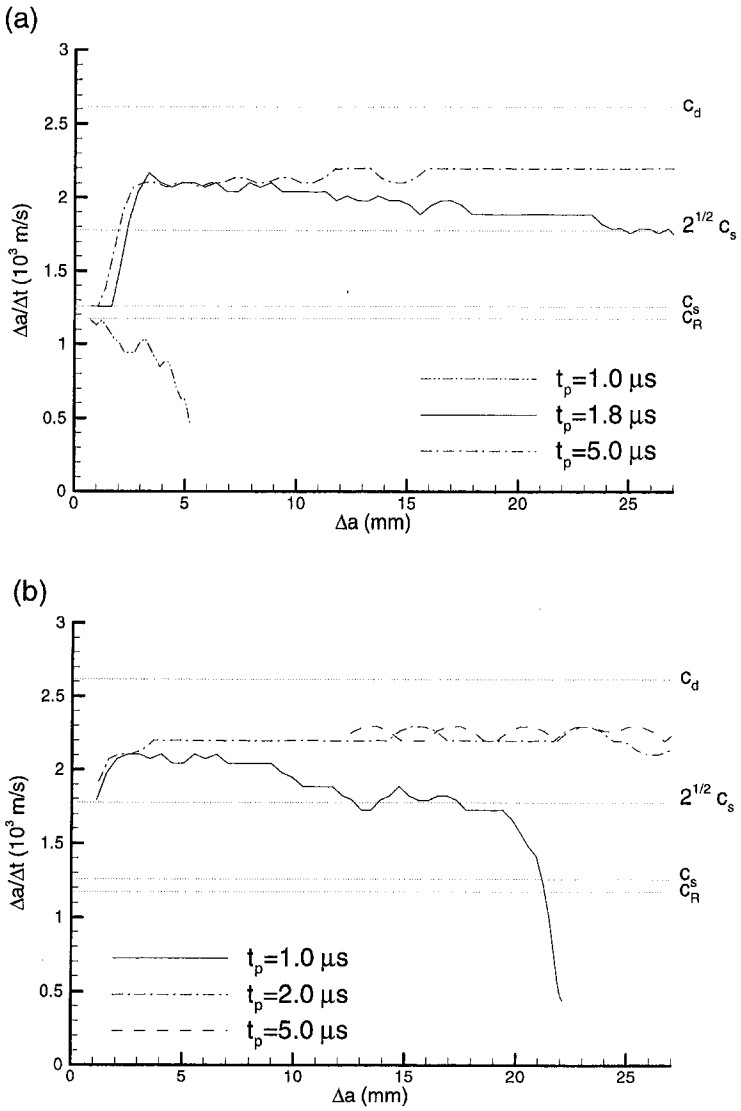


Fig. 6 Curves of crack speed, $\Delta a/\Delta t$ versus crack length, Δa, showing the effect of pulse time on the crack growth history. δ_n = 0.4 μm and q = 1. (*a*) $\tau_{max} = \sigma_{max}$ = 60 MPa. (*b*) $\tau_{max} = \sigma_{max}$ = 30 MPa.

crack. This microcrack then propagates intersonically. This mechanism of microcrack nucleation providing the transition between subsonic crack speeds and intersonic crack speeds has also been seen in the calculations of Andrews (1976), Needleman and Rosakis (1999), and Abraham and Gao (1999).

Since microcrack nucleation mediates the transition, it is not surprising that the value of cohesive strength at which it occurs and the time when it occurs are very sensitive to the details of the cohesive characterization. This is seen in Fig. 4 where the crack speed histories for $\sigma_{max} = \tau_{max} = 68.5$ MPa with $q = 0.9986$ and $\sigma_{max} = \tau_{max} = 66$ MPa with $q = 1$ are compared. The fact that the transition occurs at different times in these two cases indicates that the transition time is not set by the arrival of an elastic wave, as it was in Needleman and Rosakis (1999).

In Fig. 5, the nominal crack speed (after the initial crack acceleration) is plotted against cohesive strength for the calculations where $q = 0.9986$. The sharp transition at $\sigma_{max} \approx 68.5$ MPa is seen. Cohesive strength values up to 106 MPa were considered and for all values considered greater than 69 MPa, the crack speed is about c_R. Clearly, for a high enough cohesive strength crack growth will not initiate during the initial loading wave with $V_1 = 26$ m/s.

The effect of pulse time is explored in Fig. 6. In these calculations, $q = 1$ and in Fig. 6(a), $\sigma_{max} = 60$ MPa, while in Fig. 6(b), $\sigma_{max} = 30$ MPa. For $t_p = 5$ μs in Fig. 6(a), the crack speed increases to a more or less constant value of $\approx$ 2200 m/s, pretty much as when $t_p = \infty$. With $t_p = 1.8$ μs, the crack speed reaches a maximum and then decreases to a value of about $\sqrt{2}c_s$ (1775 m/s for Homalite), which is the trend seen in the experiments of Rosakis et al. (1999). When the pulse time is reduced to $t_p = 1$ μs, the driving force for crack growth is less than required for much crack growth to occur at c_R. With the cohesive strength at 30 MPa, Fig. 6(b), the crack speed history is essentially identical for $t_p = 5$ μs and $t_p = 2$ μs. For $t_p = 1$ μs, the crack speed increases rapidly initially and then decreases to about $\sqrt{2}c_s$. When that speed can no longer be sustained, the crack speed drops quickly to less than c_R.

Figure 7 shows contours of the stress component S^{22} at $t = 21$ μs and $t = 22$ μs for the calculation with $\tau_{max} = \sigma_{max} = 64$ MPa, $q = 1$ and $t_p = \infty$. At $t = 21$ μs, the crack speed is 1155 m/s and the crack is at $\Delta a = 12.3$ mm. Under mode I loading conditions, S^{22} would be the opening stress, but here it is negative in the vicinity of the crack tip. At $t = 22$ μs, a microcrack has nucleated ahead of the main crack, at $\Delta a \approx 15$ mm, and the apparent crack speed is now about 2500 m/s ($2c_s$). It is because of such micro-

Downloaded 04 May 2010 to 171.66.16.27. Redistribution subject to ASME license or copyright; see http://www.asme.org/terms/Terms_Use.cfm

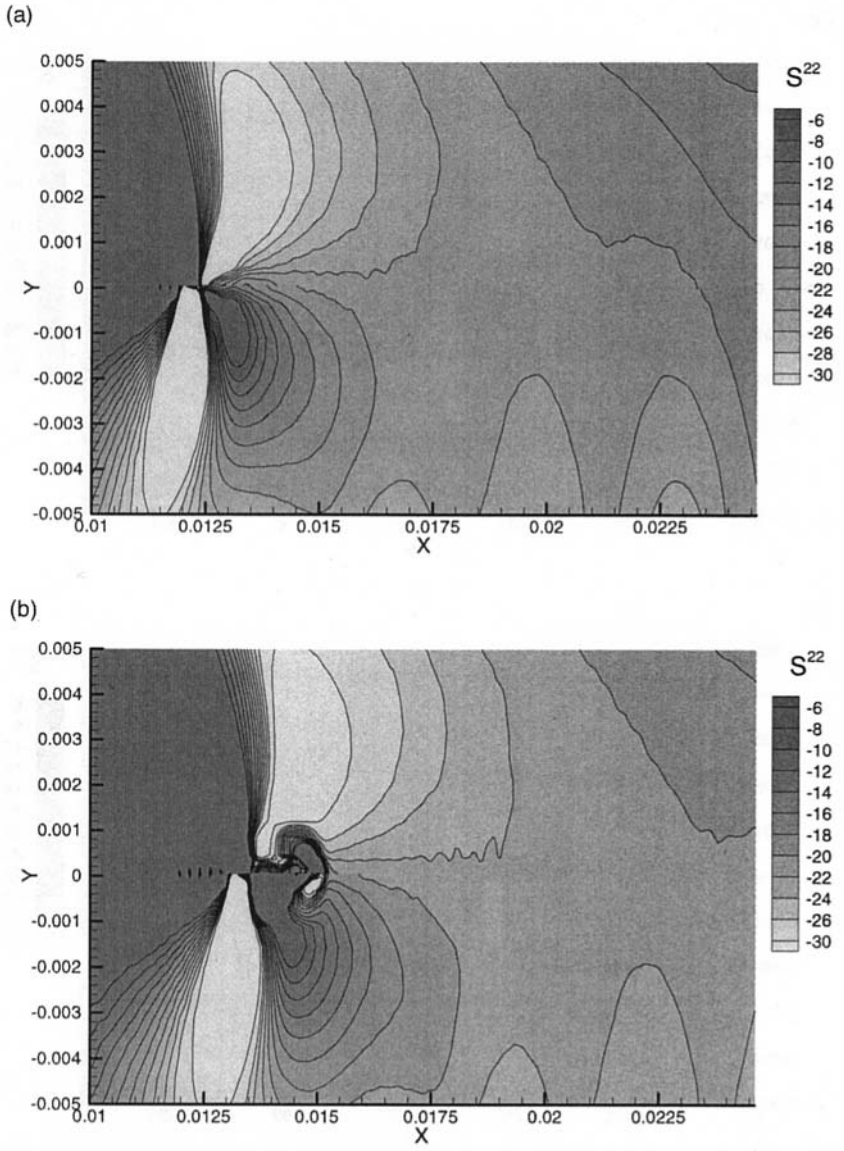


Fig. 7 Contours of the stress component S^{22} in the vicinity of the current crack tip for σ_{max} = 64 MPa, q = 1 and $t_p = \infty$. Stress values are in units of MPa and distances are in meters. (*a*) t = 21 μs. (*b*) t = 22 μs.

crack nucleation that the crack speed appears to jump in Figs. 3 and 4.

The S^{22} contours at two later times, $t = 23$ μs ($\Delta a = 17.4$ mm) and $t = 24$ μs ($\Delta a = 19.8$ mm) in Fig. 8, show the high gradients at the crack tip that are indicative of a shock-like field, although the numerical scheme used here cannot represent the abrupt jump associated with a shock. A well-defined shock front is seen in the calculations of Abraham and Gao (1999). The crack speed in Fig. 8 is in the range 2300–2400 m/s ($1.83c_s$ to $1.91c_s$), which would indicate a shock angle, given by $\sin^{-1}([c_s/\Delta a/\Delta t])$, of 32 deg–33 deg. From the contours in Fig. 8 this angle is about 34 deg–37 deg, which is not too different from what is expected based on the crack speed.

Figure 9 shows contours of S^{22} for $\tau_{max} = \sigma_{max} = 30$ MPa and $t_p = 1.0$ μs at $t = 15$ μs, where $\Delta a/\Delta t \approx 2000$ m/s ($1.59c_s$) and at $t = 20$ μs, where $\Delta a/\Delta t \approx \sqrt{2}c_s$. In Fig. 9(*a*), $\Delta a = 9.2$ mm while in Fig. 9(*b*) $\Delta a = 18.4$ mm. The decrease in the near-tip stress gradient at the lower crack speed is evident, but the angular structure of the shock-like field can still be seen. About 1 μs after the stage shown in Fig. 9(*b*), the crack speed drops abruptly and the crack then arrests.

Consider a crack tip moving along $y^2 = 0$ with instantaneous speed $\partial a/\partial t$ in the reference configuration in an elastic solid surrounded by a contour Γ that translates with the crack tip. Moving the development in Freund (1998) to the reference configuration gives the instantaneous rate of energy flow through a contour Γ with normal ν_j to the crack tip as

$$L(\Gamma) = -\frac{\partial a}{\partial t}\int_{\Gamma} P^j \nu_j ds \tag{13}$$

where

$$P^j = -\left[(W+T)\delta_1^j + \frac{1}{\partial a/\partial t}(\delta_k^j + u_{,k}^j)S^{ki}\frac{\partial u_i}{\partial t}\right] \tag{14}$$

with W the strain energy density in (8) and T the kinetic energy density given by

$$T = \frac{1}{2}\rho\frac{\partial u^i}{\partial t}\frac{\partial u_i}{\partial t}. \tag{15}$$

The sign in (14) is chosen so that the vector **P** pointing toward the crack tip corresponds to an energy flux into the crack tip.

Downloaded 04 May 2010 to 171.66.16.27. Redistribution subject to ASME license or copyright; see http://www.asme.org/terms/Terms_Use.cfm

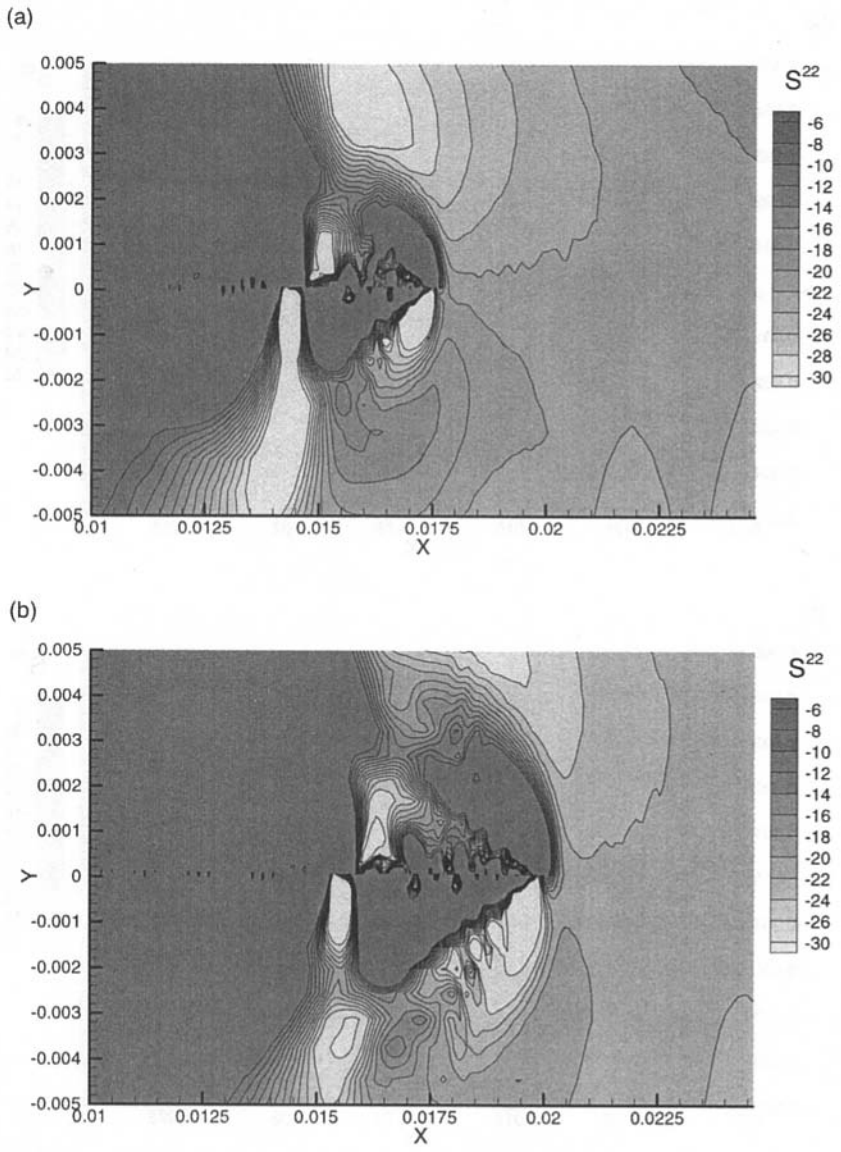


Fig. 8 Contours of the stress component S^{22} in the vicinity of the current crack tip for σ_{max} = 64 MPa, $q = 1$ and $t_p = \infty$. Stress values are in units of MPa and distances are in meters. (*a*) t = 23 μs. (*b*) t = 24 μs.

Figure 10 shows the orientation of the energy flux vector in the vicinity of the current crack tip for the calculation with $\tau_{max} = \sigma_{max} = 64$ MPa, $q = 1$ and $t_p = \infty$ at $t = 21$ μs and $t = 24$ μs. In this figure, all vectors are the same length so that the orientation, but not the magnitude, of P^j is indicated. Well in front of the crack tip the energy flux is from the lower half of the specimen ($y^2 < 0$) to the upper half ($y^2 > 0$). At $t = 21$ μs, the crack speed is approximately the Rayleigh wave speed and the energy flux near the crack tip is away from the crack tip region for $y^2 < 0$ and toward the crack tip region for $y^2 > 0$. In Fig. 10(*b*), where the crack speed is intersonic, the abrupt change in orientation of the energy flux vector along the shock is clearly seen. Here, the energy flux is toward the crack-tip region in front of the shock for both $y^2 < 0$ and $y^2 > 0$.

4 Concluding Remarks

Dynamic shear crack growth along a weak plane in an elastic solid has been analyzed using a cohesive surface framework where the crack growth history is a direct outcome of the analysis, determined by the cohesive properties of the bond line (mainly the strength and the work of separation), by the material properties and by the imposed loading. A material length scale enters the formulation through the cohesive surface characteristic length. The main features of the experimental observations of Rosakis et al. (1999) emerge from the calculations.

In addition, the parameter dependence of the response was explored by varying the cohesive strength of the bond and the pulse time, with all other material, geometric, and loading parameters kept fixed. For a sufficiently low value of the cohesive strength and a sufficiently long pulse time, the crack speed rapidly rises to a value between $\sqrt{2}c_s$ and c_d (wave speeds are defined in (9)) that decreases with increasing cohesive strength. The crack speed then remains more or less constant. Hence, with a fixed impact velocity, the amount of energy that needs to be expended for decohesion of the bond line appears significant in setting the attainable crack speed. The calculations in Fig. 3 suggest that the attainable crack speed approaches c_d in the limit of vanishing cohesive strength so that the dilational wave speed serves as the upper limit of possible crack speeds in the situation modeled here. It remains to be seen whether or not there is some criterion involving, say, maximization of energy flux into the decohesion region or minimization of energy radiated away from it, that serves to set the crack speed.

Downloaded 04 May 2010 to 171.66.16.27. Redistribution subject to ASME license or copyright; see http://www.asme.org/terms/Terms_Use.cfm

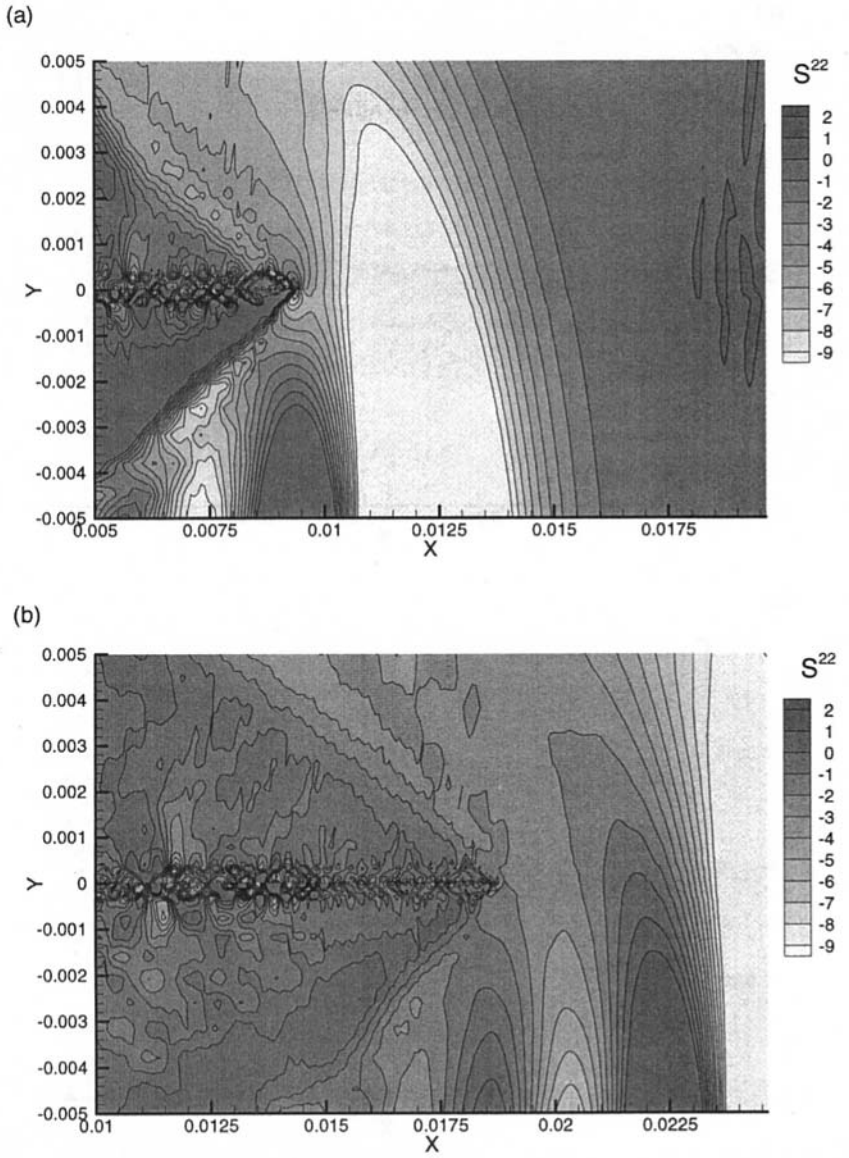


Fig. 9 Contours of the stress component S^{22} in the vicinity of the current crack tip for σ_{max} = 30 MPa, q = 1 and t_p = 1.0 μs. Stress values are in units of MPa and distances are in meters. (*a*) t = 15 μs. (*b*) t = 20 μs.

For larger values of the cohesive strength, the crack speed is maintained at about c_R, at least for the amount of crack growth considered in the computations. For values of the cohesive strength between these two regimes, the crack speed jumps from c_R to a speed between $\sqrt{2}c_s$ and c_d (Fig. 5). The mechanism for this transition is the nucleation of a microcrack ahead of the main crack, as in the numerical studies of Andrews (1976) and Abraham and Gao (1999). The fact that the cohesive characterizations in Andrews (1976), Abraham and Gao (1999) and here are very different shows that the existence of the transition is independent of the details of the cohesive model. It is worth noting that while the Lennard-Jones potential used by Abraham and Gao (1999) gave rise to a significant asymmetric crack opening accompanying shearing, no such opening occurs with the cohesive description used in the present calculations, indicating that the crack opening does not play an essential role in the transition.

Calculations for slightly different cohesive characterizations give rise to the crack speed transition taking place at different times, Fig. 4, so that the transition appears to involve an inherent instability of a mode II crack running at c_R, rather than, for example, being the result of a reflected wave giving an additional impetus to the crack. As the crack propagates at c_R, the stress and deformation ahead of the crack intensify until the conditions for microcrack nucleation are met. When this occurs depends on the cohesive properties of the weak plane. This also suggests the possibility that a transition to intersonic crack speeds might occur with the higher values of cohesive strength used here if the computations were continued for sufficiently large amounts of crack growth.

The asymptotic elastic crack field gives a vanishing energy flux into the crack tip for crack speeds above the Rayleigh wave speed except at $\sqrt{2}c_s$, since there is a square root singularity for intersonic crack speeds only when $\partial a/\partial t = \sqrt{2}c_s$ (Burridge et al., 1979). The vector plot in Fig. 10(*b*) shows that there is an energy flux into the region directly ahead of the crack tip from both halves of the specimen when the shock-like intersonic field in Fig. 8 has formed. The finite extent of the region over which decohesion takes place is key in this regard.

Pulse times are found for which the crack speed increases rapidly to a value greater than $\sqrt{2}c_s$ and then decreases more or less gradually to about $\sqrt{2}c_s$ (the values of pulse time for which

Downloaded 04 May 2010 to 171.66.16.27. Redistribution subject to ASME license or copyright; see http://www.asme.org/terms/Terms_Use.cfm

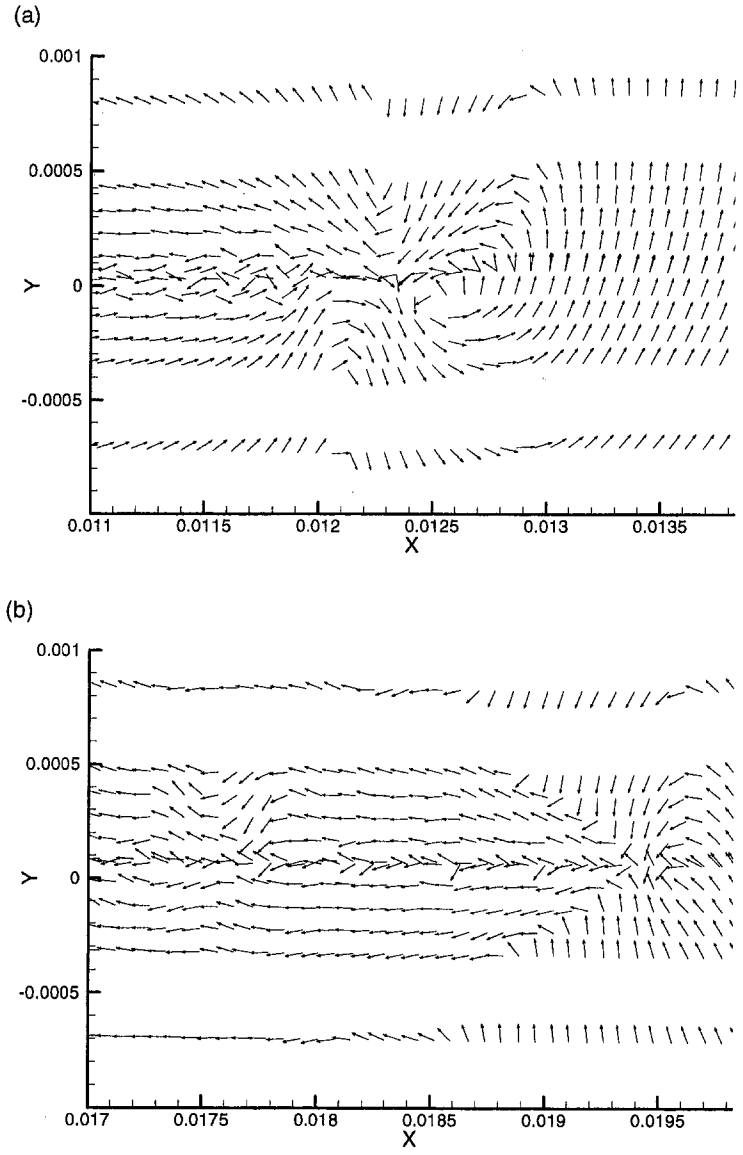


Fig. 10 The orientation of the energy flux vector P^j in (14) for σ_{max} = 64 MPa, q = 1 and $t_p = \infty$. Stress values are in units of MPa and distances are in meters. (*a*) t = 21 μs. (*b*) t = 24 μs.

this is the case depend on the cohesive strength). This is the sort of crack speed history seen in the experiments of Rosakis et al. (1999). Once the crack speed becomes significantly less than $\sqrt{2}c_s$, it decreases rapidly to below c_R, which is consistent with the conclusion of Burridge et al. (1979) that crack speeds between c_s and $\sqrt{2}c_s$ are unstable.

Acknowledgments

Support from Sandia Corporation through grant LG-3057 is gratefully acknowledged. I am indebted to Prof. A. J. Rosakis of Caltech for helpful discussions. The computations reported on here were carried out on the Cray T90 at the San Diego Supercomputer Center and at the Theoretical Physics Computing Facility at Brown University. My work on the energy flux into intersonic cracks in elastic solids began during my participation in the 1997 program "Quantitative Methods in Materials Research" at the Institute of Theoretical Physics, University of California, Santa Barbara. I am very grateful for the hospitality and intellectual stimulation I enjoyed during that visit.

References

Abraham, F. F., and Gao, H., 1999, "How Fast Can Cracks Propagate?" submitted for publication.

Andrews, D. J., 1976, "Rupture Velocity of Plane Strain Shear Cracks," *J. Geophys. Res.*, Vol. 81, pp. 5679–5687.

Archuleta, R. J., 1982, "Analysis of Near-Source Static and Dynamic Measurements From the 1979 Imperial Valley Earthquake," *Bull. Seismological Soc. Am.*, Vol. 72, pp. 1927–1956.

Belytschko, T., Chiapetta, R. L., and Bartel, H. D., 1976, "Efficient Large Scale Non-linear Transient Analysis by Finite Elements," *Int. J. Numer. Meth. Engr.*, Vol. 10, pp. 579–596.

Broberg, K. B., 1989, "The Near-Tip Field at High Crack Velocities," *Int. J. Fract.*, Vol. 39, pp. 1–13.

Broberg, K. B., 1994, "Intersonic Bilateral Slip," *Geophys. J. Int.*, Vol. 119, pp. 706–714.

Burridge, R., Conn, G., and Freund, L. B., 1979, "The Stability of a Rapid Mode II Shear Crack With Finite Cohesive Traction," *J. Geophys. Res.*, Vol. 85, pp. 2210–2222.

Freund, L. B., 1998, *Dynamic Fracture Mechanics*, Cambridge University Press, Cambridge, UK.

Johnson, E., 1990, "On the Initiation of Unidirectional Slip," *Geophys. J. Int.*, Vol. 101, pp. 125–132.

Krieg, R. O., and Key, S. W., 1973, "Transient Shell Response by Numerical Time Integration," *Int. J. Numer. Meths. Engrg.*, Vol. 7, pp. 273–286.

Lambros, J., and Rosakis, A. J., 1995c, "Shear Dominated Transonic Interfacial

Downloaded 04 May 2010 to 171.66.16.27. Redistribution subject to ASME license or copyright; see http://www.asme.org/terms/Terms_Use.cfm

Crack Growth in a Bimaterial—I. Experimental Observations," *J. Mech. Phys. Solids,* Vol. 43, pp. 169–188.

Liu, C., Huang, Y., and Rosakis, A. J., 1995, "Shear Dominated Transonic Interfacial Crack Growth in a Bimaterial—II. Asymptotic Fields and Favorable Velocity Regimes," *J. Mech. Phys. Solids,* Vol. 43, pp. 189–206.

Liu, C., Lambros, J., and Rosakis, A., 1993, "Highly Transient Elasto-Dynamic Crack Growth in a Bimaterial Interface: Higher Order Asymptotic Analysis and Optical Experiment," *J. Mech. Phys. Solids,* Vol. 41, pp. 1887–1954.

Needleman, A., 1987, "A Continuum Model for Void Nucleation by Inclusion Debonding," ASME JOURNAL OF APPLIED MECHANICS, Vol. 54, pp. 525–531.

Needleman, A., and Rosakis, A. J., 1999, "The Effect of Bond Strength and Loading Rate on the Conditions Governing the Attainment of Intersonic Crack Growth Along Interfaces," *J. Mech. Phys. Solids,* Vol. 47, pp. 2411–2449.

Ravi-Chandar, K., and Knauss, W. G., 1984, "An Experimental Investigation Into Dynamic Fracture: III." On Steady-State Crack Propagation and Crack Branching," *Int. J. Fract.,* Vol. 26, pp. 141–154.

Rosakis, A. J., Samudrala, O., and Coker, D., 1999, "Cracks Faster Than the Shear Wave Speed," *Science,* Vol. 284, pp. 1337–1340.

Sharon, E., and Fineberg, J., 1996, "Microbranching Instability and the Dynamic Fracture of Brittle Materials," *Phys. Rev.,* Vol. B54, pp. 7128–7139.

Sharon, E., and Fineberg, J., 1999, "Confirming the Continuum Theory of Dynamic Brittle Fracture for Fast Cracks," *Nature,* Vol. 397, pp. 333–335.

Singh, R. P., and Shukla, A., 1996, "Subsonic and Intersonic Crack Growth Along a Bimaterial Interface," ASME JOURNAL OF APPLIED MECHANICS, Vol. 63, pp. 919–924.

Singh, R. P., Lambros, J., Shukla, A., and Rosakis, A., 1997, "Investigation of the Mechanics of Intersonic Crack Propagation Along a Bimaterial Interface Using Coherent Gradient Sensing and Photoelasticity," *Proc. Roy. Soc. Lond.,* Vol. A453, pp. 2649–2667.

Xu, X.-P., and Needleman, A., 1993, "Void Nucleation by Inclusion Debonding in a Crystal Matrix," *Modell. Simul. Mat. Sci. Engin.,* Vol. 1, pp. 111–132.

Xu, X.-P., and Needleman, A., 1994, "Numerical Simulations of Fast Crack Growth in Brittle Solids," *J. Mech. Phys. Solids,* Vol. 42, pp. 1397–1434.

Xu, X.-P., and Needleman, A., 1996, "Numerical Simulations of Dynamic Crack Growth Along an Interface," *Int. J. Fract.,* Vol. 74, pp. 289–324.

Downloaded 04 May 2010 to 171.66.16.27. Redistribution subject to ASME license or copyright; see http://www.asme.org/terms/Terms_Use.cfm

Consistent Hashin-Shtrikman Bounds on the Effective Properties of Periodic Composite Materials

P. Bisegna
University of Roma "Tor Vergata,"
Department of Civil Engineering,
00133 Rome, Italy

R. Luciano
University of Cassino,
Department of Industrial Engineering,
03043 Cassino, Italy

In this paper the four classical Hashin-Shtrikman variational principles, applied to the homogenization problem for periodic composites with a nonlinear hyperelastic constitutive behavior, are analyzed. It is proved that two of them are indeed minimum principles while the other two are saddle point principles. As a consequence, every approximation of the former ones provide bounds on the effective properties of composite bodies, while approximations of the latter ones may supply inconsistent bounds, as it is shown by two numerical examples. Nevertheless, the approximations of the saddle point principles are expected to provide better estimates than the approximations of the minimum principles.

1 Introduction

One of the most important aims in micromechanics is to estimate the effective elastic properties of multiphase composite materials (Willis, 1981; Mura, 1987; Christensen, 1990; Aboudi, 1991). In many applications it is sufficient to bound the overall response of the composite. This task can be accomplished by using the classical minimum principles of potential or complementary energy. In particular, elementary bounds are due to Voigt (1928) and Reuss (1929).

Hashin and Shtrikman (1962a, b) proposed four variational principles able to yield bounds on the overall elastic properties of macroscopically isotropic composite materials. Their bounds depend upon the volume fractions and the elastic properties of the constituents.

The Hashin-Shtrikman variational principles were variously generalized. Composites reinforced by random or aligned anisotropic inclusions were considered by Walpole (1966, 1981). The effective properties of nonlinear composites were studied by Talbot and Willis (1985), Ponte Castañeda (1991), and Willis (1991). Bounds on the overall properties of periodic composites were carried out by Milton and Kohn (1988), Suquet (1990), Nemat-Nasser et al. (1993), and Mulinec and Suquet (1994), by taking into account the actual geometry of the microstructure.

The physical idea underlying the Hashin-Shtrikman variational principles is to substitute the heterogeneous body with a homogeneous reference body subject to polarization fields, used to simulate the different elastic responses of the constituents (Eshelby, 1957). Hence the Hashin-Shtrikman principles are characterized by two nested stationary problems: The first one, called auxiliary problem, is the elastostatic problem of the homogeneous reference body subject to a given polarization field; the second one is an optimization problem which has as unknown the optimal polarization field which exactly simulates the actual microstructure of the original heterogeneous material.

In this paper the classical Hashin-Shtrikman principles are used to approach the homogenization problem of periodic composites with nonlinear hyperelastic constitutive relationships. The aim of this work is to show that two of the Hashin-Shtrikman principles are indeed minimum principles, while the other two are saddle point principles. As a consequence, every approximation of the former ones is able to supply bounds on the overall properties of composite bodies, while approximations of the latter ones may lead to inconsistent bounds. As a matter of fact, in order to obtain bounds by using the saddle-point principles, it is necessary to exactly solve the corresponding auxiliary problems. In the last section of the paper it is shown that there exist approximations of the saddle-point principles which do lead to inconsistent bounds. On the other hand, the approximations of the saddle-point principles are expected to provide better estimates than the ones supplied by the minimum principles, at the same computational effort.

2 Notation

The three-dimensional Euclidean vector space is denoted by $\mathcal{V}$; the space of symmetric second-order tensors on $\mathcal{V}$ is denoted by Sym. The inner product is indicated by a dot $(\cdot)$, the vector product by a cross $(\times)$ and the outer product by a dyad $(\otimes)$. The skew second-order tensor W_a, where $\mathbf{a} \in \mathcal{V}$, acts as the vector product operator $\mathbf{a} \times$:

$$W_a[\mathbf{b}] = \mathbf{a} \times \mathbf{b} \quad \forall\, \mathbf{b} \in \mathcal{V}. \tag{1}$$

The algebraic constructs $\mathbf{a} \otimes \mathbf{Q} \otimes \mathbf{b}$ and $\mathbf{a} \cdot C \cdot \mathbf{b}$, where $\mathbf{a}, \mathbf{b} \in \mathcal{V}$, $\mathbf{Q} \in$ Sym and C is a second-order tensor over Sym, are defined by

$$(\mathbf{a} \otimes \mathbf{Q} \otimes \mathbf{b}) \cdot (\mathbf{C} \otimes \mathbf{D}) = \mathbf{Q}[\mathbf{C}[\mathbf{a}]] \cdot \mathbf{D}[\mathbf{b}] \quad \forall\, \mathbf{C}, \mathbf{D} \in \text{Sym}$$

$$(\mathbf{a} \cdot C \cdot \mathbf{b}) \cdot (\mathbf{c} \otimes \mathbf{d}) = C[\text{sym}\,(\mathbf{a} \otimes \mathbf{c})] \cdot \text{sym}\,(\mathbf{b} \otimes \mathbf{d}) \quad \forall\, \mathbf{c}, \mathbf{d} \in \mathcal{V}, \tag{2}$$

where sym denotes the symmetric part.

A heterogeneous infinite hyperelastic body with a periodic microstructure is considered. Let C denote the parallelepipedic unit cell of the body, and v the volume of C. In the formulation of the homogenization problem, the strain field $\boldsymbol{\epsilon}$ and the stress field $\boldsymbol{\sigma}$, with values in Sym, are involved. They are assumed to be C-periodic and square-integrable over C. Hence, it is convenient to introduce the function space $\mathcal{H}$ of C-periodic symmetric second-order tensor fields which are square-integrable over C. $\mathcal{H}$ is an Hilbert space, endowed with the inner product defined by

Contributed by the Applied Mechanics Division of THE AMERICAN SOCIETY OF MECHANICAL ENGINEERS for publication in the ASME JOURNAL OF APPLIED MECHANICS.
Discussion on the paper should be addressed to the Technical Editor, Professor Lewis T. Wheeler, Department of Mechanical Engineering, University of Houston, Houston, TX 77204-4792, and will be accepted until four months after final publication of the paper itself in the ASME JOURNAL OF APPLIED MECHANICS.
Manuscript received by the ASME Applied Mechanics Division, July 30, 1996; final revision, Feb. 20, 1999. Associate Technical Editor: J. L. Bassani.

 Copyright © 1999 by ASME

Downloaded 04 May 2010 to 171.66.16.27. Redistribution subject to ASME license or copyright; see http://www.asme.org/terms/Terms_Use.cfm

$$\int_C \mathbf{A}(p) \cdot \mathbf{B}(p) dv, \tag{3}$$

for $\mathbf{A}, \mathbf{B} \in \mathcal{H}$, where p is the typical point of C and dv is the infinitesimal volume element. The norm and the average over C of the typical field $\mathbf{A} \in \mathcal{H}$ are denoted by $\|\mathbf{A}\|$ and $\langle \mathbf{A} \rangle$, respectively.

As a consequence of the Helmholtz decomposition theorem, the space $\mathcal{H}$ turns out to be the direct sum of three mutually orthogonal closed subspaces:

$$\mathcal{H} = \mathcal{H}_0 \oplus \mathcal{E} \oplus \mathcal{T}, \tag{4}$$

where

(i) $\mathcal{H}_0$ is the space of *constant* fields, identified with Sym;

(ii) $\mathcal{E}$ is the closure in $\mathcal{H}$ of the class of all C^∞-smooth null-average fields $\mathbf{A} \in \mathcal{H}$ such that

$$\text{curl curl } \mathbf{A} = \mathbf{0}; \tag{5}$$

hence, $\mathcal{E}$ is the space of null-average *compatible* strain fields;

(iii) $\mathcal{T}$ is the closure in $\mathcal{H}$ of the class of all C^∞-smooth null-average fields $\mathbf{A} \in \mathcal{H}$ such that

$$\text{div } \mathbf{A} = \mathbf{0}; \tag{6}$$

hence, $\mathcal{T}$ is the space of null-average *self-equilibrated* stress fields.

3 Hyperelastic Constitutive Relationships

The potential energy of the unit cell C of the body is denoted by $\Phi(\boldsymbol{\epsilon})$ and is defined by

$$\Phi(\boldsymbol{\epsilon}) = \int_C \varphi(\boldsymbol{\epsilon}(p), p) dv, \tag{7}$$

where φ is the potential-energy density functional and is defined on Sym $\times$ C. The functional Φ is assumed to be convex, lower semicontinuous, and proper (Ekeland and Temam, 1976). Moreover, the following coercivity property of Φ is enforced:

$$\lim_{\|\boldsymbol{\epsilon}\| \to +\infty} \Phi(\boldsymbol{\epsilon}) = +\infty. \tag{8}$$

The functional Φ is used to define the global constitutive relationship of the body, by stipulating that a stress field $\boldsymbol{\sigma} \in \mathcal{H}$ corresponds to a given strain field $\boldsymbol{\epsilon} \in \mathcal{H}$ when

$$\boldsymbol{\sigma} \in \partial_{\boldsymbol{\epsilon}} \Phi(\boldsymbol{\epsilon}), \tag{9}$$

where $\partial_{\boldsymbol{\epsilon}}$ is the subdifferential operator with respect to $\boldsymbol{\epsilon}$. Equation (9) describes a quite general class of hyperelastic materials, including nonlinear behaviors. It is worth noting that, since Φ need not be differentiable, multivalued constitutive relationships can be considered.

The complementary energy $\Psi(\boldsymbol{\sigma})$ of the unit cell C is the Fenchel conjugate of Φ:

$$\Psi(\boldsymbol{\sigma}) = \sup_{\boldsymbol{\epsilon} \in \mathcal{H}} \left\{ \int_C \boldsymbol{\sigma} \cdot \boldsymbol{\epsilon} dv - \Phi(\boldsymbol{\epsilon}) \right\}. \tag{10}$$

Also the functional Ψ can be used to define the global constitutive relationship of the body by the equation

$$\boldsymbol{\epsilon} \in \partial_{\boldsymbol{\sigma}} \Psi(\boldsymbol{\sigma}). \tag{11}$$

The issue of consistency among (9) and (11) is a standard matter of convex analysis (Ekeland and Temam, 1976).

It can be proved (Panagiotopoulos, 1985) that also Ψ admits a space density ψ, which is just the Fenchel conjugate of φ with respect to $\boldsymbol{\epsilon}$.

For a *linear* hyperelastic material, the densities φ and ψ are quadratic functionals of the strain and stress, respectively, and are usually written as

$$\varphi(\boldsymbol{\epsilon}) = \tfrac{1}{2} C[\boldsymbol{\epsilon}] \cdot \boldsymbol{\epsilon} \quad \text{and} \quad \psi(\boldsymbol{\sigma}) = \tfrac{1}{2} \mathcal{D}[\boldsymbol{\sigma}] \cdot \boldsymbol{\sigma} \tag{12}$$

where the elasticity tensor C and the compliance tensor $\mathcal{D} = C^{-1}$ have been introduced. They are, in general, functions of the point in the body.

4 Homogenization of Hyperelastic Composites With Periodic Microstructure

The homogenized potential-energy density is defined as

$$\bar{\varphi}(\bar{\boldsymbol{\epsilon}}) = \frac{1}{v} \inf_{\boldsymbol{\epsilon} \in \mathcal{E}} \Phi(\bar{\boldsymbol{\epsilon}} + \boldsymbol{\epsilon}), \quad \bar{\boldsymbol{\epsilon}} \in \text{Sym}. \tag{13}$$

To find the infimum in (13) amounts to solving the equilibrium problem for the body subject to mean strain $\bar{\boldsymbol{\epsilon}}$. In fact, from the stipulated properties of Φ, the infimum in (13) is attained (Ekeland and Temam, 1976), say at $\hat{\boldsymbol{\epsilon}} \in \mathcal{E}$, and every field

$$\boldsymbol{\sigma} \in \partial_{\boldsymbol{\epsilon}} \Phi(\bar{\boldsymbol{\epsilon}} + \hat{\boldsymbol{\epsilon}}) \tag{14}$$

can be represented as $\boldsymbol{\sigma} = \bar{\boldsymbol{\sigma}} + \hat{\boldsymbol{\sigma}}$, for some $\bar{\boldsymbol{\sigma}} \in \text{Sym}$ and $\hat{\boldsymbol{\sigma}} \in \mathcal{T}$. Hence, the compatible strain field $\bar{\boldsymbol{\epsilon}} + \hat{\boldsymbol{\epsilon}}$ and the self-equilibrated stress field $\bar{\boldsymbol{\sigma}} + \hat{\boldsymbol{\sigma}}$ constitute the solution of the equilibrium problem for the body subject to mean strain $\bar{\boldsymbol{\epsilon}}$. These fields need not be uniquely defined; they are unique if Φ is strictly convex and differentiable. The homogenized constitutive relationship of the composite body maps $\bar{\boldsymbol{\epsilon}}$ into $\bar{\boldsymbol{\sigma}}$ and can be written as

$$\bar{\boldsymbol{\sigma}} \in \partial_{\bar{\boldsymbol{\epsilon}}} \bar{\varphi}(\bar{\boldsymbol{\epsilon}}). \tag{15}$$

As a matter fact, from (13) and (14), it turns out that, for every $\bar{\boldsymbol{\delta}} \in \text{Sym}$,

$$\begin{aligned} \bar{\varphi}(\bar{\boldsymbol{\delta}}) &= \frac{1}{v} \inf_{\boldsymbol{\epsilon} \in \mathcal{E}} \Phi(\bar{\boldsymbol{\delta}} + \boldsymbol{\epsilon}) \\ &\geq \frac{1}{v} \inf_{\boldsymbol{\epsilon} \in \mathcal{E}} \left[\Phi(\bar{\boldsymbol{\epsilon}} + \hat{\boldsymbol{\epsilon}}) + \int_C (\bar{\boldsymbol{\sigma}} + \hat{\boldsymbol{\sigma}}) \cdot (\bar{\boldsymbol{\delta}} - \bar{\boldsymbol{\epsilon}} + \boldsymbol{\epsilon} - \hat{\boldsymbol{\epsilon}}) dv \right] \\ &= \bar{\varphi}(\bar{\boldsymbol{\epsilon}}) + \bar{\boldsymbol{\sigma}} \cdot (\bar{\boldsymbol{\delta}} - \bar{\boldsymbol{\epsilon}}), \end{aligned} \tag{16}$$

and hence (15) follows.

On the other hand, the homogenized complementary-energy density is defined as

$$\bar{\psi}(\bar{\boldsymbol{\sigma}}) = \frac{1}{v} \inf_{\boldsymbol{\sigma} \in \mathcal{T}} \Psi(\bar{\boldsymbol{\sigma}} + \boldsymbol{\sigma}), \quad \bar{\boldsymbol{\sigma}} \in \text{Sym}. \tag{17}$$

To find the infimum with respect to $\boldsymbol{\sigma} \in \mathcal{T}$ in (17) amounts to solving the compatibility problem for the body subject to mean stress $\bar{\boldsymbol{\sigma}}$, and leads to a homogenized constitutive relationship governed by $\bar{\psi}$:

$$\bar{\boldsymbol{\epsilon}} \in \partial_{\bar{\boldsymbol{\sigma}}} \bar{\psi}(\bar{\boldsymbol{\sigma}}). \tag{18}$$

The issue of consistency among (15) and (18) easily follows from the conjugacy of $\bar{\varphi}$ and $\bar{\psi}$:

$$\bar{\psi}(\bar{\boldsymbol{\sigma}}) = \sup_{\bar{\boldsymbol{\epsilon}} \in \text{Sym}} \{ \bar{\boldsymbol{\sigma}} \cdot \bar{\boldsymbol{\epsilon}} - \bar{\varphi}(\bar{\boldsymbol{\epsilon}}) \}. \tag{19}$$

This equation can be proved by the following argument (Willis, 1989):

Downloaded 04 May 2010 to 171.66.16.27. Redistribution subject to ASME license or copyright; see http://www.asme.org/terms/Terms_Use.cfm

$$\bar{\psi}(\bar{\boldsymbol{\sigma}}) = \frac{1}{v} \inf_{\boldsymbol{\sigma} \in \mathcal{T}} \Psi(\bar{\boldsymbol{\sigma}} + \boldsymbol{\sigma})$$

$$= \frac{1}{v} \inf_{\boldsymbol{\sigma} \in \mathcal{T}} \sup_{\boldsymbol{\epsilon} \in \mathcal{H}} \left[\int_C (\bar{\boldsymbol{\sigma}} + \boldsymbol{\sigma}) \cdot \boldsymbol{\epsilon} dv - \Phi(\boldsymbol{\epsilon}) \right]; \quad (20)$$

the infimum and the supremum at the right-hand side of (20) can be exchanged (Ekeland and Temam, 1976), and the right-hand side of (20) becomes

$$\frac{1}{v} \sup_{\boldsymbol{\epsilon} \in \mathcal{T}^\perp} \left[\int_C \bar{\boldsymbol{\sigma}} \cdot \boldsymbol{\epsilon} dv - \Phi(\boldsymbol{\epsilon}) \right]$$

$$= \frac{1}{v} \sup_{\bar{\boldsymbol{\epsilon}} \in \mathrm{Sym}} \sup_{\boldsymbol{\delta} \in \mathcal{E}} \left[\int_C \bar{\boldsymbol{\sigma}} \cdot \bar{\boldsymbol{\epsilon}} dv - \Phi(\bar{\boldsymbol{\epsilon}} + \boldsymbol{\delta}) \right]$$

$$= \sup_{\bar{\boldsymbol{\epsilon}} \in \mathrm{Sym}} \{ \bar{\boldsymbol{\sigma}} \cdot \bar{\boldsymbol{\epsilon}} - \bar{\varphi}(\bar{\boldsymbol{\epsilon}}) \}, \quad (21)$$

where the superscript $\perp$ denotes the orthogonal complement. Hence, (19) is proved.

5 Hashin-Shtrikman Variational Principles

In this section the four well-known Hashin-Shtrikman variational principles are briefly recalled (Hashin and Shtrikman, 1962a, b). It is pointed out here that two of them are indeed minimum principles, while the other two are saddle point principles.

The main idea underlying the Hashin-Shtrikman principles is to substitute the composite body with a homogeneous linear reference body subject to polarization fields, which are assumed as the main unknowns of the homogenization problem. Let the potential and complementary energy of the reference material be Φ_0 and Ψ_0, respectively. Their space densities are $\varphi_0(\boldsymbol{\epsilon}) = C_0[\boldsymbol{\epsilon}] \cdot \boldsymbol{\epsilon}/2$ and $\psi_0(\boldsymbol{\sigma}) = \mathcal{D}_0[\boldsymbol{\sigma}] \cdot \boldsymbol{\sigma}/2$, where C_0 and $\mathcal{D}_0 = C_0^{-1}$ are positive-definite symmetric second-order tensors over Sym.

5.1 Variational Principles Involving $\bar{\varphi}$. First, it is supposed that a reference material can be chosen such that $\Phi - \Phi_0$ is convex. It is observed that the convexity of $\Phi - \Phi_0$ is assured by the convexity of $\varphi - \varphi_0$ *at each point* of the body (Panagiotopoulos, 1985).

Let $\Psi_\Phi(\boldsymbol{\sigma}^*)$ denote the convex conjugate of $\Phi - \Phi_0$:

$$\Psi_\Phi(\boldsymbol{\sigma}^*) = \sup_{\boldsymbol{\epsilon} \in \mathcal{H}} \left\{ \int_C \boldsymbol{\sigma}^* \cdot \boldsymbol{\epsilon} dv - \Phi(\boldsymbol{\epsilon}) + \Phi_0(\boldsymbol{\epsilon}) \right\}. \quad (22)$$

The inverse relation of (22) is

$$\Phi(\boldsymbol{\epsilon}) - \Phi_0(\boldsymbol{\epsilon}) = \sup_{\boldsymbol{\sigma}^* \in \mathcal{H}} \left\{ \int_C \boldsymbol{\sigma}^* \cdot \boldsymbol{\epsilon} dv - \Psi_\Phi(\boldsymbol{\sigma}^*) \right\}. \quad (23)$$

In particular, by taking $\boldsymbol{\epsilon} = \bar{\boldsymbol{\epsilon}} + \hat{\boldsymbol{\epsilon}}$ with $\bar{\boldsymbol{\epsilon}} \in \mathrm{Sym}$ and $\hat{\boldsymbol{\epsilon}} \in \mathcal{E}$, using the fact that Φ_0 is a quadratic functional and rearranging the terms, (23) becomes

$$\Phi(\bar{\boldsymbol{\epsilon}} + \hat{\boldsymbol{\epsilon}}) - \Phi_0(\bar{\boldsymbol{\epsilon}}) = \sup_{\boldsymbol{\sigma}^* \in \mathcal{H}} \left\{ \int_C \langle \boldsymbol{\sigma}^* \rangle \cdot \bar{\boldsymbol{\epsilon}} dv - \Psi_\Phi(\boldsymbol{\sigma}^*) + \int_C \boldsymbol{\sigma}^* \cdot \hat{\boldsymbol{\epsilon}} dv + \Phi_0(\hat{\boldsymbol{\epsilon}}) \right\}. \quad (24)$$

Then, the infimum over $\hat{\boldsymbol{\epsilon}} \in \mathcal{E}$ of both sides of (24) is taken. From the positive definiteness of Φ_0, it follows that the resulting infimum and supremum at the right-hand side can be exchanged, leading to

$$\bar{\varphi}(\bar{\boldsymbol{\epsilon}}) - \varphi_0(\bar{\boldsymbol{\epsilon}}) = \frac{1}{v} \sup_{\boldsymbol{\sigma}^* \in \mathcal{H}} \left\{ \int_C \langle \boldsymbol{\sigma}^* \rangle \cdot \bar{\boldsymbol{\epsilon}} dv - \Psi_\Phi(\boldsymbol{\sigma}^*) + \inf_{\hat{\boldsymbol{\epsilon}} \in \mathcal{E}} F_{\Phi_0}^{(\boldsymbol{\sigma}^*)} \right\}, \quad (25)$$

where the quadratic functional $F_{\Phi_0}^{(\boldsymbol{\sigma}^*)}$ is defined as follows:

$$F_{\Phi_0}^{(\boldsymbol{\sigma}^*)} : \hat{\boldsymbol{\epsilon}} \in \mathcal{E} \to \int_C \boldsymbol{\sigma}^* \cdot \hat{\boldsymbol{\epsilon}} dv + \Phi_0(\hat{\boldsymbol{\epsilon}}). \quad (26)$$

It is now supposed that a reference material can be chosen such that $\Phi - \Phi_0$ is concave: In this case, by a similar procedure, it turns out that

$$\bar{\varphi}(\bar{\boldsymbol{\epsilon}}) - \varphi_0(\bar{\boldsymbol{\epsilon}}) = \frac{1}{v} \inf_{\boldsymbol{\sigma}^* \in \mathcal{H}} \left\{ \int_C \langle \boldsymbol{\sigma}^* \rangle \cdot \bar{\boldsymbol{\epsilon}} dv - \Psi_\Phi(\boldsymbol{\sigma}^*) + \inf_{\hat{\boldsymbol{\epsilon}} \in \mathcal{E}} F_{\Phi_0}^{(\boldsymbol{\sigma}^*)} \right\}, \quad (27)$$

where $\Psi_\Phi(\boldsymbol{\sigma}^*)$ denotes the concave conjugate of $\Phi - \Phi_0$:

$$\Psi_\Phi(\boldsymbol{\sigma}^*) = \inf_{\boldsymbol{\epsilon} \in \mathcal{H}} \left\{ \int_C \boldsymbol{\sigma}^* \cdot \boldsymbol{\epsilon} dv - \Phi(\boldsymbol{\epsilon}) + \Phi_0(\boldsymbol{\epsilon}) \right\}. \quad (28)$$

Equations (25) and (27) are the eigenstress-based Hashin-Shtrikman variational principles: indeed, the field $\boldsymbol{\sigma}^*$, with respect to which the supremum in (25) or the infimum in (27) have to be performed, is usually called *polarization field* or *eigenstress field.* It is worth noting that (25) is a saddle point principle, while (27) is a minimum principle.

5.2 Variational Principles Involving $\bar{\psi}$. In this subsection, variational principles involving the homogenized complementary-energy density $\bar{\psi}$ are deduced by arguing as in the previous subsection: For the sake of brevity, only the results are reported.

When a reference material can be chosen such that $\Psi - \Psi_0$ is convex, it turns out that

$$\bar{\psi}(\bar{\boldsymbol{\sigma}}) - \psi_0(\bar{\boldsymbol{\sigma}}) = \frac{1}{v} \sup_{\boldsymbol{\epsilon}^* \in \mathcal{H}} \left\{ \int_C \langle \boldsymbol{\epsilon}^* \rangle \cdot \bar{\boldsymbol{\sigma}} dv - \Phi_\Psi(\boldsymbol{\epsilon}^*) + \inf_{\hat{\boldsymbol{\sigma}} \in \mathcal{T}} F_{\Psi_0}^{(\boldsymbol{\epsilon}^*)} \right\}, \quad (29)$$

where $\Phi_\Psi(\boldsymbol{\epsilon}^*)$ is the convex conjugate of $\Psi - \Psi_0$, and the quadratic functional $F_{\Psi_0}^{(\boldsymbol{\epsilon}^*)}$ is defined as follows:

$$F_{\Psi_0}^{(\boldsymbol{\epsilon}^*)} : \hat{\boldsymbol{\sigma}} \in \mathcal{T} \to \int_C \boldsymbol{\epsilon}^* \cdot \hat{\boldsymbol{\sigma}} dv + \Psi_0(\hat{\boldsymbol{\sigma}}). \quad (30)$$

On the other hand, when a reference material can be chosen such that $\Psi - \Psi_0$ is concave, it turns out that

$$\bar{\psi}(\bar{\boldsymbol{\sigma}}) - \psi_0(\bar{\boldsymbol{\sigma}}) = \frac{1}{v} \inf_{\boldsymbol{\epsilon}^* \in \mathcal{H}} \left\{ \int_C \langle \boldsymbol{\epsilon}^* \rangle \cdot \bar{\boldsymbol{\sigma}} dv - \Phi_\Psi(\boldsymbol{\epsilon}^*) + \inf_{\hat{\boldsymbol{\sigma}} \in \mathcal{T}} F_{\Psi_0}^{(\boldsymbol{\epsilon}^*)} \right\}, \quad (31)$$

where $\Phi_\Psi(\boldsymbol{\epsilon}^*)$ denotes the concave conjugate of $\Psi - \Psi_0$.

Equations (29) and (31) are the eigenstrain-based Hashin-Shtrikman variational principles: Indeed, the field $\boldsymbol{\epsilon}^*$, with respect to which the supremum in (29) or the infimum in (31) have to be performed, is usually called *polarization field* or *eigenstrain field.* It is worth noting that (29) is a saddle point principle, while (31) is a minimum principle.

Downloaded 04 May 2010 to 171.66.16.27. Redistribution subject to ASME license or copyright; see http://www.asme.org/terms/Terms_Use.cfm

5.3 Auxiliary Problems. The Hashin-Shtrikman variational principles (25) and (27) (respectively, (29) and (31)) involve an auxiliary problem, which consists in the minimization of the functional $F_{\Phi_0}^{(\boldsymbol{\sigma}^*)}$ (respectively, $F_{\Psi_0}^{(\boldsymbol{\epsilon}^*)}$). It amounts to solving the equilibrium (respectively, compatibility) problem for the reference homogeneous body subject to the given eigenstress field $\boldsymbol{\sigma}^*$ (respectively, eigenstrain field $\boldsymbol{\epsilon}^*$).

Because of the C-periodicity of the polarization field $\boldsymbol{\sigma}^*$ [or $\boldsymbol{\epsilon}^*$], the auxiliary problem is more easily solved by a transformation from the space domain to the Fourier domain. A Cartesian frame $(0, x_1, x_2, x_3)$ is chosen, with the x_1, x_2, and x_3 axes parallel to the edges L_1, L_2, and L_3 of C, respectively. Cartesian components are denoted by subscript indices. The typical symmetric second-order tensor field $\mathbf{A} \in \mathcal{H}$ can be represented by a Fourier series as follows:

$$\mathbf{A}(\mathbf{x}) = \sum_{\mathbf{k} \in Z} \mathbf{A}_{\mathbf{k}} \exp(j \boldsymbol{\xi}_{\mathbf{k}} \cdot \mathbf{x}), \tag{32}$$

where exp denotes the exponential function, Z is the set $Z \times Z \times Z$, Z is the set of integer numbers, $\mathbf{x} = (x_1, x_2, x_3)$ is the position vector of the typical point $p \in C$, $\mathbf{k} = (k_1, k_2, k_3)$, $\boldsymbol{\xi}_{\mathbf{k}} = (2\pi k_1/L_1, 2\pi k_2/L_2, 2\pi k_3/L_3)$, $\mathbf{A}_{\mathbf{k}} \in$ Sym and $j = \sqrt{-1}$. In particular, the Fourier coefficients $\mathbf{A}_{\mathbf{k}}$ of a real field $\mathbf{A}$ satisfy the equation

$$\mathbf{A}_{-\mathbf{k}} = \mathbf{A}_{\mathbf{k}}^c, \tag{33}$$

where the superscript c denotes the complex conjugate. A null-average field $\boldsymbol{\epsilon} \in \mathcal{H}$ belongs to $\hat{\mathcal{E}}$ if and only if

$$W_{\boldsymbol{\xi}_{\mathbf{k}}} \boldsymbol{\epsilon}_{\mathbf{k}} W_{\boldsymbol{\xi}_{\mathbf{k}}} = \mathbf{0} \quad \forall\, \mathbf{k} \in \hat{Z}, \tag{34}$$

where $\hat{Z} = Z \backslash \{(0 \times 0 \times 0)\}$. Moreover, a null-average field $\boldsymbol{\sigma} \in \mathcal{H}$ belongs to $\hat{\mathcal{T}}$ if and only if

$$\boldsymbol{\sigma}_{\mathbf{k}}[\boldsymbol{\xi}_{\mathbf{k}}] = \mathbf{0} \quad \forall\, \mathbf{k} \in \hat{Z}. \tag{35}$$

By adopting the Fourier representation, the functional $F_{\Phi_0}^{(\boldsymbol{\sigma}^*)}$ is transformed into

$$F_{\Phi_0}^{(\boldsymbol{\sigma}^*)} = v \sum_{\mathbf{k} \in \hat{Z}} \{\tfrac{1}{2} C_0[\boldsymbol{\epsilon}_{\mathbf{k}}] \cdot \boldsymbol{\epsilon}_{\mathbf{k}}^c + \boldsymbol{\epsilon}_{\mathbf{k}} \cdot \boldsymbol{\sigma}_{\mathbf{k}}^{*c}\}. \tag{36}$$

This functional has to be minimized with respect to all $\boldsymbol{\epsilon}_{\mathbf{k}}$ satisfying (34). After a simple algebra, it follows that the optimal $\boldsymbol{\epsilon}_{\mathbf{k}}$ is given by

$$\boldsymbol{\epsilon}_{\mathbf{k}}^{\text{opt}} = -\boldsymbol{\xi}_{\mathbf{k}} \otimes (\boldsymbol{\xi}_{\mathbf{k}} \cdot C_0 \cdot \boldsymbol{\xi}_{\mathbf{k}})^{-1} \otimes \boldsymbol{\xi}_{\mathbf{k}}[\boldsymbol{\sigma}_{\mathbf{k}}^*] \tag{37}$$

and hence

$$\inf_{\hat{\boldsymbol{\epsilon}} \in \mathcal{E}} F_{\Phi_0}^{(\boldsymbol{\sigma}^*)} = -\frac{v}{2} \sum_{\mathbf{k} \in \hat{Z}} \boldsymbol{\xi}_{\mathbf{k}} \otimes (\boldsymbol{\xi}_{\mathbf{k}} \cdot C_0 \cdot \boldsymbol{\xi}_{\mathbf{k}})^{-1} \otimes \boldsymbol{\xi}_{\mathbf{k}}[\boldsymbol{\sigma}_{\mathbf{k}}^*] \cdot \boldsymbol{\sigma}_{\mathbf{k}}^{*c}. \tag{38}$$

Analogously, the functional $F_{\Psi_0}^{(\boldsymbol{\epsilon}^*)}$ can be written as

$$F_{\Psi_0}^{(\boldsymbol{\epsilon}^*)} = v \sum_{\mathbf{k} \in \hat{Z}} \{\tfrac{1}{2} \mathcal{D}_0[\boldsymbol{\sigma}_{\mathbf{k}}] \cdot \boldsymbol{\sigma}_{\mathbf{k}}^c + \boldsymbol{\sigma}_{\mathbf{k}} \cdot \boldsymbol{\epsilon}_{\mathbf{k}}^{*c}\}. \tag{39}$$

This functional has to be minimized with respect to all $\boldsymbol{\sigma}_{\mathbf{k}}$ satisfying (35). After a simple algebra, it follows that the optimal $\boldsymbol{\sigma}_{\mathbf{k}}$ is given by

$$\boldsymbol{\sigma}_{\mathbf{k}}^{\text{opt}} = -[C_0 - C_0 \boldsymbol{\xi}_{\mathbf{k}} \otimes (\boldsymbol{\xi}_{\mathbf{k}} \cdot C_0 \cdot \boldsymbol{\xi}_{\mathbf{k}})^{-1} \otimes \boldsymbol{\xi}_{\mathbf{k}} C_0][\boldsymbol{\epsilon}_{\mathbf{k}}^*] \tag{40}$$

and hence

$$\inf_{\hat{\boldsymbol{\sigma}} \in \mathcal{T}} F_{\Psi_0}^{(\boldsymbol{\epsilon}^*)} = -\frac{v}{2} \sum_{\mathbf{k} \in \hat{Z}} [\mathcal{D}_0 - \boldsymbol{\xi}_{\mathbf{k}} \otimes (\boldsymbol{\xi}_{\mathbf{k}} \cdot C_0 \cdot \boldsymbol{\xi}_{\mathbf{k}})^{-1} \otimes \boldsymbol{\xi}_{\mathbf{k}}] \times [C_0[\boldsymbol{\epsilon}_{\mathbf{k}}^*]] \cdot C_0[\boldsymbol{\epsilon}_{\mathbf{k}}^{*c}]. \tag{41}$$

6 Bounds on the Homogenized Densities $\bar{\varphi}$ and $\bar{\psi}$

The homogenized potential and complementary-energy densities $\bar{\varphi}$ and $\bar{\psi}$ can be obtained by performing the minimizations involved in Eqs. (13) and (17), respectively. When those minimizations are performed over finite-dimensional subspaces, say $\mathcal{E}_f$ and $\mathcal{T}_f$ of the original spaces $\mathcal{E}$ and $\mathcal{T}$, upper bounds on $\bar{\varphi}$ and $\bar{\psi}$ are obtained:

$$\bar{\varphi}(\bar{\boldsymbol{\epsilon}}) \leq \frac{1}{v} \inf_{\boldsymbol{\epsilon} \in \mathcal{E}_f} \Phi(\bar{\boldsymbol{\epsilon}} + \boldsymbol{\epsilon}) \quad \text{and}$$

$$\bar{\psi}(\bar{\boldsymbol{\sigma}}) \leq \frac{1}{v} \inf_{\boldsymbol{\sigma} \in \mathcal{T}_f} \Psi(\bar{\boldsymbol{\sigma}} + \boldsymbol{\sigma}). \tag{42}$$

On the other hand, $\bar{\varphi}$ and $\bar{\psi}$ can be carried out also by using the Hashin-Shtrikman variational principles (25), (27), (29), and (31). If the optimizations with respect to the polarization fields are performed over a finite-dimensional subspace $\mathcal{H}_f$ of $\mathcal{H}$, upper or lower bounds on the involved homogenized energy densities are obtained. In particular,

(i) if $\Phi - \Phi_0$ is convex (or $\Psi - \Psi_0$ is concave), then

$$\bar{\varphi}(\bar{\boldsymbol{\epsilon}}) - \varphi_0(\bar{\boldsymbol{\epsilon}}) \geq \frac{1}{v} \sup_{\boldsymbol{\sigma}^* \in \mathcal{H}_f} \left\{ \int_C \langle \boldsymbol{\sigma}^* \rangle \cdot \bar{\boldsymbol{\epsilon}} dv - \Psi_\Phi(\boldsymbol{\sigma}^*) + \inf_{\hat{\boldsymbol{\epsilon}} \in \mathcal{E}} F_{\Phi_0}^{(\boldsymbol{\sigma}^*)} \right\} \tag{43}$$

and

$$\bar{\psi}(\bar{\boldsymbol{\sigma}}) - \psi_0(\bar{\boldsymbol{\sigma}}) \leq \frac{1}{v} \inf_{\boldsymbol{\epsilon}^* \in \mathcal{H}_f} \left\{ \int_C \langle \boldsymbol{\epsilon}^* \rangle \cdot \bar{\boldsymbol{\sigma}} dv - \Phi_\Psi(\boldsymbol{\epsilon}^*) + \inf_{\hat{\boldsymbol{\sigma}} \in \mathcal{T}} F_{\Psi_0}^{(\boldsymbol{\epsilon}^*)} \right\}; \tag{44}$$

(ii) if $\Phi - \Phi_0$ is concave (or $\Psi - \Psi_0$ is convex), then

$$\bar{\varphi}(\bar{\boldsymbol{\epsilon}}) - \varphi_0(\bar{\boldsymbol{\epsilon}}) \leq \frac{1}{v} \inf_{\boldsymbol{\sigma}^* \in \mathcal{H}_f} \left\{ \int_C \langle \boldsymbol{\sigma}^* \rangle \cdot \bar{\boldsymbol{\epsilon}} dv - \Psi_\Phi(\boldsymbol{\sigma}^*) + \inf_{\hat{\boldsymbol{\epsilon}} \in \mathcal{E}} F_{\Phi_0}^{(\boldsymbol{\sigma}^*)} \right\} \tag{45}$$

and

$$\bar{\psi}(\bar{\boldsymbol{\sigma}}) - \psi_0(\bar{\boldsymbol{\sigma}}) \geq \frac{1}{v} \sup_{\boldsymbol{\epsilon}^* \in \mathcal{H}_f} \left\{ \int_C \langle \boldsymbol{\epsilon}^* \rangle \cdot \bar{\boldsymbol{\sigma}} dv - \Phi_\Psi(\boldsymbol{\epsilon}^*) + \inf_{\hat{\boldsymbol{\sigma}} \in \mathcal{T}} F_{\Psi_0}^{(\boldsymbol{\epsilon}^*)} \right\}. \tag{46}$$

Equations (43) and (45) (respectively, (44) and (46)) require the computation of the infimum of the functional $F_{\Phi_0}^{(\boldsymbol{\sigma}^*)}$ (respectively, $F_{\Psi_0}^{(\boldsymbol{\epsilon}^*)}$). To this end, Eq. (38) (respectively, (41)) can be adopted. It involves an infinite sum over $\mathbf{k}$ which cannot be generally expressed in a closed form. As a consequence, it has generally to be computed numerically (Iwakuma and Nemat-Nasser, 1983). In this case $\mathbf{k}$ cannot range over the whole $\hat{Z}$, but it must range only over a finite subset $\hat{Z}_f$ of $\hat{Z}$. In other words, the functional $F_{\Phi_0}^{(\boldsymbol{\sigma}^*)}$ (respectively, $F_{\Psi_0}^{(\boldsymbol{\epsilon}^*)}$) is computed by taking $\boldsymbol{\epsilon}_{\mathbf{k}} = \mathbf{0}$ (respectively, $\boldsymbol{\sigma}_{\mathbf{k}} = \mathbf{0}$) for $\mathbf{k} \notin \hat{Z}_f$ instead of the optimal value (37) (respectively, (40)). Hence, every numerical estimate of the infinite sum in (38) (respectively, (41)) is indeed an upper bound on the infimum of $F_{\Phi_0}^{(\boldsymbol{\sigma}^*)}$ (respectively, $F_{\Psi_0}^{(\boldsymbol{\epsilon}^*)}$):

Downloaded 04 May 2010 to 171.66.16.27. Redistribution subject to ASME license or copyright; see http://www.asme.org/terms/Terms_Use.cfm

$$\inf_{\hat{\boldsymbol{\sigma}}\in\mathcal{T}} F_{\Phi_0}^{(\boldsymbol{\sigma}^*)} \le -\frac{v}{2}\sum_{\mathbf{k}\in\hat{\mathcal{Z}}_f} \boldsymbol{\xi}_{\mathbf{k}} \otimes (\boldsymbol{\xi}_{\mathbf{k}}\cdot C_0\cdot\boldsymbol{\xi}_{\mathbf{k}})^{-1} \otimes \boldsymbol{\xi}_{\mathbf{k}}[\boldsymbol{\sigma}_{\mathbf{k}}^*]\cdot\boldsymbol{\sigma}_{\mathbf{k}}^{*c} \tag{47}$$

(respectively,

$$\inf_{\hat{\boldsymbol{\epsilon}}\in\mathcal{T}} F_{\Psi_0}^{(\boldsymbol{\epsilon}^*)} \le -\frac{v}{2}\sum_{\mathbf{k}\in\hat{\mathcal{Z}}_f} [\mathcal{D}_0 - \boldsymbol{\xi}_{\mathbf{k}} \otimes (\boldsymbol{\xi}_{\mathbf{k}}\cdot C_0\cdot\boldsymbol{\xi}_{\mathbf{k}})^{-1} \otimes \boldsymbol{\xi}_{\mathbf{k}}] \times [C_0[\boldsymbol{\epsilon}_{\mathbf{k}}^*]]\cdot C_0[\boldsymbol{\epsilon}_{\mathbf{k}}^{*c}]\Big). \tag{48}$$

From a mechanical point of view, by taking $\boldsymbol{\epsilon}_{\mathbf{k}} = \mathbf{0}$ (respectively $\boldsymbol{\sigma}_{\mathbf{k}} = \mathbf{0}$) for $\mathbf{k} \notin \hat{\mathcal{Z}}_f$, an approximate auxiliary-problem solution is found, which is compatible [respectively, equilibrated] but not exactly equilibrated [respectively, compatible].

Under the hypothesis that $\Phi - \Phi_0$ is concave (respectively, $\Psi - \Psi_0$ is concave), the following upper bound on $\bar{\varphi}$ (respectively, $\bar{\psi}$) is obtained from Eqs. (45) and (47) (respectively, (44) and (48)):

$$\bar{\varphi}(\bar{\boldsymbol{\epsilon}}) - \varphi_0(\bar{\boldsymbol{\epsilon}}) \le \frac{1}{v}\inf_{\boldsymbol{\sigma}^*\in\mathcal{H}_f}\left\{\int_C \langle\boldsymbol{\sigma}^*\rangle\cdot\bar{\boldsymbol{\epsilon}}\,dv - \Psi_\Phi(\boldsymbol{\sigma}^*) - \frac{v}{2}\sum_{\mathbf{k}\in\hat{\mathcal{Z}}_f} \boldsymbol{\xi}_{\mathbf{k}} \otimes (\boldsymbol{\xi}_{\mathbf{k}}\cdot C_0\cdot\boldsymbol{\xi}_{\mathbf{k}})^{-1} \otimes \boldsymbol{\xi}_{\mathbf{k}}[\boldsymbol{\sigma}_{\mathbf{k}}^*]\cdot\boldsymbol{\sigma}_{\mathbf{k}}^{*c}\right\} \tag{49}$$

(respectively,

$$\bar{\psi}(\bar{\boldsymbol{\sigma}}) - \psi_0(\bar{\boldsymbol{\sigma}}) \le \frac{1}{v}\inf_{\boldsymbol{\epsilon}^*\in\mathcal{H}_f}\left\{\int_C \langle\boldsymbol{\epsilon}^*\rangle\cdot\bar{\boldsymbol{\sigma}}\,dv - \Phi_\Psi(\boldsymbol{\epsilon}^*) - \frac{v}{2}\sum_{\mathbf{k}\in\hat{\mathcal{Z}}_f} [\mathcal{D}_0 - \boldsymbol{\xi}_{\mathbf{k}} \otimes (\boldsymbol{\xi}_{\mathbf{k}}\cdot C_0\cdot\boldsymbol{\xi}_{\mathbf{k}})^{-1} \otimes \boldsymbol{\xi}_{\mathbf{k}}] \times [C_0[\boldsymbol{\epsilon}_{\mathbf{k}}^*]]\cdot C_0[\boldsymbol{\epsilon}_{\mathbf{k}}^{*c}]\right\}\Big). \tag{50}$$

It is emphasized that, for *every* choice of $\mathcal{H}_f \subset \mathcal{H}$ *and* $\mathcal{Z}_f \subset \mathcal{Z}$, an upper bound on $\bar{\varphi}$ (respectively, $\bar{\psi}$) is obtained by Eq. (49) (respectively, (50)). Larger $\mathcal{H}_f$ and $\mathcal{Z}_f$ are chosen, better the upper bound is computed.

On the other hand, under the hypothesis that $\Phi - \Phi_0$ is convex (respectively, $\Psi - \Psi_0$ is convex), a lower bound on $\bar{\varphi}$ (respectively, $\bar{\psi}$) is given in Eq. (43) (respectively, (46)). Clearly, in this case equation (47) (respectively, (48)) is not useful. Moreover, in the next section it will be proved by simple examples that there exist sets $\mathcal{H}_f \subset \mathcal{H}$ and $\mathcal{Z}_f \subset \mathcal{Z}$ such that the inequality

$$\bar{\varphi}(\bar{\boldsymbol{\epsilon}}) - \varphi_0(\bar{\boldsymbol{\epsilon}}) \ge \frac{1}{v}\sup_{\boldsymbol{\sigma}^*\in\mathcal{H}_f}\left\{\int_C \langle\boldsymbol{\sigma}^*\rangle\cdot\bar{\boldsymbol{\epsilon}}\,dv - \Psi_\Phi(\boldsymbol{\sigma}^*) - \frac{v}{2}\sum_{\mathbf{k}\in\hat{\mathcal{Z}}_f} \boldsymbol{\xi}_{\mathbf{k}} \otimes (\boldsymbol{\xi}_{\mathbf{k}}\cdot C_0\cdot\boldsymbol{\xi}_{\mathbf{k}})^{-1} \otimes \boldsymbol{\xi}_{\mathbf{k}}[\boldsymbol{\sigma}_{\mathbf{k}}^*]\cdot\boldsymbol{\sigma}_{\mathbf{k}}^{*c}\right\} \tag{51}$$

(respectively,

$$\bar{\psi}(\bar{\boldsymbol{\sigma}}) - \psi_0(\bar{\boldsymbol{\sigma}}) \ge \frac{1}{v}\sup_{\boldsymbol{\epsilon}^*\in\mathcal{H}_f}\left\{\int_C \langle\boldsymbol{\epsilon}^*\rangle\cdot\bar{\boldsymbol{\sigma}}\,dv - \Phi_\Psi(\boldsymbol{\epsilon}^*) - \frac{v}{2}\sum_{\mathbf{k}\in\hat{\mathcal{Z}}_f} [\mathcal{D}_0 - \boldsymbol{\xi}_{\mathbf{k}} \otimes (\boldsymbol{\xi}_{\mathbf{k}}\cdot C_0\cdot\boldsymbol{\xi}_{\mathbf{k}})^{-1} \otimes \boldsymbol{\xi}_{\mathbf{k}}] \times [C_0[\boldsymbol{\epsilon}_{\mathbf{k}}^*]]\cdot C_0[\boldsymbol{\epsilon}_{\mathbf{k}}^{*c}]\right\}\Big) \tag{52}$$

does not hold. As a matter of fact, in order to obtain a lower bound on $\bar{\varphi}$ (respectively, $\bar{\psi}$), the infimum of the functional $F_{\Phi_0}^{(\boldsymbol{\sigma}^*)}$ (respectively, $F_{\Psi_0}^{(\boldsymbol{\epsilon}^*)}$) must be *exactly* evaluated. In other words, the sum in Eq. (38) (respectively, (41)) must be evaluated over *all* the infinite set $\hat{\mathcal{Z}}$. This fact rules numerical computations out unless the set $\mathcal{H}_f$ be constituted by fields having only a finite number of Fourier coefficients different from zero.

However, it is pointed out that, if an upper bound ψ^+ on $\bar{\psi}$ (respectively, an upper bound φ^+ on $\bar{\varphi}$) is available, then a lower bound on $\bar{\varphi}$ (respectively, $\bar{\psi}$) can be easily obtained as the Fenchel conjugate of ψ^+ (respectively, φ^+):

$$\bar{\varphi}(\bar{\boldsymbol{\epsilon}}) \le \sup_{\bar{\boldsymbol{\sigma}}\in\mathrm{Sym}} \{\bar{\boldsymbol{\sigma}}\cdot\bar{\boldsymbol{\epsilon}} - \psi^+(\bar{\boldsymbol{\sigma}})\} \tag{53}$$

(respectively,

$$\bar{\psi}(\bar{\boldsymbol{\sigma}}) \le \sup_{\bar{\boldsymbol{\epsilon}}\in\mathrm{Sym}} \{\bar{\boldsymbol{\sigma}}\cdot\bar{\boldsymbol{\epsilon}} - \varphi^+(\bar{\boldsymbol{\epsilon}})\}). \tag{54}$$

7 Applications

A composite body reinforced by parallel fibers in a periodic square arrangement is considered. The unit cell C is chosen with three mutually orthogonal sides in the directions of the fibers and of the fibers arrangement.

The matrix (m) and the fibers (f) are assumed to be made of homogeneous linear elastic transversely-isotropic materials, with the axis of transverse isotropy in the fibers direction.

It is a simple matter to verify that the homogenized potential and complementary-energy densities $\bar{\varphi}$ and $\bar{\psi}$ are quadratic functionals, and hence can be written as

$$\bar{\varphi}(\bar{\boldsymbol{\epsilon}}) = \tfrac{1}{2}\,\bar{\boldsymbol{\epsilon}}\cdot\bar{C}[\bar{\boldsymbol{\epsilon}}] \quad\text{and}\quad \bar{\psi}(\bar{\boldsymbol{\sigma}}) = \tfrac{1}{2}\,\bar{\boldsymbol{\sigma}}\cdot\bar{\mathcal{D}}[\bar{\boldsymbol{\sigma}}], \tag{55}$$

respectively. It is observed that the homogenized material is not, in general, transversely isotropic, but is at least orthotropic tetragonal.

Poor bounds on $\bar{C}$, due to Voigt (1928) and Reuss (1929), can be obtained by choosing the spaces $\mathcal{E}_f$ and $\mathcal{T}_f$ in Eqs. (42) as the null vector space:

$$\bar{C} \le c_m C_m + c_f C_f \quad\text{and}\quad \bar{C} \ge (c_m\mathcal{D}_m + c_f\mathcal{D}_f)^{-1}, \tag{56}$$

where c_m and c_f are the volume fractions of the matrix and the fibers, respectively (of course, $c_f + c_m = 1$). Better bounds on $\bar{C}$ can be carried out by choosing $\mathcal{E}_f$ and $\mathcal{T}_f$ according to the Ritz or finite element method.

On the other hand, bounds on $\bar{C}$ can be also derived by using (49) and (50), involving a reference material, which is assumed to be transversely isotropic, with the axis of transverse isotropy in the fibers direction. Simple explicit formulas of those bounds can be obtained by taking the space $\mathcal{H}_f$ of polarization fields as follows:

Downloaded 04 May 2010 to 171.66.16.27. Redistribution subject to ASME license or copyright; see http://www.asme.org/terms/Terms_Use.cfm

Table 1 Coefficients γ_1 and γ_3, in the case of square (*s*) or circular (*c*) fibers, for $c_f = 0.6$ and some values of N

N	1	2	5	10	20	50	100	200
γ_1^s	0.053272	0.086443	0.099626	0.107413	0.111490	0.113633	0.114424	0.114806
γ_3^s	0.001837	0.003806	0.004536	0.004734	0.004786	0.004798	0.004800	0.004801
γ_1^c	0.069778	0.088182	0.102115	0.105461	0.107803	0.109164	0.109638	0.109875
γ_3^c	0.000041	0.003929	0.007230	0.008490	0.009173	0.009596	0.009740	0.009812

$$\mathcal{H}_f = \{\mathbf{A}(x_1, x_2, x_3): \mathbf{A} = [1 - \chi_f(x_1, x_2)]\mathbf{A}_m + \chi_f(x_1, x_2)\mathbf{A}_f,\ \mathbf{A}_m,\ \mathbf{A}_f \in \mathrm{Sym}\}, \quad (57)$$

where χ_f is the characteristic function of the fiber.

If both $C_m - C_0$ and $C_f - C_0$ are negative (respectively, positive) definite, then by (49) (respectively, (50)) the following eigenstress-based upper bound (respectively, eigenstrain-based lower bound) can be derived:

$$\bar{C} \le C_0 + c_f \,\mathrm{sym}\, \Sigma_f + c_m \,\mathrm{sym}\, \Sigma_m \quad (58)$$

(respectively,

$$\bar{C} \ge (\mathcal{D}_0 + c_f \,\mathrm{sym}\, \Xi_f + c_m \,\mathrm{sym}\, \Xi_m)^{-1}), \quad (59)$$

where

$$\Sigma_f = [\Delta_f - \Gamma\Delta_m^{-1}\Gamma/(c_f c_m)]^{-1}(I + \Gamma\Delta_m^{-1}/c_f)$$
$$\Sigma_m = [\Delta_m - \Gamma\Delta_f^{-1}\Gamma/(c_f c_m)]^{-1}(I + \Gamma\Delta_f^{-1}/c_m) \quad (60)$$

(respectively,

$$\Xi_f = [\Theta_f - \Lambda\Theta_m^{-1}\Lambda/(c_f c_m)]^{-1}(I + \Lambda\Theta_m^{-1}/c_f)$$
$$\Xi_m = [\Theta_m - \Lambda\Theta_f^{-1}\Lambda/(c_f c_m)]^{-1}(I + \Lambda\Theta_f^{-1}/c_m)), \quad (61)$$

I denotes the fourth-order identity tensor and

$$\Delta_f = (C_f - C_0)^{-1} + \Gamma/c_f, \quad \Delta_m = (C_m - C_0)^{-1} + \Gamma/c_m \quad (62)$$

(respectively,

$$\Theta_f = (\mathcal{D}_f - \mathcal{D}_0)^{-1} + \Lambda/c_f, \quad \Theta_m = (\mathcal{D}_m - \mathcal{D}_0)^{-1} + \Lambda/c_m). \quad (63)$$

The tensors Γ and Λ, respectively related to the equilibrium and compatibility auxiliary problems, follow from Eqs. (38) and (41), respectively:

$$\Gamma_{1111} = \frac{\gamma_1}{C_{1111}} + \frac{\gamma_3}{C_{1212}}, \quad \Gamma_{2222} = \frac{\gamma_5}{C_{1111}} + \frac{\gamma_3}{C_{1212}},$$
$$\Gamma_{1212} = \frac{\gamma_3}{C_{1111}} + \frac{\gamma_1 - 2\gamma_3 + \gamma_5}{4C_{1212}},$$
$$\Gamma_{1122} = \Gamma_{2211} = \frac{\gamma_3}{C_{1111}} - \frac{\gamma_3}{C_{1212}},$$
$$\Gamma_{1112} = \Gamma_{1211} = \frac{\gamma_2}{C_{1111}} + \frac{\gamma_4 - \gamma_2}{2C_{1212}},$$
$$\Gamma_{2212} = \Gamma_{1222} = \frac{\gamma_4}{C_{1111}} + \frac{\gamma_2 - \gamma_4}{2C_{1212}},$$
$$\Gamma_{2323} = \frac{\gamma_8}{4C_{2323}}, \quad \Gamma_{2331} = \Gamma_{3123} = \frac{\gamma_7}{4C_{2323}},$$
$$\Gamma_{3131} = \frac{\gamma_6}{4C_{2323}} \quad (64)$$

and

$$\Lambda = C_0(\mathcal{D}_0\gamma_9 - \Gamma)C_0, \quad (65)$$

where the constants C_{ijhk} are the coefficients of the tensor C_0 and the following symbols have been introduced:

$$\gamma_1 = \sum_{k_1,k_2} |c_{(k_1,k_2)}|^2 \frac{\xi_1^4}{(\xi_1^2 + \xi_2^2)^2}, \quad \gamma_2 = \sum_{k_1,k_2} |c_{(k_1,k_2)}|^2 \frac{\xi_1^3\xi_2}{(\xi_1^2 + \xi_2^2)^2},$$
$$\gamma_3 = \sum_{k_1,k_2} |c_{(k_1,k_2)}|^2 \frac{\xi_1^2\xi_2^2}{(\xi_1^2 + \xi_2^2)^2}, \quad \gamma_4 = \sum_{k_1,k_2} |c_{(k_1,k_2)}|^2 \frac{\xi_1\xi_2^3}{(\xi_1^2 + \xi_2^2)^2},$$
$$\gamma_5 = \sum_{k_1,k_2} |c_{(k_1,k_2)}|^2 \frac{\xi_2^4}{(\xi_1^2 + \xi_2^2)^2}, \quad \gamma_6 = \sum_{k_1,k_2} |c_{(k_1,k_2)}|^2 \frac{\xi_1^2}{\xi_1^2 + \xi_2^2},$$
$$\gamma_7 = \sum_{k_1,k_2} |c_{(k_1,k_2)}|^2 \frac{\xi_1\xi_2}{\xi_1^2 + \xi_2^2}, \quad \gamma_8 = \sum_{k_1,k_2} |c_{(k_1,k_2)}|^2 \frac{\xi_2^2}{\xi_1^2 + \xi_2^2},$$
$$\gamma_9 = \sum_{k_1,k_2} |c_{(k_1,k_2)}|^2, \quad (66)$$

Here $|\cdot|$ denotes the modulus of the argument, the sums are performed over $[-N \ldots N] \times [-N \ldots N] \times \{0\} - \{(0, 0, 0)\}$ for some natural number N, and $c_{(k1,k2)}$ are the Fourier coefficients of the function χ_f:

$$c_{(k_1,k_2)} = \frac{1}{v}\int_c \chi_f(x_1, x_2)\, \exp[-j(\xi_1 x_1 + \xi_2 x_2)]dv. \quad (67)$$

It is a simple matter to verify that the coefficients γ_i are related by the equations

$$\gamma_1 + \gamma_3 = \gamma_6, \quad \gamma_5 + \gamma_3 = \gamma_8,$$
$$\gamma_2 + \gamma_4 = \gamma_7, \quad \text{and} \quad \gamma_6 + \gamma_8 = \gamma_9. \quad (68)$$

Moreover, since the geometry of the fibers has a square symmetry, it turns out that

$$\gamma_1 = \gamma_5, \quad \gamma_2 = \gamma_4 = 0, \quad \gamma_7 = 0 \quad \text{and} \quad \gamma_6 = \gamma_8. \quad (69)$$

The coefficients γ_1 and γ_3 have been numerically computed for several values of N, in the cases of square or circular centered fiber with volume fraction $c_f = 0.6$. The results obtained are reported in Table 1. The other coefficients can be easily deduced from γ_1 and γ_3 by using (68) and (69).

On the other hand, if both $C_m - C_0$ and $C_f - C_0$ are positive (respectively, negative) definite, then by (51) (respectively, (52)) the following eigenstress-based lower bound (respectively, eigenstrain-based upper bound) is derived:

$$\bar{C} \ge C_0 + c_f \,\mathrm{sym}\, \Sigma_f + c_m \,\mathrm{sym}\, \Sigma_m \quad (70)$$

(respectively,

$$\bar{C} \le (\mathcal{D}_0 + c_f \,\mathrm{sym}\, \Xi_f + c_m \,\mathrm{sym}\, \Xi_m)^{-1}), \quad (71)$$

which is correct only when Σ_f and Σ_m (respectively, Ξ_f and Ξ_m) are computed by taking $N \to +\infty$.

Downloaded 04 May 2010 to 171.66.16.27. Redistribution subject to ASME license or copyright; see http://www.asme.org/terms/Terms_Use.cfm

Table 2 Graphite-epoxy composite. Material properties of the constituents. Voigt and Reuss bounds. Ritz upper (U) and lower (L) bounds obtained by 400 or 900 Fourier terms.

	Epoxy	Graphite	Reuss	Voigt	Ritz (L) 400	Ritz (L) 900	Ritz (U) 400	Ritz (U) 900
C_{1111}	5.5731	14.2531	8.6222	10.7811	9.4067	9.4108	9.5270	9.4897
C_{3333}	5.5731	168.4727	12.0549	103.3128	96.3122	98.5177	103.1167	103.1115
C_{1212}	1.5923	6.0000	2.8438	4.2334	2.9348	2.9385	3.0061	2.9835
C_{1122}	2.3885	2.2600	2.9288	2.3125	2.5070	2.5061	2.4774	2.4857
C_{1133}	2.3885	4.9545	3.4653	3.9281	3.5741	3.5751	3.6013	3.5926
C_{2323}	1.5923	27.5800	3.6586	17.1840	5.4848	5.4946	6.1590	5.9398

An interesting particular case takes place when the constituent phases are well ordered, i.e., when $C_f - C_m$ is positive or negative definite. Indeed, in this case the reference material can coincide with either one of the constituent materials. Clearly, the polarization field vanishes on the constituent material assumed as reference material.

For the sake of brevity, only the case $C_f > C_m$ is considered in what follows. In this hypothesis, by taking $C_0 = C_f$ in Eq. (49) the eigenstress-based upper bound follows:

$$\bar{C} \leq C_f + c_m[(C_m - C_f)^{-1} + \Gamma/c_m]^{-1}, \tag{72}$$

while, by taking $C_0 = C_m$ in Eq. (50) the eigenstrain-based lower bound follows:

$$\bar{C} \geq (\mathcal{D}_m + c_f[(\mathcal{D}_f - \mathcal{D}_m)^{-1} + \Lambda/c_f]^{-1})^{-1}. \tag{73}$$

Moreover, by taking $C_0 = C_m$ in Eq. (51), the following eigenstress-based lower bound is obtained:

$$\bar{C} \geq C_m + c_f[(C_f - C_m)^{-1} + \Gamma/c_f]^{-1}, \tag{74}$$

while, by taking $C_0 = C_f$ in Eq. (52), the eigenstrain-based upper bound is derived:

$$\bar{C} \leq (\mathcal{D}_f + c_m[(\mathcal{D}_m - \mathcal{D}_f)^{-1} + \Lambda/c_m]^{-1})^{-1}. \tag{75}$$

It is worth noting that the bounds (74) and (75) are correct only in the limit case $N \to +\infty$.

Two numerical examples are presented. The elastic moduli are reported in GPa.

As a first example, a graphite fiber-reinforced epoxy composite, realized by circular fibers with $c_f = 0.6$ is considered. Since in this

Table 3 Graphite-epoxy composite. Eigenstress-based Hashin-Shtrikman upper bounds for some values of *N*. Graphite reference material.

N	1	2	5	10	20	50	100	200
C_{1111}	10.3676	10.1865	10.0060	9.9541	9.9210	9.9010	9.8940	9.8906
C_{3333}	103.2408	103.2162	103.1920	103.1859	103.1818	103.1793	103.1784	103.1781
C_{1212}	3.6259	3.4219	3.1941	3.1417	3.1033	3.0805	3.0725	3.0685
C_{1122}	2.3256	2.3705	2.4162	2.4340	2.4443	2.4508	2.4531	2.4542
C_{1133}	3.8080	3.7671	3.7267	3.7164	3.7096	3.7055	3.7041	3.7034
C_{2323}	15.1374	14.3720	13.5767	13.3690	13.9222	13.1455	13.1162	13.1015

Table 4 Graphite-epoxy composite. Eigenstrain-based Hashin-Shtrikman lower bounds for some values of *N*. Epoxy reference material.

N	1	2	5	10	20	50	100	200
C_{1111}	9.0664	9.1823	9.3034	9.3270	9.3451	9.3556	9.3592	9.3611
C_{3333}	19.1286	26.2288	46.8789	60.4876	75.7816	89.6575	95.8514	99.3194
C_{1212}	2.8441	2.8754	2.9032	2.9141	2.9202	2.9239	2.9252	2.9259
C_{1122}	2.6735	2.6169	2.5524	2.5427	2.5339	2.5288	2.5271	2.5262
C_{1133}	3.5219	3.5398	3.5567	3.5606	3.5637	3.5653	3.5659	3.5662
C_{2323}	4.3567	4.6619	5.0101	5.1069	5.1735	5.2140	5.2282	5.2354

Table 5 Graphite-epoxy composite. Eigenstress-based Hashin-Shtrikman incorrect lower bounds for some values of *N*. Epoxy reference material.

N	1	2	5	10	20	50	100	200
C_{1111}	9.9809	9.8056	9.4888	9.4309	9.3968	9.3767	9.3698	9.3634
C_{3333}	103.1728	103.1394	103.1109	103.1044	103.1001	103.0976	103.0967	103.0963
C_{1212}	3.1976	3.0727	2.9703	2.9523	2.9391	2.9317	2.9291	2.9278
C_{1122}	2.3350	2.4244	2.4838	2.5044	2.5148	2.5211	2.5232	2.5243
C_{1133}	3.6948	3.6390	3.5916	3.5806	3.5735	3.5693	3.5679	3.5672
C_{2323}	6.9634	6.0943	5.5092	5.3894	5.3146	5.2718	5.2573	5.2500

Table 6 Graphite-epoxy composite. Eigenstrain-based Hashin-Shtrikman incorrect upper bounds for some values of *N*. Graphite reference material.

N	1	2	5	10	20	50	100	200
C_{1111}	9.5290	9.6846	9.8230	9.8495	9.8685	9.8794	9.8832	9.8851
C_{3333}	82.2214	92.2505	99.6305	101.2103	102.2086	102.7837	102.9805	103.0789
C_{1212}	2.8448	2.9353	3.0082	3.0352	3.0495	3.0584	3.0614	3.0629
C_{1122}	2.5153	2.4868	2.4595	2.4591	2.4570	2.4561	2.4557	2.4555
C_{1133}	3.6133	3.6514	3.6847	3.6926	3.6977	3.7006	3.7017	3.7022
C_{2323}	10.2266	11.5243	12.5611	12.7929	12.9412	13.0274	13.0570	13.0718

Downloaded 04 May 2010 to 171.66.16.27. Redistribution subject to ASME license or copyright; see http://www.asme.org/terms/Terms_Use.cfm

case the constituent materials are well ordered, the reference material is chosen to coincide with either matrix or fibers. The material constants of matrix and fibers, the Voigt and Reuss bounds, as well as the upper (U) and lower (L) bounds obtained via the Ritz method by using 400 or 900 Fourier series terms are reported in Table 2. The eigenstress-based upper bound, the eigenstrain-based lower bound, the incorrect eigenstress-based lower bound, and the incorrect eigenstrain-based upper bound, obtained by Eqs. (72), (73), (74), and (75), respectively, are reported in Tables 3, 4, 5, and 6 for different values of N.

As a second example, a square-fiber-reinforced composite with $c_f = 0.6$, realized by isotropic ill-ordered constituent materials, is considered. The first Lamé constant and the bulk modulus of the constituents and of the reference materials (stiffer (h) and softer (s) than the constituents) are $\mu_m = 1$, $\kappa_m = 20$, $\mu_f = 10$, $\kappa_f = 15$, $\mu_h = 10.001$, $\kappa_h = 20.001$, $\mu_s = 0.9999$, and $\kappa_s = 14.999$. The Voigt and Reuss bounds, as well as the upper (U) and lower (L) bounds obtained via the finite element method by using a 10×10 or 20×20 discretization of the unit cell are reported in Table 7. The eigenstress-based upper bound, the eigenstrain-based lower bound, the incorrect eigenstress-based lower bound, and the incorrect eigenstrain-based upper bound, obtained by equations (72), (73), (74), and (75), respectively, are reported in Tables 8, 9, 10, and 11 for different values of N.

It is worth noting that the bounds (72) and (73), obtained by using the minimum principles and reported in Tables 3, 4, 8, and 9, improve as N grows up. On the other hand, the incorrect bounds (74) and (75), obtained by using the mixed variational principles and reported in Tables 5, 6, 10, and 11, become worse as N grows up. Moreover, the results marked with an underline in the latter tables are inconsistent with the bounds reported in Tables 2 and 7.

Table 7 Composite with ill-ordered constituents. Voigt and Reuss bounds. Finite element (FEM) upper (U) and lower (L) bounds obtained by a 10 × 10 or 20 × 20 discretization of the unit cell.

	Reuss	Voigt	FEM (L) 10×10	FEM (L) 20×20	FEM (U) 10×10	FEM (U) 20×20
C_{1111}	19.5652	25.5333	23.6835	23.8620	24.3527	24.1726
C_{3333}	19.5652	25.5333	23.5097	23.8067	24.1441	24.1327
C_{1212}	2.1739	6.4000	2.2646	2.2668	2.2879	2.2797
C_{1122}	15.2174	12.7333	13.9786	14.0459	13.8222	14.0015
C_{1133}	15.2174	12.7333	12.8749	12.6840	12.4807	12.4787
C_{2323}	2.1739	6.4000	2.9559	2.9737	3.0049	2.9873

The previous examples show that the approximations of the saddle-point Hashin-Shtrikman principles (25) and (29) may really lead to erroneous bounds. This conclusion does not clearly appear when a large value of N is adopted (e.g., Nemat-Nasser and Hori, 1993). Nevertheless, a bound has been *surely* computed by approximating (25) or (29) only if the involved auxiliary problem has been *exactly* solved ($N \to \infty$ in Eqs. (51) and (52)).

On the other hand, the numerical results show the capability of the mixed variational principles to provide excellent estimates on the overall properties of heterogeneous materials even if a small numerical effort is used (e.g., Iwakuma and Nemat-Nasser, 1993; Luciano and Barbero, 1994).

Table 8 Composite with ill-ordered constituents. Eigenstress-based Hashin-Shtrikman upper bounds for some values of *N*. Reference material stiffer than the constituents.

N	1	2	5	10	20	50	100	200
C_{1111}	25.1808	24.8951	24.7725	24.7065	24.6733	24.6563	24.6501	24.6471
C_{3333}	25.1112	24.8167	24.6941	24.6221	24.5844	24.5646	24.5572	24.5537
C_{1212}	5.2855	4.1735	3.5698	3.1451	2.8982	2.7608	2.7086	2.6832
C_{1122}	13.0580	13.3241	13.4387	13.5000	13.5306	13.5463	13.5520	13.5548
C_{1133}	12.6566	12.6030	12.5807	12.5677	12.5608	12.5572	12.5559	12.5552
C_{2323}	5.8905	5.4828	5.2981	5.1851	5.1245	5.0923	5.0804	5.0745

Table 9 Composite with ill-ordered constituents. Eigenstrain-based Hashin-Shtrikman lower bounds for some values of *N*. Reference material softer than the constituents.

N	1	2	5	10	20	50	100	200
C_{1111}	20.3867	21.4686	22.2249	22.8549	23.2659	23.5125	23.6101	23.6577
C_{3333}	20.3154	21.4429	22.3114	23.0599	23.5640	23.8718	23.9942	24.0550
C_{1212}	2.2009	2.2312	2.2429	2.2462	2.2469	2.2471	2.2472	2.2472
C_{1122}	14.9598	14.7180	14.6072	14.5327	14.4956	14.4773	14.4704	14.4680
C_{1133}	14.7745	14.0972	13.5722	13.1187	12.8130	12.6262	12.5520	12.5150
C_{2323}	2.4311	2.6630	2.7772	2.8507	2.8903	2.9119	2.9205	2.9239

Table 10 Composite with ill-ordered constituents. Eigenstress-based Hashin-Shtrikman incorrect lower bounds for some values of *N*. Reference material softer than the constituents.

N	1	2	5	10	20	50	100	200
C_{1111}	24.5916	24.0083	23.8233	23.7558	23.7280	23.7159	23.7125	23.7100
C_{3333}	24.8030	24.4128	24.2716	24.1937	24.1541	24.1337	24.1263	24.1227
C_{1212}	3.1177	2.5456	2.3954	2.3178	2.2799	2.2608	2.2540	2.2506
C_{1122}	13.6268	14.1842	14.3599	14.4223	14.4474	14.4582	14.4612	14.4634
C_{1133}	12.6006	12.5296	12.5039	12.4898	12.4826	12.4789	12.4775	12.4768
C_{2323}	3.9562	3.2934	3.1066	3.0132	2.9672	2.9443	2.9366	2.9320

Table 11 Composite with ill-ordered constituents. Eigenstrain-based Hashin-Shtrikman incorrect upper bounds for some values of *N*. Reference material softer than the constituents.

N	1	2	5	10	20	50	100	200
C_{1111}	22.6755	23.8572	24.2379	24.4466	24.5513	24.6052	24.6249	24.6343
C_{3333}	22.7132	23.8474	24.1988	24.3818	24.4716	24.5173	24.5339	24.5419
C_{1212}	2.3660	2.5616	2.6317	2.6505	2.6553	2.6566	2.6567	2.6568
C_{1122}	14.2506	13.8529	13.7174	13.6368	13.5952	13.5734	13.5654	13.5616
C_{1133}	13.5007	12.9083	12.7298	12.6381	12.5934	12.5708	12.5625	12.5586
C_{2323}	3.8357	4.5706	4.8154	4.9463	5.0112	5.0446	5.0568	5.0625

Downloaded 04 May 2010 to 171.66.16.27. Redistribution subject to ASME license or copyright; see http://www.asme.org/terms/Terms_Use.cfm

8 Conclusions

In this work the problem of bounding the overall elastic properties of heterogeneous media was approached via the Hashin-Shtrikman variational principles. It was shown that two of the Hashin-Shtrikman principles are indeed minimum principles, while the other two are saddle point principles. As a consequence, every approximation of the former ones is able to supply bounds on the overall properties of composite bodies, while approximations of the latter ones may lead to inconsistent bounds.

It is worth noting that similar situations take place when bounds on the overall electric, piezoelectric, or other properties of heterogeneous media are searched for via the Hashin-Shtrikman variational principles.

Acknowledgments

The authors wish to thank Prof. Franco Maceri for valuable comments on this paper.

The financial supports of the Italian National Research Council (CNR), of the Italian Ministry of University and Research (MURST), and of the Italian Space Agency (ASI) are gratefully acknowledged.

References

Aboudi, J., 1991, *Mechanics of Composite Materials: A Unified Micromechanical Approach,* Elsevier, Amsterdam.

Christensen, R. M., 1990, "A Critical Evaluation for a Class of Micromechanics Models," *J. Mech Phys. Solids,* Vol. 38, pp. 379–404.

Ekeland, I., and Temam, R., 1976, *Convex Analysis and Variational Problems,* North-Holland, Amsterdam, pp. 34–45, 165–185.

Eshelby, J. D., 1957, "The Determination of the Elastic Field of an Ellipsoidal Inclusion, and Related Problems," *Proc. R. Soc. London,* Vol. A241, pp. 376–396.

Hashin, Z., and Shtrikman, S., 1962a, "On Some Variational Principles in Anisotropic and Nonhomogeneous Elasticity," *J. Mech. Phys. Solids,* Vol. 10, pp. 335–342.

Hashin, Z., and Shtrikman, S., 1962b, "A Variational Approach to the Theory of the Elastic Behavior of Multiphase Materials," *J. Mech. Phys. Solids,* Vol. 11, pp. 127–140.

Iwakuma, T., and Nemat-Nasser, S., 1983, "Composites With Periodic Microstructure," *Comput. Structures,* Vol. 16, pp. 13–19.

Luciano, R., and Barbero, E., 1994, "Formulas for the Stiffness of Composites With Periodic Microstructure," *Int. J. Solids Struct.,* Vol. 31, pp. 2933–2944.

Milton, W., and Kohn, R. V., 1988, "Variational Bounds on the Effective Moduli of Anisotropic Composites," *J. Mech. Phys. Solids,* Vol. 36, pp. 597–629.

Mulinec, H., and Suquet, P., 1994, "A Fast Numerical Method for Computing the Linear and Nonlinear Mechanical Properties of Composites," *C. R. Acad. Sci. Paris II,* Vol. 318, pp. 1417–1423.

Mura, T., 1987, *Micromechanics of Defects in Solids,* Martinus Nijhoff, Dordrecht.

Nemat-Nasser, S., Yu, N., and Hori, H., 1993, "Bounds and Estimates of Overall Moduli of Composites With Periodic Microstructure," *Mech. Mater.,* Vol. 15, pp. 163–181.

Panagiotopoulos, P. D., 1985, *Inequality Problems in Mechanics and Applications,* Birkhäuser, Boston, pp. 61–114.

Ponte Castañeda, P., 1991, "The Effective Mechanical Properties of Nonlinear Isotropic Composites," *J. Mech. Phys. Solids,* Vol. 39, pp. 45–71.

Reuss, A., 1929, "Berechnung der Fliessgrenze von Mischkristallen auf Grund der Plastizitätsbedingung für Einkristalle," *Z. Angew. Math. Mech.,* Vol. 9, pp. 49–58.

Suquet, P., 1990, "A Simplified Method for the Prediction of Homogenized Elastic Properties of Composites With a Periodic Structure," *C. R. Acad. Sci. Paris II,* Vol. 311, pp. 769–774.

Talbot, D. R. S., and Willis, J. R., 1985, "Variational Principles for Inhomogeneous Nonlinear Media," *IMA J. Appl. Math.,* Vol. 35, pp. 39–54.

Voigt, W., 1928, *Lehrbuch der Kristallphysik,* Teubner, Leipzig.

Walpole, L. J., 1966, "On Bounds for the Overall Elastic Moduli of Inhomogeneous Systems—I and II," *J. Mech. Phys. Solids,* Vol. 14, pp. 151–162, 289–301.

Walpole, L. J., 1981, "Elastic Behavior of Composite Materials: Theoretical Foundations," *Advances in Applied Mechanics,* Vol. 21, C. S. Yih, ed., Academic Press, New York, pp. 169–242.

Willis, J. R., 1981, "Variational and Related Methods for the Overall Properties of Composites," *Advances in Applied Mechanics,* Vol. 21, C. S. Yih, ed., Academic Press, New York, pp. 1–78.

Willis, J. R., 1989, "The Structure of Overall Constitutive Relations for a Class of Nonlinear Composites," *IMA J. Appl. Math.,* Vol. 43, pp. 231–242.

Willis, J. R., 1991, "On Methods for Bounding the Overall Properties of Nonlinear Composites," ASME JOURNAL OF APPLIED MECHANICS, Vol. 39, pp. 73–86.

Downloaded 04 May 2010 to 171.66.16.27. Redistribution subject to ASME license or copyright; see http://www.asme.org/terms/Terms_Use.cfm

M. M. Carroll
Rice University,
George R. Brown School of Engineering,
6100 Main Street, MS 364
Houston, TX 77005-1892
Fellow ASME

F. J. Rooney
Department of Civil Engineering,
University of California,
Berkeley, CA 94720
Mem. ASME

Singular Solutions in Second-Order Elasticity

The problems of a concentrated point force in an infinite medium (Kelvin's problem), or applied normal to the boundary of a half-space (Boussinesq's problem), as well as the corresponding problems for a concentrated couple, are solved to second order for incompressible isotropic elastic solids. The solutions are based on a simplified form of the second-order equations, obtained previously, and use of the Love's function representation for axisymmetric problems in the linear theory.

1 Introduction

For a broad class of problems in finite elastostatics, the boundary conditions allow definition of a small parameter (ϵ, say), and solutions may be obtained by successive approximations. When the loading is specified with respect to the undeformed body, the solution for the displacement and stress to order ϵ^n may be obtained by solving a sequence of n linear problems on the undeformed region. For compressible materials, each of these problems is a classical problem of linear elastostatics. For incompressible materials, it is necessary to introduce appropriate transformations in order to reduce the incompressibility condition to the classical form (cf. Chan and Carlson, 1970; Hill, 1973). In particular, the second-order problems, for compressible or incompressible materials, involve induced body forces, and surface displacements or tractions, which are of the second degree in the classical first-order solutions.

In an earlier paper (Carroll and Rooney, 1984), we simplified the second-order problem for incompressible isotropic solids, by identifying that part of the body force which is conservative and so can be absorbed into the pressure. For some problems, including Saint Venant torsion, plane strain and antiplane strain, the entire second-order body force is conservative and so the second-order problem reduces to a classical problem with no body force.

Even when the total second-order body force is not conservative, the identification of a conservative part (Carroll and Rooney, 1984) simplifies the second-order problem. We now take advantage of this simplification to solve some singular problems to second order. Specifically, we treat a concentrated point force acting in an infinite medium (Kelvin's problem), or applied normal to the boundary of a half-space (Boussinesq's problem) together with the corresponding problems of a couple in an infinite medium and applied normal to the boundary of a half-space.

We make use of the Love's function representation of solutions of axisymmetric problems with axial body forces. The solution of the second-order problems for media of infinite extent involves finding particular integrals of the inhomogeneous biharmonic equation. The solution of Kelvin's problem was given previously by Selvadurai (1970). The first-order stresses, for both problems, are such that the plane normal to the direction of the force or couple is free of traction except at the point of application. Thus, the first-order solutions for the infinite medium are also the first-order solution for the corresponding half-space problems. For the second-order problems, the solutions for the whole space give normal tractions on the boundary of the half-space. These tractions vary as r^{-4} for the concentrated force problem, and as r^{-6} for the concentrated moment problem, where r is the radial coordinate in a cylindrical polar system. For such singular tractions, the Hankel transform method (Terezawa, 1951) leads to divergent integrals. However, we solve the problem by finding the appropriate Love function.

2 Basic Equations

Consider a homogeneous, isotropic, incompressible elastic body, which occupies a region R_0 with boundary ∂R_0 in an undistorted reference configuration, and is held in equilibrium and occupies a region R with boundary ∂R. Suppose that there is no applied body force and that tractions are specified on ∂R_0.

Let $\mathbf{X}$ and $\mathbf{x}$ denote the position vectors of a particle before and after deformation. The governing equations are (a) the incompressibility condition

$$\det \mathbf{F} = 1; \quad \mathbf{F} = \text{Grad } \mathbf{x}, \tag{2.1}$$

(b) the equilibrium equation

$$\text{Div } \mathbf{P} = \mathbf{0}, \tag{2.2}$$

where $\mathbf{P}$ is the nonsymmetric Piola-Kirchoff stress tensor, (c) the constitutive equation

$$\mathbf{P} = -\Pi(\mathbf{F}^{-1})^T + \frac{\partial W}{\partial \mathbf{F}}, \tag{2.3}$$

where Π is an undetermined pressure and

$$W = W(I_1, I_2); \quad I_1 = \text{tr } \mathbf{B}; \quad I_2 = \text{tr } \mathbf{B}^{-1}; \quad \mathbf{B} = \mathbf{F}\mathbf{F}^T, \tag{2.4}$$

and (d) the boundary condition

$$\mathbf{P}\mathbf{n} = \epsilon \mathbf{s}(\mathbf{X}) \quad \text{on} \quad \partial R_0, \tag{2.5}$$

where $\mathbf{n}$ is the unit outward normal on ∂R_0 and ϵ is some small parameter.

Assume that the displacements and stresses admit power series expansions in ϵ, so that

$$\mathbf{x} - \mathbf{X} = \epsilon \mathbf{u} + \epsilon^2 \mathbf{v} + \ldots \tag{2.6}$$

and

$$\mathbf{P} = \epsilon \mathbf{S} + \epsilon^2 \mathbf{T} + \ldots \tag{2.7}$$

where $\mathbf{u}$, $\mathbf{v}$, $\mathbf{S}$, and $\mathbf{T}$ are functions of $\mathbf{X}$. We introduce material constants μ and κ, defined by

$$\mu = 2(C_1 + C_2); \quad \kappa = C_1 - C_2; \quad C_i = \frac{\partial W}{\partial I_i}(3, 3). \tag{2.8}$$

Contributed by the Applied Mechanics Division of THE AMERICAN SOCIETY OF MECHANICAL ENGINEERS for publication in the ASME JOURNAL OF APPLIED MECHANICS.
Discussion on the paper should be addressed to the Technical Editor, Professor Lewis T. Wheeler, Department of Mechanical Engineering, University of Houston, Houston, TX 77204-4792, and will be accepted until four months after final publication of the paper itself in the ASME JOURNAL OF APPLIED MECHANICS.
Manuscript received by the ASME Applied Mechanics Division, June 26, 1997; final revision, Aug. 16, 1999. Associate Technical Editor: L. T. Wheeler.

 Copyright © 1999 by ASME

Downloaded 04 May 2010 to 171.66.16.27. Redistribution subject to ASME license or copyright; see http://www.asme.org/terms/Terms_Use.cfm

Substituting the power series expansions (2.6) and (2.7) into the governing equations and equating the coefficients of ϵ and ϵ^2 to zero gives the first-order and second-order equations.

The First-Order Problem. The first-order equations are

$$\text{Div } \mathbf{u} = 0 \tag{2.9}$$

$$\text{Div } \mathbf{S} = \mathbf{0} \tag{2.10}$$

$$\mathbf{S} = -p\mathbf{1} + 2\mu\mathbf{E}; \quad \mathbf{E} = \tfrac{1}{2}\{\text{Grad } \mathbf{u} + (\text{Grad } \mathbf{u})^T\} \tag{2.11}$$

where p is the first-order pressure, $\mathbf{1}$ is the unit tensor, and

$$\mathbf{Sn} = \mathbf{s} \quad \text{on} \quad \partial R_0. \tag{2.12}$$

This is the classical problem for an incompressible, isotropic material with shear modulus μ, and $\mathbf{E}$ is the infinitesimal strain tensor.

The Second-Order Problem. The second-order equations are

$$\text{Div } \mathbf{v} = \tfrac{1}{2} \text{ tr } \{(\text{Grad } \mathbf{u})^2\} \tag{2.13}$$

$$\text{Div } \mathbf{T} = \mathbf{0} \tag{2.14}$$

$$\mathbf{T} = -q\mathbf{1} + \mu[\text{Grad } \mathbf{v} + (\text{Grad } \mathbf{v})^T - \{(\text{grad } \mathbf{u})^2\}^T] + p(\text{Grad } \mathbf{u})^T - 8C_2\mathbf{E}^2 \tag{2.15}$$

where q is the second-order pressure, and

$$\mathbf{Tn} = \mathbf{0} \quad \text{on} \quad \partial R_0. \tag{2.16}$$

There is an additional condition (Signorini's compatibility condition)

$$\int_{\partial R_0} \mathbf{u} \times \mathbf{s} dA = \mathbf{0} \tag{2.17}$$

on the first-order solution. This serves to determine the first-order rigid displacement so that the second-order problem is well posed.

The second-order problem can be reduced to a classical linear problem on R_0 (cf. Chan and Carlson, 1970)

$$\text{Div } \mathbf{v}' = 0 \tag{2.18}$$

$$\text{Div } \mathbf{T}' + \mathbf{f}' = \mathbf{0} \tag{2.19}$$

$$\mathbf{T}' = -q'\mathbf{1} + \mu\{\text{Grad } \mathbf{v}' + (\text{Grad } \mathbf{v}')^T\} \tag{2.20}$$

$$\mathbf{T}'\mathbf{n} = \mathbf{t}' \quad \text{on} \quad \partial R_0 \tag{2.21}$$

where

$$\mathbf{v}' = \mathbf{v} - \tfrac{1}{2}\mathcal{D}\mathbf{u}; \quad \mathcal{D} = \mathbf{u} \cdot \text{Grad} \tag{2.22}$$

$$\mathbf{T}' = \mathbf{T} - q^+\mathbf{1} - \mathbf{T}^* \tag{2.23}$$

$$\mathbf{f}' = 4\kappa \text{ Div } \mathbf{E}^2 \tag{2.24}$$

$$\mathbf{t}' = -(q^+\mathbf{1} + \mathbf{T}^*)\mathbf{n} \tag{2.25}$$

and

$$q^+ = -\tfrac{1}{2}(\mathcal{D}p - \mu \text{ tr } \mathbf{E}^2) \tag{2.26}$$

$$\mathbf{T}^* = \mu(\mathcal{D}\mathbf{E} + \mathbf{EW} + \mathbf{WE}) + p(\mathbf{E} - \mathbf{W}) + (4\kappa - 2\mu)\mathbf{E}^2 \tag{2.27}$$

$$\mathbf{W} = \tfrac{1}{2}\{\text{Grad } \mathbf{u} + (\text{Grad } \mathbf{u})^T\}. \tag{2.28}$$

Love's Stress Function. It will be convenient to use Love's stress function representation for the solution of axisymmetric problems with axial body forces (cf. Little, 1973). In a cylindrical system (r, θ, z), with unit base vectors $(\mathbf{e}_r, \mathbf{e}_\theta, \mathbf{e}_z)$, the solution of the system (2.18)–(2.20), with body force field

$$\mathbf{f}' = F(r, z)\mathbf{e}_z \tag{2.29}$$

is given by

$$2\mu\mathbf{v}' = (\nabla^2\Phi)\mathbf{e}_z - \text{Grad } \frac{\partial\Phi}{\partial z} \tag{2.30}$$

and

$$\mathbf{T}' = \tfrac{1}{2}\nabla^2 \frac{\partial\Phi}{\partial z}\mathbf{1} + \mu\{\text{Grad } \mathbf{v}' + (\text{Grad } \mathbf{v}')^T\} \tag{2.31}$$

where Φ satisfies

$$\nabla^4\Phi = -2F. \tag{2.32}$$

3 Kelvin's Problem

In the linear theory, the displacement field $\mathbf{u}$ in an infinite medium, with a concentrated force of strength A acting at the origin, is given by (cf. Carroll and Rooney, 1984)

$$\mathbf{u} = \frac{A}{4\pi\mu R^3}\{rz\mathbf{e}_r + (r^2 + 2z^2)\mathbf{e}_z\}; \quad R^2 = r^2 + z^2 \tag{3.1}$$

where (r, θ, z) are cylindrical polar coordinates, $(\mathbf{e}_r, \mathbf{e}_\theta, \mathbf{e}_z)$ are unit base vectors, and the concentrated force acts in the positive z-direction. It is convenient to introduce a length L, such that

$$\epsilon = \frac{A}{4\pi\mu L^2} \tag{3.2}$$

is a small parameter, and to nondimensionalise lengths with respect to L. It is evident from (3.1) and (3.2) that displacement gradients at a distance L from the origin are of order ϵ. Thus, L might be considered the distance from the point of application of the force at which the linear solution is acceptable.

With this nondimensionalisation, the first-order solution is generated by the Love function $\Phi = 2\mu R$, with first-order displacement field

$$\mathbf{u} = \frac{1}{R^3}\{rz\mathbf{e}_r + (r^2 + 2z^2)\mathbf{e}_z\}. \tag{3.3}$$

The first-order strain, rotation, and stress are

$$\mathbf{E} = \frac{z}{R^5}\{(-2r^2 + z^2)\mathbf{e}_r \otimes \mathbf{e}_r + (r^2 + z^2)\mathbf{e}_\theta \otimes \mathbf{e}_\theta + (r^2 - 2z^2)\mathbf{e}_z \otimes \mathbf{e}_z - 3rz(\mathbf{e}_r \otimes \mathbf{e}_z + \mathbf{e}_z \otimes \mathbf{e}_r) \tag{3.4}$$

$$\mathbf{W} = \frac{r}{R^3}(\mathbf{e}_r \otimes \mathbf{e}_z - \mathbf{e}_z \otimes \mathbf{e}_r) \tag{3.5}$$

$$\mathbf{S} = -p\mathbf{1} + 2\mu\mathbf{E}; \quad p = 2\mu z/R^3. \tag{3.6}$$

The second-order body force $\mathbf{f}'$ is given by (2.24) and (3.4), and it may be written as

$$\mathbf{f}' = 4\kappa\left(\text{Grad } \frac{2z^2}{R^6} - \frac{2z}{R^6}\mathbf{e}_z\right). \tag{3.7}$$

The first term is conservative and can be absorbed into the pressure, thus

$$\mathbf{T}' = -q^{(1)}\mathbf{1} + \mathbf{T}^{(2)}; \quad q^{(1)} = \frac{8\kappa z^2}{R^6} \tag{3.8}$$

and

Downloaded 04 May 2010 to 171.66.16.27. Redistribution subject to ASME license or copyright; see http://www.asme.org/terms/Terms_Use.cfm

$$\text{Div } \mathbf{T}^{(2)} - \frac{8\kappa z}{R^6}\,\mathbf{e}_z = \mathbf{0}. \tag{3.9}$$

A particular solution of (2.32), with body force in (3.9), is

$$\Phi^{(2)} = \frac{-2\kappa z}{R^2}. \tag{3.10}$$

The corresponding displacement, given by (2.30) and (3.10), is

$$\mathbf{v}' = \mathbf{v}^{(2)} = \frac{2\kappa}{\mu R^6}\{r(3z^2 - r^2)\mathbf{e}_r + 2z(z^2 - r^2)\mathbf{e}_z\}. \tag{3.11}$$

The stress is given by (2.31), (3.10), and (3.11) as

$$\mathbf{T}' = \mathbf{T}^{(2)} = \frac{2\kappa}{R^8}\begin{pmatrix} 7r^4 - 38r^2z^2 + 3z^4 & 0 & 4rz(5r^2 - 7z^2) \\ 0 & R^2(3z^2 - r^2) & 0 \\ 4rz(5r^2 - 7z^2) & 0 & -3(r^4 - 10r^2z^2 + 5z^4) \end{pmatrix}. \tag{3.12}$$

The second-order displacement is given by (2.22), (3.3), and (3.11) as

$$\mathbf{v}^{(K)} = \frac{r}{2\mu R^6}(\mu - 4\kappa)(r^2 - 3z^2)\mathbf{e}_r + \frac{2z}{\mu R^6}\{-\mu z^2 + 2\kappa(z^2 - r^2)\}\mathbf{e}_z \tag{3.13}$$

where the superscript K has been attached for later reference. The second-order stress is given by the formulae (2.23), (2.26), (2.27) and the results obtained in this section as

$$\mathbf{T}^{(K)} = \frac{3\mu}{R^8}\begin{pmatrix} -r^4 + 3r^2z^2 + z^4 & 0 & -3r^3z \\ 0 & z^2R^2 & 0 \\ rz(2z^2 - r^2) & 0 & z^2(z^2 - 2r^2) \end{pmatrix} + \frac{2\kappa}{R^8}\begin{pmatrix} 7r^4 - 34r^2z^2 + z^4 & 0 & 2rz(10r^2 - 11z^2) \\ 0 & R^2(z^2 - r^2) & 0 \\ 2rz(10r^2 - 11z^2) & 0 & -3r^4 + 28r^2z^2 - 11z^4 \end{pmatrix}. \tag{3.14}$$

This second-order solution of Kelvin's problem is in agreement with that of Selvadurai (1970).

4 Boussinesq's Problem

The problem of Boussinesq is that of a concentrated normal force on the boundary of a half-space ($z > 0$, say). The solution must satisfy the following conditions:

(a) All stress components tend to zero at infinity.
(b) The stress singularity at the origin is equivalent to a concentrated force $A\mathbf{e}_z$.
(c) The tractions vanish elsewhere on the boundary $z = 0$.

In the classical linear theory, for incompressible isotropic solids, the solution of Kelvin's problem is also the solution of Boussinesq's problem. This is evident from (3.4) and (3.6), since the tractions associated with the first-order stress $\mathbf{S}$ vanish on $z = 0$. The solution of Kelvin's problem to second order, however, is not a solution of Boussinesq's problem. In fact, it follows from (3.14) that the Kelvin solution gives second-order tractions on the plane $z = 0$, which are given by

$$-\mathbf{T}^{(K)}\mathbf{e}_z|_{z=0} = \frac{6\kappa}{r^4}\,\mathbf{e}_z. \tag{4.1}$$

Accordingly, the solution of Boussinesq's problem to second order is found by superposing on the Kelvin solution a solution of the classical linear problem, with no body force, which meets condition (a) above and gives rise to normal tractions on $z = 0$ which cancel those in (4.1).

The solution of this linear problem presents some difficulty. First, the Hankel transform technique developed by Terezawa (Sneddon, 1951) does not work for the normal loading Cr^{-4}, because the inverse transform integral diverges (see Selvadurai, 1970). Secondly, elementary Love functions involving powers of z and R generate solutions with normal tractions Cr^{-n} on $z = 0$ only if n is an odd integer. However, it can be shown that the appropriate Love function for the problem under consideration is

$$\Phi^{(3)} = \frac{3\kappa}{2}\left\{\frac{R^2 + z^2}{R^3}\log\left(\frac{R + z}{R^2}\right) - \frac{2R + z}{R^2}\right\}. \tag{4.2}$$

The corresponding displacement $\mathbf{v}^{(3)}$ and stress $\mathbf{T}^{(3)}$ are obtained from (2.30) and (2.31). The second-order displacement for Boussinesq's problem is obtained by adding $\mathbf{v}^{(3)}$ to $\mathbf{v}^{(K)}$, given in (3.13), leading to

$$v_r^{(B)} = \frac{3\kappa rz}{4\mu R^7}\left\{3(r^2 - 4z^2)\log\left(\frac{R + z}{R^2}\right) + r^2 + \frac{z(13r^2 - 2z^2)}{R + z}\right\} + \frac{r}{2\mu R^6}(\mu - 4\kappa)(r^2 - 3z^2)$$

$$v_z^{(B)} = \frac{3\kappa}{4\mu R^7}\left\{(r^4 + 8r^2z^2 - 8z^4)\log\left(\frac{R + z}{R^2}\right) - zR(r^2 - 14z^2) + 4z^2(r^2 - 3z^2)\right\} + \frac{2z}{\mu R^6}\{-\mu z^2 + 2\kappa(z^2 - r^2)\}. \tag{4.3}$$

The second-order stress components are obtained by adding $\mathbf{T}^{(3)}$ to $\mathbf{T}^{(K)}$, given in (3.14), leading to

$$T_{rr}^{(B)} = \frac{3\kappa}{2}\left\{\left(-\frac{21z}{R^5} + \frac{120z^3}{R^7} - \frac{105z^5}{R^9}\right)\log\left(\frac{R + z}{R}\right) + \frac{1}{R(R + z)}\left(\frac{z}{R^3} - \frac{3z^2}{R^5}\right)\right\} + \frac{\mu}{R^8}(-3r^4 + 9r^2z^2 + 3z^4) + \kappa\left\{\frac{20}{R^4} - \frac{21z}{R^5} - \frac{219z^2}{R^6} + \frac{192z^3}{R^7} + \frac{512z^4}{2R^8} - \frac{213z^5}{R^9}\right\}$$

$$T_{\theta\theta}^{(B)} = \frac{3\kappa}{2}\left\{-\frac{6z}{R^5}\log\frac{R + z}{R^2} - \frac{1}{R(R + z)}\left(\frac{z}{R^3} - \frac{3z^2}{R^5}\right)\right\} + \frac{3\mu z^2}{R^6} + \kappa\left\{\frac{8}{R^4} - \frac{6z}{R^5} - \frac{z^2}{2R^6}\right\}$$

$$T_{zz}^{(B)} = \frac{3\kappa}{2}\left\{\left(-\frac{75z^3}{R^7} + \frac{105z^5}{R^9}\right)\log\left(\frac{R + z}{R}\right)\right\} + \mu\left\{-\frac{6z^2}{R^6} + \frac{9z^4}{R^8}\right\} + \kappa\left\{\frac{128z^2}{R^6} - \frac{120z^3}{R^7} - \frac{513z^4}{2R^8} + \frac{213z^5}{R^9}\right\}$$

$$T_{rz}^{(B)} = \frac{3\kappa}{2}\left\{\left(-\frac{45rz^2}{R^7} + \frac{105rz^4}{R^9}\right)\log\left(\frac{R + z}{R^2}\right) + \left(\frac{9z^2}{R^5} - \frac{15z^4}{R^7}\right)\frac{r}{R(R + z)}\right\} + \kappa\left\{\frac{64rz}{R^6} - \frac{72rz^2}{R^7} - \frac{219rz^3}{R^8} + \frac{213rz^4}{R^9}\right\} - \frac{9\mu r^3 z}{R^8}$$

Downloaded 04 May 2010 to 171.66.16.27. Redistribution subject to ASME license or copyright; see http://www.asme.org/terms/Terms_Use.cfm

$$T^{(B)}_{zr} = \frac{3\kappa}{2}\left\{\left(-\frac{45rz^2}{R^7}+\frac{105rz^4}{R^9}\right)\log\left(\frac{R+z}{R^2}\right)+\frac{r}{R(R+z)}\left(\frac{9z^2}{R^5}-\frac{15z^4}{R^7}\right)\right\}+\kappa\left\{\frac{64rz}{R^6}-\frac{72rz^2}{R^7}-\frac{219rz^3}{R^8}+\frac{213rz^4}{R^9}\right\}+\mu\left\{-\frac{3rz}{R^6}+\frac{9rz^3}{R^8}\right\}. \quad (4.4)$$

6 Concentrated Moment in an Infinite Medium

The first-order displacement field resulting from a concentrated couple of strength B acting at the origin with its axis in the z-direction is

$$\mathbf{u} = \frac{3Br}{4\pi\mu R^3}\mathbf{e}_\theta. \quad (5.1)$$

We again introduce a length l so that

$$\epsilon = \frac{3B}{4\pi\mu l^3} \quad (5.2)$$

is a small parameter and nondimensionalize with respect to l. Again we may regard l as the distance from the point of application at which the linear solution is acceptable. After nondimensionalizing, the first-order displacement field is

$$\mathbf{u} = \frac{r}{R^3}\mathbf{e}_\theta. \quad (5.3)$$

The first-order strain and rotation are

$$\mathbf{E} = -\frac{3r}{2R^5}\{r(\mathbf{e}_r\otimes\mathbf{e}_\theta+\mathbf{e}_\theta\otimes\mathbf{e}_r)+z(\mathbf{e}_\theta\otimes\mathbf{e}_z+\mathbf{e}_z\otimes\mathbf{e}_\theta)\} \quad (5.4)$$

$$\mathbf{W} = \frac{1}{2R^5}\{(r^2-2z^2)(\mathbf{e}_r\otimes\mathbf{e}_\theta-\mathbf{e}_\theta\otimes\mathbf{e}_r)-3rz(\mathbf{e}_\theta\otimes\mathbf{e}_z-\mathbf{e}_z\otimes\mathbf{e}_\theta)\} \quad (5.5)$$

and the first-order pressure is zero, so

$$\mathbf{S} = 2\mu\mathbf{E}. \quad (5.6)$$

The second-order body force is given by (2.24) and (5.4), and may be written as

$$\mathbf{f}' = \frac{3\kappa}{2}\,\mathrm{Grad}\left(\frac{5r^2+2z^2}{R^8}\right)+\frac{18\kappa z}{R^8}\mathbf{e}_z. \quad (5.7)$$

The first term may be absorbed into the pressure, so that

$$\mathbf{T}' = -q^{(1)}\mathbf{1}+\mathbf{T}^{(2)};\quad q^{(1)} = \frac{3\kappa(5r^2+2z^2)}{R^8} \quad (5.8)$$

and

$$\mathrm{Div}\,\mathbf{T}^{(2)}+\frac{18\kappa z}{R^8}\mathbf{e}_z = \mathbf{0}. \quad (5.9)$$

A particular solution of (2.32) with this body force is

$$\Phi^{(2)} = -\frac{\kappa z}{2R^4} \quad (5.10)$$

and the corresponding displacement, given by (2.30) and (5.10), is

$$\mathbf{v}' = \mathbf{v}^{(2)} = -\frac{\kappa}{\mu R^8}\{r(r^2-5z^2)\mathbf{e}_r+2z(2r^2-z^2)\mathbf{e}_z\}. \quad (5.11)$$

The stress $\mathbf{T}^{(2)}$ is given by (2.31), (5.10), and (5.11) as

$$\mathbf{T}^{(2)} = \frac{3\kappa}{R^{10}}\begin{pmatrix}3r^4-24r^2z^2+5z^4 & 0 & 2rz(7r^2-9z^2)\\ 0 & -R^2(r^2-5z^2) & 0\\ 2rz(7r^2-9z^2) & 0 & -3r^4+24r^2z^2-5z^4\end{pmatrix}. \quad (5.12)$$

The second-order displacement is given by (2.22), (5.3), and (5.11) as

$$\mathbf{v}^{(M)} = -\frac{r}{2\mu R^8}\{\mu R^2+2\kappa(r^2-5z^2)\}\mathbf{e}_r-\frac{2\kappa z}{\mu R^8}(2r^2-z^2)\mathbf{e}_z. \quad (5.13)$$

The second-order stress is given by the formulae (2.23), (2.26), and (2.27) and the results obtained in this section as

$$\mathbf{T}^{(M)} = \frac{3\mu}{4R^{10}}\begin{pmatrix}r^2(r^2+7z^2) & 0 & 2rz(2z^2-r^2)\\ 0 & -7r^2R^2 & 0\\ -6r^3z & 0 & 3r^2(r^2-z^2)\end{pmatrix}+\frac{3\kappa}{2R^{10}}\begin{pmatrix}7r^4-55r^2z^2+8z^4 & 0 & 2rz(17r^2-18z^2)\\ 0 & -R^2(r^2-8z^2) & 0\\ 2rz(17r^2-18z^2) & 0 & -(r^2-4z^2)(11r^2-3z^2)\end{pmatrix}. \quad (5.14)$$

6 Concentrated Normal Moment at the Boundary of a Half-Space

The first-order stress (5.6) is such that the plane $z = 0$ is free of traction except for the concentrated moment at the origin. So just as for the concentrated force, the half-space solution is identical to the solution for the infinite medium. The first-order solution is given by (5.3)–(5.6). In order to solve the problem to second order it is necessary to solve a classical linear problem, with no body force, but with stresses that vanish at infinity and which cancel the tractions associated with the second-order stress $\mathbf{T}^{(M)}$ on $z = 0$, so that

$$\mathbf{T}\mathbf{e}_z|_{z=0} = -\frac{\xi}{r^6}\mathbf{e}_z;\quad \xi = \frac{3}{4}(3\mu-22\kappa). \quad (6.1)$$

The appropriate Love function for this problem is

$$\Phi^{(4)} = \frac{\xi}{64}\left\{\left(-\frac{1}{R^3}-\frac{6z^2}{R^5}+\frac{15z^4}{R^7}\right)\log\left(\frac{R+z}{R^2}\right)+\frac{z}{R^4}-\frac{4z^2}{R^5}-\frac{15z^3}{R^6}+\frac{16z^4}{R^7}\right\}. \quad (6.2)$$

The corresponding displacements are obtained from (2.30) and are given by

$$v_r^{(4)} = -\frac{\xi}{128\mu}\left\{\left(\frac{45rz}{R^7}-\frac{630rz^3}{R^9}+\frac{945rz^5}{R^{11}}\right)\log\left(\frac{R+z}{R^2}\right)+\frac{r}{R(R+z)}\left[-\frac{9z}{R^5}+\frac{90z^3}{R^7}-\frac{105z^5}{R^9}\right]+\frac{48rz}{R^7}+\frac{330rz^2}{R^8}-\frac{852rz^3}{R^9}-\frac{840rz^4}{R^{10}}+\frac{1488rz^5}{R^{11}}\right\}$$

$$v_z^{(4)} = \frac{\xi}{128\mu}\left\{\left(-\frac{9}{R^5}-\frac{135z^2}{R^7}+\frac{945z^4}{R^9}-\frac{945z^6}{R^{11}}\right)\times\log\left(\frac{R+z}{R^2}\right)-\frac{6}{R^5}+\frac{9z}{R^6}-\frac{144z^2}{R^7}-\frac{630z^3}{R^8}+\frac{1278z^4}{R^9}+\frac{945z^5}{R^{10}}-\frac{1488z^6}{R^{11}}\right\}. \quad (6.3)$$

The corresponding components of stress can be obtained from (2.31) as

Downloaded 04 May 2010 to 171.66.16.27. Redistribution subject to ASME license or copyright; see http://www.asme.org/terms/Terms_Use.cfm

$$T_{rr}^{(4)} = \frac{\xi}{64}\left[\frac{15z}{R^7}\left\{33 - 427\left(\frac{z}{R}\right)^2 + 1071\left(\frac{z}{R}\right)^4 - 693\left(\frac{z}{R}\right)^6\right\} \times \log\left(\frac{R+z}{R^2}\right) + \frac{1}{(R+z)R^5}\left\{8 - 91\left(\frac{z}{R}\right) + 72\left(\frac{z}{R}\right)^2 + 1512\left(\frac{z}{R}\right)^3 - 408\left(\frac{z}{R}\right)^4 - 3663\left(\frac{z}{R}\right)^5 + 360\left(\frac{z}{R}\right)^6 + 2250\left(\frac{z}{R}\right)^7\right\} + \frac{1}{R^6}\left\{-72 + 618\left(\frac{z}{R}\right) + 2982\left(\frac{z}{R}\right)^2 - 9922\left(\frac{z}{R}\right)^3 - 10827\left(\frac{z}{R}\right)^4 + 27186\left(\frac{z}{R}\right)^5 + 8145\left(\frac{z}{R}\right)^6 - 18258\left(\frac{z}{R}\right)^7\right\}\right]$$

$$T_{\theta\theta}^{(4)} = \frac{\xi}{64}\left[\frac{60z}{R^7}\left\{3 - 7\left(\frac{z}{R}\right)^2\right\}\log\left(\frac{R+z}{R^2}\right) + \frac{1}{(R+z)R^5}\left\{-1 + 8\left(\frac{z}{R}\right) - 6\left(\frac{z}{R}\right)^2 - 96\left(\frac{z}{R}\right)^3 + 15\left(\frac{z}{R}\right)^4 + 120\left(\frac{z}{R}\right)^5\right\} + \frac{1}{R^6}\left\{-63 + 192\left(\frac{z}{R}\right) + 411\left(\frac{z}{R}\right)^2 - 568\left(\frac{z}{R}\right)^3 - 120\left(\frac{z}{R}\right)^4\right\}\right]$$

$$T_{zz}^{(4)} = \frac{\xi}{64}\left[\frac{15z^3}{R^7}\left\{245 - 882\left(\frac{z}{R}\right)^2 + 693\left(\frac{z}{R}\right)^4\right\} \times \log\left(\frac{R+z}{R^2}\right) + \frac{1}{R^6}\left\{-64 - 1344\left(\frac{z}{R}\right)^2 + 4970\left(\frac{z}{R}\right)^3 + 9765\left(\frac{z}{R}\right)^4 - 20832\left(\frac{z}{R}\right)^5 - 10395\left(\frac{z}{R}\right)^6 + 18258\left(\frac{z}{R}\right)^7\right\}\right]$$

$$T_{rz}^{(4)} = T_{zr}^{(4)} = \frac{\xi}{64}\left[\frac{315rz^2}{R^9}\left\{5 - 30\left(\frac{z}{R}\right)^2 + 33\left(\frac{z}{R}\right)^4\right\} \times \log\left(\frac{R+z}{R^2}\right) + \frac{15rz^2}{(R+z)R^8}\left\{-15 + 70\left(\frac{z}{R}\right)^2 - 63\left(\frac{z}{R}\right)^4\right\} + \frac{6rz}{R^8}\left\{-64 + 355\left(\frac{z}{R}\right) + 980\left(\frac{z}{R}\right)^2 - 2480\left(\frac{z}{R}\right)^3 - 1575\left(\frac{z}{R}\right)^4 + 3043\left(\frac{z}{R}\right)^5\right\}\right]. \quad (6.4)$$

The complete second-order solution is

$$\mathbf{v} = \mathbf{v}^{(M)} + \mathbf{v}^{(4)} \quad (6.5)$$

$$\mathbf{T} = \mathbf{T}^{(M)} + \mathbf{T}^{(4)} \quad (6.6)$$

where $\mathbf{v}^{(M)}$ and $\mathbf{T}^{(M)}$ are given by (5.13) and (5.14), respectively.

References

Carroll, M. M., and Rooney, F. J., 1984, "Simplification of the Second Order Problem for Incompressible Solids," *Quart. J. Mech. Appl. Math.*, Vol. 37, pp. 261–272.

Chan, C., and Carlson, E. E., 1970, "Second-Order Incompressible Elastic Torsion," *In. J. Engng. Sci*, Vol. 8, pp. 415–430.

Hill, J. M., 1973, note on "Second-Order Incompressible Elastic Torsion," *Int. J. Engng. Sci.*, Vol. 11, pp. 331–336.

Little, R. M., 1973, *Elasticity*, Prentice-Hall, Englewood Cliffs, NJ.

Selvadurai, A. P. S., 1970, "Problems in Second-Order Elasticity," Ph.D. thesis, The University of Nottingham.

Sneddon, I. N., 1951, *Fourier Transforms*, McGraw-Hill, New York.

Downloaded 04 May 2010 to 171.66.16.27. Redistribution subject to ASME license or copyright; see http://www.asme.org/terms/Terms_Use.cfm

H. J. Golden

T. W. Strganac[1]

Department of Aerospace Engineering,
Texas A&M University,
College Station, TX 77843-3141

R. A. Schapery
Department of Aerospace Engineering
And Engineering Mechanics,
The University of Texas at Austin,
Austin, TX 78712-1085

An Approach to Characterize Nonlinear Viscoelastic Material Behavior Using Dynamic Mechanical Tests and Analyses

Linear viscoelastic properties may be rapidly identified using dynamic mechanical analysis methods, yet these traditional methods do not properly identify nonlinear viscoelastic response. Herein, dynamic mechanical methodologies are extended to provide an approach for nonlinear characterization. The proposed method is based on Schapery's nonlinear viscoelastic model extended to dynamic mechanical theory. The oscillatory loading during a dynamic test is addressed within the nonlinear viscoelastic model. An experimental protocol is established. Analyses and experiments are performed for the characterization of thin-film polyethylene to validate the approach.

Introduction

The research herein is driven by the need to characterize thin films used in the construction of high-altitude scientific balloons. The need for balloon systems to fly longer, higher, and with heavier payload weights, has required the development of higher performance materials. The use of dynamic mechanical test and analysis (DMTA) methodologies has been proven to accurately characterize the linear properties of material behavior with a substantially reduced time for experiments. However, DMTA is limited to the linear range because the theory and test protocol does not properly address nonlinear behavior. Following conventional viscoelasticity terminology, the use of "dynamic" refers to steady-state harmonic input, not inertial effects; the latter are negligible here.

Many investigators have examined approaches to characterize thin-film materials. Schapery (1966; 1968; 1969a, b, 1997) developed a nonlinear constitutive model based on irreversible thermodynamic theory for nonlinear viscoelastic materials. Wilbeck (1981) used Schapery's model to predict creep with temperature and strain histories. His studies show that thin-film polyethylene exhibits nonlinear behavior due to the dependence of the behavior on the load history. Strganac et al. (1991) and Letton et al. (1992) examined thin-film polyethylene retrieved from NASA's Long Duration Exposure Facility (LDEF). Dynamic mechanical methods were used to characterize the effects of low-earth orbit environment on the viscoelastic material properties. These studies confirm that, although the linear approach provides an accurate approximation for small strains or loads, predictions based upon a linear test and analysis deteriorate for moderate to high stress levels.

Dillard et al. (1987) compared several models for predicting the nonlinear behavior of graphite/epoxy composites and determined that Schapery's model was the most general and adaptable to computational methodologies. Smart and Williams (1972) compared three single integral methods for nonlinear viscoelastic modeling of polypropylene and polyvinylchloride, and determined that Schapery's model predicted stress loading and unloading more accurately using either the stress or strain formulations. Rand et al. (1996a, b) presented uniaxial and biaxial predictions using Schapery's model and material parameters obtained from traditional creep measurements. The predictions show good agreement with measurements; however, their technique requires significant time for measurement and subsequent analysis to identify the constitutive properties, and the low-temperature short-time scale components of the viscoelastic response are difficult to determine. These earlier studies have shown that Schapery's theory is the most promising of the examined techniques.

Strganac et al. (1995) briefly examined DMTA for nonlinear characterization, but the quality of the experimental data was limited by the test equipment. Strganac and Golden (1996) predicted nonlinear viscoelastic response using a hybrid set of measurements applied to Schapery's nonlinear model. The experimental data was derived from both DMTA (Biskup, 1994) and creep tests (Rand et al., 1996b) at various temperatures and stresses. This approach, although it used DMTA, still required creep data and was only appropriate for constant load conditions.

Regardless of limitations, the advantages that DMTA offers for rapid and accurate nonlinear material characterization is desirable. The technique described herein is a novel approach to use DMTA for characterization of nonlinear viscoelastic material properties. The technique incorporates a combined preload and oscillatory load in Schapery's nonlinear model. As a consequence, the technique enables rapid characterization of the nonlinear material parameters required to predict arbitrary viscoelastic behavior due to time-varying loads.

Model

The stress formulation of Schapery's (1969b) model is

$$\epsilon(t) = D_0 g_0 \sigma + g_1 \int_0^t \hat{D}(\Psi - \Psi') \frac{d(g_2\sigma)}{d\tau} d\tau \qquad (1)$$

where ϵ and σ are uniaxial strain and stress, respectively; D_0 is the linear elastic creep compliance component; $\hat{D}$ is the linear transient creep compliance component which is dependent on time and temperature; and, g_0, g_1, and g_2 are the nonlinear viscoelastic parameters which may depend on stress and temperature.

The parameters Ψ and Ψ' are reduced time variables defined as

[1] To whom correspondence should be addressed.

Contributed by the Applied Mechanics Division of THE AMERICAN SOCIETY OF MECHANICAL ENGINEERS for publication in the ASME JOURNAL OF APPLIED MECHANICS.

Discussion on the paper should be addressed to the Technical Editor, Professor Lewis T. Wheeler, Department of Mechanical Engineering, University of Houston, Houston, TX 77204-4792, and will be accepted until four months after final publication of the paper itself in the ASME JOURNAL OF APPLIED MECHANICS.

Manuscript received by the ASME Applied Mechanics Division, Sept. 30, 1997; final revision, July 29, 1998. Associate Technical Editor: I. M. Daniel.

 Copyright © 1999 by ASME

Downloaded 04 May 2010 to 171.66.16.27. Redistribution subject to ASME license or copyright; see http://www.asme.org/terms/Terms_Use.cfm

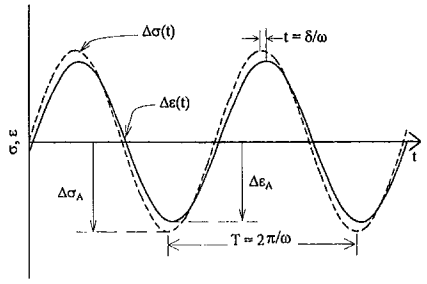


Fig. 1 An oscillatory load (stress) input and deformation (strain) response is shown

$$\Psi = \Psi(t, \sigma, T) = \int_0^t \frac{dt'}{a_\sigma a_T} \quad \text{and}$$

$$\Psi' = \Psi'(\tau, \sigma, T) = \int_0^\tau \frac{dt'}{a_\sigma a_T} \tag{2a}$$

where a_σ is the stress and possibly temperature-dependent shift factor and a_T is the temperature-dependent shift factor at zero stress. These factors are determined using time-temperature superposition, and represent a compression or expansion on the time scale due to temperature or preload effects. Time-temperature superposition principles (Ferry, 1980) are typically employed to characterize viscoelastic material behavior. The approach permits properties measured at one temperature and/or preload to be directly related to those properties at other temperatures or preloads through the shift factor a_T and/or a_σ. Thus,

$$D(t, T) = D(t/a_T) \tag{3}$$

where D represents the creep compliance and T is temperature. An important feature of time-temperature superposition is the ability to measure properties over the same time scale and simply relate the material response obtained at different temperatures.

Schapery's nonlinear viscoelastic model is rewritten as

$$\epsilon = \epsilon_e + g_1 \int_0^t \hat{D}(\Psi - \Psi') \frac{d(\hat{g}_2)}{d\tau} d\tau \tag{4}$$

where $\epsilon_e = D_0 g_0 \sigma$ (the elastic strain response) and $\hat{g}_2 = g_2 \sigma$. The oscillatory stress input of DMTA measurements will be considered by using a Taylor series expansion of stress. Thus, the stress input is defined as $\sigma(t) = \sigma_m + \Delta\sigma(t)$ in which σ_m represents the mean value of stress due to preload at $t = 0$ and $\Delta\sigma$ represents the oscillatory stress. The expanded form of Eq. (4), with second and higher-order terms in $\Delta\sigma$ removed, is

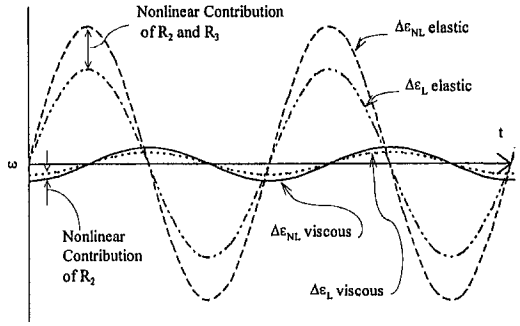


Fig. 2 Contributions from several nonlinearities in the strain response are shown

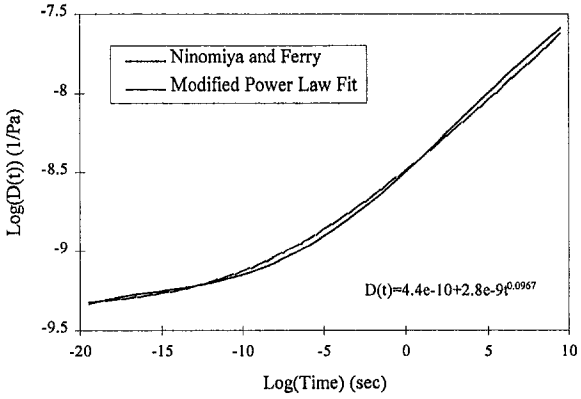


Fig. 3 The linear creep compliance master curve for Stratofilm-372 is shown for tests in the machine direction (reference temperature is 23°C)

$$\epsilon(\sigma_m + \Delta\sigma) = \epsilon_{e,m} + \left(\frac{d\epsilon_e}{d\sigma}\right)_{\sigma_m} \Delta\sigma + (g_{1,m} + \Delta g_1) \int_0^t \hat{D}(\Psi - \Psi') \frac{d(\hat{g}_{2,m} + \Delta\hat{g}_2)}{d\tau} d\tau \tag{5}$$

where

$$\Delta g_1 = \left(\frac{dg_1}{d\sigma}\right)_{\sigma_m} \Delta\sigma \quad \text{and} \quad \Delta\hat{g}_2 = \left(\frac{d\hat{g}_2}{d\sigma}\right)_{\sigma_m} \Delta\sigma$$

and where the use of the subscript "m" on a variable indicates that the variable is associated with σ_m. The reduced time variable, Ψ, is also a function of stress and is expanded in a similar manner. Thus, for constant temperature,

$$\Psi = \Psi_m - \frac{1}{a_{\sigma,m}^2} \frac{da_{\sigma,m}}{d\sigma} \int_0^t \Delta\sigma dt' \quad \text{and} \tag{6a}$$

$$\Psi' = \Psi'_m - \frac{1}{a_{\sigma,m}^2} \frac{da_{\sigma,m}}{d\sigma} \int_0^\tau \Delta\sigma dt. \tag{6b}$$

With substitution of Eq. (6*a*) and Eq. (6*b*), Eq. (5) is separated into a transient and oscillatory strain response, $\epsilon = \epsilon_{tran} + \Delta\epsilon$. Full development is described in Golden et al. (1996). The transient strain response is identified as

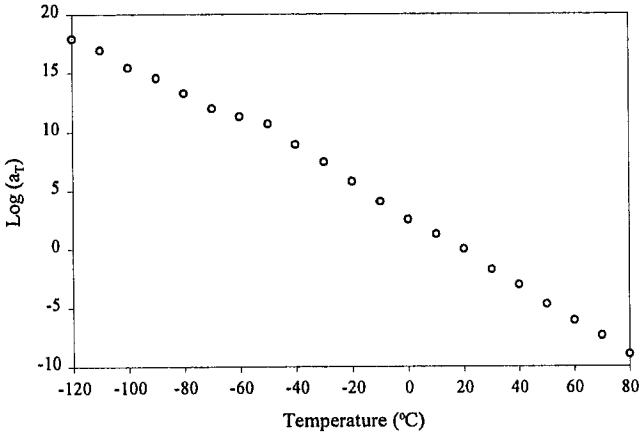


Fig. 4 The temperature-dependent shift factor associated with the linear creep compliance master curve are shown (reference temperature is 23°C)

Downloaded 04 May 2010 to 171.66.16.27. Redistribution subject to ASME license or copyright; see http://www.asme.org/terms/Terms_Use.cfm

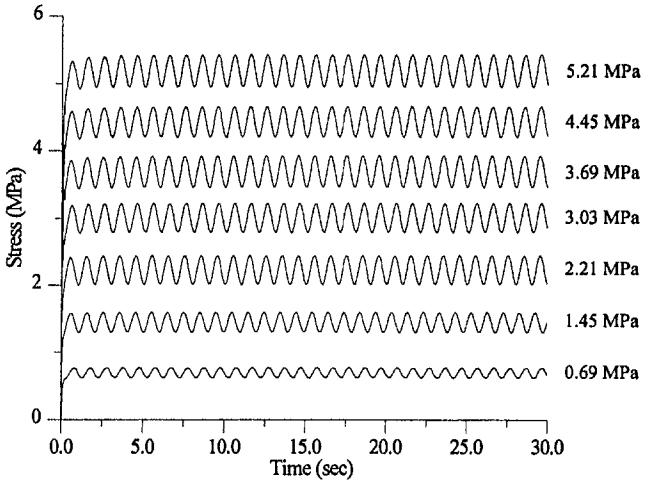


Fig. 5 Measurements of the oscillatory stress input are shown for several preloads

$$\epsilon_{\text{tran}} = \epsilon_{e,m} + g_{1,m} g_{2,m} \hat{D}\left(\frac{t}{a_{\sigma,m}}\right)\sigma_m. \tag{7a}$$

Assuming the initial transients occur during the first few oscillations and may be ignored (an assumption to be validated through subsequent measurements), the oscillatory strain is

$$\Delta\epsilon = \left(\left(\frac{d\epsilon_e}{d\sigma}\right)_{\sigma_m} + g_{1,m}\frac{d\hat{g}_{2,m}}{d\sigma}\hat{D}^* + \hat{g}_{2,m}\frac{dg_{1,m}}{d\sigma}\hat{D}\left(\frac{t}{a_{\sigma,m}}\right)\right)\Delta\sigma \tag{7b}$$

where $\hat{D}^*$ is the linear complex compliance defined as

$$\hat{D}^* = |\hat{D}^*|e^{-i\hat{\delta}} = |\hat{D}^*|(\cos(\hat{\delta}) - i\sin(\hat{\delta})) = \hat{D}' - i\hat{D}''$$

in which $\Delta\sigma$ is a complex exponential in Eq. (7*b*) and

$$\hat{D}' = \hat{\omega}\int_0^\infty \hat{D}(\xi)\sin(\hat{\omega}\xi)d\xi,$$

$$\hat{D}'' = -\hat{\omega}\int_0^\infty \hat{D}(\xi)\cos(\hat{\omega}\xi)d\xi,$$

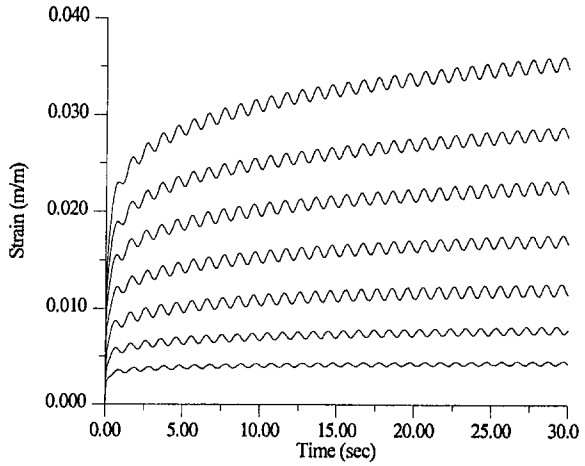


Fig. 6 Measurements of the total strain response from the input stress (Fig. 5) are shown

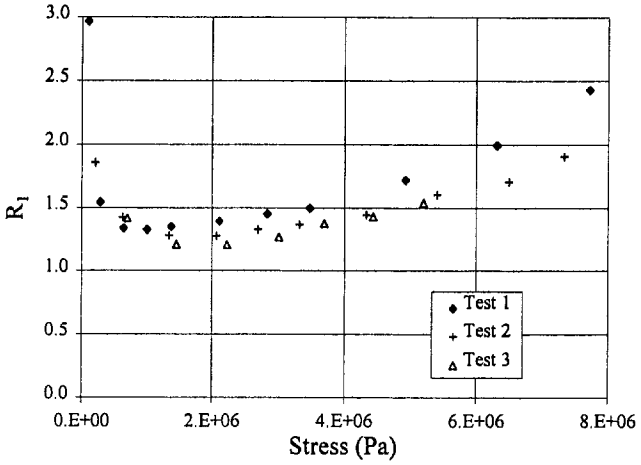


Fig. 7 Measurements of the nonlinear parameter group R_1 are shown

$$\tan(\hat{\delta}) = \frac{\hat{D}''}{\hat{D}'}, \quad |\hat{D}^*| = \sqrt{\hat{D}'^2 + \hat{D}''^2}, \quad \text{and} \quad \hat{\omega} = \omega a_{\sigma,m}.$$

If the linear transient compliance may be represented by a power-law (again, an assumption to be validated through subsequent measurements), such that $\hat{D}(t) = D_1 t^n$, then Eq. (7*a*) reduces to

$$\epsilon_{\text{tran}} = \epsilon_{e,m} + \frac{g_{1,m}g_{2,m}}{a^n_{\sigma,m}} D_1 t^n \sigma_m. \tag{8a}$$

Equation (7*b*), with the identification of a nonlinear complex compliance (D^*_{NL}), may be written as

$$\Delta\epsilon = D^*_{NL}\Delta\sigma \tag{8b}$$

where

$$D^*_{NL} = D'_{NL} - iD''_{NL}.$$

Components of the nonlinear complex compliance are

$$D'_{NL} = \frac{d\epsilon_{e,m}}{d\sigma} + \left[\frac{g_{1,m}}{a^n_{\sigma,m}}\frac{d\hat{g}_{2,m}}{d\sigma}\right]D' + \left[\frac{\hat{g}_{2,m}}{a^n_{\sigma,m}}\frac{dg_{1,m}}{d\sigma}\right]D_1 t^n \tag{9a}$$

and

$$D''_{NL} = \left[\frac{g_{1,m}}{a^n_{\sigma,m}}\frac{d\hat{g}_{2,m}}{d\sigma}\right]D'' \tag{9b}$$

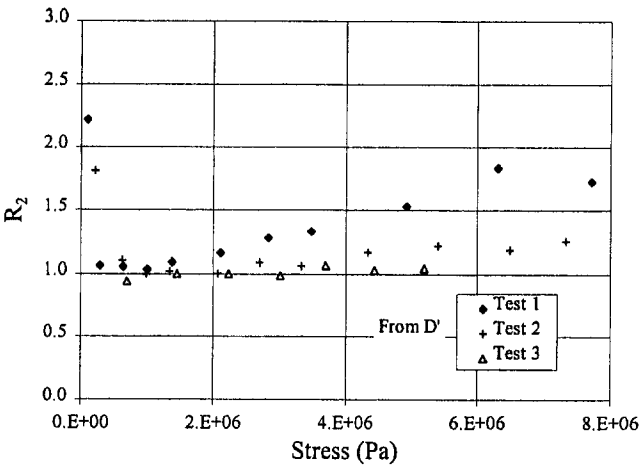


Fig. 8 Measurements of the nonlinear parameter group R_2 are shown (derived from the nonlinear storage compliance)

Downloaded 04 May 2010 to 171.66.16.27. Redistribution subject to ASME license or copyright; see http://www.asme.org/terms/Terms_Use.cfm

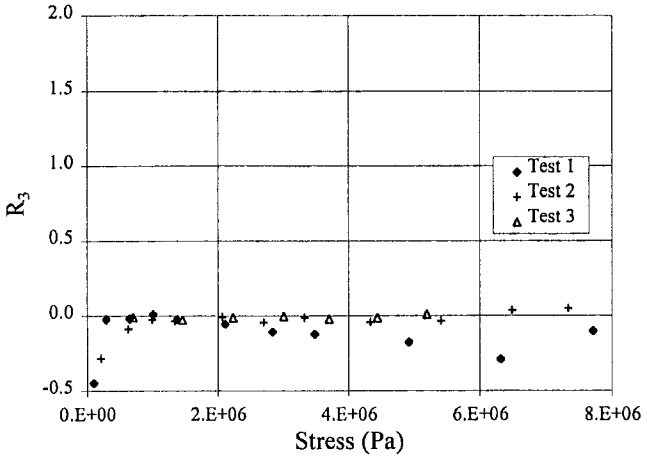


Fig. 9 Measurements of the nonlinear parameter group R_3 are shown

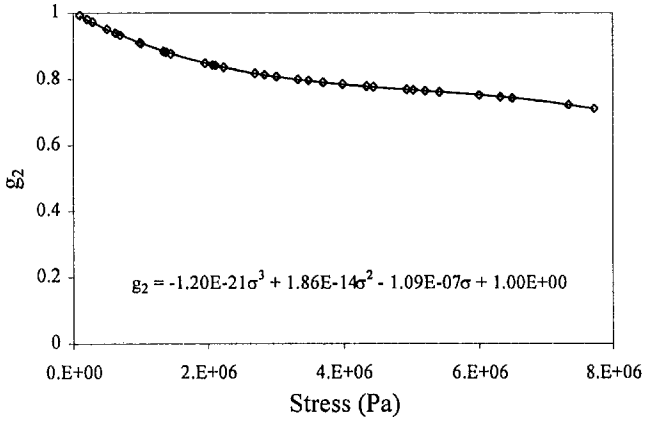


Fig. 10 The nonlinear parameter g_2 is found from integration of the measured R parameters

where

$$\frac{d\epsilon_{e,m}}{d\sigma} = D_0\left(g_{0,m} + \sigma_m \frac{dg_{0,m}}{d\sigma}\right),$$

$$D' = D_1\Gamma(1+n)\cos(\hat{\delta})(\omega)^{-n},$$

$$D'' = D_1\Gamma(1+n)\sin(\hat{\delta})(\omega)^{-n}, \quad \text{and} \quad \hat{\delta} = \frac{n\pi}{2}$$

and Γ is the gamma function.

The transient strain response defined by Eq. (8*a*) is the response due to the application of a constant preload. It is observed that Eq. (8*a*) will reduce to the linear formulation if the nonlinear parameters are set to unity. Combining Eq. (8*a*) and Eq. (8*b*), the total strain response is

$$\epsilon(\sigma_m + \Delta\sigma) = \left(D_0 g_0 + \frac{g_{1,m}g_{2,m}}{a^n_{\sigma,m}} D_1 t^n\right)\sigma_m + D^*_{NL}\Delta\sigma, \quad (10)$$

in which $\epsilon_{e,m} = D_0 g_0 \sigma_m$ and the real part of the last term is used.

Experiment

With consideration of the theoretical model for nonlinear DMTA, a methodology for measuring the nonlinear viscoelastic parameters is presented. Several steps are outlined that identify the individual nonlinear parameters from experimental data.

First, the transient strain response is separated from the oscillatory strain response defined by Eq. (8*a*) and Eq. (8*b*). The oscillatory portion is the difference between the transient strain and the total measured strain, $\Delta\epsilon(t) = \epsilon(t) - \epsilon_{\text{tran}}$; thus, the transient response is found by removing the oscillatory portion of the strain response from the total measured strain. The transient strain response is further separated into the elastic and transient components defined by Eq. (8*a*). The elastic component of Eq. (8*a*) is identified by the instantaneous strain response, $\epsilon_{e,m}$, due to the mean stress, σ_m, of the applied step load. The nonlinear parameter g_0 is identified by the deviation from linearity of the initial elastic response due to changes in the mean stress. Since the transient strain response is measured and the elastic contribution is identified from the strain response, the only unknown variables in Eq. (8*a*) appear as a collection of individual nonlinear parameters. Herein, this collection of parameters is defined as R_1,

$$R_{1,m} = R_1(\sigma_m) = \frac{g_{1,m}g_{2,m}}{a^n_{\sigma,m}}, \quad (11)$$

which is experimentally evaluated. If the material is linear within the load (stresses) examined, then the value of $R_{1,m}$ will be unity for this range of loads. Note, the individual nonlinear parameters contained within $R_{1,m}$ must still be uniquely identified.

Next, the measured oscillatory strain response is separated into the nonlinear complex compliance components defined in Eq. (8*b*). In complex notation, the steady-state strain response due to an oscillatory stress input, $\Delta\sigma = \Delta\sigma_A e^{i\omega t}$, is $\Delta\epsilon = \Delta\epsilon_A e^{i(\omega t - \delta)}$. Therefore, with substitution into Eq. (8*b*), the complex compliance is defined as

$$D^*_{NL} = \frac{\Delta\epsilon_A}{\Delta\sigma_A} e^{-i\delta}$$

from which the complex compliance components are

$$D'_{NL} = \frac{\Delta\epsilon_A}{\Delta\sigma_A}\cos(\delta) \quad \text{and} \quad D''_{NL} = \frac{\Delta\epsilon_A}{\Delta\sigma_A}\sin(\delta). \quad (12a)$$

From the experimental data, $\Delta\epsilon_A$ is the measured amplitude of the output oscillatory strain, $\Delta\sigma_A$ is the prescribed amplitude of the input oscillatory stress, and δ is the measured phase difference between the stress and the strain (see Fig. 1). As illustrated in Fig. 2, the complex compliance parameters contribute to two parts of the oscillatory strain response—the in-phase storage compliance (elastic contribution) and the out-of-phase loss compliance (viscous contribution). These complex compliance components are equivalent to the terms in Eq. (9*a*) and Eq. (9*b*).

Then, consider the three individual terms of Eq. (9*a*). The first term is already identified from the elastic part of the transient strain data. The second two terms must be identified; and, it is observed that one term is independent of time and the other term is transient.

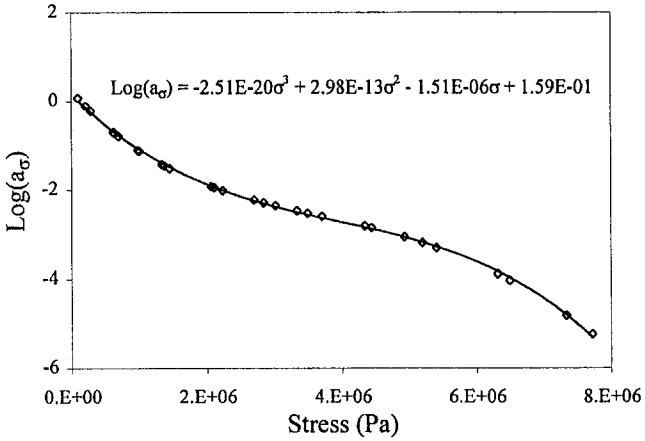


Fig. 11 The nonlinear parameter a_σ is derived from the R parameters

Downloaded 04 May 2010 to 171.66.16.27. Redistribution subject to ASME license or copyright; see http://www.asme.org/terms/Terms_Use.cfm

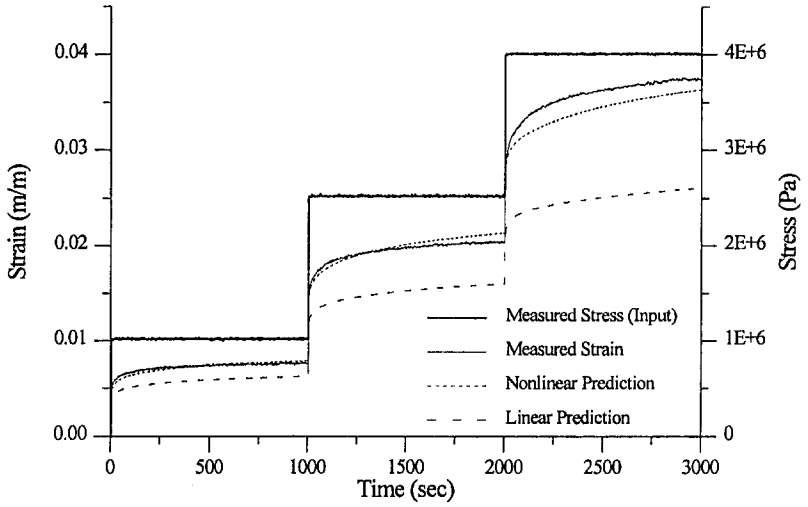


Fig. 12 Comparisons between measured and predicted strain response are shown for a three step load history

All terms not within brackets in Eq. (9*a*) are associated with the linear compliance model. Two collections of nonlinear parameters appear within the brackets, and are defined herein as $R_{2,m}$ and $R_{3,m}$. Thus,

$$R_{2,m} = R_2(\sigma_m) = \frac{g_{1,m}}{a^n_{\sigma,m}} \frac{d\hat{g}_{2,m}}{d\sigma} \tag{13a}$$

and

$$R_{3,m} = R_3(\sigma_m) = \frac{\hat{g}_{2,m}}{a^n_{\sigma,m}} \frac{dg_{1,m}}{d\sigma}. \tag{13b}$$

The contributions of each of these collections are illustrated in Fig. 2. $R_{2,m}$ is a parameter that accounts for variation from linearity of the storage and loss compliance magnitude. $R_{3,m}$ is a parameter that accounts for any transient behavior exhibited by the storage compliance. With consideration of the experiment, $R_{2,m}$ and $R_{3,m}$ are extracted from a fit of the measured storage compliance (all other variables are known). Alternatively, or as a verification, $R_{2,m}$ may be determined directly from Eq. (9*b*).

Finally, it is noted that $R_{1,m}$, $R_{2,m}$, and $R_{3,m}$ are functions of the mean stress level, σ_m, at an applied preload. These three collections each contain different combinations of the individual nonlinear parameters g_1, g_2, and a_σ,

$$R_1(\sigma) = \frac{g_1 g_2}{a^n_\sigma}, \quad R_2(\sigma) = \frac{g_1}{a^n_\sigma}\left(g_2 + \sigma \frac{dg_2}{d\sigma}\right), \quad \text{and}$$

$$R_3(\sigma) = \frac{\hat{g}_2}{a^n_\sigma} \frac{dg_1}{d\sigma}. \tag{14}$$

Essentially, three equations with three unknowns are present. The nonlinear parameter g_2 is determined through integration of the ratio R_2/R_1, thus,

$$\int_0^{\sigma_m} \left(\frac{R_2}{R_1} - 1\right) \frac{d\sigma}{\sigma} = \int_0^{\sigma_m} d \ln (g_2) = \ln (g_2(\sigma_m)). \tag{15}$$

The nonlinear parameter g_1 is determined through integration of the ratio R_3/R_1, thus,

$$\int_0^{\sigma_m} \frac{R_3}{R_1 \sigma} d\sigma = \int_0^{\sigma_m} d \ln (g_1) = \ln (g_1(\sigma_m)). \tag{16}$$

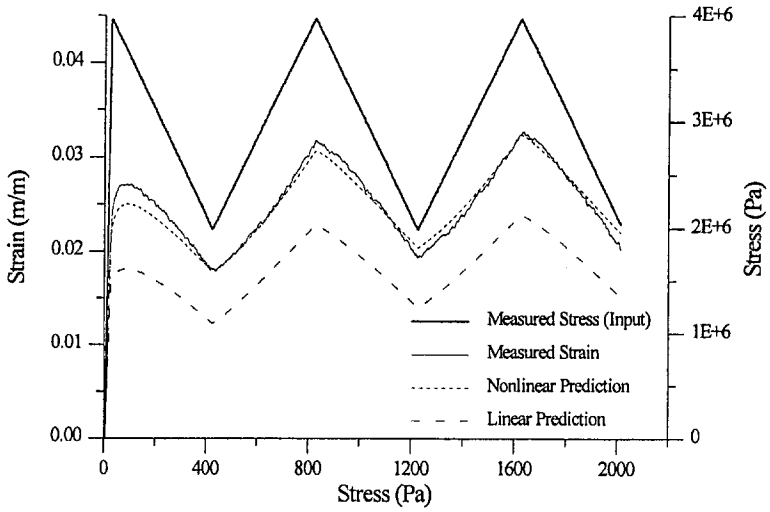


Fig. 13 Comparisons between measured and predicted strain response are shown for a large-amplitude sawtooth load history

Downloaded 04 May 2010 to 171.66.16.27. Redistribution subject to ASME license or copyright; see http://www.asme.org/terms/Terms_Use.cfm

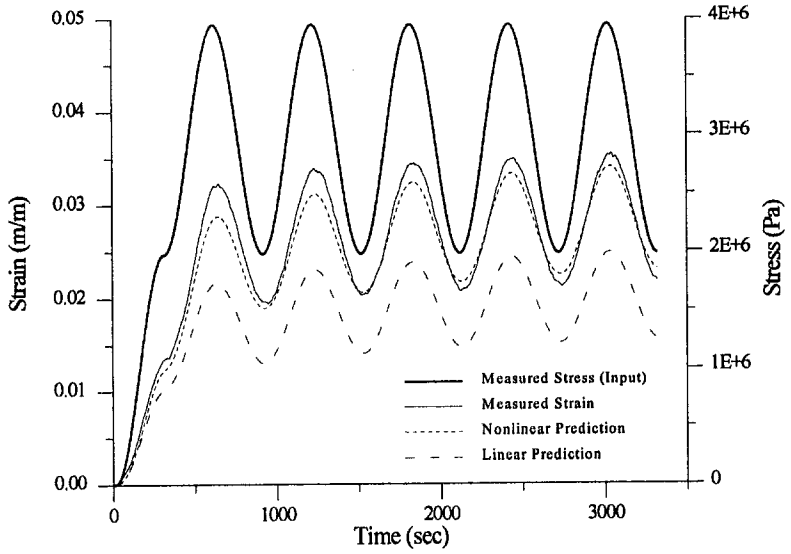


Fig. 14 Comparisons between measured and predicted strain response are shown for a large-amplitude oscillatory load history

The individual nonlinear parameters g_0, g_1, and g_2 are now identified, and the one remaining nonlinear parameter, a_σ, is found by back substitution into one of the R_i in Eq. (14).

Results

Measurements were performed on Stratofilm®-372 (SF-372), a linear low density polyethylene film, to validate the nonlinear DMTA procedure. The constitutive properties for this material—manufactured through a blown-film extrusion process—are direction-dependent; herein, measurements are performed for the machine direction. The nonlinear characterization was performed at room temperature (23°C). Nonlinear measurements used a MTS load frame and servo-hydraulic control system. The MTS 810 test system includes a 20 kip load frame, a 20 kip hydraulic actuator, the MTS 458.20 MicroConsole™, the MTS 458.91 MicroProfiler™, and a SM-10 Interface S-type load cell.

Thin-film specimens are not conducive to standard strain measuring devices; thus, strain was determined using the displacement of the driving piston and the specimen gauge length (defined as the length of the specimen between grips). Piston displacement may be measured to an accuracy of ±0.003175 mm (±0.000125 in.). The SM-10 Interface S-type load cell was calibrated for a full scale range of ±11.12 N (±2.5 lbs.). The resolution of the force transducer is ±0.00334 N (±0.00075 lbs.). A data acquisition system (486 class/33 MHz PC with a ComputerBoards CIO-AD16jr analog-to-digital data acquisition board) was used for recording the loads and displacements.

Nonlinear material characterization uses certain properties derived from a linear model. For the linear model, the procedure and measured data as described by Biskup (1994) was utilized. For the results presented herein, the linear range was confirmed by measurements that have no sensitivity to preload. The linear complex compliance data is obtained with detailed DMTA, and this data is used to determine the creep compliance in the time domain. The method of Ninomiya and Ferry (Ferry, 1980) is used for the transformation of the complex compliance data to the creep compliance,

$$D(t) = D'(\omega) + 0.4D''(0.4\omega) - 0.14D''(10\omega)|_{t=1/\omega}. \quad (23)$$

Comparisons with other methods are presented by Biskup (1994) and show this method to be valid. The creep compliance master curve is shown in Fig. 3. As is also presented in Fig. 3, a modified power-law fit is used to model the linear creep compliance. The reference temperature is 20°C, and the associated temperature-dependent shift factor is shown in Fig. 4.

Nonlinear dynamic mechanical tests were performed at several levels of mean stress due to preload, and tests were repeated for three specimens. A series of tests performed on SF-372 are shown in Figs. 5 and 6. Figure 5 shows the input stress due to load and Fig. 6 shows the resulting strain response. The mean value of stress is indicated. The magnitude of the oscillatory stress was maintained at an order of magnitude less than the mean stress, and does not exceed 0.172 MPa (25 psi).

Evaluation of the nonlinear parameter terms R_1, R_2, and R_3 was performed, and the results are shown in Figs. 7, 8, and 9. Each figure shows three separate tests that are used to find the nonlinear parameters. Examining Fig. 9, the value of R_3 is essentially zero; therefore, the nonlinear parameter g_1 is unity. In addition, measurements for all preloads of interest indicate no nonlinear contributions related to the elastic response; thus, g_0 is unity for this material. Using Eqs. (15) and (16), the nonlinear parameters g_2 and a_σ are determined. These parameters are shown in Figs. 10 and 11.

Schapery's model (see Eq. (1)) is numerically evaluated using the nonlinear parameters derived by experiments. Thus, the nonlinear strain response of a uniaxially loaded specimen may be predicted. An obvious test of the presented approach is prediction of the strain response that was used to determine the individual nonlinear parameters. In other words, do the nonlinear parameters (see Figs. 10 and 11) and the load histories of Fig. (5) predict the responses measured in Fig. 6? The answer is yes and, in essence, Fig. 6 could be duplicated with a simple change in the caption from "predictions" to "measurements."

Golden et al. (1996) examined the long-term response of balloon materials (Stratofilm®-372) for stress levels representative of flight conditions. Those results were limited to a constant preload case which may be modeled solely by the R_1 parameter; however, those results clearly defined the linear range for the material, as well as showed excellent long-term predictions (on the order of six months) when compared with exact measurements.

Several cases of new, different load histories are examined to provide a more substantial validation of the approach. Case 1 examines a load history consisting of a series of discrete step load inputs as shown in Fig. 12. Case 2 examines a load history consisting of a large-amplitude sawtooth oscillation as shown in Fig. 13. Case 3 examines a load history consisting of a large-amplitude sinusoidal oscillation as shown in Fig. 14. In each of these figures, the predictions of strain response using both the traditional linear approach and, as developed herein, the nonlinear approach are compared to direct measurements. In all cases, the predicted response using the linear model is ex-

Downloaded 04 May 2010 to 171.66.16.27. Redistribution subject to ASME license or copyright; see http://www.asme.org/terms/Terms_Use.cfm

tremely poor whereas the predicted response using the nonlinear model is very good.

Conclusions

A nonlinear viscoelastic methodology for dynamic mechanical test and analysis (DMTA) is introduced. Schapery's nonlinear viscoelastic theory is used as a basis to extend the DMTA approach to nonlinear characterization. Theoretical and experimental developments are described that characterize the individual nonlinear parameters found in Schapery's nonlinear model. These developments are limited to viscoelastic behavior, albeit nonlinear, and consequently do not account for unrecoverable deformations due to plasticity and aging.

Experimental characterization and validation was performed on Stratofilm®-372 (SF-372), a linear low-density polyethylene film. Studies on other materials have not been performed; thus, applicability to other classes of materials has not been validated. The linear compliance model was determined using the principles associated with linear DMTA and linear material characterization. This characterization was performed such that the mean stress level, as well as any other possible nonlinear contribution, is essentially zero during DMTA procedures. Time-temperature superposition principles and time-frequency transformations were used to construct a linear creep compliance master curve from DMTA measurements.

As a validation to the methodology, three additional load cases are examined to demonstrate the nonlinear DMTA approach and experiment protocol. Characterization tests require small oscillatory loads about a constant preload in accordance with the supporting nonlinear theory as described. Although nonlinear contributions due to large amplitude oscillatory loads may be of concern for certain classes of material, predictions of arbitrary response, such as those shown for the large oscillatory loading for the material examined herein, show good agreement with measurements. The properties representative of one material are examined at a specific temperature, and comparisons between predictions and experimental data show a promising method that will produce much improved results over linear theory. In addition, the time required to determine the nonlinear parameters is substantially reduced using the nonlinear DMTA methodology compared to creep and recovery tests.

Acknowledgments

This work has been performed under NASA Grant NAG5-673. The authors thank the staff of the Balloon Projects Branch at NASA's Goddard Space Flight Center for their support.

References

Biskup, B. A., 1994, "Characterization of the Viscoelastic Properties of Thin-Film Materials Using Dynamic-Mechanical Testing Techniques," MS thesis, Texas A&M University, College Station, TX.

Dillard, D. A., Straight, M. R., and Brinson, H. F., 1987, "The Nonlinear Viscoelastic Characterization of Graphite/Epoxy Composites," *Polymer Engineering and Science,* Vol. 27, No. 2, pp. 116–123.

Ferry, J. D., 1980, *Viscoelastic Properties of Polymers,* 3rd Ed., John Wiley and Sons, New York.

Golden, H., Strganac, T., and Schapery, R., 1996, "A Test and Analysis Protocol to Rapidly Characterize Nonlinear Viscoelastic Properties of Balloon Materials," AIAA Paper 96-0572, AIAA 34th Aerospace Sciences Meeting & Exhibit, Reno, NV.

Letton, A., Farrow, D. A., and Strganac, T. W., 1992, "Viscoelastic Characterization of Thin-Film Polymers Exposed to Low-Earth Orbit," *Proceedings of LDEF-69 Months in Space, Second Post-Retrieval Symposium,* NASA CP-3194, Part 3, San Diego, CA, NASA, Office of Management Science and Technology Information Program, Washington, DC, pp. 849–866.

Rand, J. L., Grant, D. A., and Strganac, T., 1996a, "The Nonlinear Biaxial Characterization of Balloon Film," AIAA Paper 96-0574, AIAA 34th Aerospace Sciences Meeting & Exhibit, Reno, NV.

Rand, J. L., Henderson, J. K., and Grant, D. A., 1996b, "Nonlinear Behavior of Linear Low Density Polyethylene," *Polymer Engineering and Science,* Vol. 36, No. 8, pp. 1058–1064.

Schapery, R. A., 1966, "A Theory of Nonlinear Thermoviscoelasticity Based on Irreversible Thermodynamics," *Proceedings of the 5th U.S. National Congress of Applied Mechanics,* ASME, New York, pp. 511–530.

Schapery, R. A., 1968, "On a Thermodynamic Constitutive Theory and Its Application to Various Nonlinear Materials," *Proceedings of the IUTAM Symposium,* Springer-Verlag, New York.

Schapery, R. A., 1969a, "Further Development of a Thermodynamic Constitutive Theory: Stress Formulation," Purdue University, Report AA & ES 69-2.

Schapery, R. A., 1969b, "On the Characterization of Nonlinear Viscoelastic Materials," *Polymer Engineering and Science,* Vol. 9, No. 4, pp. 295–310.

Schapery, R. A., 1971, "Viscoelastic Characterization of a Nonlinear Fiber-Reinforced Plastic," *Journal of Composite Materials,* Vol. 5, pp. 208–234.

Schapery, R. A., 1997, "Nonlinear Viscoelastic and Viscoplastic Constitutive Equations Based on Thermodynamics," *Mechanics of Time-Dependent Materials,* Vol. 1, pp. 209–240.

Smart, J., and Williams, J. G., 1972, "A Comparison of Single-Integral Nonlinear Viscoelasticity Theories," *Journal of the Mechanics and Physics of Solids,* Vol. 20, pp. 313–324.

Strganac, T. W., Letton, A., Farrow, D. A., Rock, N. I., and Williams, K. D., 1991, "The Investigation of Balloon Materials Exposed to the Low Earth Orbit Environment," AIAA Paper No. 91-3657, *Proceedings of the AIAA International Balloon Technology Conference,* Albuquerque, NM, American Institute of Aeronautics and Astronautics, Reston, VA.

Strganac, T. W., Letton, A., Payne, D. F., and Biskup, B. A., 1995, "Characterization of Nonlinear Viscoelastic Behavior using a Dynamic Mechanical Approach," *AIAA Journal,* Vol. 33, No. 5, pp. 904–910.

Strganac, T. W., and Golden, H. J., 1996, "Predictions of Nonlinear Viscoelastic Behavior Using a Hybrid Approach," *International Journal of Solids and Structures,* Vol. 33, No. 30, pp. 4561–4570.

Wilbeck, J. S., 1981, "Nonlinear Viscoelastic Characterization of Thin Polyethylene Film," NASA Contract Report 156876.

Downloaded 04 May 2010 to 171.66.16.27. Redistribution subject to ASME license or copyright; see http://www.asme.org/terms/Terms_Use.cfm

On the Dynamic Growth of a Spherical Inclusion With Dilatational Transformation Strain in Infinite Elastic Domain

B. Wang[1]
School of MPE,
Nanyang Technological University,
Singapore

Q. Sun
Department of Mechanical Engineering,
The Hong Kong University of Science and Technology,
Clear Water Bay,
Kowloon, Hong Kong

Z. Xiao
School of MPE,
Nanyang Technological University,
Singapore

In this paper, the dynamic effect was incorporated into the initiation and propagation process of a transformation inclusion. Based on the time-varying propagation equation of a spherical transformation inclusion with pure dilatational eigenstrain, the dynamic elastic fields both inside and outside the inclusion were derived explicitly, and it is found that when the transformation region expands at a constant speed, the strain field inside the inclusion is time-independent and uniform for uniform eigenstrain. Following the basic ideas of crack propagation problems in dynamic fracture mechanics, the reduction rate of the mechanical part of the free energy accompanying the growth of the transformation inclusion was derived as the driving force for the move of the interface. Then the equation to determine the propagation speed was established. It is found that there exists a steady speed for the growth of the transformation inclusion when time is approaching infinity. Finally the relation between the steady speed and the applied hydrostatic stress was derived explicitly.

Introduction

Martensitic-type phase transformations can happen in many kinds of solid materials. These materials can be certain metals, such as shape memory alloys and TRIP steels, as well as ceramics like zirconia. Extensive investigations have been done in the past decades to understand and model the mechanical behavior of materials during transformation (for example, Sun and Hwang, 1993a, b; Wang, 1997; Sano et al., 1992; Silling, 1992; Stam, 1994; etc.). Here we only mention a few papers, more completed literature may be found in a recent review paper by Ficher et al. (1996). However, most of these investigations are limited to the quasi-static cases.

In fact, a certain incubation time will be necessary for transformation to start, i.e., nucleation, but this is only in the order of hundreds of nanoseconds. Once the transformation has initiated, it will typically proceed throughout the crystal as growth of inclusion with very high speed, even over 1000 m/s. For such a high-speed propagation process of martensite, it is extremely difficult to investigate its nature using an experimental approach. The research work on dynamic analysis of transformation are far few compared with those on quasi-static analysis. One approach to study the propagation behavior of martensitic transformation is to assume that the growth of martensite takes place by the propagation of waves throughout the materials. By assuming the growth velocity according to the velocity of stress waves, one could predict the final morphology of martensitic transformation. For example, Meyers (1980) described the growth of lenticular martensite typically occurring in the Fe-Ni and Fe-C systems in terms of the propagation of transformation waves, and his model could determine the shape of a growing martensite plate. Whereas it is a well-known fact that in reality, only a few martensitic transformations can take place in the order of wave speed. Later Yu and Clapp (1989a) used both the magnetic induction and acoustic emission method to measure the velocity of martensitic growth, and then they (1989b) used molecular dynamics simulations to investigate the growth process. Mikata and Nemat-Nasser (1988) solved the eigenstrain problem wherein the transformation strain is spatially uniform in the inclusion and is time-harmonic, but the boundary of the inclusion is fixed. The key to the growth dynamics of martensitic transformation is the growth velocity of the moving interface and how it is affected by various driving forces and resisting forces in connection with temperature or external load. To the author's knowledge, no widely accepted conclusions exist about it at present stage.

In this paper, the objective is to incorporate the dynamic effect into the propagation process of a transformation inclusion. Based on the propagation equation of a spherical transformation inclusion with pure dilatational eigenstrain, the dynamic elastic fields both inside and outside the inclusion were derived explicitly first. Then following the basic ideas of crack propagation problems in dynamic fracture mechanics (Freund, 1990), the reduction rate of the mechanical part of the free energy accompanying the growth of the transformation inclusion was derived as the driving force for the propagation of the interface. Based on such an energy equation, the equation for determining the propagation speed was established. Although all the explicit expressions obtained are for self-similar growth of a spherical transformation region, some conclusions reveal some general characteristics of the growth stage. And the idea of this paper can also be extended easily to study the growth process of more realistic martensitic morphology.

2 The Stress Fields in an Elastic Solid With a Growing Martensitic Inclusion

2.1 Basic Equations for Dynamic Eigenstrain Problem. Using the convention that repeated suffixes imply summation, the equation of motion can be written in the form as

$$\frac{\partial \sigma_{jk}}{\partial x_k} + f_j = \rho \frac{\partial^2 u_j}{\partial t^2} \tag{1}$$

[1]On leave from Harbin Institute of Technology, China.

Contributed by the Applied Mechanics Division of THE AMERICAN SOCIETY OF MECHANICAL ENGINEERS for publication in the ASME JOURNAL OF APPLIED MECHANICS.

Discussion on the paper should be addressed to the Technical Editor, Professor Lewis T. Wheeler, Department of Mechanical Engineering, University of Houston, Houston, TX 77204-4792, and will be accepted until four months after final publication of the paper itself in the ASME JOURNAL OF APPLIED MECHANICS.

Manuscript received by the ASME Applied Mechanics Division, June 17, 1998; final revision, Dec. 14, 1998. Associate Technical Editor: J. W. Ju.

 Copyright © 1999 by ASME

Downloaded 04 May 2010 to 171.66.16.27. Redistribution subject to ASME license or copyright; see http://www.asme.org/terms/Terms_Use.cfm

where $u_i(\mathbf{x}, t)$ is the total displacement field, ρ is the density of the medium, and f_j is the body-force per unit volume.

Let us consider a body that tends to undergo a nonelastic small deformation $e^0_{jk}(\mathbf{x}, t)$. Suppose that the body occupies a volume D and is bounded by the traction-free surface L, then the stress σ_{jk} is given as

$$\sigma_{jk} = C_{jklm}(e_{lm} - e^0_{lm}) = \tau_{jk} - C_{jklm}e^0_{lm} \tag{2}$$

where $e_{ij} = \frac{1}{2}(u_{i,j} + u_{j,i})$ is the total strain, and $\tau_{jk} = C_{jklm}e_{lm}$ is the stress that would be produced if the displacement $u_i(\mathbf{x}, t)$ were completely elastic. Inserting (2) into the equation of motion with no body forces, we obtain

$$\frac{\partial \tau_{jk}}{\partial x_k} - \rho \frac{\partial^2 u_j}{\partial t^2} = C_{jklm} \frac{\partial e^0_{lm}}{\partial x_k} \tag{3}$$

with the boundary condition that $\tau_{jk}n_k - C_{jklm}n_k e^0_{lm} = 0$ on L. Comparing Eqs. (1) and (3), we see that the nonelastic deformation $e^0_{jk}(\mathbf{x}, t)$ produces the same total displacement as that by a body force $f_j = -C_{jklm}\partial e^0_{lm}/\partial x_k$ throughout D and surface traction $F_j = C_{jklm}n_k e^0_{lm}$ over L. By introducing the dynamic Green's function $G_{ij}(\mathbf{x}' - \mathbf{x}; t' - t)$, which means the x'_j-component of the displacement produced at $(\mathbf{x}'; t')$ by a concentrated impulsive unit force in the x_i-direction at $(\mathbf{x}, t)$, one obtains (Willis, 1965; Mura, 1987) for the case without external surface force

$$u_i(\mathbf{x}', t') = \int_{-\infty}^{\infty} dt \int_D C_{jklm}e^0_{lm}(\mathbf{x}, t) \frac{\partial G_{ij}(\mathbf{x}' - \mathbf{x}; t' - t)}{\partial x_k} dv(\mathbf{x}). \tag{4}$$

If the action of external surface force is considered, Eq. (4) becomes

$$u_i(\mathbf{x}', t') = \int_{-\infty}^{\infty} dt \int_D C_{jklm}e^0_{lm}(\mathbf{x}, t) \frac{\partial G_{ij}(\mathbf{x}' - \mathbf{x}; t' - t)}{\partial x_k} dv(\mathbf{x}) + \int_{-\infty}^{\infty} dt \int_L F_j(\mathbf{x}; t) G_{ij}(\mathbf{x}' - \mathbf{x}; t' - t) ds(\mathbf{x}). \tag{5}$$

2.2 Solution for Spherical Inclusion. Now we consider a transformation inclusion as a region Ω with boundary Γ inside elastic medium D, which undergoes a spontaneous uniform nonelastic deformation e^0_{lm} (Fig. 1).

Considering the growth of the inclusion, the eignstrain is expressed as

$$e^0_{lm} = \epsilon^T_{lm}(t)H(R(t) - |\mathbf{x}|) \tag{6}$$

where $R(t)$ is the radius of the inclusion, and $H(\cdot)$ is the Heaviside's function. For $R(t)$ = constant, it corresponds to Nemat-Nasser's work when ϵ^T_{lm} is time harmonic. Here for simplicity, the current problem involves a time-independent ϵ^T_{lm}, and the self-similar growth of spherical inclusion was considered. If the boundary L is traction free, the total displacement field is derived by inserting Eq. (6) into Eq. (5) and using Gauss's theorem,

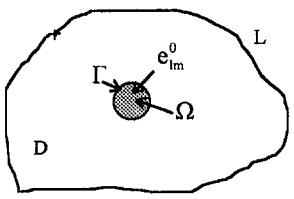


Fig. 1 A growth inclusion in infinite medium

$$u_i(\mathbf{x}', t') = \int_{-\infty}^{\infty} dt \int_{\Omega(R)} C_{jklm}\epsilon^T_{lm}H(R(t) - |\mathbf{x}|) \times \frac{\partial G_{ij}(\mathbf{x}' - \mathbf{x}; t' - t)}{\partial x_k} dv(\mathbf{x}) = \int_{-\infty}^{\infty} dt \int_\Gamma C_{jklm}\epsilon^T_{lm}n_k G_{ij}(\mathbf{x}' - \mathbf{x}; t' - t) ds(\mathbf{x}), \tag{7}$$

where Γ is the surface of the spherical inclusion and n_k is the outward normal to the surface.

In an isotropic medium, the appropriate expression for dynamic Green's function $G_{ij}(\mathbf{x}; t)$ has been given by Love (1944) as follows:

$$G_{ij}(\mathbf{X}; t) = \frac{1}{4\pi\rho}\left\{\frac{\delta(x - bt)}{bx}\delta_{ij} + \frac{\partial^2 x^{-1}}{\partial x_i \partial x_j}t + \frac{x_i x_j}{x^3}\left[\frac{\delta(x - at)}{a} - \frac{\delta(x - bt)}{b}\right]\right\} \quad 0 \le bt \le x \le at$$
$$= 0 \quad \text{otherwise} \tag{8}$$

where $\delta(\cdot)$ is Dirac's delta function, $a^2 = (\lambda + 2\mu)/\rho$, $b^2 = \mu/\rho$ and $x^2 = x_j x_j$, and λ, μ are Lame's constants.

We consider the spherical transformation inclusion undergoing a uniform dilatation ϵ^T throughout its volume, and having the same elastic moduli as the matrix. Hence

$$\epsilon^T_{lm} = \epsilon^T\delta_{lm}. \tag{9}$$

Substitution of Eq. (9) into Eq. (7) yields

$$u_i(\mathbf{x}', t') = (3\lambda + 2\mu)\int_{-\infty}^{\infty} dt \int_{S(R)} \epsilon^T \frac{x_j}{R(t)} G_{ij}(\mathbf{x}' - \mathbf{x}; t' - t) ds(\mathbf{x}). \tag{10}$$

By symmetry, in polar coordinates (r, θ, ϕ), the only nonzero displacement is $u_r(r, t')$, which coincides with $u_3(\mathbf{x}'; t')$ at any point $\mathbf{x}' = (0, 0, r)$ of the x'_3-axis. Therefore,

$$u_r(r, t') = u_3(0, 0, r; t') = (3\lambda + 2\mu)\int_{-\infty}^{\infty} dt \int_{S(R)} \frac{x_j}{R(t)} G_{3j}(\mathbf{x}' - \mathbf{x}; t' - t) ds(\mathbf{x})$$
$$= \frac{3\lambda + 2\mu}{2\rho}\int_{-\infty}^{\infty} dt \int_0^{\pi}\left\{\frac{\cos\theta\,\delta(x - bt)}{bx} + \frac{1}{x^5}[3(r\cos\theta - R)(r - R\cos\theta) - x^2\cos\theta] + \frac{(r\cos\theta - R)(r - R\cos\theta)}{x^3}\left[\frac{\delta(x - at)}{a} - \frac{\delta(x - bt)}{b}\right]\right\} R^2(t)\sin\theta d\theta \tag{11}$$

where we have substituted for G_{3j} from Eq. (8) with $\mathbf{x}' = (0, 0, r)$ and $\mathbf{x} = (R\sin\theta\cos\phi, R\sin\theta\sin\phi, R\cos\theta)$, and performed the trivial integration with respect to ϕ. The θ-integration can be carried out by transforming the independent variable to x as follows:

Downloaded 04 May 2010 to 171.66.16.27. Redistribution subject to ASME license or copyright; see http://www.asme.org/terms/Terms_Use.cfm

$$\cos\theta = \frac{R^2(t) + r^2 - x^2}{2R(t)r} \tag{12}$$

and the integration range for θ is $(0, \pi)$, which should change to $(|r - R|, r + R)$ for x. By considering the nonzero range of G_{3j} given by Eq. (8), the integration range should be (bt, at) for x. Through the integration, one can find that the components with speed b canceled each other. One obtains

$$u_r(r, t') = u_3(0, 0, r; t') = \frac{3\lambda + 2\mu}{2\rho} \cdot \frac{\epsilon^T}{a} \int_{t_L}^{t_U} \psi(t'; t)dt \tag{13}$$

where (t_L, t_U) are the lower and upper limits of the integration and are determined by $|r - R(t)| \le a(t' - t) \le r + R(t)$, and

$$\psi(t'; t) = \begin{cases} \dfrac{r^2 + R^2(t) - a^2(t' - t)^2}{2r^2}; \\ \qquad |r - R(t)| \le a(t' - t) \le r + R(t) \\ 0; \quad \text{otherwise.} \end{cases} \tag{14}$$

If we know the propagation equation $R(t)$ of the transformation inclusion, we can derive the dynamical displacement field both inside and outside the inclusion through Eq. (13).

2.3 Spherical Inclusion With Constant Propagation Velocity

(1) Interior Points. If the point **x** is inside the inclusion ($r - R(t) < 0$ or $r < R(t)$), equations for determining the upper and lower limits of the integration variable t are as follows:

$$a(t' - t_U^I) - R(t_U^I) + r \ge 0 \tag{15}$$

$$a(t' - t_L) - R(t_L) - r \le 0. \tag{16}$$

If we further assume that the inclusion expands at constant speed v, $R(t) = vt$. Equations (15) and (16) give the integration range

$$\frac{at' - r}{a + v} \le t \le \frac{at' + r}{a + v}. \tag{17}$$

Carrying out the integration (13) on the range (17) gives radial displacement inside the inclusion as follows:

$$u_r^I(t) = \frac{3\lambda + 2\mu}{3\rho a(a + v)^2}(a + 2v)r\epsilon^T \tag{18}$$

The total strain inside the inclusion is given by

$$\epsilon_r = \frac{\partial u_r}{\partial r} = \epsilon_t = \frac{u_r}{r} = \frac{3\lambda + 2\mu}{3\rho a(a + v)^2}(a + 2v)\epsilon^T. \tag{19}$$

For isotropic materials, the stress inside the inclusion can be obtained as follows:

$$\begin{aligned} \sigma_{ij}^I &= C_{ijkl}(\epsilon_{kl}^I - \epsilon_{kl}^T) \\ &= [\lambda\delta_{ij}\delta_{kl} + \mu\delta_{ik}\delta_{jl} + \mu\delta_{il}\delta_{jk}](\epsilon_r - \epsilon^T)\delta_{kl} \\ &= \left[\frac{1}{\left(1 + \dfrac{4\mu}{3\lambda + 2\mu}\right)\left(1 + \dfrac{v^2}{a(a + v)}\right)} - 1\right] \\ &\qquad \times (3\lambda + 2\mu)\epsilon^T\delta_{ij}. \end{aligned} \tag{20}$$

It is interesting to note that inside an expanding inclusion at a constant velocity, the elastic field is time-independent and the strain and stress are constant for uniform eignstrain as the case of a static inclusion problem (Mura, 1987). If the growth speed v approaches zero, Eqs. (18) and (19) approaches the result of the static inclusion problem by substituting $a^2 = (\lambda + 2\mu)/\rho$ into them. It can be found through Eq. (20) that if the eigenstrain of the inclusion is extension, the stresses inside the spherical inclusion are always hydrostatic compressive as expected. Further, the compressive stress will increase with the increasing speed of inclusion expansion. If the growth speed of the inclusion reaches the speed a of irrotational waves, the total extension strain will be reduced 25 percent as compared with the total strain of the static case (see Eq. (19)), and the hydrostatic compressive stress inside inclusion increases by 25 percent as given by Eq. (20).

(2) Exterior Points. In such case, the equation for determining the upper and lower limits of the integration is given by

$$a(t' - t_U^O) + R(t_U^O) - r \ge 0 \tag{21}$$

$$a(t' - t_L) - R(t_L) - r \le 0. \tag{22}$$

For uniform expansion inclusion, the integration range is given by

$$\frac{at' - r}{a + v} \le t \le \frac{at' - r}{a - v}. \tag{23}$$

Substitution of Eq. (23) into Eq. (13) gives

$$\begin{aligned} u_r^O(t) = \frac{(3\lambda + 2\mu)\epsilon^T}{4\rho a r^2(a^2 - v^2)^3}\Big\{ & 2vr^2(at - r)(a^2 - v^2)^2 \\ & + \frac{2}{3}v^3(at - r)^3(3a^2 + v^2) + \frac{1}{3}a^2[(r - vt)^3(a + v)^3 \\ & - (r + vt)^3(a - v)^3]\Big\} \end{aligned} \tag{24}$$

$$\sigma_{rr}^O = (\lambda + 2\mu)\frac{\partial u_r^o}{\partial r} + 2\lambda\frac{u_r^o}{r}. \tag{25}$$

One can check easily that on the surface of the inclusion (i.e., $r = vt$)

$$u_r^I(t) = u_r^O(t) \tag{26}$$

which satisfies the continuity condition on the surface.

3 Energy Concepts and the Equation of Martensitic Inclusion Growth

Accompanying the propagation of the transformation inclusion, the energy will change. Similar to the dynamic fracture process (Freund, 1990), the released energy serves as a generalized driving force for the growth of the inclusion. In this section, we will derive the expression of the energy release rate, and establish the equation to determine the growth rate of the inclusion.

3.1 The Rate of Mechanical Energy. Consider a finite body D containing a transformation inclusion Ω. Along the surface S of D, the external force is $T_i = \sigma_{ij}n_j$, and the inner and outer surfaces of Ω are denoted as Γ^-, Γ^+ (Fig. 2).

The mechanical part of the internal energy involves the elastic energy plus the kinetic energy. Therefore, the rate of elastic strain energy inside D is given by

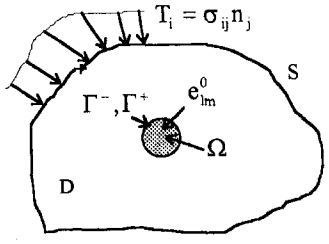


Fig. 2 A transformation inclusion in elastic medium

Downloaded 04 May 2010 to 171.66.16.27. Redistribution subject to ASME license or copyright; see http://www.asme.org/terms/Terms_Use.cfm

$$\dot{W} = \frac{d}{dt}\left[\frac{1}{2}\int_D \sigma_{ij} e_{ij} dv\right] \tag{27}$$

where

$$\sigma_{ij} = C_{ijkl}(\epsilon_{kl} - \epsilon^T_{kl}) \tag{28}$$

$$e_{ij} = \epsilon_{ij} - \epsilon^T_{ij}. \tag{29}$$

Substitution of Eqs. (28), (29) into Eq. (27) yields

$$\begin{aligned}\dot{W} &= \frac{1}{2}\int_D \frac{d}{dt}\{\sigma_{ij}(\epsilon_{ij} - \epsilon^T_{ij})\}dv \\ &= \frac{1}{2}\int_D \frac{d}{dt}\left\{C_{ijkl}\left(\frac{\partial u_i}{\partial x_j} - \epsilon^T_{ij}\right)\left(\frac{\partial u_k}{\partial x_l} - \epsilon^T_{kl}\right)\right\}dv \\ &= \int_D C_{ijkl}\left(\frac{\partial \dot{u}_i}{\partial x_j} - \dot{\epsilon}^T_{ij}\right)\left(\frac{\partial u_k}{\partial x_l} - \epsilon^T_{kl}\right)\Big\}dv \\ &= \int_D \sigma_{ij}\left(\frac{\partial \dot{u}_i}{\partial x_j} - \dot{\epsilon}^T_{ij}\right)dv. \end{aligned} \tag{30}$$

By substituting Eq. (1) into Eq. (30), the first term of Eq. (30) can be written as

$$\begin{aligned}\int_D \sigma_{ij}\frac{\partial \dot{u}_i}{\partial x_j}dv &= \int_D \frac{\partial}{\partial x_j}(\sigma_{ij}\dot{u}_i)dv - \int_D \sigma_{ij,j}\dot{u}_i dv \\ &= \int_D \frac{\partial}{\partial x_j}(\sigma_{ij}\dot{u}_i)dv - \int_D \rho\ddot{u}_i\dot{u}_i dv. \end{aligned} \tag{31}$$

In an elastic medium with a growing inclusion, we cannot use Gauss's theorem directly to the first term in Eq. (31), since across the boundary of the inclusion, the integrand is not continuous. So we divide the integral into two parts as follows:

$$\begin{aligned}\int_D \frac{\partial}{\partial x_j}(\sigma_{ij}\dot{u}_i)dv &= \int_\Omega \frac{\partial}{\partial x_j}(\sigma_{ij}\dot{u}_i)dv + \int_{D-\Omega} \frac{\partial}{\partial x_j}(\sigma_{ij}\dot{u}_i)dv \\ &= \int_{\Gamma^-} \sigma_{ij}\dot{u}_i n_j ds - \int_{\Gamma^+} \sigma_{ij}\dot{u}_i n_j ds \\ &\quad + \int_S \sigma_{ij}\dot{u}_i n_j ds \\ &= -\int_\Gamma [\sigma_{ij}\dot{u}_i]n_j ds + \int_S \sigma_{ij}\dot{u}_i n_j ds \end{aligned} \tag{32}$$

where Γ is the surface of the inclusion, n_j is the exterior unit vector normal to Γ, and

$$[\sigma_{ij}\dot{u}_i] = (\sigma_{ij}\dot{u}_i)_{\text{out}} - (\sigma_{ij}\dot{u}_i)_{\text{in}}. \tag{33}$$

The change rate of the kinetic energy is given by

$$\dot{K} = \int_D \rho\dot{u}_i\ddot{u}_i dv. \tag{34}$$

Therefore the change rate of the internal energy is given by

$$\begin{aligned}\dot{E} &= \dot{W} + \dot{K} \\ &= -\int_\Gamma [\sigma_{ij}\dot{u}_i]n_j ds - \int_D \sigma_{ij}\dot{\epsilon}^T_{ij}dv + \int_S \sigma_{ij}\dot{u}_i n_j ds. \end{aligned} \tag{35}$$

The rate of work done by the external force T_i is given by

$$U = \int_S T_i\dot{u}_i ds = \int_S \sigma_{ij}n_j\dot{u}_i ds. \tag{36}$$

Therefore the energy release rate accompanying the growth of the transformation inclusion can be obtained as follows:

$$\dot{\Pi} = U - \dot{E} = \int_\Gamma [\sigma_{ij}\dot{u}_i]n_j ds + \int_\Omega \sigma_{ij}\dot{\epsilon}^T_{ij}dv. \tag{37}$$

According to Eqs. (6) and (9), one can obtain

$$\dot{e}^0_{ij} = \epsilon^T\delta_{ij}\delta(R(t) - |x|)\dot{R}(t). \tag{38}$$

The volume integral in Eq. (37) can be carried out first on $|x|$, and one obtains

$$\dot{\Pi} = \int_\Gamma \{[\sigma_{ij}\dot{u}_i]n_j + \sigma_{ii}\epsilon^T\dot{R}(t)\}ds. \tag{39}$$

Eshelby proposed the famous energy-momentum tensor as the driving force for a defect to propagate in materials (Eshelby, 1970). In fact, Eq. (39) gives the rate of the driving force for a transformation region to expand in the same sense. $\dot{\Pi}$ also means the reduction rate of the mechanical part of the free energy accompanying the growth of the transformation inclusion. For spherical inclusion with pure dilatational eigenstrain as discussed in this paper, Eq. (39) becomes

$$\begin{aligned}\dot{\Pi} &= \int_\Gamma \{[\sigma_{ij}\dot{u}_i]n_j + \sigma_{ii}\epsilon^T\dot{R}(t)\}ds \\ &= S(R)\{[\sigma_{rr}\dot{u}_r] + \sigma_{ii}\epsilon^T\dot{R}(t)\} \\ &= S(R)\Bigg\{(\lambda + 2\mu)\left[\frac{\partial u^O_r}{\partial r}\dot{u}^O_r - \left(\frac{\partial u^I_r}{\partial r} - \epsilon^T\right)\dot{u}^I_r\right] \\ &\quad + 2\lambda\left[\frac{u^O_r}{r}\dot{u}^O_r - \left(\frac{u^I_r}{r} - \epsilon^T\right)\dot{u}^I_r\right] \\ &\quad + \epsilon^T\dot{R}(t')\Bigg[\sigma^0_{ii} + (3\lambda + 2\mu) \\ &\qquad \times \left(\frac{\partial u^I_r}{\partial r} + 2\frac{u^I_r}{r} - 3\epsilon^T\right)\Bigg]\Bigg\}\Bigg| r = R(t') \end{aligned} \tag{40}$$

where $S(R)$ is the surface area of the inclusion. The radial displacements u^I_r, u^O_r inside and outside the inclusion are given by Eq. (13) as follows:

$$u^I_r = C\int_{t_L}^{t^I_u} \psi(t'; t)dt \tag{41}$$

$$u^O_r = C\int_{t_L}^{t^O_u} \psi(t'; t)dt \tag{42}$$

where $C = (3\lambda + 2\mu)\epsilon^T/2\rho a$, $\psi(t'; t)$ is given by Eq. (14), and t_L, t^I_U, t^O_U can be determined by Eqs. (15), (16), and (21), respectively. It can be found easily that

Downloaded 04 May 2010 to 171.66.16.27. Redistribution subject to ASME license or copyright; see http://www.asme.org/terms/Terms_Use.cfm

$$\left\{ t_U^I = t_U^O = t';\ \frac{\partial t_U^I}{\partial t'} = \frac{\partial t_U^O}{\partial t'} = 1 \right\} \Big| \, r = R(t'). \tag{43}$$

Therefore

$$\dot{u}_r^O = \dot{u}_r^I = C\left[\int_{t_L}^{t'} \frac{\partial \psi(t';\, t)}{\partial t'}\, dt + 1 - \psi(t';\, t_L)\, \frac{\partial t_L}{\partial t'} \right] \tag{44}$$

$$\frac{\partial u_r^O}{\partial r} = C\left[\int_{t_L}^{t'} \frac{\partial \psi(t';\, t)}{\partial r}\, dt + \frac{\partial t_U^O}{\partial r} - \psi(t';\, t_L)\, \frac{\partial t_L}{\partial r} \right] \tag{45}$$

$$\frac{\partial u_r^I}{\partial r} = C\left[\int_{t_L}^{t'} \frac{\partial \psi(t';\, t)}{\partial r}\, dt + \frac{\partial t_U^I}{\partial r} - \psi(t';\, t_L)\, \frac{\partial t_L}{\partial r} \right]. \tag{46}$$

Substitution of Eqs. (44), (45), and (46) into Eq. (40) yields

$$\dot{\Pi} = S(R)\Bigg\{ C\left[(3\lambda + 2\mu)\epsilon^T - \frac{2aC}{a^2 - \dot{R}^2(t')}\,(\lambda + 2\mu) \right] \times \left[\int_{t_L}^{t'} \frac{\partial \psi(t';\, t)}{\partial t'}\, dt + 1 - \psi(t';\, t_L)\, \frac{\partial t_L}{\partial t'} \right] + \epsilon^T \dot{R}(t') \Bigg\{ \sigma_{ii}^0 - 3(3\lambda + 2\mu)\epsilon^T + (3\lambda + 2\mu)C\left[\int_{t_L}^{t'} \frac{\partial \psi(t';\, t)}{\partial r}\, dt + \frac{\partial t_U^I}{\partial r} - \psi(t';\, t_L)\, \frac{\partial t_L}{\partial r} + 2\int_{t_L}^{t'} \psi(t';\, t)\, dt/R(t') \right] \Bigg\} \Bigg\}. \tag{47}$$

$\dot{\Pi}$ can also be expressed in the form as

$$\dot{\Pi} = g\dot{R}(t) \tag{48}$$

where $g = \partial\Pi/\partial R$, is the rate of mechanical energy reduction per unit increase of the inclusion radius.

3.2 The Rate of Chemical and Surface Free Energy. If the reduction of surface energy per unit area and the reduction of the chemical free energy per unit volume are denoted as ΔU_s, $\Delta U_{ch} = -\Delta S(T_0 - T)$, where ΔS is the transformational entropy change, T is the temperature (Wang, 1997), and the total free energy release rate per unit increase of R is given by

$$G = g + 4\pi R^2 \Delta U_{ch} + 8\pi R \Delta U_s = \frac{\dot{\Pi}}{\dot{R}} - 4\pi R^2 \Delta S(T_0 - T) + 8\pi R \Delta U_s. \tag{49}$$

Considering that the energy will be dissipated in the process of the transformation, one can establish the growth criterion of the transformation region as follows:

$$G = G_c \tag{50}$$

where G_c is the material constant, which represents the dissipated part of the energy. Through Eq. (50), one can obtain the radius of the transformation inclusion as a function of time under different external conditions.

4 Discussion and Some Concluding Remarks

If we take the assumption that after time t_0, the inclusion will grow in constant speed V, therefore, from t_L to t', it expands also in the constant speed, and one obtains

$$t_L = \frac{a - V}{a + V}\, t' - \frac{2[R(t_0) - Vt_0]}{a + V} \tag{51}$$

$$R(t) = R(t_0) + V(t - t_0). \tag{52}$$

Substitution of Eqs. (51), (52) into Eq. (13), then into Eq. (47) yields

$$\dot{\Pi} = S(R)\Bigg\{ C\left[(3\lambda + 2\mu)\epsilon^T - \frac{2aC}{a^2 - V^2}\,(\lambda + 2\mu) \right]\left[\frac{R^3(t_L)}{3R^3(t')} + \frac{8a^2V}{3(a+V)^3} - \frac{2a^2}{(a+V)^2} + \frac{2}{3} - \left(\frac{R^2(t_L)}{2R^2(t')} - \frac{2a^2}{(a+V)^2} + \frac{1}{2} \right)\frac{a - V}{a + V} \right] + \epsilon^T V \Bigg\{ \sigma_{ii}^0 - 3(3\lambda + 2\mu)\epsilon^T + \frac{(3\lambda + 2\mu)C}{a + V}\left[\frac{R^2(t_L)}{2R^2(t')} - \frac{2a^2}{(a+V)^2} + \frac{7}{2} \right] \Bigg\} \Bigg\}. \tag{53}$$

Substitution of Eq. (53) into Eq. (49), then into Eq. (50) yields an equation for determining the speed V of the inclusion propagation. It can be found that the speed depends on the time t' through the terms involving $R(t_L)/R(t')$. When the time $t' \to \infty$, one finds

$$\lim_{t' \to \infty} \frac{R(t_L)}{R(t')} = \frac{a - V}{a + V}. \tag{54}$$

Substitution of Eq. (54) into Eq. (53) gives

$$\dot{\Pi} = S(R)\Bigg\{ C\left[(3\lambda + 2\mu)\epsilon^T - \frac{2aC}{a^2 - V^2}\,(\lambda + 2\mu) \right] \times \left[\frac{(a - V)^3}{3(a+V)^3} + \frac{8a^2V}{3(a+V)^3} - \frac{2a^2}{(a+V)^2} + \frac{2}{3} - \left(\frac{(a - V)^2}{2(a+V)^2} - \frac{2a^2}{(a+V)^2} + \frac{1}{2} \right)\frac{a - V}{a + V} \right] + \epsilon^T V \Bigg\{ \sigma_{ii}^0 - 3(3\lambda + 2\mu)\epsilon^T + \frac{(3\lambda + 2\mu)C}{a + V}\left[\frac{(a - V)^2}{2(a+V)^2} - \frac{2a^2}{(a+V)^2} + \frac{7}{2} \right] \Bigg\} \Bigg\}. \tag{55}$$

Substitution of Eq. (55) into Eq. (49), then into Eq. (50) yields an equation for determining the steady speed of the inclusion expansion when $t' \to \infty$.

If it is assumed that the boundary of the transformation inclusion grows in constant speed V, one can write

$$t_L = \frac{a - V}{a + V}\, t',\ R(t) = Vt. \tag{56}$$

Therefore, from Eq. (47), one can find that reduction rate of the mechanical part of the free energy $\dot{\Pi}$ is also given by Eq. (55). Substitution of Eq. (55) into Eq. (49), then into Eq. (50) yields

$$\frac{4\pi R^2}{V}\Bigg\{ C\left[(3\lambda + 2\mu)\epsilon^T - \frac{2aC}{a^2 - V^2}\,(\lambda + 2\mu) \right]\left[\frac{(a - V)^3}{3(a+V)^3} + \frac{8a^2V}{3(a+V)^3} - \frac{2a^2}{(a+V)^2} + \frac{2}{3} - \left(\frac{(a - V)^2}{2(a+V)^2} - \frac{2a^2}{(a+V)^2} + \frac{1}{2} \right)\frac{a - V}{a + V} \right] + \epsilon^T V \Bigg\{ \sigma_{ii}^0 - 3(3\lambda + 2\mu)\epsilon^T + \frac{(3\lambda + 2\mu)C}{a + V}\left[\frac{(a - V)^2}{2(a+V)^2} - \frac{2a^2}{(a+V)^2} + \frac{7}{2} \right] \Bigg\} \Bigg\} - 4\pi R^2 \Delta S(T_0 - T) + 8\pi R \Delta U_s = G_c. \tag{57}$$

Using Eq. (57), one can determine the constant growth speed of the transformation inclusion according to the applied environment temperature and hydrostatic load for different materials. The dis-

Downloaded 04 May 2010 to 171.66.16.27. Redistribution subject to ASME license or copyright; see http://www.asme.org/terms/Terms_Use.cfm

sipated part of the energy can be assumed to be proportional to the volume of the inclusion, therefore G_c can be expressed in the form as

$$G_c = 4\pi R^2 \xi_c \tag{58}$$

where ξ_c is the dissipated energy for creating unit volume of martensite. Substitution of Eq. (58) into Eq. (57) yields

$$\frac{1}{V}\left\{C\left[(3\lambda+2\mu)\epsilon^T - \frac{2aC}{a^2-V^2}(\lambda+2\mu)\right]\left[\frac{(a-V)^3}{3(a+V)^3} + \frac{8a^2V}{3(a+V)^3} - \frac{2a^2}{(a+V)^2} + \frac{2}{3} - \left(\frac{(a-V)^2}{2(a+V)^2} - \frac{2a^2}{(a+V)^2} + \frac{1}{2}\right)\frac{a-V}{a+V}\right] + \epsilon^T V\left\{\sigma_{ii}^0 - 3(3\lambda+2\mu)\epsilon^T + \frac{(3\lambda+2\mu)C}{a+V}\left[\frac{(a-V)^2}{2(a+V)^2} - \frac{2a^2}{(a+V)^2} + \frac{7}{2}\right]\right\}\right\} - \Delta S(T_0 - T) + \frac{2}{R}\Delta U_s = \xi_c. \tag{59}$$

From Eq. (59), we know, if the surface energy ΔU_s can be neglected, under the action of constant hydrostatic tension, or constant temperature, the interface of martensitic inclusion can grow in constant speed, whereas if the surface energy cannot be neglected, to obtain the constant speed for martensite growth, the applied external condition must change in proportion to $\propto 1/R$.

If we further assume that the reduction of the chemical free energy compensates for the dissipation energy in the transformation process, i.e., $\Delta U_{ch} = -\Delta S(T_0 - T) = \xi_c$, one obtains

$$\frac{1}{V}\left\{C\left[(3\lambda+2\mu)\epsilon^T - \frac{2aC}{a^2-V^2}(\lambda+2\mu)\right]\left[\frac{(a-V)^3}{3(a+V)^3} + \frac{8a^2V}{3(a+V)^3} - \frac{2a^2}{(a+V)^2} + \frac{2}{3} - \left(\frac{(a-V)^2}{2(a+V)^2} - \frac{2a^2}{(a+V)^2} + \frac{1}{2}\right)\frac{a-V}{a+V}\right] + \epsilon^T V\left\{\sigma_{ii}^0 - 3(3\lambda+2\mu)\epsilon^T + \frac{(3\lambda+2\mu)C}{a+V}\left[\frac{(a-V)^2}{2(a+V)^2} - \frac{2a^2}{(a+V)^2} + \frac{7}{2}\right]\right\}\right\} + \frac{2}{R}\Delta U_s = 0. \tag{60}$$

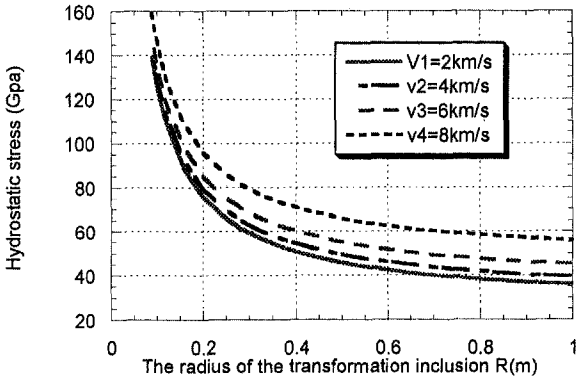


Fig. 3 The applied hydrostatic stress versus the size of the transformation inclusion for growth velocities; *v*1 = 2 km/s, *v*2 = 4 km/s, *v*3 = 6 km/s, *v*4 = 8 km/s

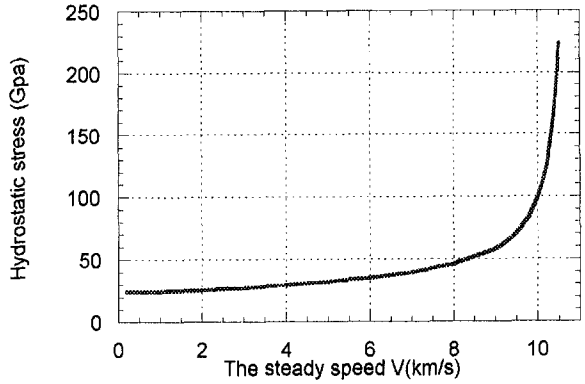


Fig. 4 The applied hydrostatic stress versus steady speed of the inclusion expansion

Using Eq. (60), one can derive σ_{ii}^0 required to keep the interface propagating in constant speed as a function of the inclusion size. If we take the ceramic material as an example, whose constants are $\lambda = 130.77$ Gpa, $\mu = 80.15$, $\rho = 2500$ kg/m^3, $\epsilon^T = 0.04$, $\Delta U_s = -200$ Mpa, the applied hydrostatic stress was shown in Fig. 3. The results shown here do not correspond to any practical case.

The applied hydrostatic stress versus the steady speed was shown in Fig. 4. It is obvious that the growth speed is always lower than the speed $a = 10790$ m/s of irrotational waves.

Acknowledgments

The authors appreciate the support by the National Natural Science Foundation of China through the Fund for Excellent Young Investigators.

References

Eshelby, J. D., 1970, "Energy Relations and the Energy-Momentum Tensor in Continuum Mechanics," *Inelastic Behavior of Solids,* M. F. Kanninen, W. F. Adler, A. R. Rosenfield, and R. I. Jaffee, eds., McGraw-Hill, New York, pp. 77–115.

Fischer, F. D., Sun, Q. P., and Tanaka, T., 1996, "Transformation-Induced Plasticity," ASME *Applied Mechanics Reviews,* Vol. 49, pp. 317–364.

Freund, L. B., 1990, *Dynamic Fracture Mechanics,* Cambridge University Press, London.

Love, A. E. H., 1944, *A Treatise on the Mathematical Theory of Elasticity,* 4th Ed., Dover, New York.

Meyers, M. A., 1980, "On the Growth of Lenticular Martensite," *Acta Metallurgica,* Vol. 28, pp. 757–770.

Mikata, Y., and Nemat-Nasser, S., 1988, "First-Order Dynamic Eshelby Tensor," *Proceedings of 25th Annual Technical Meeting Society of Engineering Science,* CA.

Mura, T., 1987, *Micromechanics of Defects in Solids,* 2nd Rev. Ed., Martinus Nijhoff, Dordrecht, The Netherlands.

Sano, Y., Chang, S. N., Meyers, M. A., and Nemat-Nasser, S., 1992, "Identification of Stress-Induced Nucleation Sites for Martensite in Fe-31.8 wt% Ni-0.02 wt% C Alloy," *Acta Metall. Mater.,* Vol. 40, p. 413.

Silling, S. A., 1992, "Dynamic Growth of Martensitic Plates in an Elastic Material," *Journal of Elasticity,* Vol. 28, pp. 143–164.

Sun, Q. P., and Hwang, K. C., 1993, "Micromechanics Modeling for Constitutive Behavior of Polycrystalline Shape Memory Alloys–I. Derivation of General Relations," *J. Mech. Phys. Solids,* Vol. 41, p. 1.

Sun, Q. P., and Hwang, K. C., 1993, "Micromechanics Modeling for Constitutive Behavior of Polycrystalline Shape Memory Alloys–II. Study of the Individual Phenomena," *J. Mech. Phys. Solids,* Vol. 41, p. 19.

Stam, G. Th. M., 1994, "A Micromechanical Approach to Transformation Toughening in Ceramics," Ph.D. thesis, Delft University of Technology.

Wang, B., 1997, "Some Special Characteristics of Stress-Induced Martensitic Transformations Predicted by a Statistical Model," *Acta Mater.,* Vol. 45, No. 4, pp. 1551–1556.

Willis, J. R., 1965, "Dislocations and Inclusions," *J. Mech. Phys. Solids,* Vol. 13, pp. 377–395.

Yu, Z-H., and Clapp, P. C., 1989, "Growth Dynamics Study of the Martensitic Transformation in Fe-30 Pct Ni Alloys: Part I. Quantitative Measurements of Growth Velocity," *Metallurgical Transaction A,* Vol. 20, pp. 1601–1615.

Yu, Z-H., and Clapp, P. C., 1989, "Growth Dynamics Study of the Martensitic Transformation in Fe-30 Pct Ni Alloys: Part II. Computer Simulation of Martensitic Growth," *Metallurgical Transaction A,* Vol. 20, pp. 1617–1629.

Downloaded 04 May 2010 to 171.66.16.27. Redistribution subject to ASME license or copyright; see http://www.asme.org/terms/Terms_Use.cfm

Application of Finite-Part Integrals to Planar Interfacial Fracture Problems in Three-Dimensional Bimaterials

M.-C. Chen[1]
Department of Mechanical Engineering,
East China Jiaotong University,
Nanchang 330013, Jiangxi, P.R. China

N.-A. Noda
Department of Mechanical Engineering,
Kyushu Institute of Technology,
Kitakyushu 804-8550, Japan

R.-J. Tang
Department of Engineering Mechanics,
Shanghai Jiao Tong University,
Shanghai 200030, P.R. China

This paper deals with linear elastic fracture problems for a planar crack on an interface between two dissimilar elastic half-space solids bonded together. The finite-part integral concept is used to derive hypersingular integro-differential equations for the interfacial crack from the point-force solutions for a bimaterial space. Investigations on the singularities and the singular stress fields in the vicinity of the crack are made by the dominant-part analysis of the two-dimensional hypersingular integrals. Thereafter the stress intensity factor K-fields and the energy release rate G are exactly obtained by using the definitions of stress intensity factors and the principle of virtual work, respectively. The results show that, unlike the homogenous case, the asymptotic fields always consist of all three modes of fracture. Finally, some numerical examples of various aspects of elliptical cracks subjected to constant pressures are given.

Introduction

With the rapidly increasing use of composites for engineering structures, much attention has been paid to the interfacial crack by more researchers. It is useful to design and manufacture composite materials for which we know the fracture behavior of their interface. During the past few years, considerable analyses have been performed, and many problems regarding the mechanics of interfacial fracture have been discussed. However, these studies generally involved two-dimensional interfacial crack modeling; little work, theoretical work in particular, on the three-dimensional aspect of crack problems has been carried out except those of specially shaped cracks (Wills, 1972; Erdogan and Arin, 1972; Kassir and Bregman, 1972; Shibuya et al., 1989; Nakamura, 1991; Yuuki and Xu, 1992). This is mainly due to the extreme difficulties of solving such problems by mathematics and mechanics, or to the substantial computation required in the numerical analyses.

The purpose of this paper is to make more systematic and painstaking theoretical studies of a three-dimensional planar interfacial crack on a bimaterial interface by the use of hypersingular integral equation method. The key to the utilization of the hypersingular integral equation method is the availability of known point-force fundamental solutions expressed in tensor form obtained by the authors (1997) and the concept of the finite-part integral introduced by Hadamard (1952). Two-dimensional hypersingular integral equations with unknown displacement jumps across the crack surfaces are first derived for an arbitrarily shaped crack parallel to a bimaterial interface, then based on these equations, use is further made of limit theory and Taylor series expansions to obtain hypersingular integro-differential equations for the interfacial planar crack. In order to determine the stress singularities near the interfacial crack front edge, the hypersingular integro-differential equations are investigated by the dominant-part analysis of the two-dimensional hypersingular integrals. Starting strictly from the three-dimensional theory of elasticity, the dominant-part analysis of the two-dimensional hypersingular integrals is also applied to study the singular stress fields ahead of the interfacial crack front edge. The stress intensity factor K-fields for the three-dimensional planar interfacial cracks are arrived at in the light of similar definitions of K-fields for the two-dimensional interfacial cracks (Hutchinson et al., 1987; Rice, 1988). In addition, energy release rate G is analyzed by the principle of virtual work. Finally, some numerical examples of planar interfacial elliptical cracks under the normal uniform loading are given.

Hypersingular Integral Equation for a Planar Crack Parallel to a Bimaterial Interface

A fixed rectangular Cartesian coordinate system x_i is used. Subscripts of English letters always take the values 1, 2, 3 and those of Greek letters, 1, 2. The Einstein summation convention is assumed. We consider two dissimilar elastic half-spaces bonded together along the $x_1 - x_2$ plane (see Fig. 1). Suppose that the upper half-space is occupied by an elastic medium with constants (μ_1, υ_1) and the lower half-space by an elastic medium with constants (μ_2, υ_2), where μ is shear modulus and υ Poisson's ratio. The planar crack is assumed to be located at a distance h above, and parallel to, the bimaterial interface. The external forces acting on the planar crack surfaces $(S^{\pm})$ are in self-equilibrium. The displacements and the stresses are presumed to decrease to zero at infinity.

The displacement in the upper space I due to the crack disturbance can be expressed in terms of Somigliana's identity (Brebbia, 1981) as

$$u_i^{\mathrm{I}}(\mathbf{x}) = -\int_{S^+} T_{ij}^{\mathrm{I}+}(\mathbf{x}, \boldsymbol{\xi}) \Delta u_j^{\mathrm{I}}(\boldsymbol{\xi}) dS(\boldsymbol{\xi}), \tag{1}$$

in which the superscript I means the upper half-space I; $\Delta u_j^{\mathrm{I}}(\boldsymbol{\xi})$ are the unknown displacement jumps across the crack surfaces $(S^{\pm})$, i.e.,

$$\Delta u_j^{\mathrm{I}}(\boldsymbol{\xi}) = \{u_j^{\mathrm{I}}(\boldsymbol{\xi})\}_{x_3=h^+} - \{u_j^{\mathrm{I}}(\boldsymbol{\xi})\}_{x_3=h^-}$$

and $T_{ij}^{\mathrm{I}+}(\mathbf{x}, \boldsymbol{\xi})$ denote the tractions in the i direction at a point $\mathbf{x}$ generated by a unit concentrated body force in the j direction

[1] On leave from Kyushu Institute of Technology, Kitakyushu, Japan.

Contributed by the Applied Mechanics Division of THE AMERICAN SOCIETY OF MECHANICAL ENGINEERS for publication in the ASME JOURNAL OF APPLIED MECHANICS.
Discussion on the paper should be addressed to the Technical Editor, Professor Lewis T. Wheeler, Department of Mechanical Engineering, University of Houston, Houston, TX 77204-4792, and will be accepted until four months after final publication of the paper itself in the ASME JOURNAL OF APPLIED MECHANICS.
Manuscript received by the ASME Applied Mechanics Division, Sept. 23, 1998; final revision, Feb. 19, 1999. Associate Technical Editor: W. J. Drugan.

 Copyright © 1999 by ASME

Downloaded 04 May 2010 to 171.66.16.27. Redistribution subject to ASME license or copyright; see http://www.asme.org/terms/Terms_Use.cfm

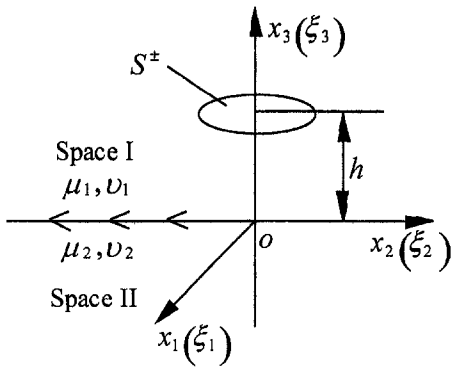


Fig. 1 A planar crack parallel to a bimaterial interface

applied at a point $\boldsymbol{\xi}$ in the upper half-space I (Chen and Tang, 1997).

By using (1) and the generalized Hooke's law, the corresponding stress fields read

$$\sigma_{ij}^{\mathrm{I}}(\mathbf{x}) = -C_{ijkl}^{\mathrm{I}} \int_{S^+} \frac{\partial T_{km}^{\mathrm{I}+}(\mathbf{x}, \boldsymbol{\xi})}{\partial x_l} \Delta u_m^{\mathrm{I}}(\boldsymbol{\xi}) dS(\boldsymbol{\xi}), \tag{2}$$

where C_{ijkl}^{I} are the components of the elastic modulus tensor in the upper half-space I, given by

$$C_{ijkl}^{\mathrm{I}} = \frac{2\upsilon_1\mu_1}{1-2\upsilon_1}\delta_{ij}\delta_{kl} + \mu_1(\delta_{ik}\delta_{jl} + \delta_{il}\delta_{jk}),$$

where δ_{mn} is the Kronecker delta.

Noting that the differentiations of $T_{ij}^{\mathrm{I}+}(\mathbf{x}, \boldsymbol{\xi})$ in (2) have hypersingularities of $O(r^3)$ as the point $\mathbf{x}$ approaches the point $\boldsymbol{\xi}$ on the crack surfaces $S^+(x_3 \to h)$ and the boundary conditions over the upper crack surface $\sigma_{3i}^{\mathrm{I}}(x_1, x_2, h^+) = -p_i^{\mathrm{I}}(x_1, x_2, h^+)$, we must employ the concept of the finite-part integral while obtaining the limits of the stress components $\sigma_{3i}^{\mathrm{I}}(x_1, x_2, h^+)$ which give the crack surface tractions.

After lengthy manipulations, a system of two-dimensional hypersingular integral equations for the planar crack parallel to the bimaterial interface is written as

$$\begin{aligned}
&\oint\!\!\!\!\!\!-_{S^+} \left[\frac{2(\kappa_1-1)}{r^3}\delta_{\alpha\beta} + \frac{3(3-\kappa_1)(x_\alpha-\xi_\alpha)(x_\beta-\xi_\beta)}{r^5}\right]\Delta u_\beta^{\mathrm{I}}(\boldsymbol{\xi})dS(\boldsymbol{\xi}) \\
&\quad + \int_{S^+} K_{\alpha j}^{\mathrm{I}}(\mathbf{x}, \boldsymbol{\xi})\Delta u_j^{\mathrm{I}}(\boldsymbol{\xi})dS(\boldsymbol{\xi}) \\
&\qquad = -\frac{4\pi(\kappa_1+1)}{\mu_1} p_\alpha^{\mathrm{I}}(x_1, x_2, h^+), \quad x_1, x_2 \in S^+, \quad (3a)
\end{aligned}$$

$$\begin{aligned}
&\oint\!\!\!\!\!\!-_{S^+} \frac{4}{r^3}\Delta u_3^{\mathrm{I}}(\boldsymbol{\xi})dS(\boldsymbol{\xi}) + \int_{S^+} K_{3j}^{\mathrm{I}}(\mathbf{x}, \boldsymbol{\xi})\Delta u_j^{\mathrm{I}}(\boldsymbol{\xi})dS(\boldsymbol{\xi}) \\
&\qquad = -\frac{4\pi(\kappa_1+1)}{\mu_1} p_3^{\mathrm{I}}(x_1, x_2, h^+), \quad x_1, x_2 \in S^+, \quad (3b)
\end{aligned}$$

in which

$$\kappa_1 = 3 - 4\upsilon_1; \quad r^2 = \delta_{\alpha\beta}(x_\alpha - \xi_\alpha)(x_\beta - \xi_\beta);$$

$\oint\!\!\!\!\!\!-_{S^+}$ means the finite-part integral of Hadamard (1952) and the kernels $K_{ij}^{\mathrm{I}}(\mathbf{x}, \boldsymbol{\xi})$ read

$$\begin{aligned}
K_{11}^{\mathrm{I}}(\mathbf{x}, \boldsymbol{\xi}) &= -2[(\kappa_1-1) + (\kappa_1+1)(\Lambda_1+\Lambda_2-2\Lambda)]/R^3 \\
&\quad + 3\{4h^2[(\kappa_1-5) + 2(\kappa_1+1)(3\Lambda_1-\Lambda)] \\
&\quad - (x_1-\xi_1)^2[(3-\kappa_1) + 2(\kappa_1+1)(\Lambda-\Lambda_1-\Lambda_2)]\}/R^5 \\
&\quad + 120[1-(\kappa_1+1)\Lambda_1]h^2[4h^2 + 3(x_1-\xi_1)^2]/R^7 \\
&\quad - 3360[1-(\kappa_1+1)\Lambda_1]h^4(x_1-\xi_1)^2/R^9, \\
K_{21}^{\mathrm{I}}(\mathbf{x}, \boldsymbol{\xi}) &= -3(x_1-\xi_1)(x_2-\xi_2)\{[(3-\kappa_1) \\
&\quad + 2(\kappa_1+1)(\Lambda-\Lambda_1-\Lambda_2)]/R^5 - 40[1-(\kappa_1+1)\Lambda_1]h^2 \\
&\quad \times (3/R^7 + 28h^2/R^9)\}, \\
K_{31}^{\mathrm{I}}(\mathbf{x}, \boldsymbol{\xi}) &= -12h(x_1-\xi_1)\{(\kappa_1+1)(\Lambda_1-\Lambda_2)/R^5 \\
&\quad - 20[1-(\kappa_1+1)\Lambda_1]h^2(3/R^7 + 28h^2/R^9)\} \\
K_{33}^{\mathrm{I}}(\mathbf{x}, \boldsymbol{\xi}) &= -2[2-(\kappa_1+1)(\Lambda_1+\Lambda_2)]/R^3 \\
&\quad + 24h^2\{[(\kappa_1+1)(2\Lambda_1-\Lambda_2)-1]/R^5 \\
&\quad - 80[1-(\kappa_1+1)\Lambda_1]h^2(1/R^7 - 7h^2/R^9)\}, \\
K_{22}^{\mathrm{I}}(\mathbf{x}, \boldsymbol{\xi}) &= K_{11}^{\mathrm{I}}\{x_1 \to x_2, \xi_1 \to \xi_2\}, \\
K_{12}^{\mathrm{I}}(\mathbf{x}, \boldsymbol{\xi}) &= K_{21}^{\mathrm{I}}\{x_1 \leftrightarrow \xi_1, x_2 \leftrightarrow \xi_2\}, \\
K_{32}^{\mathrm{I}}(\mathbf{x}, \boldsymbol{\xi}) &= K_{31}^{\mathrm{I}}\{x_1 \to x_2, \xi_1 \to \xi_2\}, \\
K_{13}^{\mathrm{I}}(\mathbf{x}, \boldsymbol{\xi}) &= K_{31}^{\mathrm{I}}\{x_1 \leftrightarrow \xi_1, x_2 \leftrightarrow \xi_2\}, \\
K_{23}^{\mathrm{I}}(\mathbf{x}, \boldsymbol{\xi}) &= K_{32}^{\mathrm{I}}\{x_1 \leftrightarrow \xi_1, x_2 \leftrightarrow \xi_2\}
\end{aligned} \tag{4}$$

where

$$\Lambda = \mu_2/(\mu_1+\mu_2), \quad \Lambda_1 = \mu_2/(\mu_1+\kappa_1\mu_2),$$
$$\Lambda_2 = \mu_2/(\mu_2+\kappa_2\mu_1), \quad R^2 = r^2 + 4h^2, \quad \kappa_2 = 3 - 4\upsilon_2.$$

Hypersingular Integro-differential Equation for the Planar Interfacial Crack

It can be seen from (4) that moving the planar crack to the bimaterial interface ($h \to 0$) leads to $R = r$ in the expressions of $K_{ij}^{\mathrm{I}}(\mathbf{x}, \boldsymbol{\xi})$ and that the kernels $K_{ij}^{\mathrm{I}}(\mathbf{x}, \boldsymbol{\xi})$ have subsequently hypersingularities of Hadamard (1952) as $\mathbf{x} \to \boldsymbol{\xi}$. To regularize the kernels $K_{ij}^{\mathrm{I}}(\mathbf{x}, \boldsymbol{\xi})$, $\Delta u_j^{\mathrm{I}}(\boldsymbol{\xi})$ can be expanded in a two-term Taylor series in the neighborhood of the point $\mathbf{x}$, that is

$$\begin{aligned}
\Delta u_j^{\mathrm{I}}(\boldsymbol{\xi}) &= \Delta u_j^{\mathrm{I}}(x_1, x_2) + \frac{\partial \Delta u_j^{\mathrm{I}}(x_1, x_2)}{\partial x_1}(\xi_1 - x_1) \\
&\quad + \frac{\partial \Delta u_j^{\mathrm{I}}(x_1, x_2)}{\partial x_2}(\xi_2 - x_2) + O(r^2).
\end{aligned} \tag{5}$$

Substituting (5) into (3), we have

$$\begin{aligned}
&\mu_1(\Lambda_2-\Lambda_1)\frac{\partial \Delta u_3^{\mathrm{I}}(x_1, x_2)}{\partial x_\alpha} + \mu_1\frac{(2\Lambda-\Lambda_1-\Lambda_2)}{2\pi} \\
&\quad \times \oint\!\!\!\!\!\!-_{S^+} \frac{1}{r^3}\delta_{\alpha\beta}\Delta u_\beta^{\mathrm{I}}(\boldsymbol{\xi})dS(\boldsymbol{\xi}) + 3\mu_1\frac{(\Lambda_1+\Lambda_2-\Lambda)}{2\pi} \\
&\quad \times \oint\!\!\!\!\!\!-_{S^+} \frac{(x_\alpha-\xi_\alpha)(x_\beta-\xi_\beta)}{r^5}\Delta u_\beta^{\mathrm{I}}(\boldsymbol{\xi})dS(\boldsymbol{\xi}) = -p_\alpha^{\mathrm{I}}(x_1, x_2), \\
&\qquad\qquad x_1, x_2 \in S^+, \quad (6a)
\end{aligned}$$

Downloaded 04 May 2010 to 171.66.16.27. Redistribution subject to ASME license or copyright; see http://www.asme.org/terms/Terms_Use.cfm

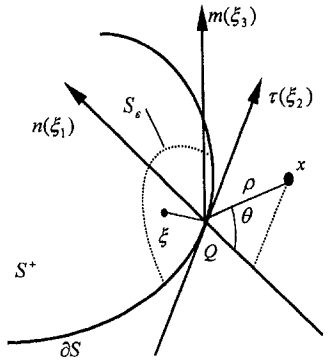


Fig. 2 A local intrinsic coordinate system

$$\mu_1(\Lambda_1 - \Lambda_2)\frac{\partial \Delta u_\alpha^1(x_1, x_2)}{\partial x_\alpha} + \mu_1\frac{(\Lambda_1 + \Lambda_2)}{2\pi}\int_{S^+}\frac{\Delta u_3^1(\boldsymbol{\xi})}{r^3}dS(\boldsymbol{\xi}) = -p_3^1(x_1, x_2), \quad x_1, x_2 \in S^+. \quad (6b)$$

Equations (6) are the very hypersingular integro-differential equations for the three-dimensional fields of a planar crack on a bimaterial interface. Obviously, if the two dissimilar materials bounded together are the same, that is, $\mu_1 = \mu_2$, $\upsilon_1 = \upsilon_2$, then $\Lambda = 1/2$, $\Lambda_1 = \Lambda_2$, and (6) degenerate into the results for the infinite homogeneous and isotropic body obtained by Takakuda (1985) and Qin and Tang (1993). We are not aware of any published research on the hypersingular integro-differential equations or other similar integral equations of the three-dimensional interfacial crack fields which are helpful for us to study three-dimensional interfacial crack problems.

Stress Singularity Near the Planar Interfacial Crack Front

As shown in Fig. 2, introduce a local triple orthogonal intrinsic coordinate system: $(n, \tau, m) := (\xi_1, \xi_2, \xi_3)$ at a point Q along the smooth periphery ∂S of the planar crack and a small sector shape of S_ϵ in the osculating plane around the point Q. In terms of the theory of elasticity (Parton and Perlin, 1984), the displacements surrounding the point Q can be decomposed into combinations of those for the plane-strain case with those for the antiplane case, and are related to only coordinates ξ_1 in the normal plane through the point Q as well as the position of the point Q along the contour of the crack, i.e.,

$$\Delta u_i^1(\boldsymbol{\xi}) = A_i(Q)\xi_1^{\alpha_i}. \quad (7)$$

Here the repeated indices are not summed; $A_i(Q)$ are complex constants concerning with the position of the point Q and α_i are unknown singularities which take values within range $0 < \mathrm{Re}(\alpha_i) < 1$.

If bounded internal pressures are applied on the crack surfaces, inserting (7) into (3) and using a similar method to what was previously mentioned, we give by the dominant-part analysis of the two-dimensional hypersingular integrals

$$\lim_{x\to Q}\int_{S_\epsilon}\frac{1}{r^3}\Delta u_m^1(\boldsymbol{\xi})dS(\boldsymbol{\xi}) = -2A_m(Q)x_1^{\alpha_m - 1}\alpha_m\pi\cot(\alpha_m\pi), \quad (8a)$$

$$\lim_{x\to Q}\int_{S_\epsilon}\frac{(x_\beta - \xi_\beta)^2}{r^5}\Delta u_\beta^1(\boldsymbol{\xi})dS(\boldsymbol{\xi}) = -\frac{2}{3}(2\delta_{\beta 1} + \delta_{\beta 2})A_\beta(Q)x_1^{\alpha\beta - 1}\alpha_\beta\pi\cot(\alpha_\beta\pi), \quad (8b)$$

$$\lim_{x\to Q}\lim_{h\to 0}\int_{S_\epsilon}K_{nm}^1(\mathbf{x}, \boldsymbol{\xi})\Delta u_m^1(\boldsymbol{\xi})dS(\boldsymbol{\xi}) = 2\{2[2 - (\kappa_1 + 1)(\Lambda_1 + \Lambda_2)](\delta_{n1}\delta_{m1} + \delta_{n3}\delta_{m3}) + (\kappa_1 + 1)(1 - 2\Lambda)\delta_{n2}\delta_{m2} + 2(\kappa_1 + 1)(\Lambda_1 - \Lambda_2) \times (\delta_{n3}\delta_{m1} - \delta_{n1}\delta_{m3})\tan(\alpha_m\pi)\} \times A_m(Q)x_1^{\alpha_m - 1}\alpha_m\pi\cot(\alpha_m\pi) \quad (8c)$$

in which the repeated indices are not summed. Substituting (8) into (3), then multiplying both sides of (3) by $x_1^{1-\alpha_m}$ and setting $\alpha_1 = \alpha_3 = \alpha$, yield

$$A_1(Q)(\Lambda_1 + \Lambda_2)\alpha\cot(\pi\alpha) + A_3(Q)(\Lambda_1 - \Lambda_2)\alpha = 0, \quad (9a)$$

$$A_2(Q)\cot(\pi\alpha_2) = 0, \quad (9b)$$

$$A_1(Q)(\Lambda_1 - \Lambda_2)\alpha - A_3(Q)(\Lambda_1 + \Lambda_2)\alpha\cot(\pi\alpha) = 0. \quad (9c)$$

For nontrivial solutions of $A_i(Q)$, the determinant of their coefficients must vanish. Because $\alpha = 0$ is not a solution of above equations in the present case, the following two characteristic equations are obtained:

$$\cot\pi\alpha_2 = 0, \quad (10a)$$

$$\cot^2\pi\alpha + \left(\frac{\Lambda_1 - \Lambda_2}{\Lambda_1 + \Lambda_2}\right)^2 = 0. \quad (10b)$$

It is seen that (10*a*) corresponds to antiplane problems (Zak and Williams, 1963) and (10*b*) to plane-strain problems (Williams, 1959). Therefore, the solutions of (10) read

$$\alpha_2 = \frac{1}{2}; \quad \alpha = \frac{1}{2} \pm i\gamma, \quad \gamma = \frac{1}{2\pi}\ln\left(\frac{\mu_1 + \kappa_1\mu_2}{\mu_2 + \kappa_2\mu_1}\right). \quad (11)$$

Here $i = \sqrt{-1}$. From (9*a*), (9*c*), and (10*b*), we find

$$A_1(Q) = \pm iA_3(Q). \quad (12)$$

As the displacement must be a real number, in terms of (7), (11), and (12), the displacement jumps near the planar interfacial crack front edge can be expressed as

$$\Delta u_3^1(\boldsymbol{\xi}) - i\Delta u_1^1(\boldsymbol{\xi}) = [A_R(Q) + iA_I(Q)]\xi_1^\alpha = A(Q)\xi_1^\alpha, \quad (13a)$$

$$\Delta u_2^1(\boldsymbol{\xi}) = A_2(Q)\xi_1^{1/2}. \quad (13b)$$

Singular Stress Field Ahead of the Planar Interfacial Crack Front

The stress fields at any point interior to the upper half-space, caused by the planar interfacial crack, have been given by the first author (1997) and take the following form:

$$\sigma_{3\alpha}^1(\mathbf{x}) = \frac{\mu_1}{2\pi}\int_{S^+}\left\{\left[\left(\frac{2\Lambda - \Lambda_1 - \Lambda_2}{r_1^3} + \frac{3(2\Lambda_1 - \Lambda)}{r_1^5}x_3^2\right)\delta_{\alpha\beta} + \left(\frac{3(\Lambda_1 + \Lambda_2 - \Lambda)}{r_1^5} - \frac{30\Lambda_1}{r_1^7}x_3^2\right)(x_\alpha - \xi_\alpha)(x_\beta - \xi_\beta)\right]\Delta u_\beta^1(\boldsymbol{\xi}) + \left(\frac{3(3\Lambda_1 - \Lambda_2)}{r_1^5} - \frac{30\Lambda_1}{r_1^7}x_3^2\right)x_3(x_\alpha - \xi_\alpha)\Delta u_3^1(\boldsymbol{\xi})\right\}dS(\boldsymbol{\xi}), \quad (14a)$$

Downloaded 04 May 2010 to 171.66.16.27. Redistribution subject to ASME license or copyright; see http://www.asme.org/terms/Terms_Use.cfm

$$\sigma_{33}^{I}(\mathbf{x}) = \frac{\mu_1}{2\pi}\int_{S^+}\left\{\left(\frac{3(\Lambda_1+\Lambda_2)}{r_1^5} - \frac{30\Lambda_1}{r_1^7}x_3^2\right)\right.$$

$$\times x_3(x_\beta - \xi_\beta)\Delta u_\beta^I(\boldsymbol{\xi}) + \left(\frac{(\Lambda_1+\Lambda_2)}{r_1^3} + \frac{3(5\Lambda_1-\Lambda_2)}{r_1^5}\right.$$

$$\left.\left.\times x_3^2 - \frac{30\Lambda_1}{r_1^7}x_3^4\right)\Delta u_3^I(\boldsymbol{\xi})\right\}dS(\boldsymbol{\xi}), \quad (14b)$$

where

$$r_1^2 = (x_1-\xi_1)^2 + (x_2-\xi_2)^2 + x_3^2.$$

To get the singular stress fields ahead of the periphery of the planar interfacial crack we use a method similar to that of Qin and Tang (1993). As shown in Fig. 2, introducing a polar coordinate system (ρ, θ) referring to the negative normal direction in the normal plane (Q, n, m) through the point Q leads to the following coordinates at the point $\mathbf{x}$ ahead of the crack front:

$$x_1 = -\rho\cos\theta, \quad x_2 = 0, \quad x_3 = \rho\sin\theta, \quad (15a)$$

$$r_1^2 = (\xi_1 + \rho\cos\theta)^2 + \xi_2^2 + (\rho\sin\theta)^2. \quad (15b)$$

Substituting (13) and (15) into (14), we obtain dominant-part integrals as follows:

$$\lim_{\mathbf{x}\to Q}\int_{S_\epsilon}\frac{\Delta u_m^I(\boldsymbol{\xi})}{r_1^3}dS(\boldsymbol{\xi}) = \frac{2\pi}{\rho\sin\theta}\left\{-\delta_{m1}\,\mathrm{Re}\left[iA(Q)\rho^\alpha\frac{\sin\alpha\theta}{\sin\alpha\pi}\right]\right.$$

$$\left. + \delta_{m3}\,\mathrm{Im}\left[iA(Q)\rho^\alpha\frac{\sin\alpha\theta}{\sin\alpha\pi}\right]\right\}, \quad (16a)$$

$$\lim_{\mathbf{x}\to Q}\int_{S_\epsilon}\frac{(x_1-\xi_1)\Delta u_m^I(\boldsymbol{\xi})}{r_1^5}dS(\boldsymbol{\xi})$$

$$= \frac{2\pi}{3\rho\sin\theta}\left\{\delta_{m1}\,\mathrm{Re}\left[iA(Q)\alpha\rho^{\alpha-1}\frac{\sin(\alpha-1)\theta}{\sin\alpha\pi}\right]\right.$$

$$\left. - \delta_{m3}\,\mathrm{Im}\left[iA(Q)\alpha\rho^{\alpha-1}\frac{\sin(\alpha-1)\theta}{\sin\alpha\pi}\right]\right\}, \quad (16b)$$

$$\lim_{\mathbf{x}\to Q}\int_{S_\epsilon}\frac{(x_1-\xi_1)(x_2-\xi_2)\Delta u_m^I(\boldsymbol{\xi})}{r_1^5}dS(\boldsymbol{\xi}) = 0, \quad (16c)$$

$$\lim_{\mathbf{x}\to Q}\int_{S_\epsilon}\frac{(x_1-\xi_1)^2\Delta u_m^I(\boldsymbol{\xi})}{r_1^5}dS(\boldsymbol{\xi})$$

$$= \frac{2\pi}{3}\left\{\delta_{m1}\left\{\mathrm{Im}\left[iA(Q)\alpha\rho^{\alpha-1}\frac{\sin(\alpha-1)\theta}{\sin\alpha\pi}\right]\right.\right.$$

$$\left. - \frac{1}{\rho\sin\theta}\,\mathrm{Re}\left[iA(Q)\rho^\alpha\frac{\sin\alpha\theta}{\sin\alpha\pi}\right]\right\}$$

$$+ \delta_{m3}\left\{\mathrm{Im}\left[iA(Q)\alpha\rho^{\alpha-1}\frac{\sin(\alpha-1)\theta}{\sin\alpha\pi}\right]\right.$$

$$\left.\left. + \frac{1}{\rho\sin\theta}\,\mathrm{Re}\left[iA(Q)\rho^\alpha\frac{\sin\alpha\theta}{\sin\alpha\pi}\right]\right\}\right\}, \quad (16d)$$

in which $\alpha = 1/2 + i\gamma$. Putting the above results into (14), we arrive at

$$\sigma_{31}^I(\rho,\theta) = \frac{\mu_1\Lambda_1 e^{\pi\gamma}}{2\cosh\gamma\pi}\cdot\frac{1}{\sqrt{\rho}}\{[(A_R - 2\gamma A_1)\cos(\gamma\ln\rho)$$

$$- (A_I + 2\gamma A_R)\sin(\gamma\ln\rho)]\sigma_{31}^1(\theta) - [(A_I + 2\gamma A_R)$$

$$\times\cos(\gamma\ln\rho) + (A_R - 2\gamma A_1)\sin(\gamma\ln\rho)]\sigma_{31}^2(\theta)\}, \quad (17a)$$

$$\sigma_{33}^I(\rho,\theta) = \frac{\mu_1\Lambda_1 e^{\pi\gamma}}{2\cosh\gamma\pi}\cdot\frac{1}{\sqrt{\rho}}\{[(A_R - 2\gamma A_1)\cos(\gamma\ln\rho)$$

$$- (A_I + 2\gamma A_R)\sin(\gamma\ln\rho)]\sigma_{33}^2(\theta) + [(A_I + 2\gamma A_R)$$

$$\times\cos(\gamma\ln\rho) + (A_R - 2\gamma A_1)\sin(\gamma\ln\rho)]\sigma_{33}^1(\theta)\}, \quad (17b)$$

$$\sigma_{32}^I(\rho,\theta) = \frac{\mu_1\Lambda}{2}A_2(Q)\frac{1}{\sqrt{\rho}}\cos\frac{\theta}{2}, \quad (17c)$$

where $\sigma_{3m}^1(\theta)$ and $\sigma_{3m}^2(\theta)$ $(m = 1, 3)$ are nondimensional angular functions of the singular stress fields $\sigma_{3m}^I(\rho,\theta)$. They are expressed as

$$\sigma_{3m}^1(\theta) = 2\sin\frac{\theta}{2}\sinh(\pi-\theta)\gamma$$

$$+ (1-2\delta_{m1})e^{-(\pi-\theta)\gamma}\sin\theta\left(\cos\frac{3\theta}{2} - 2\gamma\sin\frac{3\theta}{2}\right),$$

$$\sigma_{3m}^2(\theta) = 2\cos\frac{\theta}{2}\cosh(\pi-\theta)\gamma$$

$$+ (1-2\delta_{m1})e^{-(\pi-\theta)\gamma}\sin\theta\left(\sin\frac{3\theta}{2} + 2\gamma\cos\frac{3\theta}{2}\right).$$

Equations (17) are the very singular stress fields ahead of the planar interfacial crack front edge in the upper half-space I. It is shown that $\sigma_{31}^I(\rho,\theta)$ and $\sigma_{33}^I(\rho,\theta)$ are oscillatory and not of a separable form. In contrast, the singular stress fields of cracks in homogenous media are separable and not oscillating (Tang and Qin, 1993). This conclusion is the same as that of plane crack problems but it is drawn strictly from the three-dimensional elasticity theory.

Stress Intensity Factor and Energy Release Rate for the Planar Interfacial Crack

Analogous to Hutchinson's definitions (Hutchinson et al., 1987) of stress intensity factors of the two-dimensional interfacial crack tip, we define the stress intensity factors associated with the three-dimensional planar interfacial crack front edge as follows:

$$K(Q) = K_1(Q) - iK_2(Q)$$

$$= \lim_{\rho\to 0}\sqrt{2}\rho^{1/2-i\gamma}[\sigma_{33}^I(\rho,\theta) - i\sigma_{31}^I(\rho,\theta)]_{\theta=0}$$

$$= \lim_{\rho\to 0}\sqrt{2}\rho^{1/2-i\gamma}[\sigma_{33}^I(\rho,0) - i\sigma_{31}^I(\rho,0)], \quad (18a)$$

$$K_{III}(Q) = \lim_{\rho\to 0}\sqrt{2\rho}\sigma_{32}^I(\rho,\theta)|_{\theta=0} = \lim_{\rho\to 0}\sqrt{2\rho}\sigma_{32}^I(\rho,0). \quad (18b)$$

From (13), (17), and (18) we obtain

$$K(Q) = \frac{\mu_1(\Lambda_1+\Lambda_2)(1+2i\gamma)}{2\cosh\pi\gamma}$$

$$\times\lim_{\xi_1\to 0}[\Delta u_3^I(\xi_1,0) - i\Delta u_1^I(\xi_1,0)]\sqrt{\frac{2}{\xi_1}}(\xi_1)^{-i\gamma}$$

$$= \frac{\mu_1\mu_2(1+2i\gamma)}{2\cosh\pi\gamma}\left(\frac{1}{\mu_1+\kappa_1\mu_2} + \frac{1}{\mu_2+\kappa_2\mu_1}\right)$$

$$\times\lim_{\xi_1\to 0}[\Delta u_3^I(\xi_1,0) - i\Delta u_1^I(\xi_1,0)]$$

$$\times\sqrt{\frac{2}{\xi_1}}(\xi_1)^{-i\gamma}, \quad (19a)$$

Downloaded 04 May 2010 to 171.66.16.27. Redistribution subject to ASME license or copyright; see http://www.asme.org/terms/Terms_Use.cfm

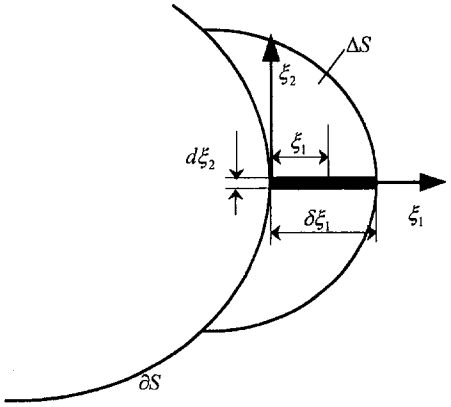


Fig. 3 A planar crack with virtual incremental area ΔS of the crack surface

$$K_{III}(Q) = \frac{\mu_1 \Lambda}{\sqrt{2}} \lim_{\xi_1 \to 0} \frac{\Delta u_2^1(\xi_1, 0)}{\sqrt{\xi_1}}$$

$$= \frac{\mu_1 \mu_2}{2(\mu_1 + \mu_2)} \lim_{\xi_1 \to 0} \Delta u_2^1(\xi_1, 0) \sqrt{\frac{2}{\xi_1}}. \quad (19b)$$

To the authors' knowledge, the present derivation of (17) and (19) is the first to do so rigorously from the three-dimensional elasticity theory.

From (19), the displacement jumps across the crack surfaces near the interfacial crack front edge take the form

$$\Delta U(\xi_1, 0) = \Delta u_3^1(\xi_1, 0) - i\Delta u_1^1(\xi_1, 0)$$

$$= \frac{K(Q)}{2(1 + 2i\gamma) \cosh \pi\gamma} \left(\frac{\kappa_1 + 1}{\mu_1} + \frac{\kappa_2 + 1}{\mu_2} \right) \times \sqrt{\frac{\xi_1}{2}} (\xi_1)^{i\gamma}, \quad (20a)$$

$$\Delta u_2^1(\xi_1, 0) = 2K_{III}(Q) \left(\frac{1}{\mu_1} + \frac{1}{\mu_2} \right) \sqrt{\frac{\xi_1}{2}}. \quad (20b)$$

By means of virtual work, the given expressions for tractions (18) and displacement fields (20), the energy release rate is readily computed from

$$G(Q) = \lim_{\Delta S \to 0} \frac{1}{2\Delta S} \int_{\Delta S} \{[\sigma_{33}^1(\xi_1; 0) - i\sigma_{31}^1(\xi_1; 0)] \cdot \Delta \bar{U}(\xi_1, 0 + \Delta S) + \sigma_{32}^1(\xi_1; 0) \Delta u_2^1(\xi_1; 0 + \Delta S)\} dS(\xi), \quad (21)$$

where $\sigma_{3i}^1(\xi_1, 0)$ are the stress components ahead of the planar interfacial crack front edge, when the increment ΔS of the crack is zero; $\Delta \bar{U}(\xi_1; 0 + \Delta S)$ is the complex conjugate to the displacement jump vector $\Delta U(\xi_1; 0 + \Delta S)$, and $\Delta u_2^1(\xi_1; 0 + \Delta S)$, the displacement jump, when the crack has advanced to the position $0 + \Delta S$. The infinitesimal amount $\delta\xi_1$ normal to the planar interfacial crack front edge ∂S is used to describe the changes of the crack surface (see Fig. 3). The total changes of the crack surface are expressed as

$$\Delta S = \int_{\partial S(\xi_2)} \delta\xi_1 d\xi_2. \quad (22)$$

Inserting (18), (20), and (22) into (21) gives

$$G(Q) = \lim_{\Delta S \to 0} \frac{1}{2 \int_{\partial S(\xi_2)} \delta\xi_1 d\xi_2} \times \int_{\partial S(\xi_2)} \int_0^{\delta\xi_1} \left[\frac{K(Q)\overline{K(Q)}}{4(1 - 2i\gamma) \cosh \pi\gamma} \times \left(\frac{\kappa_1 + 1}{\mu_1} + \frac{\kappa_2 + 1}{\mu_2} \right) \left(\frac{\delta\xi_1 - \xi_1}{\xi_1} \right)^{1/2 - i\gamma} + \frac{(\mu_1 + \mu_2) K_{III}^2(Q)}{\mu_1 \mu_2} \sqrt{\frac{\delta\xi_1 - \xi_1}{\xi_1}} \right] d\xi_1 d\xi_2 \quad (23)$$

where the inner integral of the first term is recognizable as the complex beta function $B(1/2 + i\gamma, 3/2 - i\gamma)$, and the inner integral of the second term, the real beta function $B(1/2, 3/2)$. Upon evaluation of the beta function by the gamma function $\Gamma(z)$,

$$G(Q) = \pi \left[\frac{\mu_1(\kappa_2 + 1) + \mu_2(\kappa_1 + 1)}{16\mu_1\mu_2 \cosh^2 \pi\gamma} \right] K(Q)\overline{K(Q)} + \pi \frac{(\mu_1 + \mu_2)}{4\mu_1\mu_2} K_{III}^2(Q). \quad (24)$$

Equation (24) notes that the integral in (21) has no imaginary part, a fact noticed in the general case of the two-dimensional bimaterials by Shih and Asaro (1988).

Illustrative Example

The theoretical studies in the previous sections have shown that the stress fields ahead of the planar interfacial crack have a singularity of $1/\sqrt{r} \times$ (oscillatory term) which complicates our analyses of crack problems. However, Rice (1988) and Shibuya (1989) pointed out that the phenomenon of stress oscillation occurs only in the extreme vicinity of the crack tip under tensile loading. Therefore, to reduce the efforts of our computations, we here ignore the oscillatory term in the process of numerical calculations.

As an illustration, we consider an elliptical crack under normal constant pressures. The elliptical crack with semi-major axis a and semi-minor axis b is represented as

$$\xi_1 = a\rho \cos \varphi, \quad \xi_2 = b\rho \sin \varphi,$$

where $0 \leq \rho < 1$, $0 \leq \varphi < 2\pi$.

In terms of the behavior of the displacement jumps over the

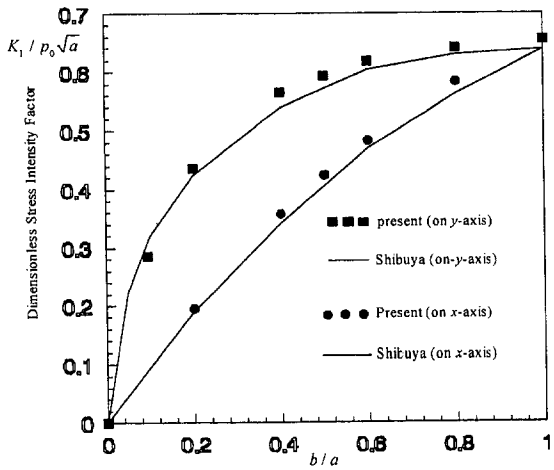


Fig. 4 Stress intensity factors of elliptical crack on x-axis and y-axis ($\mu_2/\mu_1 = 0.5$, $\nu_1 = 0.3$, $\nu_2 = 0.33$)

Downloaded 04 May 2010 to 171.66.16.27. Redistribution subject to ASME license or copyright; see http://www.asme.org/terms/Terms_Use.cfm

crack surfaces without consideration of the oscillatory term, the crack displacement jumps can be expressed in the form of Chebyshev polynomial, i.e.,

$$\Delta u_i^{\mathrm{I}}(\xi_1, \xi_2) = \sqrt{1 - (\xi_1/a)^2 - (\xi_2/b)^2} \times \sum_{n=0,2,\ldots}^{N} \sum_{m=0,2,\ldots}^{M} C_{nm}^{i} T_n(\xi_1/a) T_m(\xi_2/b), \quad (25)$$

in which C_{nm}^{i} are unknown coefficients to be determined and T_l denotes the Chebyshev polynomials of the first kind. Consequently, the mode I stress intensity factor can be obtained from the following expression (Chen, 1997):

$$K_{\mathrm{I}}(Q) = \mu_1\mu_2\left(\frac{1}{\mu_1 + \kappa_1\mu_2} + \frac{1}{\mu_2 + \kappa_2\mu_1}\right) \times \sum_{n=0,2,\ldots}^{N} \sum_{m=0,2,\ldots}^{M} C_{nm}^{3} T_n(\cos\varphi) T_m(\sin\varphi) \sqrt{\frac{1}{ab}}\, \bar{K}, \quad (26)$$

here

$$\bar{K} = (a^2 \sin^2\varphi + b^2 \cos^2\varphi)^{1/4}.$$

The calculated results on the x-axis and y-axis are depicted in Fig. 4 as a function of the aspect ratio of the elliptical crack and compared with the available solutions (Shibuya, 1989). It is seen that both results are in good agreement.

Concluding Remark

In the present paper, starting from the fundamental solution of a point force for three-dimensional elastic space problems of bimaterials, we have performed rigorous theoretical analyses of some basic interfacial crack problems by using the hypersingular integral equation method and have obtained some useful results such as a system of hypersingular integral equations for an arbitrarily shaped planar interfacial crack (6), singular stress fields (17), and stress intensity factors (18). These results are undoubtedly helpful for us to study the three-dimensional interfacial crack problems.

Acknowledgment

The first and the third authors are grateful for the financial support from the National Natural Science Foundation of China.

References

Brebbia, C. A., 1981, *Progress in Boundary Element Methods,* Vol. 1, Pentech Press, London.

Chen, M.-C., 1997, "A Hypersingular Integral Equation Method of Three-Dimensional Crack Problems Near and on an Interface of Bimaterials," Ph.D dissertation, Shanghai Jiao Tong University, Shanghai, P.R. China.

Chen, M.-C., and Tang, R.-J., 1997, "An Explicit Tensor Expressions of Fundamental Solutions of a Space Problem of Bimaterials," *Chinese Appl. Math. Mech.,* Vol. 18, pp. 331–340.

Erdogan, F., and Arin, K., 1972, "Penny-Shaped Interface Crack Between an Elastic Layer and a Half-space," *Int. J. Solids Struct.,* Vol. 8, pp. 93–109.

Hadamard, J., 1952, *Lectures on Cauchy's Problem in Linear Partial Differential Equations,* Dover, New York.

Hutchinson, J. W., Mear, M. E., and Rice, J. R., 1987, "Crack Paralleling an Interface Between Dissimilar Materials," ASME JOURNAL OF APPLIED MECHANICS, Vol. 54, pp. 828–832.

Kassir, M. K., and Bregman, A. M., 1972, "The Stress Intensity Factor for a Penny-Shaped Crack Between Two Dissimilar Materials," ASME JOURNAL OF APPLIED MECHANICS, Vol. 39, pp. 308–301.

Nakamura, T., 1991, "Three-Dimensional Stress Fields of Elastic Interface Cracks," ASME JOURNAL OF APPLIED MECHANICS, Vol. 58, pp. 939–946.

Parton, V. Z., and Perlin, P. I., 1984, *Mathematical Methods of the Theory of Elasticity,* Moscow.

Qin, T.-Y., and Tang, R.-J., 1993, "Finite-Part Integral and Boundary Element Method to Solve Embedded Planar Crack Problems," *Int. J. Fracture,* Vol. 60, pp. 373–381.

Rice, J. R., 1988, "Elastic Fracture Mechanics Concepts for Interfacial Cracks," ASME JOURNAL OF APPLIED MECHANICS, Vol. 55, pp. 98–103.

Shibuya, T., et al., 1989, "Stress Analysis of the Vicinity of an Elliptical Crack at the Interface of Two Bounded Half-Spaces," *JSME Int. J.,* Vol. 32, pp. 485–491.

Takakuda, K., Koizumi, T., and Shibuya, T., 1985, "On Integral Equation Methods for Cracks," *Bulletin of JSME,* Vol. 28, pp. 217–224.

Tang, R.-J., and Qin, T.-Y., 1993, "A Hypersingular Integral Method for Three-Dimensional Crack Problems," *Acta Mechanica Sinica,* Vol. 25, pp. 665–675.

Williams, M. L., 1959, "The Stresses Around a Fault or Crack in Dissimilar Media," *Bull. Seis. Soc. America,* Vol. 49, pp. 199–204.

Willis, J. R., 1972, "The Penny-Shaped Crack on an Interface," *Q. J. Mech. & Appl. Math.,* Vol. 25, pp. 367–385.

Yuuki, R., and Xu, J.-Q., 1992, "A BEM Analysis of a Three-Dimensional Interfacial Crack of Bimaterials," *Transactions of JSME,* Series A Vol. 58, No. 545, pp. 19–46 (in Japanese).

Zak, A. R., and Williams, M. L., 1963, "Crack Point Stress Singularities at a Bimaterial Interface," ASME JOURNAL OF APPLIED MECHANICS, Vol. 30, pp. 142–143.

Downloaded 04 May 2010 to 171.66.16.27. Redistribution subject to ASME license or copyright; see http://www.asme.org/terms/Terms_Use.cfm

Lateral Thermal Buckling of Pipelines on the Sea Bed

D. J. Miles[1]

C. R. Calladine[2]
Professor

Department of Engineering,
University of Cambridge,
Cambridge CB2 1PZ, UK

Lateral buckling can occur in a submarine pipeline laid (without trenching) on the seabed, when the oil temperature rises. Motion of the (elastic) pipe relative to the sea bed is resisted by friction. The initial buckling is a localization phenomenon, and the first buckle lobes to form grow in amplitude most rapidly as the temperature increases. But as the temperature continues to rise, these early buckles cease growing, and growth is transferred to adjacent, newly formed lobes. The lobes first formed thus eventually become "extinct." We investigate these phenomena by means of a small-scale physical model and by computer simulation. The results of many computer runs can be condensed into a few universal curves by the use of suitable dimensionless groups. Simple formulas emerge for the amplitude and wavelength of the "extinct" lobes, and for the maximum bending strain experienced by the pipeline, as a function of temperature.

1 Introduction

A submarine pipeline has been laid, untrenched, on a flat sea bed. Hot oil begins to flow through it. Potential thermal expansion is resisted by long-range frictional effects, and so there is longitudinal compressive stress in the pipeline, which increases as temperature increases. When such compressive stress reaches a critical value, the pipeline buckles laterally into a snake-like profile.

Since friction between the pipeline and the sea bed acts equally in either lateral direction, the buckled lobes are distributed on both sides of the original centerline. This phenomenon of lateral buckling is related to that of upheaval buckling of a trenched pipeline in a vertical plane (see, e.g., Maltby and Calladine, 1995a, b). But that problem is unsymmetrical, because downward movement of the pipe into the sea bed is resisted by much larger forces than upward movement towards the surface.

The phenomenon of lateral buckling in submarine pipelines is closely related to that of lateral buckling of welded railway tracks on a hot day (Kerr, 1978; Tvergaard and Needleman, 1981). That problem is known to involve a *localization* phenomenon. Thus, instead of buckling into an extensive, periodic mode shape—as it would if it were a classical elastic-beam-on-elastic-foundation—the track first buckles locally at a place where there is some sort of initial imperfection. The adjacent thermally expanded track then "feeds" into the buckles, which grow when the temperature rises further. In a pressurized pipeline, thermal expansion is augmented by longitudinal elastic straining on account of pressure-related stresses in the pipe wall. Throughout the paper we shall use the terms "temperature" and "thermal expansion" implicitly to include such pressure-related effects. (See the second footnote to Table 2.)

Lateral buckling of a pipeline does not necessarily affect its operation, provided the local bending of the pipe is not so severe as to produce an unacceptable kink, or other destabilizing local plastic deformation. It is well known, of course, that some localization phenomena concentrate practically all subsequent deformation into a single narrow zone (e.g., Tvergaard and Needleman, 1980). If that were to happen in a pipeline, it would be a source of genuine concern to the engineer.

The aim of the present paper is to investigate the phenomenon of lateral buckling in pipelines lying on the sea bed, across a wide range of pipeline parameters. In order to make the problem tractable we shall represent the pipeline as a long elastic bar supported on a flat, frictional base. Previous work on this topic has been confined to experimental tests on lateral force-displacement relations for a discrete piece of pipe dragged across various sea bed soils (e.g., Brennodden et al., 1986) and occasional computer simulation of specific pipelines (e.g., Kaye et al., 1995).

The investigation that we have conducted (Miles, 1998) involves small-scale physical model experiments on a specially built test rig, followed by a finite element computer study that replicates experimental observations and so enables us confidently to extend the computations to a range of cases involving different values of the key parameters. The results of many such computer runs may then be condensed onto a few, universal curves by means of appropriate dimensionless variables; and this leads, finally, to some simple design formulas in terms of the relevant working variables.

Throughout the work we assume that buckling has already been initiated. We are concerned here only with the post-buckling growth and development of buckles as temperature continues to rise, and with the largest bending strain that may be developed in the most critical buckled lobe, which might precipitate unacceptable localized damage if it were to cause a local bending buckle in the pipe.

2 Small-Scale Model Testing

Purely computational studies run the risk that some small feature that has been omitted by hypothesis from the computer model may actually be crucial to the physical phenomenon under investigation. We therefore began with a small-scale experimental investigation.

The basic conception of the apparatus was to use an elastic, silicone rubber strip of the order of 7 mm square in cross section and 2 m long to represent a substantial length of the prototype pipeline. Thermal expansion of the strip was simulated by a longitudinal contraction of the base slab which represented the sea bed. We found that expanded polystyrene was a suitable material for this purpose. The base slab was made from four sheets of expanded polystyrene 25 mm thick, glued together to make a slab of thickness of 50 mm. The overall dimensions of the base slab were 2.4 × 0.45 m. The arrangement is shown schematically in Fig. 1. The slab rested directly on a smooth wooden bench, which was dusted with French chalk in order to reduce friction. The ends

[1] Formerly Graduate Student. Presently at Andrew Palmer and Associates, SAIC, 40 Carden Place, Aberdeen AB10 1UP, UK.

[2] To whom all correspondence should be addressed.

Contributed by the Applied Mechanics Division of THE AMERICAN SOCIETY OF MECHANICAL ENGINEERS for publication in the ASME JOURNAL OF APPLIED MECHANICS.

Discussion on the paper should be addressed to the Technical Editor, Professor Lewis T. Wheeler, Department of Mechanical Engineering, University of Houston, Houston, TX 77204-4792, and will be accepted until four months after final publication of the paper itself in the ASME JOURNAL OF APPLIED MECHANICS.

Manuscript received by the ASME Applied Mechanics Division, May 18, 1999; final revision, Aug. 2, 1999. Associate Technical Editor: S. Kyriakides.

 Copyright © 1999 by ASME

Downloaded 04 May 2010 to 171.66.16.27. Redistribution subject to ASME license or copyright; see http://www.asme.org/terms/Terms_Use.cfm

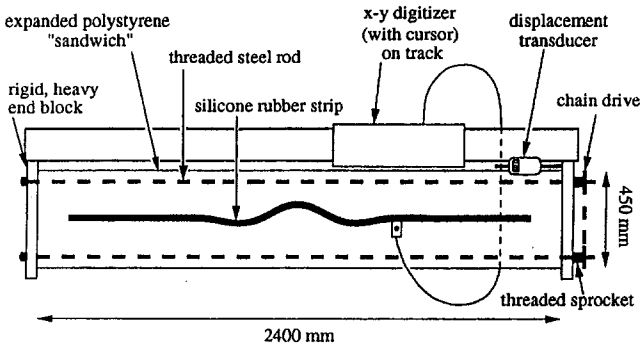


Fig. 1 Schematic plan view of the small-scale experimental apparatus

Table 1 Measured properties of two axially stiffened silicone rubber strips used in the small-scale experiments

Strip Properties		Strip Designation	
		S1	S2
Length of strip	(m)	1.8	2.0
width of strip	(mm)	9.3	5.3
depth of strip	(mm)	9.6	6.3
diameter of steel wire	(mm)	0.126	0.126
flexural stiffness, EI	(Nm^2)	1.12×10^{-3}	1.26×10^{-4}
Axial stiffness, EA	(N)	2720	2600
Weight per unit length	(Nm^{-1})	1.04	0.393
Axial friction coefficient, μ_{ax}			0.35
Lateral friction coefficient, μ_{lat}			0.35
Dimensionless group D_4			5.2×10^{-6}

of the slab abutted steel blocks 50 × 5 × 5 cm, one of which was clamped to the bench. Two long steel rods connected these end blocks. They passed through holes in the polystyrene and were threaded at the moveable end, and onto each a threaded sprocket wheel was screwed. The sprockets were rotated equally by means of a bicycle chain that passed over a third sprocket attached to a simple handle. Turning the handle thus compressed the base slab uniaxially. The relative movement of the end blocks was measured by means of a displacement transducer.

The crucial operational requirement for the base slab material is that an imposed end-to-end contraction should impart practically uniform compressive strain over the entire length of the slab; and the detailed constitutive law for the material is not directly relevant to this requirement. Extensive and detailed tests (Miles, 1998) showed that the performance of the compressible base-slab was good provided there was a pre-compression of about 5 mm, and that the base slab was not left under compression for longer than was necessary for the performance of experiments. Measurements also showed that the strain across the width of the base slab was practically zero: cf. Gibson and Ashby (1997). (See also Section 4.)

2.1 Silicone-Rubber Strips. The silicone rubber strips that were to simulate the prototype pipeline were cast in an open mould built up from steel bars, as shown in Fig. 2.

If a small-scale rubber strip is to model the thermal buckling of a prototype pipe, it is necessary that a certain dimensionless group should have the same numerical value in both the model and the prototype. It was found impractical to meet such a condition (see Section 3) with a plain silicone rubber strip of convenient size, essentially because the axial elastic stiffness of the strip was too low. Accordingly, a technique was developed for casting a fine steel wire, of diameter 0.126 mm, along the geometric centerline of the strip. During the casting process this wire was held straight under a small tension; and in order to prevent detectable gravitational sag, it was supported at regular intervals on small pads of silicone rubber. The wire was coated with Ambersil binding agent before the silicone rubber was cast. Even so, it tended to slip longitudinally relative to the rubber. This problem was overcome by depositing small blobs of solder at intervals along the wire. The cross-sectional dimensions of the silicone rubber strip were determined by the dimensions of the prototype pipeline being simulated: See Section 3 for details. After a strip had been cast, small markers (usually pin pricks filled with ink) were added to its top surface, typically at 50-mm spacing: This gave a satisfactory number of points of measurement—between three and five points—in each buckled lobe. The measuring system is described below.

Altogether, three strips were made, two of which had a central wire. Details of these two strips are given in Table 1. Most of the computations were done for strip S2, which was designed to simulate a specific pipeline (see Section 3).

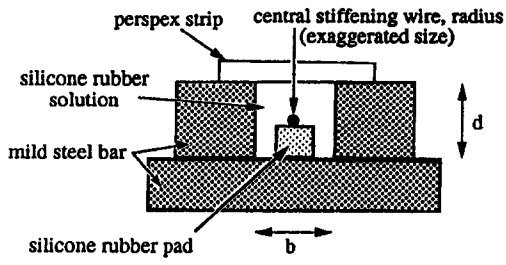


Fig. 2 Cross section of mould for forming silicone-rubber strips. *b*, *d* denote breadth and depth of the strip, respectively.

2.2 Elastic and Frictional Properties of Silicone-Rubber Strips. The elastic modulus of the silicone rubber was measured for each strip. The main method was a self-weight bending assay, in which the self-weight tip deflection of a short piece of the strip mounted as a cantilever was measured for different projecting lengths; and from these data together with weight measurements, the value of Young's modulus E could be determined. The presence of the central wire had a negligible effect on the flexural stiffness of the strip; and the central placing of the wire was confirmed by cantilever experiments on the strip in different orientations.

The axial stiffness of the composite strip was computed from the value of E thus measured, together with the calculable axial stiffness of the steel wire. In practice all but a few percent of the axial stiffness came from the wire.

The frictional characteristics of silicone rubber sliding over expanded polystyrene were determined by direct experiments on a piece of strip 0.3 m long. It was dragged over the base slab both axially and laterally by means of cotton thread, and the small forces required were measured by an instrumented steel cantilever. Frictional forces varied to some extent with speed, and friction was evidently affected by the grain texture of the expanded polystyrene surface. The full frictional force was not mobilized until the silicone rubber had moved relative to the expanded polystyrene by about 0.4 mm. A representative value of the coefficient of friction between silicone rubber and expanded polystyrene was 0.35, for relative motion in both the axial and lateral directions, and these were the base values used for the computations.

2.3 Measurement of the Position of the Strip. Positions of markers on the strip were measured in a global x, y coordinate system in the plane of the base slab by means of an acoustic digitizer, type SAC GP-9, reading to a cursor that could be located optically, without direct contact, vertically above the target points. Extensive tests on the digitizer showed that it located points to within an accuracy of about 0.3 mm over a field 1.2 m long and the full width of the slab, except when the cursor was close to an end of the digitizer. In order to cover the entire surface of the base slab, the digitizer was made movable to two discrete locations alongside

Downloaded 04 May 2010 to 171.66.16.27. Redistribution subject to ASME license or copyright; see http://www.asme.org/terms/Terms_Use.cfm

Table 2 Properties of a North Sea pipeline

Outer diameter	0.168 m
Wall thickness	0.0159 m
Flexural stiffness, EI	4.62×10^6 Nm^2
Axial stiffness, EA	1.57×10^9 N
Submerged weight (contents filled)	457 Nm^{-1}
Axial friction coefficient, μ_{ax}	0.7*
Lateral friction coefficient, μ_{lat}	0.7*
Dimensionless group D_4	5.0×10^{-6}
Effective temperature rise, ΔT†	83°C

* Assumed value: see Palmer et al. (1981, 1988).
† The contribution to longitudinal elastic expansion on account of pressure p is equivalent to a rise in temperature of $pD(1 - 2\nu)/4Et\alpha$, where D = diameter of pipe, t = thickness, ν = Poisson's ratio, and α = coefficient of linear thermal expansion. For this pipeline p = 8.4 MPa, and so the pressure-equivalent temperature rise is approximately 4°C.

the slab. In some cases all of the buckled lobes conveniently lay in range of the digitizer in just one central position. But it was not difficult to align the fields of measurement for the two different locations of the digitizer, if that was needed.

When a set of position readings had been taken for the strip in a given conformation—a task taking, typically, one or two minutes—these were processed by a Savitzky-Golay filter (Press et al., 1992, Section 14.8) which produced a smooth, continuous curve on the basis of the positions of the measured points.

2.4 Fixing the Ends of the Strip. The silicone rubber strip, about 2 m long, models a piece of pipeline typically some 0.5 km long: See Section 3 for details of the geometrical scaling procedure. The prototype pipeline is much longer than that, of course. This means that some "finite length" effects may intrude into the small-scale model experiments. In most of our tests the ends of the strip were anchored frictionally to the base slab, by means of small lead weights.

3 Dimensionless Variables

Dimensional analysis is a general tool for interpreting the results of tests on small-scale models in relation to the behaviour of the prototype. In particular, the variables of any problem must be combined into appropriate dimensionless groups.

When a buckled lobe is developing, its half-wavelength λ, amplitude a, and axial force P are the key variables, and they all depend on the current base contraction (or equivalent thermal expansion). The only relevant mechanical properties of the strip or pipeline are its flexural and axial stiffnesses EI and EA, respectively. When there is frictional sliding in the (locally) axial direction, the frictional drag is q_{ax} per unit length: This is equal to the weight of the strip (or the submerged weight of the pipeline) per unit length multiplied by an axial coefficient of friction μ_{ax}. Likewise there is a lateral frictional drag q_{lat} per unit length.

In this list of variables we have not assigned a symbol to temperature (or base slab contraction): As we shall see later, it is more convenient to incorporate temperature into another variable (f: see Section 6) that also has the advantage of enabling us to take account of any finite length effects in the experiments or the computations. There may also be other variables, that have not been mentioned so far, which may or may not play a significant part in the post-buckling behavior: See Section 7.

All of the seven quantities listed above involve only two dimensions: force and length. So we expect, by Buckingham's theorem (Taylor, 1975), to find $7 - 2 = 5$ independent dimensionless groups. These may be written as

$$\left.\begin{aligned} D_1 &= \lambda(q_{ax}/EI)^{1/3} \\ D_2 &= a(q_{ax}/EI)^{1/3} \\ D_3 &= P/EA \\ D_4 &= (EI)^{1/3} q_{ax}^{2/3}/EA \\ D_5 &= q_{lat}/q_{ax}. \end{aligned}\right\} \quad (1)$$

Groups D_1 to D_3 deal with the main variables describing lobe growth: Here we have taken $(EI/q_{ax})^{1/3}$ as a convenient reference length (using q_{ax} rather than q_{lat} for reasons that will become clear later) and EA as a convenient reference force (as in Maltby and Calladine, 1995b). Group D_4 is a dimensionless combination of the flexural and axial stiffnesses and one of the two frictional parameters; for dynamical similarity between model and prototype D_4 must have the same value in each. That is the constraint which obliged us to cast a fine steel wire along the centerline for the working silicone rubber strips. We also know that the geometric scaling factor between prototype and model is given by

$$l_{prot}/l_{mod} = (EI/q_{ax})^{1/3}_{prot}/(EI/q_{ax})^{1/3}_{mod}. \quad (2)$$

Finally, D_5 is the ratio of lateral to axial frictional drag. This ratio may be known for the prototype (see Table 2) but its experimental value in the small-scale model may be different. One of the purposes of our parametric study was to determine how the experimental results depend on D_5.

The silicone rubber strip whose parameters have been given in Table 1 was intended to model a particular physical flowline—a small-diameter intrafield pipeline—in which lateral buckling had been observed. Particulars are given in Table 2.

4 ABAQUS Finite Element Package

The ABAQUS finite element package (Hibbitt, Karlsson and Sorenson, 1995) was used in order to set up a simulation of the small-scale experimental setup. It is capable of dealing with problems involving finite rotations. With this program it was relatively straightforward to include movement of the pipe/strip elements over the base slab and to provide components q_{ax} and q_{lat} of axial and lateral frictional drag on the pipe in a local coordinate frame. For most of the computations the base slab was considered rigid and the pipe/strip underwent thermal expansion. But for some computations the base slab was modeled as it really was in the small-scale experiments, i.e., as unidirectionally contracting. Such computations were much more time-consuming, on account of the need to model the base slab as deformable.

In general there was excellent agreement between the ABAQUS computations and the small-scale experiments. An example showing a succession of measured and computed deformed profiles is given in Fig. 3. In all of the computations a mirror-symmetry boundary condition was specified at the centre of the central lobe, whereas the experiments showed a small level of asymmetry. The

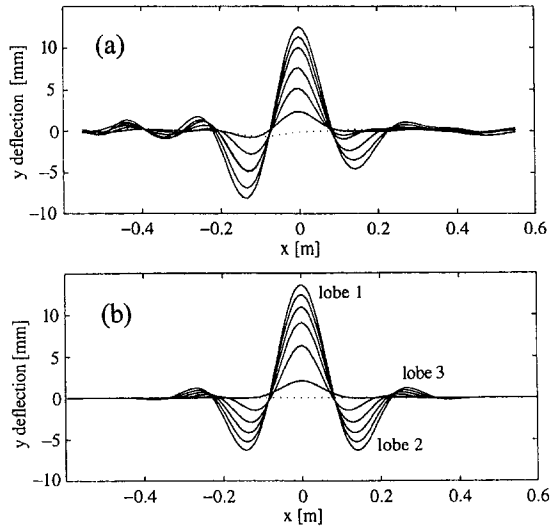


Fig. 3 Comparison of measured (*a*) and computer-generated (*b*) profiles of strip S2. Note that the *y*-scale has been exaggerated.

Downloaded 04 May 2010 to 171.66.16.27. Redistribution subject to ASME license or copyright; see http://www.asme.org/terms/Terms_Use.cfm

situation depicted in Fig. 3 is typical of many other comparisons between experiment and computation.

It must be conceded that the modeling of expansion of the strip by means of a *unidirectional* contraction of the base is not strictly valid. An *isotropic,* bi-directional contraction would correctly model an expanding strip—provided, of course, the resulting conformation of both strip and base slab were to be subsequently enlarged isotropically by the same small factor in order to restore the base slab to its original size. But isotropic bi-axial contraction would be difficult to achieve, physically. Our reason for hoping that uni-directional contraction would be adequate in the experiments was, of course, that in general the strip was lying broadly along the direction of principal contraction. In order to confirm this assumption, a separate computation was performed, in which the base slab underwent bi-axial contraction. Overall there was negligible difference between the computations using uni-axial and bi-axial contraction; which confirmed the practical validity of a uniaxially contracting base slab for modeling the thermal expansion of the pipeline.

5 Experimental Observations

In most of the experiments the strip was initially set up on the base slab against a steel straight edge. In cases where no deliberate initial imperfection was introduced to the line of the strip, the base slab contraction produced buckling lobes at a variety of locations along the strip, with preference for buckling to begin near the ends. Since it was clearly desirable to avoid end effects where possible, a deliberate imperfection was normally introduced at the center of the strip by pushing the strip sideways there after it had been laid straight. With imperfections of amplitude less than 1 mm or so, buckling involved an initial "jump" to a buckled form; whereas for imperfections of more than 2 mm there was no jump. Since we were concerned primarily with the post-buckling evolution of buckled profiles, we did not study the initial stages of buckling.

5.1 The Phenomenon of "Lobe-Extinction." The sequence of profiles in Fig. 3 show that the first lobe to be formed (lobe 1) grows rapidly at first as temperature or base contraction increases; but eventually its growth slows down and the adjacent, smaller lobes (lobes 2) take over the role of accommodating further expansion of the strip. And then lobes 2 cease growing, and lobes 3 take over. Eventually, as the temperature continues to increase, all lobes stop growing when they have reached a given amplitude and "lobe length" (i.e., half-wavelength).

We have here a phenomenon that we call "lobe extinction." It can be seen rather more clearly in computations than in experiments, because the computations can be taken artificially to a higher temperature or base slab contraction. Figure 4(*a*) shows a plot of amplitude in lobes 1, 2, and 3 against a measure of temperature in a particular case. It can be seen that the amplitude of lobe 1 is tending towards a limiting value; and that lobes 2 (and subsequent lobes) also appear eventually to be heading for the same limiting value. More complete examples will be presented below.

Figure 4(*b*) shows the corresponding plot for "lobe length" of lobes 1, 2, and 3 as the temperature steadily increases. It is clear that in general the lobe lengths increase as the amplitude increases; and it is also clear that the lobe lengths reach a single limiting value rather earlier than do the lobe amplitudes.

What is seen in Fig. 4 is, indeed, representative of a general phenomenon. Each lobe in turn is the most active lobe, growing faster than all others; yet each lobe eventually stops growing, in the same way that a mid-ocean volcano becomes extinct when the underlying "hot spot" moves on to form a new, active volcano (Clague and Jarrard, 1973). Thus we find that the initial "localization" phenomenon of buckling is overtaken by a kind of "tiredness"; and eventually a set of practically *uniform,* "extinct" buckled lobes is left on the base slab or sea bed.

In the long run, therefore, we have three distinct spatial phases

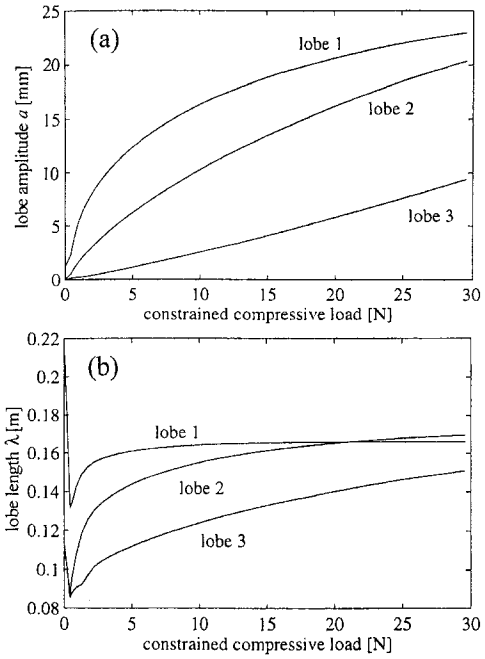


Fig. 4 Plots of lobe amplitude (*a*) and lobe length (*b*) for three lobes in a computation on strip S2. The abscissa is the calculated fully constrained compressive load in the strip at the base-slab strain.

of behavior in the lateral buckling of a pipeline as the temperature continues to rise. First, in the center and on either side of the initiating buckle lie an increasing series of uniform "extinct" lobes. That region is bordered on either side by an active, transition zone involving a few currently growing lobes. And beyond those zones the strip/pipeline has not yet begun to buckle.

The physical feature which causes lobes to stop growing appears to be the *axial friction* that has to be overcome in the active region of growing lobes; so that within the zone of "extinct" lobes there is simply not sufficient axial compressive force to increase the amplitude of these lobes any further.

The concept of "lobe extinction" is important for the engineer because it puts limits on the ultimate amplitude and half-wavelength of *all* post-buckled lobes, and hence on the greatest bending strain that can ever occur in the pipeline during the course of thermal buckling, however much the temperature may rise.

The above description of the evolution of buckling must be treated with some caution, however. It suffers from a tacit, unquantified assumption that the temperature or base contraction can go on increasing indefinitely. But it should be understood that in a given situation the rise of temperature may actually be insufficient to cause even the first lobe to approach the point of extinction.

The concept of lobe-extinction clearly needs to be made quantitative, not only in regard to the limiting half-wavelength and amplitude of the "extinct" lobes, but also with respect to the temperature increase necessary to put, say, the first lobe into the "extinct" zone.

6 Free-End Displacement

How may we characterize a given buckled profile in relation to the thermal expansion which causes it? The most useful concept that we have come across in this regard is what we call *free-end displacement, f.*

Figure 5 shows schematically the distribution of axial force P against a position coordinate x for the simpler artificial problem of a long straight pipeline *with a free end* that is subjected to a steadily increasing rise in temperature, ΔT. Remote from the free end $x = 0$ there is the fully resisted thermal expansion force, $EA\alpha\Delta T$: α is the coefficient of thermal expansion for the pipeline

Downloaded 04 May 2010 to 171.66.16.27. Redistribution subject to ASME license or copyright; see http://www.asme.org/terms/Terms_Use.cfm

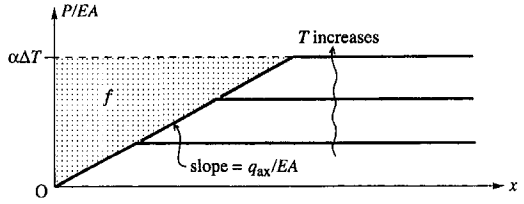


Fig. 5 Plot of *P/EA* against *x* for a long straight strip with a free end at *x* = 0. The sloping line corresponds to the region of frictional slipping, while the horizontal lines correspond to fully restrained pipe. The shaded area gives the axial displacement *f* at the free end.

material. But frictional slip occurs in a region nearer the origin, in which

$$P = q_{ax}x. \tag{3}$$

In this region the pipeline material moves to the left relative to the base; and the axial movement of the free end, f, is equal to the shaded area of the diagram, as may easily be shown:

$$f = EA(\alpha\Delta T)^2/2q_{ax}. \tag{4}$$

f is an important parameter because it turns out, in the many computed cases, that f is also practically equal to the "excess length" of the curved pipeline contour over the straight baseline, as shown schematically in Fig. 6. In broad terms, the reason for this agreement is that the distribution of axial compressive force in the strip or pipeline is not very different overall as between the actual, buckled strip on the one hand and the artificial straight strip with a free end on the other.

An important feature of the free-end displacement f is that it enables us to account in a quantitative way for the differences between a finite-length small-scale experiment on the one hand and the much longer—practically infinite—prototype pipeline on the other. In each case the "excess length" of the buckled profile corresponds to f as calculated for a straight, free-ended strip. The calculation of f as in Eq. (4) is for an infinitely long strip; but the corresponding calculation is readily done for a strip of finite length.

It follows from all of this that f is the most appropriate abscissa for plotting curves of the kind shown in Fig. 4, in order to display the way in which lobe half-wavelengths and amplitudes change as the temperature increases.

7 Parametric Study of Buckled Forms

So far, the data presented in Figs. 3 and 4 have been gathered from model tests and corresponding computations for one specific pipeline, having particular dimensions and frictional characteristics. What we now need is a thorough parametric study in which all of the defining parameters are altered in turn.

Such a study was performed by means of the computer. The "base case" was the one that we have described already, and excursions from it took the form of cases in which the parameters EI, EA, q_{lat}, and q_{ax} were changed in value—typically by factors 1.2, 1.5 or 2—either individually or together. Altogether 19 different cases were run.

The first result to emerge from this study was that the value of axial stiffness EA had no bearing on the sequence of pipeline profiles generated as the temperature increased. The explanation for this is that the sequence of profiles is determined by the flexural response of the pipeline to forces imposed by friction; and so EA only affects the behaviour through the calculation of f.

The second result was a surprising one. If a case is run with q_{lat} having, say, twice the value that it had in a previous study, with other parameters (EI, q_{ax}) unchanged, then the amplitude of "extinct" lobes turns out to be *twice* its previous value. This seems odd, because it might have been expected that *increased* lateral friction would *reduce* the amplitude of the buckled lobes.

Now in a region of uniform small-amplitude periodic buckles, the axial compressive force P is related to half-wavelength λ and amplitude a by the close approximation

$$P = \frac{\pi^2 EI}{\lambda^2} + \frac{\lambda^2 q_{lat}}{\pi^2 a}. \tag{5}$$

This result may be obtained from the governing equation, as in Maltby and Calladine (1995b). For present purposes, however, we note that the first term on the R.H.S. corresponds to the axial force required for Euler buckling of the pipeline with half-wavelength λ, in the absence of friction; while the second term corresponds approximately to the axial force carried by a shallow momentless *arch* which is loaded transversely by the resistive frictional force q_{lat}. Notice in particular that the second term *decreases* as amplitude a *increases.*

Now numerical studies show a remarkable and consistent feature among "extinct" lobes, namely that the second term on the R.H.S. of Eq. (5) is always equal to almost exactly one third of the first term. How and why this constant ratio comes about is something that we do not yet fully understand; but this empirical observation enables us to see clearly in particular that when the value of q_{lat} is doubled, then so also must be the amplitude a of the "extinct" lobes.

The best global view of the process of evolution of post-buckled lobes is obtained from plots of amplitude and half-wavelength of successive lobes against a dimensionless parameter containing f. Trial-and-error manipulation of the results of the many computer runs showed that plots of

$$L = \lambda(q_{ax}/EI)^{1/3} \quad \text{and} \quad A = a(q_{ax}/EI)^{1/3}(q_{ax}/q_{lat}), \tag{6}$$

respectively, against

$$F = f(q_{ax}/EI)^{1/3}(q_{ax}/q_{lat})^2 = D_6 \tag{7}$$

were *universal,* in the sense that curves computed for the many different parameter cases aligned well with each other, as shown in Fig. 7.

The alignment is not perfect, but nevertheless we find it convincing. There are some minor discrepancies in the dimensionless plot of A against F; but the differences are larger in the dimensionless plot of L against F. Those differences are due mainly to the way in which initial imperfections in the line of the strip were introduced in the different computed cases. Note that the "scatter" is largest for lobe 1, which is directly affected by any initial imperfection, while it is progressively smaller in lobes 2 and 3. However, we are mainly interested for present purposes in the "far post-buckling" behavior; and it is clear from Fig. 7 that initial conditions have little effect upon the ultimate extinct conformation of the lobes.

It may be seen in Fig. 7(a) that the dimensionless amplitude does not reach an absolutely constant, limiting value: instead, the curves appear to show a small positive slope. When a given lobe is actively *growing* as f increases, the increasing amplitude comes about mainly on account of some axial "feeding in" of material from the adjacent lobe or lobes. But when a lobe becomes extinct there is no more interlobe transfer of material. If the temperature still continues to rise, then the contour length *within* the lobe must continue to increase by a small amount; and it is this which accounts (quantitatively) for the small,

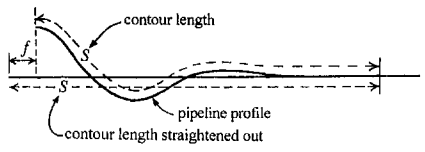


Fig. 6 Relationship between *f* and the contour length of a bucked pipe profile

Downloaded 04 May 2010 to 171.66.16.27. Redistribution subject to ASME license or copyright; see http://www.asme.org/terms/Terms_Use.cfm

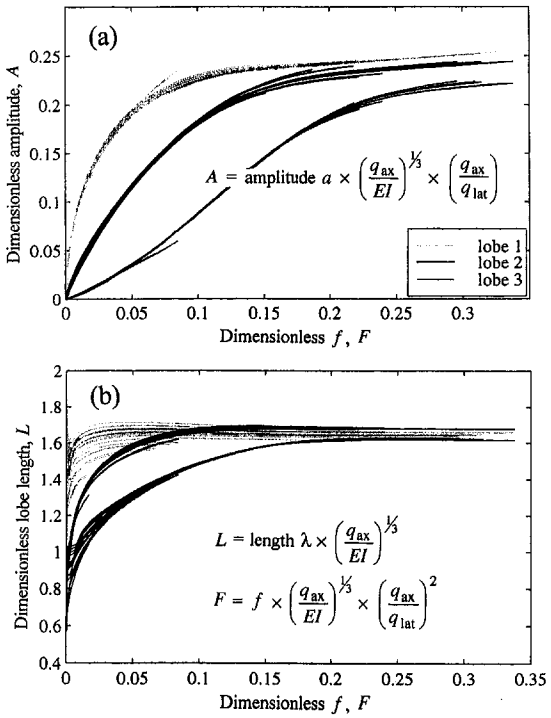


Fig. 7 Dimensionless plots of lobe amplitude and length against *f*, from 19 computer studies of strips having different values of *EI*, *EA*, q_{ax}, and q_{lat}.

positive slopes seen in Fig. 7(*a*). Notwithstanding this effect, however, it is reasonable to regard 0.25 as a limiting value for the dimensionless amplitude.

Another point to emerge from Fig. 7 is that the half-wavelengths of the lobes depend on the *axial* but not on the *lateral* frictional drag. Indeed, this is why we chose to use $(EI/q_{ax})^{1/3}$ as the reference length when setting up dimensionless groups in Section 3. This might seem strange in view of the buckling of a classical beam-on-elastic-foundation (Hetényi, 1946), where the transverse *stiffness* of the foundation plays a direct part in determining the half-wavelength of the buckles. In the present problem it seems that the axial *force* in the pipeline or strip is, somehow, primarily responsible for determining the half-wavelengths of the buckles.

8 Design Formulas

The plots of Fig. 7 indicate that "extinct" lateral-buckling lobes may be described by some very simple formulas, which should in turn be useful to the engineer from the point of view of design of a new pipeline or assessment of an existing one.

Let us make a preliminary investigation of such formulas, first of all under the implicit assumption that the temperature rise in the pipe will be sufficient to take lobe 1 into the "extinct" range; and then for lesser temperature rises.

As explained already, the maximum *bending strain* in the buckled pipe is of major importance, because if the pipeline material were to go far into the plastic range, the pipe would become unstable, leading to a damaging "kinking."

Let b be the mean radius of the initially straight pipe, and κ the magnitude of the curvature of the centerline in the deformed configuration. The bending strain ϵ, at the "extreme fiber," is given by $\epsilon = b\kappa$. Also, let $y(x)$ represent the profile of a local lobe. For a lobe of amplitude a and half-wavelength λ and assumed to be sinusoidal, and with (a/λ) sufficiently small that we may use small-deflection formulas, we find

$$|\kappa|_{max} = \pi^2 a/\lambda^2. \tag{8}$$

Taking 0.25 and 1.7, respectively, as the limiting values of the ordinates of A and L in Fig. 7(*a*) and (*b*), we have

$$a = 0.25(q_{lat}/q_{ax})(EI/q_{ax})^{1/3} \tag{9}$$

and

$$\lambda = 1.7(EI/q_{ax})^{1/3}; \tag{10}$$

hence

$$\epsilon_{max} = 0.85b\,\frac{q_{lat}}{q_{ax}}\left(\frac{q_{ax}}{EI}\right)^{1/3}. \tag{11}$$

In the case of the flowline whose particulars are given in Table 2, this gives $\epsilon_{max} = 2.7 \times 10^{-3}$. Although such a strain is within the plastic range for typical pipeline steels,—the elastic strain range is typically between 1 and 2×10^{-3}—it is not sufficient to give a local kinking of the pipe. Thus, Calladine (1983) made a study of the critical strain for local buckling to occur in a pipe under pure bending, and found experimentally that the critical strain was approximated by

$$\epsilon_{cr} \approx (0.3 \pm 0.05)(t/b) \tag{12}$$

for steel pipes, where t/b is the thickness/radius ratio. For the present pipe (see Table 2) $b/t \approx 5$, so $\epsilon_{cr} \approx 6$ percent, i.e., an order of magnitude larger than the maximum bending strain in the "extinct" lobes.

Formula (11) gives the "extreme-fiber," bending strain in a fully developed "extinct" lobe. It may be applied to any pipeline with given parameters. Now an assessment of the *submerged weight* per unit length of pipe is required for the evaluation of q_{ax}. This depends on the radius and thickness of the steel pipe, the nature of its contents and the buoyancy effect of any insulation, etc. Since we shall obtain an overestimate of ϵ_{max} if we overestimate the self-weight, we may obtain a rough approximation to the submerged weight by considering a steel pipe without insulation and full of water. This enables Eq. (11) to be simplified considerably; and using tabulated values for the density and Young's modulus of steel we obtain

$$\epsilon_{max} \approx 0.0074(\mu_{lat}/\mu_{ax}^{2/3})b^{1/3}. \tag{13}$$

The wall thickness t of the pipe does not appear in Eq. (13) because I is proportional to t and so also is the submerged weight in the special case of a water-filled pipe. Formula (13) gives $\epsilon_{max} = 2.8 \times 10^{-3}$ in the case cited above: The difference between this value and the one found from Eq. (11) by use of data from Table 2 comes from the fact that in the present case Eq. (13) overestimates the submerged weight by about 12 percent. In general, ϵ_{max} is insensitive to changes in the submerged weight, by reason of the one third power-law.

Formula (13) is useful, notwithstanding its approximate nature, in that it shows that if the radius of the pipe were to increase by an order of magnitude, to the largest size used in practice, then the value of ϵ_{max} would increase by a factor of about 2, other things being equal. For b/t values of around 30—the largest used in practice—Eq. (12) shows that the critical bending strain for local buckling is around one percent. It appears, then, that while the bending strain in the "extinct" lobes of a typical buckled pipeline may be some way into the plastic strain range, it would not normally be sufficient to cause local buckling of the pipe.

In the case of a given pipeline, Eq. (11) should be used in order to evaluate ϵ_{max}. Nevertheless, the simplified Eq. (13) may be useful in providing a rough first-order estimate of ϵ_{max}.

We have assumed explicitly throughout our analysis that the pipe remains within the elastic range; and so any predictions of straining within the plastic range must be regarded with caution and scepticism. But it is conceivable that our results may not be seriously in error if the pipe material is taken only a small way into

Downloaded 04 May 2010 to 171.66.16.27. Redistribution subject to ASME license or copyright; see http://www.asme.org/terms/Terms_Use.cfm

the plastic range; and that is a topic which clearly warrants further research.

However, all of these considerations have presupposed that the value of f is sufficient to bring lobe 1 to the point of extinction, say $F \geq 0.1$. But in a practical case the value of f may well be much smaller. Thus in the pipeline whose particulars are given in Table 2, three buckled lobes were found at a spacing of 0.5 km. In such a case $F \cong 0.1$ (see Miles, 1998, for details) so the value of A is reduced from 0.25 to 0.1, and the extreme fiber bending strain to $\sim 1 \times 10^{-3}$, which should be within the elastic range. The occurrence of buckled lobes at such a close spacing suggests that significant imperfections may have been present in the pipe, which is a factor beyond the scope of the present investigation.

9 Closing Remarks

For the sake of providing a tractable problem we have considered a simplified, or idealized, version of the actual physical situation under investigation. We have already commented on cases where bending of the pipe might strain the material into the plastic range. The assumed constant frictional force should be a satisfactory model of the actual interaction between the pipe and the sea bed provided the real behavior is not strikingly different. In this connection we may remark that in the extreme case of upheaval buckling (Maltby and Calladine, 1995a, b), where the resistive force changes strongly with deflection, a completely different problem formulation is required.

Acknowledgments

We are grateful to Prof. Andrew Palmer for continuing advice and to the U.K. Engineering and Physical Sciences Research Council, in cooperation with British Petroleum, for a "CASE" research studentship. We thank David Walker and Lawrence Tebboth of BP, who provided valuable help and advice. An anonymous referee made several comments which led to an improvement of the text.

References

Brennodden, H., Sveggen, O., Wagner, D., and Murff, J., 1986, "Full-Scale Pipe-Soil Interaction Tests," *Proceedings, Eighteenth Annual Offshore Technology Conference,* Vol. 4, Houston, ASME, New York, pp. 433–440.

Calladine, C. R., 1983, "Plastic Buckling of Tubes in Pure Bending," *Collapse,* J. M. T. Thompson, and G. W. Hunt, eds., Cambridge University Press, London.

Clague, D. A., and Jarrard, R. D., 1973, "Tertiary Pacific Plate Motion Deduced From the Hawaiian-Emperor Chain," *Bulletin of the Geological Society of America,* Vol. 84, pp. 1135–1154.

Gibson, L. J., and Ashby, M. F., 1997, *Cellular Solids,* 2nd Ed., Cambridge University Press, London.

Hetényi, M., 1946, *Beams on Elastic Foundations,* The University of Michigan Press, Ann Arbor, MI.

Hibbit, Karlsson and Sorenson, Inc., 1995, *ABAQUS Manuals* Version 5.5.

Kaye, D., LeMarchand, D., Blondin, P., and Carr, M., 1995, "Lateral Buckling Design of the Dunbar Double Wall Insulated Pipeline," *Proceedings, Eighteenth Annual Offshore Pipeline Technology Conference,* Copenhagen, IPC Technical Services, London, 15 pp. + 6 pp. of diagrams.

Kerr, A., 1978, "Analysis of Thermal Track Buckling in the Lateral Plane," *Acta Mechanica,* Vol. 30, pp. 17–50.

Maltby, T., and Calladine, C. R., 1995a, "An Investigation Into Upheaval Buckling of Buried Pipelines: I. Experimental Apparatus and Some Observations," *Int. J. Mech. Sci.,* Vol. 37, pp. 943–963.

Maltby, T., and Calladine, C. R., 1995b, "An Investigation Into Upheaval Buckling of Buried Pipelines: II. Theory and Analysis of Experimental Observations," *Int. J. Mech. Sci.,* Vol. 37, pp. 965–983.

Miles, D. J., 1998, "Lateral Thermal Buckling of Pipelines," Ph.D. dissertation, University of Cambridge, Cambridge, UK.

Palmer, A. C., and Ling, M. T. S., 1981, "Movements of Submarine Pipelines Close to Platforms," *Proceedings, Thirteenth Annual Offshore Technology Conference,* Vol. 3, Houston, ASME, New York, pp. 17–24.

Palmer, A. C., Steenfelt, J. S., Steensen-Bach, J. O., and Jacobsen, V., 1988, "Lateral Resistance of Marine Pipelines on Sand," *Proceedings, Twentieth Annual Offshore Technology Conference,* Vol. 4, Houston, ASME, New York, pp. 399–408.

Press, W. H., Tenkolsky, S. A., Vetterling, W. T., and Flannery, B. P., 1992, *Numerical Recipes in C,* 2nd Ed., Cambridge University Press, London.

Taylor, E., 1974, *Dimensional Analysis for Engineers,* Oxford University Press, Oxford.

Tvergaard, V., and Needleman, A., 1980, "On the Localisation of Buckling Patterns," ASME JOURNAL OF APPLIED MECHANICS, Vol. 47, pp. 613–619.

Tvergaard, V., and Needleman, A., 1981, "On Localised Thermal Track Buckling," *Int. J. Mech. Sci.,* Vol. 23, pp. 577–587.

Downloaded 04 May 2010 to 171.66.16.27. Redistribution subject to ASME license or copyright; see http://www.asme.org/terms/Terms_Use.cfm

A Strip Element Method for Analyzing Wave Scattering by a Crack in an Immersed Composite Laminate

G. R. Liu

Z. C. Xi

K. Y. Lam
Mem. ASME

H. M. Shang
Mem. ASME

Department of Mechanical and Production Engineering, National University of Singapore, 10 Kent Ridge Crescent, Singapore 119260

A strip element method is presented for analyzing wave scattering by a crack in a composite laminate submerged in a fluid. In this method, the fluid and laminated plate are modeled using two-nodal-line and three-nodal-line strip elements, respectively. A system of governing equations of the fluid and solid strip elements in frequency domain are derived using a variational method and the Hamilton principle, which are converted as a set of characteristic equations in wave number domain by applying Fourier transform techniques. A particular solution to the equations is obtained using a modal analysis method in conjunction with inverse Fourier transform techniques. A complementary solution to the equations is found employing horizontal boundary conditions on cross sections at the crack tips. The addition of the particular and complementary solutions yields a general solution. Numerical examples are presented for immersed steel and composite plates with either a horizontal or a vertical crack. Computed results indicate that the fluid has considerable influence on the wave fields scattered by a crack in a composite laminate.

1 Introduction

Owing to their high specific stiffness and strength, advanced fiber-reinforced composite materials have been widely used in aircraft and aerospace as well as many other industries. Cracks could occur in a composite laminate as a result of composite manufacture or through in-service use. Their growth can give rise to failure of composite structures. The ultrasonic technique is one of the most popular methods for evaluating composite cracks. It is able to provide a scattered wave field from which the characteristics of cracks can be obtained. In ultrasonics, a fluid, usually water, is generally used as a coupling medium between an ultrasonic wave generator and composite materials. As the fluid may affect the sensitivity of detecting cracks in materials, it is of importance to investigate fluid-structural coupling effects.

As wave propagation in anisotropic composite plates was well studied (Mal, 1988; Datta et al., 1988a, b), scattering of a wave by a crack in a composite plate attracted much attention in wave motion of composite materials. Karim, Kundu, and Desai (1989) analyzed dynamic responses of delamination cracks in a layered fiber-reinforced composite plate using an analytical approach. Datta, Ju, and Shah (1992) dealt with scattering of an impact wave from an infinite uniaxial graphite/epoxy plate containing a horizontal crack using a hybrid method. Kundu and Boström (1991) examined axisymmetric scattering of elastic waves by a circular crack situated in a transversely isotropic solid.

On the other hand, considerable progress also was made toward understanding the interaction of ultrasonic waves with fluid-coupled anisotropic media in the absence of cracks (Nayfeh, 1995). Dealing with wave propagation of an anisotropic half-space immersed in a fluid, Atalar (1983) investigated numerically reflection coefficients at a liquid-cubic-anisotropic crystal. In the analysis, a null in the reflection coefficient was detected for certain orientations. This study was extended to a general anisotropic half-space by Arikan, Teletar, and Atalar (1989) later on. Braga and Herrmann (1989) treated a periodically isotropic layered half-space immersed in an acoustic fluid using a propagator matrix method. Nayfeh (1991) analytically studied reflection and transmission coefficients at liquid-monoclinic half-spaces as well. The dependence of these coefficients on propagation direction and incident angles was discussed. Nayfeh and Chimenti (1988a) conducted both theoretical and experimental investigation on reflection from a unidirectional fibrous composite plate immersed in water. They found that the Cremer correspondence principle is valid only when the ratio of fluid to solid density is small. Nayfeh and Chimenti (1988b) also discussed a generally orthotropic plate. Furthermore, Chimenti and Nayfeh (1990) extended their work on the single orthotropic plate to cross-ply composite laminates using a transfer matrix approach. Nayfeh and Taylor (1988) investigated surface wave characteristics of multilayered media in contact with a fluid on one side while its other side is free or in contact with another solid substrate. Dayal and Kinra (1989) examined both analytically and experimentally the wave speed and attenuation for a symmetric cross-ply composite laminate. Mal, Xu, and Bar-Cohen (1989) performed theoretical and experimental studies on bounded plates. Liu et al. (1996) carried out a stress wave analysis of composite laminates excited by underwater explosion shocks. It is worth noting that these references confined themselves to anisotropic media without cracks. So far, only limited work is available on the interaction of ultrasonic waves with cracked anisotropic media submerged in fluid. Gracewski and Bogy (1986) investigated analytically time-harmonic elastic wave scattering by an interface crack in a layered half-space submerged in water. Variations of stress intensity factors at crack tips with incident angles were discussed for plane waves incidents from water onto an iron layer-iron half-space. The interaction of ultrasonic waves with cracked laminated composite plates immersed in a fluid remains untouched.

The purpose of this paper, therefore, is to analyze wave scattering by a crack in a composite laminate with an arbitrary number of anisotropic layers submerged in a fluid. The presence of the

Contributed by the Applied Mechanics Division of THE AMERICAN SOCIETY OF MECHANICAL ENGINEERS for publication in the ASME JOURNAL OF APPLIED MECHANICS.

Discussion on the paper should be addressed to the Technical Editor, Professor Lewis T. Wheeler, Department of Mechanical Engineering, University of Houston, Houston, TX 77204-4792, and will be accepted until four months after final publication of the paper itself in the ASME JOURNAL OF APPLIED MECHANICS.

Manuscript received by the ASME Applied Mechanics Division, Nov. 3, 1998; final revision, Apr. 2, 1999. Associate Technical Editor: A. K. Mal.

 Copyright © 1999 by ASME

Downloaded 04 May 2010 to 171.66.16.27. Redistribution subject to ASME license or copyright; see http://www.asme.org/terms/Terms_Use.cfm

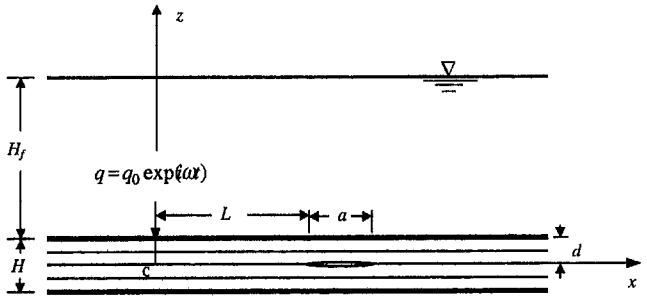


Fig. 1 Geometry of a cracked composite laminate submerged in a fluid

crack makes it difficult to obtain an analytical solution and therefore a numerical method needs to be developed. A strip element method proposed by Liu and Achenbach (1994, 1995) was shown to be capable of reducing computational labor greatly if it was used to deal with a cracked dry composite plate. In this analysis, the strip element method is extended to a cracked composite laminate immersed in a fluid. First of all, the strip element method is used to reduce a system of partial differential governing equations for both the fluid and plate to a system of ordinary differential governing equations, which are then converted as a set of characteristic equations by applying Fourier transform techniques. A particular solution to the equations is obtained using a modal analysis method in conjunction with inverse Fourier transform techniques. A complementary solution to the equations is found employing horizontal boundary conditions on cross sections at the crack tips. The addition of the particular and complementary solutions yields a general solution. Finally, numerical examples are given for immersed composite laminates with either a horizontal or a vertical crack. The effects of the fluid on the scattered wave field in fluid-loaded cracked composite laminates are discussed.

2 Statement of Problem

Consider a composite laminated plate of thickness H with either a horizontal or a vertical crack submerged in a fluid, as shown in Fig. 1. The distance from the upper surface of the plate to the fluid free surface is denoted as H_f. The plate is made of an arbitrary number of linearly elastic laminae. The bonding between plies is perfect except in the region of the crack. Deformations of the plate are assumed small under a harmonic excitation. The Cartesian coordinate system is used. The plate is infinitely long in the x direction. The length and depth of the crack are denoted by a and d, respectively. The left tip of the crack is situated at $x = L$. A transverse line load of $q = q_0 \exp(i\omega t)$ uniformly distributed along the axis y is applied on the upper surface and at $x = 0$. The fluid is assumed to be irrotational, inviscid, acoustic, and unbound in the x direction. It is of interest to find the wave scattering by the crack in the plate. Because the geometry of the plate and load are independent of the y-coordinate, the problem is a two-dimensional plane strain one in nature.

3 Fluid Strip Element

In this analysis, pressure $p(x, z, t)$ in the acoustic fluid is chosen as an unknown. The fluid governing equation in terms of the pressure $p(x, z, t)$ is given by

$$\frac{\partial^2 p}{\partial x^2} + \frac{\partial^2 p}{\partial z^2} - \frac{\partial^2 p}{c^2 \partial t^2} = 0 \tag{1}$$

where c is the speed of sound in the fluid and t is time.

In addition to Eq. (1), boundary conditions on both the fluid surface and the fluid-plate interface are needed for the determination of $p(x, z, t)$. The boundary condition on the free surface of the fluid is $p = 0$.

The boundary condition at the fluid-plate interface follows from the dynamic equilibrium equation of the fluid as well as the displacement continuity condition between the fluid and plate at the interface. The dynamic equilibrium equation of the fluid at the fluid-plate interface is given by

$$\frac{\partial p}{\partial z} + \rho_f \frac{\partial v_f}{\partial t} = 0 \tag{2}$$

where ρ_f is the density of the fluid and v_f is the z-component of the velocities of the fluid. When displacement continuity conditions between the plate and fluid at the interface are considered, the velocity of the fluid v_f may be expressed as

$$v_f = \frac{\partial w}{\partial t} \tag{3}$$

where w is the z-component of the upper surface displacements of the plate. Substitution of Eq. (3) into Eq. (2) gives the boundary condition at the fluid-plate interface

$$\frac{\partial p}{\partial z} = -\rho_f \frac{\partial^2 w}{\partial t^2}. \tag{4}$$

In what follows, formulation of a fluid strip element is derived using a variational method. In this paper, a two-nodal-line strip element shown in Fig. 2 is used to model the fluid field. P_l and P_u are, respectively, unknown pressure amplitudes at the lower and upper nodal-lines, denoted by subscripts l and u, of the fluid strip element. The pressure within the fluid strip element may be expressed in terms of nodal-line unknown pressure amplitudes as follows:

$$p(x, \eta, t) = \mathbf{N}_f(\eta)\mathbf{P}(x) \exp(i\omega t) \tag{5}$$

where $i = \sqrt{-1}$, ω is an angular frequency, $\mathbf{P}(x) = [P_l \quad P_u]^T$ is the vector of nodal-line unknown pressure amplitudes of the fluid strip element, and $\mathbf{N}_f(\eta) = [(1 - \eta) \quad \eta]$ is the shape function matrix of the fluid strip element. Here $\eta = z/h_f$ with h_f being the thickness of the fluid strip element.

It has been proved by Xi et al. (1997a, b) that Eqs. (1) and (4) are equivalent to the following functional:

$$J = \frac{1}{2}\int_0^1 \left[\left(\frac{\partial p}{\partial x}\right)^2 + \left(\frac{\partial p}{h_f \partial \eta}\right)^2 + \frac{2p}{c^2}\frac{\partial^2 p}{\partial t^2}\right] h_f d\eta + \rho_f p \frac{\partial^2 w}{\partial t^2} \tag{6}$$

where w may be expressed as follows:

$$w = \mathbf{NU}. \tag{7}$$

Here $\mathbf{n} = [0 \quad 1]$, $\mathbf{N}$ and $\mathbf{U}$ are, respectively, the shape function matrix and vector of nodal-line unknown displacement amplitudes of a solid strip element on the fluid-laminate interface, which will be introduced in the next section.

Substituting Eqs. (5) and (7) into Eq. (6) and performing variational manipulation with respect to $\mathbf{P}$ yields the following governing equation of the fluid strip element:

$$-\mathbf{A}_{2f}\frac{d^2\mathbf{P}}{dx^2} + \left(\mathbf{A}_{0f} - \frac{\omega^2}{c^2}\mathbf{M}_f\right)\mathbf{P} = \rho_f \omega^2 \mathbf{F}^T \mathbf{U} \tag{8}$$

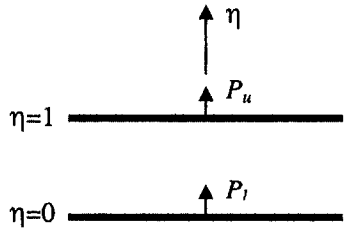


Fig. 2 Strip element for a fluid

Downloaded 04 May 2010 to 171.66.16.27. Redistribution subject to ASME license or copyright; see http://www.asme.org/terms/Terms_Use.cfm

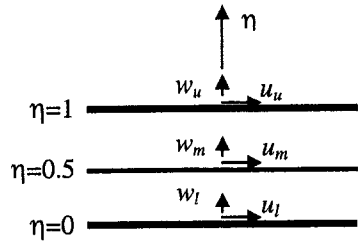


Fig. 3 Strip element for a laminated plate

where $\mathbf{A}_{if}$ ($i = 0, 2$), $\mathbf{M}_f$ and $\mathbf{F}$ are given by Xi et al. (1999). The coupling matrix $\mathbf{F}$ represents the effect of the surface displacements of the laminated plate on the acoustic pressure in the fluid.

4 Solid Strip Element

The strain-displacement relations of the plate are given by

$$\boldsymbol{\epsilon} = \mathbf{L}\mathbf{u} \tag{9}$$

where $\boldsymbol{\epsilon} = [\epsilon_x \quad \epsilon_z \quad \gamma_{xz}]^T$ is the vector of strains, $\mathbf{u} = [u \quad w]^T$ is the vector of displacements, and

$$\mathbf{L} = \begin{bmatrix} 1 & 0 \\ 0 & 0 \\ 0 & 1 \end{bmatrix} \frac{\partial}{\partial x} + \begin{bmatrix} 0 & 0 \\ 0 & 1 \\ 1 & 0 \end{bmatrix} \frac{\partial}{\partial z} = \mathbf{L}_x \frac{\partial}{\partial x} + \mathbf{L}_z \frac{\partial}{\partial z}. \tag{10}$$

The constitutive relations for a lamina are given by

$$\boldsymbol{\sigma} = \bar{\mathbf{Q}}\boldsymbol{\epsilon} \tag{11}$$

where $\boldsymbol{\sigma} = [\sigma_x \quad \sigma_z \quad \tau_{xz}]^T$ is the vector of stresses and

$$\bar{\mathbf{Q}} = \begin{bmatrix} \bar{Q}_{11} & \bar{Q}_{13} & 0 \\ \bar{Q}_{13} & \bar{Q}_{33} & 0 \\ 0 & 0 & \bar{Q}_{55} \end{bmatrix} \tag{12}$$

is the matrix of the off-principal-axis stiffness coefficients of the lamina whose expressions in terms of engineering constants are given in Vinson and Sierakowski (1987).

The formulae of a solid strip element are derived using the Hamilton principle. A three-nodal-line strip element shown in Fig. 3 is used to model the plate. u_l, w_l, u_m, w_m, u_u, and w_u are, respectively, unknown horizontal and vertical displacement amplitudes at the lower, middle, and upper nodal-lines, denoted by l, m, and u, of the solid strip element. The displacements within the solid strip element are related to the unknown displacement amplitudes at the nodal lines as

$$\mathbf{u} = \mathbf{N}(\eta)\mathbf{U}(x)\exp(i\omega t) \tag{13}$$

where $\mathbf{U}(x) = [u_l \quad w_l \quad u_m \quad w_m \quad u_u \quad w_u]^T$ is the vector of the unknown displacement amplitudes at the nodal lines of the solid strip element, and $\mathbf{N}(\eta) = \lfloor (1 - 3\eta + 2\eta^2)\mathbf{I} \quad 4(\eta - \eta^2)\mathbf{I} \quad (-\eta + 2\eta^2)\mathbf{I} \rfloor$ is the shape function matrix of the solid strip element. Here $\mathbf{I}$ is a 2 by 2 identity matrix and $\eta = z/h$ with h being the thickness of the solid strip element.

The Hamilton principle is given by

$$\int_{t_0}^{t_1} \delta(V - T)dt = 0 \tag{14}$$

where the times t_0 and t_1 are arbitrary, V and T are the potential energy and kinetic energy of the solid strip element, respectively. The potential energy of the solid strip element in the absence of body forces is given by

$$V = \tfrac{1}{2}\int_0^1 \boldsymbol{\epsilon}^T\boldsymbol{\sigma}h d\eta - wq - wp. \tag{15}$$

Substituting Eqs. (9), (10), and (11) into Eq. (15) results in

$$V = \frac{1}{2}\int_0^1 \mathbf{u}^T\left(\mathbf{D}_1\frac{\partial^2}{\partial x^2} + 2\mathbf{D}_2\frac{\partial^2}{h\partial\eta\partial x} + \mathbf{D}_3\frac{\partial^2}{h^2\partial\eta^2}\right)\mathbf{u}h d\eta - wq - wp \tag{16}$$

where $\mathbf{D}_i$ ($i = 1, 2, 3$) are given by Xi et al. (1999). The kinetic energy of the solid strip element is given by

$$T = \frac{1}{2}\int_0^1 \frac{\partial\mathbf{u}^T}{\partial t}\frac{\partial\mathbf{u}}{\partial t}\rho h d\eta \tag{17}$$

where ρ is the mass density of the material of the element.

Substituting Eqs. (16) and (17) into Eq. (14), in light of Eqs. (5), (7), and (13), and then taking variation with respect to $\mathbf{U}$ leads to the following governing equation of the solid strip element:

$$-\mathbf{A}_2\frac{d^2\mathbf{U}}{dx^2} + \mathbf{A}_1\frac{d\mathbf{U}}{dx} + (\mathbf{A}_0 - \omega^2\mathbf{M})\mathbf{U} = \mathbf{F}\mathbf{P} + \mathbf{q} \tag{18}$$

where $\mathbf{A}_i$ ($i = 0, 1, 2$), $\mathbf{M}$ and $\mathbf{q}$ are given by Xi et al. (1999). The coupling matrix $\mathbf{F}$ is the same given in Eq. (8), through which the acoustic pressure of the fluid influences the displacements of the laminated plate. As can be seen from Eqs. (8) and (18), the original partial differential equations of both the fluid and plate have been simplified to ordinary differential equation through the strip element idealization. As a result, computational labor can be greatly reduced.

5 Particular Solution for Coupled System

Equations (8) and (18) are two coupled differential equations in a frequency domain. Their particular solution can be sought in a wave number domain by a modal analysis method. To this end, the following Fourier transforms of the pressure and displacement amplitude vectors with respect to the horizontal coordinate x are introduced:

$$\tilde{\mathbf{P}}(k) = \int_{-\infty}^{\infty}\mathbf{P}(x)e^{ikx}dx, \quad \tilde{\mathbf{U}}(k) = \int_{-\infty}^{\infty}\mathbf{U}(x)e^{ikx}dx \tag{19}$$

where k is the wave number. The application of Eq. (19) to Eqs. (8) and (18) leads to the following characteristic equations of the fluid and plate in the wave number domain:

$$\left[k^2\mathbf{A}_{2f} + \mathbf{A}_{0f} - \frac{\omega^2}{c^2}\mathbf{M}_f\right]\tilde{\mathbf{P}} = \rho_f\omega^2\mathbf{F}^T\tilde{\mathbf{U}} \tag{20}$$

$$[k^2\mathbf{A}_2 + ik\mathbf{A}_1 + \mathbf{A}_0 - \omega^2\mathbf{M}]\tilde{\mathbf{U}} = \mathbf{F}\tilde{\mathbf{P}} + \mathbf{q}_0 \tag{21}$$

Note that the matrices and vectors in Eqs. (20) and (21) are for the whole domains of the fluid and laminated plate, which are obtained by assembling all the matrices and vectors for strip elements given by Xi et al. (1999). To achieve high precision, these two equations should be solved simultaneously rather than staggeringly. Therefore, they can be rewritten in a more compact form

$$[\mathbf{A} - k\mathbf{B}]\mathbf{d} = \mathbf{p} \tag{22}$$

where

$$\mathbf{A} = \begin{bmatrix} \mathbf{0} & \mathbf{0} & \mathbf{I} & \mathbf{0} \\ \mathbf{0} & \mathbf{0} & \mathbf{0} & \mathbf{I} \\ \omega^2\mathbf{M} - \mathbf{A}_0 & \mathbf{F} & -i\mathbf{A}_1 & \mathbf{0} \\ \rho_f\omega^2\mathbf{F}^T & \dfrac{\omega^2}{c^2}\mathbf{M}_f - \mathbf{A}_{0f} & \mathbf{0} & \mathbf{0} \end{bmatrix} \tag{23}$$

Downloaded 04 May 2010 to 171.66.16.27. Redistribution subject to ASME license or copyright; see http://www.asme.org/terms/Terms_Use.cfm

$$\mathbf{B} = \begin{bmatrix} \mathbf{I} & 0 & 0 & 0 \\ 0 & \mathbf{I} & 0 & 0 \\ 0 & 0 & \mathbf{A}_2 & 0 \\ 0 & 0 & 0 & \mathbf{A}_{2f} \end{bmatrix} \quad \mathbf{p} = \begin{Bmatrix} \mathbf{0} \\ \mathbf{0} \\ -\mathbf{q}_0 \\ \mathbf{0} \end{Bmatrix} \quad \mathbf{d} = \begin{Bmatrix} \tilde{\mathbf{U}} \\ \tilde{\mathbf{P}} \\ k\tilde{\mathbf{U}} \\ k\tilde{\mathbf{U}} \end{Bmatrix}. \quad (24)$$

Applying the modal analysis technique (Liu et al., 1995) to Eq. (22) gives

$$\mathbf{d} = \sum_{m=1}^{2(M+M_f)} \frac{\varphi_m^L \mathbf{P} \varphi_m^R}{(k - k_m) B_m} \quad (25)$$

where M and M_f are the number of rows of the square matrices A_i and A_{if}, respectively, $B_m = \varphi_m^L \mathbf{B} \varphi_m^R$. Here k_m, φ_m^L, and φ_m^R are, respectively, the eigenvalues and the left and right eigenvectors obtained from the following characteristic equations

$$\mathbf{0} = [\mathbf{A} - k_m \mathbf{B}] \varphi_m^R, \quad \mathbf{0} = \varphi_m^L [\mathbf{A} - k_m \mathbf{B}] \quad (26)$$

If φ_m^L and φ_m^R are rewritten in a partition form

$$\varphi_m^L = [\varphi_{m1}^L \quad \varphi_{m2}^L \quad \varphi_{m3}^L \quad \varphi_{m4}^L],$$
$$\varphi_m^R = [\varphi_{m1}^R \quad \varphi_{m2}^R \quad \varphi_{m3}^R \quad \varphi_{m4}^R]^T \quad (27)$$

where φ_{m1}^L, φ_{m3}^L, φ_{m1}^R, φ_{m3}^R have the dimension of M, and φ_{m2}^L, φ_{m4}^L, φ_{m2}^R, φ_{m4}^R have the dimension of M_f, then Eq. (25) gives

$$\tilde{\mathbf{U}}_p = -\sum_{m=1}^{2(M+M_f)} \frac{\varphi_{m3}^L \mathbf{q}_0 \varphi_{m1}^R}{(k - k_m) B_m}, \quad \tilde{\mathbf{P}}_p = -\sum_{m=1}^{2(M+M_f)} \frac{\varphi_{m3}^L \mathbf{q}_0 \varphi_{m2}^R}{(k - k_m) B_m}. \quad (28)$$

Applying the inverse Fourier transform to Eqs. (28), the displacement and pressure amplitudes in the spatial domain can be expressed by

$$\mathbf{U}_p = -\frac{1}{2\pi} \int_{-\infty}^{\infty} \sum_{m=1}^{2(M+M_f)} \frac{\varphi_{m3}^L \mathbf{q}_0 \varphi_{m1}^R}{(k - k_m) B_m} e^{-ikx} dk,$$

$$\mathbf{P}_p = -\frac{1}{2\pi} \int_{-\infty}^{\infty} \sum_{m=1}^{2(M+M_f)} \frac{\varphi_{m3}^L \mathbf{q}_0 \varphi_{m2}^R}{(k - k_m) B_m} e^{-ikx} dk. \quad (29)$$

Notice that φ_{m3}^L, φ_{m1}^R, φ_{m2}^R, $\mathbf{q}_0$, and B_m are independent of k. The integrals in Eqs. (29) are analytic functions of k, except at $2(M + M_f)$ poles ($k = k_m$). Hence, the integrations in Eqs. (29) can be carried out analytically using the Cauchy's theorem

$$\mathbf{U}_p = \begin{cases} -i \sum_{m=1}^{M+M_f} \frac{\varphi_{m3}^{+L} \mathbf{q}_0 \varphi_{m1}^{+R}}{B_m^+} e^{-ik_m^+ x}, & \text{for } x \geq 0 \\ i \sum_{m=1}^{M+M_f} \frac{\varphi_{m3}^{-L} \mathbf{q}_0 \varphi_{m1}^{-R}}{B_m^-} e^{-ik_m^- x}, & \text{for } x < 0 \end{cases} \quad (30)$$

$$\mathbf{P}_p = \begin{cases} -i \sum_{m=1}^{M+M_f} \frac{\varphi_{m3}^{+L} \mathbf{q}_0 \varphi_{m2}^{+R}}{B_m^+} e^{-ik_m^+ x}, & \text{for } x \geq 0 \\ i \sum_{m=1}^{M+M_f} \frac{\varphi_{m3}^{-L} \mathbf{q}_0 \varphi_{m2}^{-R}}{B_m^-} e^{-ik_m^- x}, & \text{for } x < 0. \end{cases} \quad (31)$$

6 General Solution for Coupled System

A complementary solution to the associated homogeneous equation of Eq. (18) can be obtained in a way similar to Liu and Achenbach (1994, 1995). Then the summation of the particular and complementary solutions yields a general solution for the fluid-loaded composite plate. To use the strip element method, the cracked plate needs to be divided into subdomains. In each subdomain, a set of equations is obtained, which establishes relationships between displacements and stresses on the vertical boundaries of the subdomain. Then sets of equations for all the subdomains are assembled applying displacement and stress continuity conditions at junctions between the subdomains. Finally, the displacements at the junctures can be obtained by solving the resulting set of equations, consequently, the entire displacement field can be obtained. For more detail, the readers are referred to Liu and Achenbach (1995).

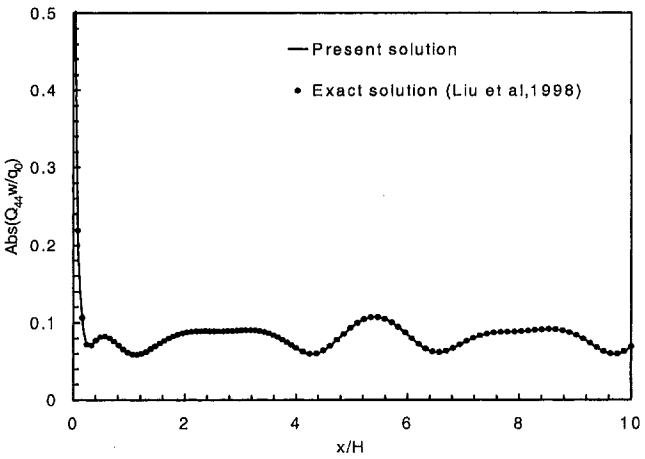


Fig. 4 Distribution of normal displacement on the upper surface of an immersed (C0/G45/G − 45)$_s$ composite laminate ($\bar{\omega} = 3.14$, $\bar{L} = 4$, $\bar{H}_f = 1$)

7 Numerical Results and Discussion

Based on the foregoing formulation, a strip element method program has been developed in FORTRAN 90 and run on an HP workstation. In this section, numerical examples are given for a steel plate, (C90/G0)$_s$, (C0/G90)$_s$, and (C90/G45/G − 45)$_s$ laminates. Numerical results are presented in the form of normal displacements on the upper surface of the plate. In the laminate code, a lamina numbering increases from the bottom to the top surface. Letters C and G represent carbon/epoxy and glass/epoxy, respectively. Numbers following the letters indicate the angle of the fiber orientation with respect to the axis x. The subscript s denotes that the composite laminate is symmetrically stacked. The material properties of the plates are taken from Liu et al. (1995). Here water is used as the coupling fluid. The density of water is $\rho_f = 1.0$ g/cm^3 and the acoustic wave velocity is $c = 1.48 \times 10^3$ m/s. In all calculations, dimensionless parameters used are as follows:

$$\bar{x} = x/H, \quad \bar{\mathbf{Q}} = \mathbf{Q}/Q_{44}, \quad \bar{w} = Q_{44} w/q_0, \quad \bar{u} = Q_{44} u/H$$

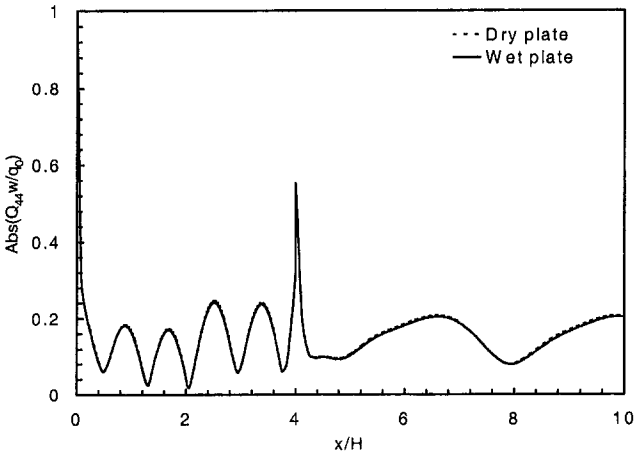
$$\bar{\omega} = \omega H/c_s, \quad \bar{c} = c/c_s, \quad c_s = \sqrt{Q_{44}/\rho}, \quad \bar{p} = p/q_0,$$

$$\bar{H}_f = H_f/H \quad \bar{L} = L/H, \quad \bar{a} = a/H, \quad \bar{\rho} = \rho_f/\rho, \quad \bar{d} = d/H$$

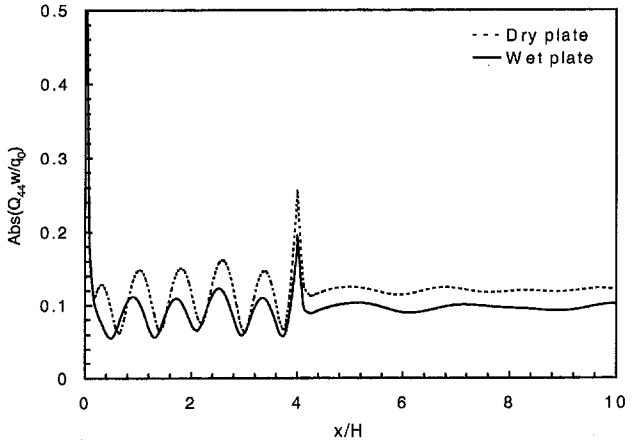
where Q_{44} and ρ are the material constant and mass density of a reference material. The reference material for a steel plate is the steel plate itself, while the reference material for a hybrid composite plate is C0.

To verify the present formulation and numerical implementation, an immersed (C90/G45/G − 45)$_s$ composite laminated plate in the absence of a crack is first calculated. In Fig. 4, computed results provided by the present analysis are compared with an exact solution recently obtained by Liu et al. (1998). Good agreement is found. Besides, this example is also used for convergence study to find the number of elements required for the analyses. For this example, each layer is divided in four elements and thus the entire plate is divided into 24 elements. The number of the fluid strip elements is identical to that of the solid strip elements. It can

Downloaded 04 May 2010 to 171.66.16.27. Redistribution subject to ASME license or copyright; see http://www.asme.org/terms/Terms_Use.cfm



(a)



(b)

Fig. 5 Distribution of normal displacement on the upper surface of plates with vertical surface-breaking cracks; (*a*) steel plate, (*b*) $(C90/G0)_s$ composite plate ($\bar{\omega} = 3.14$, $\bar{L} = 4$, $\bar{H}_f = 1$)

be seen from this figure that the results are converged to a very good degree of accuracy. Hence, in the subsequent calculations, each ply is divided into four elements and the number of elements of a plate is equal to the number of elements of each ply multiplied by the number of plies of the plate. The number of the fluid strip elements is the same as that of the solid strip elements.

Next wave scattering of cracked composite plates submerged in a fluid are studied. Figures 5(*a*) and 5(*b*) show the distribution of the normal displacement on the upper surface of submerged steel and $(C90/G0)_s$ composite plates, respectively. The plates have a vertical upper surface-breaking crack, and the crack length and depth are $\bar{a} = 0.25$ and $\bar{d} = 0$. For the sake of comparison, results for the corresponding dry plates are also plotted in the same figures (dotted lines). It is obvious from Fig. 5(*a*) that the displacement responses of the wet steel plate are almost the same as those of the corresponding dry steel plate. This observation indicates that the presence of the fluid has negligible influence on the response of the steel plate. This conclusion is correspondence with the Cremer principle. However, from Fig. 5(*b*) it is quite interesting to note that the displacement responses of the wet composite laminate are much lower than those of the corresponding dry composite laminate. This shows that the addition of the fluid can reduce significantly the magnitude of the displacement of the plate. As a result, the Cremer principle is not valid for fluid-coupled composite laminates. The reason is given as follows.

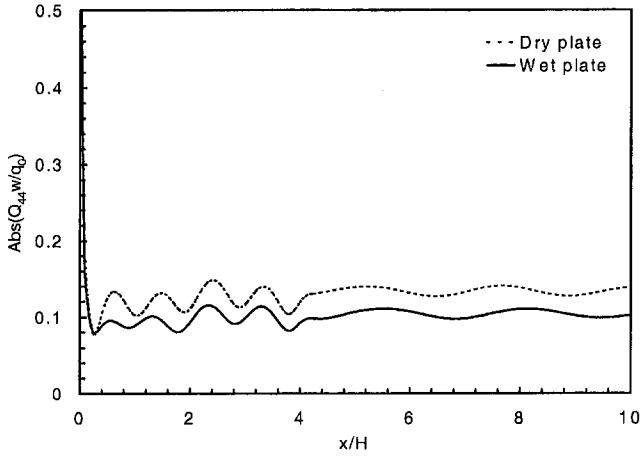


Fig. 6 Distribution of normal displacement on the upper surface of a $(C0/G90)_s$ composite plate with an interior vertical crack ($\bar{\omega} = 3.14$, $\bar{L} = 4$, $\bar{H}_f = 1$)

The effects of the fluid on the oscillating plate can be considered mainly through so-called added mass. The amount of the added mass depends on the flexibility of the plate. As the steel plate is much stiffer compared with the $(C90/G0)_s$ composite plate of the same thickness. The added mass on the $(C90/G0)_s$ plate is therefore larger than that on the steel plate. Moreover, the density of the $(C90/G0)_s$ composite plate is much smaller than that of the steel plate. The same amount of added mass should therefore affect more on the $(C90/G0)_s$ composite plate than on the steel plate. It may be mentioned here that the fluid seems to have little effect on the distribution pattern of the displacement on the plate surface. This finding is very important because crack detecting techniques proposed by Lam et al. (1997) can be developed in a similar way for submerged plates. It is also found in the calculations that as the liquid depth increases, the surface displacement of the plate decreases initially; but when the liquid depth is much larger than the thickness of the plate, the displacement of the plate converges to a certain value.

In order to further confirm the above findings, two more cracked plates immersed in a fluid are calculated. Figure 6 shows the distribution of the normal displacement on the upper surface of an immersed $(C0/G90)_s$ composite plate with an interior vertical crack. The crack length and depth are $\bar{a} = 0.5$ and $\bar{d} = 0.25$. Figure 7 shows the distribution of the normal displacement on the upper surface of a submerged $(C90/G45/G - 45)_s$ composite plate

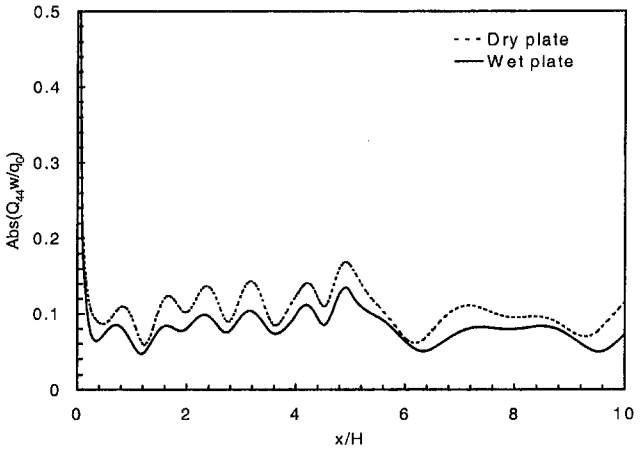


Fig. 7 Distribution of normal displacement on the upper surface of a $(C0/G45/G - 45)_s$ composite plate with a horizontal crack ($\bar{\omega} = 3.14$, $\bar{L} = 4$, $\bar{H}_f = 1$)

Downloaded 04 May 2010 to 171.66.16.27. Redistribution subject to ASME license or copyright; see http://www.asme.org/terms/Terms_Use.cfm

with a horizontal crack. The crack length and depth are $\bar{a} = 1.0$ and $\bar{d} = 0.33$. These two figures demonstrate again that the presence of the fluid has substantial impact on the displacement of the composite plate.

8 Conclusions

A strip element method has been presented for analyzing wave scattering by a crack in an immersed composite plate. The numerical results indicate that the addition of the fluid has much less influence on the wave field in steel plates, but it can reduce significantly the magnitude of the displacement response of the composite plates which are flexible and have lower mass density.

The use of strip element method not only reduces the spatial dimensions of the original problem by one, but also makes it easier to deal with composite plates made of an arbitrary number of anisotropic layers, of arbitrary lay-ups and of any types of materials. The crack in the plate can be either vertical or horizontal. The number of the elements used for the strip element method is very small compared with the conventional finite element method. Moreover, the strip elements can deal with problems with infinite domains very accurately.

References

Atalar, A., 1983, "Reflection of Ultrasonic Waves at a Liquid-Cubic-Solid Interface," *J. Acoust. Soc. Am.,* Vol. 73, No. 2, pp. 435–440.

Arikan, O., Teletar, E., and Atalar, A., 1989, "Reflection Coefficient Null of Acoustic Waves at a Liquid-Anisotropic-Solid Interface," *J. Acoust. Soc. Am.,* Vol. 85, No. 1, pp. 1–10.

Braga, A. M. B., and Herrmann, G., 1989, "Wave Propagation in Submerged Layered Composites," *Elastic Wave Propagation,* M. F. McCarthy and M. A. Hayes, eds., Elsevier, North-Holland, Amsterdam, pp. 301–306.

Chimenti, D. E., and Nayfeh, A. H., 1990, "Ultrasonic Reflection and Guided Wave Propagation in Biaxially Laminated Composite Plates," *J. Acoust. Soc. Am.,* Vol. 87, No. 4, pp. 1409–1415.

Datta, S. K., Ju, T. H., and Shah, A. H., 1992, "Scattering of an Impact Wave by a Crack in a Composite Plate," ASME JOURNAL OF APPLIED MECHANICS, Vol. 59, pp. 596–603.

Datta, S. K., Ledbetter, H. M., Shindo, Y., and Shah, A. H., 1988a, "Phase Velocity and Attenuation of Plane Elastic Waves in a Particle-Reinforced Composite Medium," *Wave Motion,* Vol. 10, No. 2, pp. 171–182.

Datta, S. K., Shah, A. H., Bratton, R. L., and Chakraborty, T., 1988b, "Wave Propagation in Laminated Composite Plates," *Journal of the Acoustical Society of America,* Vol. 83, No. 6, pp. 2020–2026.

Dayal, V., and Kinra, V. K., 1989, "Leaky Lamb Waves in an Anisotropic Plate: An Exact Solution and Experiments," *J. Acoust. Soc. Am.,* Vol. 85, No. 6, pp. 2268–2276.

Gracewski, S. M., and Bogy, D. B., 1986, "Elastic Wave Scattering From an Interface Crack in a Layered Half Space Submerged in Water, Part 1: Applied Tractions at the Liquid-Solid Interface; Part 2: Incident Plane Waves and Bounded Beams," ASME JOURNAL OF APPLIED MECHANICS, Vol. 53, pp. 326–338.

Karim, M. R., Kundu, T., and Desai, C. S., 1989, "Detection of Delamination Cracks in Layered Fiber-Reinforced Composite Plates," ASME *Journal of Pressure Vessel Technology,* Vol. 111, pp. 165–171.

Kundu, T., and Boström, A., 1991, "Axisymmetric Scattering of a Plane Longitudinal Wave by a Circular Crack in a Transversely Isotropic Solid," ASME JOURNAL OF APPLIED MECHANICS, Vol. 58, pp. 695–702.

Lam, K. Y., Liu, G. R., and Wang, Y. Y., 1997, "Time-Harmonic Response of a Vertical Crack in Plates," *Theoretical and Applied Fracture Mechanics,* Vol. 27, pp. 21–28.

Liu, G. R., and Achenbach, J. D., 1994, "A Strip Element Method for Stress Analysis of Anisotropic Linearly Elastic Solids," ASME JOURNAL OF APPLIED MECHANICS, Vol. 61, pp. 270–277.

Liu, G. R., and Achenbach, J. D., 1995, "Strip Element Method to Analyze Wave Scattering by Cracks in Anisotropic Laminated Plates," ASME JOURNAL OF APPLIED MECHANICS, Vol. 62, pp. 607–613.

Liu, G. R., Lam, K. Y., and Chan, E. S., 1996, "Stress Waves in Composite Laminates Excited by Transverse Plane Shock Waves," *Shock and Vibration,* Vol. 3, No. 6, pp. 419–433.

Liu, G. R., Wang, X. J., and Xi, Z. C., 1998, "An Exact Solution for a Wave Propagation in Composite Plate Submerged in a Fluid," *Int. J. Mech. Sci.,* submitted for publication.

Mal, A. K., 1988, "Wave Propagation in Layered Composite Laminates Under Periodic Surface Loads," *Wave Motion,* Vol. 10, pp. 257–266.

Mal, A. K., Xu, P. C., and Bar-Cohen, Y., 1989, "Analysis of Leaky Lamb Waves in Bounded Plates," *Int. J. Eng. Sci.,* Vol. 27, pp. 779–791.

Nayfeh, A. H., 1991, "Elastic Wave Reflection From Liquid-Anisotropic Substrate Interfaces," *Wave Motion,* Vol. 14, No. 1, pp. 55–67.

Nayfeh, A. H., 1995, *Wave Propagation in Layered Anisotropic Media with Applications to Composites,* North-Holland, Amsterdam.

Nayfeh, A. H., and Chimenti, D. E., 1988a, "Propagation of Guided Waves in Fluid-Coupled Plates of Fiber-Reinforced Composite," *J. Acoust. Soc. Am.,* Vol. 83, No. 5, pp. 1736–1743.

Nayfeh, A. H., and Chimenti, D. E., 1988b, "Ultrasonic Wave Reflection From Liquid Coupled Orthotropic Plates With Application to Fibrous Composites," ASME JOURNAL OF APPLIED MECHANICS, Vol. 55, pp. 863–870.

Nayfeh, A. H., and Taylor, T. W., 1988, "Surface Wave Characteristics of Fluid-Loaded Multilayered Media," *J. Acoust. Soc. Am.,* Vol. 84, pp. 2187–2191.

Vinson, J. R., and Sierakowski, R. L., 1987, "The Behavior of Structures Composed of Composite Materials," Martinus Nijhoff Publishers, Dordrecht, The Netherlands.

Xi, Z. C., Liu, G. R., Lam, K. Y., and Shang, H. M., 1999, "Detection of a Crack in a Fluid-Loaded Composite Laminate," *Proceedings of the Asia-Pacific Vibration Conference '99,* Dec. 13–15, 1999, Singapore.

Xi, Z. C., Yam, L. H., and Leung, T. P., 1997a, "Free Vibration of a Partially Fluid-Filled Cross-Ply Laminated Composite Circular Cylindrical Shell," *J. Acoust. Soc. Am.,* Vol. 101, No. 3, pp. 909–917.

Xi, Z. C., Yam, L. H., and Leung, T. P., 1997b, "Free Vibration of a Laminated Composite Circular Cylindrical Shell Partially Filled With Fluid," *Composites,* Vol. 28B, pp. 359–375.

Downloaded 04 May 2010 to 171.66.16.27. Redistribution subject to ASME license or copyright; see http://www.asme.org/terms/Terms_Use.cfm

Analysis of Thin-Walled Closed Beams With General Quadrilateral Cross Sections

J. H. Kim
Research Associate,
Institute of Advanced Machinery and Design

Y. Y. Kim
Associate Professor

School of Mechanical and
Aerospace Engineering,
Seoul National University,
Kwanak-Gu, Shinlim-Dong, San 56-1,
Seoul 151-742, Korea

This paper deals with the one-dimensional static and dynamic analysis of thin-walled closed beams with general quadrilateral cross sections. The coupled deformations of distortion as well as torsion and warping are investigated in this work. A new approach to determine the functions describing section deformations is proposed. In particular, the present distortion function satisfies all the necessary continuity conditions unlike Vlasov's distortion function. Based on these section deformation functions, a one-dimensional theory dealing with the coupled deformations is presented. The actual numerical work is carried out using two-node C^0 finite element formulation. The present one-dimensional results for some static and free-vibration problems are compared with the existing and the plate finite element results.

Introduction

Thin-walled closed beams are preferred over thin-walled open beams particularly when high torsional rigidities are required. However, it is difficult to predict their behavior accurately with simplified theories. The purpose of this paper is to analyze the static and dynamic coupled deformation of torsion, warping, and distortion of thin-walled closed beams with general quadrilateral cross sections using a one-dimensional beam theory. In particular, a function describing distortional deformation of the beam cross section is newly proposed to develop a one-dimensional theory. For the numerical analysis based on the one-dimensional beam theory, a two-node C^0 finite element formulation is performed.

Vlasov (1961) offered a most comprehensive theoretical analysis of thin-walled structures. Thereafter many papers have been published on thin-walled closed beams, and an excellent review on this subject is given in Maisel (1982). Křístek (1970) solves the problem of nonuniform torsion in tapered box beams and considers the effect force deforming the cross section. Cheung (1969) uses the finite strip method for folded plates and employs Fourier series for the expansion in the longitudinal direction. Jirousek et al. (1979) propose a macro-element, which consists of a modified Ahmad thick shell element and an assembly element.

Bažant and Nimeiri (1974) develop a skew-ended finite element for curved box beams, using a mapping process of a rectangular element with a square cross section. Considering distortion and warping, Boswell and Zhang (1983) present finite beam element formulation for the static analysis and later report some related experimental results (1985). Zhang and Lyons (1984a, 1984b) develop a multi-cell box beam finite element for the analysis of curved bridges, and Boswell and Li (1995) discuss warping functions due to torsion and distortion. Razzaqpur and Li (1991a, 1991b) consider warping and distortion deformations in the study of multi-cell box beams. They also extend their theory to the curved thin-walled box beams (1994). Mikkola and Paavola (1980) suggest a finite element method for elastic box beams. Paavola (1992) presents a discrete finite element method in which the cross sections are assumed to consist of piecewise rectilinear cross sections of separate shells. However, the focus of these papers is not on the accurate determination of the distortional shape function of thin-walled beams with general cross sections. The accurate distortional shape function, like other sectional deformation shape functions, is very important in obtaining accurate results particularly for vibration problems.

As far as the distortion shape function is concerned, Vlasov (1961) discusses the distortional shape for a rectangular box beam. Bažant and Nimeiri (1974) map the distortion shape of the rectangular box beam into that of the trapezoidal box beam. Boswell and Zhang (1984) deal with the distortion function of the box beams with one symmetry axis. Maisel (1982) also discusses distortional shapes for polygonal sectioned box beams on the assumption that the cross section can be viewed as a hinged system. However, it seems that these approaches are difficult to extend directly to beams with arbitrary cross sections including general quadrilateral cross sections. The consideration of the distortional deformation is generally more significant in dynamic analysis. For instance, the significance of sectional deformations, such as distortion, is addressed in the vibration analysis of a box-beam T-joint (Kim et al., 1995). Although several papers (Gere, 1954; Bishop et al., 1983; Friberg, 1985; Zhang and Chen, 1990; Kou et al., 1992; Kim et al., 1994a, b; Laudiero and Savoia, 1991) consider dynamic problems, these papers do not take into account both warping and distortion.

In the present paper we present a new method to determine warping and distortion functions for general quadrilateral cross-sectioned thin-walled beams. First we apply the virtual work concept to impose the orthogonality conditions of warping and distortional functions with respect to some sectional rigid-body motions, which physically correspond to extension, torsion, bending, and flexure. Although these conditions suffice for the determination of an approximate warping function, additional rotation/moment continuity conditions at the corners of the contour of the quadrilateral cross section need to be taken into account in the case of distortion functions. In finding a distortion function for rectangular cross sections, Vlasov (1961) sacrifices the displacement continuity at the corner in order to satisfy more important rotation/moment continuity conditions; the importance of the displacement continuity in rectangular cross-sectioned beam has been addressed in Kim and Kim (1999). This paper presents distortion functions that not only satisfy all the necessary continuity conditions, but also are valid for general quadrilateral cross sections.

After the warping and distortion functions are found, the variational principle is used to obtain a one-dimensional beam theory for the analysis of coupled deformation of torsion, warping, and

Contributed by the Applied Mechanics Division of THE AMERICAN SOCIETY OF MECHANICAL ENGINEERS for publication in the ASME JOURNAL OF APPLIED MECHANICS.
Discussion on the paper should be addressed to the Technical Editor, Professor Lewis T. Wheeler, Department of Mechanical Engineering, University of Houston, Houston, TX 77204-4792, and will be accepted until four months after final publication of the paper itself in the ASME JOURNAL OF APPLIED MECHANICS.
Manuscript received by the ASME Applied Mechanics Division, June 16, 1998; final revision, Jan. 6, 1999. Associate Technical Editor: J. N. Reddy.

 Copyright © 1999 by ASME

Downloaded 04 May 2010 to 171.66.16.27. Redistribution subject to ASME license or copyright; see http://www.asme.org/terms/Terms_Use.cfm

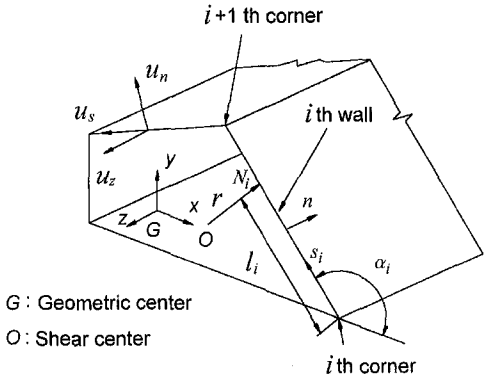


Fig. 1 Displacements at an arbitrary point on the contour of a thin-walled beam with a quadrilateral cross section

distortion. Although some closed-form solutions are possible in some special cases, we carry out numerical analysis by developing two-node C^0 finite elements. For the present finite element, only the measures of torsion, warping, and distortion are considered as the field variables. No particular effort is made in estimating the effects of the use of high-order, field-consistent, or mixed finite elements. Several numeral results by the present analysis are compared with the existing as well as the plate finite element results.

Basic Field Equation and Assumption

Figure 1 shows the contour of a thin-walled beam with a general quadrilateral cross section. The uniform contour thickness t is assumed to be much smaller than the beam length L. The contour is also assumed to be in-extensional. A right-handed curvilinear coordinate system (n, s, z) is introduced in addition to the Cartesian coordinate system (x, y, z). The tangential coordinate s is measured along the contour, and different origins are used for each wall as indicated in Fig. 1. The normal coordinate n directs outwards from the contour in the figure. The line ON_i is normal to the ith contour, where O is the shear center of the cross section and N_i is a generic point on the ith contour. The ith contour connects the ith and $(i + 1)$th corners.

It is convenient to describe the displacement of a point on the contour in terms of the normal $u_n(s, z)$, tangential $u_s(s, z)$, and axial $u_z(s, z)$ components as indicated in Fig. 1. If the beam deformation measures at given z are represented by the amounts of axial rotation $\theta(z)$, warping $U(z)$, and distortion $\chi(z)$, the shell displacements may be written as

$$u_s(s, z) = \psi_s^\theta(s)\theta(z) + \psi_s^U(s)U(z) + \psi_s^\chi(s)\chi(z) \quad (1a)$$

$$u_n(s, z) = \psi_n^\theta(s)\theta(z) + \psi_n^U(s)U(z) + \psi_n^\chi(s)\chi(z) \quad (1b)$$

$$u_z(s, z) = \psi_z^\theta(s)\theta(z) + \psi_z^U(s)U(z) + \psi_z^\chi(s)\chi(z) \quad (1c)$$

where $\psi(s)$ denote the preassigned functions of s describing the contour deformations in the n-s plane per unit value of U, θ, and χ. A major issue in the thin-walled beam analysis is how to find the correct form of $\psi(s)$, particularly the form of $\psi^\chi(s)$.

By considering the rotation $\theta(z)$ of the beam cross section about the positive z-axis, one can identify $\psi^\theta(s)$ as

$$\psi_s^\theta(s) = r(s)$$

$$\psi_n^\theta(s) = -l_i + s$$

$$\psi_z^\theta(s) = 0 \quad (2)$$

where $r(s)$ is the distance normal to the contour from the shear center O, and l_i denotes the distance from the origin of the s coordinate on the ith wall to the point N_i.

When the warping deformation $U(z)$ is considered, only the axial displacement $u_z(s, z)$ is significant so that one may assume that

$$\psi_s^U(s) = 0, \quad \psi_n^U(s) = 0, \quad \psi_z^U(s) \neq 0 \quad (3)$$

where $\psi_z^U(s)$ will be determined in the next section.

For the consideration of the in-plane distortional (or lozenging) deformation $\chi(z)$, the axial displacement can be assumed to be zero.

$$\psi_s^\chi(s) \neq 0, \quad \psi_n^\chi(s) \neq 0, \quad \psi_z^\chi(s) = 0 \quad (4)$$

The specific functional form of $\psi_s^\chi(s)$ and $\psi_n^\chi(s)$ will be investigated in the next section. As pointed out in the Introduction, one of the major contributions of this work is to determine the correct form of these functions, which is valid for general quadrilateral cross sections.

Once the shell displacements are found, three-dimensional displacements $\tilde{u}_n$, $\tilde{u}_s$, and $\tilde{u}_z$ can be found on the assumption that the beam wall thickness is much smaller than the beam length.

$$\tilde{u}_n(n, s, z) \approx u_n(s, z) = \psi_n^\theta(s)\theta(z) + \psi_n^\chi(s)\chi(z) \quad (5a)$$

$$\tilde{u}_s(n, s, z) \approx u_s(s, z) + n\frac{\partial u_n(s, z)}{\partial s}$$

$$\approx \psi_s^\theta(s)\theta(z) + \psi_s^\chi(s)\chi(z) + n\frac{d\psi_n^\chi(s)}{ds}\chi(z) \quad (5b)$$

$$\tilde{u}_z(n, s, z) \approx u_z(s, z) = \psi_z^U(s)U(z) \quad (5c)$$

Equations (5) are then used to find the following three-dimensional strain components:

$$\epsilon_{zz} = \frac{\partial \tilde{u}_z}{\partial z} = \psi_z^U(s)\frac{dU(z)}{dz} \quad (6a)$$

$$\epsilon_{zs} = \frac{1}{2}\left(\frac{\partial \tilde{u}_z}{\partial s} + \frac{\partial \tilde{u}_s}{\partial z}\right)$$

$$\approx \frac{1}{2}\left(\frac{d\psi_z^U(s)}{ds}U(z) + \psi_s^\theta(s)\frac{d\theta(z)}{dz} + \psi_s^\chi(s)\frac{d\chi(z)}{dz}\right) \quad (6b)$$

$$\epsilon_{ss} = \frac{\partial \tilde{u}_s}{\partial s} = n\frac{\partial^2 u_n}{\partial s^2} = n\frac{d^2\psi_n^\chi}{ds^2}\chi(z). \quad (6c)$$

Other strain components are negligible in comparison with these components.

Once the strain components are defined, the corresponding stresses can be easily found from the following constitutive relation:

$$\sigma_{zz} = E_1(\epsilon_{zz} + \nu\epsilon_{ss})$$

$$\sigma_{ss} = E_1(\epsilon_{ss} + \nu\epsilon_{zz})$$

$$\sigma_{sz} = 2G\epsilon_{sz} \quad (7)$$

with

$$E_1 \equiv \frac{E}{1 - \nu^2}$$

where E, G are Young's and shear moduli, respectively, and ν is Poisson's ratio. If needed, the shear stress components σ_{xz} and σ_{yz} can be computed from

$$\sigma_{xz} = \sigma_{sz}\cos\alpha_i$$

$$\sigma_{yz} = \sigma_{sz}\sin\alpha_i \quad (8)$$

where α_i is the angle between the horizontal axis (x-axis) and the tangential direction of each wall, as shown in Fig. 1. For more

Downloaded 04 May 2010 to 171.66.16.27. Redistribution subject to ASME license or copyright; see http://www.asme.org/terms/Terms_Use.cfm

detailed accounts of the basic field equations and assumptions see Vlasov (1961).

Warping and Distortion Functions

In this section, the procedure to determine the approximate form of the warping (ψ_z^U) and distortion (ψ_s^χ, ψ_n^χ) functions will be presented. As the underlying concept to find approximate warping and distortion functions, we propose to impose the condition such that the virtual work done by the warping and distortion stress vanishes under certain rigid-body virtual displacement fields. We denote the rigid-body virtual translations and rotations in the directions of x, y, and z by (δU_x, δU_y, δU_z) and ($\delta\Theta_x$, $\delta\Theta_y$, $\delta\Theta_z$), respectively.

1 Warping Function. The warping function is much easier to find in comparison with the distortion function. However, the understanding of this procedure is very important for the determination of the distortion function, which will be discussed shortly.

From Eqs. (6), (7), the nonzero stress components by warping, which will be superscribed by U, are given by

$$\sigma_{zz}^U(z) = E_1\psi_z^U(s)\frac{dU(z)}{dz}, \quad \sigma_{sz}^U = G\frac{d\psi_z^U}{ds}U(z). \tag{9}$$

It is noted that the warping deformations generally result from flexural and torsional deformations. This means that the following virtual work due to δU_x, δU_y, and $\delta\Theta_z$ does not generally vanish, so that no condition to determine the function ψ_z^U can be obtained from this consideration.

$$\delta W_{\text{warping}} = \int_A [r(s)\sigma_{sz}^U\delta\Theta_z + \sigma_{xz}^U\delta U_x + \sigma_{yz}^U\delta U_y]dA \tag{10}$$

However, a condition to determine the warping function can be found from the fact that no virtual work should be done by the warping stress due to the rigid-body motions associated with axial extensional and bending motions. This statement can be expressed as

$$0 = \delta W_{\text{warping}} = \int_A \sigma_{zz}^U[\delta U_z - y(s)\delta\Theta_x + x(s)\delta\Theta_y]dA \tag{11}$$

Since Eq. (11) holds for arbitrary virtual displacements δU_z, $\delta\Theta_x$, and $\delta\Theta_y$, the following conditions must be satisfied:

$$\int_A \psi_z^U dA = 0 \tag{12a}$$

$$\int_A \psi_z^U \cdot y(s)dA = 0 \tag{12b}$$

$$\int_A \psi_z^U \cdot x(s)dA = 0. \tag{12c}$$

To find a warping function satisfying Eqs. (12), one may assume further that the warping function $\psi_z^U(s)$ is a piecewise linear function of s. Thus the warping function $\psi_z^U(s)$ can be written in a finite series consisting of the so-called hat function $\psi_{zi}^U(s)$.

$$\psi_z^U(s) = \sum_{i=1}^{4} C_i\psi_{zi}^U(s) \tag{13}$$

The linearly varying hat function $\psi_{zi}^U(s)$ has a unit value at the ith corner and vanishes at all other corners. Applying the three conditions stated by Eqs. (12), the functional form of $\psi_z^U(s)$ can be determined where any one of constants C_i can be set equal to 1. The three-dimensional warping functions are shown in Fig. 2 for some beam cross sections.

The usual approach (see Gjelsvik, 1981) to find the warping function for thin-walled closed beams would yield

$$\psi_z^U(s) = \int_0^s (r - r_n)dA. \tag{14}$$

In Eq. (14), $r_n = 2A_1/\oint ds$ where A_1 and $\oint ds$ are the area enclosed by and the total length of the contour, respectively. The expression given by Eq. (14) agrees with the present result, but yields a trivial warping function in the case of a square cross section while the present analysis gives a nontrivial result even for a square cross section.

2 Distortion Functions. Now we will discuss the method to determine the distortion functions $\psi_s^\chi(s)$ and $\psi_n^\chi(s)$ analytically. To the authors' knowledge, the present method is developed here for the first time. The validity of the present distortion function will be verified in the subsequent section.

In investigating the deformation due to distortion, the underlying assumption is that each wall of the contour is in-extensional.

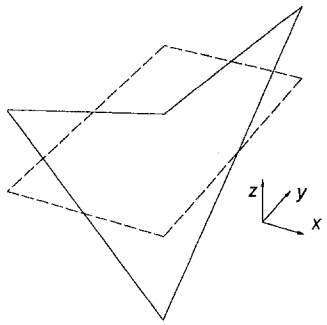


Fig. 2(*a*)

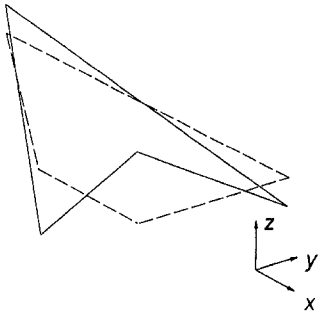


Fig. 2(*b*)

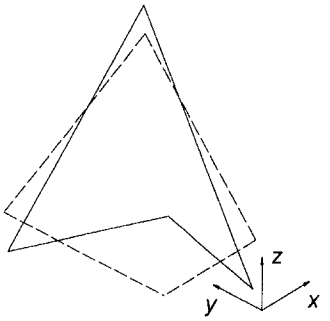


Fig. 2(*c*)

Fig. 2 Warping functions for (*a*) rectangular, (*b*) trapezoidal, and (*c*) general cross sections. (Solid lines: deformed, dotted lines: undeformed.)

Downloaded 04 May 2010 to 171.66.16.27. Redistribution subject to ASME license or copyright; see http://www.asme.org/terms/Terms_Use.cfm

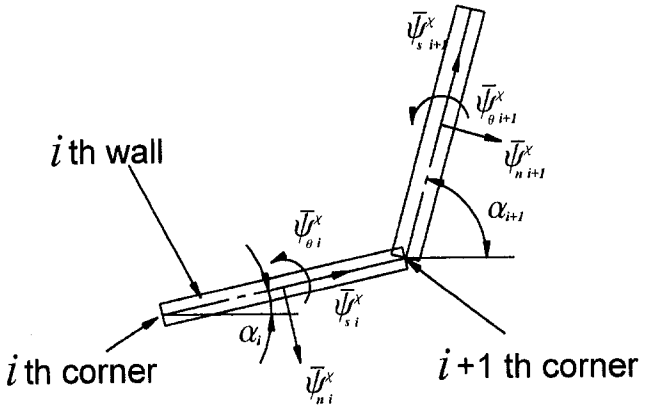


Fig. 3 Variables used to define the in-plane rigid-body deformation of the ith wall, which are associated with the contour distortion

Therefore, we first assume that each wall deforms just like a rigid body in the plane of the cross section. The amount of this deformation may be best described by the amount of rigid-body tangential ($\bar{\psi}^{\chi}_{si}$) and normal ($\bar{\psi}^{\chi}_{ni}$) translations and a rigid-body rotation ($\bar{\psi}^{\chi}_{\theta i}$) of the ith wall ($i = 1, 2, 3, 4$), measured at the center of each wall. (See Fig. 3.) In terms of these quantities, the tangential ($\psi^{\chi}_{si}(s_i)$) and normal ($\psi^{\chi}_{ni}(s_i)$) displacements in the ith wall may be expressed as

$$\psi^{\chi}_{si}(s_i) = \bar{\psi}^{\chi}_{si} \tag{15a}$$

$$\psi^{\chi}_{ni}(s_i) = \bar{\psi}^{\chi}_{ni} - (s_i - b_i/2)\bar{\psi}^{\chi}_{\theta i} \quad (0 \le s_i \le b_i,\ i = 1, 2, 3, 4) \tag{15b}$$

where b_i denotes the length of the ith wall.

The displacement continuity conditions at the corners may be expressed as

$$\psi^{\chi}_{si}|_{s_i=b_i} = \psi^{\chi}_{si+1}|_{s_{i+1}=0} \cos(\alpha_{i+1} - \alpha_i) - \psi^{\chi}_{ni+1}|_{s_{i+1}=0} \sin(\alpha_{i+1} - \alpha_i) \tag{16a}$$

$$\psi^{\chi}_{ni}|_{s_i=b_i} = \psi^{\chi}_{si+1}|_{s_{i+1}=0} \sin(\alpha_{i+1} - \alpha_i) + \psi^{\chi}_{ni+1}|_{s_{i+1}=0} \cos(\alpha_{i+1} - \alpha_i) \quad (\text{for } i = 1, 2, 3, 4;\ 5 \rightarrow 1). \tag{16b}$$

In addition to the continuity conditions expressed by Eqs. (16), the distortion displacement field must satisfy the condition similar to Eq. (11). In this case, we impose the condition that the virtual work by the distortion stress $\sigma^{\chi}_{sz}(s)$ due to the rigid-body virtual displacements δU_x, δU_y, and $\delta\Theta_z$ corresponding to flexural and torsional deformations must vanish:

$$0 = \delta W_{\text{distortion}} = \int_A [r(s)\sigma^{\chi}_{sz}\delta\Theta_z + \sigma^{\chi}_{zx}\delta U_x + \sigma^{\chi}_{zy}\delta U_y]dA. \tag{17}$$

Since $\delta\Theta_z$, δU_x, and δU_y are arbitrary, the condition stated by Eq. (17) is equivalent to the following three independent conditions:

$$\sum_{i=1}^{4} \int r(s_i)(\sigma^{\chi}_{sz})_i dA = 0 \tag{18a}$$

$$\sum_{i=1}^{4} \int (\sigma^{\chi}_{sz})_i \cos\alpha_i dA = 0 \tag{18b}$$

$$\sum_{i=1}^{4} \int (\sigma^{\chi}_{sz})_i \sin\alpha_i dA = 0 \tag{18c}$$

where subscribed quantities are associated with the ith wall. Equations (16) and (18) give 11 conditions to determine 12 unknown variables, $\bar{\psi}^{\chi}_{si}$, $\bar{\psi}^{\chi}_{ni}$, and $\bar{\psi}^{\chi}_{\theta i}$ ($i = 1, 2, 3, 4$). (Note that any one of 12 unknowns can be set arbitrary.)

It should be noted that Eqs. (15) alone represent a displacement field with rotation discontinuity at the corners; corners behave as hinges with this displacement field. Vlasov (1961) suggests a modification of the distortion function form in order to satisfy the rotation continuity. Though Vlasov's modification is useful for stress analysis, Vlasov's modified distortion function for rectangular cross sections now violates the displacement continuity at the corners. Subsequently, his approach does not seem to be proper for dynamic problems and is difficult to extend for general quadrilateral cross sections.

In what follows we propose a new method which guarantees the rotation/moment as well as the displacement continuities at the corners. In order to meet the rotation/moment continuity, the normal displacement $\psi^{\chi}_{ni}(s_i)$ is replaced by a cubic function

$$\psi^{\chi}_{ni}(s_i) = D_{i0} + D_{i1}s_i + D_{i2}s_i^2 + D_{i3}s_i^3 \tag{19}$$

while the tangential displacement $\psi^{\chi}_{si}(s_i)$ given by Eq. (15a) remains unchanged. For subsequent analysis, it is convenient to introduce new quantities $\beta_{i(i)}$ and $\beta_{i(i+1)}$, which are defined as the rotations of the ith wall at the ith and $(i + 1)$th corners.

The constants D_{i0} through D_{i3} in Eq. (19) must be selected to satisfy the following conditions:

$$\psi^{\chi}_{ni}|_{s_i=0} = \bar{\psi}^{\chi}_{ni} + \bar{\psi}^{\chi}_{\theta i}\frac{b_i}{2} \tag{20a}$$

$$\psi^{\chi}_{ni}|_{s_i=b_i} = \bar{\psi}^{\chi}_{ni} - \bar{\psi}^{\chi}_{\theta i}\frac{b_i}{2} \tag{20b}$$

$$\frac{d}{ds_i}[\psi^{\chi}_{ni}(s_i)]_{s_i=0} = \beta_{i(i)} \tag{20c}$$

$$\frac{d}{ds_i}[\psi^{\chi}_{ni}(s_i)]_{s_i=b_i} = \beta_{i(i+1)}. \tag{20d}$$

Then Eq. (19) can be written as

$$\psi^{\chi}_{ni}(s_i) = \left[-\frac{2}{b_i^2}(-\beta_{i(i)} - \bar{\psi}^{\chi}_{\theta i}) + \frac{\beta_{i(i+1)} - \beta_{i(i)}}{b_i^2}\right]s_i^3 + \left[\frac{3}{b_i}(-\beta_{i(i)} - \bar{\psi}^{\chi}_{\theta i}) - \frac{\beta_{i(i+1)} - \beta_{i(i)}}{b_i}\right]s_i^2 + \beta_{i(i)}s_i + \bar{\psi}^{\chi}_{\theta i}\frac{b_i}{2} + \bar{\psi}^{\chi}_{ni}. \tag{21}$$

The deformed contour shape determined by Eq. (21) is plotted in Fig. 4.

It should be noted that Eqs. (20a, b) are exactly the same conditions used to determine $\psi^{\chi}_{ni}(s_i)$ in Eq. (15b). Since four constants $\bar{\psi}^{\chi}_{ni}$ have already been selected to satisfy the conditions expressed by Eqs. (16) and (18), the normal displacement expressed by Eq. (21) automatically satisfies these conditions. Therefore, only the additional conditions to determine $\beta_{i(i)}$ and $\beta_{i(i+1)}$ are needed.

The equations to determine eight coefficients $\beta_{i(i)}$ and $\beta_{i(i+1)}$ are provided by the rotation and moment continuity at the corners:

$$\beta_{i(i+1)} = \beta_{i+1(i+1)} \tag{22a}$$

$$\bar{M}_{i(i+1)} = \bar{M}_{i+1(i+1)} \quad (i = 1, 2, 3, 4;\ 5 \rightarrow 1). \tag{22b}$$

Downloaded 04 May 2010 to 171.66.16.27. Redistribution subject to ASME license or copyright; see http://www.asme.org/terms/Terms_Use.cfm

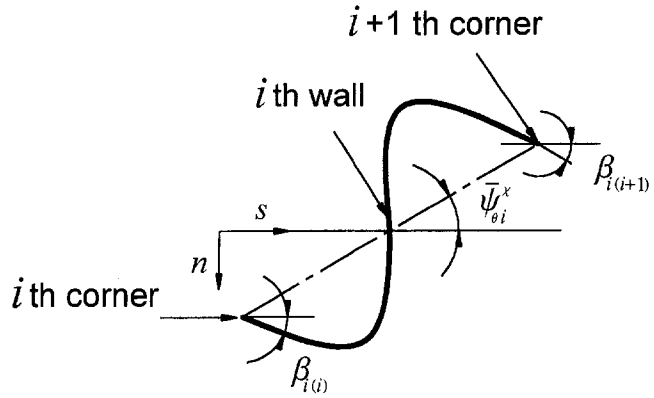


Fig. 4 A typical deformed shape of the *i*th wall of a thin-walled beam. (The displacement and rotation/moment continuities at the corner can be achieved with this distortion shape function.)

The moments $\bar{M}_{i(i)}$ and $\bar{M}_{i(i+1)}$ of the ith wall at the ith and $(i+1)$th corners are given by

$$\bar{M}_{i(i)} = M_i(s_i = 0), \quad \bar{M}_{i(i+1)} = M_i(s_i = b_i).$$

The moment $M_i(s_i)$ can be approximated by a classical beam theory:

$$M_i(s_i) = \frac{Et^3}{12} \frac{d^2\psi^{\chi}_{ni}(s_i)}{ds_i^2}$$

The corresponding bending strain through the wall thickness is given by Eq. (6*c*) where the dependence on the normal coordinate n is explicitly stated.

It is important to note again that the use of $\psi^{\chi}_{ni}(s_i)$ in Eq. (21) instead of $\psi^{\chi}_{ni}(s_i)$ in Eq. (15*b*) does not alter the displacement conditions at the corners stated by Eqs. (16) and (18). Vlasov's distortional function, valid only up to rectangular cross sections, satisfies Eqs. (22), but not (16). However, the present distortion functions $\psi^{\chi}_{ni}(s_i)$ and $\psi^{\chi}_{si}(s_i)$ satisfy all the underlying conditions. Figure 5 shows the distortion functions obtained from the present analysis for some cross sections.

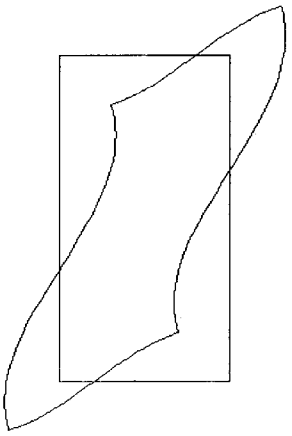


Fig. 5(*a*)

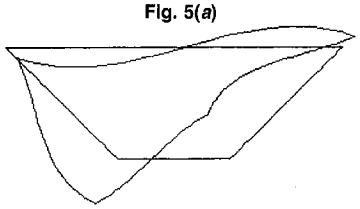


Fig. 5(*b*)

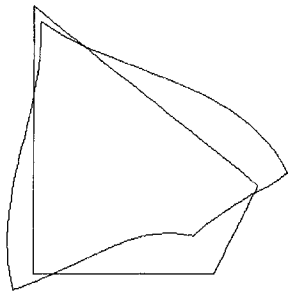


Fig. 5(*c*)

Fig. 5 Distortion functions for (*a*) rectangular, (*b*) trapezoidal, and (*c*) general cross sections

One-Dimensional Analysis

The static equilibrium equations can be obtained from the principle of the minimum potential energy (Washizu, 1982) where the potential energy Π is expressed as

$$\Pi = \tfrac{1}{2}\int \sigma_{ij}\epsilon_{ij}dV - \int (p\tilde{u}_z + q\tilde{u}_s)dV \qquad (23)$$

where p and q are the external loads in the axial and tangential directions. Substituting Eqs. (5)–(7) into Eq. (23) and integrating over the beam cross section A yields

$$\Pi = \tfrac{1}{2}\int \{aE_1U'^2 + cE_1\chi^2 + G(b_1U^2 + b_1^*\theta'^2 + b_5\chi'^2) + 2G(b_2U\theta' + b_3U\chi' + b_4\theta'\chi')\}dz - \int (p_1U + q_1\theta + q_2\chi)dz \qquad (24)$$

where $(\,)'$ denotes the differentiation with respect to z. Constants a, b_1^*, b_1, b_2, b_3, b_4, b_5 and c in Eq. (24) are

$$a = \int_A (\psi_z^U)^2 dA$$

$$b_1^* = \int_A (\psi_s^{\theta})^2 dA, \quad b_1 = \int_A \left(\frac{d\psi_z^U}{ds}\right)^2 dA$$

$$b_2 = \int_A \psi_s^{\theta}\frac{d\psi_z^U}{ds}dA, \quad b_3 = \int_A \psi_s^{\chi}\frac{d\psi_z^U}{ds}dA$$

$$b_4 = \int_A \psi_s^{\theta}\psi_s^{\chi}dA, \quad b_5 = \int_A (\psi_s^{\chi})^2 dA$$

$$c = \int_A n^2\left(\frac{d^2\psi_n^{\chi}}{ds^2}\right)^2 dA$$

and p_1, q_1, and q_2 are one dimensional load terms defined as

$$p_1 = \int_A p\psi_z^U dA; \quad q_1 = \int_A q\psi_s^{\theta}dA; \quad q_2 = \int_A q\psi_s^{\chi}dA.$$

Note that Eq. (24) is the one-dimensional version of the energy expression of Eq. (23) and constants a_1, etc., depend on the choice of $\psi^{\theta}(s)$, $\psi^U(s)$, and $\psi^{\chi}(s)$. Invoking the stationary condition on Π in Eq. (24) yields the following set of governing equations:

Downloaded 04 May 2010 to 171.66.16.27. Redistribution subject to ASME license or copyright; see http://www.asme.org/terms/Terms_Use.cfm

$$-E_1 aU'' + Gb_1 U + Gb_2\theta' + Gb_3\chi' = 0 \quad (25a)$$

$$-Gb_2 U' - Gb_1^*\theta'' - Gb_4\chi'' = 0 \quad (25b)$$

$$-Gb_3 U' - Gb_4\theta'' - Gb_5\chi'' + E_1 c\chi = 0. \quad (25c)$$

One may also identify the following generalized stress resultants H, B, and Q by examining the boundary terms appearing in the first variation of Π.

$$H \equiv \int_A \sigma_{zs}\psi_s^\theta dA = G(b_1^*\theta' + b_2 U + b_4\chi') \quad (26a)$$

$$B \equiv \int_A \sigma_{zz}\psi_z^U dA = E_1 aU' \quad (26b)$$

$$Q \equiv \int_A \sigma_{zs}\psi_s^\chi dA = G(b_5\chi' + b_3 U + b_4\theta') \quad (26c)$$

Note that these resultants H, B, and Q are the energy conjugates of Θ, U and χ, respectively.

To carry out numerical analysis, we employ a standard two-node displacement-based C^0-continuous finite element approach based on the energy form (24).[1] Following the standard procedure, the matrix equation can be obtained:

$$\mathbf{Kd} = \mathbf{P} + \mathbf{Q} \quad (27)$$

where the nodal displacement vector $\mathbf{d}$ is defined as

$$\mathbf{d} = \{\Theta_1 \quad U_1 \quad \chi_1 \quad \Theta_2 \quad U_2 \quad \chi_2\}^T. \quad (28)$$

The subscripts 1 and 2 denote the node numbers in an element level.

The load vectors $\mathbf{P}$ and $\mathbf{Q}$ are defined as

$$\mathbf{P} = \int_{-1}^{1} \mathbf{N}^T\mathbf{R}|J|d\xi \quad (29)$$

$$\mathbf{Q} = \{H_1 \quad B_1 \quad Q_1 \quad H_2 \quad B_2 \quad Q_2\}^T. \quad (30)$$

In Eq. (29), the matrix $\mathbf{N}$ is the linear shape function matrix defined as

$$\mathbf{N} = \begin{bmatrix} \frac{1}{2}(1-\xi) & 0 & 0 & \frac{1}{2}(1+\xi) & 0 & 0 \\ 0 & \frac{1}{2}(1-\xi) & 0 & 0 & \frac{1}{2}(1+\xi) & 0 \\ 0 & 0 & \frac{1}{2}(1-\xi) & 0 & 0 & \frac{1}{2}(1+\xi) \end{bmatrix} \quad (31)$$

and ξ in Eq. (29) is the dimensionless coordinate:

$$\xi = \frac{2z - (z_1 + z_2)}{z_2 - z_1} = \frac{2z - (z_1 + z_2)}{l}$$

where z_1 and z_2 are the axial coordinates of the beam elements and l is the beam element length. The Jacobian $|J|$ is simply $l/2$. The vector denoting one-dimensional load terms is defined as

$$\mathbf{R} = \{q_1 \quad p_1 \quad q_2\}^T.$$

The stiffness matrix $\mathbf{K}$ in Eq. (27) may be written explicitly as

$$\mathbf{K} = \begin{bmatrix} G\frac{b_1^*}{l} & -G\frac{b_2}{2} & G\frac{b_4}{l} & -G\frac{b_1^*}{l} & -G\frac{b_2}{2} & -G\frac{b_4}{l} \\ & E_1\frac{a}{l} + G\frac{b_1 l}{3} & -G\frac{b_3}{2} & G\frac{b_2}{2} & -E_1\frac{a}{l} + G\frac{b_1 l}{6} & G\frac{b_3}{2} \\ & & G\frac{b_5}{l} + E_1\frac{cl}{3} & -G\frac{b_4}{l} & -G\frac{b_3}{2} & -G\frac{b_5}{l} + E_1\frac{cl}{6} \\ & & & G\frac{b_1^*}{l} & G\frac{b_2}{2} & G\frac{b_4}{l} \\ & \text{—sym—} & & & E_1\frac{a}{l} + G\frac{b_1 l}{3} & G\frac{b_3}{2} \\ & & & & & G\frac{b_5}{l} + E_1\frac{cl}{3} \end{bmatrix}.$$

For dynamic analysis, Eq. (27) is replaced by

$$\mathbf{M}\frac{d^2\mathbf{d}}{dt^2} + \mathbf{Kd} = \mathbf{P} + \mathbf{Q} \quad (32)$$

where $\mathbf{d}$, $\mathbf{P}$, and $\mathbf{Q}$ are interpreted as functions of time t, and the consistent mass matrix $\mathbf{M}$ can be obtained explicitly as

$$\mathbf{M} = \rho\begin{bmatrix} (b_1^* + d_1)\frac{l}{3} & 0 & (b_4 + d_3)\frac{l}{3} & (b_1^* + d_1)\frac{l}{6} & 0 & (b_4 + d_3)\frac{l}{6} \\ & a\frac{l}{3} & 0 & 0 & a\frac{l}{6} & 0 \\ & & (b_5 + d_2)\frac{l}{3} & (b_4 + d_3)\frac{l}{6} & 0 & (b_5 + d_2)\frac{l}{6} \\ & & & (b_1^* + d_1)\frac{l}{3} & 0 & (b_4 + d_3)\frac{l}{3} \\ & \text{—sym} & & & a\frac{l}{3} & 0 \\ & & & & & (b_5 + d_2)\frac{l}{3} \end{bmatrix}$$

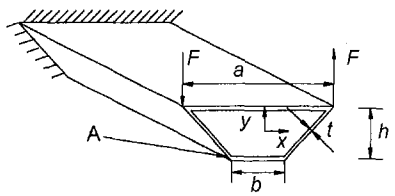


Fig. 6 Geometry of a thin-walled cantilevered beam, which may be subjected to a couple

[1] The exact solution based on the present one-dimensional theory is also given in the Appendix.

Downloaded 04 May 2010 to 171.66.16.27. Redistribution subject to ASME license or copyright; see http://www.asme.org/terms/Terms_Use.cfm

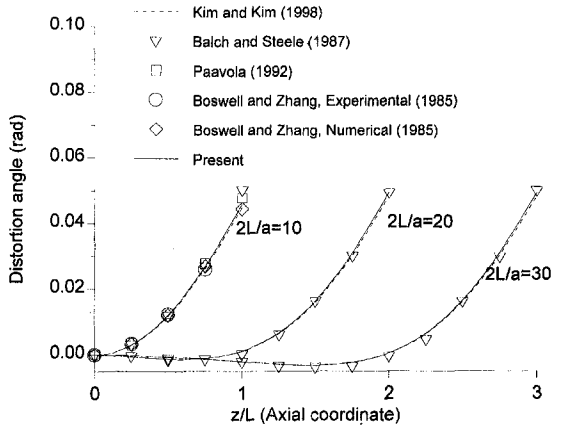


Fig. 7 Distortion of a rectangular box beam ($a = b = 300$ mm, $h = 150$ mm, $L = 1500$ mm)

where ρ is the beam density and constants d_1, d_2, and d_3 are defined as

$$d_1 = \int_A (\psi_n^\theta)^2 dA$$

$$d_2 = \int_A (\psi_n^\chi)^2 dA$$

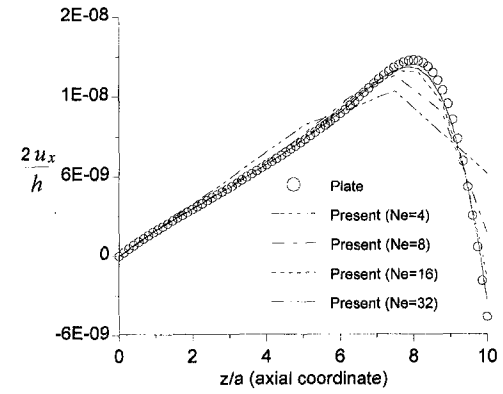


Fig. 8(*a*)

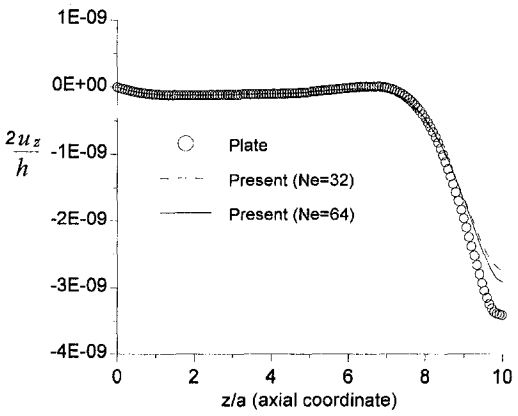


Fig. 8(*b*)

Fig. 8 The axial variation of the dimensionless displacements (*a*) $2u_x/h$, (*b*) $2u_z/h$ along corner *A* of the trapezoidal box beam subjected to a couple

Table 1 The first two eigenfrequencies for a rectangular box beam

Mode number	1	2
Method 1 (Kim and Kim; 1999)	858.69 Hz	2484.5 Hz
Method 2 (Kim and Kim; 1999)	947.39 Hz	2859.5 Hz
Present	928.95 Hz	2879.4 Hz
Plate (NASTRAN)	926.45 Hz	2836.5 Hz

$$d_3 = \int_A \psi_n^\theta \psi_n^\chi dA.$$

Once **d** is found either form Eq. (27) or Eq. (32), the stress and displacement can be calculated from the standard approach used in the finite element analysis.

Numerical Results

Example 1 *A cantilever rectangular box beam subjected to a couple.*

Before considering thin-walled beams with general quadrilateral cross sections, a rectangular box beam is first investigated to confirm the validity of the present approach. A cantilever rectangular box beam under a couple has been a subject of many earlier investigations (Boswell and Zhang, 1985; Balch and Steele, 1987; Paavola, 1992; Kim and Kim, 1999). This beam can be considered as a degenerate case with $a = b$ from the beam shown in Fig. 6 ($a = b = 300$ mm, $h = 150$ mm, $L = 1500$ mm, $t = 3.18$ mm, $E = 196.2$ kN/mm^2, $\nu = 0.27$). The magnitude of the two point loads is 4905 N, and the magnitude of the resulting torque is 1422.5 Nm (=4905 N $\times$ 290 mm). Figure 7 compares the present results for the distortional angle with the existing results; observe that the present result agrees well with the analytic solutions by Balch and Steele (1987), who employed more elaborate theories.

Example 2 *A cantilever thin-walled trapezoidal beam subjected to a couple.*

As the second example, a trapezoidal cross section ($a = 75$ mm, $b = 25$ mm, $h = 25$ mm, $t = 1$ mm, $L = 750$ mm in Fig. 6) under two point forces of unit magnitude at the free edge is considered. The material properties are $E = 200$ kN/mm^2, $\nu = 0.3$ and $\rho = 7.8 \times 10^{-6}$ kg/mm^3. The same material properties will be used in the subsequent problems. Since no published report is available for general quadrilateral cross sections, the present result will be compared with that obtained by the plate finite element analysis. Since the direct comparison for θ, χ, and U is difficult, we examine the dimensionless displacements $2u_x/h$, $2u_z/h$. Figures 8(*a, b*) indicate that the present one-dimensional result matches well with the NASTRAN (1989) *plate* finite element result.[2] As the number N_e of the present elements increases, the present results approach the plate finite element result. Somewhat slow convergence is attributed to the exponential behavior of the solution near the ends. Improved convergence may be achieved by the use of higher-order elements, but this is not the main concern of this paper.

The present exact solution for this example is also given in the Appendix, and is compared with the finite plate element result.

Example 3 *Free vibration of a free-free rectangular box beam ($a = b = 50$ mm, $h = 25$ mm, $t = 1$ mm, $L = 500$ mm).*

The advantage of the present technique is that it can be applied for both static and dynamic problems without any modification. This is due to the fact that the distortion functions ψ_n^χ and ψ_s^χ are so selected as to satisfy both the displacement and rotation (and moment) continuities at the contour corners. As a verification example of the present approach for dynamic analysis, we start with the free vibration of a thin-walled rectangular box beam with no end constraint.

Table 1 lists the first two eigenfrequencies associated with

[2] The plate results given here are converged results.

Downloaded 04 May 2010 to 171.66.16.27. Redistribution subject to ASME license or copyright; see http://www.asme.org/terms/Terms_Use.cfm

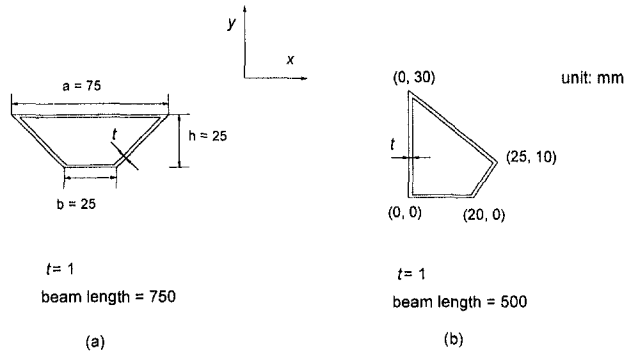


Fig. 9 The geometry of freely supported beams with (*a*) a trapezoidal and (*b*) general quadrilateral cross sections

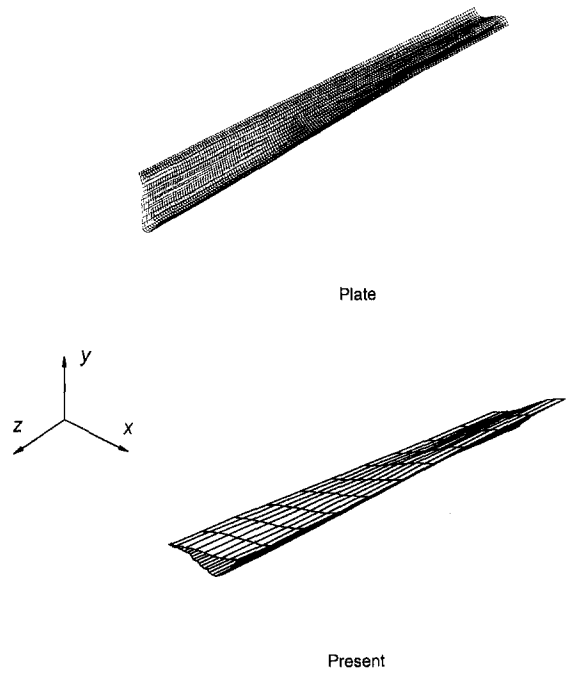


Fig. 10 The first mode of a freely supported trapezoidal box beam

torsion and distortion. Although not plotted here, the first vibration mode is a distortion-dominant one coupled with torsional deformation, and the second mode is a torsion-dominant mode.

In Table 1, Method 1 refers to the analysis using the same distortion function, obtained directly from Vlasov's theory, in the construction of both stiffness and mass matrices. On the other hand, Method 2 refers to the analysis using statically admissible and kinematically compatible distortion functions for the stiffness and mass matrices, respectively (see Kim and Kim, 1999). Although Method 2 yields as good results as and is simpler than the present method, Method 2 is limited only to rectangular box beams. Excellent agreement between the present and the plate finite element results is observed in Table 1.

Example 4 *Free vibration of freely supported thin-walled beams: (a) a trapezoidal cross section and (b) a general cross section.*

Now we consider the free vibration problems for (a) a trapezoidal and (b) general quadrilateral cross sections as shown in Fig. 9. The first two eigenfrequencies associated with torsional and distortional deformations are tabulated in Table 2, which compare the results from the present and NASTRAN plate finite elements. As shown in Table 2, the present analysis predicts very well the first two eigenfrequencies while the conventional theory, which considers torsion alone, cannot predict the second eigenfrequency and yields a considerably higher value for the first frequency than the present analysis.

The present first vibration mode shape for the trapezoidal box beam is reconstructed from the one-dimensional analysis, and compared in Fig. 10 with that from the plate finite element analysis. It appears from this figure that the first mode is dominated by torsional deformation. However, the effect of distortional deformation is not negligible: see Table 2.

Conclusions

New distortion shape functions are proposed for general quadrilateral cross-sectioned closed thin-walled beams. Based on these shape functions, a new one-dimensional theory dealing with coupled deformations of torsion, warping, and distortion of the thin-walled beam is presented. Several numerical results obtained by the one-dimensional finite element analysis based on the present theory have confirmed the validity of the present approach. The importance of the consideration of distortional deformation is also addressed, particularly for the dynamic analysis of thin-walled beams.

Table 2 The first two eigenfrequencies of freely supported beams in Fig. 9

Trapezoidal section shown in Fig. 9 (a)			
Mode number	Plate	Conventional beam	Present (N_e=10)
1	911.8 Hz	1258.1 Hz	909.6 Hz
2	1666.5 Hz	N/A	1696.6 Hz
General section shown in Fig. 9 (b)			
Mode number	Plate	Conventional beam	Present (N_e=10)
1	2348.3 Hz	2413.9 Hz	2335.0 Hz
2	3090.8 Hz	N/A	2951.6 Hz

Acknowledgments

The authors are grateful for the support provided by a grant from the Korea Science & Engineering Foundation (KOSEF) and Safety and Structural Integrity Research Center at the Sung Kyun Kwan University.

References

Balch, C. D., and Steele, C. R., 1987, "Asymptotic Solutions for Warping and Distortion of Thin-Walled Box Beams," ASME JOURNAL OF APPLIED MECHANICS, Vol. 54, pp. 165–173.

Bažant, Z. P., and Nimeiri, M. E., 1974, "Stiffness Method for Curved Box Girders at Initial Stress," *Journal of the Structural Division,* Vol. 100, No. ST10, pp. 2071–2090.

Bishop, R. E. D., Price, W. G., and Cheng, Z. X., 1983, "On the Structural Dynamics of a Vlasov Beam," *Proceedings of the Royal Society of London,* Vol. A388, pp. 49–73.

Boswell, L. F., and Li, Q., 1995, "Consideration of the Relationships Between Torsion, Distortion, and Warping of Thin-Walled Beams," *Thin-Walled Structures,* Vol. 21, pp. 147–161.

Boswell, L. F., and Zhang, S. H., 1983, "A Box Beam Finite Element for the Elastic Analysis of Thin-Walled Structures," *Thin-Walled Structures,* Vol. 1, pp. 353–383.

Boswell, L. F., and Zhang, S. H., 1984, "The Effect of Distortion in Thin-Walled Box-Spine Beams," *International Journal of Solids and Structures,* Vol. 20, No. 9–10, pp. 845–862.

Boswell, L. F., and Zhang, S. H., 1985, "An Experimental Investigation of the Behavior of Thin-Walled Box Beams," *Thin-Walled Structures,* Vol. 3, pp. 35–65.

Cheung, Y. K., 1969, "Folded Plate Structures by Finite Strip Method," *Journal of the Structural Division, Proceedings of ASCE,* Vol. 95, No. ST12, pp. 2963–2979.

Friberg, P. O., 1985, "Beam Element Matrices Derived From Vlasov's Theory of Open Thin-Walled Elastic Beams," *International Journal for Numerical Methods in Engineering,* Vol. 21, pp. 1205–1228.

Gere, J. M., 1954, "Torsional Vibrations of Beams of Thin-Walled Open Section," ASME JOURNAL OF APPLIED MECHANICS, pp. 381–387.

Gjelsvik, A., 1981, *The Theory of Thin Walled Bars,* John Wiley and Sons, New York.

Jirousek, J., Bougerguig, A., and Saygun, A., 1979, "A Macro-Element Analysis of Prestressed Curved Box-Girder Bridges," *Computers & Structures,* Vol. 10, pp. 467–482.

Kim, M. Y., Chang, S. P., and Kim, S. B., 1994a, "Spatial Stability and Free Vibration of Shear Flexible Thin-Walled Elastic Beams. I: Analytical Approach," *International Journal for Numerical Methods in Engineering,* Vol. 37, pp. 4097–4115.

Kim, M. Y., Chang, S. P., and Kim, S. B., 1994b, "Spatial Stability and Free Vibration of Shear Flexible Thin-Walled Elastic Beams. II: Numerical Approach,"

Downloaded 04 May 2010 to 171.66.16.27. Redistribution subject to ASME license or copyright; see http://www.asme.org/terms/Terms_Use.cfm

International Journal for Numerical Methods in Engineering, Vol. 37, pp. 4117–4140.

Kim, Y. Y., Yim, H. J., Kang, J. H., and Kim, J. H., 1995, "Reconsideration of the Joint Modelling Technique: in a Box-Beam T-Joint," SAE paper 951108, pp. 275–279.

Kim, Y. Y., and Kim, J. H., 1999, "Thin-Walled Closed Box Beam Element for Static and Dynamic Analysis," *International Journal for Numerical Methods in Engineering,* Vol. 45, pp. 473–490.

Kou, C. H., Benzley, S. E., Huang, J. Y., and Firmage, D. A., 1992, "Free Vibration Analysis of Curved Thin-Walled Girder Bridges," *Journal of Structural Engineering,* Vol. 118, No. 10, pp. 2890–2910.

Křístek, V., 1970, "Tapered Box Girders of Deformable Cross Section," *Journal of the Structural Division, ASCE,* Vol. 96, No. ST8, Proc. Paper 7489, pp. 1761–1793.

Laudiero, F., and Savoia, M., 1991, "The Shear Strain Influence on the Dynamics of Thin-Walled Beams," *Thin-Walled Structures,* Vol. 11, pp. 375–407.

Maisel, B. I., 1982, "Analysis of Concrete Box Beams Using Small-Computer Capacity," Cement and Concrete Association, Development Report 5, London.

Mikkola, M. J., and Paavola, J., 1980, "Finite Element Analysis of Box Girders," *Journal of the Structural Division, ASCE,* Vol. 106, No. ST6, pp. 1343–1357.

MSC/NASTRAN, 1989, *User's Manual,* The McNeal Schwendler Corporation, Los Angeles.

Paavola, J., 1992, "A Finite Element Technique for Thin-Walled Girders," *Computers & Structures,* Vol. 44, No. 1–2, pp. 159–175.

Razzaqpur, A. G., and Li, H. G., 1991a, "Thin-Walled Multicell Box Girder Finite Element," *Journal of Structural Engineering, ASCE,* Vol. 117, No. 10, pp. 2953–2971.

Razzaqpur, A. G., and Li, H. G., 1991b, "A Finite Element With Exact Shape Functions for Shear Lag Analysis in Multi-Cell Box-Girders," *Computers & Structures,* Vol. 39, No. 1–2, pp. 155–163.

Razzaqpur, A. G., and Li, H. G., 1994, "Refined Analysis of Curved Thin-Walled Multicell Box Girders," *Computers & Structures,* Vol. 53, No. 1, pp. 131–142.

Vlasov, V. Z., 1961, *Thin Walled Elastic Beams,* Israel Program for Scientific Translations, Jerusalem.

Washizu, K., 1982, *Variational Methods in Elasticity and Plasticity,* 3rd Ed., Pergamon Press, London.

Zhang, Z., and Chen, S., 1990, "Dynamic Finite-Element Method of Thin-Walled Beams," *AIAA Journal,* Vol. 28, No. 5, pp. 910–914.

Zhang, S. H., and Lyons, L. P. R., 1984a, "A Thin-Walled Box Beam Finite Element for Curved Bridge Analysis," *Computers & Structures,* Vol. 18, No. 6, pp. 1035–1046.

Zhang, S. H., and Lyons, L. P. R., 1984b, "The Application of the Thin-Walled Box Beam Element to Multibox Bridge Analysis," *Computer & Structures,* Vol. 18, No. 5, pp. 795–802.

APPENDIX

In order to find the closed-form solution of Eqs. (25), we introduce a function $f(z)$ such that

$$U = f'$$

$$\chi = \frac{ab_5}{cb_3} f^{(4)} - \frac{G}{E_1} \frac{b_1^*(b_1 b_5 - b_3^2) - b_2^2 b_5}{cb_3 b_1^*} f^{(2)}$$

$$\theta = \frac{-ab_5}{cb_2} f^{(4)} + \left[\frac{E_1}{G} \frac{a}{b_2} + \frac{G}{E_1} \frac{b_1^*(b_1 b_5 - b_3^2) - b_2^2 b_5}{cb_2 b_1^*} \right] f^{(2)} - \frac{b_1}{b_2} f \quad \text{(A1)}$$

where $f^{(n)}$ denotes the nth derivative of $f(z)$ with respect to z. The function f is selected to satisfy Eq. (25*a*). This approach was proposed in Vlasov (1961) for rectangular cross-sectioned beam analysis. Now the substitution of Eq. (A1) into Eq. (25*b*) or (25*c*) gives

$$f^{(6)} - 2r^2 f^{(4)} + s^4 f^{(2)} = 0 \quad \text{(A2)}$$

where

$$r^2 = \frac{1}{2} \left[\frac{b_1^*(b_1 b_5 - b_3^2) - b_2^2 b_5}{ab_5 b_1^*} \frac{G}{E_1} + \frac{c}{b_5} \frac{E_1}{G} \right]$$

$$s^4 = \frac{cb_1}{ab_5} - \frac{cb_2^2}{ab_5 b_1^*}.$$

The general solution of Eq. (A2) can be written as

$$f(z) = f_1\phi_1(z) + f_2\phi_2(z) + f_3\phi_3(z) + f_4\phi_4(z) + f_5 z + f_6 \quad \text{(A3)}$$

where f_i (i = 1, 2, 3, 4, 5, 6) are unknown coefficients to be determined from the boundary conditions. The functions ϕ_i (i = 1, 2, 3, 4) take on the following form:

$$\phi_1 = \cosh \alpha z \sin \beta z$$

$$\phi_2 = \cosh \alpha z \cos \beta z$$

$$\phi_3 = \sinh \alpha z \sin \beta z$$

$$\phi_4 = \sinh \alpha z \cos \beta z$$

where α and β are defined as

$$\alpha = \sqrt{\frac{s^2 + r^2}{2}}, \quad \beta = \sqrt{\frac{s^2 - r^2}{2}}.$$

This closed-form solution is used to solve the problem given in Example 2 and the result is compared with the finite plate element result (See Fig. A1). The present dimensionless displacement $2u_x/h$ at corner A agrees well with the finite element result, and the axial distributions of the rotation angle θ and the distortion angle γ are also plotted in Fig. A1.

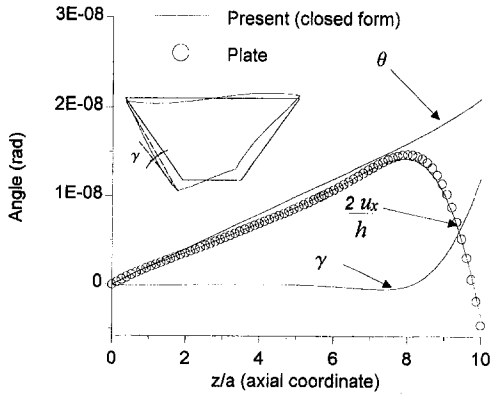


Fig. A1 The axial variation of the rotation angle θ, the distorted angle γ at an edge and the dimensionless displacement $2u_x/h$ along corner *A* of the trapezoidal box section beam subjected to a couple

Downloaded 04 May 2010 to 171.66.16.27. Redistribution subject to ASME license or copyright; see http://www.asme.org/terms/Terms_Use.cfm

W. Yang

H. Pan
Professor

D. Zheng
Professor

Q. Cai
Professor

Central Iron and Steel Research Institute,
Beijing 100081, P. R. China

An Energy Method for Analyzing Magnetoelastic Buckling and Bending of Ferromagnetic Plates in Static Magnetic Fields

Based on an energy method analyses of magnetoelastic buckling and bending of ferromagnetic thin plates in transverse, oblique, and longitudinal fields are performed in this paper. A general expression of the critical magnetic field of the plate in a transverse field is presented. It is shown that the critical magnetic field is not only related to the ratio of the thickness to the cantilevered length, but also to the susceptibility and the demagnetizing factors that are primarily dependent on the ratios of the thickness to width and the thickness to the total length. In different cases, main factors that affect the critical magnetic field are discussed. Theoretical predictions agree with experimental results reasonably.

1 Introduction

About 30 years ago, Moon and Pao (1968) gave a first theoretical analysis of the problem of magnetoelastic buckling of a ferromagnetic plate in a transverse magnetic field. The problem was formulated, similar to Euler buckling problem, in terms of analysis of applied loads and the deflection of the plate. The difference between Euler buckling and magnetoelastic buckling is that the load in the Euler problem is a mechanical force while the load in the magnetoelastic buckling problem is magnetic forces. Based on the magnetic force on the distributed dipoles and the theory of thin plates, the authors obtained an analytical expression of the critical magnetic field B_{cr}, which is dependent on the ratio of the thickness h to the length l of the plate, as $B_{cr} \propto (h/l)^{3/2}$. (Throughout this paper the notation B_{cr} always denotes the critical field of a plate in a *transverse* magnetic field.) Compared with the experimental results, their theoretical predictions are of an overestimation by a factor of about 2. Moreover, experiments (Moon and Pao, 1968; Dalrymple, Peach, and Viegelahn, 1976) showed that the B_{cr} increased with the width-to-thickness ratio, which could not be reflected in the Moon-Pao theory since it was assumed that both the plate and the magnetic field were infinite. Afterwards, research was mainly concentrated on the effect of edge on the critical field (e.g., Miya, Hara, and Someya, 1978; Dalrymple, Peach, and Viegelahn, 1977). Essentially the effort made in these studies may be considered as complementary within the framework of the Moon-Pao theory. The fact that such research had not given a substantial improvement of the prediction of the B_{cr} indicates that the prediction error in the Moon-Pao theory was not mainly due to the edge effect. Dalrymple, Peach, and Viegelahn (1976); Christopherson and Peach (1989), and Peach, Christopherson, Darlymple, and Viegelahn (1988) studied the magnetoelastic buckling problem experimentally and compared their experiment results with the Moon-Pao model. It seems that no further progress has been made in theoretical analysis since the Moon-Pao theory was presented.

Magnetoelastic buckling of a ferromagnetic plate in a transverse magnetic field is analyzed in the present paper by using the energy method. From the viewpoint of energy, the spontaneous tendency of a plate in the field is always to be in a state of minimum energy. So the buckling problem can be formulated in terms of the extreme value of energy. The Euler equation is obtained from the variation of energy functional. The eigenvalue of the Euler equation determines directly a general expression of the critical field. Factors that influence the critical field, such as the width, the inserting depth, and susceptibility of the plate, are included in this expression. In practice, the plane of the plate may not be exactly situated in the vertical plane of the magnetic field so that, strictly speaking, there is no buckling phenomenon. In such cases, instead, the plate will be bent and the deflection will increase monotonously with magnetic field. However, the deflection of the plate is related to the ratio of the applied field to the B_{cr}. The analysis of the deformation of a plate in an oblique field is also given in this paper. From an analysis of a plate in a longitudinal field it is shown that the plate will neither buckle nor bend.

It is assumed that materials are isotropic and the magnetostrictive effect is neglected. Assume that the deflection u of the plate is of an infinitesimal value so that the relationship $\theta \approx u' = du/dx \ll 1$ holds.

2 Buckling of a Plate in a Transverse Static Magnetic Field

We will mainly study the case of a cantilever plate shown in Fig. 1(*a*). Let l_0, l, h, and w denote the total length, the cantilevered length, the thickness, and the width of the plate, respectively. The coordinate systems used are shown in Fig. 1(*b*). The plate is fixed in a transverse field $\mathbf{B}_0$, i.e., before deformation the middle plane of the plate is vertical to the direction of the field $\mathbf{B}_0$ and situated on the x-z plane. Let $\mathbf{n}$, $\mathbf{s}$, and θ represent unit vectors that are normal to and along the rotated surface and the rotation of the middle plane, respectively. It is necessary to introduce the total length l_0 of the plate into the analysis when analyzing the magnetic energy.

2.1 Energy Analysis. The total energy in a deformed plate consists of the elastic strain energy, applied magnetic energy, and demagnetization energy, which will be expressed in the forms of the energy of the plate per unit width. Applied magnetic energy is the reciprocal action energy between the magnetization and the applied magnetic field when the magnetic body is set in the applied magnetic field. For a magnetic body with finite dimensions, its

Contributed by the Applied Mechanics Division of THE AMERICAN SOCIETY OF MECHANICAL ENGINEERS for publication in the ASME JOURNAL OF APPLIED MECHANICS.
Discussion on the paper should be addressed to the Technical Editor, Professor Lewis T. Wheeler, Department of Mechanical Engineering, University of Houston, Houston, TX 77204-4792, and will be accepted until four months after final publication of the paper itself in the ASME JOURNAL OF APPLIED MECHANICS.
Manuscript received by the ASME Applied Mechanics Division, Apr. 14, 1998; final revision, Feb. 2, 1999. Associate Technical Editor: R. C. Benson.

 Copyright © 1999 by ASME

Downloaded 04 May 2010 to 171.66.16.27. Redistribution subject to ASME license or copyright; see http://www.asme.org/terms/Terms_Use.cfm

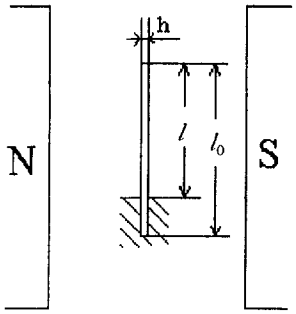


Fig. 1(*a*) A ferromagnetic thin plate is situated in a uniform magnetic field

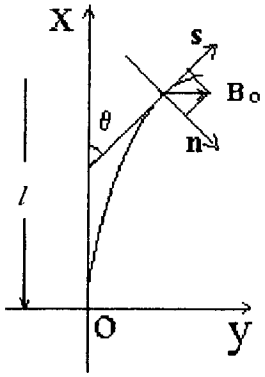


Fig. 1(*b*) Coordinate systems and geometry of a deformed plate

internal magnetic field $\mathbf{H}$ is smaller than the applied field $\mathbf{H}_0$ because of the existence of a demagnetizing field $\mathbf{H}_d$ due to the magnetization. The resultant magnetic field $\mathbf{H}$ is expressed in terms of vectors as follows:

$$\mathbf{H} = \mathbf{H}_0 + \mathbf{H}_d. \tag{1}$$

Similarly, demagnetization energy is the reciprocal action energy between the magnetization and the demagnetization field. Both applied magnetic energy and demagnetization energy is the potential energy that the magnetic body possesses in the applied field and demagnetizing field, respectively.

2.1.1 Elastic Strain Energy. Neglecting the longitudinal (along the length direction of the meddle plane) strain of the thin plate, the elastic energy consists of bending strain energy E_b only, which can be expressed as

$$E_b = \int_{-(l_0-l)}^{l} \tfrac{1}{2}D(u'')^2dx = \int_0^l \tfrac{1}{2}D(u'')^2dx = \int_0^l \tfrac{1}{2}D\theta'^2dx \tag{2}$$

where $D = Eh^3/12(1 - \nu^2)$, and E and ν denote Young's modulus and Poisson's ratio of the plate, respectively.

2.1.2 Magnetic Energy. The total magnetic energy E_m is the sum of the applied magnetic energy E_H and the demagnetization energy E_d,

$$E_m = E_H + E_d = -\int_V \mu_0\mathbf{H}_0\cdot\mathbf{M}dV - \tfrac{1}{2}\int_V \mu_0\mathbf{H}_d\cdot\mathbf{M}dV, \tag{3}$$

where $\mathbf{M}$ is the magnetization vector, and μ_0 vacuum permeability.

The relations between the quantities $\mathbf{H}$, $\mathbf{M}$ and $\mathbf{H}_d$ are as follows:

$$\mathbf{H}_d = -N\mathbf{M}; \quad \mathbf{M} = \chi\mathbf{H} \tag{4}$$

where N denotes the demagnetizing factor in the direction of $\mathbf{M}$ and χ magnetic susceptibility.

Substituting (1) and (4) into (3), one obtains

$$E_m = -\frac{\mu_0}{2}\int_V \frac{H_0^2\left(N+\frac{2}{\chi}\right)}{\left(N+\frac{1}{\chi}\right)^2}dV. \tag{5}$$

Since it is difficult to determine the demagnetizing factor N for the deformed plate, we rewrite E_m as the sum of the two parts, normal to and along the meddle plane of the rotated plate (refer to Fig. 1(*b*)),

$$E_m = -\frac{\mu_0}{2}\int_{-(l_0-l)}^{l} \frac{N_l+\frac{2}{\chi}}{\left(N_l+\frac{1}{\chi}\right)^2}H_0^2(\sin\theta)^2hdx - \frac{\mu_0}{2}\int_{-(l_0-l)}^{l} \frac{N_h+\frac{2}{\chi}}{\left(N_h+\frac{1}{\chi}\right)^2}H_0^2(\cos\theta)^2hdx \tag{5a}$$

where N_l and N_h denote the longitudinal and transverse demagnetizing factor, respectively.

Here, we neglect the effect of the small deformation on the demagnetizing factors. The components of the field used in (5*a*) will not satisfy the continuous conditions of normal component of $\mathbf{B}$ and the tangential component of $\mathbf{H}$. However, if the plate thickness is small enough compared to its length and the assumption of infinitesimal deflection holds, (5*a*) is a valid approximation.

Noticing that $\theta = 0$ in the fixed part and using the general relation $B_0 = \mu_0 H_0$, E_m can be written in the following form:

$$E_m = -\tfrac{1}{2}\int_0^l P\sin^2\theta dx + E_{t0} \tag{6}$$

where

$$P = \left[\frac{N_l+\frac{2}{\chi}}{\left(N_l+\frac{1}{\chi}\right)^2} - \frac{N_h+\frac{2}{\chi}}{\left(N_h+\frac{1}{\chi}\right)^2}\right]\frac{B_0^2}{\mu_0}h,$$

$$E_{t0} = -\frac{\mu_0\left(N_h+\frac{2}{\chi}\right)}{2\left(N_h+\frac{1}{\chi}\right)^2}H_0^2hl_0. \tag{7a,b}$$

E_{t0} stands for the total magnetic energy as the plate is in the position before deformation.

2.1.3 Energy Functional and its Variation. The energy functional E_t is obtained from (2) and (6):

$$E_t = E_b + E_m = \int_0^l (\tfrac{1}{2}D\theta'^2 - \tfrac{1}{2}P\sin^2\theta)dx + E_{t0}. \tag{8}$$

Its Euler equation is

$$D\theta'' + \tfrac{1}{2}P\sin 2\theta = 0. \tag{9}$$

Noticing $\sin\theta \approx \theta$, (9) can be rewritten as

$$D\theta'' + P\theta = 0. \tag{10}$$

Downloaded 04 May 2010 to 171.66.16.27. Redistribution subject to ASME license or copyright; see http://www.asme.org/terms/Terms_Use.cfm

Table 1 Comparison of theoretical and experimental results

$w = 6$ mm							
$l_0 = 90$mm				$l_0 = 70$mm			
l	$B_{cr}{}^e$	$B_{cr}{}^t$	Δ%	l	$B_{cr}{}^e$	$B_{cr}{}^t$	Δ%
65	780	693	-11	55	989	950	-3.9
70	715	643	-10	60	910	871	-4.3
80	632	563	-11	65	833	804	-3.5
$w = 12$mm							
$l_0 = 90$mm				$l_0 = 70$mm			
l	$B_{cr}{}^e$	$B_{cr}{}^t$	Δ%	l	$B_{cr}{}^e$	$B_{cr}{}^t$	Δ%
65	960	800	-17	55	1220	1112	-8.9
70	850	743	-12	60	1048	1019	-2.8
80	745	650	-13	65	1022	941	-7.9

*The units of l and B_{cr} ($B_{cr}{}^e$ and $B_{cr}{}^t$) are mm and 10^{-4} Tesla respectively, $B_{cr}{}^e$ and $B_{cr}{}^t$ are respectively experimental and theoretical critical field and $\Delta\% = \dfrac{B_{cr}{}^t - B_{cr}{}^e}{B_{cr}{}^e} \times 100$.

The eigenvalue of (10) can be obtained by using suitable boundary conditions. For a cantilevered plate, the boundary conditions are $\theta(0) = 0$ and $\theta'(l) = 0$. The lowest critical P_{cr} is determined:

$$P_{cr} = \pi^2 D/(4l^2). \tag{11}$$

2.2 Calculation of Demagnetizing Factor. The demagnetizing factor is primarily dependent on the geometrical shape of the magnetic body. Here we adopt a traditional method described by Zhong (1992) to calculate the demagnetizing factor. Based on the principle of equivalent magnetization sphere, and regarding the ferromagnetic plate as a longitudinally magnetized isolated magnetic body, the longitudinal demagnetizing factor can be obtained as follows:

$$N_l = \frac{1}{1 + \dfrac{l_e}{h}\sqrt{\pi}\sqrt{\dfrac{l_0}{h}\left(\dfrac{h}{w}\right)^2 + \dfrac{h}{w}\left(1 + \dfrac{l_0}{h}\right)}} \tag{12}$$

where l_e is the length of magnetic circuit.

In the case of the nonuniform magnetization and that the length of magnetic circuit is not equal to the length of the plate, $l_e = 0.7\, l_0$ when $l_0/h \gg 9$ (Zhong, 1992).

Similarly, the transverse demagnetizing factor is

$$N_h = \frac{1}{1 + \sqrt{\pi}\dfrac{h}{l_0}\sqrt{\dfrac{l_0 h}{w^2} + \dfrac{h}{w} + \dfrac{l_0}{w}}}. \tag{13}$$

2.3 Expression of Critical Field B_{cr}. Substituting (12) and (13) into (7*a*), and then using (11), the expression of critical field B_{cr} can be obtained. In the case of the ferromagnetic thin plate and $l_0/h \gg 1$, which is studied in this paper, one has $N_h \approx 1 \gg N_l \approx (1.43/\sqrt{\pi})(h/l_0)^{3/2}[(h/w)^2 + (h/w)]^{-1/2}$. Hence compared with the first term in the bracket in Eq. (7*a*), the second term can be ignored. Thus B_{cr} can then be expressed as follows:

$$\frac{B_{cr}}{\sqrt{\mu_0 E}} = \frac{\pi}{\sqrt{12(1-\nu^2)}} \times \frac{(1.43/\sqrt{\pi})(h/l_0)^{3/2}[(h/w)^2 + (h/w)]^{-1/2} + 1/\chi}{\sqrt{(1.43/\sqrt{\pi})(h/l_0)^{3/2}[(h/w)^2 + (h/w)]^{-1/2} + 2/\chi}} \left(\frac{h}{2l}\right). \tag{14}$$

This is a general expression of critical field B_{cr} of a cantilevered plate in a transverse field. The expression shows that the critical field is not only influenced by the ratio (h/l), but also by the ratios (h/l_0) and (h/w) and the susceptibility χ. It is not surprised that the ratio (h/l_0) has an influence on B_{cr} since the demagnetizing factor is related to it. This point is confirmed by our experimental results shown later in Table 1. Noticing that in the expression (14) only the factor $(h/2l)$ is dependent on the mechanical boundary conditions, the corresponding expression of critical field for different mechanical boundary conditions can be simply obtained by alternating the factor $(h/2l)$ in (14) appropriately. For example, for a simply supported plate, one can give its expression of the critical field by replacing the factor $(h/2l)$ with (h/l).

Similarly, the expression of B_{cr} of a circular rod in a transverse field is given by Yang (1998).

2.4 Discussion on Application of the Eq. (14) in Different Cases.

Case of $1/\chi \ll N_l$. This condition is satisfied for a high permeability plate with finite dimensions. Let $\bar{B}$ denote $(B_{cr}/\sqrt{\mu_0 E})$ which is a nondimensional quantity, then (14) can be rewritten as

$$\bar{B} = \frac{\pi^{3/4}}{\sqrt{33.6(1-\nu^2)}}\left(\frac{l}{l_0}\right)^{3/4}\left[\left(\frac{h}{w}\right)^2 + \frac{h}{w}\right]^{-1/4}\left(\frac{h}{l}\right)^{7/4}. \tag{14a}$$

It shows that B_{cr} is only related to the dimensions of the plate and $B_{cr} \propto (h/l)^{7/4}$ for a given (h/w). Here a comparison of (14*a*) with experimental results given by Moon and Pao (1968) is shown in Fig. 2. In the comparison it is assumed that $\nu = 0.3$. The width of these specimens is about 6 mm, and since Moon and Pao (1968) did not give the data of l_0 it is believable to assume that the real value of the fixed part $l_0 - l$ is in the range from 5 to 35 mm (about 0.2 to 1.4 inches). The prediction error of the expression (14*a*) is less than 9.5 percent when taking $l_0 - l = 25.4$ mm (1 inch). It is evident in Fig. 2 that the agreement of the present theory with the experiment is satisfactory. Furthermore, Eq. (14) demonstrates that the larger the (w/h) ratio, the larger the critical field for a given (h/l_0) and (h/l). This coincides with Moon's experimental results.

Case of $N_l \ll 1/\chi$. This condition is satisfied for an infinite plate or a low susceptibility plate with finite dimensions. To this end (14) can be simplified as

Downloaded 04 May 2010 to 171.66.16.27. Redistribution subject to ASME license or copyright; see http://www.asme.org/terms/Terms_Use.cfm

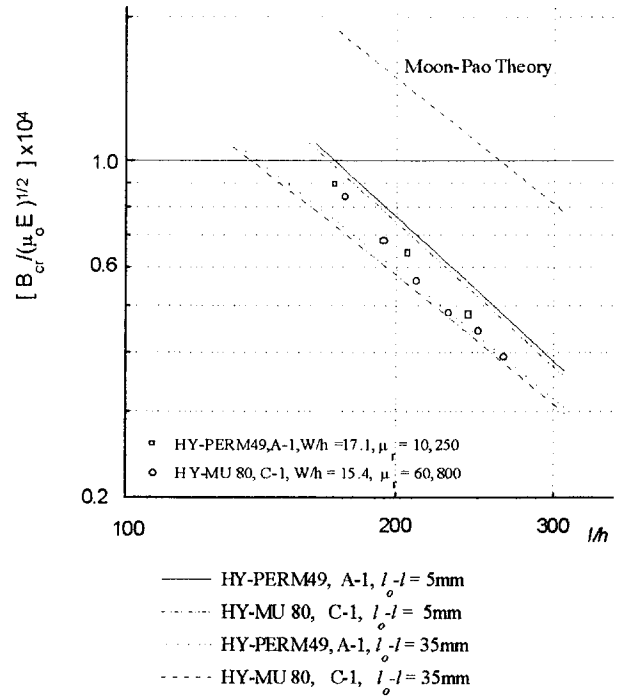


Fig. 2 Comparison of theoretical with experimental results

$$\bar{B} = \frac{\pi}{\sqrt{96\chi(1-\nu^2)}}\left(\frac{h}{l}\right). \tag{14b}$$

Equation (14*b*) shows that the relationship between B_{cr} and (h/l) is linear. From the experiment results on Martensitic stainless steel (Sandvik HT-9) (Moon, 1984; Moon and Hara 1982), it is found that the relationship between B_{cr} and (h/l) is close to 1.18 power.

Similarly, the relationship between B_{cr} and (d/l) is also linear when $N_l \ll 1/\chi$ for a circular rod in a transverse field, where d is the diameter of the rod (Yang, 1998). Experimental results given by Moon (1984) show that the relationship is 1.1 power.

It is seen from two extreme cases discussed above that the relationship between B_{cr} and (h/l) is in the range from 1 to $\frac{7}{4}$ power. The power is close to 1 when the susceptibility is very low, and the power is close to $\frac{7}{4}$ when the susceptibility is very high for a finite plate.

Case of $N_l \sim 1/\chi$. We performed an experiment using nonorientated silicon steel of grade DW310 with thickness 0.5 mm. The diameter of magnetic poles used in the experiment was 100 mm. The change of the field between the 70-mm dia circle was less than six percent and between 90-mm dia circle close to 16 percent. The change of the field from pole to pole was less than five percent. Permeability data measured by testing standard ring specimens is $\mu_r = 1200$ at $H = 0.8$ A/m. (It has an increase of not more than ten percent at $H = 10$ A/m.) The Young's modulus and possion's ratio are $E = 210$ GPa and $\nu = 0.28$, respectively. Listed in Table 1 is a comparison of theoretical with experimental results in various dimensions.

It is seen from Table 1, the total length l_0 and the width w evidently influence the critical field. It displays that, just as the theory predicted, a shorter total length and/or a wider plate has a larger critical field for a given cantilevered length. In Table 1 the agreement between experiments and theoretical predictions is generally good, especially for smaller specimens. It is in accordance with the fact that the applied field has less nonuniformity within a smaller diameter.

It is worth mentioning that in both cases $N_l \ll 1/\chi$ and $N_l \sim 1/\chi$, the $\bar{B}$ is related to current susceptibility χ. When χ varies appreciably with the applied field, it is necessary to use iteration in the calculation of $\bar{B}$.

3 Deformation of a Plate in an Oblique Field

3.1 Theory. The typical imperfection of magnetoelastic buckling is misalignment, i.e., there is a small angle α between the field direction and the normal to the middle plane of the undeformed plate. In other words, the plate is fixed in an oblique field. Here, let θ denote the rotation of the plate resulting from the action of the field. Again assume that θ is a small quantity. Then the angle between the field direction and the normal to the middle plane of the plate in its deformed configuration is $(\alpha + \theta)$. The Euler equation of the energy functional of a plate in an oblique field can be rewritten as

$$D\theta'' + \tfrac{1}{2}P \sin 2(\alpha + \theta) = 0. \tag{15}$$

Here we give the approximate solution of (15) when $\alpha \ll 1$. Since $\alpha + \theta \ll 1$, (15) can be approximately written as

$$D\theta'' + P(\alpha + \theta) = 0. \tag{15a}$$

The boundary conditions are $\theta(0) = 0$ and $\theta'(l) = 0$ for a cantilevered plate. In this case, there is a unique solution to (15*a*). Noticing (11) and (7*a*), i.e., $\sqrt{(P_{cr}/D)} \cdot l = \pi/2$ and $P/P_{cr} = (B_0/B_{cr})^2$, the solution is

$$\theta = \alpha \tan\beta \cdot \sin\left(\frac{x}{l}\beta\right) + \alpha\cos\left(\frac{x}{l}\beta\right) - \alpha \tag{16}$$

where $\beta = (B_0/B_{cr}) \cdot (\pi/2)$.

Then the deflection δ of the free end of the plate is given as follows:

$$\delta = \alpha \cdot l\left(\sec\beta \cdot \frac{\sin\beta}{\beta} - 1\right), \tag{17}$$

where $\sin\beta/\beta$ is a monotone decreasing function when $0 < \beta \le \pi/2$, i.e., $0 < B_0 \le B_{cr}$. Its range is $[2/\pi, 1)$.

When $\alpha \neq 0$, Eq. (17) indicates that $\delta \neq 0$, once a small B_0 is applied. It means that the plate will deform in a manner of bending. So in this case there is no ideal buckling phenomenon. In the limit case that $\alpha = 0$, Eq. (17) indicates that $\delta = 0$ for an arbitrary $B_0 < B_{cr}$. The δ will be an indeterminate of the type $0 \cdot \infty$ once $B_0 = B_{cr}$. It is the characteristic that only bifurcation or ideal buckling possesses.

The relation of δ/h versus B_0/B_{cr} shown in Fig. 3 is nonlinear.

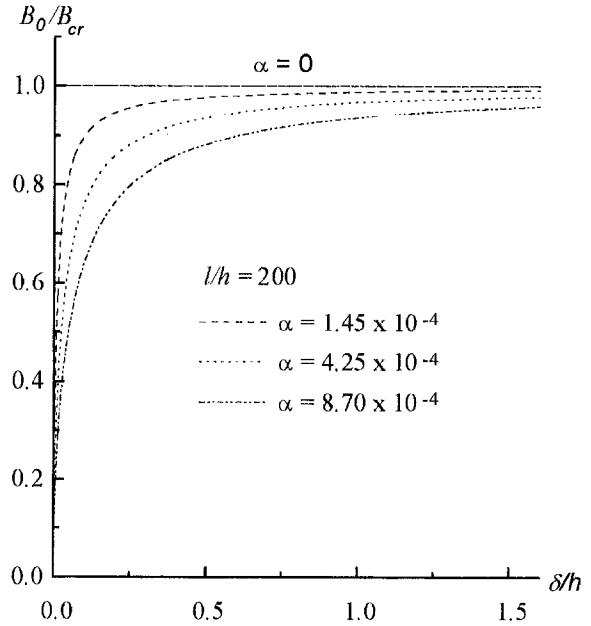


Fig. 3 Magnetic field versus top deflection of cantilever plates for different α

Downloaded 04 May 2010 to 171.66.16.27. Redistribution subject to ASME license or copyright; see http://www.asme.org/terms/Terms_Use.cfm

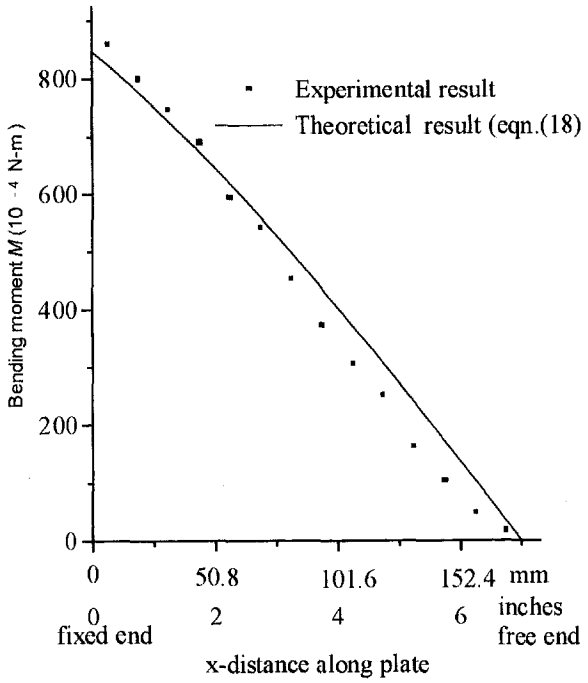


Fig. 4 A comparison of theoretical bending moments with experimental results

The increase of δ/h is very slow at the beginning and then gets fast when B_0/B_{cr} increases, finally δ/h snaps suddenly into a large quantity when B_0/B_{cr} is very close to unity. The B_{cr} is always an asymptotic value of B_0 in the curve of δ versus B_0 and is independent of α. Therefore one can take the asymptotic value of B_0 in the experimental relation of δ versus B_0 as an approximation of the B_{cr} when the misalignment is unavoidable in practice.

3.2 Comparison of Theoretical With Experimental Results. Peach and Christopherson (1988) and Christopherson and Peach (1989) carried out an experiment in which $\alpha = 5$ deg. They measured the strains in different stations on the surface of the deformed plate by using strain gauges. From the strain measurements they gave the values of the bending moment and then the values of the plate curvature θ' and rotation θ. Substituting their experimental data $\theta = 357.298 \times 10^{-4}$ at $x = l/2$ into (16), one has $\beta = 0.87195$. The error of β obtained by using their data at different stations is less than three percent. The expression of bending moment M is derived from (16):

$$M = D\theta' = D\frac{\alpha\beta}{l}\left[\tan\beta\cos\left(\frac{x}{l}\beta\right) - \sin\left(\frac{x}{l}\beta\right)\right]. \quad (18)$$

Rotation θ and bending moment M are obtained by substituting $\beta = 0.87195$ and $D = 0.1663\text{N-m}^2(1.663 \times 10^8\text{dyne-cm}^2)$ into (16) and (18). The comparison of theoretical with experimental bending moments is shown in Fig. 4.

4 The Response of a Plate in a Longitudinal Field

Now image that the field direction is parallel to the x-axis, i.e., $\alpha = 90$ deg. in (15). Then one can obtain

$$D\theta'' - \tfrac{1}{2}P\sin 2\theta = 0. \quad (19)$$

Under the assumption of small deflection, (19) can be approximately rewritten as

$$D\theta'' - P\theta = 0. \quad (20)$$

There is no nonzero solution to (20) for a cantilevered and/or simply supported plate. It implies that the undeformed state is a state of the lowest energy for a plate in a longitudinal field and so the plate will neither bend nor buckle.

Summarily, we have analyzed the behavior of a plate in a transverse, an oblique, and a longitudinal field. It is obvious that the cases of a plate in a transverse and a longitudinal field can be regarded as special cases of an oblique field taking $\alpha = 0$ deg and $\alpha = 90$ deg, respectively. Due to the introduction of the demagnetizing factor into the analysis, other than the ratio of (h/l) and the susceptibility χ, factors influencing the critical field such as the ratios of (h/l_0) and (h/w) also appeared in our results. Following this work, we have performed the analysis of the vibration problem of a plate in a transverse and a longitudinal field (Yang, 1998). The results show that the natural frequency of a plate in a longitudinal field will increase with the field.

Acknowledgment

The authors are indebted to Prof. Lichi Tai for his encouragement.

References

Christopherson, N. S., Peach, M. O., and Darlymple, J. M., 1989, "Magnetostatic Deformation Experiment: Bending of a Thin Plate," *Experimental Mechanics,* Vol. 29, pp. 432–436.

Dalrymple, J. M., Peach, M. O., and Viegelahn, G. L., 1976, "Magnetoelastic buckling: Theory versus Experiment," *Experimental Mechanics,* Vol. 16, pp. 26–31.

Dalrymple, J. M., Peach, M. O., and Viegelahn, G. L., 1977, "Edge Effect Influence on Magnetoelastic Buckling of Rectangular Plates," ASME JOURNAL OF APPLIED MECHANICS, Vol. 44, pp. 305–310.

Miya, K., Hara, K., and Someya, K., 1978, "Experimental and Theoretical Study on Magnetoelastic Buckling of a Ferromagnetic Cantilevered Beam-plate," ASME JOURNAL OF APPLIED MECHANICS, Vol. 45, pp. 355–360.

Moon, F. C., and Pao, Y. H., 1968, "Magnetoelastic Buckling of a Thin Plate," ASME JOURNAL OF APPLIED MECHANICS, Vol. 35, pp. 53–58.

Moon, F. C., and Hara, K., 1982, "Buckling Induced Stresses in Martensitic Stainless Steels for Magnetic Fusion Reactors," *Nuclear Engineering and Design,* Vol. 71, pp. 27–31.

Moon, F. C., 1984, *Magneto-solid Mechanics,* John Wiley and Sons, New York, pp. 166–169.

Peach, M. O., Christopherson, N. S., Darlymple, J. M., and Viegelahn, G. L., 1988, "Magnetoelastic Buckling: Why Theory and Experiment Disagree," *Experimental Mechanics,* Vol. 28, pp. 65–69.

Yang, Wentao, 1998, "An Investigation on Magnetoelastic Buckling and Vibration of a Thin Plate in magnetic fields," Ph.D. dissertation, Central Iron and Steel Research Institute, Beijing, P. R. China.

Zhong, Wending, 1992, *Ferromagnetism,* Beijing: Science Press pp. 478–482 (in Chinese).

Downloaded 04 May 2010 to 171.66.16.27. Redistribution subject to ASME license or copyright; see http://www.asme.org/terms/Terms_Use.cfm

Effective Constitutive Properties of Linear Elastic Cellular Solids With Randomly Oriented Cells

Z. Dimitrovová
Departamento de Engenharia Mecanica, IDMEC,
Instituto Superior Tecnico,
Av. Rovisco Pais 1,
1096 Lisboa, Portugal
e-mail: zdimitro@dem.ist.utl.pt

A new methodology to derive the linear effective constitutive law for a group of composites with random microstructure of a special kind is described as an extension of the methodology proposed in Warren and Kraynik (1988) and of the methodology used in polycrystal theory. The results are expressed in the form of specific bounds on effective elastic constants. Practical importance is in the specific bounds when the methodology is applied to cellular solids. Several examples are shown and compared with other published results. The new contribution of this paper lies in the presentation of the methodology, derivation of new specific bounds in two dimensions, and comments related to already published works on cellular solids.

1 Introduction

Proper description of the macroscopic behavior of composites has been the subject of considerable research for many years; thus several methodologies and techniques have been developed in this area. This paper starts with a short outline of homogenization techniques for composite materials and some remarks related to cellular solids.

In many types of statistically homogeneous composites the ratio of the characteristic size of heterogeneities to the size of the full medium, δ, is very small, making numerical solutions that account completely for these heterogeneities (for instance, by finite elements) almost impossible. Thus homogenization techniques are often used. When solving mechanical problems, one replaces the original problem by a problem defined on a fictitious homogeneous medium with certain effective properties. These properties depend on the mechanical properties of the phases, their volume fractions, and the particular microstructure. The fictitious homogeneous medium is the limit (as δ tends to zero) of a sequence of heterogeneous media. Actual composites correspond to very small but nonzero δ, and thus the effective properties must be understood in an approximate sense.

There are two limit cases of actual composites that require different modeling in order to determine the effective properties: composites with a random microstructure (random composites) and composites with a periodic microstructure (periodic composites). In deterministic theories, the first type allows the introduction of a representative volume element (RVE), which is, roughly speaking, the smallest possible region of the composite with the same effective properties as the original one (Hashin, 1970; 1983; Nemat-Nasser and Hori, 1993; Ostoja-Starzewski, 1998). In the case of a periodic microstructure, a basic cell, defined as the (smallest possible) region which can construct the full medium by periodic repetition, can be introduced (Duvaut, 1976; Bensoussan, Lions, and Papanicolau, 1978; Suquet, 1985a, b; Bakhvalov and Panasenko, 1989; Guedes, 1990; Nemat-Nasser and Hori, 1993). In both cases two levels are involved: the macrolevel, which is the level of the fictitious medium, and the microlevel, i.e., the level of the (rescaled) RVE or basic cell. If the microscale is defined such that the basic cell has a unit volume, the term unit cell is often used instead.

For periodic composites, effective properties related to some particular microstructure are obtainable in an exact form, at least numerically. However, due to the complexity of the random microstructure, effective properties of random composites can only be expressed either in the form of representative functions (usually semiempirical) or in the form of bounds. For effectively isotropic two-phase composites (with perfectly bonded phases) the well-known Voigt and Reuss bounds were improved using the Hashin-Shtrikman variational principle (Hashin and Shtrikman, 1962a, 1963) in Hashin and Shtrikman (1963), giving the Hashin-Shtrikman bounds. They are optimal if, besides the phase properties, only the information about the phase volume fractions is available.

In stochastic theories, additional quantitative characterization of the microstructure can be expressed by n-point correlation functions (Torquato and Stell, 1982) permitting the determination of improved bounds for specific models of microstructures: spherical inclusion models (Torquato, 1991, 1994, 1998), cell models (Lu and Torquato, 1990), etc. In addition, a local effective property may be defined for a mesoscale window (statistical volume element corresponding to a lower scale than a RVE). This approach forms the base of stochastic finite elements (Ostoja-Starzewski, 1993, 1994, 1998), permitting a numerical calculation of effective properties again in the form of bounds.

Along this line, the polycrystal theory was developed. The first Voigt and Reuss bounds on their effective constitutive properties were improved using the already mentioned Hashin-Shtrikman variational principle for polycrystals with various types of single-crystal symmetry in Hashin and Shtrikman (1962b), Peselnick and Meister (1965), Meister and Peselnick (1966), Watt (1979, 1980), and Watt and Peselnick (1980). More recent work on polycrystals has been devoted to the optimality of the Voigt and Reuss bounds (Avellaneda and Milton, 1989).

Cellular solids can be either found in the nature (cork, coral, stalk and leaves of plants, some biomaterials, etc.) or manufactured by foaming of polymers, metals, and ceramics or by other technologies. They can be used for absorption of the kinetic energy, for thermal insulation, etc. The importance of cellular materials as well as the necessity of suitable methodologies allowing a detailed description of their properties increases.

A cellular solid (foam) is composed of an interconnected network of solid struts and shell parts, which can be assigned to cells that are (usually with some modifications) repeated in the medium, not necessarily in a periodic manner. Cellular solids can be classified as open-cell foams, consisting only of solid struts, and

Contributed by the Applied Mechanics Division of THE AMERICAN SOCIETY OF MECHANICAL ENGINEERS for publication in the ASME JOURNAL OF APPLIED MECHANICS.
Discussion on the paper should be addressed to the Technical Editor, Professor Lewis T. Wheeler, Department of Mechanical Engineering, University of Houston, Houston, TX 77204-4792, and will be accepted until four months after final publication of the paper itself in the ASME JOURNAL OF APPLIED MECHANICS.
Manuscript received by the ASME Applied Mechanics Division, Sept. 30, 1998; final revision, Apr. 29, 1999. Associate Technical Editor: M.-J. Pindera.

 Copyright © 1999 by ASME

Downloaded 04 May 2010 to 171.66.16.27. Redistribution subject to ASME license or copyright; see http://www.asme.org/terms/Terms_Use.cfm

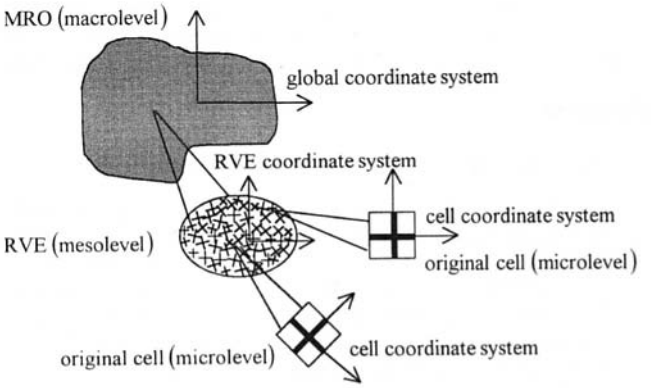


Fig. 1 Medium consisting of randomly oriented cells

closed-cell foams, containing mainly shell parts; see the main monograph on cellular solids by Gibson and Ashby (1988). Actual foams can be partly open and partly closed. Cellular solids can be viewed as composites with void and solid (generally nonhomogeneous) phases.

One of the main parameters that characterize a particular foam is the relative density, s (the ratio of the foam density to the solid phase density), which is low, usually limited by $s = 0.3$ (Gibson and Ashby, 1988). Due to this fact at least one dimension of the solid phase (thickness) at the cell level is small compared to the characteristic cell size. This condition provides motivation for the application of structural theories in homogenization calculations, as shown in Dimitrovová (1997) for periodic foams and in Dimitrovová (1997) and Dimitrovová and Faria (1999), where bounds on the effective properties of open-cell foams were derived. Since they are strictly lower than the bounds for foams (including closed-cell ones), they cannot be obtained by adapting, e.g., the two-phase composite Hashin-Shtrikman bounds. Characterization of random foams by representative functions, fitting some experimental data, can be found in Gibson and Ashby (1988) or Christensen (1994). Effective property calculation for some open-cell foams is presented in Warren and Kraynik (1988).

This paper provides a generalization of Warren and Kraynik's methodology, which is also an extension of the polycrystal methodology, allowing a determination of the effective constitutive properties of some random composites by terms closely related to their particular microstructure.

2 Composites With Randomly Oriented Cells

Two-phase composites with linear homogeneous isotropic phases (and the related foams) are only considered in this paper. The proposed methodology relates to composites with random microstructure of a special kind, named media consisting of randomly oriented cells (MRO). Before their definition, some auxiliary terms are introduced. Let a periodic composite and its possible basic cell be given and defined as the original periodic medium (OPM) and the original cell, respectively. Let us fix the local coordinate system in the basic cell and call it the cell coordinate system. Then MRO (Fig. 1) are defined as random media satisfying the following requirements: (i) particular original cells appear in a RVE with all possible rotations of the cell coordinate system; (ii) all rotational angles of the cell coordinate system are present in a RVE with the same probability. Consequently, the effective isotropy of MRO is ensured.

In order to calculate MRO (effective) properties, in addition to the micro and macrolevel used in homogenization techniques, it is necessary to introduce the mesolevel (Fig. 1). Thus, the original cells correspond to meso-points forming the RVE. Each meso-point is characterized by the same OPM (effective) properties and the nonhomogeneity in MRO is caused by the different rotations of

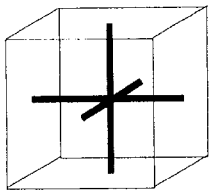


Fig. 2 A basic cell of the regular cubic lattice

the meso-points. This description is similar to the polycrystal model (Hashin and Shtrikman, 1962b), if single crystals are considered as the original cells. However, as in (Warren and Kraynik, 1988), we assume that the original cell size does not vary, otherwise relative volumes of equally oriented original cells would have to be considered (Hashin and Shtrikman, 1962b), (Ferrari and Johnson, 1988).

The partition of the RVE into original cells requires an approximation, but the error (smaller for foams due to the large volume fraction of the void phase) introduced in this way is not important due to the different scales. The reasons why OPM was introduced are: (a) MRO phase volume fractions can be easily kept and (b) OPM permits a unique characterization of the meso-point effective properties (meso-properties). MRO model was already used in Warren and Kraynik (1988) with OPM as the cubic lattice (Fig. 2).

In the polycrystal theory, the boundary of the single crystals need not be considered, thus no assumption about the single-crystal shapes is required. However, for specific purposes, the polycrystal microstructure may be idealized, e.g., by Voronoi cells (Werner, Siegmund, Weinhandl, and Fischer, 1994; Ostoja-Starzewski, 1993, 1994) or by spheres or layered models (Schulgasser, 1983; Avellaneda and Milton, 1989).

In some cases, it may be preferable to define MRO by repeated elements fulfilling the requirements (i) and (ii) in a RVE, but to which no OPM can be related as, e.g., in the example of the tetrahedral lattice (Fig. 3) in (Warren and Kraynik, 1988). In order to calculate effective properties of a repeated element or, in other words, to characterize the meso-properties, boundary conditions like uniform strain, uniform stress or others can be imposed on the boundary. Meso-properties are not uniquely stated, but usually it is possible to determine whether the calculated properties correspond to an upper or a lower estimate of the actual properties.

The following condition holds for the tensor of MRO elastic stiffnesses in matrix representation, $\mathbf{C}^{\mathrm{MRO}}$, which is to be determined:

$$\boldsymbol{\Sigma}^{\mathrm{MRO}} = \mathbf{C}^{\mathrm{MRO}} \cdot \mathbf{E}^{\mathrm{MRO}}, \tag{1}$$

where $\cdot$ stands for the matrix multiplication and $\boldsymbol{\Sigma}^{\mathrm{MRO}}$ and $\mathbf{E}^{\mathrm{MRO}}$ for the macro-stress and macro-strain tensor in vector representation, respectively. The macro-stress (macro-strain) is defined as the volume average of the micro-stress (micro-strain) over a RVE. In MRO model averaging can be divided into two steps. In the first step the microlevel fields are averaged with respect to the cell coordinate system in each original cell separately, giving OPM stress $\boldsymbol{\Sigma}^{\mathrm{OPM}}$ and strain $\mathbf{E}^{\mathrm{OPM}}$. In the second step $\boldsymbol{\Sigma}^{\mathrm{OPM}}$ and $\mathbf{E}^{\mathrm{OPM}}$ are rotated in each original cell (meso-point) to the RVE coordinate

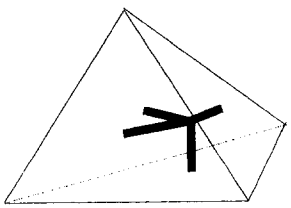


Fig. 3 A repeated element in the tetrahedral lattice

Downloaded 04 May 2010 to 171.66.16.27. Redistribution subject to ASME license or copyright; see http://www.asme.org/terms/Terms_Use.cfm

system and then the averaging operator is applied. The second step is equivalently given by the orientational average of OPM values, which is expressed by the invariant integral (Lagzdins, Tamuzs, Teters and Kregers, 1992). We use the notation $\mathbf{\Sigma}^{\mathrm{MRO}} = [\mathbf{\Sigma}^{\mathrm{OPM}}]$ and $\mathbf{E}^{\mathrm{MRO}} = [\mathbf{E}^{\mathrm{OPM}}]$ in this case.

Due to the complexity of the MRO microstructure it is obvious that $\mathbf{C}^{\mathrm{MRO}}$ cannot be generally available in an exact form, but only in the form of specific MRO bounds. We state them in Section 3 under the assumption of uniform meso-strain or meso-stress, justifying the usage of the names specific MRO Voigt and Reuss bounds. They are expressed in terms of OPM properties and thus are closely related to the particular microstructure. The distance between them depends on the level of the OPM anisotropy. Specific MRO Voigt (Reuss) bound must not be confused with the two-phase composite Voigt (Reuss) bound resulting from the assumption of uniform micro-strain (micro-stress).

The above bounds can be improved using the Hashin-Shtrikman variational principle (Hashin and Shtrikman, 1962a, 1963) in cases, where the related OPM has some kind of effective symmetry, yielding the specific MRO Hashin-Shtrikman bounds. In Section 4 the case when the related OPM possesses a cubic (square in two dimensions) symmetry is treated. Let k and K be bulk moduli in two and three dimensions, respectively, ${}^{1}G$ and ${}^{2}G$ be two shear moduli (the isotropy condition is ${}^{1}G = {}^{2}G = G$), then in two dimensions under plane stress (superscript σ) ${}^{\sigma}\mathbf{C}^{\mathrm{OPM}}$ reads as

$$\begin{bmatrix} {}^{\sigma}k^{\mathrm{OPM}} + {}^{\sigma,1}G^{\mathrm{OPM}} & {}^{\sigma}k^{\mathrm{OPM}} - {}^{\sigma,1}G^{\mathrm{OPM}} & 0 \\ {}^{\sigma}k^{\mathrm{OPM}} - {}^{\sigma,1}G^{\mathrm{OPM}} & {}^{\sigma}k^{\mathrm{OPM}} + {}^{\sigma,1}G^{\mathrm{OPM}} & 0 \\ 0 & 0 & {}^{\sigma,2}G^{\mathrm{OPM}} \end{bmatrix}. \quad (2)$$

If the generalized plane-strain assumption is adopted, (2) is extended in a usual way, the "in-plane" part is formally the same, but the moduli correspond to the plane-strain assumption (superscript ϵ). $\mathbf{C}^{\mathrm{OPM}}$ in three dimensions is given by

$$\begin{bmatrix} K^{\mathrm{OPM}} + 4\,{}^{1}G^{\mathrm{OPM}}/3 & K^{\mathrm{OPM}} - 2\,{}^{1}G^{\mathrm{OPM}}/3 & K^{\mathrm{OPM}} - 2\,{}^{1}G^{\mathrm{OPM}}/3 & 0 & 0 & 0 \\ K^{\mathrm{OPM}} - 2\,{}^{1}G^{\mathrm{OPM}}/3 & K^{\mathrm{OPM}} + 4\,{}^{1}G^{\mathrm{OPM}}/3 & K^{\mathrm{OPM}} - 2\,{}^{1}G^{\mathrm{OPM}}/3 & 0 & 0 & 0 \\ K^{\mathrm{OPM}} - 2\,{}^{1}G^{\mathrm{OPM}}/3 & K^{\mathrm{OPM}} - 2\,{}^{1}G^{\mathrm{OPM}}/3 & K^{\mathrm{OPM}} + 4\,{}^{1}G^{\mathrm{OPM}}/3 & 0 & 0 & 0 \\ 0 & 0 & 0 & {}^{2}G^{\mathrm{OPM}} & 0 & 0 \\ 0 & 0 & 0 & 0 & {}^{2}G^{\mathrm{OPM}} & 0 \\ 0 & 0 & 0 & 0 & 0 & {}^{2}G^{\mathrm{OPM}} \end{bmatrix}. \quad (3)$$

In Section 5 the four specific bounds are applied to cellular solids, explicit analytical results are presented, compared with results published in Warren and Kraynik (1988), Gibson and Ashby (1988), and Christensen (1994), and some conclusions are stated.

The first contribution of this paper is in the extension of the polycrystal methodology to MRO and the key issue in the proposed methodology is the proper characterization of the meso-properties. Furthermore, the specific MRO Hashin-Shtrikman bounds derived in Section 4 for two-dimensional media have not been previously published (analogous bounds for three-dimensional media can be adapted from polycrystal bounds by replacing the single-crystal properties by the OPM properties).

The second contribution of this paper is in the generalization of the methodology proposed in Warren and Kraynik (1988). The calculation of effective properties is shown there only for foams consisting of straight equilateral struts and it is not presented in a general way. The final result corresponds to the specific MRO Voigt bound, thus here a correct interpretation of this result is provided, along with the establishment of a link between the methodology in Warren and Kraynik (1988) and the methodology for polycrystals.

3 Specific MRO Voigt and Reuss Bounds

It holds (based on the polycrystal theory) that the specific MRO Voigt (Reuss) bound on $\mathbf{C}^{\mathrm{MRO}}$ can be obtained by orientational average (orientational average and inverse) of the OPM elastic stiffnesses $\mathbf{C}^{\mathrm{OPM}}$ (compliances $\mathbf{D}^{\mathrm{OPM}}$). The statement can be justified as follows: let a MRO and its RVE be taken. Let us assume that (in the vector representation) $(\mathbf{E}^{\mathrm{MRO}})_1 = E_{11}^{\mathrm{MRO}} = \alpha = [\mathbf{E}^{\mathrm{OPM}}]_1$, while the other components are zero. Then

$$\mathbf{\Sigma}^{\mathrm{MRO}} = [\mathbf{\Sigma}^{\mathrm{OPM}}] = [\mathbf{C}^{\mathrm{OPM}} \cdot \mathbf{E}^{\mathrm{OPM}}] = \alpha[\mathbf{C}^{\mathrm{OPM}}]_1, \quad (4)$$

where $[\mathbf{C}^{\mathrm{OPM}}]_1$ denotes the first column of $[\mathbf{C}^{\mathrm{OPM}}]$. Consequently, taking into account the assumption about uniform meso-strain, $[\mathbf{C}^{\mathrm{OPM}}] \geq \mathbf{C}^{\mathrm{MRO}}$ and $[\mathbf{C}^{\mathrm{OPM}}]$ is the specific MRO Voigt (upper) bound on $\mathbf{C}^{\mathrm{MRO}}$. Inequalities between matrices are taken in the sense that the corresponding difference is positive (negative) semi-definite.

Analogously, when the only nonzero component is $\Sigma_{11}^{\mathrm{MRO}} = \beta = [\mathbf{\Sigma}^{\mathrm{OPM}}]_1$, one gets

$$\mathbf{E}^{\mathrm{MRO}} = [\mathbf{E}^{\mathrm{OPM}}] = [\mathbf{D}^{\mathrm{OPM}} \cdot \mathbf{\Sigma}^{\mathrm{OPM}}] = \beta[\mathbf{D}^{\mathrm{OPM}}]_1, \quad (5)$$

where $[\mathbf{D}^{\mathrm{OPM}}]_1$ denotes the first column of $[\mathbf{D}^{\mathrm{OPM}}]$, consequently $[\mathbf{D}^{\mathrm{OPM}}]^{-1} \leq \mathbf{C}^{\mathrm{MRO}}$ and $[\mathbf{D}^{\mathrm{OPM}}]^{-1}$ is the specific MRO Reuss (lower) bound on $\mathbf{C}^{\mathrm{MRO}}$.

Summing up,

$$[\mathbf{D}^{\mathrm{OPM}}]^{-1} \leq \mathbf{C}^{\mathrm{MRO}} \leq [\mathbf{C}^{\mathrm{OPM}}]. \quad (6)$$

$[\mathbf{C}^{\mathrm{OPM}}]$ and $[\mathbf{D}^{\mathrm{OPM}}]$ are not mutually inverse and equalities in (6) are saturated only for $\mathbf{C}^{\mathrm{OPM}} = [\mathbf{C}^{\mathrm{OPM}}]$ (equivalently $\mathbf{D}^{\mathrm{OPM}} = [\mathbf{D}^{\mathrm{OPM}}]$) holding, e.g., for an effectively isotropic OPM.

Let us determine $[\mathbf{C}^{\mathrm{OPM}}]$ and $[\mathbf{D}^{\mathrm{OPM}}]$. An arbitrary rotation of the cell coordinates in three dimensions is described by three independent parameters. Direction cosines are not convenient (they give nine parameters with six additional constraints of orthonormality), thus it is usual to use Eulerian angles. The choice is not unique; we adopt the one from (Warren and Kraynik, 1988), zxz with the link to φ, θ, ψ. The invariant integral for a fourth-order tensor $\mathbf{R}$ is defined as

$$[\mathbf{R}]_{ijkr} = \frac{1}{8\pi^2} \int_0^{2\pi} \int_0^{\pi} \int_0^{2\pi} R_{mnpq} T_{im} T_{jn} T_{kp} T_{rq} \sin\theta d\varphi d\theta d\psi. \quad (7)$$

In (7), the summation convention was adopted, all subscripts take values 1, 2, 3, and the transformation matrix $\mathbf{T}$ is

Downloaded 04 May 2010 to 171.66.16.27. Redistribution subject to ASME license or copyright; see http://www.asme.org/terms/Terms_Use.cfm

$$\mathbf{T} = \begin{bmatrix} \cos\varphi\cos\psi - \sin\varphi\cos\theta\sin\psi & \sin\varphi\cos\psi + \cos\varphi\cos\theta\sin\psi & \sin\theta\sin\psi \\ -(\cos\varphi\sin\psi + \sin\varphi\cos\theta\cos\psi) & -(\sin\varphi\sin\psi - \cos\varphi\cos\theta\cos\psi) & \sin\theta\cos\psi \\ \sin\varphi\sin\theta & -\cos\varphi\sin\theta & \cos\theta \end{bmatrix}. \tag{8}$$

When expressing $[\mathbf{C}^{\mathrm{OPM}}]$ and $[\mathbf{D}^{\mathrm{OPM}}]$ we used an adjustment of (7) to the matrix representation of fourth-order constitutive tensors according to (Lekhnitskii, 1981). $[\mathbf{C}^{\mathrm{OPM}}]$ or $[\mathbf{D}^{\mathrm{OPM}}]$ can be given in the form of single contributions of $\mathbf{C}^{\mathrm{OPM}}$ or $\mathbf{D}^{\mathrm{OPM}}$ components, which is summarized in Table 1. Only components ij with $i, j = 1, 2, 3$ and components 44, 55, and 66 of $\mathbf{C}^{\mathrm{OPM}}$ or $\mathbf{D}^{\mathrm{OPM}}$ contribute to $[\mathbf{C}^{\mathrm{OPM}}]$ and $[\mathbf{D}^{\mathrm{OPM}}]$. One can conclude from Table 1 that $[\mathbf{C}^{\mathrm{OPM}}]$ and $[\mathbf{D}^{\mathrm{OPM}}]$ are isotropic and that the specific bounds on K^{MRO} and G^{MRO} are (subscripts V and R stand for Voigt and Reuss bounds, respectively)

$$K_V^{\mathrm{MRO}} = \frac{C_{11}^{\mathrm{OPM}} + C_{22}^{\mathrm{OPM}} + C_{33}^{\mathrm{OPM}} + 2(C_{23}^{\mathrm{OPM}} + C_{31}^{\mathrm{OPM}} + C_{12}^{\mathrm{OPM}})}{9},$$

$$K_R^{\mathrm{MRO}} = \frac{1}{D_{11}^{\mathrm{OPM}} + D_{22}^{\mathrm{OPM}} + D_{33}^{\mathrm{OPM}} + 2(D_{23}^{\mathrm{OPM}} + D_{31}^{\mathrm{OPM}} + D_{12}^{\mathrm{OPM}})},$$

$$G_V^{\mathrm{MRO}} = \frac{C_{11}^{\mathrm{OPM}} + C_{22}^{\mathrm{OPM}} + C_{33}^{\mathrm{OPM}} - (C_{23}^{\mathrm{OPM}} + C_{31}^{\mathrm{OPM}} + C_{12}^{\mathrm{OPM}}) + 3(C_{44}^{\mathrm{OPM}} + C_{55}^{\mathrm{OPM}} + C_{66}^{\mathrm{OPM}})}{15},$$

$$G_R^{\mathrm{MRO}} = \frac{15}{4(D_{11}^{\mathrm{OPM}} + D_{22}^{\mathrm{OPM}} + D_{33}^{\mathrm{OPM}}) - 4(D_{23}^{\mathrm{OPM}} + D_{31}^{\mathrm{OPM}} + D_{12}^{\mathrm{OPM}}) + 3(D_{44}^{\mathrm{OPM}} + D_{55}^{\mathrm{OPM}} + D_{66}^{\mathrm{OPM}})}. \tag{9}$$

Let the generalized plane-strain assumption be adopted and the independence of the MRO microstructure on coordinate 1 be assumed in the two-dimensional case. The invariant integral is

$$[\mathbf{R}]_{ijkr} = \frac{1}{2\pi}\int_0^{2\pi} R_{mnpq}T_{im}T_{jn}T_{kp}T_{rq}\,d\varphi, \tag{10}$$

where

$$\mathbf{T} = \begin{bmatrix} 1 & 0 & 0 \\ 0 & \cos\varphi & \sin\varphi \\ 0 & -\sin\varphi & \cos\varphi \end{bmatrix}. \tag{11}$$

Table 2 summarizes the results in the same way as Table 1; if contributions of $\mathbf{D}^{\mathrm{OPM}}$ are different from those of $\mathbf{C}^{\mathrm{OPM}}$, they are written in brackets. Components 24, 34, 56 and 42, 43, 65 should be included in Table 2, but due to the symmetry of $\mathbf{C}^{\mathrm{OPM}}$ and $\mathbf{D}^{\mathrm{OPM}}$, their contributions to $[\mathbf{C}^{\mathrm{OPM}}]$ and $[\mathbf{D}^{\mathrm{OPM}}]$ cancel. One can conclude from Table 2 that MRO are transversely isotropic and that the specific bounds on in-plane constants can be written as (for the sake of simplicity superscripts ϵ or σ in $\mathbf{C}^{\mathrm{OPM}}$ and $\mathbf{D}^{\mathrm{OPM}}$ components are omitted):

$${}^{\epsilon}k_V^{\mathrm{MRO}} = \frac{C_{22}^{\mathrm{OPM}} + C_{33}^{\mathrm{OPM}} + 2C_{23}^{\mathrm{OPM}}}{4},$$

$${}^{\epsilon}k_R^{\mathrm{MRO}} = \frac{D_{11}^{\mathrm{OPM}}}{D_{11}^{\mathrm{OPM}}(D_{22}^{\mathrm{OPM}} + D_{33}^{\mathrm{OPM}} + 2D_{23}^{\mathrm{OPM}}) - (D_{12}^{\mathrm{OPM}} + D_{13}^{\mathrm{OPM}})^2},$$

$${}^{\epsilon}G_V^{\mathrm{MRO}} = \frac{C_{22}^{\mathrm{OPM}} + C_{33}^{\mathrm{OPM}} - 2C_{23}^{\mathrm{OPM}} + 4C_{44}^{\mathrm{OPM}}}{8},$$

$${}^{\epsilon}G_R^{\mathrm{MRO}} = \frac{2}{D_{22}^{\mathrm{OPM}} + D_{33}^{\mathrm{OPM}} - 2D_{23}^{\mathrm{OPM}} + D_{44}^{\mathrm{OPM}}}. \tag{12}$$

In the case of plane stress the only formal difference is in k_R^{MRO}:

$${}^{\sigma}k_R^{\mathrm{MRO}} = \frac{1}{D_{22}^{\mathrm{OPM}} + D_{33}^{\mathrm{OPM}} + 2D_{23}^{\mathrm{OPM}}}, \tag{13}$$

Table 1 Contributions of $\mathbf{C}^{\mathrm{OPM}}$ and $\mathbf{D}^{\mathrm{OPM}}$ components to $[\mathbf{C}^{\mathrm{OPM}}]$ and $[\mathbf{D}^{\mathrm{OPM}}]$, respectively, in the three-dimensional case

Contributions to $[\mathbf{C}^{\mathrm{OPM}}]$ or $[\mathbf{D}^{\mathrm{OPM}}]$ components	Components from $\mathbf{C}^{\mathrm{OPM}}$				Components from $\mathbf{D}^{\mathrm{OPM}}$			
	ii for i=1,2,3	ij for i≠j, i,j=1,2,3	ii for i=4,5,6	rest	ii for i=1,2,3	ij for i≠j, i,j=1,2,3	ii for i=4,5,6	rest
ii for i=1,2,3	1/5	1/15	4/15	0	1/5	1/15	1/15	0
ij for i≠j, i,j=1,2,3	1/15	2/15	-2/15	0	1/15	2/15	-1/30	0
ii for i=4,5,6	1/15	-1/30	1/5	0	4/15	-2/15	1/5	0
rest	0	0	0	0	0	0	0	0

Table 2 Contributions of $\mathbf{C}^{\mathrm{OPM}}$ and $\mathbf{D}^{\mathrm{OPM}}$ components to $[\mathbf{C}^{\mathrm{OPM}}]$ and $[\mathbf{D}^{\mathrm{OPM}}]$, respectively, in the two-dimensional case

Contributions to $[\mathbf{C}^{\mathrm{OPM}}]$ ($[\mathbf{D}^{\mathrm{OPM}}]$) components	Components from $\mathbf{C}^{\mathrm{OPM}}$ ($\mathbf{D}^{\mathrm{OPM}}$)						
	11	12,13	21,31	55,66	22,33	23,32	44
11	1	0	0	0	0	0	0
12,13	0	1/2	0	0	0	0	0
21,31	0	0	1/2	0	0	0	0
55,66	0	0	0	1/2	0	0	0
22,33	0	0	0	0	3/8	1/8	1/2 (1/8)
23,32	0	0	0	0	1/8	3/8	-1/2 (-1/8)
44	0	0	0	0	1/8 (1/2)	-1/8 (-1/2)	1/2

Downloaded 04 May 2010 to 171.66.16.27. Redistribution subject to ASME license or copyright; see http://www.asme.org/terms/Terms_Use.cfm

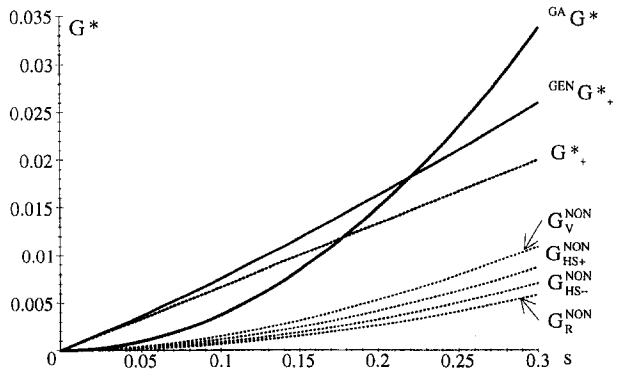


Fig. 4 Comparison of the proposed curve ${}^{GA}G^*$ with the upper bound (linearized form, G_+^*; with nonlinear effect included, ${}^{GEN}G_+^*$) and with the specific MRO bounds if OPM is the nonaligned lattice (G_V^{NON}, G_R^{NON}, G_{HS+}^{NON} and G_{HS-}^{NON})

but, in fact, all bounds differ since the $\mathbf{C}^{OPM}$ and $\mathbf{D}^{OPM}$ components must be also taken in accordance with the assumption of plane stress.

If only some estimate of meso-properties is available (either it is difficult to express OPM properties using the periodicity boundary conditions or only repeated elements are introduced in MRO characterization) it can be easily verified that introducing $\mathbf{C}_{est}^{OPM}$ and $(\mathbf{C}_{est}^{OPM})^{-1}$ with $\mathbf{C}_{est}^{OPM} \geq \mathbf{C}^{OPM}$, specific upper and lower bounds from (9) and (12)–(13) are still upper and lower bounds. This does not hold for $\mathbf{C}_{est}^{OPM} < \mathbf{C}^{OPM}$.

If the related OPM possesses effective cubic or square symmetry, its bulk modulus is invariant under rotation, so $K^{OPM} = K_V^{OPM} = K_R^{OPM} = K^{MRO}$ or $k^{OPM} = k_V^{OPM} = k_R^{OPM} = k^{MRO}$ (in two dimensions this holds for plane stress as well as generalized plane strain). Then in three dimensions,

$$G_V^{MRO} = \frac{2\,{}^1G^{OPM} + 3\,{}^2G^{OPM}}{5}, \quad G_R^{MRO} = \frac{5}{\frac{2}{{}^1G^{OPM}} + \frac{3}{{}^2G^{OPM}}}, \tag{14}$$

and in two dimensions (with the corresponding superscript),

$$G_V^{MRO} = \frac{{}^1G^{OPM} + {}^2G^{OPM}}{2}, \quad G_R^{MRO} = \frac{2}{\frac{1}{{}^1G^{OPM}} + \frac{1}{{}^2G^{OPM}}}. \tag{15}$$

We stated in Section 2 that the distance between the specific bounds depends on the level of OPM anisotropy, which is now expressible as the ratio between ${}^1G^{OPM}$ and ${}^2G^{OPM}$.

4 Specific MRO Hashin-Shtrikman Bounds

In this section the specific MRO Hashin-Shtrikman bounds, as improvements of (15), are derived for two-dimensional media, if the related OPM is effectively square symmetric. Three-dimensional analogs of these bounds, i.e., improvements of (14), can be taken from Hashin and Shtrikman (1962b), provided that single-crystal properties are replaced by OPM properties.

The improvement of (15), based on the Hashin-Shtrikman variational principle, follows the basic steps from Hashin and Shtrikman (1962b). Let us adopt the generalized plane-strain assumption and let U^{MRO} stand for the strain energy density in the given MRO. It is proved in Hashin and Shtrikman (1962a) that U^{MRO} is the stationary value of some functional U^P. In addition to terms related to the MRO, the functional U^P contains characteristics of a reference medium, which is geometrically identical to the MRO. The reference medium is assumed to be homogeneous, transversely isotropic (at the mesolevel in our case). Its properties are unknown and chosen in a way to optimize the bounds, derived later on. The most important term in U^P is the stress polarization tensor $\mathbf{P}$ given by $\mathbf{P} = \boldsymbol{\Sigma}^{MRO} - \mathbf{C}^0 \cdot \mathbf{E}^{MRO}$, where $\mathbf{C}^0$ are effective elastic stiffnesses of the reference medium.

If $\mathbf{C}^{MRO} - \mathbf{C}^0$ is positive (negative) definite, U^{MRO} is the absolute maximum (minimum) of U^P. In the derivation of the bounds a special kind of the stress polarization field $\mathbf{P}$ is chosen, and then, $\mathbf{P}$ can be taken as the only variable in U^P. Consequently, the extreme condition is obtained by taking the variation of U^P with respect to $\mathbf{P}$. Let us denote the polarization field that satisfies this extreme condition by $\mathbf{P}^S$. The stationary value $U^{P,S}$ is

$$U^{P,S} = U^0 + \tfrac{1}{2}[\mathbf{P}^S] \cdot \mathbf{E}^0, \tag{16}$$

where $\mathbf{E}^0$ is the macro-strain in the reference medium. Since the orientational average $[\mathbf{P}^S]$ has to be introduced into (16), not $\mathbf{P}^S$ but $[\mathbf{P}^S]$ can be solved from the extreme condition. Using the same notation B_2 and β as in (Hashin and Shtrikman, 1962b), one obtains

$$[\mathbf{P}^S] = \frac{2B_2}{1 + 2\beta B_2}\,\mathbf{E}^0. \tag{17}$$

The constant β is determined in (Hashin, 1965) in terms of the (not yet specified) moduli ${}^\epsilon k^0$ and ${}^\epsilon G^0$, but obviously ${}^\epsilon k^0 = {}^\epsilon k^{OPM}$. Thus

$$\beta({}^\epsilon k^{OPM}, {}^\epsilon G^0) = -\frac{{}^\epsilon k^{OPM} + 2\,{}^\epsilon G^0}{4\,{}^\epsilon G^0({}^\epsilon k^{OPM} + {}^\epsilon G^0)}. \tag{18}$$

B_2 is a component with subscript 44 of the orientational average of matrix representation of a tensor $((\mathbf{C}^{OPM} - \mathbf{C}^0)^{-1} - \beta\mathbf{I})^{-1}$, where $\mathbf{I}$ is the identity tensor. It is given by

$$B_2 = \frac{1}{\frac{2}{{}^{\epsilon,1}G^{OPM} - {}^\epsilon G^0} - 4\beta({}^\epsilon k^{OPM}, {}^\epsilon G^0)} + \frac{1}{\frac{2}{{}^{\epsilon,2}G^{OPM} - {}^\epsilon G^0} - 4\beta({}^\epsilon k^{OPM}, {}^\epsilon G^0)}. \tag{19}$$

The specific bounds on ${}^\epsilon G^{MRO}$ can then be expressed from the following expression:

$${}^\epsilon G^0 + \frac{B_2}{1 + 2B_2\beta({}^\epsilon k^{OPM}, {}^\epsilon G^0)}. \tag{20}$$

If $\mathbf{C}^{OPM} - \mathbf{C}^0$ is positive definite (${}^{\epsilon,1}G^{OPM} > {}^\epsilon G^0$ and ${}^{\epsilon,2}G^{OPM} > {}^\epsilon G^0$), (20) yields the lower bound; the upper bound is obtained when $\mathbf{C}^{OPM} - \mathbf{C}^0$ is negative definite (${}^{\epsilon,1}G^{OPM} < {}^\epsilon G^0$ and ${}^{\epsilon,2}G^{OPM} < {}^\epsilon G^0$). Since (20) is a monotonically increasing function of ${}^\epsilon G^0$, the best lower (upper) bound is obtained for the highest (lowest) possible ${}^\epsilon G^0$ ensuring that $\mathbf{C}^{OPM} - \mathbf{C}^0$ is still positive definite (negative definite). Let, e.g., ${}^{\epsilon,1}G^{OPM} > {}^{\epsilon,2}G^{OPM}$. Consequently (+ and − stand for the upper and the lower bounds, respectively, HS refers to Hashin-Shtrikman bounds):

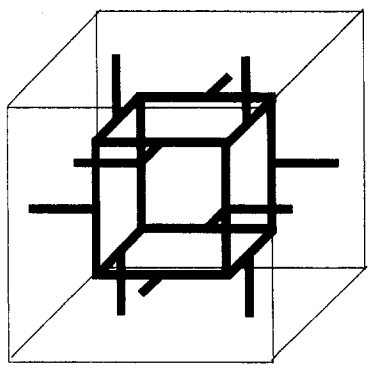


Fig. 5 A basic cell of the nonaligned lattice

Downloaded 04 May 2010 to 171.66.16.27. Redistribution subject to ASME license or copyright; see http://www.asme.org/terms/Terms_Use.cfm

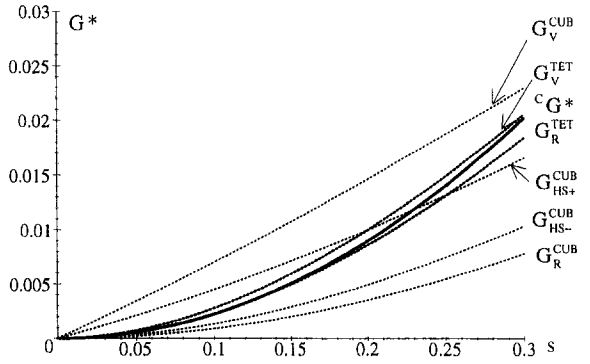


Fig. 6 Comparison of the specific MRO bounds of the tetrahedral lattice (G_V^{TET} and G_R^{TET}) and the specific MRO bounds if OPM is the regular cubic lattice (G_V^{CUB}, G_R^{CUB}, G_{HS+}^{CUB}, and G_{HS-}^{CUB}) with the proposed curve $^cG^*$ (full line)

$$^{\epsilon}G_{HS+}^{MRO} = {}^{\epsilon,1}G^{OPM} + \frac{1}{2\left(\frac{1}{{}^{\epsilon,2}G^{OPM} - {}^{\epsilon,1}G^{OPM}} - \beta({}^{\epsilon}k^{OPM}, {}^{\epsilon,1}G^{OPM})\right)} \quad \text{and}$$

$$^{\epsilon}G_{HS-}^{MRO} = {}^{\epsilon,2}G^{OPM} + \frac{1}{2\left(\frac{1}{{}^{\epsilon,1}G^{OPM} - {}^{\epsilon,2}G^{OPM}} - \beta({}^{\epsilon}k^{OPM}, {}^{\epsilon,2}G^{OPM})\right)}. \quad (21)$$

The case when ${}^{\epsilon,1}G^{OPM} < {}^{\epsilon,2}G^{OPM}$ can be treated similarly, yielding the same results, only + and − have to be exchanged. The bounds under the plane-stress assumption are formally equal, only the plane-strain shear and bulk moduli are replaced by the plane-stress ones.

In the three-dimensional case when, e.g., ${}^1G^{OPM} > {}^2G^{OPM}$, it holds

$$G_{HS+}^{MRO} = {}^1G^{OPM} + \frac{3}{\frac{5}{{}^2G^{OPM} - {}^1G^{OPM}} - 4\beta(K^{OPM}, {}^1G^{OPM})} \quad \text{and}$$

$$G_{HS-}^{MRO} = {}^2G^{OPM} + \frac{2}{\frac{5}{{}^1G^{OPM} - {}^2G^{OPM}} - 6\beta(K^{OPM}, {}^2G^{OPM})}, \quad (22)$$

where $\beta(K^{OPM}, G^0)$ is given by

$$\beta(K^{OPM}, G^0) = -\frac{3(K^{OPM} + 2G^0)}{5G^0(3K^{OPM} + 4G^0)}. \quad (23)$$

5 Examples and Comparisons

Let us apply the above theory to foams. We restrict ourselves to open-cell foams, since then explicit analytical results of OPM properties can be simply obtained, see (Dimitrovová, 1997).

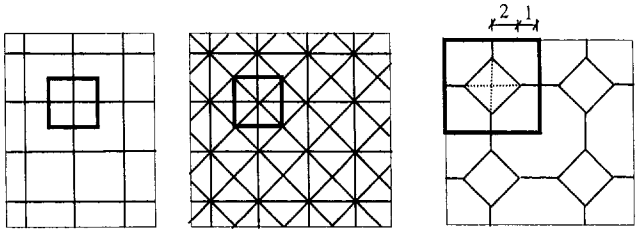


Fig. 7 The regular square, the square with two obliques, and the diamond lattices

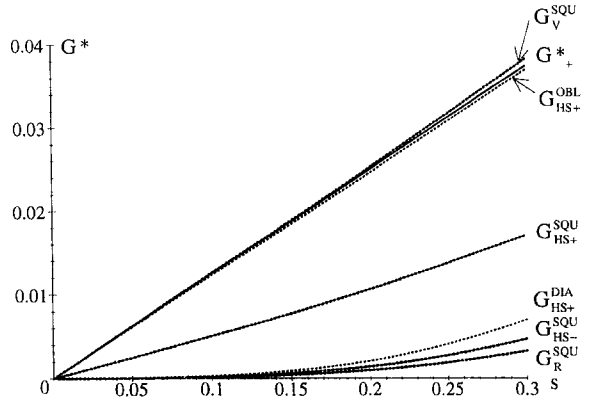


Fig. 8 Comparison of the specific MRO bounds related to the regular square lattice (G_V^{SQU}, G_R^{SQU}, G_{HS+}^{SQU}, and G_{HS-}^{SQU}), the square lattice with two obliques (G_{HS+}^{OBL}) and the diamond lattice (G_{HS+}^{DIA}) with the linearized upper bound G_+^* (full line)

Mainly OPM with cubic (square in two dimensions) effective symmetry are assumed and the struts composing the foams are taken with constant square cross-sectional areas. In two-dimensional cases the plane stress assumption is adopted. All curves in the graphs are plotted as functions of the relative density s and in a dimensionless form (divided by the Young's modulus of the solid phase), however, for the sake of simplicity the notation from the previous sections is not altered.

The first comments are related to the proposed function for dimensionless effective shear modulus G^* of isotropic open-cell foams from (Gibson and Ashby, 1988), ${}^{GA}G^* = 3s^2/8$. This function is compared in Fig. 4 with the linearized upper bound $G_+^* = s/15$ of open-cell foams derived in (Dimitrovová, 1997) and with four specific bounds (superscript NON) related to MRO with OPM as the nonaligned lattice (Fig. 5). The choice of the basic cell was inspired by Gibson and Ashby (1988), who did not use it as a periodic cell but rather as a conceptual cell expressing the bending response of open-cell foams. The specific bounds G_{HS+}^{NON} and G_{HS-}^{NON} are quite close, allowing a good estimate of an actual MRO response. The response is soft and so this particular MRO could be used as a model for very soft open-cell foams. It is seen that, although ${}^{GA}G^*$ is fitted to the experimental data, it is above G_+^* for higher s (69 percent for $s = 0.3$). To explain this fact: first, it should be pointed out that G_+^* does not include the bending contribution (it was shown in (Dimitrovová, 1997) that it is small and it is not well defined since it varies for different optimal media) and that s in G_+^* is expressed from a simplified relation. For the optimal medium derived in (Dimitrovová, 1997) and for $s = 0.3$ the increase in G_+^* due to the bending contribution is five percent (it is little different for another cross-sectional shape) and the increase due to the higher-order terms in s is 22 percent; the curve with both nonlinear effects, ${}^{GEN}G_+^*$, is also included in Fig. 4. Second, recent experimental data for G^* in (Gibson and Ashby, 1988) are available only for $s \in [0.01, 0.03]$. The extension of ${}^{GA}G^*$ from low values of s (where it reflects only the bending response) to high values of s neglects the axial contribution, which now becomes more important. It would make the curve representing G^* more straight and lower, see (Dimitrovová, 1997). Moreover, for high values of s, ${}^{GA}G^*$ coincides with the data for closed-cell foams, which are generally stiffer. As regards the other data presented in (Gibson and Ashby, 1988) as data of open-cell foams, G^* could be calculated from the data of Young's modulus and Poisson's ratio obtained by Gent and Thomas (1959). Such values follow the curve ${}^{GA}G^*$. Gent and Thomas' data are for $s \in [0.1, 1]$. Close to $s = 1$, when the specimens are not any more cellular, the significance of the data is questionable in our context. Also, no photographs are shown in Gent and Thomas (1959), the specimens for s close to 0.3 may be partly closed-cell foams, since the data basically coincide with other data of closed-cell foams.

Downloaded 04 May 2010 to 171.66.16.27. Redistribution subject to ASME license or copyright; see http://www.asme.org/terms/Terms_Use.cfm

Other comments are related to the paper by Warren and Kraynik (1988). The first example there, the tetrahedral lattice (superscript TET), is MRO composed of repeated elements (Fig. 3). Meso-properties are calculated (for an arbitrarily rotated element) under uniform boundary strain applied at the center of the strut cross sections and under no restriction on cross-sectional rotations. Repeated elements are self-equilibrated, but it is difficult to justify the equilibrium between neighboring ones. Meso-properties thus correspond to some upper estimate. The final result in (Warren and Kraynik, 1988) is in fact G_V^{TET}, which should not be presented as the actual response. Also the calculation could be reduced by calculating the meso-properties with respect to some fixed coordinates and then introducing them into (9). $\mathbf{C}^{\mathrm{TET}}$ does not possess cubic symmetry, thus specific bounds from (22) are not applicable, but $K_V^{\mathrm{TET}} = K_R^{\mathrm{TET}}$. Two specific bounds G_V^{TET} and G_R^{TET} are compared in Fig. 6 with a function for open-cell foams with mainly bending response proposed in (Christensen, 1994), ${}^{c}G^* = 9s^2/40$, and with four specific bounds (superscript CUB) related to the second example in (Warren and Kraynik, 1988), where OPM is the regular cubic lattice (Fig. 2). Boundary conditions of the kind described above incidentally coincide with the periodicity boundary conditions, however, again only G_V^{CUB} (its linearization coincides with G_+^*) is presented in (Warren and Kraynik, 1988). It is seen from Fig. 6 that G_V^{TET} and G_R^{TET} are quite close and that ${}^{c}G^*$ (which was also fitted to experimental data) shows an excellent agreement with them. It can be thus concluded that the tetrahedral lattice is a very good model for an open-cell foam representation. The distance between the other four specific bounds is very large ($G_{\mathrm{HS}+}^{\mathrm{CUB}}$ and $G_{\mathrm{HS}-}^{\mathrm{CUB}}$ provide a significant improvement of G_V^{CUB} and G_R^{CUB}), since ${}^{1}G^{\mathrm{OPM}}$ expresses only axial response, while ${}^{2}G^{\mathrm{OPM}}$ expresses only bending response. In the specific bounds the axial response becomes the essential one, since the curves are almost straight. It is seen that in this case the estimate of the actual response by G_V^{CUB} could lead to a significant discrepancy. Thus a proper understanding of the results is very important.

To conclude the comparative remarks, we also show some two-dimensional examples in order to justify the specific bounds (21) proved in Section 4. Related OPM are the following: the regular square, the square with two obliques and the diamond lattices (Fig. 7; basic cells are marked by bold lines). In Fig. 8 the specific bounds (superscripts SQU, OBL, and DIA) are compared with the linearized upper bound $G_+^* = s/8$ (Dimitrovová and Faria, 1999). Since the square with two obliques (strong medium) and the diamond lattice (soft medium) are "almost" effectively isotropic, the specific bounds practically coincide and in Fig. 8 only $G_{\mathrm{HS}+}^{\mathrm{OBL}}$ and $G_{\mathrm{HS}+}^{\mathrm{DIA}}$ are plotted. The regular square lattice possesses a high level of anisotropy, which justifies the distances between the four specific bounds (Fig. 8). As was found for the three-dimensional analog of this medium, G_V^{SQU} in its linearized form coincides with G_+^*.

6 Conclusions

In this paper a simple and practical way of expressing effective elastic constants of MRO in the form of specific bounds is proposed. The distances between the specific bounds depend on the level of the OPM anisotropy. Several examples of open-cell foams where the specific bounds can be expressed in an explicit analytical form were shown. From the three-dimensional examples we conclude that: (i) the proposed function in Gibson and Ashby (1988) should reflect the axial response of open-cell foams for higher relative densities and should be slightly lower there; (ii) the basic cell of the nonaligned lattice taken as an original cell forms a very soft MRO medium, which is not convenient to use as a general characterization; (iii) the tetrahedral lattice, with very close specific bounds (permitting a good estimate of the actual response) provides a very good model for open-cell foam characterization; (iv) MRO with OPM with a high level of anisotropy cannot be characterized by the specific Voigt bound. This is also the reason why we provided improvements of specific Voigt and Reuss bounds in two-dimensional case, for MRO with effectively square symmetric OPM, which is a common property of many two-dimensional media. As an additional result, related to Dimitrovová (1997) and Dimitrovová and Faria (1999), we found two more G^*-optimal media, namely, MRO with OPM as the regular cubic or square lattice.

The simplifying assumptions stated in the beginning of Section 2 are not inevitable for the proposed methodology; thus an extension of the methodology to more general composites can be developed.

References

Avellaneda, M., and Milton, G. W., 1989, "Optimal Bounds on the Effective Bulk Modulus of Polycrystals," *SIAM Journal of Applied Mathematics,* Vol. 49, pp. 824–837.

Bakhvalov, N., and Panasenko, G., 1989, *Homogenization: Averaging Processes in Periodic Media,* Kluwer, Dordrecht, The Netherlands.

Bensoussan, A., Lions, J. L., and Papanicolau, G., 1978, *Asymptotic Analysis for Periodic Structures,* North-Holland, Amsterdam.

Christensen, R. M., 1994, "Heterogeneous Material Mechanics at Various Scales," ASME *Applied Mechanics Reviews,* Vol. 47, pp. S20–S33.

Dimitrovová, Z., 1997, "Mechanical Properties of Cellular Materials," Ph.D. dissertation, Instituto Superior Técnico, Lisbon, Portugal.

Dimitrovová, Z., and Faria, L., 1999, "New Methodology to Establish Bounds on Effective Properties of Cellular Solids," *Mechanics of Composite Materials and Structures,* Vol. 6, pp. 331–346.

Duvaut, G., 1976, "Homogeneization et Materiaux Composite," *Theoretical and Applied Mechanics,* ed. P. Ciarlet and M. Rouseau, eds. North-Holland, Amsterdam.

Ferrari, M., and Johnson, G. C., 1988, "The Equilibrium Properties of a 6 mm Polycrystal Exhibiting Transverse Isotropy," *Journal of Applied Physics,* Vol. 63, pp. 4460–4468.

Gent, A. N., and Thomas, A. G., 1959, "The Deformation of Foamed Elastic Materials," *Journal of Applied Polymer Science,* Vol. 1, pp. 107–113.

Gibson, L. J., and Ashby, M. F., 1988, *Cellular Solids. Structure and Properties,* Pergamon Press, Oxford.

Guedes, J. M., 1990, "Nonlinear Computational Models for Composite Materials Using Homogenization," Ph.D. dissertation, The University of Michigan, Ann Arbor, MI.

Hashin, Z., 1965, "On Elastic Behavior of Fibre Reinforced Materials of Arbitrary Transverse Phase Geometry," *Journal of the Mechanics and Physics of Solids,* Vol. 13, pp. 119–134.

Hashin, Z., 1970, "Theory of Composite Materials," *Mechanics of Composite Materials,* F. W. Wendt, H. Liebowitz, and N. Perrone, eds., Pergamon Press, Oxford.

Hashin, Z., 1983, "Analysis of Composite Materials—A Survey," ASME JOURNAL OF APPLIED MECHANICS, Vol. 50, pp. 481–505.

Hashin, Z., and Shtrikman, S., 1962a, "On Some Variational Principles in Anisotropic and Nonhomogeneous Elasticity," *Journal of the Mechanics and Physics of Solids,* Vol. 10, pp. 335–342.

Hashin, Z., and Shtrikman, S., 1962b, "A Variational Approach to the Theory of the Elastic Behavior of Polycrystals," *Journal of the Mechanics and Physics of Solids,* Vol. 10, pp. 343–352.

Hashin, Z., and Shtrikman, S., 1963, "A Variational Approach to the Theory of the Elastic Behavior of Multiphase Materials," *Journal of the Mechanics and Physics of Solids,* Vol. 11, pp. 127–140.

Lagzdins, A., Tamuzs, V., Teters, G., and Kregers, A., 1992, *Orientational Averaging in Mechanics of Solids,* Longman Group, London.

Lekhnitskii, S. G., 1981, *Theory of Elasticity of an Anisotropic Body,* Mir, Moscow.

Lu, B., and Torquato, S., 1990, "*n*-Point Probability Functions for a Lattice Model of Heterogeneous Media," *Physical Review B,* Vol. 42, pp. 4453–4459.

Meister, R., and Peselnick, L., 1966, "Variational Method of Determining Effective Moduli of Polycrystals with Tetragonal Symmetry," *Journal of Applied Physics,* Vol. 37, pp. 4121–4125.

Nemat-Nasser, S., and Hori, M., 1993, *Micromechanics: Overall Properties of Heterogeneous Materials* (North-Holland Series in Applied Mathematics and Mechanics), Vol. 37, ed. J. D. Achenbach, B. Budiansky, H. A. Lauwerier, P. G. Saffman, L. Van Wijngaarden, and J. R. Willis, eds., North-Holland Amsterdam.

Ostoja-Starzewski, M., 1993, "Micromechanics as a Basis of Stochastic Finite Elements and Differences: An Overview," ASME *Applied Mechanics Reviews,* Vol. 46, pp. S136–S147.

Ostoja-Starzewski, M., 1994, "Micromechanics as a Basis of Continuum Random Fields," ASME *Applied Mechanics Reviews,* Vol. 47, pp. S221–S230.

Ostoja-Starzewski, M., 1998, "Random Field Models of Heterogeneous Materials," *International Journal of Solids and Structures,* Vol. 35, pp. 2429–2455.

Peselnick, L., and Meister, R., 1965, "Variational Method of Determining Effective Moduli of Polycrystals: (A) Hexagonal Symetry, (B) Trigonal Symmetry," *Journal of Applied Physics,* Vol. 36, pp. 2879–2884.

Schulgasser, K., 1983, "Sphere Assemblage Model for Polycrystals and Symmetric Materials," *Journal of Applied Physics,* Vol. 54, pp. 1380–1382.

Suquet, P. M., 1985a, "Elements of Homogenization for Inelastic Solid Mechanics," *Homogenization Techniques for Composite Media,* Proceedings, Udine, Italy, E. Sanchez-Palencia, and A. Zaoui, eds., Lecture Notes in Physics, 272, Springer-Verlag, New York, pp. 193–278.

Downloaded 04 May 2010 to 171.66.16.27. Redistribution subject to ASME license or copyright; see http://www.asme.org/terms/Terms_Use.cfm

Suquet, P. M., 1985b, "Local and Global Aspects in the Mathematical Theory of Plasticity," *Plasticity Today—Modeling Methods and Applications,* A. Sawczuk, and G. Bianchi, Elsevier, London, pp. 279–310.

Torquato, S., 1991, "Random Heterogeneous Media: Microstructure and Improved Bounds on Effective Properties," ASME *Applied Mechanics Reviews,* Vol. 44, pp. 37–76.

Torquato, S., 1994, "Macroscopic Behavior of Random Media from the Microstructure," ASME *Applied Mechanics Reviews,* Vol. 47, pp. S29–S37.

Torquato, S., 1998, "Morphology and Effective Properties of Disordered Heterogeneous Media," *International Journal of Solids and Structures,* Vol. 35, pp. 2385–2406.

Torquato, S., and Stell, G., 1982, "Microstructure of Two-Phase Random Media. I. The *n*-Point Probability Functions," *Journal of Chemical Physics,* Vol. 77, pp. 2071–2077.

Warren, W. E., and Kraynik, A. M., 1988, "The Linear Elastic Properties of Open-Cell Foams," ASME JOURNAL OF APPLIED MECHANICS, Vol. 55, pp. 341–346.

Watt, J. P., 1979, "Hashin-Shtrikman Bounds on the Effective Elastic Moduli of Polycrystals With Orthorhombic Symmetry," *Journal of Applied Physics,* Vol. 50, pp. 6290–6295.

Watt, J. P., 1980, "Hashin-Shtrikman Bounds on the Effective Elastic Moduli of Polycrystals with Monoclinic Symmetry," *Journal of Applied Physics,* Vol. 51, pp. 1520–1524.

Watt, J. P., and Peselnick, L., 1980, "Clarification of the Hashin-Shtrikman Bounds on the Effective Elastic Moduli of Polycrystals with Hexagonal, Trigonal, and Tetragonal Symmetries," *Journal of Applied Physics,* Vol. 51, pp. 1525–1531.

Werner, E., Siegmund, T., Weinhandl, H., and Fischer, F. D., 1994, "Properties of Random Polycrystalline Two-Phase Materials," ASME *Applied Mechanics Reviews,* Vol. 47, pp. S231–S240.

Downloaded 04 May 2010 to 171.66.16.27. Redistribution subject to ASME license or copyright; see http://www.asme.org/terms/Terms_Use.cfm

T. A. Godfrey
Research Engineer,
U.S. Army Soldier and Biological
Chemical Command,
Natick Soldier Center,
Mail Stop AMSSB-RSS-M,
Natick, MA 01760-5020
e-mail: tgodfrey@natick-emh2.army.mil
Mem. ASME

J. N. Rossettos
Professor,
Department of Mechanical, Industrial
and Manufacturing Engineering,
Northeastern University,
Boston, MA 02115
Fellow ASME

The Onset of Tear Propagation at Slits in Stressed Uncoated Plain Weave Fabrics

A simple micromechanical model is developed to predict the onset of tear propagation at slit-like damage sites (i.e., a series of consecutive aligned yarn breaks) in biaxially stressed plain weave fabrics under increasing loading. A crucial aspect of the model is the treatment of the frictional slip of yarns near the damage site. Although the actual configuration of slipping regions is complex, the onset of tear propagation in large slits (i.e., more than, say, 35 breaks) is dominated by slip occurring on the first few intact yarns adjacent to the breaks. The assumptions in the mathematical model were motivated by both experimental observations and calculations for key configurations. Analytical results obtained for this simple model exhibit good agreement with experimental results, which are presented for a variety of fabrics with initial slits of 35 and 45 breaks.

Introduction

Bi-axially stressed woven fabrics are used in inflatable and tension structures, parachute canopies, and, increasingly, in geotextile-reinforced geotechnical structures. In end-use, fabrics are often accidentally cut or punctured by a sharp edge or by impact with projectiles. Under sufficiently high remote tension, the local damage provides the starting point for a rapidly propagating tear that results in catastrophic failure of the fabric structure. The problem was recognized in connection with early fabric-covered military aircraft and was addressed by investigators empirically using the *wounded tensile test* (Harrison, 1960). Although the phenomenon has long been known, it has not been the subject of intense fundamental study (i.e., involving multiple investigators over a period of years) and, therefore, progress has been modest.

Installed geotextiles contain holes created by accidental damage, e.g., during compaction of the backfill (Troost and Ploeg, 1990), as well as purposefully made holes to incorporate specific design features of the project. The growth of tears arising from one of these damage sites can lead to sudden failure of the geotechnical structure (Koerner et al., 1987). Given the impact the proper functioning of these structures (e.g., municipal landfills, hazardous waste landfills, levees, etc.) has on the safety and health of local human populations, study of the tear propagation phenomenon is now extremely relevant to the national interest.

Hedgepeth (1961) provided the first micromechanical analysis of a damaged filamentary structure. His analysis, based on shear lag theory, has been applied to fiber/matrix composites, where the matrix transfers the load from broken to unbroken fibers by means of shear. The original work has been the basis of numerous extensions and modifications (see review by Rossettos and Godfrey, 1998). Hedgepeth regarded his shear lag model, where the fibers carry axial loads and the matrix is assumed to carry only shear, to apply to coated woven fabrics as well, where the coating transfers shear between yarns. In bi-axially stressed *uncoated* woven fabrics, load transfer between yarns of a given yarn set is accomplished by rotation of the tensioned crossing yarns in the fabric plane. In this regard, the fabric acts mechanically like a remotely stressed plane pin-jointed net and the shear stiffness is stress-induced, rather than an intrinsic property of the fabric. This stress-stiffening effect has been noted by Christoffersen (1980) and by Topping (1961). The ultimate transfer of load to a given yarn arises through frictional contact between warp and fill yarns at the crossover point.

Christoffersen (1980) derived a general theory for a continuum model of the fabric as a deformable orthotropic plate that allows for elastic stretching along two orthotropic directions and is capable of stress-free deformation in shear. He applied his general theory to the problem of an isolated slit and demonstrated that harmonic problems (Laplace's equation) arise when yarn rotations are small and normal stress is constant in one of the orthotropic directions, as in the case of for the slit interrupting only a single yarn system. It is assumed that sufficient friction or other means prevents yarn slippage at crossover points. This latter assumption is appropriate for coated fabrics, but not for most uncoated fabrics, where yarn slip appears to have an important toughening effect. To capture the frictional slip of discrete yarns, a micromechanical approach is necessary.

The experimental results of Abbott and Skelton (1972) suggest that yarn slip at crossover points may significantly toughen slit-damaged woven fabrics against tear propagation. Abbott and Skelton considered slit damage introduced suddenly into uniaxially loaded fabrics, measuring the critical tension at which tear propagation from the initial slit occurs. In tests of otherwise identical coated and uncoated fabrics, critical tensions for the uncoated specimens were higher by as much as a factor of two. Popova and Iliev (1993) remark on the significant yarn slippage exhibited in experiments on uncoated slitted fabric specimens under uniaxial loading as compared to the behavior of the same fabrics after application of an elastomeric coating.

Godfrey and Rossettos (1998) have introduced a micromechanical modeling approach that addresses the tendency of individual yarns to slip near the damage region. They identify two types of frictional slip that occur near the damage site: type 1 involves slip occurring on yarns broken in the initial slit, and type 2 involves slip occurring on intact yarns in the damage growth path near the tip of the slit. Tear propagation is assumed to occur when the maximum yarn tension in the intact yarn adjacent to the last yarn break approaches the yarn breaking load. Although the basic governing equations are simple, implementing the approach to address a damage configuration involving a practical number of breaks involves considerable difficulty in defining regions on each yarn where slip is occurring. Nonetheless, preliminary experimental results (Godfrey and Rossettos, 1999) demonstrate, through

Contributed by the Applied Mechanics Division of THE AMERICAN SOCIETY OF MECHANICAL ENGINEERS for publication in the ASME JOURNAL OF APPLIED MECHANICS.
Discussion on the paper should be addressed to the Technical Editor, Professor Lewis T. Wheeler, Department of Mechanical Engineering, University of Houston, Houston, TX 77204-4792, and will be accepted until four months after final publication of the paper itself in the ASME JOURNAL OF APPLIED MECHANICS.
Manuscript received by the ASME Applied Mechanics Division, Dec. 2, 1998; final revision, May 11, 1999. Associate Technical Editor: M.-J. Pindera.

 Copyright © 1999 by ASME

Downloaded 04 May 2010 to 171.66.16.27. Redistribution subject to ASME license or copyright; see http://www.asme.org/terms/Terms_Use.cfm

correlation with dimensionless parameters in the model, that the present approach captures the essential physics of the phenomenon.

In this work, we adopt a micromechanical modeling approach (Godfrey and Rossettos, 1998) for considering large slits where type 2 slip is assumed to occur on the first few intact yarns at the tip of the slit. For clarity of exposition, some of the original development given in Godfrey and Rossettos (1998) will be summarized here. It will be shown that type 2 slip occurring on the first few intact yarns exerts a dominant influence over the onset of tear propagation in fabrics containing large slits. Experimental results for the onset of tear propagation at 35 and 45 break slits in a variety of biaxially stressed plain weave fabrics are presented and exhibit good agreement with the analytical predictions.

Micromechanical Model

In this section, we summarize the main features of a micromechanics-based mathematical model originally developed in more detail by Godfrey and Rossettos (1998). Consider a plain weave fabric with damage consisting of a slit-like series of consecutive yarn breaks arrayed parallel to the x_2-coordinate direction at $x_1 = 0$, where the x_1x_2-coordinate system is aligned with the yarn directions. The microstructural geometry and nomenclature pertaining to the damaged fabric is indicated in Fig. 1. The slit interrupts only number one (# 1) yarns, referring to yarns parallel to the x_1 and x_2-directions as # 1 and number two (# 2) yarns, respectively. The plain weave unit cell dimensions are y_{01} along the x_1-axis (the spacing of the # 2 yarns) and y_{02} along the x_2-axis (the spacing of the # 1 yarns). Remote biaxial membrane stresses (i.e., having dimensions of force/length) are applied to the fabric such that the stress in the x_2 direction, T_2, is held constant while the stress in the x_1 direction, T_1, is increased quasi-statically. The global configuration of the damage and remote loading is shown in Fig. 2. At the microstructural level, the membrane stresses are viewed as individual remote yarn tensions such that # 2 yarns are under constant remote tensions F_2^* and # 1 yarns are under quasistatically increasing remote tensions p (i.e., $T_1 = p/y_{02}$, $T_2 = F_2^*/y_{01}$). As x_1-direction loading increases, the # 1 yarns exhibit displacements in the x_1-direction and the # 2 yarns exhibit x_1-direction displacements and small rotations in the fabric plane (Fig. 3). With continued increasing loading, the # 1 and # 2 yarns may be observed to slip at crossover points in a region near the

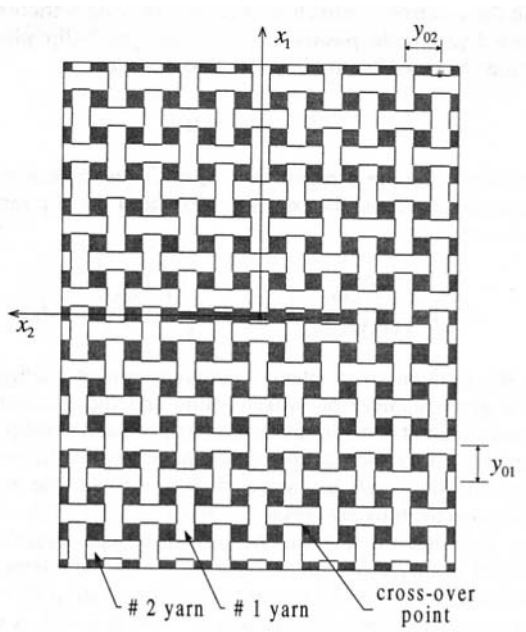


Fig. 1 Microstructural geometry of fabric containing five break slit-like damage

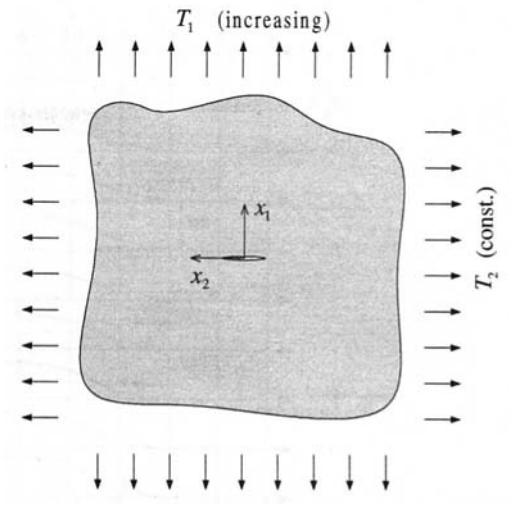


Fig. 2 Configuration of biaxial remote stresses on damaged fabric

breaks (Fig. 4). When p reaches a critical value p_c, the initial slit damage propagates through rupture of the intact # 1 yarns on either side of the breaks roughly along the line $x_1 = 0$.

Appropriate differential equations that describe the equilibrium of yarns in regions where slip at crossover points occurs, and in the region where slip does not occur, can easily be derived (Godfrey and Rossettos, 1998). For instance, in the region where crossover point slip does not occur, equilibrium of the # 1 yarns can be derived by taking into account the load transfer to the # 1 yarns that occurs due to the rotated tensioned # 2 yarns in the fabric plane. For small rotations, the angles are indicated in Fig. 3(*b*). The component of the # 2 yarn tension along the # 1 yarn can then be written. Introduce u_n^j as the x_1-displacement of the jth crossover point on the nth # 1 yarn, where the reference state for displacements are the positions of points on an otherwise identical stressed fabric *without damage*. In the development of the mathematical model, analytical and experimental curves (Godfrey and Rossettos, 1998) of yarn force versus strain in the x_1-direction for Kevlar® and Dacron® fabrics have shown good agreement, thereby lending validity to the crimp interchange mechanics used in the model. For sufficiently high values of the loading, p, the # 1 yarns are assumed to be in a nearly straightened out condition, and display an effective constant axial stiffness property $(EA)_{\text{eff}}$ having the dimension of force. Rotation of the # 2 yarns is represented by relative displacements at points on adjacent # 1 yarns. Considering the crossover point unit cell as a free body, Fig. 3(*b*), the component of force in the x_1-direction acting on the # 2 yarn entry and exit boundaries will be $F_2^*(u_{n-1}^j - u_n^j)/y_{02}$ and $-F_2^*(u_n^j - u_{n+1}^j)/y_{02}$. Therefore, equilibrium of the jth crossover unit cell in the x_1-direction is written as

$$F_{1n}^{j+1} - F_{1n}^j + \frac{u_{n-1}^j - 2u_n^j + u_{n+1}^j}{y_{02}} F_2^* = 0. \tag{1}$$

Replace the jth and $j+1$th F_{1n} terms with differences of crossover point displacements $(EA)_{\text{eff}}(u_n^j - u_n^{j-1})/y_{01}$ and $(EA)_{\text{eff}}(u_n^{j+1} - u_n^j)/y_{01}$, respectively. These terms are strains on either side of crossover point j multiplied by $(EA)_{\text{eff}}$. Equation (1) becomes

$$\frac{(EA)_{\text{eff}}}{y_{01}}(u_n^{j-1} - 2u_n^j + u_n^{j+1}) + \frac{F_2^*}{y_{02}}(u_{n-1}^j - 2u_n^j + u_{n+1}^j) = 0. \tag{2}$$

Smearing out the interaction with the # 2 yarns and regarding u_n as a continuous function of position x_1, this equilibrium equation, for nonslipping yarns, can then be written as

Downloaded 04 May 2010 to 171.66.16.27. Redistribution subject to ASME license or copyright; see http://www.asme.org/terms/Terms_Use.cfm

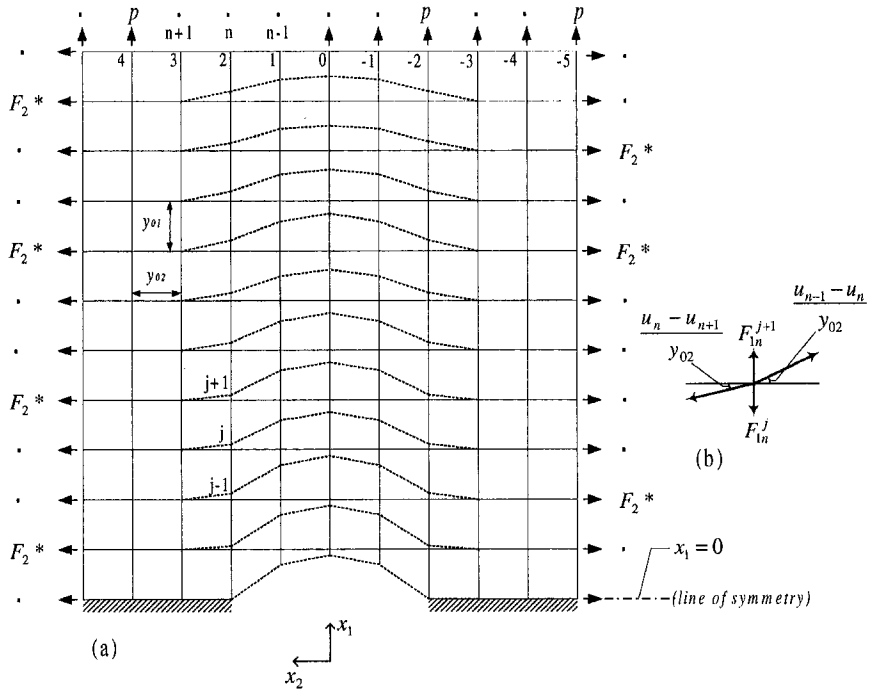


Fig. 3 (*a*) Geometry of damaged fabric indicating the elastic (nonslipping) deformation. Highly schematic, only yarn centerlines are shown. Breaks in # 1 yarns, dashed lines represent deformed # 2 yarns. (*b*) Equilibrium of the *j*th crossover point unit cell.

$$\frac{d^2u_n}{dx_1^2} + \frac{F_2^*}{(EA)_{\text{eff}}y_{01}y_{02}}(u_{n-1} - 2u_n + u_{n+1}) = 0. \tag{3}$$

Equation (3) is written in dimensionless form as

$$U_n'' + U_{n-1} - 2U_n + U_{n+1} = 0 \tag{4}$$

using the following nondimensionalization:

$$x_1 = \sqrt{\frac{(EA)_{\text{eff}}y_{01}y_{02}}{F_2^*}}\,\xi, \quad u_n = p\sqrt{\frac{y_{01}y_{02}}{(EA)_{\text{eff}}F_2^*}}\,U_n \tag{5}$$

where primes denote differentiation with respect to ξ.

Crossover point slip is assumed to occur in a region near the breaks, $0 < x_1 < l_n$, where l_n denotes the extent of the slip region on the nth # 1 yarn. In the slipping region, the yarn is assumed to experience a periodic array of frictional tractions f of constant value (simple slip assumption (Godfrey and Rossettos, 1998)), the period corresponding to the crossover point spacing. The equilibrium equation can be written as

$$\frac{d^2u_n}{dx_1^2} \mp \frac{f}{(EA)_{\text{eff}}y_{01}} = 0 \tag{6}$$

where the minus sign applies for slip of a broken yarn and the plus sign applies for slip occurring on an intact yarn. It is noted that yarns that are broken (# 1 yarns) will slip in the positive x_1-direction relative to the crossing # 2 yarns (Fig. 4), thereby incurring a friction force in the negative x_1-direction (type 1 slip: minus sign). In the slip that occurs on an intact yarn, the # 2 yarns slip in the positive x_1-direction (Fig. 4), applying a friction force on the # 1 yarn in the positive x_1-direction (type 2 slip: plus sign). Equation (6) is written in dimensionless form as

$$U_n'' \mp \hat{f} = 0 \tag{7}$$

where slip occurs in a region $0 < \xi < \hat{l}_n$ and a dimensionless loading parameter and dimensionless extent of the slip region are introduced:

$$f = p\sqrt{\frac{F_2^*y_{01}}{(EA)_{\text{eff}}y_{02}}}\,\hat{f}, \quad l_n = \sqrt{\frac{(EA)_{\text{eff}}y_{01}y_{02}}{F_2^*}}\,\hat{l}_n. \tag{8}$$

In the solution of problems involving various configurations with a given number of broken yarns and the associated slip regions, continuity conditions between the slip and nonslip regions are applied, in addition to appropriate boundary conditions. Since the broken yarn ends are stress free at the slit, the boundary condition on the broken yarns at $\xi = 0$ is $U_n' = -1$. The -1 is due to the fact that the sum of the reference state strain and the additional strain du_n/dx_1 must vanish at $\xi = 0$; the reference state strain is $du_R/dx_1 = p/(EA)_{\text{eff}}$ and, using (5), get $dU_R/d\xi = 1$. For intact yarns, symmetry requires that $U_n = 0$ at $\xi = 0$. A uniform strain is assumed far from the breaks, therefore, for all yarns we require that $U_n' = 0$ at $\xi = \infty$.

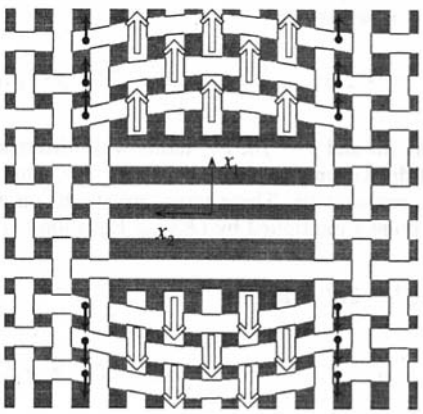


Fig. 4 Yarn slip and deformation pattern near slit. White arrows indicate motion of broken # 1 yarns in type 1 slip. Black arrows indicate motion of # 2 yarns in type 2 slip. Highly schematic.

Downloaded 04 May 2010 to 171.66.16.27. Redistribution subject to ASME license or copyright; see http://www.asme.org/terms/Terms_Use.cfm

Application to Large Slits—Type 2 Slip

The essential mechanisms of the model are depicted by the equilibrium equations, i.e., (4) and (7), and appropriate boundary and continuity conditions as discussed above. Although the basic equations are simple, the opportunity for each yarn near the damage site to slip over a unique slip extent, l_n, creates significant difficulty in implementing the model to treat specific numbers of breaks. For larger slits, the actual configuration of the slipping regions may be expected to become increasingly complex. For predicting the onset of tear propagation, our interest is in the stress concentration in the first intact yarn at the tip of the slit. Since knowledge of the complete deformation field of the fabric under increasing load is not our goal, we exploit simplifications designed to approximate the fabric's behavior in the immediate vicinity of the first intact yarn at loads corresponding to the onset of tear propagation.

As previously mentioned, type 2 slip is the slip that occurs when a rotated crossing yarn slips in the positive x_1-direction at a crossover point with an intact yarn, straightening the kink that occurs at the crossover point to a degree (Fig. 4). Type 1 slip is the slip that occurs on broken yarns as they displace relative to the crossing yarns, moving away from the initial line of breaks (Fig. 4). For slits involving small numbers of breaks, where high remote loads may be attained, type 1 slip may be easily observed in testing because the slip displacements are significant; the broken ends of the yarns often slip far enough to disengage from their interlacings with several crossing yarns.

Consider the damaged fabric under a slowly increasing remote yarn load p starting from zero. Initially, for large slits, the fabric behaves elastically (no slip) until p attains the threshold value p_{limit}, when type 2 slip begins along the first intact # 1 yarn at the tip of the slit. As the load is increased further, the type 2 slip extent grows and a second load threshold is reached when type 1 slip begins at the outermost broken yarn. For further increases in the load, the type 1 slip extent will increase approximately linearly with the load, as shown by calculations in Godfrey and Rossettos (1998), but, for some regime of load, the type 1 slip extent will remain significantly smaller than the type 2 slip extent. Since, for increasingly large slits, tear propagation can be expected to occur at smaller values of p (larger stress concentrations), the loading regime in which either type 2 slip occurs alone, or occurs over a much larger extent than type 1 slip, encompasses the loads over which tear propagation occurs in many stressed fabrics. Post-test inspection of experimental specimens confirms this expectation, where little evidence of type 1 slip is exhibited by the most damage sensitive fabrics.

Comparison of the post-test permanent deformation patterns in the vicinity of slit damage in fabric specimens with small and large slits supports the notion that the type 2 slip mechanism becomes increasingly important in larger slits. Specimens of a continuous filament polyester fabric with damage consisting of three (small slit) and 45 (large slit) consecutive aligned fill yarn breaks were tested under the considered bi-axial loading. The fabric, and the method and conditions of the biaxial testing, are described in the experimental section of this paper. The polyester fabric is the most damage tolerant of those studied here and, therefore, exhibits the largest and most well developed slip regions. The post-test configuration of the three break specimen, after removal of the external loads, is exhibited in Fig. 5. As can be seen, tear propagation *did not* occur at the initial damage site; the test ended in a "jaw break" type failure. The deformation pattern provides clear evidence of substantial type 1 slip: the cut ends of the three broken yarns have displaced far enough to disengage from interlacings with seven or eight # 2 yarns; the three broken yarns exhibit a distinct wiggly appearance for some length starting at the cut ends, suggestive of a slipped yarn region adjacent to an unslipped region of the broken yarns further away from the origin. The overall waviness exhibited by all # 1 yarns in the figure is due to the general plastic deformation of the # 1 yarns in the specimen caused

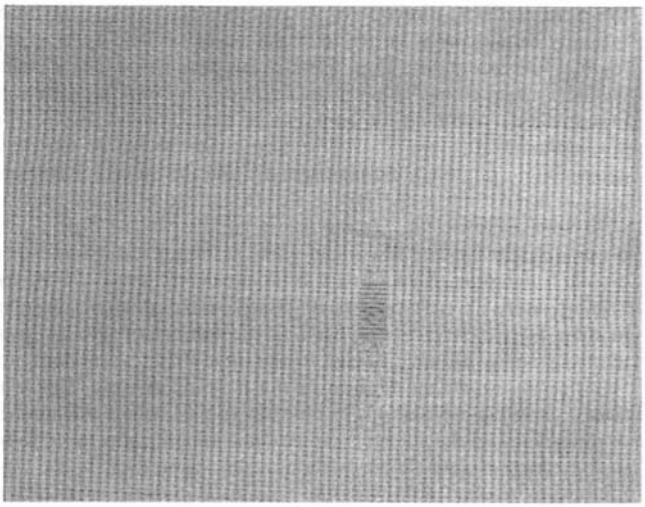


Fig. 5 Post-test permanent deformation pattern in three break specimen, polyester fabric

by the high value of the remote tension, p, experienced in this test. Examination of the # 2 yarns in this specimen reveals that they remain essentially straight and parallel to the x_2-coordinate axis in the vicinity of the local damage, a fact that is consistent with the hypothesis that very little, if any, slip occurred at crossover points along the intact yarns (type 2 slip). The post-test configuration of the 45 break specimen, after removal of external loads, is exhibited in Fig. 6. This test ended in tear propagation, as evidenced by the frayed looking yarn ends resulting from the rupture of the initially intact # 1 yarns along the line $x_1 \cong 0$. The displacement of the cut yarn ends seen here, similar to that seen in the three break specimen, also indicates substantial type 1 slip. In the 45 break case, however, the # 2 yarns are permanently curved such that, as they approach their crossover points with the broken # 1 yarns, the # 2 yarns move away from the line of initial breaks. Crossover points on any particular # 2 yarn, where it is interlaced with the 45 initially broken # 1 yarns, are seen to lie at greater distances from the line $x_1 \cong 0$ than cross-over points where the # 2 yarn is interlaced with the initially intact # 1 yarns (except in the region of complicated deformation very near the cut ends). This pattern can be seen in the entire field of view of Fig. 6. The occurrence of type 2 slip along several intact # 1 yarns at the tips of the slit provides a plausible explanation of the observed deformation pattern. The fact that the pattern extends to the edge of the figure suggests that

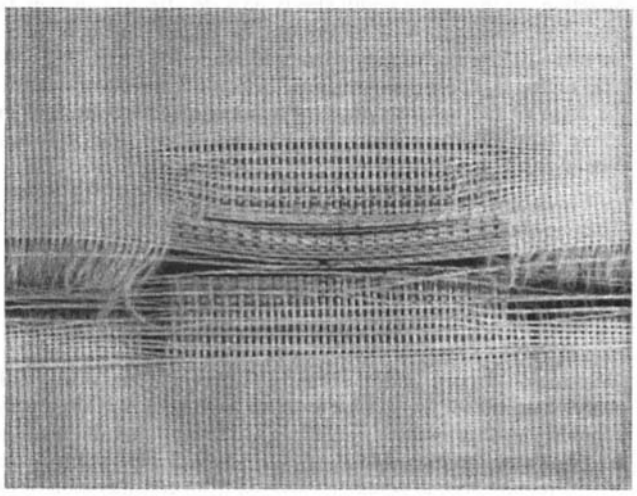


Fig. 6 Post-test permanent deformation pattern in 45 break specimen, polyester fabric

Downloaded 04 May 2010 to 171.66.16.27. Redistribution subject to ASME license or copyright; see http://www.asme.org/terms/Terms_Use.cfm

the extent in the x_1-direction of the region experiencing type 2 slip is likely significantly larger than the extent of the type 1 slip region. Taken together, Figs. 5 and 6 suggest that, as the considered slit size becomes larger, type 2 slip becomes the predominant inelastic mechanism in the response of the damaged fabric. The predominance of type 2 slip in large slits is apt to be most applicable to relatively damage sensitive fabrics, where tear propagation occurs before the type 1 slip extent grows significantly.

In what follows, we assume for large slits, that a type 2 slip occurs in only the first few intact yarns at the tip of the slit over a common extent, l. Type 1 slip is assumed *not to occur* on the broken yarns. These simple assumptions on slip configuration are justified by two observations. First, the occurrence of type 2 slip on yarns at some distance ahead of the first intact yarn does not significantly affect the tension in the first intact yarn. This was demonstrated in calculations by Godfrey (1998), where the number of intact yarns at the slit tip assumed to be slipping was taken to be in the range of four to ten without affecting tension in the first intact yarn. Second, following the discussion given in the previous paragraphs, it can be shown for large slits a posteriori from results of the calculation, using (7), that, for values of the remote load that are of interest, type 1 slip either will not occur or its extent will be small (note that, if $U''_N(0^+) \le \hat{f}$, where yarn N is the last broken yarn, no type 1 slip will occur). This suggests that type 2 slip will have the primary influence over the stress concentration in the first intact yarn.

We consider a finite width configuration of $2q + 1$ # 1 yarns with $2N + 1$ consecutive aligned breaks (slit) centered at the zeroth yarn. Yarns in the positive x_2 half-plane are numbered so that n equals 1 to q. Yarns in the negative x_2 half-plane are numbered -1 to $-q$. The series of breaks is symmetrical about the center yarn, so that, concerning ourselves only with nonnegative n, yarns numbered $0 \le n \le N$ are broken and yarns numbered $n > N$ are intact. Because of symmetry, we need only consider equations for yarns $n = 0$ to $n = q$.

The fabric is divided into regions I, $0 < \xi < \hat{l}$, where type 2 slip is occurring on yarns $n = N + 1$ to $n = N + s$, and II, $\xi \ge \hat{l}$, where no slip is occurring. In the analysis, we will arbitrarily take s to be four, for definiteness. As mentioned, varying the value of s from four to ten has an insignificant effect on the stress concentration in the first intact yarn (Godfrey, 1998). The value of q is assumed to be sufficiently large such that the behavior of the finite width configuration closely approximates that of an infinite fabric with an isolated slit. Similar studies in composite sheets containing matrix yield zones near the slit tip (Rossettos and Shishesaz, 1987; Rossettos and Olia, 1995), where the structure of the equations is the same (Rossettos and Godfrey, 1998) and the slip zone in fabrics plays an analogous role as the matrix yield zone in composites, have shown exponential decay in the width direction, so that finite width sheets provide effective models for the infinite sheet problems. Therefore, the displacements of yarn q are taken to be those of the undamaged reference, i.e., $U_q(\xi) = 0$.

In region II (nonslipping region), the equilibrium equations have the form of (4), where symmetry about the center yarn and the above assumption regarding the qth yarn, lead to the following special forms for yarns 0 and $q - 1$, written as

$$U''_0 - 2U_0 + 2U_1 = 0 \tag{9}$$

and

$$U''_{q-1} + U_{q-2} - 2U_{q-1} = 0, \tag{10}$$

respectively.

In region I, (4), and the special forms (9) and (10), hold everywhere except for yarns $n = N$ through $n = N + 5$. For the slipping yarns, $N + 1 \le n \le N + 4$, the equilibrium equations are (7) where the plus sign is taken for type 2 slip. Yarns N and $N + 5$ require special equations derived from consideration of the equilibrium and deformation of that portion of a crossing (# 2) yarn that spans the crossover points on # 1 yarns from yarn N to yarn $N + 5$. The derivation proceeds as follows. It is assumed that the # 2 yarns behave as classical taut strings under transverse loads, f, at the four slipping crossover points. The displacement of the crossing (# 2) yarns in the x_1-direction at the slipping crossover points is denoted by δ_n, $N + 1 \le n \le N + 4$. Force equilibrium in the x_1-direction is written for each of the slipping crossover points on the # 2 yarns, where force components arise from the small rotations of the tensioned # 2 yarns and the small rotation angles are indicated by differences of displacements, i.e., $(\delta_{n-1} - \delta_n)/y_{02}$. This leads to a system of four linear equations for the four unknown # 2 yarn displacements: $(u_N - 2\delta_{N+1} + \delta_{N+2})F_2^*/y_{02} = f$, $(\delta_{N+1} - 2\delta_{N+2} + \delta_{N+3})F_2^*/y_{02} = f, \ldots, (\delta_{N+3} - 2\delta_{N+4} + u_{N+5})F_2^*/y_{02} = f$. Using (5) to nondimensionalize both # 1 and # 2 displacements (i.e., u_n and δ_n), and (8) to nondimensionalize f, the four equations take the form: $U_N - 2\Delta_{N+1} + \Delta_{N+2} = \hat{f}$, $\Delta_{N+1} - 2\Delta_{N+2} + \Delta_{N+3} = \hat{f}$, $\Delta_{N+2} - 2\Delta_{N+3} + \Delta_{N+4} = \hat{f}$, and $\Delta_{N+3} - 2\Delta_{N+4} + U_{N+5} = \hat{f}$, where the Δ_n are the dimensionless displacements of the # 2 yarn crossover points. Observing that the equation for the Nth # 1 yarn will have the form $U''_N + U_{N-1} - 2U_N + \Delta_{N+1} = 0$, and that of the $N + 5$th # 1 yarn will have the form $U''_{N+5} + \Delta_{N+4} - 2U_{N+5} + U_{N+6} = 0$, the solution for Δ_{N+1} and Δ_{N+4}, obtained from the four equations for the Δ_n, may be substituted into the equations for the Nth and $N + 5$th # 1 yarn to obtain

$$U''_N + U_{N-1} - \tfrac{6}{5}U_N + \tfrac{1}{5}U_{N+5} = 2\hat{f} \tag{11}$$

and

$$U''_{N+5} + \tfrac{1}{5}U_N - \tfrac{6}{5}U_{N+5} + U_{N+6} = 2\hat{f}. \tag{12}$$

As previously discussed, the boundary conditions may be written for intact and broken yarns as

$$U_n(0) = 0,\ n \ge N + 1; \quad U'_n(0) = -1,\ n \le N; \tag{13}$$

at $\xi = 0$ and as

$$U'_n(\infty) = 0 \tag{14}$$

for all yarns, $0 \le n \le q - 1$, at $\xi = \infty$. Since all yarns are continuous at $\xi = \hat{l}$, the following continuity conditions hold, where roman numeral subscripts I and II refer to the solution in regions I and II, respectively,

$$U_{In}(\hat{l}) = U_{IIn}(\hat{l}); \quad U'_{In}(\hat{l}) = U'_{IIn}(\hat{l}). \tag{15}$$

An additional continuity condition arises from the assumption that slipping is approached in a continuous fashion. This may be illustrated by considering a point at $x_1 = a$ on yarn $n = N + 1$. As the remote load p is increased, a value of p is reached that just starts slip with the extent $l = 0^+$. As the load is increased further, the slip extent l increases, but, as long as $l < a$, no slip occurs at

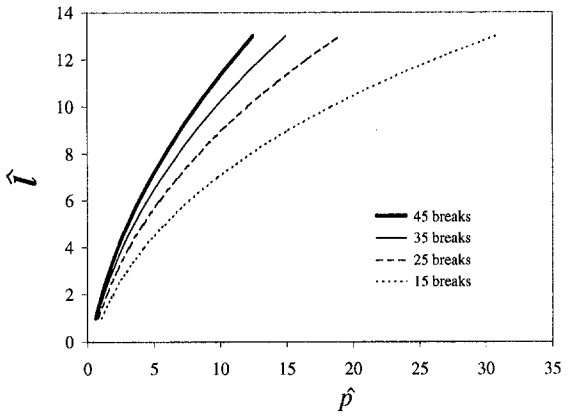


Fig. 7 Behavior of type 2 slip extent, $\hat{l}$, with increasing dimensionless applied load, $\hat{p}$

Downloaded 04 May 2010 to 171.66.16.27. Redistribution subject to ASME license or copyright; see http://www.asme.org/terms/Terms_Use.cfm

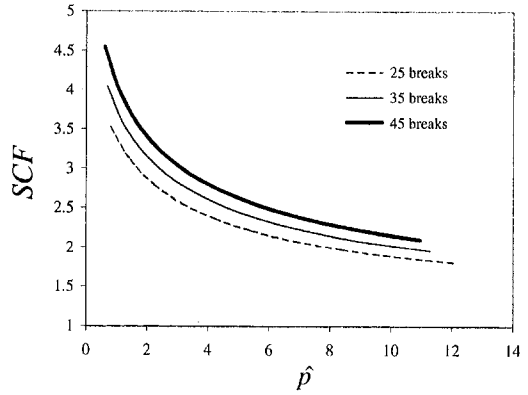


Fig. 8 SCF versus $\hat{p}$ for slits of various numbers of breaks, large-slit analysis

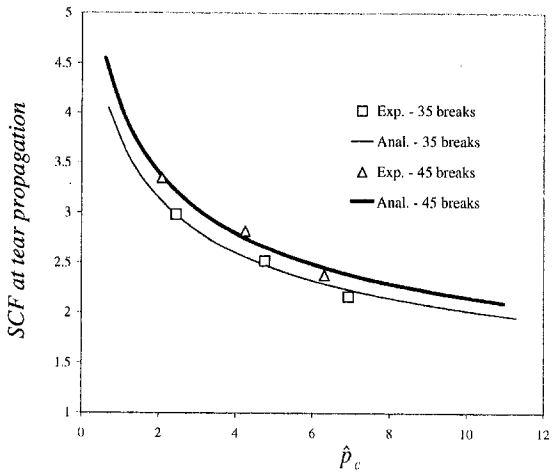


Fig. 9 Comparison of analytical and experimental SCF_{tp} versus $\hat{p}_c$ behavior for 35 and 45 break slits

the point $x_1 = a$. During this time, the frictional forces at the nonslipping crossover points in the neighborhood of $x_1 = a$ increase continuously, until they reach a maximum value of f (on the verge of slip) as the slip extent l approaches a. Therefore, the frictional force on yarn $N + 1$ (proportional to U''_{N+1}) is taken to be continuous at $x_1 = l$, which may be stated in the dimensionless variables, using (4) and (7), as

$$\{U_N - 2U_{N+1} + U_{N+2}\}_{II}|_{\xi=\hat{l}} = \hat{f}. \tag{16}$$

The system of second order differential equations, namely (4), (9), (10), (11), and (12), for the nonslipping yarns in region I may be written in matrix form as

$$\mathbf{U}''_I - \mathbf{L}\mathbf{U}_I = \mathbf{Q} \tag{17}$$

where $\mathbf{L}$ is banded, $\mathbf{U}_I^T = [U_0, U_1, \ldots, U_N, U_{N+5}, U_{N+6}, \ldots, U_{q-2}, U_{q-1}]$, and the elements of $\mathbf{Q}$ are all zero except the $N + 1$th and $N + 2$th element (corresponding to equations for yarns N and $N + 5$), which are $2\hat{f}$. A homogeneous solution to (17) is assumed in the form $\mathbf{U}_I = \mathbf{R}e^{\lambda\xi}$, where $\mathbf{U}_I$ and $\mathbf{R}$ are vectors of order $q - 4$. The resulting eigenvector problem, $(\mathbf{L} - \lambda^2\mathbf{I}) = \mathbf{0}$, leads to eigenvalues λ_i^2 and eigenvectors $\mathbf{R}^i$. The solution $\mathbf{U}_I$ can be written by the superposition of eigenvectors as the expansion

$$\mathbf{U}_I = \sum_{i=1}^{q-4} \mathbf{R}^i(B_i e^{-\lambda_i\xi} + C_i e^{\lambda_i\xi}) + \mathbf{U}_P \tag{18}$$

where the particular solution, $\mathbf{U}_P$, has been added to satisfy (17). The solution for the slipping yarns in region I, which involves (7), is

$$U_{In} = -\frac{\hat{f}}{2}\xi^2 + A_n\xi, \quad N + 1 \le n \le N + 4. \tag{19}$$

The system of second-order differential equations, namely (4), (9), and (10), for region II may similarly be written in matrix form and the solution may be written as the eigenvector expansion

$$\mathbf{U}_{II} = \sum_{i=1}^{q} \mathbf{Y}^i D_i e^{-\gamma_i\xi} \tag{20}$$

where the $+\gamma_i$ have been discarded to satisfy (14), $\mathbf{U}_{II}$ and $\mathbf{Y}$ are vectors of order q, and $\mathbf{U}_{II}^T = [U_0, U_1, \ldots, U_{q-2}, U_{q-1}]$.

To complete the solution process, we select values for the slip extent, $\hat{l}$, and determine the values of the constants (i.e., A_i, B_i, C_i, and D_i) and the parameter, $\hat{f}$, using the boundary conditions, (13), and the continuity conditions, (15) and (16). Observing from (8) that the parameter $\hat{f}$ is inversely proportional to the applied load, p, we introduce a dimensionless applied load, $\hat{p}$, which we define as $\hat{p} = \hat{f}^{-1}$, in the interest of clarity in the presentation and interpretation of the results.

Analytical Results—Type 2 Slip

As indicated above, the behavior of type 2 slip extent, $\hat{l}$, with increasing dimensionless applied load, $\hat{p}$, may be obtained by selecting values of $\hat{l}$ and solving the defined boundary value problem to yield $\hat{f}$, where $\hat{p} = \hat{f}^{-1}$. In Fig. 7, $\hat{l}$ is plotted against $\hat{p}$ for various numbers of breaks. It is seen that larger slits (i.e., involving greater numbers of breaks) yield significantly greater slip extents for given values of $\hat{p}$.

The stress concentration factor (SCF) is defined here as the ratio of the maximum tension in the intact yarn adjacent to the yarn break at the tip of the slit to the remote applied load, p_{max}/p. Using

Table 1 Fabric properties

Fabric	# 1 yarn system	y_{01}, cm	y_{02}, cm	p_u, N	$(EA)_{eff}$, N	F_2^*, N	f, N
Cotton	fill	0.0334	0.0379	1.93	32.3	0.569	0.0328
Polyester, continuous filament	fill	0.0348	0.0686	6.36	23.9	0.888	0.0582
Cotton/polyester blend	fill	0.0334	0.0391	2.27	40.4	0.569	0.0356
Cotton/polyester blend	warp	0.0391	0.0334	2.50	71.2	0.388	0.0166

Downloaded 04 May 2010 to 171.66.16.27. Redistribution subject to ASME license or copyright; see http://www.asme.org/terms/Terms_Use.cfm

Table 2 Tear propagation results for 35 and 45 break slits

Fabric	# 1 yarn system	35 break slit $\hat{p}_c$	35 break slit SCF_{tp}	45 break slit $\hat{p}_c$	45 break slit SCF_{tp}
Cotton	fill	2.45 (0.612)†	2.98 (0.364)	—	—
Polyester, continuous filament	fill	6.94 (0.944)	2.16 (0.018)	6.31 (0.883)	2.38 (0.080)
Cotton/polyester blend	fill	—	—	2.09 (0.449)	3.35 (0.155)
Cotton/polyester blend	warp	4.76 (0.571)	2.52 (0.144)	4.25 (0.551)	2.82 (0.212)

† Standard deviations indicated in parenthesis.

the displacement reference and the nondimensionalization scheme, it is straightforward to show that the SCF can be written as SCF = $U'_{N+1}(0) + 1$. The SCF due to slits containing various numbers of breaks is plotted against $\hat{p}$ in Fig. 8.

Experiments

To investigate the predictive ability of the simple micromechanical large-slit model, a number of plain weave fabrics have been studied experimentally. Particular aspects of the experimental methods are described in more detail by Godfrey and Rossettos (1999), where preliminary results for 26 break slits are given. The methods used to obtain the present results differ only in that an improved specimen is used that provides a larger (15 cm × 15 cm) bi-axially stressed region.

It is assumed that the onset of tear propagation occurs when the maximum yarn tension in the fabric, p_{max}, occurring in the $N + 1$th (first intact) yarn attains the value of the in situ ultimate breaking load of the # 1 yarn, p_u. The SCF in a particular fabric, under specific crossing yarn tension F_2^*, for a slit consisting of a given number of # 1 yarn breaks, takes on a special value at the onset of tear propagation, which we denote SCF_{tp}. Since the applied load has the value p_c (*p critical*) at the instant of tear propagation, we may write SCF_{tp} as $SCF_{tp} = p_u/p_c$. The SCF versus $\hat{p}$ behavior, exhibited in Fig. 8, may be interpreted as representing the SCF_{tp} versus $\hat{p}_c$ behavior of fabrics, where $\hat{p}_c$ is the dimensionless applied load at the onset of tear propagation, written, using (8), as

$$\hat{p}_c = \frac{p_c}{f}\sqrt{\frac{F_2^* y_{01}}{(EA)_{\text{eff}} y_{02}}}. \tag{21}$$

We will present our experimental results, which are essentially values of p_c measured in a variety of stressed fabrics for slits of 35 and 45 breaks, through the dimensionless parameters, SCF_{tp} and $\hat{p}_c$.

The selection of 35 and 45 breaks for study was motivated by previous work with 26 breaks and the desire to study larger damage sizes. Much larger sizes were not considered because of limitations in existing experimental means, as well as the concern that very large slits may violate some of the fundamental modeling assumptions, such as the small # 2 yarn rotation assumption.

The experimental set-up uses cruciform-shaped specimens where a fixed stress is applied in the x_2-direction (a force on each # 2 yarn of F_2^*) using an air cylinder actuated frame and a varying stress (from zero to high values) is applied in the x_1-direction by a servo-hydraulic test machine. In tear propagation experiments, the initial slit-like damage is created in the center of the specimen by carefully cutting consecutive # 1 yarns using a sharp razor. The damaged specimen is mounted in the frame and F_2^* is applied. The value of the remote load p is increased monotonically from zero until tear propagation occurs; the maximum value of p is taken to be p_c.

To evaluate the dimensionless parameters, the values for y_{01}, y_{02}, p_u, and $(EA)_{\text{eff}}$ are determined for the particular fabric and orientation under consideration. In addition, the value of f is determined for the specific value of F_2^* to be used in the tear propagation tests. Measurements of the in situ yarn stiffness and strength, $(EA)_{\text{eff}}$ and p_u, respectively, are made using uniaxially loaded "ravel strip" specimens. The value of $(EA)_{\text{eff}}$ is determined from the slope of the load/strain curve in the region where the loaded yarns have straightened out. The crossover point slip frictional force, f, is measured indirectly using a cruciform specimen with a small number of breaks (five to seven) observed under magnification on a video monitor, where the deflections of the # 2 yarns caused by interaction with slipping # 1 yarns are used to calculate f. The frictional forces balance components of the forces in the tensioned crossing (# 2) yarns as they rotate through small angles. These angles, and therefore the frictional forces, can be calculated from the deflections. The selection of five to seven breaks for the measurements is a trade-off between two competing effects: Smaller numbers of breaks yield less deformation in the # 2 yarns and, therefore, make measurements more difficult; using larger numbers of breaks introduces the possibility that not all of the broken # 1 yarns will be slipping simultaneously at crossover points on the # 2 yarn selected for measurement. Attempts to measure f with larger numbers of breaks (fifteen) resulted in lower values, which is consistent with the notion that not all crossover points were contributing the maximum frictional force associated with slip.

A 100 percent cotton staple yarn fabric, a cotton/polyester blend staple yarn fabric, and a continuous multifilament polyester yarn fabric are studied here. All fabrics are plain weave and somewhat sheer, i.e., exhibit easily observed open space between yarns, in order to mitigate the effects of near contact between adjacent yarns of the same yarn system. The fabric constructions are 30.0 by 26.4, 30.0 by 25.6, and 28.7 by 14.6, warp yarns/cm by filling yarns/cm, and the areal densities are 113 g/m^2, 107 g/m^2, and 83.0 g/m^2, for the cotton, cotton/polyester, and polyester fabrics, respectively. The microstructural properties pertaining to the present tear propagation experiments are given in Table 1.

The results of tear propagation experiments are given in Table 2 for initial slit-like damage consisting of 35 and 45 breaks. Standard deviations are determined based on approximate formulas for propagation of error in calculated quantities (Taylor, 1990), where the variability of p_c, p_u, and f has been taken into account. Most of the variability exhibited by $\hat{p}_c$ stems from variability in f. The measurement of f is difficult, particularly for the staple yarn fabrics. For each case, three measurements of f, three measurements of p_c and three to six measurements of p_u were made.

Comparison of Analytical and Experimental Results

The experimental results given in Table 2 are plotted with the predictions made using our large-slit analysis for 35 and 45 breaks

Downloaded 04 May 2010 to 171.66.16.27. Redistribution subject to ASME license or copyright; see http://www.asme.org/terms/Terms_Use.cfm

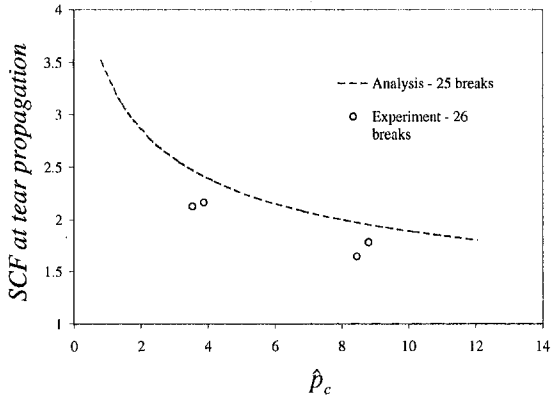


Fig. 10 Comparison of analytical 25 break slit SCF_{tp} versus $\hat{p}_c$ behavior with experimental results for 26 break slits given in Godfrey and Rossettos (1999)

in Fig. 9. The experimental and analytical results are seen to be in good agreement. In Fig. 10, preliminary experimental results given by Godfrey and Rossettos (1999) for 26 breaks are plotted with the analytical curve for 25 breaks (the present model has only been implemented for odd numbers of breaks). For this case, the analytical SCF_{tp} is consistently higher than that measured, suggesting two possibilities: (1) the 26 break slit is not sufficiently large to be well approximated by our large-slit approach; and (2) the smaller specimen size used in the earlier work affects the experimental results.

Conclusions

A simple micromechanical model has been developed to predict the onset of tear propagation at slit-like damage sites in biaxially stressed plain weave fabrics under increasing loading perpendicular to the line of breaks. The analysis has been specialized for large slits parallel to a yarn direction, where it is assumed that slip occurs at crossover points in a region along the first few intact yarns near the tip of the slit. The simplified slipping configuration applies to slits involving greater than, say, 35 breaks, where it can be shown a posteriori that the slip mechanism assumed in the analysis is the one that dominates for remote load values of interest. Experimental results have been presented for the onset of tear propagation in a variety of stressed cotton and polyester fabrics containing 35 and 45 break slits that agree well with predictions made using the present large-slit analysis.

References

Abbott, N. J., and Skelton, J., 1972, "Crack Propagation in Woven Fabrics," *Journal of Coated Fibrous Materials,* Vol. 1, pp. 234–252.

Christoffersen, J., 1980, "Fabrics: Orthotropic Materials With a Stress-Free Shear Mode," ASME JOURNAL OF APPLIED MECHANICS, Vol. 47, pp. 71–74.

Godfrey, T. A., 1998, "A Micromechanical Model for Damage Growth in Stressed Plain Weave Fabrics," Doctoral dissertation, Department of Mechanical, Industrial and Manufacturing Engineering, Northeastern University, Boston, MA.

Godfrey, T. A., and Rossettos, J. N., 1998, "Damage Growth in Prestressed Plain Weave Fabrics," *Textile Research Journal,* Vol. 68, pp. 359–370.

Godfrey, T. A., and Rossettos, J. N., 1999, "A Parameter for Comparing the Damage Tolerance of Stressed Plain Weave Fabrics," *Textile Research Journal,* Vol. 69, pp. 503–511.

Harrison, P. W., 1960, "The Tearing Strength of Fabrics," *Journal of the Textile Institute,* Vol. 51, pp. 91–131.

Hedgepeth, J. M., 1961, "Stress Concentrations in Filamentary Structures," NASA Technical Note D-882.

Koerner, R. M., Hwu, B., and Wayne, M. H., 1987, "Soft Soil Stabilization Designs Using Geosynthetics," *Geotextiles and Geomembranes,* Vol. 6, pp. 31–51.

Popova, M. B., and Iliev, V. D., 1993, "Simulation of the Tearing Behavior of Anisotropic Geomembrane Composites," *Geotextiles and Geomembranes,* Vol. 12, pp. 729–738.

Rossettos, J. N., and Godfrey, T. A., 1998, "Damage Analysis in Fiber Composite Sheets and Uncoated Woven Fabrics," ASME *Applied Mechanics Reviews,* Vol. 51, pp. 373–385.

Rossettos, J. N., and Olia, M., 1995, "On the Hybrid Effect and Matrix Yielding at Fibre Breaks in Hybrid Composite Sheets," *Mechanics of Composite Materials and Structures,* Vol. 2, pp. 275–280.

Rossettos, J. N., and Shishesaz, M., 1987, "Stress Concentration in Fiber Composite Sheets Including Matrix Extension," ASME JOURNAL OF APPLIED MECHANICS, Vol. 54, pp. 723–724.

Taylor, J. K., 1990, *Statistical Techniques for Data Analysis,* Lewis Publishers, Chelsea, MI.

Topping, A. D., 1961, "An Introduction to Biaxial Stress Problems in Fabric Structures," *Aerospace Engineering,* Vol. 20, pp. 18–19 and 53–57.

Troost, G. H., and Ploeg, N. A., 1990, "Influence of Weaving Structure and Coating on the Degree of Mechanical Damage of Reinforcing Mats and Woven Geogrids Caused by Different Fills During Installation," *Proc. 4th Int'l Conference on Geotextiles, Geomembranes and Related Products,* Vol. 2, G. den Hoedt, ed. A. A. Balkema, Rotterdam.

Downloaded 04 May 2010 to 171.66.16.27. Redistribution subject to ASME license or copyright; see http://www.asme.org/terms/Terms_Use.cfm

Microstructural Stress Tensor of Granular Assemblies With Volume Forces

K. Bagi
Department of Structural Mechanics,
TU Budapest,
Muegyetem rkp. 3. K.mf.35,
H-1521 Budapest, Hungary

This paper focuses on the discrete expression of stress tensors of assemblies containing discrete particles with volumetric loads acting on them in addition to boundary forces. Instead of the concept of continuum point, a domain containing a finite number of grains is considered. This domain is replaced by a suitably chosen equivalent continuum whose average stress is expressed—assuming that the grains are in equilibrium—in terms of contact forces and properly defined branch vectors. Symmetry of the stress tensor is also analyzed.

1 Introduction

The aim of this paper is to analyze the definition of microstructural stress tensors for random granular assemblies with volumetric loads. The term "granular assembly" denotes a set of separate grains of arbitrary convex shape. Depending on the mechanical characteristics of the contacts between them, grains may slide and roll along each other, contacts can be created or deleted, etc., so the internal geometrical structure is able to rearrange under the effect of external mechanical loading.

Because of the discrete nature of the material, the definition of a stress tensor is not self-evident. There are different approaches to find a theoretically correct definition and express the stress in terms of forces transmitted between contacting particles. One possibility is to build the definition on the average force acting on an arbitrary plane that cuts through the packing: There is a nice introduction to this method in Jagota et al. (1988), together with those important references like Weber (1966) or Mehrabadi et al. (1982). Another possibility is to consider a finite-size domain containing several particles, and express its average stress in terms of contact forces and other necessary quantities. Several studies followed this second approach: Kanatani (1981), Rothenburg et al. (1981), Christofferssen et al. (1981), etc., analyzed the effect of external forces acting on the boundary of the domain in which the grains are acted upon by contact forces from their neighbors. However, these studies neglect the weight of the grains as well as any other volume forces, and this can be a rather rough estimation in many cases.

Our earlier studies (Bagi, 1996a) followed the second approach, and aimed to find a theoretically and physically established microstructural definition for both the stress and the strain tensors as volume-averaged quantities. Similarly to the previous papers, volumetric loads were excluded from the calculations. The definitions were based on two cell systems, the "material cell system" and the "space cell system," that were introduced to replace the discrete assembly by continuous domains for the continuum-mechanical analysis. (These systems are dual to each other in topological sense, and they can be considered as the generalization of Voronoi and Delaunay systems for the case of irregular grains, as introduced in Bagi (1996b) in detail.) The stress tensor was defined as the volume average of the stresses in the material cells, and the strain as the volume average of the strains (symmetric part of the displacement gradient tensor) of the space cells. Applying then the equilibrium condition of grains, the above-defined stress tensor could be expressed in terms of discrete microvariables:

$$\bar{\sigma}_{ij} = \frac{1}{V}\sum_{(L)} V^L \bar{\sigma}^L_{ij} = \frac{1}{V}\sum_{(c)} l^c_i F^c_j \tag{1}$$

and the displacement gradient tensor could also be written in a discrete form (showing an obvious duality with (1)):

$$\bar{e}_{ij} = \frac{1}{V}\sum_{(K)} V^K \bar{e}^K_{ij} = \frac{1}{V}\sum_{(c)} d^c_i \Delta u^c_j. \tag{2}$$

Here $\bar{\sigma}_{ij}$ is the average stress tensor belonging to the considered finite subassembly and $\bar{e}_{ij}$ is the average displacement gradient tensor (its symmetric part is the linear strain tensor); F_j and Δu_j are the contact force and the relative translation between neighbouring grains; l_i is the branch vector (see Fig. 3.) and d_i is the corresponding complementary area vector (exact definition on d_i, the dual quantity of branch vector, is given in Bagi (1996b)).

The present paper concentrates on the above *stress definition* and intends to *generalize* its field of validity. Introducing the details of the analysis, its aim is to show how can the definition be applied in case of *volume forces acting on the particles* beside surface forces. Section 2 recalls the continuum-mechanical fundaments; Section 3 introduces the geometrical background (how to assign an "equivalent continuum" to the particulate material); then Section 4 derives the expression of average stress in terms of discrete microvariables.

2 Continuum-Mechanical Background

Consider a closed continuous domain loaded by volumetric forces $g_i(x_i)$ on its volume V and by distributed forces $p_i(x_i)$ on its surface S. The Cauchy equations (3) should hold in every point of V, and the boundary conditions (4) in every point of S:

$$\sigma_{kj,k} + g_j = 0 \tag{3}$$

$$\sigma_{ij} n_j = p_i \tag{4}$$

Applying the identity (5) and the Gauss-Ostrogradskij theorem (6),

$$\sigma_{ij} = (x_i \sigma_{kj})_{,k} - x_i (\sigma_{kj})_{,k} \tag{5}$$

$$\int_{(V)} (x_i \sigma_{kj})_{,k} dV = \int_{(S)} x_i \sigma_{kj} n_k dS, \tag{6}$$

the volume average of the stress tensor in V can be written as (7)

Contributed by the Applied Mechanics Division of THE AMERICAN SOCIETY OF MECHANICAL ENGINEERS for publication in the ASME JOURNAL OF APPLIED MECHANICS.
Discussion on the paper should be addressed to the Technical Editor, Professor Lewis T. Wheeler, Department of Mechanical Engineering, University of Houston, Houston, TX 77204-4792, and will be accepted until four months after final publication of the paper itself in the ASME JOURNAL OF APPLIED MECHANICS.
Manuscript received by the ASME Applied Mechanics Division, Dec. 23, 1997; final revision, Feb. 10, 1999. Associate Technical Editor: J. T. Jenkins.

 Copyright © 1999 by ASME

Downloaded 04 May 2010 to 171.66.16.27. Redistribution subject to ASME license or copyright; see http://www.asme.org/terms/Terms_Use.cfm

$$\bar{\sigma}_{ij} = \frac{1}{V}\int_{(V)} \sigma_{ij} dV = \frac{1}{V}\int_{(S)} x_i p_j dS + \frac{1}{V}\int_{(V)} x_i g_j dV. \quad (7)$$

Now divide the domain into subdomains: V^L and S^L are the volume and surface of the Lth subdomain; $p_i(x_i)$ acts on S^L (partly from the neighboring subdomains and partly—where S^L has a common part with S—from the external surface loads). Expression (7) can be applied to express the volume average of the stresses of the subdomains:

$$\bar{\sigma}_{ij} = \frac{1}{V}\sum_{(L)} V^L \bar{\sigma}^L_{ij} = \frac{1}{V}\sum_{(L)} \left(\int_{(S^L)} x_i p_j dS + \int_{(V^L)} x_i g_j dV \right) \quad (8)$$

(since the surface integrals in the inside of the domain cancel out in the summation, this expression equals to (7)).

The above expressions will be written in a discretized form in the following way. First, to replace the distributed volume forces on subdomain "L".

$$x^L_{G_i} G^L_j = \int_{(V)} x_i g_j dV \quad (9)$$

where G^L_j is the resultant of the considered volume forces, and x^L_{Gi} is its point of action. This expression exactly holds if $g_i(x_i)$ is constant (for example, gravity forces acting on a domain having the same density in every point); however, in case of generally varying (nonuniform, nonparallel) volume forces the above expression can be considered as an estimation only.

Second, to replace the surface forces $p_i(x_i)$, consider the common faces S^{L1}, S^{L2}, ... S^{Lc}, ... of the analyzed subdomain "L" with its 1st, 2nd, ... cth, ... neighbors. For each of these subsurfaces apply the replacement

$$x^c_i F^c_j = \int_{(S^{Lc})} x_i p_j dS. \quad (10)$$

This expression can be considered to be exact if $p_i(x_i)$ acts on a very small (point-like) part of the surface (like contact forces between two touching grains); otherwise, this is also an estimation whose exactness would need further analysis.

Applying the above two expressions, the average stress in "L" is

$$\bar{\sigma}^L_{ij} = \frac{1}{V^L}\sum_{(c)} x^c_i F^c_j + \frac{1}{V^L} x^L_{G_i} G^L_j. \quad (11)$$

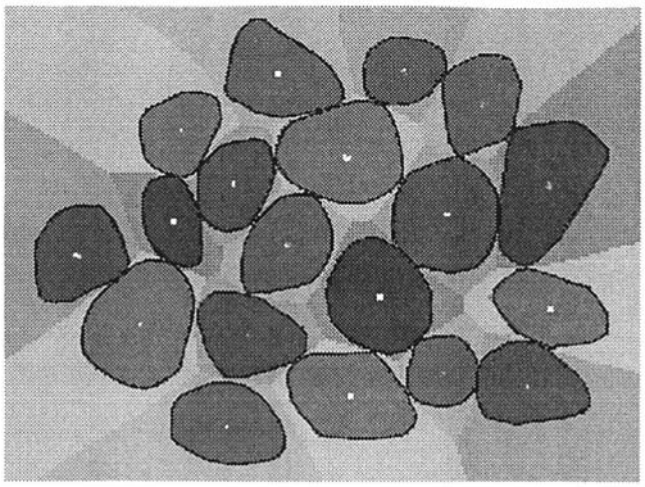


Fig. 1

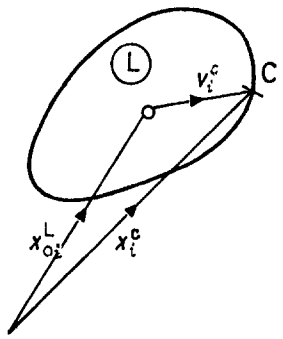


Fig. 2

Since the forces acting between neighboring domains cancel out in the summation, averaging these subdomain stresses for the entire domain leads to the following expression as the discrete version of (7)

$$\bar{\sigma}_{ij} = \frac{1}{V}\sum_{(L)} V^L \bar{\sigma}^L_{ij} = \frac{1}{V}\sum_{(k)} x^k_i F^k_j + \frac{1}{V}\sum_{(L)} x^L_{G_i} G^L_j \quad (12)$$

where the summation with index "k" runs over those subsurfaces only which belong to the external boundary of the whole analyzed domain.

3 The Material Cell System

This system was defined in order to replace the granular assembly with a suitable *equivalent continuum.* The definition can be summarized as follows (see Bagi, 1996a, or Bagi, 1996b, for more details):

Consider an assembly in two-dimensional or three-dimensional Euclidean space that consists of grains having arbitrary convex shape. Analyze a point of the space: Determine its distance from every grain, and then assign the point to that grain from which the point has the smallest distance. Executing the same analysis for all points of the space, contiguous "cells" will form around the grains (each cell containing exactly one grain). Fig. 1 illustrates such a system.

Any set of grains whose material cells are finite will be called a *finite subassembly* of the analyzed system. (In general case there are, of course, several different ways to select finite subassemblies in a given assembly.)

4 Granular Assemblies

Now consider an assembly consisting of grains of any arbitrary convex shape. Prepare its material cell system, and consider a finite subassembly whose stress state will be analyzed. The domain determined by the corresponding material cells is loaded on its boundary points x^1_i, x^2_i, ..., x^k_i, ... by concentrated forces F^1_i, F^2_i, ..., F^k_i, ... and by the resultants of volume forces on the individual grains. Assume that the resultants of volume forces act in the grain centroids: G^1_i in x^1_{0i}, G^2_i in x^2_{0i}, ..., G^L_i in x^L_{0i}, ... The Lth cell receives contact forces F^1_i, F^2_i, ..., F^c_i, ... at the contact points x^1_i, x^2_i, ..., x^c_i, ..., and the volume force G^L_i at x^L_{0i}. Average stress in this cell is given by (11); this expression will be written now in a new form. Figure 2 illustrates that x^c_i can be decomposed into two parts as $x^c_i = x^L_{0i} + v^c_i$, so the average stress of the cell is

$$\bar{\sigma}^L_{ij} = \frac{1}{V^L}\sum_{(c)} v^c_i F^c_j + \frac{1}{V^L} x^L_{0_i} \sum_{(c)} F^c_j + \frac{1}{V^L} x^L_{0_i} G^L_j$$

$$= \frac{1}{V^L}\sum_{(c)} v^c_i F^c_j + \frac{1}{V^L} x^L_{0_i} \left(G^L_j + \sum_{(c)} F^c_j \right). \quad (13)$$

Downloaded 04 May 2010 to 171.66.16.27. Redistribution subject to ASME license or copyright; see http://www.asme.org/terms/Terms_Use.cfm

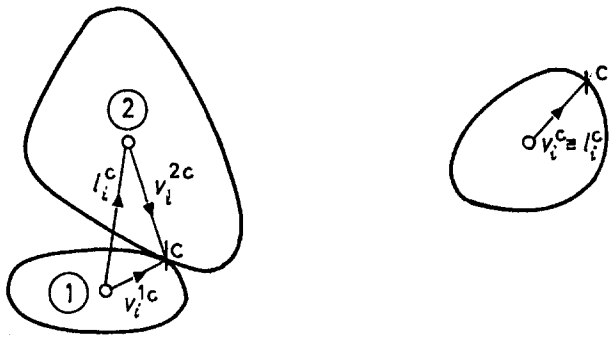


Fig. 3

where the last term vanishes if the grain is in equilibrium.

Note that the condition of moment equilibrium of the Lth grain can be formulated as

$$\sum_{(c)} \nu_i^c F_j^c - \sum_{(c)} \nu_j^c F_i^c = 0 \tag{14}$$

for every $i \neq j$ pairs; consequently, in case of moment equilibrium $\bar{\sigma}_{ij}^L$ is symmetric.[1]

Finally, Fig. 3 defines the *branch vector* l_i^c belonging to a face "c." The definition for those faces in the inside of the analysed domain is: $l_i^c = \nu_{1i}^c - \nu_{2i}^c$; and for those faces on the boundary: $l_i^c = \nu_i^c$.

Applying this definition of the branch vector, volume average of stress tensor for the entire domain can be written as

$$\bar{\sigma}_{ij} = \frac{1}{V} \sum_{(L)} V^L \bar{\sigma}_{ij}^L = \frac{1}{V} \sum_{(c)} l_i^c F_j^c. \tag{15}$$

The left Eq. (15) is the *suggested definition of a stress tensor for granular assemblies.* The equation on the right shows how the volume average of stresses in the material cells can be *expressed in terms of contact forces and branch vectors.*

5 Discussion

At first sight, the above result in (15) seems to be equivalent to those existed previously in the literature. However, there are significant differences:

1 A basic difference from the theoretical point of view is that the transition between the discrete material and the continuum is properly established with the help of the suitably chosen *equivalent continuum.*

2 From a practical point of view it can be a significant improvement that the *weight of the grains* is taken into account.

3 The terms belonging to the boundary forces are correctly taken into consideration through the *two different definitions of the branch vector* for the internal and the boundary contacts.

[1] It is worthwhile to mention that the stress tensor, defined as the volume-average of cell stresses, is symmetric even in the case of eccentric volume forces, assuming that the grains are in equilibrium for moment. This can be shown as follows. Release the restriction that the resultants of volume forces acting on the individual grains should act in the centroids; instead, let G_i^L act at the points x_{Gi}^L for every grain (but still keep the assumption described in (9)). The position vector x_{Gi}^L can be decomposed into two parts: $x_{Gi}^L = x_{0i}^L + \nu_{Gi}^L$ where ν_{Gi}^L is the vector pointing from the centroid of grain "L" to the point of action of G_i^L. The average stress for cell "L," according to (11), is

$$\bar{\sigma}_{ij}^L = \frac{1}{V^L} \sum_{(c)} \nu_i^c F_j^c + \frac{1}{V^L} x_{0i}^L \sum_{(c)} F_j^c + \frac{1}{V^L} x_{Gi}^L G_j^L$$
$$= \frac{1}{V^L} \left(\sum_{(c)} \nu_i^c F_j^c + \nu_{Gi}^L G_j^L \right) + \frac{1}{V^L} x_{0i}^L \left(\sum_{(c)} F_j^c + G_j^L \right)$$

where the last term vanishes in equilibrium. On the other hand, the condition for moment equilibrium of grain "L" is

$$\sum_{(c)} \nu_i^c F_j^c + \nu_{Gi}^L G_j^L - \sum_{(c)} \nu_j^c F_i^c - \nu_{Gj}^L G_i^L = 0 \quad \text{for every } i \neq j$$

which means that the stress tensor is symmetric.

References

Bagi, K., 1996a, "Stress and Strain in Granular Assemblies," *Mechanics of Materials,* Vol. 22, pp. 165–177.

Bagi, K., 1996b, "Geometrical Modelling of Granular Assemblies," *Acta Technica Acad. Sci. Hung, 1995–96,* Vol. 107, 1–2, pp. 1–16.

Christoffersen, J., Mehrabadi, M. M., and Nemat-Nasser, S., 1981, "A Micromechanical Description of Granular Material Behavior," ASME JOURNAL OF APPLIED MECHANICS, Vol. 48, pp. 339–344.

Jagota, A., Dawson, P. R., and Jenkins, J. T., 1988, "An Anisotropic Continuum Model for the Sintering and Compaction of Powder Packings," *Mechanics of Materials,* Vol. 7, pp. 255–269.

Kanatani, K., 1981, "A Theory of Contact Force Distribution in Granular Materials," *Powder Technology,* Vol. 28, pp. 167–172.

Mehrabadi, M. M., Nemat-Nasser, S., and Oda, M., 1982, "On Statistical Description of Stress and Fabric in Granular Materials," *Int. J. Numer. Anal. Geomech.,* Vol. 6, pp. 95–108.

Rothenburg, L., and Selvadurai, A. P. S., 1981, "A Micromechanical Definition of the Cauchy Stress Tensor for Particulate Media," *Proc. Intl. Symp. on the Mechanical Behavior of Structured Media,* Pt. B., Ottawa, Selvadurai, ed., pp. 469–486.

Weber, J., 1966, "Recherches Concernant les Contraintes Intergranulaires dans les Milieux Pulvérulents Application a la Rhéologie de ces Milieux," *Conférence au Groupe Francais de Rhéologie,* pp. 161–170.

Downloaded 04 May 2010 to 171.66.16.27. Redistribution subject to ASME license or copyright; see http://www.asme.org/terms/Terms_Use.cfm

M. Kazic
Associate Professor.

R. Bulatovic
Professor.

Department of Mechanical Engineering,
University of Montenegro,
Cetinjski put b.b.,
81000 Podgorica, Yugoslavia

On the Equilibrium Conditions of Nonstationary Mechanical Systems

The equilibrium problem of nonstationary systems is studied. The starting point is the principle of virtual work (PVW). Contrary to stationary problems, some additional conditions (along with PVW) should be satisfied. Proof of Gantmacher's postulate is derived. A new approach is given, and some results of other authors are discussed.

1 Introduction

Equilibrium problems of mechanical systems, studied via analytical statics, refer mostly to the cases where active forces and constraints do not depend explicitly on time (stationary problems). In the case of stationary (scleronomic) constraints, rest is always one of the possible kinematical states so that the presence or absence of equilibrium depends only on the active forces applied to the system, assuming that constraints are ideal. More precisely, if at a given moment in some arbitrary position the system is motionless, forces can always be chosen in such a way that the system remains in that position. On the other hand, if active forces are given, equilibrium can rarely be maintained in all possible configurations. Moreover, in some problems it cannot be maintained at all. Necessary and sufficient conditions of such problems are given either by the principle of virtual work (PVW) or by equilibrium equations, in Cartesian coordinates (with Lagrange multipliers), or in generalized coordinates.

Although the equilibrium of nonstationary systems is possible it is not typical. Here, in contrast to scleronomic systems, rest is not always a possible kinematical state. In addition, explicit dependence of forces and/or constraints on time entails specific qualities which are the source of ambiguities and errors in studies of equilibrium problems. Problems arise, in particular, when equilibrium of these systems is studied in generalized coordinates.

In this paper, we shall first in Section 2 postulate the problem. Then, following up the traditional concept, in Section 3 it will be shown that the PVW, as defined by Gantmacher in the form of an independent axiom, provides necessary and sufficient conditions of equilibrium of a nonstationary system. In Section 4 we shall give an alternative formulation of PVW which is suitable for finding equilibrium positions and, on that basis, we shall state equations which contain necessary and sufficient conditions of equilibrium for the system under consideration. In Section 5 results and conclusions of other authors will be studied and discussed, as well as compared to the results of Section 4. Both results (of Section 4 and Section 5) will be illustrated by simple examples.

2 Preliminaries

A system of N particles M_i, of masses m_i, whose position in inertial three-dimensional Euclidean space is described by N vectors $r_i = x_i i + y_i j + z_i k (x_i, y_i, z_i$–Cartesian coordinates) is studied. The motion of the system is constrained by k ideal, holonomic, nonstationary constraints

$$f_\alpha(r_i, t) = 0 \quad (\alpha = 1, \ldots k < 3N) \tag{1}$$

while active forces $F_i(r_j, V_j, t)$ $(i, j = 1 \ldots N)$ are applied to the system.

Equilibrium of the system is a position of the system in which it will stay all the time ($r_i(t) \equiv$ const), if it occupied this position in the initial moment and if initial velocities of all the particles were equal zero ($V_i(t_o) = 0$).

In order that some r_{io} be an equilibrium position it should satisfy the constraints for all time, i.e.,

$$f_\alpha(r_i = r_{i0}, t) = 0, \quad \forall\, t \geq t_o. \tag{2}$$

Positions of the system which satisfy conditions (2) are kinematically possible equilibrium positions.

With the help of generalized coordinates $q = (q^1 \ldots q^n)$, $n = 3N - k$, whose choice is, to some degree, arbitrary, position vectors r_i are given in the form $r_i = r_i(q, t)$. The "motion" $q = q(t)$ in $V\{q\}$ coordinate space describe the possible equilibrium position in an inertial reference system only if the following conditions are satisfied:

$$r_i = r_i(q(t), t) \equiv r_{io} \quad \text{for} \quad t \geq t_o$$

which is equivalent to

$$g_{iv}(q(t), t)\dot{q}^v(t) + g_{io}(q(t), t) \equiv 0 \quad \text{for} \quad t \geq t_o$$

where

$$g_{iv} = \frac{\partial r_i}{\partial q^v} \quad g_{io} = \frac{\partial r_i}{\partial t}.$$

It should be pointed out that in a possible equilibrium position generalized coordinates need not be fixed, neither fixed generalized coordinates describe equilibrium. But if the possible equilibrium r_{io} is known, generalized coordinates can always be chosen in a way that in this position all of them are fixed, $r_i(q = q_o, t) \equiv r_{io}$, $t \geq t_o$.

3 Proof of Gantmacher's Postulate

Gantmacher (1970) gives PVW as an independent axiom:

- For some position (compatible with constraints) of a system to be an equilibrium position it is necessary and sufficient that in this position the sum of works of all effective forces on any virtual displacement of the system be zero.

The additional conditions that the constraints and PVW are satisfied for any t, if $r_i = r_o$ and $V_i = 0$, are given without explanation.

Contributed by the Applied Mechanics Division of THE AMERICAN SOCIETY OF MECHANICAL ENGINEERS for publication in the ASME JOURNAL OF APPLIED MECHANICS.
Discussion on the paper should be addressed to the Technical Editor, Professor Lewis T. Wheeler, Department of Mechanical Engineering, University of Houston, Houston, TX 77204-4792, and will be accepted until four months after final publication of the paper itself in the ASME JOURNAL OF APPLIED MECHANICS.
Manuscript received by the ASME Applied Mechanics Division, Dec. 3, 1997; final revision, Jan. 19, 1999. Associate Technical Editor: A. A. Ferri.

 Copyright © 1999 by ASME

Downloaded 04 May 2010 to 171.66.16.27. Redistribution subject to ASME license or copyright; see http://www.asme.org/terms/Terms_Use.cfm

The PVW for nonstationary systems, along with the mentioned Gantmacher's conditions, can be given as the following theorem:

THEOREM:

- An initially motionless system in some position r_{io} will remain in this position if and only if for any $t \geq t_o$ the following conditions are satisfied.

$$(a)\ \sum F_i(t, r_j = r_{jo}, V_j = 0) \cdot \delta r_i = 0, \quad (b) f_\alpha(t, r_{io}) = 0 \quad (3)$$

where δr_i is any virtual displacement from r_{io}.

Proof:

Let r_{io} be equilibrium position: $r_i(t) = r_{io}$, $t \geq t_o$.

In that case condition (3*b*) is satisfied. According to Newton's second law, when $a = \ddot{r}_i(t) \equiv 0$ and $V_i = \dot{r}_i(t) \equiv 0$, it follows that

$$\sum \{F_i(r_j = r_{jo}, V_j = 0, t) + R_i\} \cdot \delta r_i = 0 \quad (4)$$

which for ideal constraints (i.e., $\Sigma R_i \cdot \delta r_i = 0$) implies condition (3*a*).

Let $r_i(t_o) = r_{io}$, $V_i(t_o) = 0$ and suppose that conditions (3) are satisfied. It will be shown that, under these conditions, the system will not leave this position.

Fulfillment of condition (3*b*) means that r_{io} is a possible equilibrium position, which enables us to choose generalized coordinates (see Section 2) in such a way that

$$r_i(q = 0, t) \equiv r_{io} \quad t \geq t_o. \quad (5)$$

From (5) it follows that

$$\frac{\partial^s r_i}{\partial t^s}(q = 0, t) \equiv 0 \quad s = 1, 2 \quad t \geq t_o. \quad (6)$$

The virtual displacements from r_{io} are

$$\delta r_i = \frac{\delta r_i}{\partial q^v}(q = 0, t)\delta q^v = g_{iv}(q = 0, t) \cdot \delta q^v. \quad (7)$$

Since the variations δq^v are arbitrary, condition (3*a*) is equivalent to the n conditions

$$Q_v^* = \sum_i F_i(r_j = r_{jo}, V_j = 0, t) \cdot \frac{\partial r_i}{\partial q^v}(q = 0, t)$$

$$= 0 (v = 1 \ldots n). \quad (8)$$

Let the motion of the system be described by Lagrange's equations:

$$\frac{d}{dt}\frac{\partial T}{\partial \dot{q}^v} - \frac{\partial T}{\partial q^v} = Q_v \quad (v = 1 \ldots n) \quad (9)$$

where

$$T = \tfrac{1}{2} a_{\mu v}(q, t)\dot{q}^\mu \dot{q}^v + a_\mu(q, t)\dot{q}^\mu + a_o(q, t) \quad (10)$$

$$a_{\mu v} = \sum m_i \frac{\partial r_i}{\partial q^v} \cdot \frac{\partial r_i}{\partial q^\mu},$$

$$a_{\mu o} = \sum m_i \frac{\partial r_i}{\partial q^\mu} \cdot \frac{\partial r_i}{\partial t},$$

$$a_{oo} = \frac{1}{2} \sum m_i \left(\frac{\partial r_i}{\partial t}\right)^2 \quad (11)$$

$$Q_v = \sum F_i(t, r_j(q, t), V_j(q, \dot{q}, t)) \cdot \frac{\partial r_i}{\partial q^v}. \quad (12)$$

Comparing (12) to (8) it is obvious that

$$Q_v^* = Q_v(q = 0, \dot{q} = 0, t) \quad (v = 1 \ldots n) \quad (13)$$

while from (11) and (6) it follows that

$$\left.\frac{d}{dt}\frac{\partial T}{\partial \dot{q}^v}\right|_{q=\dot{q}=0} = a_{\mu v}(q = 0, t)\ddot{q}^\mu$$

$$\text{and} \quad \left.\frac{\partial T}{\partial q^v}\right|_{q=\dot{q}=0} = 0. \quad (14)$$

Existence of the relations (14), (8), and (13) enables us to come to the conclusion that the differential equations of motion (9) have the trivial solution $q(t) = 0$.

Furthermore, conditions $q(t_o) = 0$, $\dot{q}(t_o) = 0$ imply $r_i(t_o) = r_{io}$ and $V_i(t_o) = 0$ and vice versa, which under the assumption that the solution is unique (Newton-Laplace's principle of causality) brings us to the conclusion that the system, under conditions (3) will be all the time in rest (in r_{io}).

It should be underlined that without postulation the causality condition, PVW would give only the necessary conditions of equilibrium. This statement can easily be described by the example[1] of the unit mass particle constrained to move along the x-axes under the force $F = \sqrt[3]{6x}\, i$. In this case, along with the solution $x_1(t) = 0$, of the differential equation of motion, there exist the solutions $x_{2,3} = \pm(t^3/6)$ which satisfy the initial conditions $x(0) = 0$, $\dot{x}(0) = 0$.

4 Equilibrium Equations

In the previous section necessary and sufficient equilibrium conditions of nonstationary systems were derived in variational form. These conditions are equivalent to the following equations:

$$(a)\ F_i(r_j, V_j = 0, t) + \sum \lambda_\alpha \frac{\partial f_\alpha}{\partial r_i} = 0 \quad (b)\ f_\alpha(r_j, t) = 0 \quad (15)$$

where the λ_α are Lagrange's multipliers.

Now, we are going to express these conditions in generalized coordinates. The first step is to reformulate the theorem given in Section 3.

The necessary and sufficient conditions for the equilibrium of a nonstationary system is that the system of Eqs. (15) has solutions r_i which do not depend on time. These conditions in generalized coordinates become

$$(a)\ Q_v = \sum F_i(r_j, V_j = 0, t) \cdot \frac{\partial r_i}{\partial q^v} = 0$$

$$(b)\ (g_{vi}\dot{q}^v + g_{io})|_{q^*} = 0 \quad (16)$$

where q^* is the solution of the (16*a*).

Equations (16) will be named "equilibrium equations" rather than conditions of equilibrium. By this name we want to underline that they do not only give the necessary and sufficient equilibrium conditions but describe the equilibrium position as well (if it exists). This means that it is not possible to find out that some systems can attain equilibrium, without calculating the equilibrium position. The problem is being solved in the following way: First, the solution $q^{*v} = q^{*v}(t)$ that is the possible equilibrium position is calculated from (16*a*); then this solution is tested on the condition (16*b*). If these conditions are satisfied, solution q^{*v} describes the equilibrium position. One simple example will illustrate the proposed procedure.

[1] Geronimus, J. L., 1973, *Theoretical Mechanics,* Moscow, pp. 350–351 (in Russian).

Downloaded 04 May 2010 to 171.66.16.27. Redistribution subject to ASME license or copyright; see http://www.asme.org/terms/Terms_Use.cfm

Example 1. Particle of weight G is moving along the constraint surface $f = x^2 + y^2 + (z - e^t)^2 - e^{2t} = 0$. Generalized coordinates: φ, θ; $x = e^t \sin\varphi \cos\theta$, $y = e^t \sin\varphi \sin\theta$, $z = e^t(1 - \cos\varphi)$

$$(Q_\varphi = -Ge^t \sin\varphi,\ Q_\theta = 0) \rightarrow \varphi_1 = 0,\ \varphi_2 = \pi \quad (16a)$$

$$(g_{\varphi\varphi}\dot{\varphi} + g_{\theta\theta}\dot{\theta} + g_{o})|_{\varphi_1} = 0;$$

$$g_{\varphi\varphi}\dot{\varphi} + g_{\theta\theta}\dot{\theta} + g_{o}|_{\varphi_2} = 2e^t \neq 0 \quad (16b)$$

φ_1 is the equilibrium position.

5 Comments

Besides the already mentioned Gantmacher's axiom, there are a few other works dealing with the problem of equilibrium in a nonstationary case. What is in common for all these works is the statement that, contrary to stationary (scleronomic) case, the PVW is only a necessary condition of equilibrium. Differences and mistakes appear in postulating additional conditions.

Papastavridis (1989) derived necessary and sufficient conditions for equilibrium, from the Lagrange-d'Alembert's Principle, which in a case of systems subjected to holonomic rheomic ideal constraints reduce to

$$(a)\ \sum F_i \delta r_i = 0 \quad (b)\ \int_{t_o}^{t} \sum m_i a_i \cdot \frac{\partial r_i}{\partial t}\, dt = 0. \quad (17)$$

(It is assumed that system is initially motionless.)

Let $r_i^* = r_i^*(t)$ be such kinematically possible motion which satisfy initial conditions: $r_i^*(t_o) = r_{io}^*$, $\dot{r}_i^*(t_o) = V_{io} = 0$ as well as the variational Eq. (17a).

It does not necessarily follow from (17b) that $\Sigma\, m_i \dot{r}_i^*(t) \cdot \delta r_i^* = 0$, i.e., $r_i^*(t)$ need not be a real motion. This means that (17) are not sufficient conditions for equilibrium. In the same paper the author compares Eqs. (17) with the Hamel conditions (see Papastavridis, 1989)

$$(a)\ \sum F_i \delta r_i = 0 \quad (b)\ \frac{\partial r_i}{\partial t} = 0, \quad (18)$$

asserting that they are equivalent. These conditions are not equivalent, because conditions (17b) are satisfied not only when (18b) are satisfied but for $a_i = 0$, or $a_i \perp (\partial r_i/\partial t)$. Conditions (18$b$) are equivalent to $\dot{q}^v = 0$ which (according to Section 2) need not describe the equilibrium, because we are dealing with absolute equilibrium.

Example 2. A particle is constrained to move along the x-axes under the action of the force $F = (t^2 - x)i$. ($m = 1$, $x_o = \dot{x}_o = 0$); generalized coordinate: x; $r = xi \rightarrow \partial r/\partial t = 0$. From PVW it follows that $r^* = t^2 i$, which obviously does not describe equilibrium, although (17b) and (18b) are satisfied. The motion of the particle in this study is described by $r = (2\cos t + t^2 - 2)i$ which means that $r^* = t^2 i$ is not a real motion.

Example 3. A heavy particle in constrained to move along the vertical circle of the radius a which rotates about its center. Angular velocity of this rotation is $\dot{\theta}(t)$. Generalized coordinate: φ; $r = a\cos(\theta(t) + \varphi)i + a\sin(\theta(t) + \varphi)j$ Application of the Eqs. (16) gives the equilibrium positions

$$\varphi_1 = \pi/2 - \theta(t), \quad \varphi_2 = 3\pi/2 - \theta(t)$$

although condition (18b) is not satisfied.

In Vujičić (1988) from equilibrium equations in vectorial form

$$\mathbf{F}_i + \mathbf{R}_i = 0 \wedge \mathbf{V}_i = 0, \quad (19)$$

the following equilibrium conditions are derived:

$$(a)\ \mathbf{F}_i + \sum_\alpha \lambda_\alpha \operatorname{grad}_{r_i} f_\alpha = 0 \quad (b)\ \frac{\partial f_\alpha}{\partial t} = 0 \quad (20)$$

where conditions (20b) are calculated in the equilibrium position $r_i = r_{io}$.

In the same paper, conditions of equilibrium in generalized coordinates are given by

$$(a)\ \mathbf{Q}_\alpha = 0 \quad (b)\ \mathbf{Q}_o + \mathbf{R}_o = 0 \quad (21)$$

where

$$Q_\alpha = \sum \mathbf{F}_i \cdot \frac{\partial r_i}{\partial q^\alpha}, \quad Q_0 = \sum \mathbf{F}_i \cdot \frac{\partial r_i}{\partial t}, \quad R_o = \sum \mathbf{R}_i \cdot \frac{\partial r_i}{\partial t}.$$

If the conditions (20) or (21) are applied to the aforementioned Example 2, they give the same result ($r_i = t^2 i$) as conditions (17) and (18).

References

Gantmacher, F., 1970, *Lectures in Analytical Mechanics,* Mir, Moscow, p. 22 (originally in Russian, 1966).

Kiltchevski, N. A., 1977, *A Course in Theoretical Mechanics,* t.2., Moscow, pp. 107–111 (in Russian).

Papastavridis, J., 1989, "On the Sufficentcy of the Principle of Virtual Work for Mechanical Equilibrium: A Critical Reexamination," ASME JOURNAL OF APPLIED MECHANICS, Vol. 56, pp. 704–707.

Vujičić, V., 1988, "On the Principle of Possible Displacements for Rheonomic Systems," *Prikladnaja Mehanika,* t. 24. No. 2, Kiev, pp. 125–127.

Downloaded 04 May 2010 to 171.66.16.27. Redistribution subject to ASME license or copyright; see http://www.asme.org/terms/Terms_Use.cfm

Representation of Stokes Flow Through a Planar Contraction by Papkovich-Fadle Eigenfunctions

M. A. Rogerson[1]

Y. L. Yeow

Department of Chemical Engineering,
The University of Melbourne,
Parkville 3052, Australia

Stokes flow through a planar contraction is represented by matching together two series of Papkovich-Fadle eigenfunctions. Each series represents the solution in one of the unbounded rectangular regions upstream and downstream of the contraction plane. The coefficients of the series are obtained by weakly enforcing C^3 matching conditions at the contraction plane using the Galerkin method. A post-processing technique is used to improve the appearance of the streamline plots near the singularity in the solution at the re-entrant corner of the channel. The pressure variation along the channel, as well as the excess pressure drop due to the contraction and the size of the upstream recirculating zone versus the contraction ratio, are presented. Channel contraction ratios of between two and six are considered.

Introduction

Papkovich-Fadle eigenfunctions satisfy identically the biharmonic equation of Stokes flow. They also satisfy many of the commonly encountered boundary conditions of laminar flow. Such functions are therefore well suited to represent Stokes flow through a planar contraction. Purely numerical techniques such as the finite element method often have difficulties in coping with large contractions due to the prohibitive computational requirements. These numerical techniques must also artificially impose a fully developed flow profile at some finite distance upstream and downstream of the contraction. The use of the Papkovich-Fadle eigenfunctions does not incur these disadvantages. Furthermore, the use of such eigenfunction representations has been greatly facilitated in recent years due to the advent of computer software, such as Mathematica and Maple, which is capable of performing symbolic mathematical manipulations.

Accurate flow characteristics over a wide range of contraction ratios are thus easily obtainable, and the results applicable in the many practical instances where slow viscous Newtonian flow through a channel contraction is found.

The results of this investigation can be compared against a number of other studies of this problem. For example, Davies et al. (1984) used finite difference and finite element techniques, Dennis and Smith (1980) used a finite difference technique, Ingham and Kelmanson (1984) used boundary integral procedures, while Karageorghis and Phillips (1989, 1991) used a Chebyshev and Laguerre series representation to approximate the channel contraction flow.

The use of Papkovich-Fadle eigenfunctions to solve other Stokes flow problems can be found in Joseph and Sturges (1978) and Trogdon and Joseph (1982). These investigations, however, use a biorthogonal operator method to determine the series coefficients rather than the Galerkin method employed here.

[1] Currently at the Department of Chemical Engineering, University of Cambridge, Cambridge CB2 3RA, UK.

Contributed by the Applied Mechanics Division of THE AMERICAN SOCIETY OF MECHANICAL ENGINEERS for publication in the ASME JOURNAL OF APPLIED MECHANICS. Discussion on the paper should be addressed to the Technical Editor, Professor Lewis T. Wheeler, Department of Mechanical Engineering, University of Houston, Houston, TX 77204-4792, and will be accepted until four months after final publication of the paper itself in the ASME JOURNAL OF APPLIED MECHANICS.

Manuscript received by the ASME Applied Mechanics Division, Aug. 27, 1997; final revision, May 3, 1999. Associate Technical Editor: D. A. Siginer.

Formulation

The problem domain is shown in Fig. 1. The velocity is symmetrical about the channel centerline so that only half the channel width need be considered. The contraction ratio is $\Lambda > 1$. The coordinate system is chosen such that the origin is located on the channel centerline at the contraction plane.

The no-slip condition is imposed on all solid boundaries, and a fully developed flow profile is imposed at $x \to \infty$ and $x \to -\infty$.

The velocity in the channel $u(x, y)\mathbf{i} + v(x, y)\mathbf{j}$ is expressed in terms of the stream function ψ where

$$u = \frac{\partial \psi}{\partial y} \quad v = -\frac{\partial \psi}{\partial x}. \tag{1}$$

The continuity equation is thus automatically satisfied and the equation of motion for steady planar Stokes flow reduces to the biharmonic equation:

$$\nabla^4 \psi = 0. \tag{2}$$

In terms of the stream function, the usual viscous flow boundary conditions are

$$\psi(x, \Lambda) = 1, \quad \frac{\partial \psi}{\partial y}(x, \Lambda) = 0, \quad -\infty < x \le 0 \tag{3}$$

$$\psi(0, y) = 1, \quad \frac{\partial \psi}{\partial x}(0, y) = 0, \quad 1 \le y \le \Lambda \tag{4}$$

$$\psi(x, 1) = 1, \quad \frac{\partial \psi}{\partial y}(x, 1) = 0, \quad 0 \le x < \infty \tag{5}$$

$$\psi(x, 0) = 0, \quad \frac{\partial^2 \psi}{\partial y^2}(x, 0) = 0, \quad -\infty < x < \infty \tag{6}$$

$$\psi(x, y) \to \frac{3}{2}\left(\frac{y}{\Lambda} - \frac{1}{3}\left(\frac{y}{\Lambda}\right)^3\right) \quad \text{as} \quad x \to -\infty, \quad 0 \le y \le \Lambda \tag{7}$$

$$\psi(x, y) \to \tfrac{3}{2}(y - \tfrac{1}{3}y^3) \quad \text{as} \quad x \to \infty, \quad 0 \le y \le 1. \tag{8}$$

Papkovich-Fadle Eigenfunction Representation

The problem domain is decomposed into the two unbounded rectangular regions I and II (Fig. 1). Separate representations ψ^I

 Copyright © 1999 by ASME

Downloaded 04 May 2010 to 171.66.16.27. Redistribution subject to ASME license or copyright; see http://www.asme.org/terms/Terms_Use.cfm

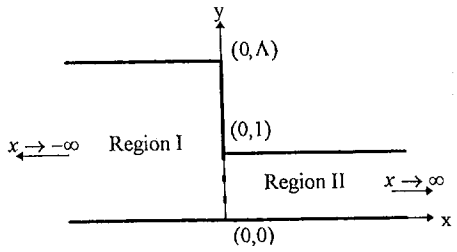


Fig. 1 The problem domain

and ψ^{II} are used to represent the stream function ψ in these respective regions. This division allows the boundary conditions (3)–(8) with the exception of (4) to be inherently satisfied by the series solutions based on the Papkovich-Fadle eigenfunctions.

The form of ψ^{I} and ψ^{II} is given in (9) and (10). The first term represents the fully developed flow profile in the channel. The second term is a series of odd-valued Papkovich-Fadle eigenfunctions. For a discussion of the mathematical properties of the Papkovich-Fadle eigenfunctions, the reader is referred to Smith (1952). This second series term represents the perturbation of the fully developed profile close to the contraction. The diminution of this perturbation further from the contraction is ensured by the exponential part of the eigenfunction.

$$\psi^{I} = \frac{3}{2}\left(\frac{y}{\Lambda} - \frac{1}{3}\left(\frac{y}{\Lambda}\right)^3\right) + \mathrm{Re}\left\{\sum_{n=1}^{N} C_n^{I} \frac{\phi_n\left(\frac{y}{\Lambda}\right)}{p_n^2} e^{p_n(x/\Lambda)}\right\} \qquad x \le 0, \quad 0 \le y \le \Lambda \quad (9)$$

$$\psi^{II} = \frac{3}{2}\left(y - \frac{1}{3}y^3\right) + \mathrm{Re}\left\{\sum_{n=1}^{N} C_n^{II} \frac{\phi_n(y)}{p_n^2} e^{-p_n x}\right\} \qquad x \ge 0, \quad 0 \le y \le 1 \quad (10)$$

The eigenvalues p_n are the complex roots of

$$\sin(2p_n) = 2p_n$$

in the first quadrant of the $x + iy$ complex plane (Smith, 1952).

The sequence of functions ϕ_n are given by

$$\phi_n(y) = p_n \cos(p_n) \sin(yp_n) - yp_n \sin(p_n) \cos(yp_n).$$

C_n^{I}, C_n^{II} are the complex valued coefficients of the series and N is the number of terms at which the series is truncated.

It is easily verified that (9) and (10) satisfy the biharmonic Eq. (2) and boundary conditions (3), (5), (6), (7), and (8).

The following matching conditions must be imposed between ψ^{I} and ψ^{II} so that the velocities and stresses are continuous at the interface between regions I and II:

$$\psi^{I}(0, y) = \psi^{II}(0, y) \quad 0 \le y \le 1 \quad (11)$$

$$\frac{\partial \psi^{I}}{\partial x}(0, y) = \frac{\partial \psi^{II}}{\partial x}(0, y) \quad 0 \le y \le 1 \quad (12)$$

$$\frac{\partial^2 \psi^{I}}{\partial x^2}(0, y) = \frac{\partial^2 \psi^{II}}{\partial x^2}(0, y) \quad 0 \le y \le 1 \quad (13)$$

$$\frac{\partial^3 \psi^{I}}{\partial x^3}(0, y) = \frac{\partial^3 \psi^{II}}{\partial x^3}(0, y) \quad 0 \le y \le 1. \quad (14)$$

Solution Method

The coefficients C_n^{I}, C_n^{II} in (9), (10) are determined by weakly enforcing the noninherently satisfied boundary condition (4) and the matching conditions (11), (12), (13), and (14).

A measure of how well these conditions are satisfied is given by the functional R:

$$R = \int_{1+\delta}^{\Lambda} [\psi^{I} - 1]^2 + \left[\frac{\partial \psi^{I}}{\partial x}\right]^2 dy + \int_{0}^{1-\delta} [\psi^{I} - \psi^{II}]^2 + \left[\frac{\partial \psi^{I}}{\partial x} - \frac{\partial \psi^{II}}{\partial x}\right]^2 + \left[\frac{\partial^2 \psi^{I}}{\partial x^2} - \frac{\partial^2 \psi^{II}}{\partial x^2}\right]^2 + \left[\frac{\partial^3 \psi^{I}}{\partial x^3} - \frac{\partial^3 \psi^{II}}{\partial x^3}\right]^2 dy \quad \text{on} \quad x = 0. \quad (15)$$

The small region $1 - \delta < y < 1 + \delta$ near the re-entrant corner on the contraction plane $x = 0$, is excluded from the functional R. It was found that this greatly improves the numerical performance of the solution scheme developed below. Typically $\delta = 0.1$. The singularity in the solution at the re-entrant corner is responsible for the deterioration of the numerical performance if this region is not excluded.

The coefficients C_n^{I}, C_n^{II} are obtained by minimizing R, that is solving

$$\frac{\partial R}{\partial C_i^{I}} = 0 \quad \text{and} \quad \frac{\partial R}{\partial C_i^{II}} = 0 \quad i: 1, 2, 3 \ldots N. \quad (16a)$$

Equation (16a) reduces to

$$\int_{1+\delta}^{\Lambda} \phi_i\left(\frac{y}{\Lambda}\right)\left([\psi^{I} - 1]\frac{1}{p_i^2} + \left[\frac{\partial \psi^{I}}{\partial x}\right]\frac{1}{\Lambda p_i}\right) dy + \int_{0}^{1-\delta} \phi_i\left(\frac{y}{\Lambda}\right)\left([\psi^{I} - \psi^{II}]\frac{1}{p_i^2} + \left[\frac{\partial \psi^{I}}{\partial x} - \frac{\partial \psi^{II}}{\partial x}\right]\frac{1}{\Lambda p_i} + \left[\frac{\partial^2 \psi^{I}}{\partial x^2} - \frac{\partial^2 \psi^{II}}{\partial x^2}\right]\frac{1}{\Lambda^2} + \left[\frac{\partial^3 \psi^{I}}{\partial x^3} - \frac{\partial^3 \psi^{II}}{\partial x^3}\right]\frac{p_i}{\Lambda^3}\right) dy = 0$$

and

$$\int_{0}^{1-\delta} \phi_i(y)\left(-[\psi^{I} - \psi^{II}]\frac{1}{p_i^2} + \left[\frac{\partial \psi^{I}}{\partial x} - \frac{\partial \psi^{II}}{\partial x}\right]\frac{1}{p_i} - \left[\frac{\partial^2 \psi^{I}}{\partial x^2} - \frac{\partial^2 \psi^{II}}{\partial x^2}\right] + \left[\frac{\partial^3 \psi^{I}}{\partial x^3} - \frac{\partial^3 \psi^{II}}{\partial x^3}\right]p_i\right) dy = 0.$$

$$i: 1, 2, 3 \ldots N \quad \text{on} \quad x = 0. \quad (16b)$$

The $2N$ equations, (16b), linear in the unknown coefficients C_1^{I} to C_N^{I} and C_1^{II} to C_N^{II}, are solved simultaneously by LU decomposition of the matrix of coefficients.

The form of (16b) shows that this solution method is equivalent to the Galerkin method. See, for example, Forray (1968).

Post-Processing Technique and Treatment of the Singularity

The behavior of the solution based on ψ^{I} and ψ^{II} was necessarily poor in the vicinity of the re-entrant corner where the boundary and matching conditions were not applied. To improve the visual appearance of the streamline plots in this region, the same type of post-processing technique as applied by Phillips and Davies (1988) was used. A separate solution ψ^{c} was used to replace the ψ^{I} and ψ^{II} solution in a small circular region (Region C) centerd on the re-entrant corner. The minimum radius required for Region C was typically 2δ. This region is shown in Fig. 2.

ψ^{c} is expressed in terms of the well-known symmetrical and antisymmetrical series used to describe Stokes flow near a corner of angle 2α, where $\alpha = 3\pi/4$ in the present case. See, for example, Leal (1992).

Downloaded 04 May 2010 to 171.66.16.27. Redistribution subject to ASME license or copyright; see http://www.asme.org/terms/Terms_Use.cfm

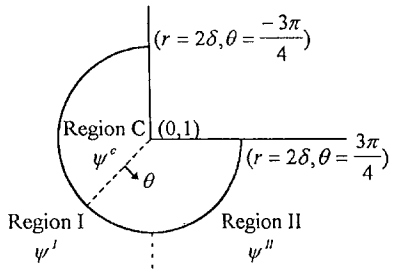


Fig. 2 The post processed region: C

$$\psi^c = \mathrm{Re}\{\sum_{i=1}^{M} \beta_i^A r^{\lambda_i^A}(\cos((\lambda_i^A - 2)\alpha)\cos(\lambda_i^A\theta) - \cos((\lambda_i^A - 2)\theta)\cos(\lambda_i^A\alpha)) + \beta_i^S r^{\lambda_i^S}(\sin((\lambda_i^S - 2)\alpha) \times \sin(\lambda_i^S\theta) - \sin((\lambda_i^S - 2)\theta)\sin(\lambda_i^S\alpha))\}$$

$$0 \le r \le 2\delta, \quad \frac{-3\pi}{4} \le \theta \le \frac{3\pi}{4} \qquad (17)$$

Terms with superscript A belong to the antisymmetrical solution and those with superscript S belong to the symmetrical solution.

λ_i^A and λ_i^S are the eigenvalues of these solutions given by the roots, with real part greater than 1, of

$$\sin(2\alpha(\lambda_i^A - 1)) = -(\lambda_i^A - 1)\sin(2\alpha)$$

and

$$\sin(2\alpha(\lambda_i^S - 1)) = +(\lambda_i^S - 1)\sin(2\alpha).$$

These eigenvalues ensure that the no-slip boundary condition on the solid wall is satisfied by ψ^c. The complex valued coefficients β_i^A and β_i^S are chosen by collocation so that ψ^c and $\partial\psi^c/\partial r$ match that of the ψ^I and ψ^{II} solution on the circumference $r = 2\delta$. Only a small number of terms in the series (17) are needed to adequately represent the solution at the corner.

Results

ψ^I, ψ^{II}, and ψ^c were used to represent the stream function ψ for planar Stokes flow through contractions of $\Lambda = 2$, 3, 4, 5, and 6. The series representing ψ^I and ψ^{II} (9) and (10) were truncated at 50 terms ($N = 50$) to satisfy the boundary and matching conditions to a maximum absolute error of 10^{-4}. The series representing ψ^c, the post-processed corner expansion (17), was truncated at four terms ($M = 4$) to give smooth contours in the immediate vicinity of the re-entrant corner.

The streamline patterns for $\Lambda = 2$, 3, and 4 are shown in Figs. 3, 4, and 5, respectively. The irregularities on the solid wall at the contraction plane are a consequence of not satisfying boundary condition (4) exactly. These can be reduced by increasing the number of terms N in the series in (9) and (10) and increasing the number of significant figures kept in the computation.

A characteristic feature of the streamline patterns is the recirculating zone upstream of the contraction plane. The size of this zone has been studied by a number of investigators. See, for example, Boger (1987). The distance of the attachment point of the primary separating streamline from the contraction plane can be used as a measure of the size of this recirculating zone. The size is made dimensionless with respect to the downstream channel halfwidth w. This dimensionless size depends on the contraction ratio Λ. A plot of the dimensionless recirculating zone size, as generated by the series solution, versus Λ is shown in Fig. 6.

Another important feature of channel contraction flow is the variation of the pressure drop with contraction ratio Λ. The pressure is nondimensionalised with respect to $\mu u_{av}/w$ where μ is the viscosity of the fluid and u_{av} is the average velocity in the downstream channel. Figure 7 is a plot of this dimensionless pressure along the centerline of the channel when $\Lambda = 2$. The pressure is arbitrarily taken to be zero at the contraction plane. The two straight lines in Fig. 7 are the pressure in the upstream

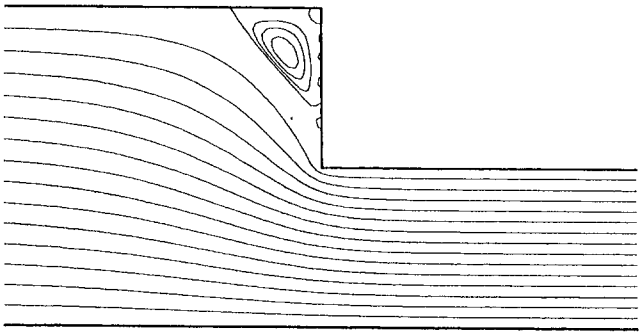


Fig. 3 Streamline plot for $\Lambda = 2$

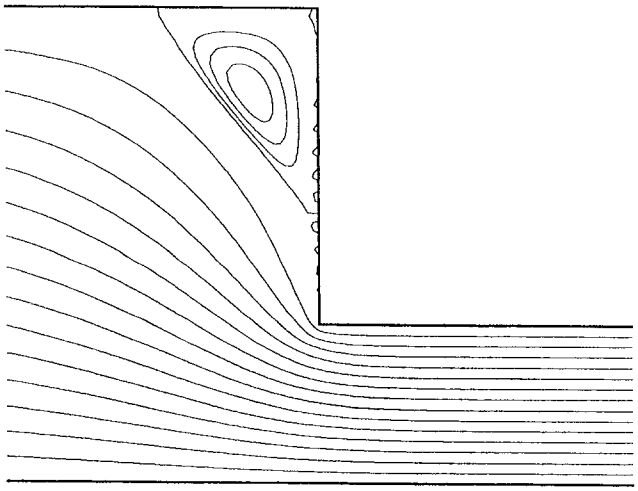


Fig. 4 Streamline plot for $\Lambda = 3$

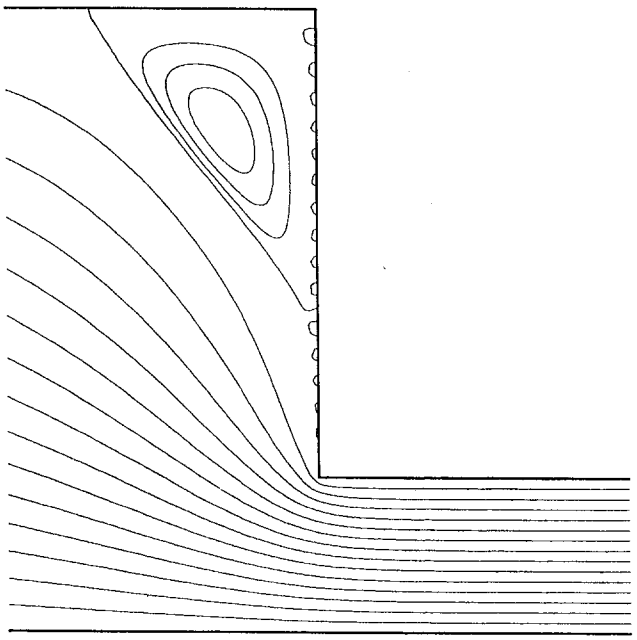


Fig. 5 Streamline plot for $\Lambda = 4$

Downloaded 04 May 2010 to 171.66.16.27. Redistribution subject to ASME license or copyright; see http://www.asme.org/terms/Terms_Use.cfm

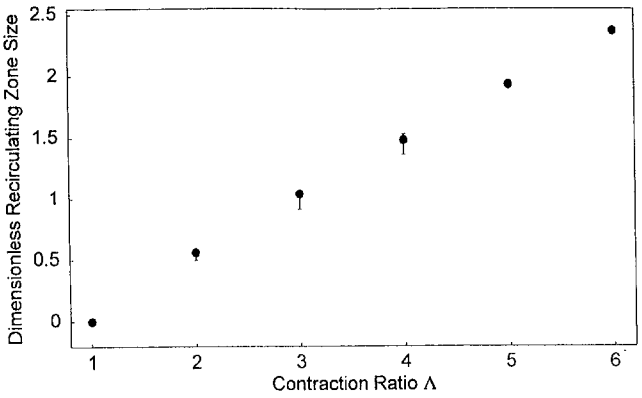


Fig. 6 Dimensionless size of the recirculating zone versus contraction ratio

and downstream channels if the velocity rearrangement brought about by the contraction is ignored. Comparing the pressure profile for this idealized case with the actual pressure profile allows the excess dimensionless pressure drop introduced by the contraction to be evaluated. The excess dimensionless pressure drop is, as expected, a function of the contraction ratio. A plot of the dimensionless excess pressure drop as a function of Λ is shown in Fig. 8. The error bars in this figure are estimated from the variation in the predicted pressure drop with the number of terms N included in the series representations ψ^{I} and ψ^{II}.

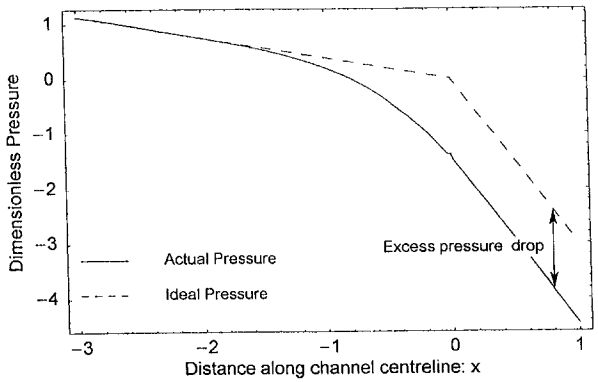


Fig. 7 Dimensionless pressure along the channel centerline when Λ = 2 and excess pressure drop

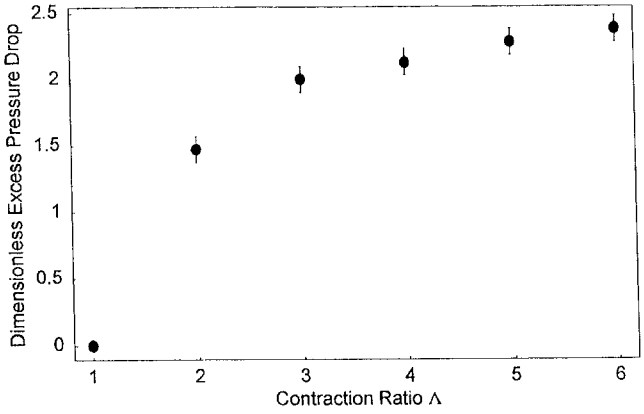


Fig. 8 Dimensionless excess pressure drop versus contraction ratio

Discussion

The stream function for planar Stokes flow through channels with contraction ratios between two and six has been successfully approximated with a series of Papkovich-Fadle eigenfunctions. Comparable results, using a variety of other techniques, have been published for contraction ratios of between two and four. The streamline plots in Figs. 3–5 are very similar to the finite element results of Davies et al. (1984), the finite difference results of Dennis and Smith (1980), the boundary integral procedures of Ingham and Kelmanson (1984), and the Chebyshev and Laguerre series representations of Karageorghis and Phillips (1989, 1991). The maximum differences between the sizes of the predicted recirculating zones using the present results and the results of these workers are denoted by the error bars in Fig. 6.

A search of the literature has failed to locate any published results on the pressure variation along the channel centreline of a constricted channel. The pressure variation at small contraction ratios (Fig. 7 and Fig. 8) compare well, however, with the authors own finite element method investigation. This finite element method investigation was limited to small contraction ratios because of the large computational requirements of the finite element method.

In their investigation of the planar contraction problem, Karageorghis and Phillips (1991) split the problem domain (Fig. 1) into three regions rather than two, eliminating the singularity at the re-entrant corner of the channel. This resulted in improved convergence of their series compared with this investigation.

An attempt was made in which the coefficients C_n^{I}, C_n^{II} and β_i^A, β_i^S for the series representation in Regions I and II and the re-entrant corner Region C were determined simultaneously by ensuring C^3 continuity across all the boundaries between these regions. For $N = 15$ and $M = 3$ terms, the results obtained were not reliable. It was surmised that the disparity in the length of the boundaries and consequently the emphasis between the corner region and that of the upstream and downstream regions may be the source of the numerical problem. This could be overcome by suitably adjusting the weighting of the various terms in the modified expression for R, but was not attempted.

Conclusions

The problem of Stokes flow through a planar contraction can be solved using a Papkovich-Fadle eigenfunction representation. Apart from generating the streamline plots, this approach also allows the excess pressure drop to be computed with relative ease.

Acknowledgments

This project was supported by Grant S89711261 from the Australian Research Council. The authors are grateful to Dr. M. R. Davidson of the Department of Chemical Engineering at The University of Melbourne for his helpful comments on the formulation of this problem.

References

Boger, D. V., 1987, "Viscoelastic Flows Through Contractions," *Annual Review of Fluid Mechanics,* Vol. 19, pp. 157–182.

Davies, A. R., Lee, S. J., and Webster, M. F., 1984, "Numerical Simulations of Viscoelastic Flow: The Effect of Mesh Size," *Journal of Non-Newtonian Fluid Mechanics,* Vol. 16, pp. 117–139.

Dennis, S. C. R., and Smith, F. T., 1980, "Steady Flow Through a Channel with a Symmetrical Constriction in the Form of a Step," *Proceedings of the Royal Society London,* Vol. A372, pp. 393–414.

Forray, M. J., 1968, *Variational Calculus in Science and Engineering,* McGraw-Hill, New York.

Ingham, D. B., and Kelmanson, M. A., 1984, *Boundary Integral Equation Analyses of Singular, Potential, and Biharmonic Problems* (Lecture Notes in Engineering), C. A. Brebbia and S. A. Orszag, eds, Springer-Verlag, Berlin.

Joseph, D. D., and Sturges, L., 1978, "The Convergence of Biorthogonal Series for Biharmonic and Stokes Flow Edge Problems: Part II," *SIAM Journal of Applied Mathematics,* Vol. 34, No. 1, pp. 7–26.

Downloaded 04 May 2010 to 171.66.16.27. Redistribution subject to ASME license or copyright; see http://www.asme.org/terms/Terms_Use.cfm

Karageorghis, A., and Phillips, T. N., 1989, "Spectral Collocation Methods for Stokes Flow in Contraction Geometries and Unbounded Domains," *Journal of Computational Physics,* Vol. 80, pp. 314–330.

Karageorghis, A., and Phillips, T. N., 1991, "Conforming Chebyshev Spectral Collocation Methods for the Solution of Laminar Flow in a Constricted Channel," *IMA Journal of Numerical Analysis,* Vol. 11, pp. 33–54.

Leal, L. G., 1992, *Laminar Flow and Convective Transport Processes,* Butterworth-Heinemann, London.

Phillips, T. N., and Davies, A. R., 1988, "On Semi-Infinite Spectral Elements for Poisson Problems With Re-entrant Boundary Singularities," *Journal of Computational and Applied Mathematics,* Vol. 21, pp. 173–188.

Smith, R. C. T., 1952, "The Bending of a Semi-Infinite Strip," *Australian Journal of Scientific Research,* Vol. 5, pp. 227–237.

Trogdon, S. A., and Joseph, D. D., 1982, "Matched Eigenfunction Expansions for Slow Flow Over a Slot," *Journal of Non-Newtonian Fluid Mechanics,* Vol. 10, pp. 185–213.

Downloaded 04 May 2010 to 171.66.16.27. Redistribution subject to ASME license or copyright; see http://www.asme.org/terms/Terms_Use.cfm

Impulsive Squeezing With Suction and Injection

E. A. Hamza
Department of Mathematics and Statistics,
College Science,
Sultan Qaboos University,
P. O. Box 36,
Al-Khod 123,
Muscat, Sultanate of Oman

This paper is concerned with the motion of a fluid film squeezed between two parallel plane surfaces with suction or injection at the porous surface. Attention is given to the case of impulsive squeezing. Analytic solutions based on the regular perturbation technique and on the linearized analysis of the resulting nonlinear partial differential equation are presented. The effects of injection and suction on the velocity profiles and on the normal forces which the fluid exerts on the surfaces are studied.

1 Introduction

The behavior of a thin film of liquid squeezed between two parallel plane surfaces has for long been recognized to be one of the most basic problems in lubrication theory. Many theoretical and experimental investigations into the problem have been motivated by role of lubrication in engineering practice and its obvious relevance to our technology-based world. Reynolds (1886) appears to have been the first to derive an equation which governs the pressure distribution in lubricating films. In his equation he assumed that the inertia terms are negligible in comparison to viscous terms. Modern lubrication theory deals in large with departures from the classical lubrication theory set by Reynolds. One such departure is to include the inertia effects. Studies of the importance of inertia effects have been motivated by the increase in speed of modern machines and, in special applications, the use of low-viscosity lubricants to reduce energy losses. The mathematical analysis, when inertia terms are included, has up to the present been based on an iteration or perturbation scheme which relies on the assumption that the Reynolds number, Re, is not large. Authors who have studied the role played by fluid inertia include Ishizawa (1966), Kuzma (1967), Tichy and Winer (1970), Jones and Wilson (1975), and Hamza and MacDonald (1981). Kuzma obtained correct approximations to the radial pressure gradient and the velocity distribution to the first order of Re. The second-order perturbation solution was included in a wide-ranging study of the squeezed-film problem by Ishizawa. He drew attention to the rapid decrease in magnitude of the universal functions f_i which occur in the perturbation expansion (it has been shown by MacDonald (1977) that $f_{i+1} = O(10^{-2} f_i)$, $0 \le i \le 5$). Expermintal results have been provided by Tichy and Winer, who considered Reynolds numbers in the range $8 < \mathrm{Re} < 14.2$ and by Kuzma who considered numbers as high as 60. Although one would expect agreement for small values of Re, the authors just mentioned, respectively, found that good agreement prevailed at values of $\mathrm{Re} = 10$ and $\mathrm{Re} = 50$. Although Tichy and Winer use of the perturbation solutions for the case when $\mathrm{Re} = 10$ can be explained by reference to the remarkable decrease in the magnitude of the functions f_i, $i \ge 1$, the Kuzma agreement between the first order and experiment in the upper range of Re is surprising. Jones and Wilson and Hamza and MacDonald considered the initial motion in the fluid and studied the length of the transition period during which the regular perturbation solution will not accurately approximate the exact solution, regardless of the value of the Reynolds number. Hamza and MacDonald's results which were obtained from the solution of the full nonlinear equations of motion by employing a finite difference scheme suggest that the first-order perturbation theory is meaningful except in the immediate vicinity of the time $t = 0$. The good agreement between first-order perturbation theory and Kuzma's experimental results for a range of Reynolds numbers extending to $\mathrm{Re} = 60$ can be seen in the light of this fact.

Suction and injection effects in lubrication have received considerable attention due to the important roles they play in many industrial applications; especially in situations where it is not possible to avoid the use of liquid-metal lubricants in preference to the convential lubricants. They also have effects in the fields of biomechanics, e.g., in cases of alternation between contraction and expansion of the blood vessels.

In this paper we examine the motion of an incompressible viscous flow between two parallel plane disks where one disk is fixed and the other is rapidly accelerated from a state of rest to a state of uniform motion in the presence of suction or injection of fluid through the fixed disk. The motivation of this study is to see the way in which the lubricant flow patterns and the load capacity change with time and to investigate their responses to suction and injection.

2 Equations of Motion

The geometry with which we shall be concerned is that of two parallel plane surfaces which initially are separated by a thin film of lubricant of thickness a_0. We select cylindrical polar coordinates (r^*, θ^*, z^*), in terms of which the lower fixed surface is described by $z^* = 0$ and the upper surface by $z^* = a(t^*)$, where $a(0) = a_0$. The corresponding velocity components are (u^*, v^*, w^*). We shall assume that the lubricant is at rest for $t^* < 0$ and that at $t^* = 0$ the upper surface moves impulsively towards the lower one with constant velocity V. For $t^* > 0$, fluid is injected or sucked from the lower surface with constant velocity V_0. We transform to nondimensional form by referring all lengths to a_0, all velocities to V, time to a_0/V, and pressure to ρV^2, where ρ denotes density. The corresponding dimensionless variables are those without the asterisks. The configuration is sketched in Fig. 1.

The nondimensional equations governing the flow are

$$\frac{\partial u}{\partial t} + u\frac{\partial u}{\partial r} + w\frac{\partial u}{\partial z} = -\frac{\partial p}{\partial r} + \frac{1}{\mathrm{Re}}\left(\frac{\partial^2 u}{\partial^2 z} + \frac{\partial^2 u}{\partial^2 r} + \frac{1}{r}\frac{\partial u}{\partial r} - \frac{u}{r^2}\right),$$

$$\frac{\partial w}{\partial t} + u\frac{\partial w}{\partial r} + w\frac{\partial w}{\partial z} = -\frac{\partial p}{\partial z} + \frac{1}{\mathrm{Re}}\left(\frac{\partial^2 w}{\partial^2 z} + \frac{\partial^2 w}{\partial^2 r} + \frac{1}{r}\frac{\partial w}{\partial r}\right),$$

$$\frac{\partial}{\partial r}(ru) + r\frac{\partial w}{\partial z} = 0,$$

where $\mathrm{Re} = Va_0/\nu$ (ν denotes kinematic viscosity).

The boundary conditions are

$$u = 0 \quad \text{at} \quad z = 0 \quad \text{and} \quad \text{at} \quad z = 1 - t,$$

Contributed by the Applied Mechanics Division of THE AMERICAN SOCIETY OF MECHANICAL ENGINEERS for publication in the ASME JOURNAL OF APPLIED MECHANICS.
Discussion on the paper should be addressed to the Technical Editor, Professor Lewis T. Wheeler, Department of Mechanical Engineering, University of Houston, Houston, TX 77204-4792, and will be accepted until four months after final publication of the paper itself in the ASME JOURNAL OF APPLIED MECHANICS.
Manuscript received by the ASME Applied Mechanics Division, Feb. 3, 1998; final revision, June 25, 1999. Associate Technical Editor: D. A. Siginer.

 Copyright © 1999 by ASME

Downloaded 04 May 2010 to 171.66.16.27. Redistribution subject to ASME license or copyright; see http://www.asme.org/terms/Terms_Use.cfm

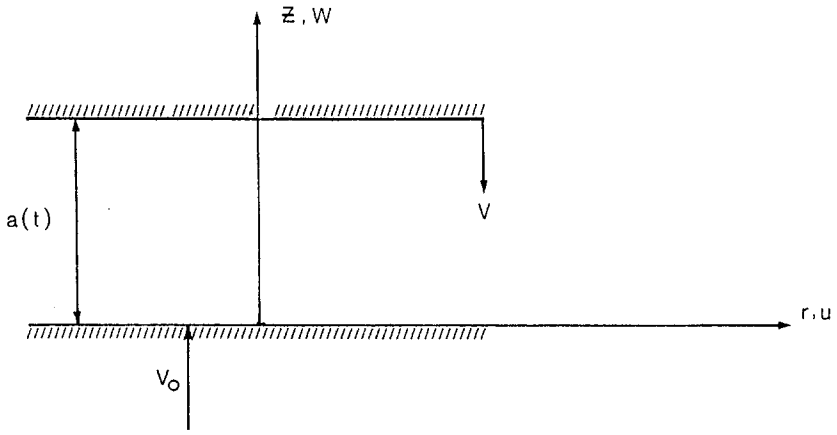


Fig. 1 System configuration at time t

$$w = V_0/V \quad \text{at} \quad z = 0 \quad \text{and} \quad w = -1 \quad \text{at} \quad z = 1 - t.$$

The mass conservation equation is satisfied by a stream function $F(z, t)$ which is such that

$$u = rF_z, \quad w = -2F,$$

so that the above nondimensional momentum equations may be expressed in the form

$$F_{zt} + F_z^2 - 2FF_{zz} = -\frac{1}{r}p_r + \frac{1}{\mathrm{Re}}F_{zzz}, \tag{1}$$

$$F_t - 2FF_z = \frac{1}{2}p_z + \frac{1}{\mathrm{Re}}F_{zz}. \tag{2}$$

Further Eqs. (1) and (2) show that p is of the form

$$p = \tfrac{1}{2}r^2P_1(t) + P_2(z, t),$$

where differentiation of Eq. (1) with respect to z and then use of the change of variables

$$y = z/T, \quad T = 1 - t,$$

leads to the equation

$$\mathrm{Re}\{yTF_{yyy} + 2TF_{yy} - T^2F_{yyT} - 2TFF_{yyy}\} = F_{yyyy}. \tag{3}$$

The transformed boundary conditions are

$$F = A, \quad F_y = 0, \quad y = 0; \quad F = 1/2, \quad F_y = 0, \quad y = 1, \tag{4}$$

where $A = V_o/2V$ is a constant parameter such that $A > 0$ corresponds to suction and $A > 0$ corresponds to injection.

The radial pressure gradient $P_1(t)$ is given by

$$T^3P_1 = (\mathrm{Re})^{-1}F_{yyy} - yTF_{yy} + T^2F_{yT} - TF_y - TF_y^2 + 2TFF_{yy}. \tag{5}$$

The initial condition, which states that for $y \neq 0, 1$, the vorticity is zero at time $t = 0^+$,

$$F = \tfrac{1}{2}y, \quad \text{when} \quad T = 1^-, \tag{6}$$

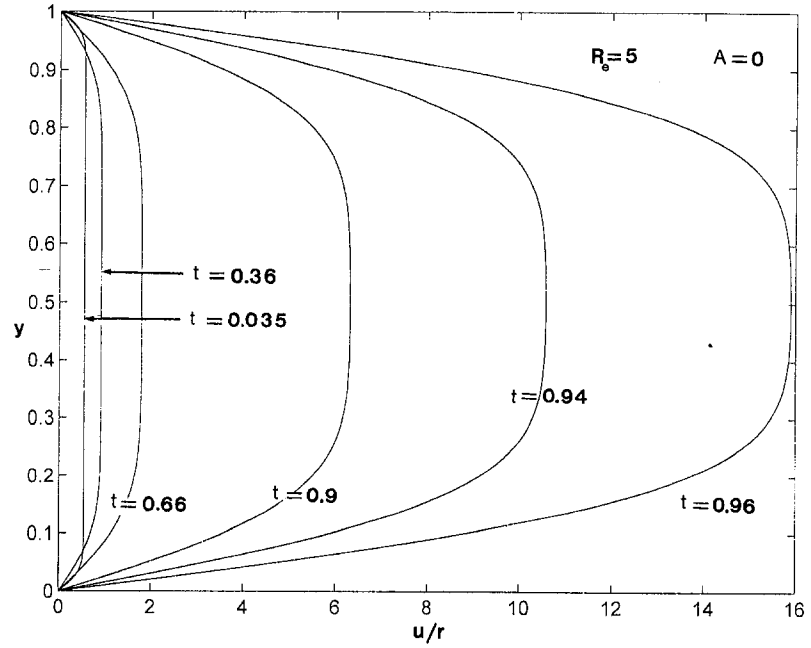


Fig. 2(*a*)

Downloaded 04 May 2010 to 171.66.16.27. Redistribution subject to ASME license or copyright; see http://www.asme.org/terms/Terms_Use.cfm

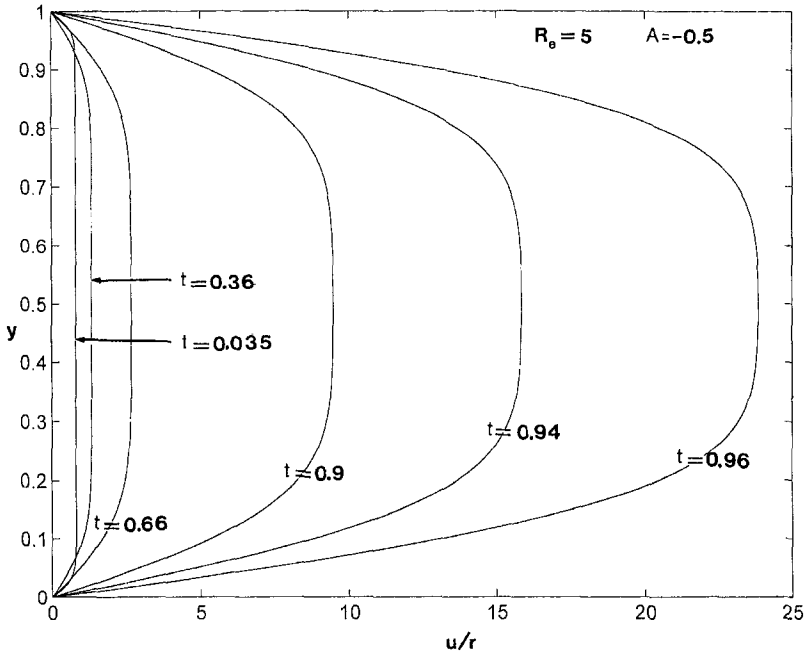


Fig. 2(*b*)

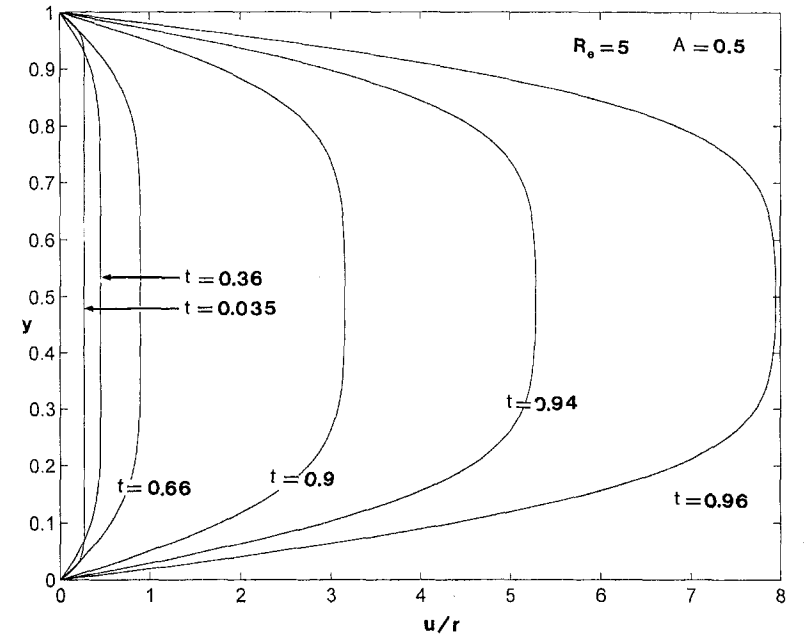


Fig. 2(*c*)

Fig. 2 Radial velocity profile development with time *t* when Re = 5 and *A* = 0, *A* = −0.5, *A* = 0.5

(i.e., at $t = 0^+$ the radial velocity u outside the infinitesimally thin sheets of vorticity which are formed on the surfaces is the inviscid velocity given by the continuity equation

$$\pi(r^*)^2 V \delta t^* = 2\pi r^* u^* a_0 \delta t^*,$$

i.e.,

$$\frac{u^*}{V} = \frac{r^*}{2a_0}, \quad \text{i.e.,} \quad \frac{u}{r} = \frac{1}{2}\Big).$$

If the upper disk is assumed to be of radius c and of negligible thickness, the resultant normal force, or load W, is given by

$$W = 2\pi \int_0^c r[p(r, h, t) - p_0]dr,$$

where p_0 is the nondimensional pressure at $r = c$, $z = a$. Thus the above result may be expressed in the form

$$W = -\pi \int_0^c r^3 P_1 dr. \tag{7}$$

Downloaded 04 May 2010 to 171.66.16.27. Redistribution subject to ASME license or copyright; see http://www.asme.org/terms/Terms_Use.cfm

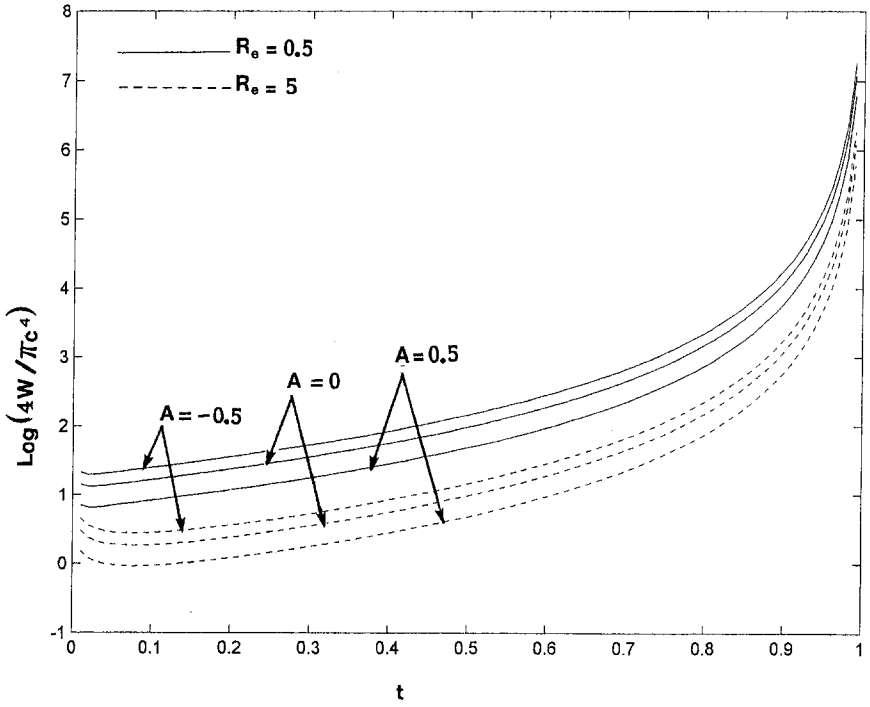


Fig. 3 Normal force, or load, variation with time t when Re = 0.5, Re = 5 and $A = 0$, $A = -0.5$, $A = 0.5$

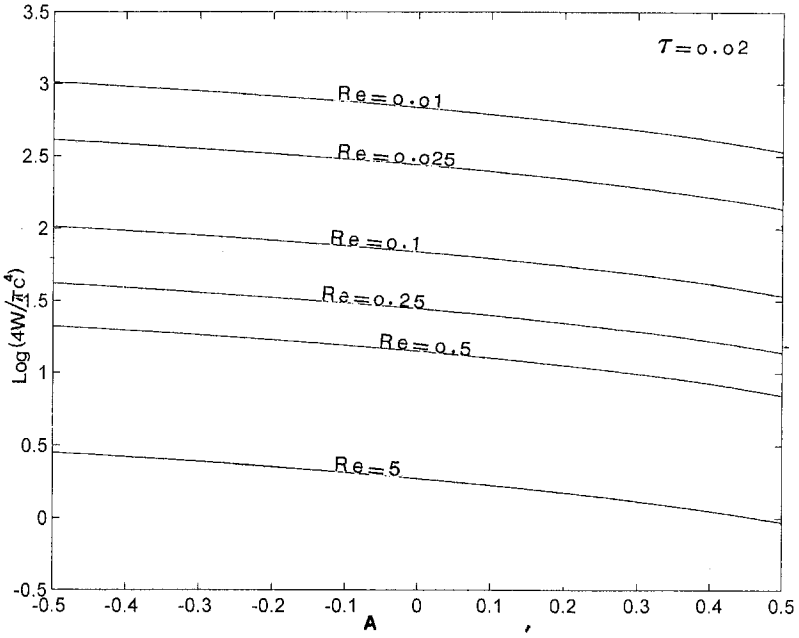


Fig. 4 Normal force, or load, variation with A and Re when $\tau = 0.02$

3 Analytic Solutions

The nonlinear partial differential Eq. (3) with conditions (4) and (6) can be solved for special practical when cases Re, A, and t are small.

3.1 Solution for Small Re. By ignoring the initial condition (6), we can obtain from Eqs. (3) and (4) the terms of the perturbation expansion

$$F = \sum_{n=0}^{\infty} (\mathrm{Re}T)^n f_n(y). \tag{8}$$

The first three terms are

Table 1 Comparison of the solution based on Eq. (13) (L) and the first-order perturbation results (P) for the radial pressure gradient: percent error = $100(L-P)/L$

	Re				
τ	0.01	0.025	0.1	0.25	0.5
.002	59.48	59.37	58.83	57.75	55.95
.005	41.88	41.73	40.95	39.40	36.82
.010	26.58	26.39	25.41	23.45	20.20
.020	11.99	11.76	10.58	08.25	04.38
.025	08.14	07.90	06.67	04.24	00.22
.040	03.27	03.01	01.72	00.83	05.01
.060	05.20	04.95	03.69	01.21	02.82
.080	00.07	00.34	01.67	04.27	08.46
.100	00.16	00.42	01.75	04.33	08.46
.150	00.18	00.44	01.76	04.30	08.26
.200	00.18	00.44	01.75	04.24	08.04

Downloaded 04 May 2010 to 171.66.16.27. Redistribution subject to ASME license or copyright; see http://www.asme.org/terms/Terms_Use.cfm

Table 2 Comparison of the solution of Eq. (13) by (i) Laplace transform method (LT) and (ii) separation of variables method (SV) for the radial pressure gradient: percent error = 100(LT–SV)/LT

τ	.002	.004	.008	.010	.020	.025	.040	.060	.080	.100	.150	.200
% error	19.88	7.17	1.10	0.44	0.01	0.03	0.89	4.88	10.77	16.99	31.13	42.93

$$f_0 = \frac{A}{2} + y^2(1-A)\left(\frac{3}{2} - y\right),$$

$$f_1 = \frac{1}{140}\, y^2(1-A)(y-1)^2[y^2(1-A)(3-2y) - y(13+8A) + 22A + 6],$$

$$f_2 = -\frac{1}{1293600}\, y^2(1-A)(y-1)^2(g+h+q) \qquad (9)$$

where

$$g = 504y^6(1-A)^2(2y-7) + 7y^4(1-A)(26y(2A+53) - 5(476A+437)),$$

$$h = -12y^3(1417A^2 - 1910 - 1047) - y^2(19868A^2 + 34877A + 5315),$$

$$q = 2y(20974A^2 + 10027A - 47) - 16356A^2 + 295A + 507.$$

The radial pressure gradient P_1 is given by

$$P_1 = \frac{1}{r}\, p_r = -6(1-A)(\mathrm{Re}T^3)^{-1}\left\{1 + \frac{\mathrm{Re}T}{140}(52A+25) + \frac{(\mathrm{Re}T)^2}{323400}(18665A^2 + 4866A - 277)\right\}. \qquad (10)$$

This is the solution which does not satisfy the initial condition (6) and so we expect it not to be valid in the vicinity of $t = 0$. However, for t not small and $\mathrm{Re} = o(1)$, the solution is a good approximation to the motion of the fluid. When $A = 0$, the solution reduces to the forced solution given by Ishizawa (1966) and Jones and Wilson (1975). They obtained the solution correct to $O(\mathrm{Re}^2)$. Good agreement with experiment, even when the Reynolds number was an order of magnitude greater than unity, was reported by Tichy and Winer (1970) and Kuzma (1967). The good agreement between theory and experiment at values of $\mathrm{Re} > 1$ can be explained by reference to the remarkable decrease in magnitude of the functions f_i, $i > 0$.

3.2 Solution for Small *t*. To prepare the ground for a study of the flow field when $0 < t \ll 1$ the following transformation is introduced:

$$T = 1 - \mathrm{Re}\tau, \quad \text{i.e.,} \quad t = \mathrm{Re}\tau.$$

Equation (3) becomes

$$y[\mathrm{Re} - \mathrm{Re}^2\tau]F_{yyy} + 2[\mathrm{Re} - \mathrm{Re}^2\tau]F_{yy} + [\mathrm{Re}^2\tau^2 - 2\,\mathrm{Re}\tau + 1]F_{yy\tau} + 2[\mathrm{Re}^2\tau - \mathrm{Re}]FF_{yyy} = F_{yyyy}, \qquad (11)$$

with initial condition

$$F = \tfrac{1}{2}y \quad \text{when} \quad \tau = 0^+, \quad y \neq 0, 1. \qquad (12)$$

The leading terms of Eq. (11) are now

$$F_{yy\tau} = F_{yyyy}, \qquad (13)$$

an equation of diffusion type which can be solved subject to conditions (4) and (12).

To solve these equations, we shall employ two different techniques: (a) the method of separation of variables (Jones and Wilson, 1975) to obtain the solution for F in terms of an infinite series which we expect to be slowly convergent for $\tau \ll 1$, and (b) Laplace transformation (Hamza and MacDonald, 1981) to get a solution which is rapidly convergent for $\tau \to 0$. A comparison between the two solutions will be given.

Separation of Variables Solution. The outline of the solution starts by changing the nonhomogeneous boundary conditions (4) to homogeneous ones. Putting

$$F(y,\tau) = G(y,\tau) + (1-A)y^2\left(\frac{3}{2} - y\right) + \frac{A}{2},$$

Eq. (13) reduces to

$$G_{yy\tau} = G_{yyyy}, \qquad \text{(i)}$$

with boundary conditions

$$G = G_y = 0 \quad \text{on} \quad y = 0; \quad G = G_y = 0 \quad \text{on} \quad y = 1. \qquad \text{(ii)}$$

The solution by separation of variables gives

$$F = (1-A)y^2\left(\frac{3}{2} - y\right) + \frac{A}{2} + \sum_{n=1}^{\infty} C_n Y_n(y) e^{-k_n^2\tau}, \qquad (14)$$

where the eigenvalues k_n satisfy

$$k_n \sin k_n + 2\cos k_n - 2 = 0, \qquad \text{(iii)}$$

and the eigenfunctions Y_n are given by

$$Y_n = \frac{\cos k_n - 1}{\sin k_n - k_n}(\sin k_n y - k_n y) + (1 - \cos k_n y), \qquad \text{(iv)}$$

and the constants C_n are determined from the initial condition (12). The eigenfunctions can be shown to be orthogonal in the sense that

$$\int_0^1 Y_n'(y)Y_m'(y)dy = 0 \quad \text{for} \quad m \neq n.$$

Hence, the constants C_n are given by

$$C_n = \frac{\displaystyle\int_0^1 [1/2 + 3(1-A)y(y-1)]Y_n'dy}{\displaystyle\int_0^1 [Y_n']^2 dy}. \qquad \text{(v)}$$

The eigenvalues are in two groups. The first group is $k_n = 2n\pi$, $n = 1, 2, 3 \ldots$ while the second group is the solution of the transcendental equation $\tan(k_n/2) = k_n/2$, where the first two values (see Abramowitz and Stegun, 1970, p. 224) are $k_1 = 8.9868$ and $k_2 = 15.4505$. When $k_n = 2n\pi$, the corresponding eigenfunctions are $\{1 - \cos(2n\pi y)\}$ and these give $C_n = 0$. So we are left only with the second group. In this case Eqs. (iv) and (v) reduce to

$$Y_n = \frac{2}{k_n}(\sin k_n y - k_n y) + (1 - \cos k_n y) \qquad \text{(vi)}$$

Downloaded 04 May 2010 to 171.66.16.27. Redistribution subject to ASME license or copyright; see http://www.asme.org/terms/Terms_Use.cfm

and

$$C_n = \frac{2(1-A)}{k_n^2}. \tag{vii}$$

The radial pressure gradient is given by

$$P_1 = \frac{1}{\mathrm{Re}T^3}[F_{yyy} - F_{y\tau} + O(\mathrm{Re}\tau)] + O(1),$$

$$= -6(\mathrm{Re}T^3)^{-1}(1-A)\{(1 + \tfrac{2}{3}e^{-k_1^2\tau} + \dots) + O(\mathrm{Re})\}. \tag{15}$$

The term $\frac{2}{3}\exp(-k_1^2\tau)$ is the correction of the first term in Eq. (10). It is the contribution of the initial condition. Hence for the initial condition to be negligible, we must have $\frac{2}{3}\exp(-k_1^2\tau) = \frac{2}{3}\exp(-80.8t/\mathrm{Re}) \ll 1$.

So the neglect of the initial condition cannot be justified when the squeeze Reynolds number Re is greater than 280, (the variable t runs from 0 to 1). On the other hand, when Re is small the initial condition becomes negligible for $\tau = t/\mathrm{Re} > (\ln 20/3)/80.8 \approx 0.0235$ to obtain less than ten percent error in the pressure gradient.

Laplace Transform Solution. Integrating Eq. (13) with respect to y twice, multiplying the resulting equation by $e^{-s\tau}$, and then integrating with respect to τ over $[0, \infty)$, we obtain, on using the conditions (12) and (4),

$$\bar{F}(y, s) = \frac{A}{2} + \frac{(1-A)I(s, y)}{4(1 - s^{1/2}/2)} \sum_{n=0}^{\infty} \left[\frac{1 + s^{1/2}/2}{1 - s^{1/2}/2}\right]^n e^{-ns^{1/2}},$$

where

$$\bar{F} = \int_0^\infty e^{-s\tau} F(y, \tau)\, d\tau,$$

and

$$I(s, y) = \frac{1}{s}[1 - s^{1/2}y(1 + e^{-s^{1/2}}) - e^{-s^{1/2}y} + e^{-s^{1/2}(1-y)} - e^{-s^{1/2}}].$$

For small τ

$$\bar{F}(y, s) = \frac{1}{s}\frac{[1 - s^{1/2}y - e^{-s^{1/2}y} + e^{-s^{1/2}(1-y)}]}{4(1 - s^{1/2}/2)} + O\left(\frac{e^{-s^{1/2}}}{s}\right),$$

so that

$$F(y, \tau) = (1-A)F_s(y, \tau) + \frac{A}{2}, \tag{16}$$

where F_s is the solution of the case of no injection or suction, given by Hamza and MacDonald (1981). For the benefit of the reader we rewrite the solution here.

$$F_s(y, \tau) = \frac{1}{4}\Bigg[1 + 2e^{4\tau}(y - 1/2)\,\mathrm{erfc}\,(-2\tau^{1/2}) + \mathrm{erfc}\,\frac{1-y}{2\tau^{1/2}} - \mathrm{erfc}\,\frac{y}{2\tau^{1/2}} + e^{-2y+4\tau}\,\mathrm{erfc}\left(\frac{y}{2\tau^{1/2}} - 2\tau^{1/2}\right) - e^{-2(1-y)+4\tau}\,\mathrm{erfc}\left(\frac{1-y}{2\tau^{1/2}} - 2\tau^{1/2}\right) + e^{-2+4\tau}\,\mathrm{erfc}\left(\frac{1}{2\tau^{1/2}} - 2\tau^{1/2}\right) + 2ye^{-2+4\tau}\,\mathrm{erfc}\left(\frac{1}{2\tau^{1/2}} - 2\tau^{1/2}\right) - \mathrm{erfc}\left(\frac{1}{2\tau^{1/2}}\right)\Bigg] + O(\tau^{1/2}e^{-1/4\tau}). \tag{17}$$

The radial pressure gradient, on using the conditions $F = F_y = 0$ on $y = 0$, is given by

$$P_1 = \frac{1}{\mathrm{Re}T^3}[F_{yyy}(0, \tau) - F_{y\tau}(0, \tau) + O(\mathrm{Re}\tau)],$$

i.e.,

$$P_1 = (\mathrm{Re}T^3)^{-1}(1-A)\Bigg[-2\Bigg\{e^{4\tau}\,\mathrm{erfc}\,(-2\tau^{1/2}) + e^{-2+4\tau}\,\mathrm{erfc}\left(\frac{1}{2\tau^{1/2}} - 2\tau^{1/2}\right)\Bigg\} - (\pi\tau)^{-1/2}\left\{1 + e^{-1/4\tau}\left(\frac{1}{4\tau} + 1\right)\right\}\Bigg] \tag{18}$$

The two forms (14) and (16) of the solution to Eqs. (13), (4), and (12) should give accurate results for $0 < t \ll 1$ and they can be used to estimate the importance of the initial condition. However, Eq. (16) is suitable for values of τ which satisfy $0 < \tau \ll 1$ whereas Eq. (14) is meaningful when τ is not small. For other ranges of interest, nonlinear terms must be taken into account and this necessitates a numerical solution of the full nonlinear equation.

4 Results and Discussion

We present and discuss the case where the upper surface is impulsively set in motion in such a way that the direction of motion, being towards the lower surface, is at rest. Fluid is injected ($A < 0$) or sucked ($A > 0$) with constant velocity through the lower surface. The impulsive movement of the upper surface results in impulsive movement of the fluid, the driving force being the radial pressure gradient, which does work to overcome fluid inertia and frictional resistance. Close to the start of the motion, vorticity is concentrated at the surfaces and is zero elsewhere. As t increases vorticity diffuses out from the surfaces and the approximate dimensional distance δ^* to which vorticity will have diffused in time t_m is given by

$$\delta^* = a_0 - Vt_m^* - 2(\nu t_m^*)^{1/2}.$$

So the nondimensional time required for the vorticity layers to merge can be written as

$$t_m = \frac{2}{\mathrm{Re}} + 1 - \frac{2}{\mathrm{Re}}(1 + \mathrm{Re})^{1/2}.$$

Thus for $\mathrm{Re} \ll 1$ $t_m \approx \frac{1}{4}\mathrm{Re} + O(\mathrm{Re}^2)$, whereas for $\mathrm{Re} \gg 1$ $t_m \approx 1 - 2/Re^{1/2}$.

Figure 2 shows the variation of the radial velocity profile with time t for $\mathrm{Re} = 5$ and $A = -0.5$, 0 and 0.5. The figure demonstrates the effect of vorticity diffusion on the velocity field. In the early stages of motion we notice that there are thin layers of vorticity adjacent to both surfaces with an inviscid core in between. As t increases, vorticity diffuses out from the surfaces and as $t \to 1$, the vorticity layers merge, inertial resistance becomes negligible in comparison to frictional resistance, and the radial velocity profile tends to the parabolic profile predicted by the classical lubrication theory (i.e., by f_0 in the perturbation results). The manner in which $F \to f_0$ depends on Re. The effect of suction and injection on the velocity profiles is to decrease or increase them by a factor of $(1 - A)$.

Of considerable interest is the variation of the radial pressure gradient (or equivalently the load W) with Reynolds number Re, time t, and the suction and injection parameter A. In the case of no suction or injection the normal force W exerted by the fluid on the surfaces is so directed as to push the surfaces away from each other. It is large near the start of the motion and near collision. A large force is necessary in the early stages of the motion to overcome inertial resistance and near the end of the motion to overcome frictional resistance. For $t \to 0$, it can be shown from Eq. (18) that the load behaves like $(1 - A)/(\pi\,\mathrm{Re}t)^{1/2}$, so near $t =$

Downloaded 04 May 2010 to 171.66.16.27. Redistribution subject to ASME license or copyright; see http://www.asme.org/terms/Terms_Use.cfm

0 W decreases with increase of t. Thus in the early stages of the motion W is large and is decreasing with increase of t, but for t close to 1, W is large and increasing with increase of t. The effect of suction and injection is to decrease or increase the load by a factor of $(1 - A)$. These effects can be gauged from Fig. 3.

Figure 4 presents the load variation with A in the range $-0.5 < A < 0.5$ for Reynolds numbers in the range $0.01 < \mathrm{Re} < 5.0$ when $\tau = 0.02$. The results shown in this figure indicate that for a fixed value of τ and A, the load on the disk decreases as $\mathrm{Re} = Va_0/\nu$ increases. This result states that if V and a_0 are held constant a decrease in kinematic viscosity will result in a decrease in the load. On the other hand, for a fixed value of τ and Re, there is a slight decrease in the load with increase of the magnitude of A. Thus when fluid is injected through the lower surface this will result in an increase of the load. Opposite results are noticed when suction is introduced.

In practice lubrication bearings normally operate at low Reynolds number, and if this is the case, perturbation theory is adequate to predict the motion. However, close to the start of the motion the perturbation results are not valid. It is of interest to employ the linearized analysis based on Eq. (13) to check the accuracy of the approximate results obtained in Eq. (9). For Reynolds number of 0.01, 0.025, 0.1, 0.25, 0.5 and for values of τ in the range $0.002 < \tau < 0.2$, Table 1 compares the radial pressure gradient term as computed from Laplace and separation of variables solutions of the linear equation (13) with the first-order perturbation results. The comparison reveals that the first-order perturbation results are not valid for small values of t. However, for $\tau > 0.02$, we observe that the first-order perturbation results for the radial pressure gradient are within ten percent of the correct results.

It is worthwhile to compare the radial pressure gradient obtained from the solutions to Eq. (13) by Laplace and separation of variables methods. For a range of τ extending to 0.2, this comparison is made in Table 2. The table demonstrates the remarkable agreement between the two results for $0.008 < \tau < 0.06$ and the difference outside this range.

References

Abramowitz, M., and Stegun, I. A., 1970, *Handbook of Mathematical Functions,* ninth printing, Dover, New York.

Hamza, E. A., and MacDonald, D. A., 1981, "A Fluid Film Squeezed Between Two Parallel Plane Surfaces," *Journal of Fluid Mechanics,* Vol. 109, pp. 147–160.

Ishizawa, S. A., 1966, "The Unsteady Laminar Flow Between Two Parallel Disks with Arbitrarily Varying Gap Width," *Bull. of the JSME,* Vol. 9, pp. 533–550.

Jones, A. F., and Wilson, S. D. R., 1975, "On the Failure of Lubrication Theory in Squeezing Flows," *Trans. ASME Series F,* Vol. 97, pp. 101–104.

Kuzma, D. C., 1967, "Fluid Inertia Effects in Squeeze Films," *Appl. Sc. Res.,* Vol. 18, pp. 15–20.

MacDonald, D. A., 1977, "On Asymptotic Approximation to a Class of Regular Perturbation Problems," ASME *Journal of Lubrication Technology,* Series F, Vol. 99, pp. 369–375.

Reynolds, O., 1886, "On The Theory of Lubrication and its Application to Mr. Beauchamp Tower's Experiments, Including an Experimental Determination of The Viscosity of Olive," *Phil. Trans. Roy. Soc., London,* Vol. A177, pp. 157–234.

Tichy, J. A., and Winer, W. O., 1970, "Inertial Considerations in Parallel Circular Squeeze Film Bearings," ASME *Journal of Lubrication Technology, Series F,* Vol. 92, pp. 588–592.

Downloaded 04 May 2010 to 171.66.16.27. Redistribution subject to ASME license or copyright; see http://www.asme.org/terms/Terms_Use.cfm

G. Borino
Dipartimento di Ingegneria Strutturale & Geotecnica, DISeG, Università di Palermo, Viale delle Scienze, I-90128 Palermo, Italy

P. Fuschi
Dipartimento Arte Scienza Tecnica Del Costruire, DASTEC, Università di Reggio Calabria, Via Melissari, I-89120 Reggio Calabria, Italy

C. Polizzotto
Dipartimento di Ingegneria Struttarale & Geotecnica, DISeG, Università di Palermo, Viale delle Sicenze, I-90128 Palermo, Italy

A Thermodynamic Approach to Nonlocal Plasticity and Related Variational Principles[1]

Elastic-plastic rate-independent materials with isotropic hardening/softening of nonlocal nature are considered in the context of small displacements and strains. A suitable thermodynamic framework is envisaged as a basis of a nonlocal associative plasticity theory in which the plastic yielding laws comply with a (nonlocal) maximum intrinsic dissipation theorem. Additionally, the rate response problem for a (continuous) set of (macroscopic) material particles, subjected to a given total strain rate field, is discussed and shown to be characterized by a minimum principle in terms of plastic coefficient. This coefficient and the relevant continuum tangent stiffness matrix are shown to admit, in the region of active plastic yielding, some specific series representations. Finally, the structural rate response problem for assigned load rates is studied in relation to the solution uniqueness, and two variational principles are provided for this boundary value problem.

1 Preliminaries and Motivation

Many technologically important materials (concrete, rocks, soils, ceramics, fiber-reinforced concrete, metals, etc.) exhibit a softening behavior (i.e., decrease of stress at increasing strain, or in general loss of positive definiteness of the tangent stiffness matrix), which is known to be accompanied by strain localization phenomena, that is, the formation, within a structure, of narrow regions (shear bands) where plastic deformation tends to concentrate, whereas the remainder of the structure unloads elastically. The analytical and numerical descriptions of these phenomena, precursors of failure, incur into serious difficulties due to loss of material stability and of well-posedness of the relevant boundary value problem (the latter ceases to be elliptic at the onset of strain localization), with consequent inception of equilibrium bifurcation phenomena (loss of solution uniqueness) and spurious mesh sensitivity in numerical finite element simulations. The very reason for these shortcomings with local plasticity theories is the lack of any material parameter as an internal length scale specifying the extent within which the microstructure's points influence one another. In other words, local plasticity theories, being characterized by a vanishing internal length scale, lead to indeterminacy of the width of the strain localization band, which in fact tends to become infinitely small in the continuum approaches, or takes on the size of the smallest finite element in the numerical treatments.

An abundant literature has been devoted to strain localization problems. On one hand, criteria for strain localization (i.e., the conditions in which the localization phenomenon is possible in a given state of the material) have been formulated; e.g., Rudnicki and Rice (1975), Hill and Hutchinson (1975), Hutchinson and Tvergaard (1981), Raniecki and Bruhns (1981), Loret (1987), and Borré and Maier (1989). On the other hand, a number of remedies to the ill-posedness of the boundary value problem in the presence of softening have been proposed with the common feature of introducing an internal length scale parameter into the continuum plasticity constitutive equations. Among these remedies, often referred to as localization limiters, the *nonlocal plasticity* and the *gradient plasticity* models are the most popular. In the nonlocal plasticity model (see, e.g., Bažant and Lin, 1988), the plasticity constitutive equations make use of quantities expressed as weighted values of local variables over the body's domain, or over a suitable influence volume centered at the generic spatial point. The gradient plasticity model (see, e.g., Aifantis, 1984; Coleman and Hodgdon, 1985; Larsy and Belytschko, 1988; Mühlhaus and Aifantis, 1991, de Borst et al. (1993, 1995), de Borst and Pamin, 1996), is characterized by a yield function which depends on the accumulated plastic strain, as well as on higher-order spatial gradients of it. A full discussion of the performance of these two plasticity models as localization limiters was provided by de Borst et al. (1993) together with a comparison with other types of localization limiters, i.e., the *Cosserat continuum model* (Mühlhaus and Vardulakis, 1987) and the *rate-dependent continuum model* (Needleman, 1988). Other proposed localization limiter types are of pure computational nature (e.g., Ortiz et al., 1987; Pietruszak and Mróz, 1981).

The purpose of the present paper is to address the above-mentioned constitutive models from the thermodynamic point of view. The Cosserat and rate-dependent continuum models are out of discussion because they comply with full locality (their ability to operate as localization limiters is due to their intrinsic mathematical features and their thermodynamic formulation is possible in principle). Thus only the nonlocal and gradient plasticity models need to be considered. Nonlocal plasticity is the object of this paper, whereas gradient plasticity is addressed elsewhere (Polizzotto and Borino, 1998). Some of the results herein presented have been the object of a research communication (Polizzotto et al., 1996).

Efforts to frame nonlocal plasticity within a general nonlocal theory of continua were made by Eringen (1981, 1983) and Nilsson (1994). These thermodynamically consistent formulations consider all (or almost all) the independent state variables as nonlocal and may thus be unsuitable for a wide class of strain-softening materials for which, as observed by Pijaudier-Cabot and Bažant (1987), only the variables that control strain-softening need to be treated as nonlocal. Strömberg and Ristinmaa (1996) accepted this point and accounted for the nonlocality using a non-associative plasticity model.

The thermodynamic formulation of nonlocal plasticity proposed

[1] This paper is dedicated to Prof. Giulio Maier on the occasion of his 65th birthday.

Contributed by the Applied Mechanics Division of THE AMERICAN SOCIETY OF MECHANICAL ENGINEERS for publication in the ASME JOURNAL OF APPLIED MECHANICS.

Discussion on the paper should be addressed to the Technical Editor, Professor Lewis T. Wheeler, Department of Mechanical Engineering, University of Houston, Houston, TX 77204-4792, and will be accepted until four months after final publication of the paper itself in the ASME JOURNAL OF APPLIED MECHANICS.

Manuscript received by the ASME Applied Mechanics Division, Mar. 31, 1997; final revision, Mar. 10, 1999. Associate Technical Editor: J. L. Bassani.

 Copyright © 1999 by ASME

Downloaded 04 May 2010 to 171.66.16.27. Redistribution subject to ASME license or copyright; see http://www.asme.org/terms/Terms_Use.cfm

by the present paper rests on the above observation by Pijaudier-Cabot and Bažant (1987) and is accordingly grounded upon the following premise: Plastic strain produces effects as isotropic hardening/softening not only where it occurs, but also at the other points of the body. This implies the existence of hardening/softening diffusion processes developing around the strain source points at the microstructure level, with consequent energy exchanges between different particles within some *diffusion* domain (V_D) in the body. As a consequence of this,

(i) the local action principle of thermodynamics does not hold.
(ii) the first and second principles of thermodynamics must be enforced globally for the diffusion domain V_D; or, alternatively, they can be enforced locally, but the energy exchanges between the material particles at the microstructure level need to be accounted for.
(iii) only the internal variables attached to the isotropic hardening/softening behavior are of nonlocal nature and, as a consequence, equilibrium and compatibility equations are not affected by nonlocality.

The plan of the paper is the following: In Sections 2 and 3, some thermodynamic considerations are developed in which the nonlocality nature of the material is specified by an appropriate integral-type regularization operator and the (nonlocal) Clausius-Duhem inequality is applied to derive the state equations and the expression of the nonnegative (nonlocal) intrinsic dissipation energy as well as to evaluate the nonlocality residual. In Section 4, the yielding laws are established for rate-independent associative nonlocal plasticity, showing that these laws comply with the nonlocal Clausius-Duhem inequality. In Section 5, a theorem of maximum intrinsic dissipation for nonlocal plasticity is provided. In Section 6, the response of the material to given total strain rates is discussed and shown to be—under certain conditions—uniquely determined by a minimum principle in terms of plastic coefficient. In Section 7, referring to a simplified nonlocal material model, series representations are given for this coefficient, as well as for the tangent stiffness matrix. In Section 8, the structural rate problem for given load rates is discussed together with its solution uniqueness. In Section 9, two variational statements of stationarity are provided for this boundary value problem, showing that they transform into a min-max principle and a minimum principle, respectively, in case of everywhere positive hardening modulus. In the last section, Section 10, the conclusions are drawn and possible future developments considered. The paper is closed by three appendices, one (Appendix A) devoted to the convergence of the series representations of Section 7, the other two (Appendices B and C) devoted to the proofs of the variational principles of Section 9.

Notation. A compact notation is used, with boldface letters denoting vectors or tensors. The "dot" and "colon" products between vectors and tensors denote the simple and double index saturation operations, respectively; that is, e.g., $\mathbf{u} \cdot \mathbf{v} = u_i v_i$, $\boldsymbol{\sigma} : \boldsymbol{\epsilon} = \sigma_{ij}\epsilon_{ji}$, $(\mathbf{C} : \boldsymbol{\epsilon})_{ij} = C_{ijhk}\epsilon_{kh}$, where the indices denote Cartesian components and the repeated index rule is applied. Partial derivatives are denoted as $a_{,b} = \partial a/\partial b$, where b is a scalar or vector or tensor variable; the time derivative is denoted by an upper dot, i.e., $\dot{a} = \partial a/\partial t$. $\mathbf{x} = \{x_1, x_2, x_3\}$ denotes orthogonal Cartesian coordinates. Also: ∇ = gradient operator, e.g., $\nabla\mathbf{u} = \{\partial u_j/\partial x_i\}$; $\nabla \cdot$ = divergence operator, e.g., $\nabla \cdot \boldsymbol{\sigma} = \sigma_{ji,j}$; the symbol := means equality by definition. Other symbols will be introduced in the text where they appear for the first time.

2 Thermodynamic Considerations

An elastic-plastic rate-independent material occupying the domain V exhibits an isotropic hardening/softening behavior of nonlocal nature. Due to this nonlocality of the material, the first principle of thermodynamics (see, e.g., Germain et al., 1983; Lemaitre and Chaboche, 1985) can be cast as

$$\int_{V^*} \rho \dot{e} dV = \int_{V^*} (\boldsymbol{\sigma} : \dot{\boldsymbol{\epsilon}} + r - \nabla \cdot \mathbf{q}) dV, \qquad \forall\, V^* : V_D \subseteq V^* \subseteq V \quad (1)$$

where ρ is the material density, $e = e(\boldsymbol{\epsilon}^e, s, \xi)$ is the internal energy, function of the elastic strain ($\boldsymbol{\epsilon}^e$), entropy (s) and the scalar (nonlocal) internal variable ξ related to the isotropic hardening/softening behavior; $\boldsymbol{\sigma}$ is the stress, $\dot{\boldsymbol{\epsilon}}$ the total strain rate, r the heat source by radiation, and $\mathbf{q}$ the heat flux. Also, V^* denotes any region of the material which includes the diffusion domain V_D, which in turn includes the (finite) region V_p within which a thermoplastic deformation mechanism is activated, i.e., $V_p \subseteq V_D \subseteq V$. Since V_p, hence V_D, cannot be smaller than some limit dictated by the material internal length scale, l say, Eq. (1) implies, everywhere in V:

$$\rho \dot{e} = \boldsymbol{\sigma} : \dot{\boldsymbol{\epsilon}} + r - \nabla \cdot \mathbf{q} + P, \quad (2)$$

where P is referred to as the *nonlocality residual* after Edelen and Laws (1971) and Edelen et al. (1971). P represents the (mechanical) energy transmitted to the considered material particle by the neighbor particles through the hardening/softening diffusion processes in V_D, the latter being promoted by the plastic deformation mechanism. P has a constitutive dependence from variables attached to the hardening/softening material behavior (like ξ), but this dependence will be determined later on after that the precise nonlocality features have been specified. For the moment it will suffice to note that $P = 0$ for purely thermoelastic processes and that

$$\int_{V^*} P dV = 0, \quad \forall\, V^* : V_D \subseteq V^* \subseteq V, \quad (3)$$

which implies that $P = 0$ at all points $\mathbf{x} \notin V_D$. In particular for $V^* = V_D$ Eq. (3) reads

$$\int_{V_D} P dV = 0, \quad \text{(insulation condition)} \quad (4)$$

meaning that no energy exchanges occur between the particles in V_D and the exterior world.

Let T be the absolute temperature. Using the free energy $\psi = e - sT$ and Eq. (2), one can write

$$D := T\left[\rho \dot{s} - \frac{r}{T} + \nabla \cdot \left(\frac{\mathbf{q}}{T}\right)\right] = \boldsymbol{\sigma} : \dot{\boldsymbol{\epsilon}} - \rho\dot{\psi} - \rho s \dot{T} - \nabla T \cdot \left(\frac{\mathbf{q}}{T}\right) + P \geq 0 \quad (5)$$

where the expression in square brackets is the internal entropy production rate and D, referred to as the *net dissipation density,* is non-negative by the second principle of thermodynamics (entropy inequality). Inequality (5) is the Clausius-Duhem inequality, differing from its classical format for the nonlocality residual P. The energy W globally dissipated in V^*, using Eq. (5) and remembering (3), reads

$$W := \int_{V^*} D dV = \int_{V^*} \left(\boldsymbol{\sigma} : \dot{\boldsymbol{\epsilon}} - \rho\dot{\psi} - \rho s \dot{T} - \left(\frac{\mathbf{q}}{T}\right) \cdot \nabla T\right) dV \geq 0 \qquad \forall\, V^* : V_D \subseteq V^* \subseteq V \quad (6)$$

Downloaded 04 May 2010 to 171.66.16.27. Redistribution subject to ASME license or copyright; see http://www.asme.org/terms/Terms_Use.cfm

which is an integral form of the Clausius-Duhem inequality.

Note that, denoting by $\mathbf{T}$ surface forces on ∂V, and by $\mathbf{b}$ body forces in V, assuming $\dot{\boldsymbol{\epsilon}}$ compatible with displacement rates $\dot{\mathbf{u}}$, and $\boldsymbol{\sigma}$ in equilibrium with the above loading forces, by the virtual work principle Eq. (6) written for $V^* = V$ can be rewritten as follows:

$$\int_V \rho\dot{\psi}dV \leq \int_{\partial V} \mathbf{T}\cdot\dot{\mathbf{u}}dS + \int_V \mathbf{b}\cdot\dot{\mathbf{u}}dV - \int_V \left(\rho s\dot{T} + \left(\frac{\mathbf{q}}{T}\right)\cdot\nabla T\right)dV \quad (7)$$

which constitutes a generalization of the variational inequality of Valanis (1996), (with which it coincides in case of uniform time-independent temperature).

Let the free energy be taken in the form

$$\psi = \psi_e(\boldsymbol{\epsilon}^e, T) + \psi_{\text{in}}(\xi, T) \quad (8)$$

where ψ_e and ψ_{in} are C^2-continuous functions of their arguments. Decomposing $\dot{\boldsymbol{\epsilon}}$ in the sum of elastic and plastic parts, i.e., $\dot{\boldsymbol{\epsilon}} = \dot{\boldsymbol{\epsilon}}^e + \dot{\boldsymbol{\epsilon}}^p$, and using Eq. (8), inequality (5) can be written as

$$D = \left(\boldsymbol{\sigma} - \rho\frac{\partial\psi_e}{\partial\boldsymbol{\epsilon}^e}\right) : \dot{\boldsymbol{\epsilon}}^e - \rho\left(s + \frac{\partial\psi}{\partial T}\right)\dot{T} + \boldsymbol{\sigma} : \dot{\boldsymbol{\epsilon}}^p - \rho\frac{\partial\psi_{\text{in}}}{\partial\xi}\dot{\xi} - \nabla T\cdot\left(\frac{\mathbf{q}}{T}\right) + P \geq 0 \quad (9)$$

which holds everywhere in V, but $P = 0$ in $V\backslash V_D$. Inequality (9) must be satisfied for any thermal and deformation processes of the material and it can thus be used in order to derive the constitutive restrictions on the prospected material model. As noted by Lubliner (1973) and Acharya and Shawki (1995, 1996), this derivation is by no means a trivial task. The latter authors employed the Coleman and Noll (1963) method to derive the thermodynamic compatibility conditions for an assumed evolution law of the material. Here, leaving unspecified this evolution law until the subsequent section, we follow a widely used reasoning (Coleman and Gurtin, 1967; Simo and Ju, 1987; Lemaitre and Chaboche, 1985) with the assumption that a constitutive restriction that is found to hold for the class of reversible processes hold true also for the irreversible ones.

Thus, let an arbitrary thermoelastic process with $\nabla T = 0$ be considered first. Then, since $\dot{\boldsymbol{\epsilon}}^p = \mathbf{0}$, $\dot{\xi} = 0$, $P = 0$ (no hardening/softening diffusion processes are activated), Eq. (9) simplifies as

$$\left(\boldsymbol{\sigma} - \rho\frac{\partial\psi_e}{\partial\boldsymbol{\epsilon}^e}\right) : \dot{\boldsymbol{\epsilon}}^e - \rho\left(s + \rho\frac{\partial\psi_e}{\partial T}\right)\dot{T} \geq 0. \quad (10)$$

This inequality implies the following restrictions:

$$\boldsymbol{\sigma} = \rho\frac{\partial\psi_e}{\partial\boldsymbol{\epsilon}^e}(\boldsymbol{\epsilon}^e, T), \quad s = -\rho\frac{\partial\psi}{\partial T}(\boldsymbol{\epsilon}^e, \xi, T) \quad (11)$$

which are admitted to be of general validity and in fact constitute the material state equations. Returning to the general case, as a consequence of (11), Eq. (9) reduces to

$$D = D_p + D_T \geq 0 \quad (12)$$

where D_p and D_T denote the (mechanical) net intrinsic dissipation and the thermal (diffusion) dissipation densities, respectively, that is

$$D_p = \boldsymbol{\sigma} : \dot{\boldsymbol{\epsilon}}^p - \chi\dot{\xi} + P \geq 0 \quad (13a)$$

$$D_T = -\nabla T\cdot\left(\frac{\mathbf{q}}{T}\right) \geq 0. \quad (13b)$$

Here, the new variable χ is the hardening force (or, $-\chi$ = thermodynamic force corresponding to the flux $\dot{\xi}$), defined as

$$\chi := \rho\frac{\partial\psi_{\text{in}}}{\partial\xi}(\xi, T), \quad (14)$$

which can be considered as an additional state equation. The sign constraints of Eqs. (13) are due to the circumstances that Eq. (12) must hold also in case of a purely mechanical ($\mathbf{q} = \mathbf{0}$), or purely thermal ($\dot{\boldsymbol{\epsilon}}^p = \mathbf{0}$, $\dot{\xi} = 0$, $P = 0$), processes.

The global net intrinsic dissipation in V^* by Eq. (3) reads:

$$W_p = \int_{V^*} (\boldsymbol{\sigma} : \dot{\boldsymbol{\epsilon}}^p - \chi\dot{\xi})dV \quad \forall\, V^* : V_D \subseteq V^* \subseteq V. \quad (15)$$

3 Nonlocal Isotropic Hardening and Evaluation of the Residual P

The hardening/softening diffusion processes previously mentioned can be described by an equation as

$$\dot{\xi} = \mathcal{R}(\dot{\kappa}) \quad \text{in} \quad V_D \subseteq V \quad (16)$$

where κ is a local internal variable with the meaning of (scalar) measure of plastic strain and $\mathcal{R}$ is a suitable *regularization operator*. Equation (16) reveals the nonlocal nature of the $\dot{\xi} - \dot{\kappa}$ relation in that the value of $\dot{\xi}$ at $\mathbf{x}$ depends on the values of $\dot{\kappa}$ within some region around $\mathbf{x}$ and that thus the plastic mechanism taking place in V_p produces hardening/softening effects in some diffusion region V_D, $V_p \subseteq V_D \subseteq V$. For gradient-dependent (or weakly nonlocal) plasticity, Eq. (16) expresses $\dot{\xi}$ as a function of $\dot{\kappa}$ and of some spatial gradients of it, in which case obviously it is $V_p = V_D \subseteq V$ (Polizzotto et al., 1996; Polizzotto and Borino, 1998). For (true) nonlocal plasticity, which is of concern in this paper, $\mathcal{R}$ is an integral operator and Eq. (16) expresses $\dot{\xi}(\mathbf{x})$ as a weighted value of the $\dot{\kappa}$ field. A typical $\dot{\xi} - \dot{\kappa}$ relation can be written as (Pijaudier-Cabot and Bazănt, 1987; Bazănt and Lin, 1988; Nilsson, 1994; Strömberg and Ristinmaa, 1996)

$$\dot{\xi}(\mathbf{x}) = \frac{1}{G(\mathbf{x})}\int_V g(\|\mathbf{y} - \mathbf{x}\|)\dot{\kappa}(\mathbf{y})dV(\mathbf{y}) \quad \text{for all} \quad \mathbf{x} \in V, \quad (17)$$

where $g(\|\mathbf{y} - \mathbf{x}\|)$ is some positive weighting function (typically, the error function $g(r) = \exp(-cr^2/l^2)$ with $c > 0$ constant and $r = \|\mathbf{y} - \mathbf{x}\|$) whereas $G(\mathbf{x})$ is the weight relative to the field point $\mathbf{x}$ defined as

$$G(\mathbf{x}) = \int_V g(\|\mathbf{y} - \mathbf{x}\|)dV(\mathbf{y}). \quad (18)$$

The value of $G(\mathbf{x})$ over the infinite domain, G_∞ say, is finite and depends on c, but not on $\mathbf{x}$. The condition $G_\infty(c) = V_{RP}$ where V_{RP} = *representative volume,* i.e., sphere (or circle in two dimensions, or segment in one dimension) of diameter l, is usually employed to evaluate c (Bazănt and Lin, 1988; Strömberg and Ristinmaa, 1996). It is evident from (17) that the diffusion domain turns out to coincide with V, i.e., $V_D = V$; in other words, for nonlocal plasticity the plastic mechanism over V_p is in principle able to generate hardening/softening effects in the whole body.

Continuing the reasoning on nonlocal plasticity, with its nonlocality features specified by (17), or by (16) in abridged form, the nonlocality residual P can correspondingly be uniquely determined. To this purpose, let the net intrinsic dissipation D_p of (13a) be rewritten, by (16), as

$$D_p = \boldsymbol{\sigma} : \dot{\boldsymbol{\epsilon}}^p - \chi\mathcal{R}(\dot{\kappa}) + P \geq 0. \quad (19)$$

Downloaded 04 May 2010 to 171.66.16.27. Redistribution subject to ASME license or copyright; see http://www.asme.org/terms/Terms_Use.cfm

As the plastic strain mechanism $(\dot{\boldsymbol{\epsilon}}^p, \dot{\kappa})$ takes place in $V_p \subseteq V$, D_p can be different from zero in the whole V and there it must have a bilinear form as

$$D_p = \boldsymbol{\sigma} : \dot{\boldsymbol{\epsilon}}^p - X\dot{\kappa}, \tag{20}$$

where $(\dot{\boldsymbol{\epsilon}}^p, \dot{\kappa})$ are the (local) evolutive variables (fluxes) describing the irreversible strain mechanism and $(\boldsymbol{\sigma}, -X)$ are the corresponding thermodynamic forces, with X being some (nonlocal) variable to be identified. (Note that the thermal dissipation D_T of (13*b*) has already a bilinear form with $-\nabla T$ the thermodynamic force and $\mathbf{q}/T$ the related flux.)

On comparing (20) with (19), one obtains

$$P = \chi\mathcal{R}(\dot{\kappa}) - X\dot{\kappa}; \tag{21}$$

then, the insulation condition (4) written for $V_D = V$ gives

$$\int_V [\chi\mathcal{R}(\dot{\kappa}) - X\dot{\kappa}]dV = 0. \tag{22}$$

Making use of (17) and introducing the new operator $\mathcal{R}^*$ given by

$$\mathcal{R}^*(\chi)|_{\mathbf{x}} := \int_V \frac{g(\|\mathbf{y} - \mathbf{x}\|)}{G(\mathbf{y})}\chi(\mathbf{y})dV(\mathbf{y}), \tag{23}$$

Eq. (22) becomes

$$\int_V [\mathcal{R}^*(\chi) - X]\dot{\kappa}dV = 0. \tag{24}$$

As the latter equation must be satisfied identically, that is, for any irreversible deformation mechanism and for any possible evolution law, hence independently from the way the square-bracketed function may depend on $\dot{\kappa}$, the following (necessary and sufficient) condition holds:

$$X = \mathcal{R}^*(\chi) \quad \text{in} \quad V \tag{25}$$

while the residual P is correspondingly identified as

$$P = \chi\mathcal{R}(\dot{\kappa}) - \mathcal{R}^*(\chi)\dot{\kappa}. \tag{26}$$

The latter satisfies the insulation condition (4) (with $V_D = V$), i.e.,

$$\int_V [\chi\mathcal{R}(\dot{\kappa}) - \mathcal{R}^*(\chi)\dot{\kappa}]dV = 0 \tag{27}$$

which enables the operator $\mathcal{R}^*$ to be recognized as the *adjoint* of $\mathcal{R}$.

By (26), the net intrinsic dissipation D_p of (19) reads

$$D_p = \boldsymbol{\sigma} : \dot{\boldsymbol{\epsilon}}^p - \mathcal{R}^*(\chi)\dot{\kappa} \geq 0 \tag{28}$$

from where P has disappeared, but Eq. (28) has still a nonlocal feature through the nonlocal thermodynamic force, $-\mathcal{R}^*(\chi)$, related to $\dot{\kappa}$. It is worth noting the important role played by the nonlocality residual P. It in fact renders applicable the second principle of thermodynamics (Clausius-Duhem inequality) at a local level in spite of the nonlocal nature of the material. As stated before, P represents the energy exchanges that occur between material particles at the microstructural level. Such energy exchanges can be given the following interpretation: The global plastic work $\int_{V_p} \boldsymbol{\sigma} : \dot{\boldsymbol{\epsilon}}^p dV$ redistributes throughout V (with local additions P where $P > 0$, or losses $-|P|$ where $P < 0$), in such a way that the (local) excess energy, D_p, with respect to the microstructure stored energy, $\chi\dot{\xi}$; that is, the quantity $D_p = (\boldsymbol{\sigma} : \dot{\boldsymbol{\epsilon}}^p + P) - \chi\dot{\xi} = \boldsymbol{\sigma} : \dot{\boldsymbol{\epsilon}}^p - \mathcal{R}^*(\chi)\dot{\kappa}$, turns out to be non-negative everywhere in V.

The above nonlocal material model can be notably simplified by considering that the hardening/softening diffusion processes in general decay rapidly from the source points and that they in practice remain quantitatively meaningful only within a spherical volume, V_0 say, centered at the source point and with radius R depending on l (such that $R \to 0$ as $l \to 0$). Such hardening/softening processes can be described by a weighting function $g(r)$ as the error function introduced in Eqs. (17) and (18), which decreases rapidly with increasing $r = \|\mathbf{y} - \mathbf{x}\|$ from $r = 0$ at the source point $\mathbf{x}$, such that $g(r) \simeq 0$ for $r > R$ with $R = ml$ and m sufficiently large as $m \geq 2$. With this assumption, the weight $G(\mathbf{x})$ of (18) turns out to take a constant value, i.e., $G_0 = V_{RP}$, for all points $\mathbf{x}$ in V, except for the points located close to the boundary surface ∂V at a distance smaller than R, for which $G(\mathbf{x})$ decreases from $G_0 = V_{RP}$ to $\sim G_0/2$ at (regular) points over ∂V. For greater simplicity, the weight G of (18) is taken constant throughout V, i.e., $G = G_0 = V_{RP}$, which amounts to assuming that the hardening/softening effects attenuate for the particles located close to the boundary surface ∂V. Under the above assumptions, the $\mathcal{R}$ operator can be written as

$$\xi(\mathbf{x}) = \mathcal{R}(\dot{\kappa})|_{\mathbf{x}} := \frac{1}{G_0}\int_{V_0} g(\|\mathbf{y} - \mathbf{x}\|)\dot{\kappa}(\mathbf{y})dV(\mathbf{y}), \tag{29}$$

where G_0 identifies with the representative volume V_{RP}. It can be easily recognized that the latter operator is self-adjoint, i.e., $\mathcal{R}^* \equiv \mathcal{R}$. Though the diffusion domain V_D may in this case be smaller than V, the reasoning developed previously to evaluate P remains valid and Eqs. (25) to (28) hold true with $\mathcal{R}$ in place of $\mathcal{R}^*$.

As a rule, the more general nonlocal material model will be considered in the subsequent sections, but at specific points the simplified model will be applied for special purposes. For simplicity, only mechanical processes will be considered in the following developments.

4 The Plastic Yielding Laws for Rate-Independent Associative Plasticity

Equation (28) suggests that, if plastic yielding is described by the (local) rate variables $\dot{\boldsymbol{\epsilon}}^p$ and $\dot{\kappa}$, the yield function and plastic potential should be specified as functions of the related thermodynamic forces, $\boldsymbol{\sigma}$ and $-\mathcal{R}^*(\chi)$. Thus, let the yield function F be chosen as

$$F(\boldsymbol{\sigma}, \mathcal{R}^*(\chi)) \equiv f(\boldsymbol{\sigma}) - \mathcal{R}^*(\chi) \leq 0, \tag{30}$$

where $f(\boldsymbol{\sigma})$ is a convex (and regular) function of stress only. The plastic flow laws for nonlocal and associative plasticity can be cast as follows:

$$F(\boldsymbol{\sigma}, \mathcal{R}^*(\chi)) \leq 0, \quad \dot{\lambda} \geq 0, \quad \dot{\lambda}F(\boldsymbol{\sigma}, \mathcal{R}^*(\chi)) = 0 \quad \text{in} \quad V \tag{31a}$$

$$\dot{\boldsymbol{\epsilon}}^p = \dot{\lambda}F_{,\sigma}, \quad \dot{\xi} = \mathcal{R}(\dot{\lambda}) \quad (\dot{\kappa} \equiv \dot{\lambda}) \quad \text{in} \quad V \tag{31b}$$

where $\dot{\lambda}$ is a C^0–continuous function representing the plastic (or consistency) coefficient and the condition $\dot{\lambda}F = 0$ in Eq. (31*a*) accounts for elastic unloading, e.g., Martin (1975), Lubliner (1990). Moreover, by Eqs. (11) and (14), $\dot{\boldsymbol{\sigma}}$ and $\dot{\chi}$ are expressed as

$$\dot{\boldsymbol{\sigma}} = \mathbf{C} : \dot{\boldsymbol{\epsilon}}^e, \quad \mathbf{C} := \rho\frac{\partial^2\psi_e}{\partial\boldsymbol{\epsilon}^e \otimes \partial\boldsymbol{\epsilon}^e} \tag{32a}$$

$$\dot{\chi} = h\dot{\xi}, \quad h := \rho\frac{d^2\psi_{\text{in}}}{d\xi^2} \tag{32b}$$

where $\mathbf{C}$ and h are, respectively, the (positive definite) elastic moduli tensor and the hardening modulus.

The flow laws (31) constitute a set of field equations for the domain V. At difference with gradient plasticity, Polizzotto et al. (1996), Eqs. (31) need no boundary conditions on ∂V (but $\dot{\kappa} = \dot{\lambda} =$

Downloaded 04 May 2010 to 171.66.16.27. Redistribution subject to ASME license or copyright; see http://www.asme.org/terms/Terms_Use.cfm

0 on the interface between V_p and the complementary region V_p^c for continuity reasons). These equations provide the plastic mechanism $\dot{\boldsymbol{\epsilon}}^p$, $\dot{\xi}$ that the material particles in V can undergo in a given state $\boldsymbol{\sigma}$, χ. But they also give indirectly the state $\boldsymbol{\sigma}$, χ of the material in V in which a given plastic mechanism $\dot{\boldsymbol{\epsilon}}^p$, $\dot{\xi}$ can develop. The latter task is mathematically equivalent to the inversion of Eqs. (31), which in principle can be done as follows.

Let the fields $\dot{\boldsymbol{\epsilon}}^p$ and $\dot{\xi}$ be assigned in V such that $\dot{\boldsymbol{\epsilon}}^p \neq \mathbf{0}$, $\dot{\xi} > 0$ in V_p and $\dot{\boldsymbol{\epsilon}}^p = \mathbf{0}$, $\dot{\xi} \geq 0$ in $V \backslash V_p$. Then, $\dot{\lambda}$ can be obtained by the second Eq. (31*b*), i.e.,

$$\mathcal{R}(\dot{\lambda}) = \dot{\xi}(\mathbf{x}) \quad \forall\ \mathbf{x} \in V, \tag{33}$$

with the constraints $\dot{\lambda} > 0$ in V_p and $\dot{\lambda} = 0$ in $V \backslash V_p$. Equation (33) is a (constrained) Fredholm integral equation of the first kind, stating that $\dot{\lambda}$ is a non-negative function the weighted value of which coincides with $\dot{\xi}$ everywhere in V, and in general admits a unique solution. In V_p, by inversion of the first of Eq. (31*b*), one obtains: $\boldsymbol{\sigma} = \boldsymbol{\sigma}(\dot{\boldsymbol{\epsilon}}^p/\dot{\lambda})$, whereas χ is there provided by an equation similar to (33), i.e.: $\mathcal{R}^*(\chi) = \phi(\dot{\boldsymbol{\epsilon}}^p/\dot{\lambda})$, where $\phi(\dot{\boldsymbol{\epsilon}}^p/\dot{\lambda}) = f(\boldsymbol{\sigma}(\dot{\boldsymbol{\epsilon}}^p/\dot{\lambda}))$. In the (open) complementary region V_p^c the state $\boldsymbol{\sigma}$, χ remains indeterminate, but $F(\boldsymbol{\sigma}, \mathcal{R}^*(\chi)) < 0$. This same (indirect) problem can more elegantly be solved via the maximum intrinsic dissipation theorem of the next section.

The difference between the above plastic yielding laws and those usually adopted for nonlocal plasticity, can be shown by choosing, for simplicity, $\chi = h\xi = h\mathcal{R}(\lambda)$, with h = constant. With this choice, Eq. (30) becomes

$$f(\boldsymbol{\sigma}) - h\mathcal{R}^*(\mathcal{R}(\lambda)) \leq 0, \tag{34}$$

at difference with

$$f(\boldsymbol{\sigma}) - h\mathcal{R}(\lambda) \leq 0 \tag{35}$$

which is usually employed in the literature (see, e.g., Bažant and Lin (1988), de Borst et al. (1993)), (and perhaps constitutes a good approximation to Eq. (34)).

The thermodynamic compatibility of Eqs. (31) can be assessed by showing that inequality (28), consequence of the (nonlocal) Clausius-Duhem inequality, is always guaranteed. In fact, by Eq. (31) and the convexity of $f(\boldsymbol{\sigma})$, one can write

$$D_p = \dot{\lambda}[\boldsymbol{\sigma} : f_{,\sigma} - \mathcal{R}^*(\chi)] \geq \dot{\lambda}[f(\boldsymbol{\sigma}) - \mathcal{R}^*(\chi)] = 0, \tag{36}$$

that is $D_p \geq 0$, as stated.

The yielding laws (31) can be shown to be derivable from a suitable theorem of maximum intrinsic dissipation. This task will be accomplished in the next section.

5 The Maximum Intrinsic Dissipation Theorem

This theorem is known to play a fundamental role within local associative plasticity, see, e.g., Hill (1950), Martin (1975), Simo (1988), as it can in fact be viewed as a variational formulation of the related plastic rate-form constitutive equations. It is quite natural to wonder whether such a theorem can be envisaged for nonlocal associative plasticity. This section is aimed at discussing this point.

First of all, let the yield function of Eq. (30) be considered with the variable $X := \mathcal{R}^*(\chi)$ treated as local. By the convexity of F as function of $\boldsymbol{\sigma}$ and X, and in virtue of Eqs. (31), the following inequality can be written:

$$(\boldsymbol{\sigma} - \hat{\boldsymbol{\sigma}}) : \dot{\boldsymbol{\epsilon}}^p - (X - \hat{X})\dot{\kappa} \geq 0 \tag{37}$$

which holds for arbitrary sets ($\boldsymbol{\sigma}$, X, $\dot{\boldsymbol{\epsilon}}^p$, $\dot{\kappa} > 0$), each of which complies with the plastic yielding laws (31), (with $\mathcal{R}^*(\chi)$ replaced by X), and for arbitrary plastically admissible sets ($\hat{\boldsymbol{\sigma}}$, $\hat{X}$), i.e., such that $F(\hat{\boldsymbol{\sigma}}, \hat{X}) \leq 0$. Let Eq. (37) be rewritten in the equivalent form

$$\boldsymbol{\sigma} : \dot{\boldsymbol{\epsilon}}^p - X\dot{\kappa} \geq \hat{\boldsymbol{\sigma}} : \dot{\boldsymbol{\epsilon}}^p - \hat{X}\dot{\kappa}, \tag{38}$$

and let Eq. (38) be integrated over V, so obtaining

$$\int_V [\boldsymbol{\sigma} : \dot{\boldsymbol{\epsilon}}^p - \mathcal{R}^*(\chi)\dot{\kappa}]dV \geq \int_V [\hat{\boldsymbol{\sigma}} : \dot{\boldsymbol{\epsilon}}^p - \mathcal{R}^*(\hat{\chi})\dot{\kappa}]dV \tag{39}$$

where X and $\hat{X}$ have been replaced by $\mathcal{R}^*(\chi)$ and $\mathcal{R}^*(\hat{\chi})$, respectively. Noting that the integral on the left-hand side is the global net intrinsic dissipation, Eq. (15), and applying the Green-type relation (27) to the pair ($\hat{\chi}$, $\dot{\kappa}$), Eq. (39) can be rewritten as

$$W_p[\dot{\boldsymbol{\epsilon}}^p, \dot{\xi}] \geq \int_{V_p} (\hat{\boldsymbol{\sigma}} : \dot{\boldsymbol{\epsilon}}^p - \hat{\chi}\dot{\xi})dV \tag{40}$$

where $\dot{\xi} = \mathcal{R}(\dot{\kappa})$. Equation (40) shows that the W_p, corresponding to any plastic mechanism described by the fields $\dot{\boldsymbol{\epsilon}}^p$ and $\dot{\xi} = \mathcal{R}(\dot{\kappa})$, can be obtained as the maximum value of the integral on the right-hand side of (40) with respect to $\hat{\boldsymbol{\sigma}}$ and $\hat{\chi}$ complying with the yield condition (30). We can thus write (dropping the cups for simplicity):

$$W_p = \max_{(\sigma,\chi)} \int_V (\boldsymbol{\sigma} : \dot{\boldsymbol{\epsilon}}^p - \chi\dot{\xi})dV$$

$$\text{subject to } F \equiv f(\boldsymbol{\sigma}) - \mathcal{R}^*(\chi) \leq 0 \quad \text{in} \quad V \tag{41}$$

where the fields $\dot{\boldsymbol{\epsilon}}^p$ and $\dot{\xi}$ are given in V.

It is of interest to investigate the mechanical implications of problem (41). This can be done by the Lagrange multiplier method. To this purpose, let $\dot{\lambda}(\mathbf{x}) \geq 0$ be the relevant multiplier and let the augmented Lagrangian functional be written as

$$L = -\int_V (\boldsymbol{\sigma} : \dot{\boldsymbol{\epsilon}}^p - \chi\dot{\xi})dV + \int_V \dot{\lambda}F(\boldsymbol{\sigma}, \mathcal{R}^*(\chi))dV, \tag{42}$$

the first variation of which reads

$$\delta L = -\int_V \delta\boldsymbol{\sigma} : (\dot{\boldsymbol{\epsilon}}^p - \dot{\lambda}F_{,\sigma})dV + \int_V [\delta\chi\dot{\xi} - \dot{\lambda}\mathcal{R}^*(\delta\chi)]dV + \int_V \delta\dot{\lambda}F dV, \tag{43}$$

where $\delta\dot{\lambda}$ is such that $\dot{\lambda} + \delta\dot{\lambda} \geq 0$ in V. Since, by Eq. (27), the identity

$$\int_V \dot{\lambda}\mathcal{R}^*(\delta\chi)dV = \int_V \mathcal{R}(\dot{\lambda})\delta\chi dV \tag{44}$$

holds, one finally obtains

$$\delta L = -\int_V \delta\boldsymbol{\sigma} : (\dot{\boldsymbol{\epsilon}}^p - \dot{\lambda}F_{,\sigma})dV + \int_V \delta\chi[\dot{\xi} - \mathcal{R}(\dot{\lambda})]dV + \int_V \delta\dot{\lambda}F dV. \tag{45}$$

As L must take a minimum with respect to $\boldsymbol{\sigma}$ and χ and a maximum with respect to $\dot{\lambda} \geq 0$, we realize that the Euler-Lagrange equations of problem (41) coincide with the plastic yielding laws (31) with $\dot{\kappa} \equiv \dot{\lambda}$, and thus $\dot{\lambda}$ takes on the role of consistency coefficient. It is therefore demonstrated that, like for local plasticity, the nonlocal plastic yielding laws (31) turn out to comply with a specific maximum plastic work theorem, of which they are the (necessary and sufficient) conditions.

Downloaded 04 May 2010 to 171.66.16.27. Redistribution subject to ASME license or copyright; see http://www.asme.org/terms/Terms_Use.cfm

6 The Material Response to a Given Total Strain Rate Field $\dot{\boldsymbol{\epsilon}}$

Let a body of volume V be in a known state in which the domain V can be split in separate parts as $V = V_y \cup V_y^e \cup \Gamma_y$, where V_y is the subregion where $F(\boldsymbol{\sigma}, \mathcal{R}^*(\chi)) = 0$, V_y^e is the (open) complementary region where $F(\boldsymbol{\sigma}, \mathcal{R}^*(\chi)) < 0$ and Γ_y denotes the interface between V_y and V_y^e. Let a total strain rate field $\dot{\boldsymbol{\epsilon}}$ be applied to the body and let the consequent rate problem be solved for the set of material particles constituting the body. Obviously, the rate response will be elastic in $V \backslash V_y = V_y^e \cup \Gamma_y$ and elastic-plastic in V_y, with perhaps elastic unloading somewhere in V_y. Note that, in local plasticity, it would be sufficient to determine the rate response of an individual material particle, whereas in the present case this is not possible because the behavior of every particle is influenced by the neighbor ones.

In V_y, where $F = 0$, it is $\dot{F} \leq 0$, that is, using Eqs. (32),

$$\dot{F} = f_{,\sigma} : \dot{\boldsymbol{\sigma}} - \mathcal{R}^*(\dot{\chi}) = q_\epsilon - h_c \dot{\lambda} - \mathcal{R}^*(h\dot{\xi}) \leq 0 \quad \text{in} \quad V_y \tag{46}$$

where

$$q_\epsilon := f_{,\sigma} : \mathbf{C} : \dot{\boldsymbol{\epsilon}}, \quad h_c := f_{,\sigma} : \mathbf{C} : f_{,\sigma}. \tag{47}$$

The unknown plastic coefficient $\dot{\lambda}$ can be nonzero only in some part $V_p \subseteq V_y$ in which $\dot{F} = 0$; that is, the conditions

$$\dot{F}(\boldsymbol{\sigma}, \mathcal{R}^*(\chi)) \leq 0, \quad \dot{\lambda} \geq 0, \quad \dot{\lambda}\dot{F} = 0 \quad \text{in} \quad V_y \tag{48}$$

must be satisfied. The boundary condition $\dot{\lambda} = 0$ on Γ_y is enforced for continuity reasons.

Let us consider the functional

$$\Pi[\dot{\lambda}] = \tfrac{1}{2} \int_V [h_c \dot{\lambda}^2 + h(\xi)(\mathcal{R}(\dot{\lambda}))^2] dV - \int_V q_\epsilon \dot{\lambda} dV \tag{49}$$

where $\dot{\lambda}$ is a (nontrivial) scalar field in the set Λ defined as

$$\Lambda = \{\dot{\lambda}(\mathbf{x}) \in C^0, \ \dot{\lambda} \geq 0 \quad \text{in} \quad V_y, \ \dot{\lambda} = 0 \quad \text{in} \quad V \backslash V_y\}. \tag{50}$$

For subsequent use the functional

$$Z(\dot{\lambda}) := h_c \dot{\lambda}^2 + h(\xi)(\mathcal{R}(\dot{\lambda}))^2 \tag{51}$$

is introduced. Then, the following can be proved.

Minimum Principle for a Continuous Set of Particles. In the hypothesis that $Z(\dot{\lambda})$ of Eq. (51) satisfies the condition

$$Z(\dot{\lambda}) > 0 \quad \text{in} \quad V_y, \quad Z(\dot{\lambda}) \geq 0 \quad \text{in} \quad V \backslash V_y, \quad \forall \ \dot{\lambda} \in \Lambda \tag{52}$$

then: (i) the solution to the constrained minimum problem

$$\min \Pi[\dot{\lambda}] \quad \text{subject to} \quad \dot{\lambda} \in \Lambda \tag{53}$$

solves the rate problem governed by Eq. (48), and (ii) conversely, the solution to this rate problem also solves (53).

The first part of the above proposition is primarily proved. Let $\dot{\lambda}$ solve (53) and let $\delta\dot{\lambda}$ be an arbitrary variation such that $\dot{\lambda} + \delta\dot{\lambda} \geq 0$ in V_y and $\delta\dot{\lambda} = 0$ in $V \backslash V_y$. Since, by hypothesis, $\Pi[\dot{\lambda}]$ is minimum, the first variation of it must be non-negative for arbitrary admissible variations $\delta\dot{\lambda}$, i.e.,

$$\begin{aligned} \delta\Pi &= \int_V \{h_c \dot{\lambda} \delta\dot{\lambda} + h\mathcal{R}(\dot{\lambda})\mathcal{R}(\delta\dot{\lambda}) - q_\epsilon \delta\dot{\lambda}\} dV \\ &= \int_V \{h_c \dot{\lambda} + \mathcal{R}^*(h\dot{\xi}) - q_\epsilon\} \delta\dot{\lambda} dV = -\int_{V_y} \dot{F} \delta\dot{\lambda} dV \geq 0 \end{aligned} \tag{54}$$

where Eqs. (27) and (46) have been used. It follows that all the conditions of Eq. (48), as the necessary conditions for problem (53), are satisfied and thus $\dot{\lambda}$ solves the rate problem. In order to prove the second part of the above proposition, let $\dot{\lambda}(\mathbf{x})$ be the/a solution to the rate problem and $\delta\dot{\lambda}$ be a variation such that $\dot{\lambda} + \delta\dot{\lambda} \geq 0$ in V_y and $\delta\dot{\lambda} = 0$ in $V \backslash V_y$. We can correspondingly write

$$\Pi[\dot{\lambda} + \delta\dot{\lambda}] = \Pi[\dot{\lambda}] + \delta\Pi + \tfrac{1}{2}\delta^2\Pi \tag{55}$$

where $\delta\Pi$ is formally expressed as in Eq. (54), whereas $\delta^2\Pi$ is the second variation which, considering also Eq. (51), reads:

$$\begin{aligned} \delta^2\Pi &= \int_V \{h_c \delta\dot{\lambda}^2 + h(\mathcal{R}(\delta\dot{\lambda}))^2\} dV \\ &= \int_V Z(\delta\dot{\lambda}) dV > 0 \quad \text{by Eqs. (50) and (52).} \end{aligned} \tag{56}$$

Therefore, Eq. (55) gives (using the notation $\dot{\lambda}' = \dot{\lambda} + \delta\dot{\lambda}$)

$$\Pi[\dot{\lambda}'] \geq \Pi[\dot{\lambda}] \quad \text{for any} \quad \dot{\lambda}' \in \Lambda \tag{57}$$

with the equality sign holding if, and only if, $\dot{\lambda}' \equiv \dot{\lambda}$. That is, $\dot{\lambda}$ solves problem (53) uniquely. QED.

It is to be noted that condition (52) is naturally satisfied for $h > 0$ in V. For $h \leq 0$, condition (52) turns out to be particularly restrictive to the material response $\dot{\lambda}$, but this point is not pursued here. Also, we note that in case of local plasticity condition (52) implies

$$h_c + h > 0 \quad \text{in} \quad V \tag{58}$$

where V has been placed for V_y because V_y can actually be any subdomain in V. Equation (58) is recognized as the well-known criterion for lack of snap-back material response (Bažant and Cedolin, 1991).

7 Region of Active Plastic Yielding (V_p)

Let the rate problem of Section 6 be still considered. When we know a priori the region $V_\lambda = V_p \subseteq V_y$ where active plastic yielding occurs, that is, where $\dot{\lambda} > 0$, we can compute $\dot{\lambda}$ using the equation $\dot{F} = 0$ enforced at all points in V_λ. In consideration of the interest of this problem for numerical applications, the simplified nonlocal material model of the end of Section 3 is considered in this section. Thus remembering Eq. (46), written with $\mathcal{R}^* = \mathcal{R}$ the latter being given by (29), we can obtain $\dot{\lambda}$ by solving the equation:

$$\dot{\lambda} + \mathcal{L}(\dot{\lambda}) = q_\epsilon / h_c \quad \text{in} \quad V_\lambda \tag{59}$$

where

$$\mathcal{L}(\dot{\lambda}) := \frac{1}{h_c} \mathcal{R}(h\mathcal{R}(\dot{\lambda})). \tag{60}$$

Equation (60) constitutes a Fredholm integral equation of the second kind and, as suggested, e.g., by Pijaudier-Cabot and Bažant (1977), de Borst et al. (1993), can be solved by successive iterations; that is, denoting by $\dot{\lambda}^{(n)}$ the nth iteration solution, we can write

$$\dot{\lambda}^{(n)} = \langle q_\epsilon \rangle / h_c - \mathcal{L}(\dot{\lambda}^{(n-1)}) \quad \text{in} \quad V_\lambda \tag{61}$$

where $\langle q_\epsilon \rangle = (q_\epsilon + |q_\epsilon|)/2$. Assuming $\dot{\lambda}^{(0)} \equiv 0$, Eq. (59) gives

$$\dot{\lambda}^{(1)} = \frac{\langle q_\epsilon \rangle}{h_c} \tag{62}$$

$$\dot{\lambda}^{(2)} = \frac{\langle q_\epsilon \rangle}{h_c} - \mathcal{L}\left(\frac{\langle q_\epsilon \rangle}{h_c}\right) \tag{63}$$

Downloaded 04 May 2010 to 171.66.16.27. Redistribution subject to ASME license or copyright; see http://www.asme.org/terms/Terms_Use.cfm

$$\dot{\lambda}^{(3)} = \frac{\langle q_\epsilon \rangle}{h_c} - \mathcal{L}\left(\frac{\langle q_\epsilon \rangle}{h_c}\right) + \mathcal{L}^{(2)}\left(\frac{\langle q_\epsilon \rangle}{h_c}\right) \tag{64}$$

and so on, where $\mathcal{L}^{(2)}(\cdot) = \mathcal{L}(\mathcal{L}(\cdot))$ and, similarly, $\mathcal{L}^{(n)}(\cdot) = \mathcal{L}(\mathcal{L}^{(n-1)}(\cdot))$. The solution $\dot{\lambda}$ to (59) can thus be formally represented by the series

$$\dot{\lambda} = \frac{\langle q_\epsilon \rangle}{h_c} + \sum_{n=1}^{\infty} (-1)^n \mathcal{L}^{(n)}\left(\frac{\langle q_\epsilon \rangle}{h_c}\right). \tag{65}$$

The convergence of this series can be assessed on the ground of the repetitive application of the double regularization operation (59), provided that a finite solution exists and $|h| < h_c$. (See Appendix A for the proof.)

The stress rate response $\dot{\boldsymbol{\sigma}}$, that is, by Eqs. (32*a*) and (31*b*), $\dot{\boldsymbol{\sigma}} = \mathbf{C} : (\dot{\boldsymbol{\epsilon}} - \dot{\boldsymbol{\epsilon}}^p) = \mathbf{C} : \dot{\boldsymbol{\epsilon}} - \mathbf{C} : f_{,\sigma}\dot{\lambda}$, using Eq. (65) with $q_\epsilon > 0$, can be expressed in the form

$$\dot{\boldsymbol{\sigma}} = \mathbf{D}_c : \dot{\boldsymbol{\epsilon}} - \sum_{n=1}^{\infty} (-1)^n S^{(n)}(\dot{\boldsymbol{\epsilon}}) \tag{66}$$

where $\mathbf{D}_c$ is a *local tangent stiffness* tensor, i.e.,

$$\mathbf{D}_c := \mathbf{C} - \frac{1}{h_c}\mathbf{a} \otimes \mathbf{a}^T, \quad \mathbf{a} := \mathbf{C} : f_{,\sigma}, \tag{67}$$

and $S^{(n)}$ denotes tensor-valued *stiffness integral operator* of order $n = 1, 2, \ldots$ defined as

$$S^{(n)}(\dot{\boldsymbol{\epsilon}}) := \mathbf{a}\mathcal{L}^{(n)}\left(\frac{1}{h_c}\mathbf{a}^T : \dot{\boldsymbol{\epsilon}}\right), \quad n = 1, 2, \ldots. \tag{68}$$

It is worth noting that, in the case of local plasticity (in which $\mathcal{R}(y) = y$ for all y), Eq. (65) becomes

$$\dot{\lambda} = \left[1 + \left(-\frac{h}{h_c}\right) + \left(-\frac{h}{h_c}\right)^2 + \ldots\right]\frac{\langle q_\epsilon \rangle}{h_c} \quad \text{in} \quad V_\lambda \tag{69}$$

where the series within the square brackets is the geometric series. This admits the limit $h_c/(h_c + h)$, provided that $|h| < h_c$. (In the softening case, the latter condition is satisfied if no snap-back material responses are admitted.) Therefore, Eq. (69) reads

$$\dot{\lambda} = \frac{\langle q_\epsilon \rangle}{h_c + h} \quad \text{in} \quad V_\lambda, \tag{70}$$

indeed a result obtainable directly from Eq. (61). Additionally, since, always for local plasticity, $\mathcal{L}^{(n)}(y) = (h/h_c)^n y$ for any y and $S^{(n)}(\dot{\boldsymbol{\epsilon}}) = (h^n/h_c^{n+1})\mathbf{a} \otimes \mathbf{a}^T : \dot{\boldsymbol{\epsilon}}$, Eq. (66) reads, using (67),

$$\dot{\boldsymbol{\sigma}} = \mathbf{C} : \dot{\boldsymbol{\epsilon}} - \frac{1}{h_c}\left[1 + \left(-\frac{h}{h_c}\right) + \left(-\frac{h}{h_c}\right)^2 + \ldots\right]\mathbf{a} \otimes \mathbf{a}^T : \dot{\boldsymbol{\epsilon}}$$

$$= \left(\mathbf{C} - \frac{1}{h + h_c}\mathbf{a} \otimes \mathbf{a}^T\right) : \dot{\boldsymbol{\epsilon}} = \mathbf{D}_{\text{LP}} : \dot{\boldsymbol{\epsilon}} \tag{71}$$

where $\mathbf{D}_{\text{LP}}$ is the continuum tangent stiffness matrix pertaining to local plasticity.

A simplification of the above formalism can be achieved at the moderate cost of considering h and h_c constant within the influence sphere in the second and higher-order regularization operations. With this approximation, Eq. (60) simplifies as

$$\mathcal{L}(\dot{\lambda}) = \frac{h}{h_c}\mathcal{R}(\mathcal{R}(\dot{\lambda})) = \frac{h}{h_c}\mathcal{R}^{(2)}(\dot{\lambda}) \tag{72}$$

where $\mathcal{R}^{(2)}$ is the second-order regularization operator, i.e., $\mathcal{R}^{(2)}(\cdot) = \mathcal{R}(\mathcal{R}(\cdot))$, and thus

$$\left.\begin{aligned}(-1)^n\mathcal{L}^{(n)}(\dot{\lambda}) &= \left(-\frac{h}{h_c}\right)^n \mathcal{R}^{(2n)}(\dot{\lambda}) \\ (-1)^n S^{(n)}(\dot{\boldsymbol{\epsilon}}) &= \left(-\frac{h}{h_c}\right)^n \mathbf{a}\mathcal{R}^{(2n)}\left(\frac{1}{h_c}\mathbf{a}^T : \dot{\boldsymbol{\epsilon}}\right)\end{aligned}\right\} n = 1, 2, \ldots. \tag{73}$$

In this way, Eqs. (65) and (66) can be written:

$$\dot{\lambda} = \frac{\langle \mathbf{a}^T : \dot{\boldsymbol{\epsilon}} \rangle}{h_c} + \frac{1}{h_c}\sum_{n=1}^{\infty}\left(-\frac{h}{h_c}\right)^n \mathcal{R}^{(2n)}(\langle \mathbf{a}^T : \dot{\boldsymbol{\epsilon}} \rangle) \tag{74a}$$

$$\dot{\boldsymbol{\sigma}} = \mathbf{D}_c : \dot{\boldsymbol{\epsilon}} - \frac{1}{h_c}\sum_{n=1}^{\infty}\left(-\frac{h}{h_c}\right)^n \mathbf{a}\mathcal{R}^{(2n)}(\mathbf{a}^T : \dot{\boldsymbol{\epsilon}}). \tag{74b}$$

The explicit form of the $2n$th order regularization operation reads

$$\mathcal{R}^{(2n)}(y) = \frac{1}{G_0^{2n}}\overbrace{\int_{V_0}\cdots\int_{V_0}}^{2n \text{ times}} g(r_1)g(s_1)\cdots g(r_n)g(s_n)y\left(\mathbf{x} + \sum_{i=1}^{n}(\mathbf{r}_i + \mathbf{s}_i)\right)(dV_0)^{2n} \tag{75}$$

where $r_i = \|\mathbf{r}_i\|$, $s_i = \|\mathbf{s}_i\|$ and $y(\mathbf{x})$ is a C^0–continuous scalar field.

Often the above V_λ domain is just an estimation within an iterative procedure aimed at evaluating the actual region of plastic yielding, i.e., $V_p \subseteq V_y$. Then, it is possible to check whether the domain V_λ previously considered coincides with V_p by verifying whether the condition $-\dot{F} = h_c\dot{\lambda} + h\mathcal{R}(\xi) - q_\epsilon > 0$ is satisfied everywhere in $V_y \backslash (V_\lambda \cup \Gamma_\lambda)$, where $\Gamma_\lambda = V_y \cap \partial V_\lambda$; otherwise a new tentative V_λ zone must be adopted.

8 The Structural Rate Problem for Nonlocal Plasticity

We consider an elastic-plastic solid body, or structure, of (open) domain V and boundary surface $S = \partial V$, subjected to body forces $\mathbf{b}$ in V, surface forces $\mathbf{T}$ on the (open) part S_T of S and imposed displacements $\mathbf{U}$ on $S_U = S \backslash S_T$. Imposed strains (e.g., thermal strains) are not considered for simplicity. All these actions vary in time quasi-statically and cause the body to undergo small displacements and strains. Assuming a general nonlocal material behavior as described in Section 3, the evolutive structural response may in principle be evaluated through a suitable step-by-step analysis, but here we are interested in the so-called rate response; that is, the structural response of the body being in a known state, to given load rates as $\dot{\mathbf{b}}$ in V, $\dot{\mathbf{T}}$ on S_T and $\dot{\mathbf{U}}$ on S_U.

Considering that the region $V_y \subseteq V$ where the yield condition has been attained (i.e., where $F = 0$) is known, whereas $F < 0$ in the (open) complementary region (V_y^c), the equations governing the above boundary value problem of nonlocal plasticity read

$$\dot{\boldsymbol{\epsilon}} = \nabla^s\dot{\mathbf{u}} \quad \text{in} \quad V, \quad \dot{\mathbf{u}} = \dot{\mathbf{U}} \quad \text{on} \quad S_U \quad \text{(compatibility)} \tag{76}$$

$$\nabla \cdot \dot{\boldsymbol{\sigma}} + \dot{\mathbf{b}} = \mathbf{0} \quad \text{in} \quad V, \quad \dot{\boldsymbol{\sigma}} \cdot \mathbf{n} = \dot{\mathbf{T}} \quad \text{on} \quad S_T \quad \text{(equilibrium)} \tag{77}$$

$$\dot{\boldsymbol{\sigma}} = \mathbf{C} : (\dot{\boldsymbol{\epsilon}} - \dot{\boldsymbol{\epsilon}}^p) \quad \text{in} \quad V \quad \text{(Hooke's law)} \tag{78}$$

$$\dot{F} \equiv f_{,\sigma} : \dot{\boldsymbol{\sigma}} - \mathcal{R}^*(\dot{\chi}) \le 0, \quad \dot{\lambda} \ge 0, \quad \dot{\lambda}\dot{F} = 0 \quad \text{in} \quad V_y \tag{79a}$$

Downloaded 04 May 2010 to 171.66.16.27. Redistribution subject to ASME license or copyright; see http://www.asme.org/terms/Terms_Use.cfm

$$\dot{\boldsymbol{\epsilon}}^p = \dot{\lambda} f_{,\sigma} \quad \text{in} \quad V_y, \quad \dot{\boldsymbol{\epsilon}}^p = \mathbf{0} \quad \text{in} \quad V \backslash V_y \quad (\text{where } \dot{\lambda} = 0) \tag{79b}$$

$$\xi = \mathcal{R}(\dot{\lambda}) \quad \text{in} \quad V. \tag{80}$$

Here, $\mathbf{n}$ denotes the unit external normal to S, ∇^s = symmetric part of ∇ = grad operator; also, Eqs. (79*a*, *b*) and (80) are the plastic yielding laws (31) written in a form suitable to the present case. The solution to the above problem, if exists, must be searched for within suitably regular function spaces, with $\dot{\lambda} C^0$–continuous.

It is of interest to investigate the conditions for the above equation set to admit a unique solution. This task can be pursued in a classical way by assuming the existence of two distinct solutions, respectively labeled with primed and doubly primed symbols. Then, introducing the symbol $\Delta(\cdot)$ to indicate difference between values of a variable in the two solutions, i.e., $\Delta(\cdot) = (\cdot)' - (\cdot)''$, we observe that, making use of Eqs. (79) the following inequality can be easily proved, i.e.,

$$\Delta \dot{F} \Delta \dot{\lambda} = \Delta \dot{\boldsymbol{\sigma}} : \Delta \dot{\boldsymbol{\epsilon}}^p - \mathcal{R}^*(\Delta \dot{\chi}) \Delta \dot{\lambda} \geq 0 \quad \text{in} \quad V_y, \tag{81}$$

which obviously holds also in the entire V because $\dot{\lambda}' = \dot{\lambda}'' = 0$ in $V \backslash V_y$. An integration over V and the application of the Green-type relation (27) then yields

$$\int_V [\Delta \dot{\boldsymbol{\sigma}} : \Delta \dot{\boldsymbol{\epsilon}}^p - \Delta \dot{\chi} \Delta \xi] dV \geq 0. \tag{82}$$

Since $\Delta \dot{\boldsymbol{\epsilon}}^p = \Delta \dot{\boldsymbol{\epsilon}} - \Delta \dot{\boldsymbol{\epsilon}}^e$ and $\Delta \dot{\chi} = h(\xi) \Delta \dot{\xi}$, Eq. (82) becomes

$$\int_V \Delta \dot{\boldsymbol{\sigma}} : \Delta \dot{\boldsymbol{\epsilon}} dV - \int_V \Delta \dot{\boldsymbol{\sigma}} : \Delta \dot{\boldsymbol{\epsilon}}^e dV - \int_V h(\xi) (\Delta \dot{\xi})^2 dV \geq 0. \tag{83}$$

Noting that $\Delta \dot{\boldsymbol{\sigma}}$ is in equilibrium with zero body force rates in V and zero traction rates on S_T, and also that $\Delta \dot{\boldsymbol{\epsilon}}$ is compatible with zero displacement rates on S_U, the first integral on the left-hand side of (83) vanishes and thus (83) reduces to

$$\int_V [\Delta \dot{\boldsymbol{\epsilon}}^e : \mathbf{C} : \Delta \dot{\boldsymbol{\epsilon}}^e + h(\xi) (\mathcal{R}(\Delta \dot{\lambda}))^2] dV \leq 0. \tag{84}$$

If $h(\xi) > 0$ everywhere in V, the square-bracketed quadratic function is positive definite and Eq. (74) can be satisfied only with $\Delta \dot{\boldsymbol{\epsilon}}^e = \mathbf{0}$ and $\Delta \dot{\xi} = \mathcal{R}(\Delta \dot{\lambda}) = 0$ everywhere in V, hence $\Delta \dot{\boldsymbol{\sigma}} \equiv \mathbf{0}$, $\Delta \dot{\chi} \equiv 0$, $\Delta \dot{\lambda} \equiv 0$, $\Delta \dot{\boldsymbol{\epsilon}}^p \equiv \Delta \dot{\boldsymbol{\epsilon}} \equiv \mathbf{0}$, $\Delta \dot{\mathbf{u}} \equiv \mathbf{0}$; that is, the solution is unique. Note that this result holds provided that $S_U \neq \varnothing$, as assumed; otherwise $\Delta \dot{\mathbf{u}} \neq \mathbf{0}$ would be allowed and the solution would be determinate to within a rigid-body motion.

In the case $h \leq 0$ in some (open) region $V_h \subset V$ and $h > 0$ in V_h^c = (open) complementary region of V_h, Eq. (84) can be split in two inequalities, i.e.,

$$\int_{V_h^c} [\Delta \dot{\boldsymbol{\epsilon}}^e : \mathbf{C} : \Delta \dot{\boldsymbol{\epsilon}}^e + h(\xi) (\mathcal{R}(\Delta \dot{\lambda}))^2] dV \leq 0 \tag{85a}$$

$$\int_{V_h} [\Delta \dot{\boldsymbol{\epsilon}}^e : \mathbf{C} : \Delta \dot{\boldsymbol{\epsilon}}^e - |h(\xi)| (\mathcal{R}(\Delta \dot{\lambda}))^2] dV \leq 0. \tag{85b}$$

Thus, we can state (i) in V_h^c, the solution is still unique (as in the case $h > 0$ everywhere in V), provided that $S_U \cap \partial V_h^c \neq \varnothing$; otherwise, the solution is there determinate to within a rigid-body motion $\Delta \dot{\mathbf{u}}$; (ii) in V_h, the solution may be nonunique since $\Delta \dot{\lambda} \neq 0$, hence $\dot{\lambda}' \neq \dot{\lambda}''$, is there allowed. Moreover, a nonunique $\dot{\lambda}$ solution in V_h can exist even with a unique $\dot{\boldsymbol{\sigma}}$ solution, i.e., with $\Delta \dot{\boldsymbol{\sigma}} = \mathbf{0}$, hence $\Delta \dot{\boldsymbol{\epsilon}}^e = \mathbf{0}$, in V_h and thus the fields $\dot{\boldsymbol{\epsilon}}^{p\prime}$ and $\dot{\boldsymbol{\epsilon}}^{p\prime\prime}$ may possibly differ from each other by a compatible strain rate field; additionally, by Eq. (79*a*), the condition $\mathcal{R}^*(|h| \mathcal{R}(\Delta \dot{\lambda})) = 0$ in V_h must be satisfied. Note that the latter situation certainly occurs if $h = 0$ everywhere in V_h, but $h > 0$ in V_h^c.

9 Variational Principles

The structural rate problem of the preceding section can be characterized by variational principles as in the following:

Mixed-Type Stationarity Principle. Let us consider the functional

$$L_1[\mathbf{X}_k, \mathbf{X}_s] = \tfrac{1}{2} \int_V (\dot{\boldsymbol{\epsilon}} - \dot{\boldsymbol{\epsilon}}^p) : \mathbf{C} : (\dot{\boldsymbol{\epsilon}} - \dot{\boldsymbol{\epsilon}}^p) dV + \tfrac{1}{2} \int_V h(\xi) \dot{\xi}^2 dV + \int_V (\dot{\boldsymbol{\sigma}} : \dot{\boldsymbol{\epsilon}}^p - \dot{\chi} \xi) dV - \int_V \dot{\mathbf{b}} \cdot \dot{\mathbf{u}} dV - \int_{S_T} \dot{\mathbf{T}} \cdot \dot{\mathbf{u}} dS \tag{86}$$

with the kinematic variables $\mathbf{X}_k = \{\dot{\mathbf{u}}, \dot{\boldsymbol{\epsilon}}, \dot{\boldsymbol{\epsilon}}^p, \dot{\xi}\}$ and the static variables $\mathbf{X}_s = \{\dot{\boldsymbol{\sigma}}, \dot{\chi}\}$, all of which belong to suitable functional spaces and satisfy the following constraint equations:

$$\dot{\boldsymbol{\epsilon}} = \nabla^s \dot{\mathbf{u}} \quad \text{in} \quad V, \quad \dot{\mathbf{u}} = \dot{\mathbf{U}} \quad \text{on} \quad S_U, \tag{87a}$$

$$\dot{F} \equiv f_{,\sigma} : \dot{\boldsymbol{\sigma}} - \mathcal{R}^*(\dot{\chi}) \leq 0 \quad \text{in} \quad V_y. \tag{87b}$$

The following can be proved:

The constrained fields $\mathbf{X}_k$ and $\mathbf{X}_s$ making L_1 stationary solve (together with some $\dot{\lambda}(\mathbf{x}) \geq 0$ in V_y and $\dot{\lambda}(\mathbf{x}) = 0$ in $V \backslash V_y$) the structural rate problem (76)–(80); conversely, the/a solution to the latter problem makes L_1 stationary.

The proof of the above statement is in Appendix B, where it is also shown that for $h > 0$ everywhere in V, the (unique) solution to the structural rate problem solves a min-max problem, i.e.,

$$\min_{(\mathbf{X}_k)} \max_{(\mathbf{X}_s)} L_1[\mathbf{X}_k, \mathbf{X}_s] \quad \text{subject to the constraints (87}a, b\text{)}. \tag{88}$$

Kinematic-Type Stationarity Principle. Let us consider the functional

$$L_2[\dot{\mathbf{u}}, \dot{\lambda}] = \tfrac{1}{2} \int_V (\nabla^s \dot{\mathbf{u}} - f_{,\sigma} \dot{\lambda}) : \mathbf{C} : (\nabla^s \dot{\mathbf{u}} - f_{,\sigma} \dot{\lambda}) dV + \tfrac{1}{2} \int_V h(\xi) (\mathcal{R}(\dot{\lambda}))^2 dV - \int_V \dot{\mathbf{b}} \cdot \dot{\mathbf{u}} dV - \int_{S_T} \dot{\mathbf{T}} \cdot \dot{\mathbf{u}} dS \tag{89}$$

where the unknown fields $\dot{\mathbf{u}}$, $\dot{\lambda}$ belong to a suitable functional spaces and satisfy the following constraint equations:

$$\dot{\mathbf{u}} = \dot{\mathbf{U}} \quad \text{on} \quad S_U, \tag{90a}$$

$$\dot{\lambda} \geq 0 \quad \text{in} \quad V_y, \quad \dot{\lambda} = 0 \quad \text{in} \quad V \backslash V_y. \tag{90b}$$

The following can be stated:

The constrained fields $\dot{\mathbf{u}}$, $\dot{\lambda}$ making L_2 stationary solve, together with $\dot{\boldsymbol{\epsilon}} = \nabla^s \dot{\mathbf{u}}$ and some $\dot{\boldsymbol{\sigma}}(\mathbf{x})$, $\dot{\boldsymbol{\xi}}(\mathbf{x})$, the structural rate problem (76)–(80); conversely, the/a solution $(\dot{\mathbf{u}}, \dot{\boldsymbol{\epsilon}}, \dot{\lambda}, \dot{\boldsymbol{\sigma}}, \dot{\boldsymbol{\xi}})$ to the latter rate problem is such that the subset $\dot{\mathbf{u}}$, $\dot{\lambda}$ makes L_2 stationary.

This principle is the nonlocal plasticity counterpart of the principle given by Mühlhaus and Aifantis (1991) for gradient plastic-

Downloaded 04 May 2010 to 171.66.16.27. Redistribution subject to ASME license or copyright; see http://www.asme.org/terms/Terms_Use.cfm

ity. Its proof is in Appendix C, where it is also shown that, whenever the hardening modulus h is positive everywhere in V, the above principle transforms into a minimum principle, i.e.,

$$\min_{(\dot{u},\dot{\lambda})} L_2[\dot{\mathbf{u}}, \dot{\lambda}] \quad \text{subject to the constraints } (90a, b). \tag{91}$$

which is the extension to nonlocal plasticity of an analogous one given by Capurso (1969) for local plasticity (see also Capurso and Maier, 1970).

10 Conclusions

This paper is an attempt to frame nonlocal plasticity within thermodynamics in the hypothesis that nonlocality is only determined by the diffusion processes inherent in the material isotropic hardening/softening. This goal has been achieved by applying the first and second principles of thermodynamics globally for the whole structure, or locally by taking into account, through a suitable nonlocality residual, the internal energy exchanges that accompany the above diffusion processes. Thermal effects of local nature, considered in the first part of the paper, have been then ignored. A procedure conceptually similar to that of the classic thermodynamics of irreversible deformation processes has so been rendered viable. The use of a suitable regularization operator with its adjoint and of the appropriate insulation condition for the hardening/softening diffusion processes has led to the evaluation of the nonlocality residual, as well as to the appropriate form of the nonnegativity requisite of the net intrinsic dissipation energy. Consistently with the latter results, the plastic yielding laws have been formulated for nonlocal associative plasticity (kinematic hardening not considered for simplicity) and a related theorem of the maximum intrinsic dissipation, of global integral form, has been proven.

All the above constitutes a thermodynamically consistent framework for nonlocal plasticity, within which other two main issues have been addressed. One is the (rate) response of a (continuous) set of material particles to a given total strain rate field. It has been proven that this response is unique and characterized by a minimum principle in terms of the unknown plastic coefficient, provided that some conditions are satisfied. Referring to the region where plastic yielding is active and to a simplified version of the nonlocal plasticity model, a series representation has been provided for the above coefficient, as well as for the related continuum tangent stiffness matrix, useful for numerical computations.

The other main issue addressed is the rate response problem of a structure to assigned load rates. The conditions for the uniqueness of solution to this boundary value problem have been discussed and shown to depend on the positive definiteness of some functional of the total plastic strain rates. The latter requisite is certainly satisfied in case of positive hardening modulus in the whole solid, in which case the solution is unique, but it may be nonunique if the hardening modulus is nonpositive somewhere in the body. Two variational characterizations, useful for discretization purposes, have been given for the above boundary value problem, both of which are stationarity principles, but transform into a min-max principle and a minimum principle, respectively, in the case of everywhere positive hardening modulus.

The above treatment of nonlocal plasticity constitutes, in the authors' opinion, a firm basis for further developments, to be achieved elsewhere, as numerical simulations to validate the proposed theory and numerical comparisons with existing theories. The proposed theory, due to its thermodynamic basis, turns out to be rather versatile, as in fact it is able to cover more complex material behaviors, for instance nonassociative plasticity, elastic-plastic-damage and elastic-viscoplastic-damage behaviors, and in general any material behavior that can be described within the theory of internal variables.

Additionally, this same theory exhibits a wider potentiality than shown previously: It in fact can be applied to gradient plasticity, provided that the regularization operator is suitably redefined as a differential one; Polizzotto et al. (1996) and Polizzotto and Borino (1998). All this is the object of an ongoing research.

Acknowledgment

The present work is part of a research project supported by the Ministero dell'Università e della Ricerca Scientifica e Tecnologica of Italy (MURST 40 percent).

References

Acharya, A., and Shawki, T. G., 1995, "Thermodynamic Restrictions on Constitutive Equations for Second-Deformation-Gradient Inelastic Behaviour," *J. Mech. Phys. Solids,* Vol. 43, pp. 1751–1772.

Acharya, A., and Shawki, T. G., 1996, "The Clausius-Duhem Inequality and the Structure of Rate-Independent Plasticity," *Int. J. Plasticity,* Vol. 12, pp. 229–238.

Aifantis, E. C., 1984, "On the Role of Gradients in the Localization of Deformation and Fracture," *J. Engn. Sci.,* Vol. 30, pp. 1279–1299.

Bažant, Z. P., and Lin, F.-B., 1988, "Nonlocal Yield Limit Degradation," *Int. J. Num. Meths. Engng.,* Vol. 26, pp. 1805–1823.

Bažant, Z. P., and Cedolin, L., 1991, *Stability of Structures,* Oxford University Press, New York.

Borré, G., and Maier, G., 1989, "On Linear Versus Nonlinear Flow Rules in Strain Localization Analysis," *Meccanica,* Vol. 24, pp. 36–41.

Capurso, M., 1969, "Minimum Principles in Elastic-Plastic Incremental Analysis Problems," *Atti Acc. Naz. Lincei,* Ser. VIII, Vol. XLIV, Fasc. 4–5, pp. 552–560 (in Italian).

Capurso, M., and Maier, G., 1970, "Incremental Elastoplastic Analysis and Quadratic Optimization," *Meccanica,* Vol. V, pp. 107–116.

Coleman, B. D., and Gurtin, M., 1967, "Thermodynamics With Internal Variables," *J. Chem. Phys.,* Vol. 47, pp. 597–613.

Coleman, B. D., and Hodgdon, M. L., 1985, "On Shear Bands in Ductile Materials," *Arch. Ration. Mech. Anal.,* Vol. 90, pp. 219–247.

Coleman, B. D., and Noll, W., 1963, "The Thermodynamics of Elastic Materials With Heat Conduction and Viscosity," *Arch. Ration. Mech. Anal.,* Vol. 13, pp. 167–178.

de Borst, R., and Mühlhaus, H.-B., 1992, "Gradient-Dependent Plasticity: Formulation and Algorithmic Aspects," *Int. J. Num. Meth. Eng.,* Vol. 35, pp. 521–539.

de Borst, R., Sluys, L. J., Mühlhaus, H.-B., and Pamin, J., 1993, "Fundamental Issues in Finite Element Analyses of Localization of Deformation," *Engineering Computations,* Vol. 10, pp. 99–121.

de Borst, R., Pamin, J., and Sluys, L. J., 1995, "Gradient Plasticity for Localization Problems in Quasi-Brittle and Frictional Materials," *Computational Plasticity, Fundamentals and Applications,* D. R. J. Owen, E. Onate, and E. Hinton, eds., Pineridge Press, Swansea, UK, pp. 509–533.

de Borst, R., and Pamin, J., 1996, "Gradient Plasticity in Numerical Simulation of Concrete Cracking," *Eur. J. Mech. A/Solids,* Vol. 15, pp. 295–320.

Edelen, D. G. B., Green, A. E., and Laws, N., 1971, "Nonlocal Continuum Mechanics," *Arch. Rat. Mech. Anal.,* Vol. 43, pp. 36–44.

Edelen, D. G. B., and Laws, N., 1971, "On the Thermodynamics of Systems With Nonlocality," *Arch. Rational Mech. Anal.,* Vol. 43, pp. 24–35.

Eringen, A. C., 1981, "On Nonlocal Plasticity," *Int. J. Engng. Sci.,* Vol. 19, pp. 1461–1474.

Eringen, A. C., 1983, "Theories of Nonlocal Plasticity," *Int. J. Engng. Sci.,* Vol. 21, pp. 741–751.

Germain, P., Nguyen, Q. S., and Suquet, P., 1983, "Continuum Thermodynamics," ASME JOURNAL OF APPLIED MECHANICS, Vol. 50, pp. 1010–1021.

Hill, R., 1950, *The Mathematical Theory of Plasticity,* Clarendon Press, Oxford, UK.

Hill, R., and Hutchinson, J. W., 1975, "Bifurcation Phenomena in the Plane Tensile Test," *J. Mech. Phys. Solids,* Vol. 23, pp. 239–264.

Hutchinson, J. W., and Tvergaard, V., 1981, "Shear Band Formation in Plane Strain," *Int. J. Solids Struct.,* Vol. 17, pp. 451–470.

Larsy, D., and Belytschko, T., 1988, "Localization Limiters in Transient Problems," *Int. J. Solids Struct.,* Vol. 24, pp. 581–597.

Lemaitre, J., and Chaboche, J.-L., 1990, *Mechanics of Solid Materials,* Cambridge University Press, Cambridge, UK.

Loret, B., 1987, "Non-Linearité Incrementale et Localisation des Déformations: Quelques Remarques," *J. de. Méc. Théor. Appl.,* Vol. 6, pp. 423–459.

Lubliner, J., 1973, "On the Structure of the Rate Equations of Materials With Internal Variables," *Acta Mech.,* Vol. 17, pp. 109–119.

Lubliner, J., 1990, *Plasticity Theory,* Macmillan, New York.

Martin, J. B., 1975, *Plasticity: Fundamentals and General Results,* The MIT Press, Cambridge, MA.

Mühlhaus, H.-B., and Vardulakis, I., 1987, "The Thickness of Shear Bands in Granular Materials," *Geotechnique,* Vol. 37, pp. 271–283.

Mühlhaus, H.-B., and Aifantis, E. C., 1991, "A Variational Principle for Gradient Plasticity," *Int. J. Solids Struct.,* Vol. 28, pp. 845–858.

Needleman, A., 1988, "Material Rate-Dependence and Mesh Sensitivity in Localization Problems," *Comp. Meth. Appl. Mech. Eng.,* Vol. 67, pp. 69–86.

Nilsson, C., 1994, "On Nonlocal Plasticity, Localization and Softening," Ph.D. thesis, Department of Structural Mechanics, Lund University of Technology, Sweden.

Ortiz, M., Leroy, Y., and Needleman, A., 1987, "A Finite Element Method for Localized Failure Analysis," *Comput. Meths. Appl. Mech. Engng.,* Vol. 61, pp. 189–214.

Downloaded 04 May 2010 to 171.66.16.27. Redistribution subject to ASME license or copyright; see http://www.asme.org/terms/Terms_Use.cfm

Pietruszak, S. T., and Mróz, Z., 1981, "Finite Element Analysis of Deformation of Strain Softening Materials," *Int. J. Num. Meths. Engng.*, Vol. 17, pp. 327–334.

Pijaudier-Cabot, G., and Bažant, Z. P., 1987, "Nonlocal Damage Theory," *J. Eng. Mech. ASCE*, Vol. 113, pp. 1512–1533.

Polizzotto, C., and Borino, G., 1998, "A Thermodynamics-Based Formulation of Gradient-Dependent Plasticity," *Eur. J. Mech. A/Solids*, Vol. 17, pp. 741–761.

Polizzotto, C., Borino, G., and Fuschi, P., 1998, "A Thermodynamic Consistent Formulation of Nonlocal and Gradient Plasticity," *Mech. Res. Com.*, Vol. 25, No. 1, pp. 75–82.

Raniecki, B., and Bruhns, O. T., 1981, "Bounds to Bifurcation Stresses in Solids With Non-Associated Plastic Flow Laws at Finite Strain," *J. Mech. Phys. Solids*, Vol. 29, pp. 153–172.

Rudnicki, J. W., and Rice, J. R., 1975, "Conditions for the Localization of Dilatant Materials," *J. Mech. Phys. Solids*, Vol. 23, pp. 371–394.

Simo, J. C., 1988, "A Framework for Finite Strain Elastoplasticity Based on Maximum Plastic Dissipation and the Multiplicative Decomposition: Part I. Continuum Formulation," *Comput. Meths. Appl. Mech. Engng.*, Vol. 66, pp. 199–219.

Simo, J. C., and Ju, J. W., 1987, "Stress and Strain Based Continuum Damage Models—I. Formulation," *Int. J. Solids Struct.*, Vol. 23, pp. 821–840.

Strömberg, L., and Ristinmaa, M., 1996, "FE-Formulation of a Nonlocal Plasticity Theory," *Comp. Meth. Appl. Mech. Eng.*, Vol. 136, pp. 127–144.

Valanis, K. C., 1996, "A Gradient Theory of Internal Variables," *Acta Mechanica*, Vol. 116, pp. 1–14.

APPENDIX A

This appendix is aimed at assessing the convergence of the series in Eq. (65). Remembering Eqs. (17) and (62), as well as the definition of $\mathcal{L}^{(n)}(\cdot)$, and with the position $\phi \equiv \langle q_\epsilon \rangle / h_c$, the detailed expressions of $(-1)^n \mathcal{L}^{(n)}(\phi)$ for $n = 1, 2, \ldots n$ read as follows:

$$-\mathcal{L}(\phi) = \frac{1}{G_0^2} \int_{V_0} \int_{V_0} \left[\frac{-h(\mathbf{x} + \mathbf{s}_1)}{h_c(\mathbf{x})} \right] g(s g(r_1) \phi(\mathbf{x} + \mathbf{s}_1 + \mathbf{r}_1) \times (dV_0)^2 \quad (92a)$$

$$\mathcal{L}^{(2)}(\phi) = \frac{1}{G_0^4} \int_{V_0} \int_{V_0} \int_{V_0} \int_{V_0} \left[\frac{-h(\mathbf{x} + \mathbf{s}_2)}{h_c(\mathbf{x})} \frac{-h(\mathbf{x} + \mathbf{s}_2 + \mathbf{s}_1)}{h_c(\mathbf{x} + \mathbf{s}_2)} \right] \cdot g(s_2) g(r_2) g(s_1) g(r_1) \phi(\mathbf{x} + \mathbf{s}_2 + \mathbf{s}_1 + \mathbf{r}_2 + \mathbf{r}_1) (dV_0)^4 \quad (92b)$$

$$(-1)^n \mathcal{L}^{(n)}(\phi) = \frac{1}{G_0^{2n}} \overbrace{\int_{V_0} \cdots \int_{V_0}}^{2n \text{ times}} \left[\frac{-h(\mathbf{x} + \mathbf{s}_n)}{h_c(\mathbf{x})} \frac{-h(\mathbf{x} + \mathbf{s}_n + \mathbf{s}_{n-1})}{h_c(\mathbf{x} + \mathbf{s}_n)} \cdots \frac{-h(\mathbf{x} + \mathbf{s}_n + \cdots + \mathbf{s}_1)}{h_c(\mathbf{x} + \mathbf{s}_n + \cdots + \mathbf{s}_2)} \right] \cdot g(s_n) g(r_n) \cdots g(s_1) g(r_1) \cdot \phi(\mathbf{x} + \mathbf{s}_n + \cdots + \mathbf{s}_1 + \mathbf{r}_n + \cdots + \mathbf{r}_1) (dV_0)^{2n}. \quad (92c)$$

Under the hypothesis that a (finite and continuous) solution to the problem of Eq. (59) exists, Eq. (92*c*) can be rewritten in the form

$$(-1)^n \mathcal{L}^{(n)}(\phi) = M_n \left(\frac{-h(\mathbf{x})}{h_c(\mathbf{x})} \right)^n J_n \quad (93)$$

where M_n is an appropriate (finite) constant and J_n is

$$J_n = \frac{1}{G_0^{2n}} \overbrace{\int_{V_0} \cdots \int_{V_0}}^{2n \text{ times}} g(s_n) g(r_n) \cdots g(s_1) g(r_1) \cdot \phi(\mathbf{x} + \mathbf{s}_n + \cdots + \mathbf{s}_1 + \mathbf{r}_n + \cdots + \mathbf{r}_1) (dV_0)^{2n}. \quad (94)$$

Since, by hypothesis, $\phi = \langle q_\epsilon \rangle / h_c$ remains finite, a constant M_0 exists such that $\phi \leq M_0$ in V_λ and thus Eq. (94), considered that $\int_{V_0} g(r) dV_0(r) = G_0$, gives

$$J_n \leq M_0. \quad (95)$$

With the aid of the above results, we can write the remainder R_n of the series (93) as

$$R_n = \sum_{k=n}^{\infty} (-1)^k \mathcal{L}^{(k)}(\phi) = \sum_{k=n}^{\infty} M_k \left(\frac{-h}{h_c} \right)^k J_k. \quad (96)$$

Considering that the constants M_n are finite for all $n = 1, 2, \ldots$, and that thus a constant $\bar{M} > 0$ can be found such that $|M_n| \leq \bar{M}$ for all n, one can write, using Eq. (95),

$$|R_n| \leq M_0 \bar{M} \sum_{k=n}^{\infty} q^k, \quad q := \frac{|h|}{h_c}. \quad (97)$$

The series on the right-hand side of the latter equation can be written as

$$\rho_n \equiv \sum_{k=n}^{\infty} q^k = q^n (1 + q + q^2 + \cdots). \quad (98)$$

Provided that $q < 1$, i.e., $|h| < h_c$, the geometric series on the right-hand side of Eq. (98) has the sum $1/(1 - q)$, whereas $q^n \to 0$ as $n \to \infty$. Since, therefore,

$$\rho_n = q^n / (1 - q) \to 0 \quad \text{for} \quad n \to \infty, \quad (99)$$

it results that $R_n \to 0$ as $n \to \infty$ and the series of Eq. (65) is convergent. Note that the inequality $|h| < h_c$, under which the convergence has been proved, is only a sufficient condition for convergence, not a necessary one.

APPENDIX B

This appendix is devoted to the proof of the first (mixed) stationarity principle of Section 9. First, we prove that the/a stationarity solution solves the structural rate problem (76)–(80). To this purpose, the Lagrangian multiplier method is employed. The Lagrangian functional related to (86) with the constraints (87) can be written as

$$L_1^a = L_1 - \int_V \dot{\lambda} \dot{F} dV + \int_V \dot{\boldsymbol{\tau}} : (\nabla^s \dot{\mathbf{u}} - \dot{\boldsymbol{\epsilon}}) dV - \int_{S_U} (\dot{\mathbf{u}} - \dot{\mathbf{U}}) \cdot \dot{\boldsymbol{\tau}} \cdot \mathbf{n} dS \quad (100)$$

where $\dot{\lambda}$ and $\dot{\boldsymbol{\tau}}$ are the appropriate Lagrange multipliers; namely, $\dot{\lambda}$ is a scalar such that $\dot{\lambda} \geq 0$ in V_y and $\dot{\lambda} = 0$ in $V \backslash V_y$, $\dot{\boldsymbol{\tau}}$ is a (symmetric) stress-like tensor. The first variation of L_1^a reads

$$\delta L_1^a = \int_V \delta \dot{\boldsymbol{\epsilon}} : [\mathbf{C} : (\dot{\boldsymbol{\epsilon}} - \dot{\boldsymbol{\epsilon}}^p) - \dot{\boldsymbol{\tau}}] dV + \int_V \delta \dot{\boldsymbol{\epsilon}}^p : [\dot{\boldsymbol{\sigma}} - \mathbf{C} : (\dot{\boldsymbol{\epsilon}} - \dot{\boldsymbol{\epsilon}}^p)] dV + \int_V \delta \dot{\xi} (h \dot{\xi} - \dot{\chi}) dV + \int_V \delta \dot{\boldsymbol{\sigma}} : (\dot{\boldsymbol{\epsilon}}^p - \dot{\lambda} f_{,\sigma}) dV - \int_V \delta \dot{\chi} (\dot{\xi} - \mathcal{R}(\dot{\lambda})) dV - \int_V \delta \dot{\mathbf{u}} \cdot (\nabla \cdot \dot{\boldsymbol{\tau}} + \dot{\mathbf{b}}) dV + \int_{S_T} \delta \dot{\mathbf{u}} \cdot (\dot{\boldsymbol{\tau}} \cdot \mathbf{n} - \dot{\mathbf{T}}) dS - \int_V \delta \dot{\lambda} \dot{F} dV + \int_V \delta \dot{\boldsymbol{\tau}} :$$

Downloaded 04 May 2010 to 171.66.16.27. Redistribution subject to ASME license or copyright; see http://www.asme.org/terms/Terms_Use.cfm

$$(\nabla^s \dot{\mathbf{u}} - \dot{\boldsymbol{\epsilon}})dV - \int_{S_U} (\dot{\mathbf{u}} - \dot{\mathbf{U}}) \cdot \delta\dot{\boldsymbol{\tau}} \cdot \mathbf{n} dS \quad (101)$$

where the divergence theorem and the Green-type relation (27) have been utilized. The condition $\delta L_1^a = 0$ for arbitrary variations, but $\dot{\lambda} + \delta\dot{\lambda} = 0$ in V_y and $\delta\dot{\lambda} = 0$ in $V \backslash V_y$, provides the relevant the Euler-Lagrange equations. The latter equations imply $\dot{\boldsymbol{\tau}} \equiv \dot{\boldsymbol{\sigma}}$ in V and coincide with Eqs. (76)–(80), with $\dot{\lambda}$ having the role of plastic coefficient. Since these Euler-Lagrange equations express necessary conditions, we can conclude that the/a stationarity solution also solves the mechanical rate problem.

Secondly, we want to prove that the/a solution to the mechanical rate problem also solves the stationarity problem. From Eq. (101), it is evident that, provided that $\delta\dot{\lambda} = 0$ in $V \backslash V_y$, the/a solution to problem (76)–(80) makes δL_1^a to vanish for arbitrary variations, but $\dot{\lambda} + \delta\dot{\lambda} \geq 0$ in V_y and $\delta\dot{\lambda} = 0$ in $V \backslash V_y$ and thus L_1 is correspondingly made stationary. The proof is so complete.

Additionally, let $\mathbf{X}_k^*$ and $\mathbf{X}_s^*$ denote the/a solution to Eqs. (76)–(80) and let $\delta\mathbf{X}_k$, $\delta\mathbf{X}_s$ be arbitrary variations in the same functional space as the related variables $\mathbf{X}_k$, $\mathbf{X}_s$, but such that the trial fields $\mathbf{X}_k' = \mathbf{X}_k^* + \delta\mathbf{X}_k$, $\mathbf{X}_s' = \mathbf{X}_s^* + \delta\mathbf{X}_s$ satisfy the constraints (87). Denoting by L_1' and L_1^* the values of L_1 for primed and starred variables, we can write

$$L_1' = L_1^* + \delta L_1 + \tfrac{1}{2}\delta^2 L_1 \quad (102)$$

where, with some mathematics,

$$\delta L_1 = \int_V [\delta\dot{\boldsymbol{\sigma}} : \dot{\boldsymbol{\epsilon}}^{p*} - \delta\dot{\chi}\mathcal{R}(\dot{\lambda}^*)]dV = \int_{V_y} \dot{\lambda}^* \delta\dot{F} dV \quad (103a)$$

$$\delta^2 L_1 = \int_V [(\delta\dot{\boldsymbol{\epsilon}} - \delta\dot{\boldsymbol{\epsilon}}^p) : \mathbf{C} : (\delta\dot{\boldsymbol{\epsilon}} - \delta\dot{\boldsymbol{\epsilon}}^p) + h(\xi^*)(\delta\dot{\xi})^2]dV + 2\int_V (\delta\dot{\boldsymbol{\sigma}} : \delta\dot{\boldsymbol{\epsilon}}^p - \delta\dot{\chi}\delta\dot{\xi})dV. \quad (103b)$$

Among the above variations, we consider two classes of them:

(i) Variation sets with identically vanishing static-type variations, i.e., $\delta\mathbf{X}_s = \mathbf{0}$ in V, for which we have $\delta L_1 = 0$, whereas the second variation reduces to

$$\delta^2 L_1 = \int_V [(\delta\dot{\boldsymbol{\epsilon}} - \delta\dot{\boldsymbol{\epsilon}}^p) : \mathbf{C} : (\delta\dot{\boldsymbol{\epsilon}} - \delta\dot{\boldsymbol{\epsilon}}^p) + h(\xi^*)(\delta\dot{\xi})^2]dV. \quad (104)$$

If $h > 0$ everywhere in V, we know from Section 8 that the solution $(\mathbf{X}_k^*, \mathbf{X}_s^*)$ is unique. The integrand of (104) is positive definite, hence Eq. (102) gives

$$L_1[\mathbf{X}_k'; \mathbf{X}_s^*] = L_1^* + \tfrac{1}{2}\delta^2 L_1 > L_1^* \quad (105)$$

for arbitrary not identically vanishing kinematic-type variations. Otherwise, if $h \leq 0$ in some region $V_h \subset V$, we know from Section 8 that the solution $(\mathbf{X}_k^*, \mathbf{X}_s^*)$ is not unique. As the integrand of (104) is no longer positive definite, inequality (105) cannot be inferred anymore.

(ii) Variation sets with identically vanishing kinematic-type variations, i.e., $\delta\mathbf{X}_k = \mathbf{0}$ in V, for which we have $\delta\dot{F} \leq 0$ everywhere in V_y (where $\dot{\lambda}^* > 0$), hence $\delta L_1 \leq 0$, and $\delta L_1^2 = 0$. Therefore, for hardening modulus h of any sign, Eq. (102) yields

$$L_1[\mathbf{X}_k^*; \mathbf{X}_s'] = L_1^* + \delta L_1 \leq L_1^* \quad (106)$$

where the equality sign before the last member is allowed to occur with nontrivial *plastically neutral* variations $\delta\mathbf{X}_s = \{\delta\dot{\boldsymbol{\sigma}}, \delta\dot{\chi}\}$, i.e., such that $\delta\dot{F} = f_{,\sigma} : \delta\dot{\boldsymbol{\sigma}} - \mathcal{R}(\delta\dot{\chi}) = 0$ everywhere in V_y.

Therefore, combining Eqs. (105) and (106) with each other yields the continued inequality

$$L_1[\mathbf{X}_k', \mathbf{X}_s^*] \geq L_1^* \geq L_1[\mathbf{X}_k^*; \mathbf{X}_s'] \quad (107)$$

which holds for arbitrary primed variables satisfying Eqs. (87). We remark that the equality sign on the left in Eq. (107) can occur only if $\mathbf{X}_k' = \mathbf{X}_k^*$, and additionally that the equality sign on the right is allowed to occur if $\mathbf{X}_s'$ is chosen to be plastically neutral, i.e., $\dot{\mathbf{F}}(\dot{\boldsymbol{\sigma}}', \dot{\chi}') = 0$ in V_y. We thus can conclude that, for $h > 0$ everywhere in V, the (unique) solution to the mechanical rate problem (76)–(80) also solves, though not uniquely, the min-max problem (88).

APPENDIX C

This appendix is devoted to the proof of the second (kinematic) principle of Section 9. The first part of this theorem can be proved using again the Lagrange multiplier method. Denoting by $\dot{\mathbf{p}}$ an appropriate (traction rate like) multiplier, the Lagrangian functional of (89) reads

$$L_2^a = L_2 - \int_{S_U} (\dot{\mathbf{u}} - \dot{\mathbf{U}}) \cdot \dot{\mathbf{p}} dS. \quad (108)$$

The first variation of L_2^a, after application of the divergence theorem and of the Green-type relation (27), can be written as

$$\delta L_2^a = \int_V \delta\dot{\mathbf{u}} \cdot \{\nabla \cdot [\mathbf{C} : (\nabla^s \dot{\mathbf{u}} - f_{,\sigma}\dot{\lambda})] + \dot{\mathbf{b}}\}dV - \int_V \delta\dot{\lambda}\{f_{,\sigma} : \mathbf{C} : (\nabla^s \dot{\mathbf{u}} - f_{,\sigma}\dot{\lambda}) - \mathcal{R}^*[h\mathcal{R}(\dot{\lambda})]\}dV + \int_{S_T} \delta\dot{\mathbf{u}} \cdot [\mathbf{n} \cdot \mathbf{C} : (\nabla^s \dot{\mathbf{u}} - f_{,\sigma}\dot{\lambda}) - \dot{\mathbf{T}}]dS + \int_{S_U} \delta\dot{\mathbf{u}} \cdot [\mathbf{n} \cdot \mathbf{C} : (\nabla^s \dot{\mathbf{u}} - f_{,\sigma}\dot{\lambda}) - \dot{\mathbf{p}}]dS - \int_{S_U} (\dot{\mathbf{u}} - \dot{\mathbf{U}}) \cdot \delta\dot{\mathbf{p}} dS. \quad (109)$$

The condition for which $\delta L_2^a = 0$ for arbitrary admissible variations, that is the Euler-Lagrange equations, turn out to be equivalent to Eqs. (76)–(80) with the multiplier $\dot{\mathbf{p}}$ being identified as the traction rate on S_U. In other words, the/a stationarity solution solves the mechanical rate problem (76)–(80).

The second part of the theorem can be proved by observing that the fields $(\dot{\mathbf{u}}, \dot{\lambda})$ that belong to the solution to the structural rate problem together with $\dot{\mathbf{p}} = \dot{\boldsymbol{\sigma}} \cdot \mathbf{n}$ on S_U, make δL_2 in (109) to vanish for arbitrary variations and $L_2[\dot{\mathbf{u}}, \dot{\lambda}]$ to be stationary. The theorem is so proved.

Furthermore, let the/a solution to the mechanical rate problem be denoted as $\dot{\mathbf{u}}^*$, $\dot{\boldsymbol{\epsilon}}^*$, etc., and let $\delta\dot{\mathbf{u}}$, $\delta\dot{\lambda}$ be a set of variation fields such that the trial variables $(\cdot)' = (\cdot)^* + \delta(\cdot)$ satisfy the constraint Eqs. (90), such that $\delta\dot{\lambda}' = \dot{\lambda}^* + \delta\dot{\lambda} \geq 0$ in V_y, but $\delta\dot{\lambda} = 0$ in $V \backslash V_y$, and $\delta\dot{\mathbf{u}} = 0$ on S_U. Denoting by L_2' and L_2^* the values of L_2 for the primed and starred variables, respectively, we have

$$L_2' = L_2^* + \delta L_2 + \tfrac{1}{2}\delta^2 L_2 \quad (110)$$

where the first variation is positive, i.e.,

Downloaded 04 May 2010 to 171.66.16.27. Redistribution subject to ASME license or copyright; see http://www.asme.org/terms/Terms_Use.cfm

$$\delta L_2 = -\int_V \delta\dot{\lambda}\dot{F}^* dV = -\int_{V_y} \delta\dot{\lambda}\dot{F}^* dV > 0 \qquad (111)$$

because $\delta\dot{\lambda}\dot{F}^* = \delta\dot{\lambda}'[f_{,\sigma}\dot{\boldsymbol{\sigma}}^* - \mathcal{R}(\dot{\chi}^*)] \leq 0$ in V and $\delta\dot{\lambda}$ is not a trivial field in V_y. The second variation reads

$$\delta^2 L_2 = \int_V [(\nabla^s \delta\dot{\mathbf{u}} - f_{,\sigma}\delta\dot{\lambda}) : \mathbf{C} : (\nabla^s \delta\dot{\mathbf{u}} - f_{,\sigma}\delta\dot{\lambda}) + h(\xi) \times (\mathcal{R}(\delta\dot{\lambda}))^2] dV \qquad (112)$$

which is positive definite if $h > 0$ in V, but not definite in sign if there exists a subregion $V_h \subset V$ where $h < 0$. In the former case, in which the solution to the mechanical rate problem is known to be unique, Eq. (110) gives

$$L_2[\mathbf{u}', \dot{\lambda}'] \geq L_2^*. \qquad (113)$$

Since this inequality holds for any fields $(\mathbf{u}', \dot{\lambda}')$ complying with Eqs. (90*a*, *b*), the equality sign holds only if the primed variables coincide with the (unique) solution to the rate problem (76)–(80), we can conclude that, whenever $h > 0$ in V, the latter solution solves uniquely also the minimum principle (91).

Downloaded 04 May 2010 to 171.66.16.27. Redistribution subject to ASME license or copyright; see http://www.asme.org/terms/Terms_Use.cfm

ERRATA

Rahman, M., 1999, "Some Problems of a Rigid Elliptical Disk-Inclusion Bonded Inside a Transversely Isotropic Space: Part I," *ASME Journal of Applied Mechanics,* Vol. 66, pp. 612–620.

1 The second line after Eq. (39) on page 617 in the above-mentioned article should read as follows: Furthermore, it can be easily seen that in this case on the disk where $\lambda = 0$, $V(x, y, 0)$ reduces to a polynomial in x, y of order $2l + i + j$.

2 The plus sign between the two components of the Eq. (A3) should be replaced by a minus sign. The same is true for Eq. (A4) as well. Thus, for instance, Eq. (A3) should read as

$$I^{(\lambda)}_{i+1,j} = \frac{-1}{(2i+1)a}\frac{\partial I^{(\lambda)}_{ij}}{\partial a} - \frac{1}{(2i+1)a\sqrt{(a^2+\lambda)^{2i+1}(b^2+\lambda)^{2j+1}\lambda}}\frac{\partial \lambda}{\partial a}.$$

The above changes are due to some misprints and as such have no bearing on the other results presented in the article.

Downloaded 04 May 2010 to 171.66.16.27. Redistribution subject to ASME license or copyright; see http://www.asme.org/terms/Terms_Use.cfm

The Nonlinear Gaussian Spectrum of Log-Normal Stochastic Processes and Variables

R. Ghanem
The Johns Hopkins University,
Baltimore, MD 21218

A procedure is presented in this paper for developing a representation of lognormal stochastic processes via the polynomial chaos expansion. These are processes obtained by applying the exponential operator to a gaussian process. The polynomial chaos expansion results in a representation of a stochastic process in terms of multidimensional polynomials orthogonal with respect to the gaussian measure with the dimension defined through a set of independent normalized gaussian random variables. Such a representation is useful in the context of the spectral stochastic finite element method, as well as for the analytical investigation of the mathematical properties of lognormal processes.

1 Introduction

The gaussian stochastic process is the default model used in most applications of probabilistic engineering mechanics. This is partly justified by the simple form of its marginal and joint density functions. Indeed, it is the only process for which all the joint density functions are explicitly known. Moreover, in many cases, the central limit theorem can be invoked to justify the choice of this model. The digital simulation of gaussian processes is a well developed topic with a number of very efficient techniques for effecting it (Shinozuka and Deodatis, 1991; Spanos and Zeldin, 1997).

In a number of applications of great interest, though, the gaussian model is clearly inappropriate in view of its symmetry, its infinite domain, and the rate of decay of the tail of its density function. Such examples include problems in ground water flow (Gelhar, 1993) and crack propagation (Yang and Manning, 1996). For the purpose of this paper, a lognormal process is obtained from a gaussian process by taking its exponential pointwise. Notwithstanding this simple relationship between the lognormal process and its underlying gaussian process, the correlation structure of the process is significantly altered by the exponentiation operation. Once a gaussian process has been simulated, a lognormal field can be readily obtained by taking the exponential of the generated variates. Although explicit relationships are available between the covariances of the gaussian and the lognormal processes, in a number of applications, however, a more important issue than simulating stochastic processes is that of representing them in an explicit expression that lends itself to analytical manipulations. The Karhunen-Loeve expansion and the polynomial chaos expansion are two examples of such representations (Ghanem and Spanos, 1991). In both of these expansions, a stochastic process is represented in terms of a discrete set of random variables. These expansions have proven very useful for the development of the spectral stochastic finite element method (Ghanem and Spanos, 1991). Unlike existing representations where the coefficients in the expansions are evaluated through a moment matching procedure (Winterstein, 1988), the current representation is viewed as a generalized Fourier expansion and the associated coefficients are evaluated as generalized Fourier coefficients that minimize the norm of the error associated with the approximation.

It is the purpose of this paper to develop a representation of the lognormal process in terms of the Polynomial Chaos expansion (Ghanem and Spanos, 1991, 1997; Wiener, 1938). This is a representation of an arbitrary stochastic process as an expansion in terms of multidimensional Hermite polynomials, the independent variables in the expansion consisting of a set of independent normalized gaussian variables.

The paper starts by reviewing some basic properties between lognormal random variables and their underlying gaussian variables. Following that, the case of two random variables is addressed. Then, the case of the lognormal process is treated, leading to its representation in terms of the polynomial chaos expansion. A parametric study is finally presented detailing the sensitivity of the proposed representation to the correlation length of the process and to its coefficient of variation.

2 Preliminaries

In this section a review is presented of some relations between lognormal random variables and their associated gaussian variables.

2.1 Marginal Lognormal Random Variables. Let g denote a gaussian random variable, and let l denote the random variable obtained by taking the exponential of g,

$$g = \ln l, \quad l = e^g. \tag{1}$$

Then, l is a lognormal random variable and its moments are related to those of g through the following simple relationships (Benjamin and Cornell, 1970):

$$\langle l^r \rangle = e^{r\mu_g} e^{r^2\sigma_g^2/2}, \tag{2}$$

where

$$\mu_g = \langle g \rangle, \quad \sigma_g^2 = \langle g^2 \rangle - \mu_g^2, \tag{3}$$

and where $\langle \ \rangle$ denotes ensemble averaging. Specifically, the first two moments are obtained as

Contributed by the Electrical and Electronic Packaging Division (EEPD) of THE AMERICAN SOCIETY OF MECHANICAL ENGINEERS for publication in the ASME JOURNAL OF APPLIED MECHANICS.

Discussion on this paper should be addressed to the Technical Editor, Professor Lewis T. Wheeler, Department of Mechanical Engineering, University Houston, Houston, TX 77204-4792, and will be accepted until four months after final publication of the paper itself in the ASME JOURNAL OF APPLIED MECHANICS.

Manuscript received by the Applied Mechanics Division June 23, 1997; final revision November 3, 1998. Associate Technical Editor: M. Shinozuka.

 Copyright © 1999 by ASME

Downloaded 04 May 2010 to 171.66.16.27. Redistribution subject to ASME license or copyright; see http://www.asme.org/terms/Terms_Use.cfm

$$\mu_l = e^{\mu_g} e^{\sigma_g^2/2}, \tag{4}$$

and

$$\langle l^2 \rangle = e^{2\mu_g} e^{2\sigma_g^2}, \tag{5}$$

respectively. The following relations follow immediately from Eqs. (1)–(4):

$$\mu_g = \ln \mu_l - \tfrac{1}{2}\sigma_g^2, \tag{6}$$

$$\sigma_g^2 = \ln (V_l^2 + 1), \tag{7}$$

$$V_l^2 = e^{\sigma_g^2} - 1, \tag{8}$$

and

$$\sigma_l^2 = \mu_l^2 (e^{\sigma_g^2} - 1), \tag{9}$$

where $V_l = \sigma_l/\mu_l$ denotes the coefficient of variation of the lognormal variable l.

2.2 Joint Lognormal Random Variables. Next, consider two random variables, l_1 and l_2 that are obtained as the exponentials of two jointly gaussian random variables g_1 and g_2. Without loss of generality, and to simplify the notation, consider that g_1 and g_2 (and, therefore, l_1 and l_2) have the same mean μ_g and variance σ_g^2,

$$\langle g_1 \rangle = \langle g_2 \rangle = \mu_g, \tag{10}$$

and

$$\sigma_{g_1} = \sigma_{g_2} = \sigma_g. \tag{11}$$

Then,

$$\langle l_1 \rangle = \langle l_2 \rangle = \mu_l, \tag{12}$$

and,

$$\sigma_{l_1} = \sigma_{l_2} = \sigma_l. \tag{13}$$

The covariance function of the two random variables l_1 and l_2 can then be shown to be given by (Johnson and Kotz, 1972)

$$\text{Cov}\,(l_1, l_2) = (e^{\text{Cov}(g_1, g_2)\sigma_{g_1}\sigma_{g_2}} - 1) e^{\mu_{g_1} + \mu_{g_2} + (1/2)(\sigma_{g_1}^2 + \sigma_{g_2}^2)}. \tag{14}$$

The covariance between g_1 and g_2 is then obtained through simple algebraic manipulations as,

$$\text{Cov}\,(g_1, g_2) = \log\left[\frac{\text{Cov}\,(l_1, l_2)}{\mu_l^2} + 1\right]. \tag{15}$$

This last equation gives the covariance between the two random variables g_1 and g_2, which would induce a specified covariance between their exponentials l_1 and l_2.

3 Lognormal Random Process

Let $g(\mathbf{x})$ denote a gaussian process with covariance function $R_{gg}(\mathbf{x}, \mathbf{y})$. Moreover, let the process g be represented as the sum of deterministic shape functions with random amplitudes according to,

$$g(\mathbf{x}) = \sum_{i=0}^{N} \xi_i g_i(\mathbf{x}) \equiv \sum_{i=0}^{N} \xi_i g_i, \tag{16}$$

where,

$$\langle \xi_i \rangle = 0, \quad \langle \xi_i \xi_j \rangle = \delta_{ij}, \quad i, j = 1, \ldots, \quad \xi_0 \equiv 1. \tag{17}$$

In this last equation, ξ_i denotes the random amplitude associated with the deterministic shape $g_i(\mathbf{x})$, and $g_0(\mathbf{x})$ denotes the mean of the process. An expansion in this form can be obtained, for example, through a Karhunen-Loeve representation of the stochastic process (Ghanem and Spanos, 1991), or through a harmonic superposition if the process is stationary (Shinozuka and Deodatis, 1991). In the case where such an expansion is identified with the Karhunen-Loeve expansion, the functions $g_i(\mathbf{x})$ would be associated with the solution to the following integral eigenvalue problem,

$$\int_{\mathscr{D}} R_{gg}(\mathbf{x}, \mathbf{y}) \phi_i(\mathbf{y}) d\mathbf{y} = \lambda_i \phi_i(\mathbf{x}), \quad \mathbf{x} \in \mathscr{D}, \tag{18}$$

where $\mathscr{D}$ denotes the dimensional extent (spatial or temporal) of the stochastic process. Then the functions, $g_i(\mathbf{x})$ are obtained as,

$$g_i(\mathbf{x}) = \sqrt{\lambda_i}\, \phi_i(\mathbf{x}). \tag{19}$$

It should be noted that in the case that the covariance of the process depends only on the difference between its two arguments, and the domain $\mathscr{D}$ of the process is infinite, the above expansion reduces to the harmonic superposition representation (Shinozuka and Deodatis, 1991). It should also be noted that the Karhunen-Loeve expansion is valid for stochastic processes of arbitrary probability density function. Only in the gaussian case, though, do the random variables ξ_i associated with this expansion lend themselves to a manageable explicit treatment since they form a gaussian vector.

Consider next the process $l(\mathbf{x})$ obtained from $g(\mathbf{x})$ via exponentiation, thus leading to a stochastic field having a lognormal marginal probability distribution. Formally, the process $l(\mathbf{x})$ is written as,

$$l(\mathbf{x}) = e^{g(\mathbf{x})} = \exp[\textstyle\sum \xi_i g_i]. \tag{20}$$

Clearly, expanding the exponential operator in a Taylor series gives the following polynomial representation of the lognormal process in terms of the random variables ξ_i,

$$l(\mathbf{x}) \approx 1 + \sum_{i=0}^{N} \xi_i g_i + \tfrac{1}{2} \sum_{i=0}^{N} \sum_{j=0}^{N} \xi_i \xi_j g_i g_j + \ldots. \tag{21}$$

However, these polynomials are not orthogonal, and are of limited use in the stochastic finite element method. Instead, a representation of the lognormal process in terms of polynomials that are orthogonal with respect to the gaussian measure will be sought. Such polynomials have the general form of multidimensional Hermite polynomials and have been labeled the Polynomial Chaos in various applications (Wiener, 1938; Kakutani, 1961; Kallianpur, 1970, 1972; Ghanem and Spanos, 1991). Using Ψ_i to denote these polynomials, the desired expansion has the form,

$$l(\mathbf{x}) = \sum_{i=0}^{P} \Psi_i l_i(\mathbf{x}), \tag{22}$$

where these random variables Ψ_i satisfy the following normalization conditions,

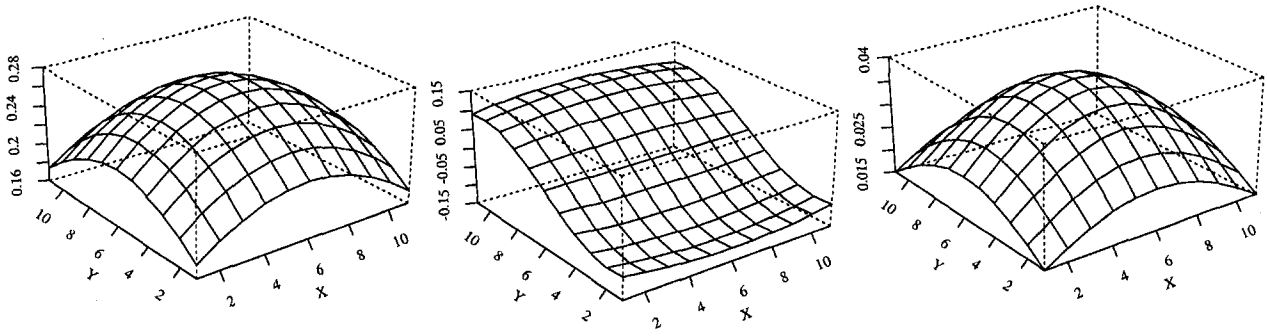
$$\langle \Psi_i \rangle = 0, \quad \langle \Psi_i \Psi_j \rangle = 0, \quad i \neq j, \quad i, j = 1, \ldots, \quad \Psi_0 \equiv 1. \tag{23}$$

Clearly, for gaussian processes, the random variables Ψ_i are gaussian, and expansion (22) is identical to expansion (16). In general, however, the process being expanded is not gaussian, and the random variables Ψ_i do not form a gaussian vector. The zero order term in the polynomial chaos expansion refers to the mean of the process and is given by,

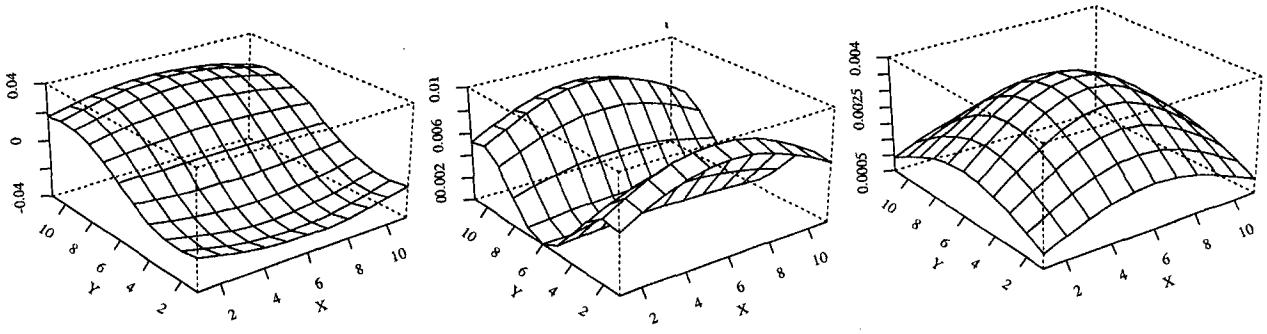
Table 1 Expressions for $\langle \Psi_i(\eta) \rangle$

$\Psi_i(\xi)$	$\Psi_i(\eta)$	$\langle \Psi_i(\eta) \rangle$
ξ_i	$\eta_i + g_i$	g_i
$\xi_i\xi_j - \delta_{ij}$	$(\eta_i + g_i)(\eta_j + g_j) - \delta_{ij}$	$g_i g_j$
$\xi_i\xi_j\xi_k - \xi_i\delta_{jk} - \xi_j\delta_{ik} - \xi_k\delta_{ij}$	$(\eta_i + g_i)(\eta_j + g_j)(\eta_k + g_k) - g_i\delta_{jk} - g_j\delta_{ik} - g_k\delta_{ij}$	$g_i g_j g_k$

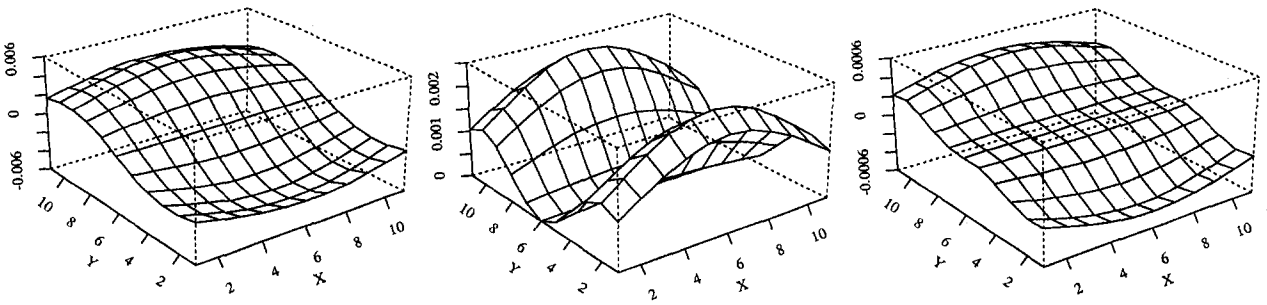
Downloaded 04 May 2010 to 171.66.16.27. Redistribution subject to ASME license or copyright; see http://www.asme.org/terms/Terms_Use.cfm



2nd Polynomial Chaos Coefficient 3rd Polynomial Chaos Coefficient 4th Polynomial Chaos Coefficient



5th Polynomial Chaos Coefficient 6th Polynomial Chaos Coefficient 7th Polynomial Chaos Coefficient



8th Polynomial Chaos Coefficient 9th Polynomial Chaos Coefficient 10th Polynomial Chaos Coefficient

Fig. 1 Coefficients in the expansions for the gaussian and lognormal processes. Third order of the polynomial chaos expansion; two terms in the Karhunen-Loeve expansion; correlation length = 1; coefficient of variation of lognormal process = 0.4.

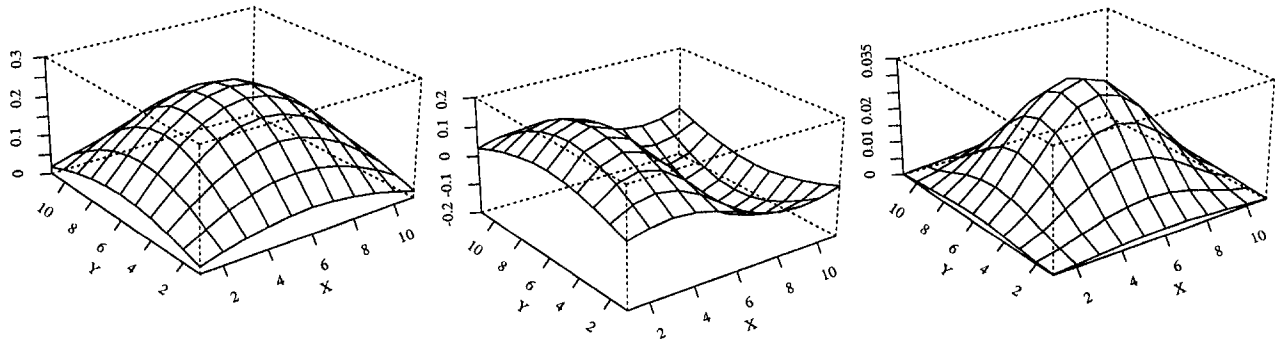
$$l_0(\mathbf{x}) = \exp\left[\mu_g + \frac{\sigma_g^2}{2}\right]. \tag{24}$$

The other coefficients can be obtained as the generalized Fourier coefficients in the expansion,

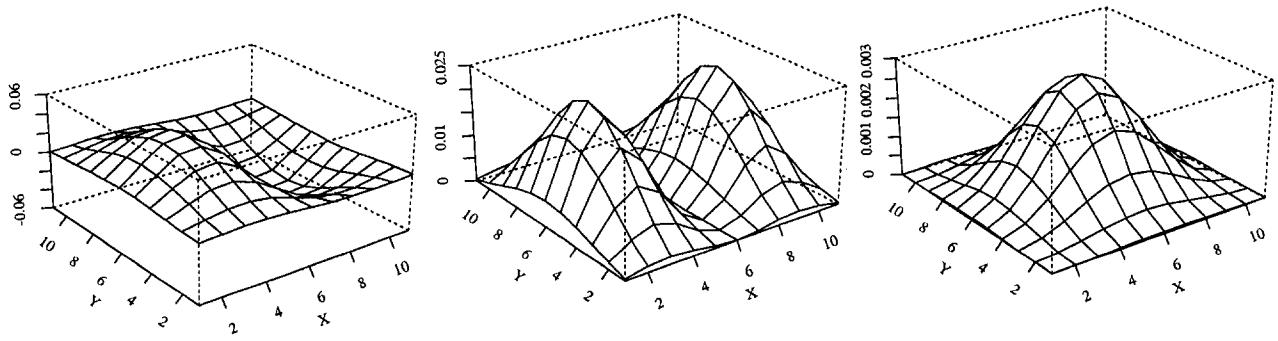
$$l_i(\mathbf{x}) = \frac{\langle l(\mathbf{x})\Psi_i\rangle}{\langle \Psi_i^2\rangle} = \frac{\langle e^{g(\mathbf{x})}\Psi_i\rangle}{\langle \Psi_i^2\rangle}, \tag{25}$$

of which equation (24) is a special case corresponding to $i = 0$. The denominator in this expression can be easily evaluated and tabulated. The numerator, on the other hand, requires some special attention. Specifically, it can be rewritten as,

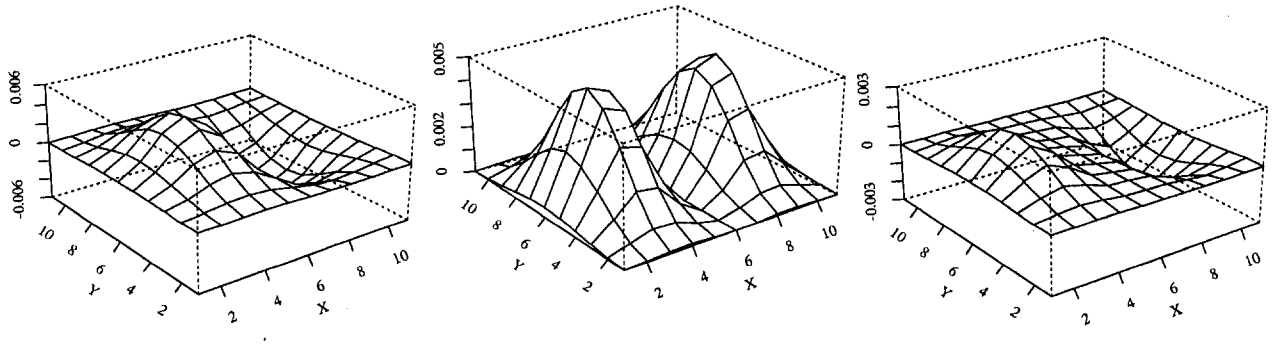
Downloaded 04 May 2010 to 171.66.16.27. Redistribution subject to ASME license or copyright; see http://www.asme.org/terms/Terms_Use.cfm



2nd Polynomial Chaos Coefficient 3rd Polynomial Chaos Coefficient 4th Polynomial Chaos Coefficient



5th Polynomial Chaos Coefficient 6th Polynomial Chaos Coefficient 7th Polynomial Chaos Coefficient



8th Polynomial Chaos Coefficient 9th Polynomial Chaos Coefficient 10th Polynomial Chaos Coefficient

Fig. 2 Coefficients in the expansions for the gaussian and lognormal processes. Third order of the polynomial chaos expansion; two terms in the Karhunen-Loeve expansion; correlation length = 0.1; coefficient of variation of lognormal process = 0.4.

$$\langle l(\mathbf{x})\Psi_i\rangle = \langle \exp[\mu_g + \sum_{i=1}^{N} \xi_i g_i]\Psi_i\rangle. \quad (26)$$

Replacing the averaging process by an integral with respect to the multidimensional gaussian variables ξ results in,

$$\langle l(\mathbf{x})\Psi_i\rangle = e^{\mu_g}\int_{-\infty}^{\infty} \exp[-\tfrac{1}{2}\sum_{j=1}^{N}\xi_j\xi_j]\exp[\sum_{j=1}^{N}\xi_j g_j]\Psi_i\, d\xi, \quad (27)$$

which can be rewritten as,

$$\langle l(\mathbf{x})\Psi_i\rangle = e^{\mu_g}\int_{-\infty}^{\infty} \exp[-\tfrac{1}{2}\sum_{j=1}^{N}(\xi_j - g_j)^2 + g_j^2]\Psi_i\, d\xi, \quad (28)$$

or,

$$\langle l(\mathbf{x})\Psi_i\rangle = \exp[\mu_g + \tfrac{1}{2}\sum_{j=1}^{N} g_j^2] \times \int_{-\infty}^{\infty} \exp[-\tfrac{1}{2}\sum_{j=1}^{N}(\xi_j - g_j)^2]\Psi_i\, d\xi. \quad (29)$$

Downloaded 04 May 2010 to 171.66.16.27. Redistribution subject to ASME license or copyright; see http://www.asme.org/terms/Terms_Use.cfm

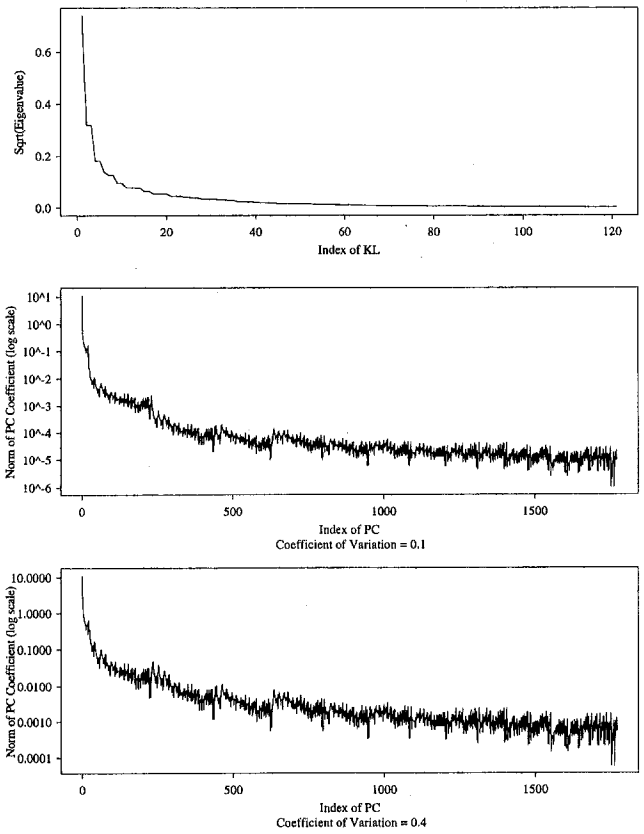


Fig. 3 Norm of the coefficients in the expansions for the gaussian and lognormal processes. Third order of the polynomial chaos expansion; 20 terms in the Karhunen-Loeve expansion; correlation length = 0.1.

Affecting a change of variable from ξ to η according to,

$$\xi_j - g_j = \eta_j, \tag{30}$$

the following expression is obtained,

$$\langle l(\mathbf{x})\Psi_i\rangle = \exp[\mu_g + \tfrac{1}{2}\sum_{j=1}^{N} g_j^2] \times \int_{-\infty}^{\infty} \exp[-\tfrac{1}{2}\sum_{j=1}^{N}\eta_j^2]\Psi_i(\eta)d\eta, \tag{31}$$

which can be simplified to,

$$\langle l(\mathbf{x})\Psi_i\rangle = \exp[\mu_g + \tfrac{1}{2}\sum_{j=1}^{N} g_j^2]\,\langle\Psi_i(\eta)\rangle. \tag{32}$$

In this last equation, the term $\langle\Psi_i(\eta)\rangle$ represents the average of the polynomial chaos centered around g_i. This average can be evaluated analytically, resulting in the values shown in Table 1. As seen from this table, the successive values of $\langle\Psi_i(\eta)\rangle$ are obtained as the homogeneous polynomials in the terms g_i. Finally, the coefficients $l_i(\mathbf{x})$ can be written as,

$$l_i(\mathbf{x}) = \frac{\langle\Psi_i(\eta)\rangle}{\langle\Psi_i^2\rangle}\exp[\mu_g + \tfrac{1}{2}\sum_{j=1}^{N} g_j^2], \tag{33}$$

where the exponential factor is equal to the mean value l_0. The lognormal process can therefore be written as,

$$l(\mathbf{x}) = l_0\Bigg(1 + \sum_{i=1}^{N}\xi_i g_i + \sum_{i=1}^{N}\sum_{j=1}^{N}\frac{(\xi_i\xi_j - \delta_{ij})}{\langle(\xi_i\xi_j - \delta_{ij})^2\rangle}g_i g_j + \ldots\Bigg). \tag{34}$$

This equation bears some resemblance to Eq. (21) with the added features that only the first term has a non-zero mean and all terms are orthogonal to each others. Given this orthogonality, a simple form can be obtained for the covariance function of the lognormal process, namely,

$$\langle l(\mathbf{x})l(\mathbf{y})\rangle = \mu_l^2\sum_{i=0}^{P}\frac{\langle\Psi_i(\eta,\mathbf{x})\rangle\langle\Psi_i(\eta,\mathbf{y})\rangle}{\langle\Psi_i^2\rangle}, \tag{35}$$

where $\Psi_i(\eta, \mathbf{x})$ indicates that the terms g_i making up $\Psi_i(\eta)$ are being evaluated at $\mathbf{x}$. Equation (35) permits the synthesis of the covariance of the lognormal process given that of the underlying gaussian process. Given the results in Table 1, Eq. (35) can be rewritten as

$$\langle l(\mathbf{x})l(\mathbf{y})\rangle = \mu_l^2\Bigg(\sum_{i=1}^{N}\frac{g_i(\mathbf{x})g_i(\mathbf{y})}{\langle\xi_i^2\rangle} + \sum_{i=1}^{N}\sum_{j=1}^{N}\frac{g_i(\mathbf{x})g_j(\mathbf{x})g_i(\mathbf{y})g_j(\mathbf{y})}{\langle(\xi_i\xi_j - \delta_{ij})^2\rangle} + \sum_{i=1}^{N}\sum_{j=1}^{N}\sum_{k=1}^{N}\frac{g_i(\mathbf{x})g_j(\mathbf{x})g_k(\mathbf{x})g_i(\mathbf{y})g_j(\mathbf{y})g_k(\mathbf{y})}{\langle(\xi_i\xi_j\xi_k - \xi_i\delta_{jk} - \xi_j\delta_{ik} - \xi_k\delta_{ij})^2\rangle} + \ldots\Bigg). \tag{36}$$

The values of the averages appearing in the denominators of Eq. (36) can be easily evaluated and tabulated (Ghanem and Spanos, 1991).

Of particular interest, is the case of a random lognormal variable. Specifically, in this case, the expansion given by Eq. (16) reduces to a single term beyond the mean. Thus, following the above notation,

$$g_1 = \sigma_g, \quad g_i = 0, \quad i > 1, \tag{37}$$

and

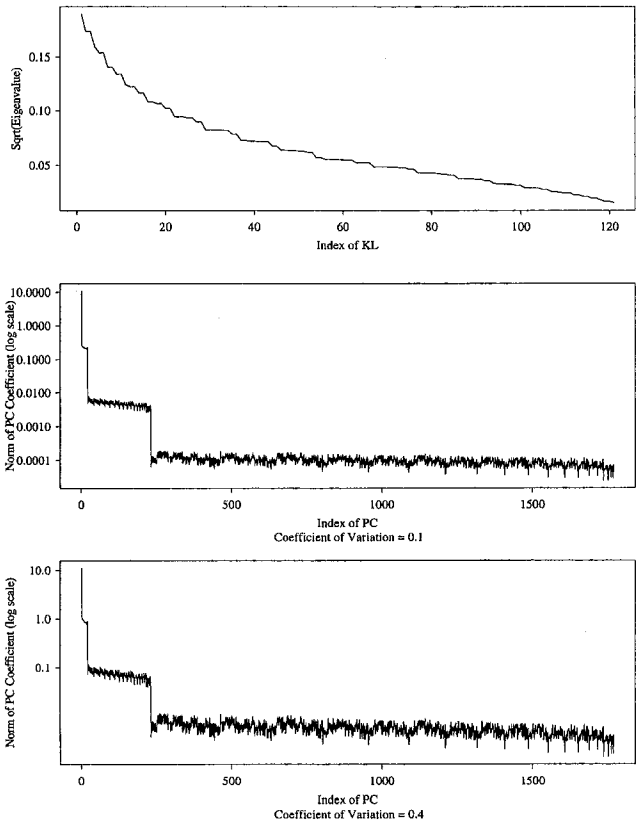


Fig. 4 Norm of the coefficients in the expansions for the gaussian and lognormal processes. Third order of the polynomial chaos expansion; 20 terms in the Karhunen-Loeve expansion; correlation length = 1.

Downloaded 04 May 2010 to 171.66.16.27. Redistribution subject to ASME license or copyright; see http://www.asme.org/terms/Terms_Use.cfm

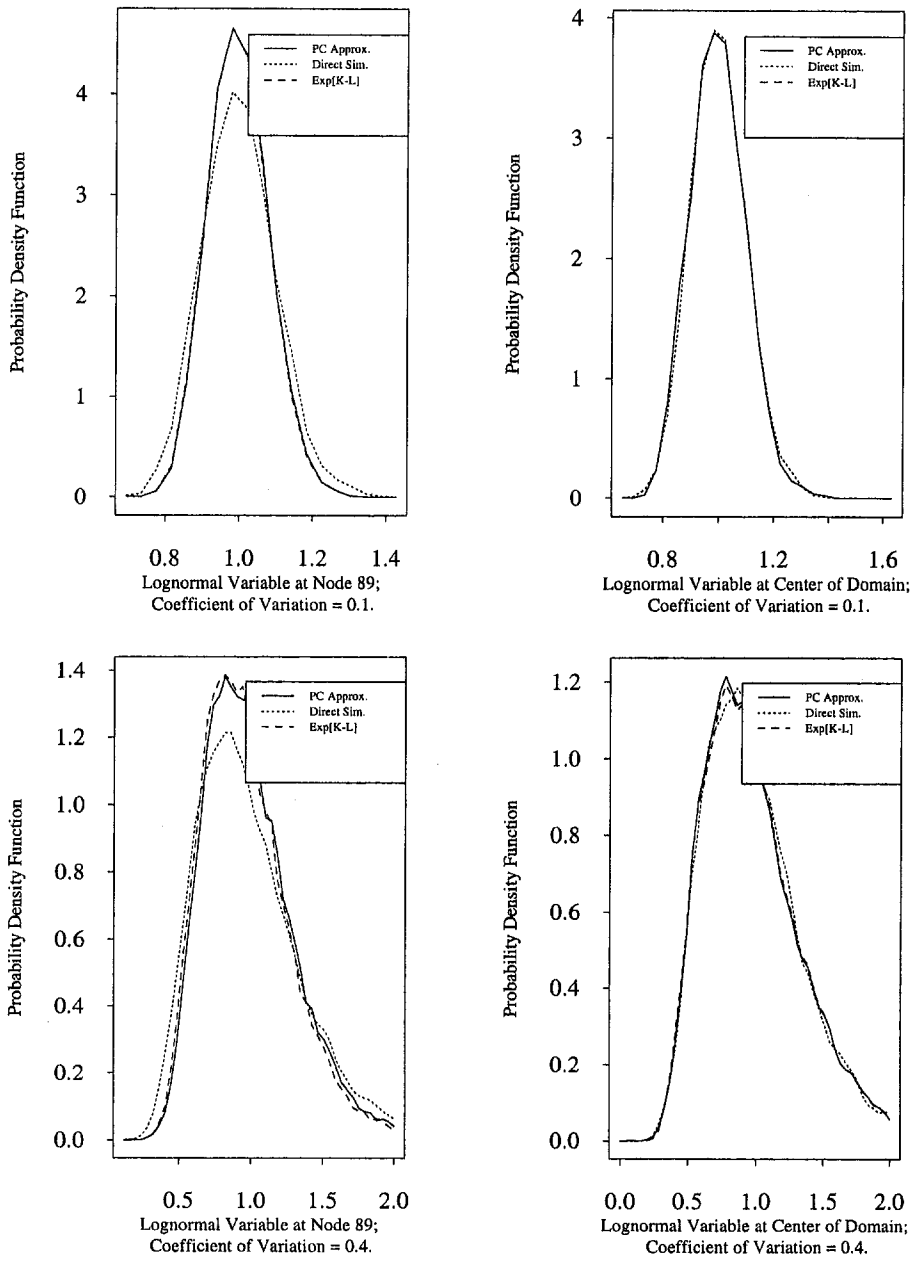


Fig. 5 Probability density function of the lognormal process. Two terms in the Karhunen-Loeve expansion; correlation length = 1.

$$g = \mu_g + \sigma_g \xi, \tag{38}$$

with

$$\langle \xi \rangle = 0, \quad \langle \xi^2 \rangle = 1. \tag{39}$$

According to the preceding development, the mean value is obtained as l_0,

$$\mu_l \equiv \langle l \rangle = l_0 = \exp[\mu_g + \tfrac{1}{2}\sigma_g^2], \tag{40}$$

and the successive terms in the expansion are obtained as,

$$l_i = \frac{\langle \Psi_i(\eta) \rangle}{\langle \Psi_i^2 \rangle} \exp\left[\mu_g + \frac{1}{2}\sigma_g^2\right]. \tag{41}$$

The lognormal random variable can thus be represented as the following polynomial in the gaussian variable ξ,

$$l = \mu_l \sum_{i=0}^{\infty} \frac{\sigma_g^i}{i!} \Psi_i$$

$$= \mu_l \left(1 + \sigma_g \xi + \frac{\sigma_g^2}{2}(\xi^2 - 1) + \frac{\sigma_g^3}{6}(\xi^3 - 3\xi) + \ldots\right) \tag{42}$$

Given the orthogonality of the polynomial chaoses, Ψ_i, the mean square of the random variable l is obtained as,

$$\langle l^2 \rangle = \sum_{i=0}^{P} l_i^2 \langle \Psi_i^2 \rangle, \tag{43}$$

or, upon substituting the expression for the generalized Fourier coefficient,

Downloaded 04 May 2010 to 171.66.16.27. Redistribution subject to ASME license or copyright; see http://www.asme.org/terms/Terms_Use.cfm

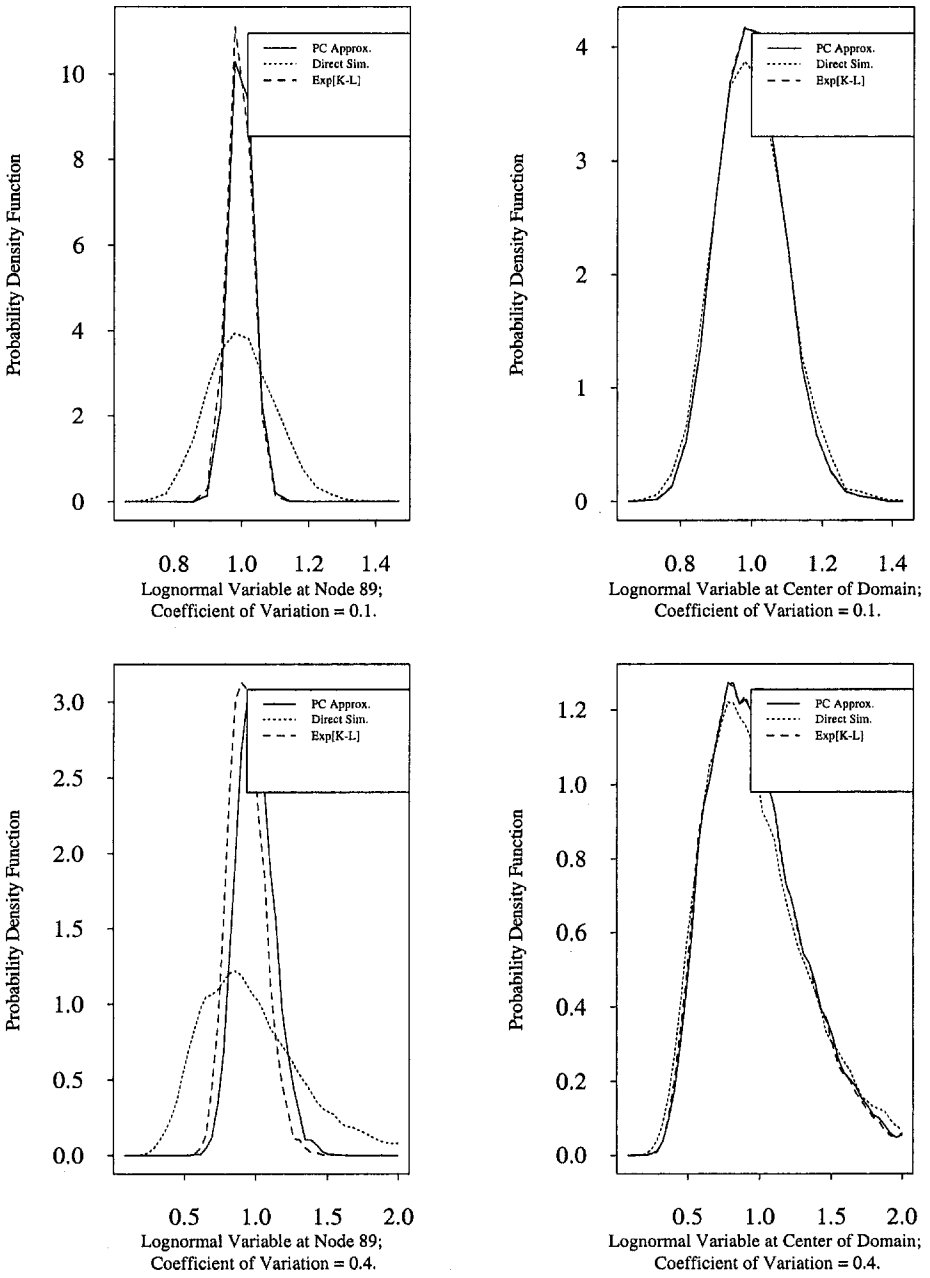


Fig. 6 Probability density function of the lognormal process. Two terms in the Karhunen-Loeve expansion; correlation length = 0.1.

$$\langle l^2 \rangle = \sum_{i=0}^{P} \frac{\langle \Psi_i(\eta) \rangle^2}{\langle \Psi_i^2 \rangle} \exp[2\mu_g + \sigma_g^2], \tag{44}$$

leading to,

$$\langle l^2 \rangle = \exp[2\mu_g + \sigma_g^2] \sum_{i=0}^{P} \frac{\langle \Psi_i(\eta) \rangle^2}{\langle \Psi_i^2 \rangle}. \tag{45}$$

Noting that this is the one-dimensional version of the preceding development, and substituting in for $\Psi_i(\eta)$ and $\langle \Psi_i^2 \rangle$, results in the following equation:

$$\langle l^2 \rangle = \exp[2\mu_g + \sigma_g^2] \sum_{i=0}^{P} \frac{\sigma_g^{2i}}{i!}, \tag{46}$$

which can be shown (Gradshteyn and Ryzhik, 1980) to converge to the following,

$$\langle l^2 \rangle = \exp[2\mu_g + 2\sigma_g^2]. \tag{47}$$

This last equation is identical to the well known expression given in Eq. (5).

Equations (34) and (42) provide, respectively, expressions for a lognormal process and a lognormal variable as a polynomial in a set of uncorrelated gaussian variables. The coefficients in these expansions are obtained via a weighted residual procedure that minimizes the norm of the error incurred by the approximation. It should be noted here that other procedures that utilized the Hermite polynomials for representing non-gaussian variables have been presented in the literature (Winterstein, 1988). Those procedures, however, evaluate the coefficients via a moment matching procedure.

4 Parametric Study

A number of factors affect the performance of the polynomial chaos expansion in representing lognormal processes. These

Downloaded 04 May 2010 to 171.66.16.27. Redistribution subject to ASME license or copyright; see http://www.asme.org/terms/Terms_Use.cfm

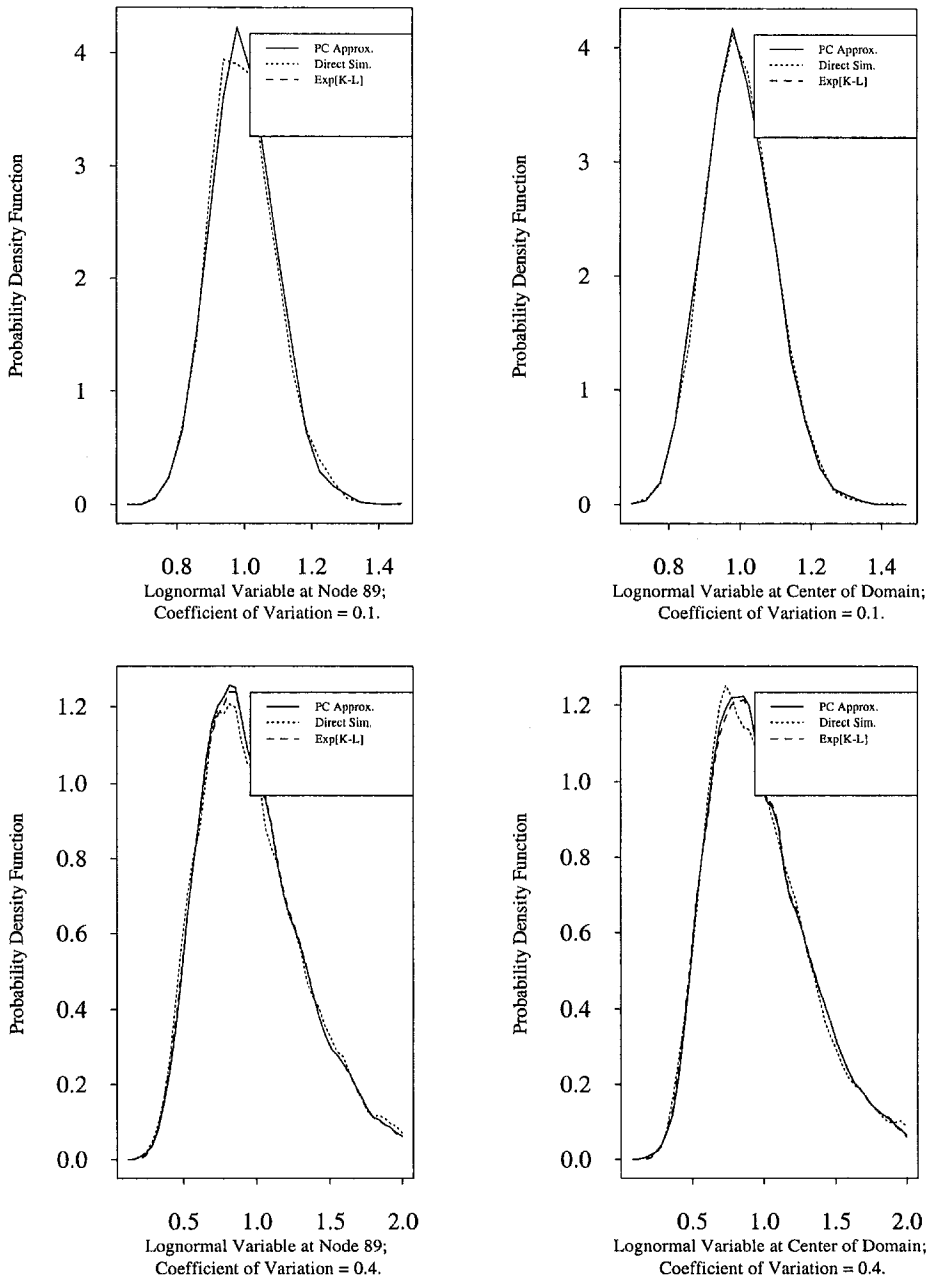


Fig. 7 Probability density function of the lognormal process. 20 terms in the Karhunen-Loeve expansion; correlation length = 1.

include the coefficient of variation of the process, the form of the covariance function of the process, the number of terms used in modeling the gaussian process in Eq. (16), and the number of terms carried through the expansion of the lognormal process in Eq. (22). A parametric study is conducted to analyze the effect of each of these features. It is expected that for small coefficients of variation, lower order terms will be needed in the polynomial chaos expansion to achieve a specified accuracy, since in that case, the lognormal process tends to a gaussian process. Moreover, for smaller correlation length, the contribution of successive terms in expansion (16) for the gaussian process decays slower than for large correlation length. In the limit of a white noise process (very small correlation), all the terms have equal contribution, while at the other limit of a random variable, only one term has a non-zero contribution. Thus, it is expected that for smaller correlation lengths, more terms will be needed in the expansion of the lognormal process.

The parametric study is conducted for a two-dimensional process defined over a square domain. A uniform mesh of 121 squares is used to define the computational domain. The integral eigenvalue problem is solved numerically (Ghanem and Spanos, 1991) over this domain.

Figures (1) and (2) show the shape of the functions $l_i(\mathbf{x})$ making up the basic scales of fluctuation of the lognormal process. Two terms are used in the Karhunen-Loeve expansion of the underlying gaussian process in this case. Thus, the first mode represents the mean process, which is constant in this case, while the second and third modes of fluctuation are proportional to those making up the gaussian process. The modes beyond the first three present the contribution from the interaction between the first two scales. The shapes have been normalized to a unit L_2 norm. Figure (1) refers to the case with a correlation length equal to 1, while Fig. (2) refers to the case with correlation length equal to 0.1. In this as well as all subse-

Downloaded 04 May 2010 to 171.66.16.27. Redistribution subject to ASME license or copyright; see http://www.asme.org/terms/Terms_Use.cfm

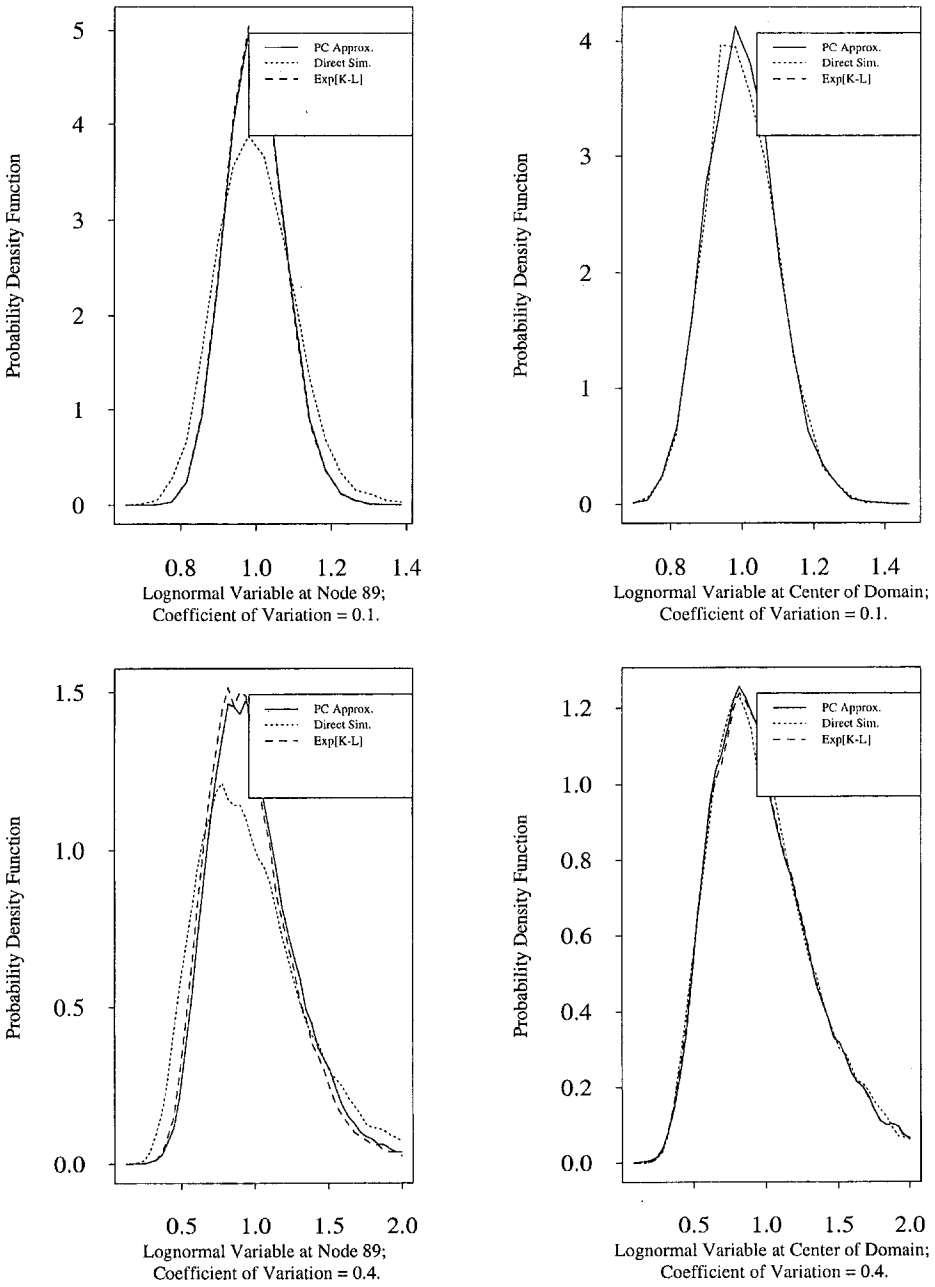


Fig. 8 Probability density function of the lognormal process. 20 terms in the Karhunen-Loeve expansion; correlation length = 0.1.

quent figures, the correlation function used is the exponentially decaying function.

Figures (3) and (4) show the decay in the norm of the coefficients in the polynomial expansion. Figure (3) shows results associated with a correlation length equal to 1 while Fig. (4) shows the results for a correlation length equal to 0.1. Each of the figures shows results associated with coefficients of variation equal to 0.1 and 0.4. Moreover, 20 terms are used in the Karhunen-Loeve expansion while all third order terms are included in the polynomial chaos expansion, totaling 1771 terms. Clearly, the rate of decay of the norm of the coefficients depends both on the coefficient of variation as well as on the correlation length of the underlying gaussian process. It should be noted that the vertical axis is shown in log-scale, thus emphasizing the rapid decay of the contributions and the fact that few terms can be used in representing the lognormal process.

Figures (5)–(8) compare the probability density function of the polynomial chaos expansion of the lognormal process with two other density functions. One of these is obtained by applying the exponential operator to the full Karhunen-Loeve expansion (including all the terms), while the other is obtained by applying the exponential operator to the Karhunen-Loeve series truncated at the level used by the polynomial chaos expansion. The first one of these is labeled "direct simulation" while the second one is labeled "exponential of KL expansion". These density functions refer to two specific points located at the center of the two-dimensional domain and another node (node 89). They are obtained by simulating uncorrelated normalized gaussian random variables and using them in the appropriate expansions to obtain corresponding realizations of the summed series. Nonparametric density estimation techniques are then used (Chambers and Hastie, 1992) to obtain a smooth approximation of the probability density function. Figures (5)

Downloaded 04 May 2010 to 171.66.16.27. Redistribution subject to ASME license or copyright; see http://www.asme.org/terms/Terms_Use.cfm

and (6) refer specifically to the case where two terms are retained in the Karhunen-Loeve expansion of the gaussian process, with a correlation length of 1 and 0.1, respectively. These probability density estimates are based on a statistical population of 10,000 samples. Note the variability of the simulated density function over the spatial domain as can be observed by the difference between the density function at the center and at node 89. Figures (7) and (8) refer to the respective cases where 20 terms are retained in the Karhunen-Loeve expansion of the gaussian process. It is clear from these results that the skewness of the probability density function is enhanced for the larger coefficients of variation. It is also clear that the adequacy of the approximation using a few terms in the Karhunen-Loeve approximation of the gaussian process decreases with the correlation length of the process, as indicated above.

5 Conclusion

A polynomial chaos expansion is developed for lognormal stochastic processes. These are processes obtained by applying the exponential operator to gaussian processes. The analytical development of the expansion is facilitated by the simple relationships between the lognormal process and the underlying gaussian process. The resulting expansion presents the lognormal process as a series of orthogonal polynomials in uncorrelated gaussian variables. The deterministic factors multiplying these polynomials represent the uncorrelated contributions to the overall process and can be viewed as the basic building blocks making up the process. The availability of such an expansion greatly facilitates the integration of the material properties modeled as lognormal processes into the spectral stochastic finite element method.

References

Benjamin, J., and Cornell, C.A., 1970, *Probability Statistics, and Decision for Civil Engineers,* McGraw-Hill, New York.

Chambers, J.M., and Hastie, T.J., 1992, *Statistical Models in S,* Wadsworth and Brooks/Cole Advanced Books and Software, Belmont, CA.

Gelhar, L., 1993, *Stochastic Subsurface Hydrology,* Prentice-Hall, Englewood Cliffs, NJ.

Ghanem, R., 1998a, "Hybrid Stochastic Finite Elements: Coupling of Spectral Expansions With Monte Carlo Simulations," submitted for review to ASME JOURNAL OF APPLIED MECHANICS.

Ghanem, R., 1998b, "Probabilistic Characterization of Transport in Random Porous Media," *Computer Methods in Applied Mechanics and Engineering,* Vol. 158, No. 3–4.

Ghanem, R., and Spanos, P., 1991, *Stochastic Finite Elements: A Spectral Approach,* Springer-Verlag, New York.

Ghanem, R., and Spanos, P., 1991, "A Spectral Stochastic Finite Element Formulation for Reliability Analysis," *ASCE Journal of Engineering Mechanics,* Vol. 117, No. 10, pp. 2351–2372.

Ghanem, R., and Spanos, P., 1993, "A Stochastic Galerkin Expansion for Nonlinear Random Vibration Analysis," *Probabilistic Engineering Mechanics,* Vol. 8, pp. 255–264.

Ghanem, R., and Kruger, R., 1996, "Numerical Solution of Spectral Stochastic Finite Element Systems," *Computer Methods in Applied Mechanics and Engineering,* Vol. 129, pp. 289–303.

Ghanem, R., and Brzkala, V., 1996, "Stochastic Finite Element Analysis for Random Layered Media," *ASCE Journal of Engineering Mechanics,* Vol. 122, No. 4, pp. 361–369.

Ghanem, R., and Spanos, P.D., 1997, "Spectral Techniques for Stochastic Finite Elements," *Archives of Computational Methods in Engineering,* Vol. 4, No. 1, pp. 63–100.

Gradshteyn, I.S., and Ryzhik, I.M., 1980, *Tables of Integrals, Series, and Products,* Academic Press, San Diego, CA.

Johnson, N.L., and Kotz, S., 1972, *Distributions in Statistics: Continuous Multivariate Distributions,* John Wiley and Sons, Inc., New York.

Kakutani, S., 1961, "Spectral Analysis of Stationary Gaussian Processes," *Proceedings, Fourth Berkeley Symposium on Mathematical Statistics and Probability,* Vol. II, J. Neyman ed., University of California, Berkeley, pp. 239–247.

Kallianpur, G., 1970, "The Role of Reproducing Kernel Hilbert Spaces in the Study of Gaussian Processes," *Advances in Probability Theory and Related Topics,* Volume 2, Peter Ney, ed., Marcel Decker, Inc., New York, pp. 49–83.

Kallianpur, G., 1972, "Homogeneous Chaos Expansions," *Statistical Models in Turbulence,* M. Rosenblatt and C. Van Atta, eds., Springer-Verlag, Berlin Heidelberg, pp. 230–254.

Li, R., and Ghanem, R., 1998, "Adaptive Polynomial Chaos Simulation Applied to Statistics of Extremes in Nonlinear Random Vibration," *Probabilistic Engineering Mechanics,* Vol. 13, No. 2, pp. 125–136.

Shinozuka, M., and Deodatis, G., 1991, "Simulation of Stochastic Processes by Spectral Representation," *Applied Mechanics Reviews,* Vol. 44, No. 4, pp. 191–204.

Spanos, P., and Ghanem, R., 1991, "Boundary Element Method Analysis for Random Vibration Problems," *ASCE Journal of Engineering Mechanics,* Vol. 117, No. 2, pp. 409–423.

Spanos, P., and Zeldin, B., 1998, "Monte Carlo Treatment of Random Fields: A Broad Perspective," *Applied Mechanics Reviews,* Vol. 51, pp. 219–237.

"State-of-the-Art Review on Computational Stochastic Mechanics," 1997, Report prepared by the Subcommittee on Computational Stochastic Mechanics, IASSAR, *Probabilistic Engineering Mechanics,* Vol. 12, No. 4, pp. 197–321.

Wiener, N., 1938, "The Homogeneous Chaos," *Amer. J. Math,* Vol. 60, pp. 897–936.

Winterstein, S., 1988, "Nonlinear Vibration Models for Extremes and Fatigue," *ASME Journal of Engineering Mechanics,* Vol. 114, No. 10, pp. 1772–1790.

Yang, J.N., and Manning, S.D., 1996, "A Simple Second Order Approximation for Stochastic Crack Growth Analysis," *Engineering Fracture Mechanics,* Vol. 53, No. 5, pp. 677–686.

Downloaded 04 May 2010 to 171.66.16.27. Redistribution subject to ASME license or copyright; see http://www.asme.org/terms/Terms_Use.cfm

R. N. Ray
Research Scholar

A. Samad
Reader

T. K. Chaudhury
Professor

Department of Mathematics,
The University of Burdwan,
Burdwan 713104,
West Bengal, India

An Exact Periodic Solution of a Hydromagnetic Flow of an Oldroyd Fluid in a Channel

The unsteady flow of a conducting Oldroyd fluid between two parallel plates, one of which is at rest and the other oscillating in its own plane with a constant mean velocity, has been investigated. Using separation of variables an exact periodic solution for the problem is obtained. Effects of viscoelastic parameters on velocity gradient, skin friction amplitude, and phase angle of the flow are discussed with graphs.

Introduction

In view of the growing importance in the chemical industries, different models of viscoelastic fluids have engaged the attention of many investigators. The Oldroyd two-constant model is one of such liquids. Mukhopadhyay and Chaudhury (1982) discussed the flow of a viscoelastic liquid of the Oldroyd type, over an infinite porous plate due to fluctuation in the main flow. Kundu (1972) gave a thorough investigation of small disturbance stability of plane Poiseuille flow of the Oldroyd fluid. Recently, Vajravelu (1988) obtained an exact periodic solution of a conducting Newtonian fluid in a horizontal channel in the presence of a magnetic field. We extend Vajravelu's problem to the class of viscoelastic liquid described by Oldroyd's (1958) two-constant model. Our solution shows some interesting effects of stress-relaxation time and strain-retardation time parameters of the liquid, on the velocity gradient, skin friction amplitude, and phase angle of the flow.

Basic Equations

The Oldroyd model (1958) for viscoelastic fluid is described by the constitutive equations

$$T_{ij} = -p\delta_{ij} + \tau_{ij} \tag{1}$$

$$(1 + \lambda_1 d/dt)\tau_{ij} = 2\eta(1 + \lambda_2 d/dt)e_{ij} \tag{2}$$

$$e_{ij} = 1/2(v_{i,j} + v_{j,i}) \tag{3}$$

where T_{ij}, τ_{ij}, e_{ij}, p, η, λ_1, λ_2 are, respectively, the total stress tensor, deviatoric stress tensor, rate of strain tensor, pressure, co-efficient of viscosity, relaxation time, and retardation time and

$$\frac{d}{dt} = \frac{\partial}{\partial t} + v_i \frac{\partial}{\partial x_i}.$$

The equation of motion is

$$\rho\left(\frac{\partial v_i}{\partial t} + v_{i,j}v_j\right) = -p_{,i} + \tau_{ij,j}. \tag{4}$$

Formulation of the Problem

We consider the unsteady flow of a conducting Oldroyd fluid between two parallel plates, one of which is at rest and the other oscillating in its own plane with a constant mean velocity. We take the x-axis along the lower plate in the direction of the flow and y-axis perpendicular to the plates.

We apply a transverse magnetic field in the direction of the flow perpendicular to the plates. For most of the practical fluids the magnetic Reynolds number is very small (Shercliff, 1965) and hence for this case we neglect the induced magnetic field. The Lorentz force in the direction of the x-axis is $-\mu\sigma H_0^2(u - U)$ where μ is the magnetic permeability and the σ is the electrical conductivity and the wall oscillating with velocity $U(t)$.

The velocity and magnetic fields are given by

$$[u(y, t) - U(y, t), 0, 0], \quad [0, H_0, 0]. \tag{5}$$

Using (5) we have, from (2) and (4),

$$\left(1 + \lambda_1 \frac{\partial}{\partial t}\right)\tau_{xy} = \eta\left(1 + \lambda_2 \frac{\partial}{\partial t}\right)\frac{\partial u}{\partial y} \tag{6}$$

$$\frac{\partial}{\partial t}(u - U) = \frac{1}{\rho}\frac{\partial}{\partial y}(\tau_{xy}) - \frac{\mu^2\sigma H_0^2}{\rho}(u - U). \tag{7}$$

The boundary conditions for the velocity field are

$$u = 0 \quad \text{at} \quad y = 0$$
$$u = U(t) \quad \text{at} \quad y = d.$$

We now introduce the following nondimensional quantities

$$u' = \frac{ud}{\nu}, \quad U' = \frac{Ud}{\nu}, \quad \xi = \frac{y}{d}, \quad t' = \frac{\nu t}{d^2}, \quad \alpha_1 = \frac{\lambda_1\nu}{d^2},$$

$$\alpha_2 = \frac{\lambda_2\nu}{d^2}, \quad M = \mu H_0 d\sqrt{\frac{\sigma}{\eta}}, \quad \tau = \frac{\tau_{xy}d^2}{\eta}.$$

Then after omitting the dashes, Eqs. (6) and (7) become

$$\left(1 + \alpha_1 \frac{\partial}{\partial t}\right)\tau = \left(1 + \alpha_2 \frac{\partial}{\partial t}\right)\frac{\partial u}{\partial \xi} \tag{8}$$

$$\frac{\partial}{\partial t}(u - U) = \frac{\partial \tau}{\partial \xi} - M^2(u - U). \tag{9}$$

Following Vajravelu (1988) we consider the case in which the unsteady velocity is given by

$$U(t) = U_d\left\{1 + \frac{\epsilon}{2}(e^{iwt} + e^{-iwt})\right\} \tag{10}$$

where w is the nondimensional frequency and U_d and ϵ are constants.

We then look for a solution of the form

Contributed by the Applied Mechanics Division of THE AMERICAN SOCIETY OF MECHANICAL ENGINEERS for publication in the ASME JOURNAL OF APPLIED MECHANICS.
Discussion on the paper should be addressed to the Technical Editor, Professor Lewis T. Wheeler, Department of Mechanical Engineering, University of Houston, Houston, TX 77204-4792, and will be accepted until four months after final publication of the paper itself in the ASME JOURNAL OF APPLIED MECHANICS.
Manuscript received by the ASME Applied Mechanics Division, July 7, 1997; final revision, Apr. 30, 1999. Associate Technical Editor: D. A. Siginer.

 Copyright © 1999 by ASME

Downloaded 04 May 2010 to 171.66.16.27. Redistribution subject to ASME license or copyright; see http://www.asme.org/terms/Terms_Use.cfm

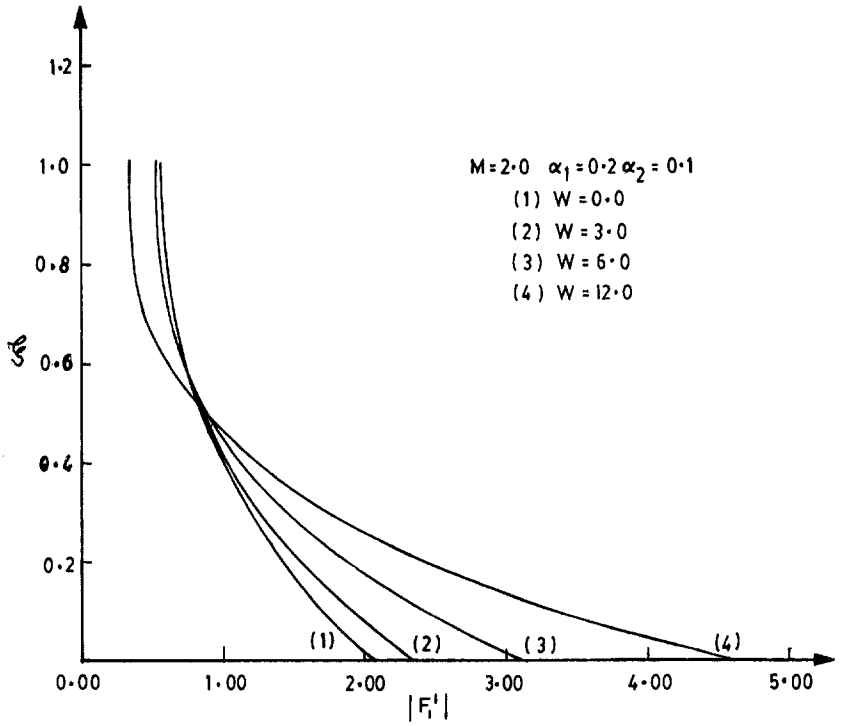


Fig. 1 Profiles of magnitude of fluctuating velocity gradient for different values of *w*

$$u = U_d\left\{F_0(\xi) + \frac{\epsilon}{2}\left(F_1(\xi)e^{iwt} + \bar{F}_1(\xi)e^{-iwt}\right)\right\}$$

$$\tau = U_d\left\{A_0(\xi) + \frac{\epsilon}{2}\left(A_1(\xi)e^{iwt} + \bar{A}_1(\xi)e^{-iwt}\right)\right\}. \quad (11)$$

Substituting (10) and (11) into (8) and (9) and equating steady and periodic terms separately to zero, we get four coupled first-order ordinary differential equations in F_0, F_1, A_0, and A_1. Finally, solving these equations with four boundary conditions for F_0 and F_1 at $\xi = 0$ and $\xi = 1$, we obtain

$$F_0(\xi) = 1 - \cosh M\xi + \coth M \sinh M\xi \quad (12)$$

$$F_1(\xi) = 1 - \cosh G\xi + \coth G \sinh G\xi \quad (13)$$

$$A_0(\xi) = M \coth M \cosh M\xi - M \sinh M\xi \quad (14)$$

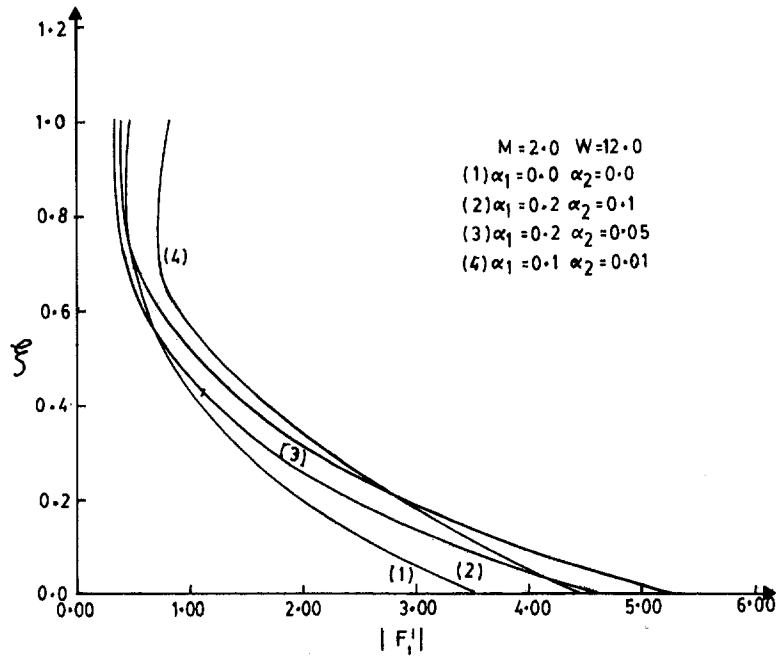


Fig. 2 Profiles of magnitude of fluctuating velocity gradient for different values of α_1 and α_2

Downloaded 04 May 2010 to 171.66.16.27. Redistribution subject to ASME license or copyright; see http://www.asme.org/terms/Terms_Use.cfm

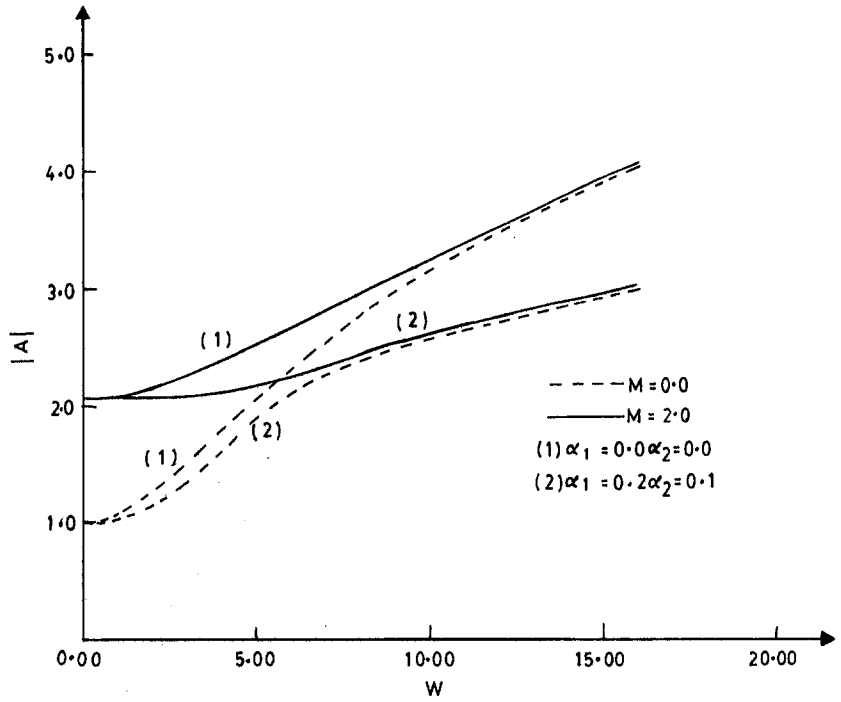


Fig. 3 Skin friction amplitude

$$A_1(\xi) = \frac{(1 + iw\alpha_2)}{(1 + iw\alpha_1)} G(\coth G \cosh G\xi - \sinh G\xi) \quad (15)$$

where

$$G = \sqrt{\frac{(iw + M^2)(1 + iw\alpha_1)}{(1 + iw\alpha_2)}}. \quad (16)$$

The shearing stress at the lower plate is given by

$$\tau_w = [\tau]_{\xi=0} = U_d\left(M \coth M + \frac{\epsilon}{2}(Ae^{iwt} + \bar{A}e^{-iwt})\right)$$

where

$$A = \frac{(1 + iw\alpha_2)}{(1 + iw\alpha_1)} G \coth G \quad (17)$$

is the stress amplitude.

The phase angle is

$$\phi_A = \tan^{-1}(A_i/A_r). \quad (18)$$

The expressions for $|F_1'|$, $|A|$ and ϕ_A are computed for several values of Oldroyd parameters α_1 and α_2 (as taken by Kundu

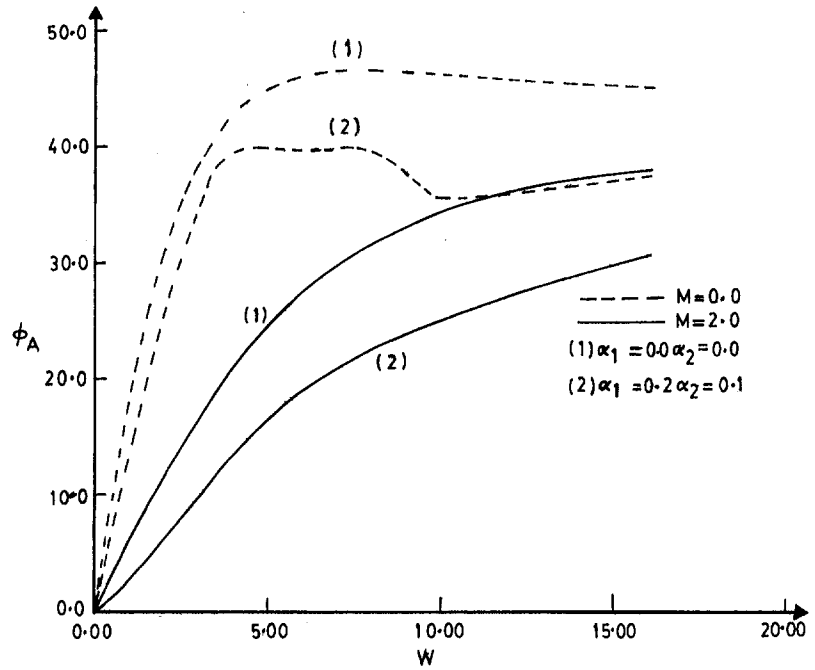


Fig. 4 Phase angle

Downloaded 04 May 2010 to 171.66.16.27. Redistribution subject to ASME license or copyright; see http://www.asme.org/terms/Terms_Use.cfm

(1972)) with different values of M and w. Numerical results are presented in the form of graphs in Figs. 1–4.

Discussion

For several values of the frequency parameter w, the distribution of the magnitude of the fluctuating velocity gradient $|F_1'|$ is shown in Fig. 1. We notice that for hydromagnetic flow ($M = 2.0$) of the Oldroyd fluid ($\alpha_1 = 0.2$, $\alpha_2 = 0.1$) $|F_1'|$ increases with frequency parameter w in the first half of the channel and then decreases in the other half, which is qualitatively the same as in the hydromagnetic flow of Newtonian fluid; however, $|F_1'|$ has higher values for the Oldroyd fluid compared to the Newtonian fluid in the first half of the channel while the opposite holds in the upper half (cf. Fig. 2, Vajravelu (1988)).

The profiles of $|F_1'|$ in the hydromagnetic case ($M = 2.0$) for $w = 12.0$ are shown in Fig. 2 for several values of α_1 and α_2 for a fixed $\alpha_1 = 0.2$. From the figure interestingly we find that $|F_1'|$ has higher values throughout for smaller values of α_2. Again, for sufficiently small α_2, the profile of $|F_1'|$ changes its nature in the sense that it attains a minimum value at a certain point in the upper half of the channel, whereafter it increases to the value at the upper plate.

The same phenomena is also observed in the hydrodynamic ($M = 0$) case. (Graphs not shown.)

Figure 3 shows the graphs of the magnitude of the amplitude $|A|$ of the fluctuating skin friction at the lower plate against w for both hydromagnetic and hydrodynamic cases for the Oldroyd as well as the Newtonian fluid ($\alpha_1 = 0$, $\alpha_2 = 0$). We find that for both hydrodynamic and hydromagnetic cases $|A|$ is smaller for an Oldroyd fluid for all w, the difference with the Newtonian fluid increasing with w. We also see that the effect of the Hartmann number M is to increase the amplitude $|A|$ for all values of w in both Newtonian and non-Newtonian cases. However, for large w, the effect of M is almost obliterated.

The profiles of the phase advance ϕ_A with w in both hydrodynamic and hydromagnetic cases are shown in Fig. 4 for the Oldroyd fluid ($\alpha_1 = 0.2$, $\alpha_2 = 0.1$) and Newtonian fluid. In the hydromagnetic case the phase angle for a Newtonian fluid slightly overshoots at some intermediate value of w and then asymptotically reaches the value 45 degrees (cf. Vajravelu). But for an Oldroyd fluid in the hydrodynamic case ϕ_A largely overshoots at some intermediate value of w, then decreases with w, and finally tends to certain mean value of about 35 degrees. In the hydromagnetic problem such overshooting does not occur in either case of a Newtonian fluid or an Oldroyd fluid ($\alpha_1 = 0.2$, $\alpha_2 = 0.1$). Furthermore, the effect of the Hartmann number is to decrease the value of ϕ_A in both hydrodynamic and hydromagnetic cases. From Fig. 4 we also notice that in both hydrodynamic and hydromagnetic problems the value of ϕ_A for any w remains smaller for an Oldroyd fluid than the corresponding value for a Newtonian fluid.

Acknowledgment

The first author is grateful to The University of Burdwan for financial assistance.

References

Kundu, P. K., 1972, "Small Disturbance Stability of Plane Poiseuille Flow of Oldroyd Fluid," *Phys. Fluids*, Vol. 15, pp. 1207–1212.

Mukhopadhyay, D. N., and Chaudhury, T. K., 1982, "On the Flow of a Viscoelastic Liquid past an infinite porous plate due to Fluctuation in the Main Flow," ASME JOURNAL OF APPLIED MECHANICS, Vol. 49, pp. 644–646.

Oldroyd, J. G., 1958, "Non-Newtonian effects in steady motion of some idealised Elastico-Viscous Liquids," *Proc. Roy. Soc. Lond.*, Vol. A245, pp. 278–297.

Shercliff, J. A., 1965, *A Text Book of Magnetohydrodynamics*, Pergamon Press, Oxford.

Vajravelu, K., 1988, "An Exact Periodic Solution of a Hydromagnetic Flow in a Horizontal Channel," ASME JOURNAL OF APPLIED MECHANICS, Vol. 55, pp. 981–983.

Downloaded 04 May 2010 to 171.66.16.27. Redistribution subject to ASME license or copyright; see http://www.asme.org/terms/Terms_Use.cfm

Integration Scheme for Elastic Deformation and Stresses

S. L. Lee
Professor

C. R. Ou
Graduate Student

Department of Power Mechanical Engineering,
National Tsing-Hua University,
Hsinchu 30043, Taiwan

The integration scheme is proposed in this paper to solve linear deformation and stresses for elastic bodies. The discretized equations are of the finite difference type such that all of the advantages in the use of a finite difference scheme are preserved. In addition, the boundary traction can be easily converted into Dirichlet boundary condition for the displacement equations without recourse to fictitious points. Three examples are illustrated in this study to examine the performances of the integration scheme. In the case of thermal loading, the integration scheme is seen to provide solution with six-place accuracy while the finite element and the boundary element solutions possess only two- to three-place accuracy at essentially the same number of grid points. A similar situation is believed to exist also in the case of pure mechanical loading, although no exact solution is available for comparison. For a square bimaterial under a thermal loading without boundary traction, the integration scheme is found to successfully predict the existence of the interface zone. Due to its simplicity and efficiency, the integration scheme is expected to have good performance for solid mechanical problems, especially when coupled with heat transfer and fluid flow inside and outside the solid.

Introduction

The finite element approach has been widely applied on solid mechanical problems. However, there are several disadvantages in the use of such a method. For instance, the shape function assumed in the finite element procedure does not necessarily satisfy the governing equations. As a result, the finite element method cannot directly solve the differential equations. It seeks only an approximation to the solution based on some concept such as the principle of minimum potential energy or the functional minimization. Furthermore, singularity problems might arise when the material is incompressible or nearly incompressible ($\nu \approx 0.5$) as remarked by Fenner (1983). Another disadvantage of the finite element method is that the resulting coefficient matrix commonly possesses a very large bandwidth, especially when clustering grids are needed.

Recently, the boundary element method (Fenner, 1983; Mukherjee and Morjaria, 1984; Ghosh and Mukherjee, 1984; Sladek et al., 1990) was successfully developed for solid mechanical problems. In a standard boundary element procedure, the governing equation is converted into an integration over the boundary of the physical domain. There is no need to solve the interior of the solution domain. However, the use of the boundary element method also poses some disadvantages (Fenner, 1983; Ghosh and Mukherjee, 1984). First, a sophisticated level of mathematics is needed. Secondly, the method is unsuitable if information is required at a large number of internal points. Third, domain integration is needed for nonhomogeneous media. Fourth, the resulting coefficient matrix is a full matrix that must be entirely stored and solved with a direct solver.

In the branch of the finite difference method, the differential equation is directly discretized into a system of algebraic equations without recourse to the minimum potential energy or a similar principle. The discretized equations are simple to code. In addition, the coefficient matrix possesses only a few diagonals that can be efficiently handled (Lee, 1989). Thus, it does show good performances in a wide variety of problems. Unfortunately, the conventional finite difference method has limited flexibility in treating the boundary conditions when applied to solid mechanical problems. It lacks a satisfying procedure for eliminating the fictitious points when the central difference scheme is applied to a boundary point with given traction. To resolve the problem, Dow et al. (1990a, b, 1992a, b) introduced a finite difference scheme based on a strain-gradient formulation. However, their procedure is quite complicated, especially for bimaterial problems due to the use of a multidimensional Taylor series expansion.

In the present study, the integration scheme is proposed to solve the displacement equations for linear elastic bodies. The discretized equations are of the finite difference type such that all of the advantages in the use of a finite difference scheme are preserved. Unlike the conventional finite difference scheme, however, the boundary traction can be easily converted into Dirichlet boundary condition for the displacement equations without the need of fictitious points. In addition, large jumps in the Young's modulus and the Poisson's ratio are allowed owing to its integration form. Three examples will be conducted to examine the performance of the integration scheme under mechanical and thermal loading for both single material and bimaterial problems.

Displacement Equation

Stress-strain and displacement-strain relations for two-dimensional plane stress linear elastic bodies are expressible as (Timoshenko and Goodier, 1970)

$$\epsilon_{xx} - \alpha\Delta T = (\sigma_{xx} - \nu\sigma_{yy})/E$$
$$\epsilon_{yy} - \alpha\Delta T = (\sigma_{yy} - \nu\sigma_{xx})/E \qquad (1a)$$

$$\epsilon_{xy} = (1 + \nu)\sigma_{xy}/E \quad \epsilon_{yx} = (1 + \nu)\sigma_{yx}/E \qquad (1b)$$

and

$$\epsilon_{xx} = \frac{\partial u}{\partial x} \quad \epsilon_{yy} = \frac{\partial v}{\partial y} \quad \epsilon_{xy} = \epsilon_{yx} = \frac{1}{2}\left(\frac{\partial v}{\partial x} + \frac{\partial u}{\partial y}\right) \qquad (2)$$

where (u, v) denotes the displacement and ΔT is the temperature change from a stress-free state. The notations α, E, and ν represent, respectively, the coefficient of thermal expansion, the Young's modulus, and the Poisson's ratio. Substitution of Eq. (2) into Eq. (1) yields

Contributed by the Applied Mechanics Division of THE AMERICAN SOCIETY OF MECHANICAL ENGINEERS for publication in the ASME JOURNAL OF APPLIED MECHANICS.
Discussion on the paper should be addressed to the Technical Editor, Professor Lewis T. Wheeler, Department of Mechanical Engineering, University of Houston, Houston, TX 77204-4792, and will be accepted until four months after final publication of the paper itself in the ASME JOURNAL OF APPLIED MECHANICS.
Manuscript received by the ASME Applied Mechanics Division, Jan. 22, 1998; final revision, Oct. 23, 1999. Associate Technical Editor: W. K. Liu.

 Copyright © 1999 by ASME

Downloaded 04 May 2010 to 171.66.16.27. Redistribution subject to ASME license or copyright; see http://www.asme.org/terms/Terms_Use.cfm

$$\frac{\sigma_{xx}}{E} = \frac{1}{1+\nu}\frac{\partial u}{\partial x} - \phi \quad \frac{\sigma_{yy}}{E} = \frac{1}{1+\nu}\frac{\partial v}{\partial y} - \phi \tag{3a}$$

$$\frac{\sigma_{xy}}{E} = \frac{1}{1+\nu}\frac{\partial u}{\partial y} + \psi \quad \frac{\sigma_{yx}}{E} = \frac{1}{1+\nu}\frac{\partial v}{\partial x} - \psi \tag{3b}$$

where

$$\phi = \frac{1}{1-\nu}\alpha\Delta T - \frac{\nu}{1-\nu^2} I \quad \psi = \frac{1}{2(1+\nu)}\omega \tag{4}$$

$$I = \frac{\partial u}{\partial x} + \frac{\partial v}{\partial y} \quad \omega = \frac{\partial v}{\partial x} - \frac{\partial u}{\partial y}. \tag{5}$$

Based on the equilibrium equations without body force (Timoshenko and Goodier, 1970) as well as the property of static equilibrium ($\sigma_{xy} = \sigma_{yx}$), the displacement equations are obtained:

$$\frac{\partial}{\partial x}\left(\frac{E}{1+\nu}\frac{\partial u}{\partial x}\right) + \frac{\partial}{\partial y}\left(\frac{E}{1+\nu}\frac{\partial u}{\partial y}\right) = \frac{\partial(E\phi)}{\partial x} - \frac{\partial(E\psi)}{\partial y} \tag{6}$$

$$\frac{\partial}{\partial x}\left(\frac{E}{1+\nu}\frac{\partial v}{\partial x}\right) + \frac{\partial}{\partial y}\left(\frac{E}{1+\nu}\frac{\partial v}{\partial y}\right) = \frac{\partial(E\psi)}{\partial x} + \frac{\partial(E\phi)}{\partial y}. \tag{7}$$

Integration Scheme

Let W, P, E be three successive grid points at (x_{i-1}, y_j), (x_i, y_j), (x_{i+1}, y_j) and the subscript "i, j" denote the value of a function at the point (x_i, y_j). Both the elastic modulus E and the Poisson ratio ν are piecewise continuous functions in the domain of $x_{i-1} \le x \le x_{i+1}$ on the line $y = y_j$. Next, let Eq. (6) be split up into a system of two ordinary differential equations

$$\frac{\partial}{\partial x}\left(\frac{E}{1+\nu}\frac{\partial u}{\partial x}\right) - \frac{\partial(E\phi)}{\partial x} = f \tag{8}$$

$$\frac{\partial}{\partial y}\left(\frac{E}{1+\nu}\frac{\partial u}{\partial y}\right) + \frac{\partial(E\psi)}{\partial y} = -f \tag{9}$$

where $f(x, y)$ is an unknown function of x and y. Integrating Eq. (8) with respect to x twice in the interval $x_i \le x \le x_{i+1}$ along the line $y = y_j$, one arrives at

$$u(x, y_j) = u_{i,j} + \int_{x_i}^{x} (1+\nu)\phi dx + \int_{x_i}^{x} \frac{1+\nu}{E}\sigma_{xx} dx \tag{10}$$

$$\sigma_{xx} = c_i + (g - \bar{g}_i) \tag{11}$$

$$c_i = \frac{u_{i+1,j} - u_{i,j} - \displaystyle\int_{x_i}^{x_{i+1}} (1+\nu)\phi dx}{\displaystyle\int_{x_i}^{x_{i+1}} \frac{1+\nu}{E} dx} \tag{12}$$

where the integration constants have been determined by the conditions $u(x_i, y_j) = u_{i,j}$ and $u(x_{i+1}, y_j) = u_{i+1,j}$. The function $g(x)$ is an antidifferential of the function $f(x, y_j)$ with respect to x. The notation $\bar{g}_i$ denotes the weighted average of the function $g(x)$ over the interval $x_i \le x \le x_{i+1}$ with respect to $(1+\nu)/E$, i.e.,

$$\bar{g}_i = \frac{\displaystyle\int_{x_i}^{x_{i+1}} \left(\frac{1+\nu}{E}\right) g dx}{\displaystyle\int_{x_i}^{x_{i+1}} \frac{1+\nu}{E} dx}. \tag{13}$$

Similarly, the displacement u and the stress σ_{xx} in the interval $x_{i-1} \le x \le x_i$ on the line $y = y_j$ have the form

$$u(x, y_j) = u_{i-1,j} + \int_{x_{i-1}}^{x} (1+\nu)\phi dx + \int_{x_{i-1}}^{x} \frac{1+\nu}{E}\sigma_{xx} dx \tag{14}$$

$$\sigma_{xx} = c_{i-1} + (g - \bar{g}_{i-1}). \tag{15}$$

Next, let both Young's modulus E and Poisson's ratio ν be continuous at $x = x_i$ such that the condition of continuous stress σ_{xx} can be imposed there for Eqs. (11) and (15), i.e.,

$$c_i - c_{i-1} = \bar{g}_i - \bar{g}_{i-1}. \tag{16}$$

This yields a relationship between the displacements at the three successive grid points (x_{i-1}, y_j), (x_i, y_j), (x_{i+1}, y_j) as

$$(a_W)_{i,j}u_{i-1,j} - ((a_W)_{i,j} + (a_E)_{i,j})u_{i,j} + (a_E)_{i,j}u_{i+1,j} = (\Re_x)_{i,j} \tag{17}$$

$$(a_W)_{i,j} = \frac{(E_{\text{eff},x})_{i-1}}{\overline{\Delta x}_i} \quad (a_E)_{i,j} = \frac{(E_{\text{eff},x})_i}{\overline{\Delta x}_i} \tag{18}$$

$$(E_{\text{eff},x})_i = \left(\int_{x_i}^{x_{i+1}} \frac{1+\nu}{E} dx\right)^{-1} \tag{19}$$

$$(\Re_x)_{i,j} = (a_E)_{i,j}\int_{x_i}^{x_{i+1}} (1+\nu)\phi dx - (a_W)_{i,j}\int_{x_{i-1}}^{x_i} (1+\nu)\phi dx + f_{i,j} \tag{20}$$

where $\Delta x_i = x_{i+1} - x_i$, $\overline{\Delta x}_i = (x_{i+1} - x_{i-1})/2$ and the approximation

$$\frac{\bar{g}_i - \bar{g}_{i-1}}{\overline{\Delta x}_i} \approx \left(\frac{dg}{dx}\right)_i = f_{i,j} \tag{21}$$

has been employed.

Finally, discretize Eq. (9) with the same procedure and add it to Eq. (17). The integration scheme for the partial differential Eq. (6) then becomes

$$(a_W)_{i,j}u_{i-1,j} + (a_E)_{i,j}u_{i+1,j} + (a_S)_{i,j}u_{i,j-1} + (a_N)_{i,j}u_{i,j+1} - (a_P)_{i,j}u_{i,j} = (a_R)_{i,j} \tag{22}$$

$$(a_W)_{i,j} = \frac{(E_{\text{eff},x})_{i-1}}{\overline{\Delta x}_i} \quad (a_E)_{i,j} = \frac{(E_{\text{eff},x})_i}{\overline{\Delta x}_i} \tag{23}$$

$$(a_S)_{i,j} = \frac{(E_{\text{eff},y})_{j-1}}{\overline{\Delta y}_j} \quad (a_N)_{i,j} = \frac{(E_{\text{eff},y})_j}{\overline{\Delta y}_j} \tag{24}$$

$$(a_P)_{i,j} = (a_W)_{i,j} + (a_E)_{i,j} + (a_S)_{i,j} + (a_N)_{i,j} \tag{25}$$

$$(a_R)_{i,j} = (a_E)_{i,j}\int_{x_i}^{x_{i+1}} (1+\nu)\phi dx - (a_W)_{i,j}\int_{x_{i-1}}^{x_i} (1+\nu)\phi dx + (a_S)_{i,j}\int_{y_{j-1}}^{y_j} (1+\nu)\psi dx - (a_N)_{i,j}\int_{y_j}^{y_{j+1}} (1+\nu)\psi dx \tag{26}$$

where the unknown function $f_{i,j}$ has been canceled. Equation (7) can be discretized with a similar procedure. Note that the algebraic Eq. (22) is of the finite difference type which can be efficiently solved by using the strongly implicit solver (Lee, 1989). For

Downloaded 04 May 2010 to 171.66.16.27. Redistribution subject to ASME license or copyright; see http://www.asme.org/terms/Terms_Use.cfm

Table 1 Dimensionless displacement ($10^3 v/L$) for Example 1 with (T_0, T_1, T_2) = (0°C, 30°C, 50°C)

		Present study			Ghosh and Mukherjee (1984)		
y/L	Exact	5 × 5	9 × 9	17 × 17	BEM(1)	BEM(2)	FEM
0.000	0.000000	0.000000	0.000000	0.000000	0.000000	0.000000	0.000000
0.125	0.090681		0.090680	0.090681		0.087158	
0.250	0.188616	0.188616	0.188616	0.188616		0.188847	0.188597
0.375	0.293806		0.293816	0.293806		0.294089	
0.500	0.406250	0.406250	0.406250	0.406250	0.406988	0.406792	0.406262
0.625	0.525949		0.525949	0.525949		0.526798	
0.750	0.652902	0.652902	0.652902	0.652902		0.653823	0.652891
0.875	0.787109		0.787110	0.787109		0.793902	
1.000	0.928571	0.928572	0.928572	0.928571	0.932955	0.931055	0.928474

BEM(1): 12 boundary nodes and 8 internal cells
BEM(2): 14 boundary nodes and 16 internal cells
FEM: 25 nodes and 8 elements

convenience, this particular scheme (22)–(26) will be referred to as the integration scheme in the present study.

In many practical applications, the boundary condition could be in the form of given traction rather than a Dirichlet boundary condition of the displacement. Under such a situation, the traction (t_x, t_y) can be converted into the form of boundary stress from the boundary conditions

$$l\sigma_{xx} + m\sigma_{xy} = t_x \tag{27a}$$

$$l\sigma_{yx} + m\sigma_{yy} = t_y \tag{27b}$$

where (l, m) are the direction cosines of the boundary surface under study. Unfortunately, there are three unknowns (i.e., $\sigma_{xy} = \sigma_{yx}$) in the two Eqs. (27). This implies that the boundary stresses cannot be completely determined by the given traction. One more condition is needed. To resolve the problem, a guessed boundary stress, σ_{xx} or σ_{yy}, from the result of the previous iteration is employed. To minimize the error, guess σ_{xx} if $l \leq m$ and vise versa (guess σ_{yy} if $l > m$). Once all of the required boundary stresses are known, a Dirichlet boundary condition for the displacement can be extrapolated from the nearest interior grid point by using an appropriate equation among Eq. (10) and

$$v(x, y_j) = v_{i,j} + \int_{x_i}^{x} (1 + \nu)\psi dx + \int_{x_i}^{x} \frac{1 + \nu}{E}\sigma_{yx} dx \tag{28a}$$

$$u(x_i, y) = u_{i,j} - \int_{y_j}^{y} (1 + \nu)\psi dy + \int_{y_j}^{y} \frac{1 + \nu}{E}\sigma_{xy} dy \tag{28b}$$

$$v(x_i, y) = v_{i,j} + \int_{y_j}^{y} (1 + \nu)\phi dy + \int_{y_j}^{y} \frac{1 + \nu}{E}\sigma_{yy} dy \tag{28c}$$

based on the previous result of displacements and stresses.

Performances of the Integration Scheme

It is interesting to note that $(E_{\text{eff},x})_i$ is an effective elastic modulus in the interval $x_i \leq x \leq x_{i+1}$ on the line $y = y_j$. Owing to its integration form, large jumps in the Young's modulus E and the Poisson's ratio ν are allowed. In addition, the integration scheme poses no truncation error, although other modes of errors might arise from the approximation (21). Thus it is expected to have a good performance in solving thermal and mechanical deformation, especially for multimaterial problems. This is one of important features of the integration scheme. Three examples will be illustrated in this section to examine the performances of the integration scheme.

Example 1. Thermoelastic Deformation of a Square Cross-Section in Plane Strain. Consider a square cross section ($0 \leq x \leq L$ and $0 \leq y \leq L$) of 304 stainless steel at a uniform temperature T_0 and a stress-free state. Let the square cross section be heated to a one-dimensional linear temperature

$$T = (T_2 - T_1)(y/L) + T_1 \tag{29}$$

while the boundary conditions of the displacement and traction are maintained at

$$u(0, y) = 0, \quad t_y(0, y) = 0, \quad u(L, y) = 0, \quad t_y(L, y) = 0$$

$$t_x(x, 0) = 0, \quad v(x, 0) = 0, \quad t_x(x, L) = 0, \quad t_y(x, L) = 0. \tag{30}$$

The material properties are assumed to be

$$E = E_{\text{ref}}(1.000 - 1.905 \times 10^{-4}T)$$

$$E_{\text{ref}} = 2.079 \times 10^{11}\ \text{N/m}^2$$

$$\nu = 0.3, \quad \alpha = 1.250 \times 10^{-5}\ (°\text{C})^{-1}. \tag{31}$$

It is noted that the Young's modulus E and the Poisson ratio ν in the plane stress formulation (1) should be replaced, respectively, by $E/(1 - \nu^2)$ and $\nu/(1 - \nu)$ for this plane-strain problem under study (Hearn, 1985). The integration scheme derived in the previous section is then employed to solve the problem on a uniform grid system of $n \times n$ points. Numerical results of dimensionless displacement v/L and dimensionless stress $\sigma_{xx}/E_{\text{ref}}$ for three grid meshes (5 × 5, 9 × 9, 17 × 17 points) are presented, respectively, in Table 1 and Table 2 under the temperatures

$$T_0 = 0°\text{C}, \quad T_1 = 30°\text{C}, \quad T_2 = 50°\text{C}. \tag{32}$$

Note also that both displacement and thermal stress in this example depend only on y.

This same problem has been solved by Ghosh and Mukherjee (1984) with a boundary element method as well as a finite element method. In the use of the boundary element method, Ghosh and Mukherjee (1984) employed two grid systems. One of them included 12 boundary nodes and 8 internal cells, while the other had 14 boundary nodes and 16 internal cells. In the finite element method, 25 nodes and 8 elements were used. These numerical results along with the exact solution are shown in Table 1 and Table 2 for comparison. For convenience, the two boundary element solutions from Ghosh and Mukherjee (1984) are referred to as BEM(1) and BEM(2), while the finite element solution is simply denoted by FEM.

From Table 1 and Table 2, one sees an excellent performance of the present integration scheme. Generally speaking, there could be a six significant-digit accuracy in the present results for both displacement and stress, while the boundary element and the finite element results from Ghosh and Mukherjee (1984) possess only

Downloaded 04 May 2010 to 171.66.16.27. Redistribution subject to ASME license or copyright; see http://www.asme.org/terms/Terms_Use.cfm

Table 2 Dimensionless stress ($-10^3\sigma_{xx}/E_{ref}$) for Example 1 with (T_0, T_1, T_2) = (0°C, 30°C, 50°C)

		Present study			Ghosh and Mukherjee (1984)		
y/L	Exact	5 × 5	9 × 9	17 × 17	BEM(1)	BEM(2)	FEM
0.0000	0.532652	0.532653	0.532653	0.532653		0.556782	
0.1250	0.576763		0.576764	0.576764		0.574710	
0.1666	0.591434				0.564877		0.589444
0.2083	0.606135					0.592604	
0.2500	0.620832	0.620833	0.620833	0.620833		0.616200	
0.2917	0.635524					0.627412	
0.3333	0.650176				0.668870		0.647928
0.3750	0.664858		0.664859	0.664859		0.661365	
0.4583	0.694173					0.695254	
0.5000	0.708842	0.708843	0.708843	0.708843	0.703575	0.704464	
0.5417	0.723505					0.712814	
0.6250	0.752783		0.752784	0.752785		0.747609	
0.6666	0.767397				0.737703		0.762438
0.7083	0.782041					0.782347	
0.7500	0.796681	0.796683	0.796683	0.796683		0.792833	
0.7916	0.811281					0.773652	
0.8333	0.825911				0.837782		0.819854
0.8750	0.840537		0.840540	0.840539		0.830881	
0.9583	0.869739					0.888015	
1.0000	0.884351	0.884354	0.884354	0.884353	0.867818	0.870229	

BEM(1): 12 boundary nodes and 8 internal cells
BEM(2): 14 boundary nodes and 16 internal cells
FEM: 25 nodes and 8 elements

two or three significant-digit accuracy. Similar situation can be found in the case with

$$T_0 = 25°C, \quad T_1 = 30°C, \quad T_2 = 125°C \tag{33}$$

as depicted in Table 3 and Table 4. The boundary element solution BEM(3) in Table 3 and Table 4 from Sladek et al. (1990) was based on a boundary element mesh with 24 boundary nodes and 8 internal cells.

Generally speaking, for a two-dimensional Cartesian grid system with $n \times n$ points, the coefficient matrix based on the present integration scheme has only 5 n^2 nonzero components (roughly). In the use of the finite element method and the boundary element method, however, there are, respectively, $(n + 2)n^2$ and $16(n - 1)^2$ components to be treated. Furthermore, each component of the matrix provided by the integration scheme (19) includes only a single integration. The formulation is quite simple as compared to that from the finite element and boundary element methods. Hence, it is believed that the integration scheme needs less CPU time than does the finite element method and the boundary element method.

Example 2. Stresses and Deformation of a Cantilever Beam Under a Uniform Load. Let a uniform load q be imposed on a two-dimensional cantilever beam of the dimension $0 \le x \le L$ and $0 \le y \le L/2$, while the surface conditions of the beam be maintained at

$$u(0, y) = 0, \quad v(0, y) = 0, \quad t_x(L, y) = 0, \quad t_y(L, y) = 0$$

$$t_x(x, 0) = 0, \quad t_y(x, 0) = 0,$$

$$t_x(x, L/2) = 0, \quad t_y(x, L/2) = -q. \tag{34}$$

The beam is assumed to have a constant elastic modulus E and a constant Poisson ratio of $\nu = 0.3$. For a uniform load of $q/E = 1/30000$, the problem is solved by using the integration scheme on a uniform grid system of 17 × 9 points ($\Delta x/L = \Delta y/L = 1/16$). Results of displacements $u(x)$ and $v(x)$ along the horizon-

Table 3 Dimensionless displacement ($10^3 v/L$) for Example 1 with (T_0, T_1, T_2) = (25°C, 30°C, 125°C)

		Present study			Sladek (1990)
y/L	Exact	5 × 5	9 × 9	17 × 17	BEM(3)
0.00	0.000000	0.000000	0.000000	0.000000	0.0
0.25	0.097935	0.097964	0.097943	0.097936	0.09747
0.50	0.333705	0.333719	0.333720	0.333707	0.3332
0.75	0.707310	0.707403	0.707283	0.707312	0.7066
1.00	1.218750	1.218270	1.218510	1.218720	1.218

BEM(3): 24 boundary nodes and 8 internal cells

Table 4 Dimensionless displacement ($-10^3\sigma_{xx}/E_{ref}$) for Example 1 with (T_0, T_1, T_2) = (25°C, 30°C, 125°C)

		Present study			Sladek (1990)
y/L	Exact	5 × 5	9 × 9	17 × 17	BEM(3)
0.00	0.089200	0.089393	0.089309	0.089252	0.090537
0.25	0.510566	0.510553	0.510573	0.510583	0.513830
0.50	0.928075	0.928005	0.928081	0.928126	0.933402
0.75	1.341725	1.342300	1.341710	1.341830	1.361675
1.00	1.751518	1.747480	1.749600	1.750690	1.778346

BEM(3): 24 boundary nodes and 8 internal cells

Downloaded 04 May 2010 to 171.66.16.27. Redistribution subject to ASME license or copyright; see http://www.asme.org/terms/Terms_Use.cfm

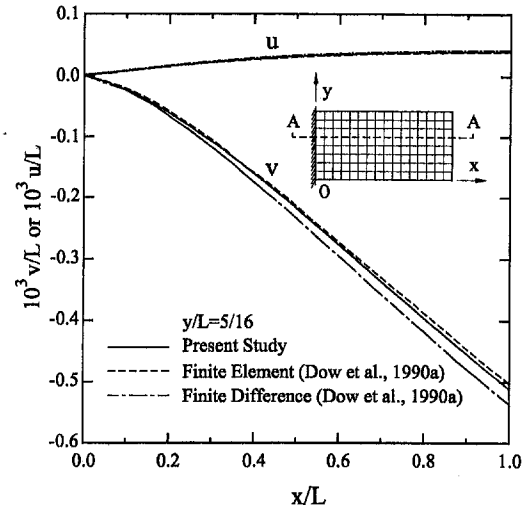


Fig. 1 Displacements (u, v) along the horizontal line y/L = 5/16 for Example 2

tal line $y/L = 5/16$ and stresses (σ_{xx}, σ_{yy}, σ_{xy}) along the vertical line $x/L = 5/16$ as a function of y are plotted in Figs. 1 and 2, respectively. Existing finite difference and finite element solutions from Dow et al. (1990a, b) for this same problem are shown also in Figs. 1 and 2 for comparison. From Fig. 1, one sees good agreements on the displacements among the three numerical results. However, the finite difference solution from Dow et al. (1990a) seems to slightly over predict the vertical displacement $|v|$. Nevertheless, good agreements on the stresses can be found among the three numerical results as observable from Fig. 2.

Example 3. Stresses in a Bimaterial Under Mechanical and Thermal Loading. As shown in Fig. 3, a steel (white region) and a brass (gray region) having the same cross section $L \times L/2$ are perfectly bonded together to form a single square cross section of $L \times L$. The two-dimensional bimaterial is assumed at stress-free state when the displacements on all of the surfaces are zero. Let $\xi = x/L$, $\eta = y/L$ and the following displacements be imposed on the surfaces of the bimaterial as a boundary condition of plane stresses

$$\frac{u}{L} = -\frac{10^{-4}}{\gamma}\frac{\nu_b g_1 - g_2}{g_3^2 g_4}, \quad \frac{v}{L} = -\frac{10^{-4}}{\gamma}\frac{\nu_b g_5 + g_6}{g_3^2 g_4} \tag{35}$$

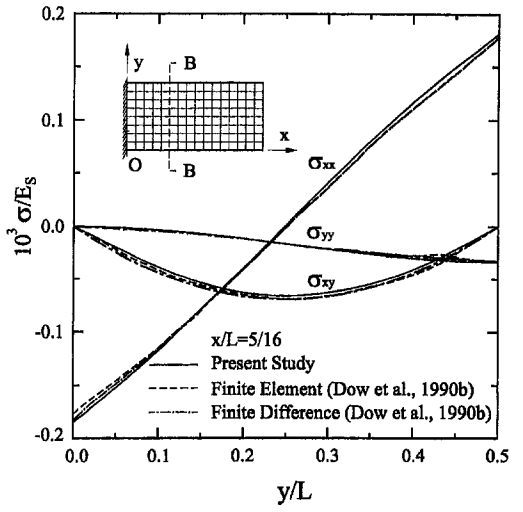


Fig. 2 Stresses (σ_{xx}, σ_{xy}, σ_{yy}) along the vertical line x/L = 5/16 for Example 2

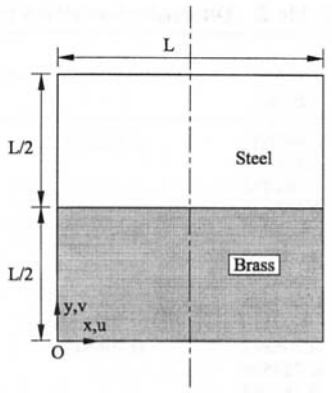


Fig. 3 Square cross section of a steel/brass bimaterial for Example 3

on $\xi = 0$ and $0 \le \eta \le 0.5$;

$$\frac{u}{L} = 10^{-4}(\beta - 1)(1 + \nu_s)(2\eta + 1)/g_4,$$

$$\frac{v}{L} = 10^{-4}(\beta - 1)(1 + \nu_s)/g_4 \tag{36}$$

on $\xi = 0$ and $0.5 \le \eta \le 1.0$;

$$\frac{u}{L} = -\frac{10^{-4}}{\gamma}\frac{\nu_b g_1 - g_2}{g_3^2 g_4}, \quad \frac{v}{L} = \frac{10^{-4}}{\gamma}\frac{\nu_b g_5 + g_6}{g_3^2 g_4} \tag{37}$$

on $\xi = 1$ and $0 \le \eta \le 0.5$;

$$\frac{u}{L} = 10^{-4}(\beta - 1)(1 + \nu_s)(2\eta + 1)/g_4,$$

$$\frac{v}{L} = -10^{-4}(\beta - 1)(1 + \nu_s)/g_4 \tag{38}$$

on $\xi = 1$ and $0.5 \le \eta \le 1.0$;

$$\frac{u}{L} = \frac{10^{-4}}{\gamma}\frac{\nu_b f_1 - f_2}{(f_3)^2(f_3 - 4)},$$

$$\frac{v}{L} = -\frac{10^{-4}}{\gamma}\frac{(\nu_b f_4 - f_5)(2\xi - 1)}{(f_3)^2(f_3 - 4)} \tag{39}$$

on $0 \le \xi \le 1$ and $\eta = 0$;

$$\frac{u}{L} = -3 \times 10^{-4}(\beta - 1)(1 + \nu_s)/f_3,$$

$$\frac{v}{L} = 10^{-4}(\beta - 1)(1 + \nu_s)(2\xi - 1)/f_3 \tag{40}$$

on $0 \le \xi \le 1$ and $\eta = 1$, where

$$f_1 = 4(\beta - 1)\xi^4 - 8(\beta - 1)\xi^3 + 4(13\beta - 6)\xi^2 - 4(12\beta - 5)\xi + (23\beta - 25)$$

$$f_2 = 4(11\beta + 1)\xi^4 - 8(11\beta + 1)\xi^3 + 4(35\beta + 6)\xi^2 - 4(24\beta + 5)\xi + (37\beta + 25)$$

$$f_3 = 2\xi^2 - 2\xi + 5$$

$$f_4 = 4(\beta - 1)\xi^4 - 8(\beta - 1)\xi^3 + 4(\beta - 6)\xi^2 + 20\xi - (\beta + 25)$$

$$f_5 = 4(3\beta + 1)\xi^4 - 8(3\beta + 1)\xi^3 + 12(5\beta + 2)\xi^2 - 4(12\beta + 5)\xi + (21\beta + 25) \tag{41}$$

Downloaded 04 May 2010 to 171.66.16.27. Redistribution subject to ASME license or copyright; see http://www.asme.org/terms/Terms_Use.cfm

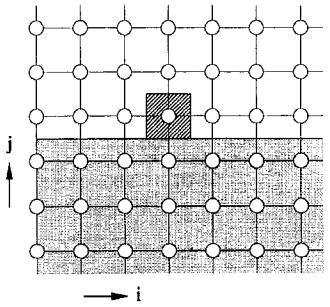


Fig. 4 Grid system in a region near the point (x/L, y/L) = (0, 0.5) for Example 3

$$g_1 = 8(3\beta + 1)\eta^5 - 4(17\beta + 11)\eta^4 + 8(4\beta + 11)\eta^3 + 4(5\beta - 16)\eta^2 + 10(\beta - 1)\eta - (23\beta - 25)$$

$$g_2 = 8(\beta - 1)\eta^5 - 44(\beta - 1)\eta^4 + 8(8\beta - 11)\eta^3 + 4(3\beta + 16)\eta^2 - 2(9\beta - 5)\eta - (37\beta + 25)$$

$$g_3 = 2\eta^2 - 6\eta + 5$$

$$g_4 = 2\eta^2 + 2\eta + 1$$

$$g_5 = 4(3\beta + 1)\eta^4 - 8(\beta + 3)\eta^3 - 4(3\beta - 14)\eta^2 - 4(2\beta + 15)\eta + (\beta + 25)$$

$$g_6 = 4(7\beta + 1)\eta^4 - 8(5\beta + 3)\eta^3 - 4(3\beta - 14)\eta^2 + 4(2\beta - 15)\eta + (21\beta + 25) \quad (42)$$

$$\beta = \frac{(1 + \nu_s)\gamma - (1 + \nu_b)}{(1 + \nu_s)\gamma + (3 - \nu_b)}. \quad (43)$$

For steel and brass, the Poisson's ratio are, respectively, $\nu_s = 0.29$ and $\nu_b = 0.33$, while their ratio of the Young's modulus is $\gamma = E_b/E_s = 0.539$. In this example, the integration scheme is employed to solve the deformation as well as the stresses on a uniform grid system of 41 × 42 points ($\Delta\xi = 1/40$ and $\Delta\eta = 1/41$). Grids in a region near the point (ξ, η) = (0, 0.5) are illustrated in Fig. 4 where the white dots denote the grid points (ξ_i, η_j) with $\xi_i = (i - 1)\Delta\xi$ and $\eta_j = (j - 1)\Delta\eta$. For convenience, the rectangular area bounded by $\xi_i \pm \Delta\xi/2$ and $\eta_j \pm \Delta\eta/2$ as the hatched region in Fig. 4 will be referred to as the control volume of the grid point (ξ_i, η_j), while the rectangle defined by four adjacent grid points, e.g., (ξ_i, η_j), (ξ_{i+1}, η_j), (ξ_{i+1}, η_{j+1}), (ξ_i, η_{j+1}) is known as the grid cell. Note that the control volumes should not cover the steel/brass interface ($\eta = y/L = 0.5$), otherwise the effective Young's modulus in the ξ-direction (19) and (23) would be difficult to define. Thus, there should be an odd number of grid cells in y-direction (η-direction) if a uniform grid system is employed.

Figure 5 shows the present numerical results of the stresses (σ_{xx}, σ_{yy}, σ_{xy}) on the vertical line $x = 0$. The exact solution from Honein and Herrmann (1990) is plotted in Fig. 5 also for comparison. Excellent agreement between the present numerical results and the exact solution is observable. This is true even when the Young's modulus of the brass is artificially decreased to $\gamma = E_b/E_s = 0.001$ as shown in Fig. 6. It should be noted here that there is a discontinuity in the stress $\sigma_{xx}(0, y)$ across the steel/brass interface. The present numerical result seems to perfectly reflect this important physical phenomenon in spite of the Young's modulus. In the present grid system (Fig. 4), the nearest grid points to the steel/brass interface are on the lines $y/L = 0.5 \pm (\Delta\eta/2)$. Hence, the present numerical result of $\sigma_{xx}(0, y)$ possesses an "inclined" line across the steel/brass interface when a linear interpolation is used. This can be improved by making extrapolations from both grid points to the interface.

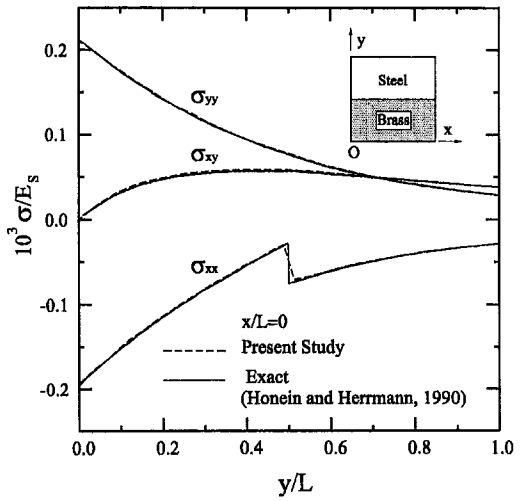


Fig. 5 Comparison of the present stresses (σ_{xx}, σ_{xy}, σ_{yy}) on the vertical surface $x/L = 0$ with the exact solution from Honein and Herrmann (1990) for the case of given surface displacements

Many approximate analytical solutions (e.g., Bogy, 1968; Munz and Yang, 1992) depict that singular stresses could exist at the free edge of bonded isotropic materials with different elastic properties under mechanical or thermal loading. However, such a stress singularity would violate the law of equilibrium (Post et al., 1994). In their studies, Post and co-workers (Post, 1987; Post and Wood, 1989; Post et al., 1994) employed a high-sensitivity moire interferometry to measure the whole-field displacements (u, v) on the free surface of a square thin plate of bimaterial (steel and brass) under a thermal loading of $\Delta T = -133°C$. The geometry of the bimaterial was similar to that shown in Fig. 3 with $L = 111.8$ mm and a thickness of 4.1 mm. The free surface stresses then were calculated from the experimental data. The normal stress σ_{yy} across the steel/brass interface was found to have a sharp tensile peak on the steel side and a sharp compressive peak on the brass side. Both peaks were very close to the steel/brass interface. The narrow region from the tensile peak to the compressive peak was called the interface zone. The normal stress σ_{yy} was a continuous function of y between the sharp turnarounds (the peaks). Unlike the existing approximate analytical solutions, however, no stress singularity could be found. The existence of the interface zone was

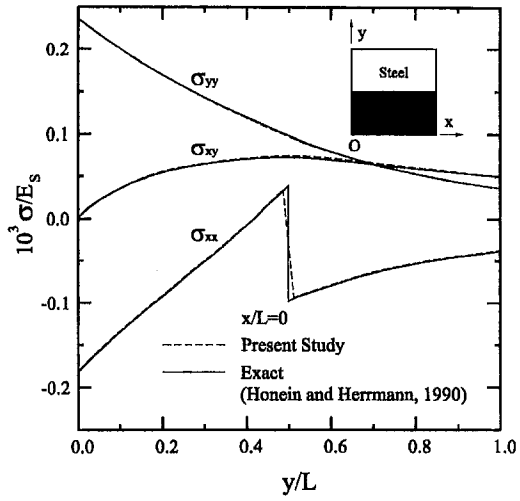


Fig. 6 Result of Fig. 5 in case the brass is replaced with an artificial material having $\nu = 0.33$ and $E = 0.001E_s$

Downloaded 04 May 2010 to 171.66.16.27. Redistribution subject to ASME license or copyright; see http://www.asme.org/terms/Terms_Use.cfm

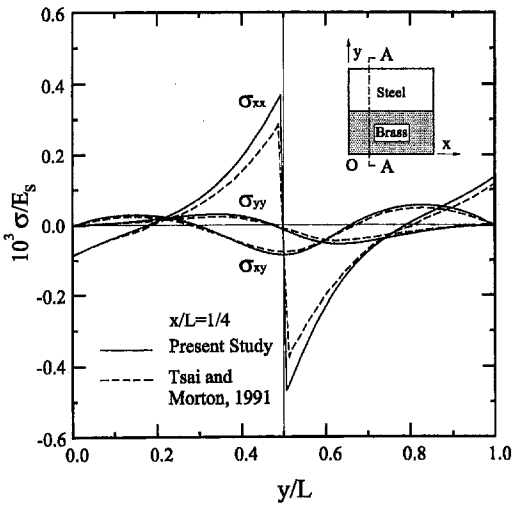


Fig. 7 Stresses (σ_{xx}, σ_{xy}, σ_{yy}) along the vertical line x/L = 1/4 for the case of thermal loading without boundary traction

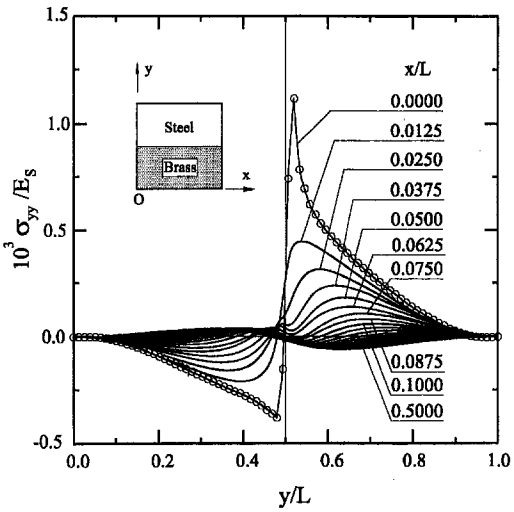


Fig. 8 Normal stresses σ_{yy} along various vertical lines for the case of thermal loading without boundary traction

confirmed by Tsai and Morton (1991) with a finite element method. Unfortunately, the surface stresses (σ_{xx}, σ_{yy}, σ_{xy}) in the interface zone obtained by Tsai and Morton (1991) did not satisfy the given boundary traction (free traction) due to the error of the finite element modeling employed by them. This will be discussed later.

To examine the performance of the integration scheme in the interface zone, let the two-dimensional bimaterial in Fig. 3 be cooled from the initial stress-free state through a temperature difference ΔT, while the surface of the bimaterial is maintained at zero traction. The linear thermal expansions in the steel and the brass are assumed to be $\alpha_s \Delta T = 1.656 \times 10^{-3}$ and $\alpha_b \Delta T = 2.592 \times 10^{-3}$, respectively. The integration scheme then is employed to solve the displacement equations on a uniform grid system of 81 × 80 points ($\Delta\xi = 1/80$ and $\Delta\eta = 1/79$). Numerical results of the stresses (σ_{xx}, σ_{yy}, σ_{xy}) along the vertical line $x/L = 1/4$ are presented in Fig. 7 as functions of y. The finite element solutions from Tsai and Morton (1991) are plotted also in Fig. 7 for comparison. From Fig. 7, one sees that both σ_{xy} and σ_{yy} are smooth functions across the steel/brass interface, while the stress σ_{xx} has a discontinuity at the interface. Satisfactory agreement can be found between the present results and the finite element solutions from Tsai and Morton (1991).

Figure 8 shows the present result of the normal stress σ_{yy} as a function of y at various x locations. The white dots on the curve of $x/L = 0$ denote the locations of the grid points. As observable from Fig. 8, the present integration scheme successfully predicts the existence of the interface zone at $y/L = 0.5$ on the free surface of the bimaterial ($x/L = 0$). Note also that in the use of the integration scheme the boundary stresses are directly imposed on the computations through Eqs. (10) and (28). Hence, the resulting boundary stresses will automatically satisfy the given boundary traction. As remarked by Tsai and Morton (1991), however, the finite element method might produce boundary stresses that does not satisfy the given boundary traction due to numerical errors especially in the interface zone. This might be attributed to the improper shape function employed in the finite element procedure. Figure 8 reveals also that on the steel side the normal stress σ_{yy} is tensile in the boundary region ($x < 0.1$) and becomes compressive in the internal region. Such a trend is reversed on the brass side. This is consistent with the physical reasoning.

As a final note, it is mentioned that the present integration scheme is equally applicable to three-dimensional problems. However, further improvement on this particular numerical method is required for problems with irregular boundaries. Such an improvement is believed to be possible as some significant progresses that have been achieved on fluid flow and heat transfer problems with an arbitrary physical domain (Hsu and Lee, 1991; Lee and Lin, 1997).

Conclusion

The finite difference scheme has many advantages over the finite element method and the boundary element method in solving a wide variety of physical problems. When applied to solid mechanical problems, however, the conventional finite difference method has limited flexibility in treating the boundary conditions. It lacks a satisfying procedure for eliminating the fictitious points when the central difference scheme is applied to a boundary point with given traction. In the present study, an integration scheme is proposed to solve linear deformation and stresses for elastic bodies. For convenience of application, the displacement equations are written in a particular form similar to a heat conduction equation. The multidimensional differential equation then is split into a system of one-dimensional equations. Instead of using the conventional Taylor series expansion, locally analytical solutions for each of the one-dimensional equations are employed to interpolate the solution between two adjacent grid points. Finally, the integration scheme is obtained by letting the stresses be in equilibrium on both sides of a grid point. Owing to its integration form, large jumps in the Young's modulus and the Poisson's ratio are allowed. This is one of the important features of the integration scheme. Through the three examples illustrated in the present study, the integration scheme shows excellent performances for linear deformation and stresses of elastic bodies under mechanical and thermal loading. Due to its simplicity and efficiency, good performances of the integration scheme are expected for solid mechanical problems especially when coupled with heat transfer and fluid flow inside and outside the solid.

Acknowledgment

The authors wish to express their appreciation to the National Science Council of Taiwan for the financial support of this work through the project NSC 84-2212-E007-052.

References

Bogy, D. B., 1968, "Edge-Bonded Dissimilar Orthogonal Elastic Wedges Under Normal and Shear Loading," ASME JOURNAL OF APPLIED MECHANICS, Vol. 35, pp. 460–466.

Dow, J. O., Jones, M. S., and Harwood, S. A., 1990a, "A Generalized Finite Difference Method for Solid Mechanics," *Numerical Methods for Partial Differential Equations,* Vol. 2, pp. 137–152.

Dow, J. O., Jones, M. S., and Harwood, S. A., 1990b, "A New Approach to

Downloaded 04 May 2010 to 171.66.16.27. Redistribution subject to ASME license or copyright; see http://www.asme.org/terms/Terms_Use.cfm

Boundary Modelling for Finite Difference Applications in Solid Mechanics," *International Journal for Numerical Methods in Engineering,* Vol. 30, pp. 99–113.

Dow, J. O., and Hardaway, J. L., 1992a, "Modeling of Multimaterial Interfaces in the Finite Difference Method," *Numerical Methods for Partial Differential Equations,* Vol. 8, pp. 493–503.

Dow, J. O., and Hardaway, J. L., 1992b, "Validation of Finite Difference Boundary Condition Models for Solid Mechanical Applications," *AIAA Journal,* Vol. 30, pp. 1864–1869.

Fenner, R. T., 1983, "The Boundary Integration Equation (Boundary Element) Method in Engineering Stress Analysis," *Journal of Strain Analysis,* Vol. 18, pp. 199–205.

Ghosh, S., and Mukherjee, S., 1984, "Boundary Element Method Analysis of Thermoelastic Deformation in Nonhomogeneous Media," *International Journal of Solids and Structures,* Vol. 20, pp. 829–843.

Hearn, E. J., 1985, *Mechanics of Materials*, 2nd Ed., Vol. 2, Pergamon Press, Oxford, p. 687.

Honein, T., and Herrmann, G., 1990, "On Bonded Inclusions With Circular or Straight Boundaries in Plane Elastostatics," ASME JOURNAL OF APPLIED MECHANICS, Vol. 57, pp. 850–856.

Hsu, K., and Lee, S. L., 1991, "A Numerical Technique for Two-Dimensional Grid Generation With Grid Control at all of the Boundaries," *Journal of Computational Physics,* Vol. 96, pp. 451–469.

Lee, S. L., 1989, "A Strongly Implicit Solver for Two-Dimensional Elliptic Differential Equations," *Numerical Heat Transfer,* Vol. 16B, pp. 161–178.

Lee, S. L., and Lin, D. W., 1997, "Transient Conjugate Heat Transfer on a Naturally Cooled Body of Arbitrary Shape," *International Journal of Heat and Mass Transfer,* Vol. 40, pp. 2133–2145.

Mukherjee, S., and Morjaria, M., 1984, "On the Efficiency and Accuracy of the Boundary Element Method and the Finite Element Method," *International Journal for Numerical Methods in Engineering,* Vol. 20, pp. 515–522.

Munz, D., and Yang, Y. Y., 1992, "Stress Singularities at the Interface in Bonded Dissimilar Materials Under Mechanical and Thermal Loading," ASME JOURNAL OF APPLIED MECHANICS, Vol. 59, pp. 857–861.

Post, D., 1987, "Moire Interferometry," *Handbook of Experimental Mechanics,* A. S. Kobayashi, ed., Prentice-Hall, Englewood Cliffs, NJ, pp. 314–387.

Post, D., and Wood, J. D., 1989, "Determination of Thermal Strains by Moire Interferometry," *Experimental Mechanics,* Vol. 29, pp. 318–322.

Post, D., Wood, J. D., Han, B., Parks, V. J., and Gerstle, Jr., F. P., 1994, "Thermal Stresses in a Bimaterial Joint: An Experimental Analysis," ASME JOURNAL OF APPLIED MECHANICS, Vol. 61, pp. 192–198.

Sladek, J., Sladek, V., and Markechova, I., 1990, "Boundary Element Method Analysis of Stationary Thermoelastic Problems in Non-homogeneous Media," *International Journal for Numerical Methods in Engineering,* Vol. 30, pp. 505–516.

Timoshenko, S. P., and Goodier, J. N., 1970, *Theory of Elasticity,* 3rd Ed., McGraw-Hill, New York, pp. 12, 27, 241, 456.

Tsai, M. Y., and Morton, J., 1991, "The Stresses in a Thermally Loaded Bimaterial Interface," *International Journal of Solids and Structures,* Vol. 28, pp. 1053–1075.

Downloaded 04 May 2010 to 171.66.16.27. Redistribution subject to ASME license or copyright; see http://www.asme.org/terms/Terms_Use.cfm

Dynamics of Serial Multibody Systems Using the Decoupled Natural Orthogonal Complement Matrices

S. K. Saha[1]
Department of Mechanical Engineering,
I.I.T., Delhi, Hauz Khas,
New Delhi 110 016, India
e-mail: saha@mech.iitd.ernet.in

Constrained dynamic equations of motion of serial multibody systems consisting of rigid bodies in a serial kinematic chain are derived in this paper. First, the Newton-Euler equations of motion of the decoupled rigid bodies of the system at hand are written. Then, with the aid of the decoupled natural orthogonal complement (DeNOC) matrices associated with the velocity constraints of the connecting bodies, the Euler-Lagrange independent equations of motion are derived. The De NOC is essentially the decoupled form of the natural orthogonal complement (NOC) matrix, introduced elsewhere. Whereas the use of the latter provides recursive order n–n being the degrees-of-freedom of the system at hand—inverse dynamics and order n^3 forward dynamics algorithms, respectively, the former leads to recursive *order n algorithms for both the cases. The order n algorithms are desirable not only for their computational efficiency but also for their numerical stability, particularly, in forward dynamics and simulation, where the system's accelerations are solved from the dynamic equations of motion and subsequently integrated numerically. The algorithms are illustrated with a three-link three-degrees-of-freedom planar manipulator and a six-degrees-of-freedom Stanford arm.*

1 Introduction

The conventional approach to obtain the dynamic model, i.e., equations of motion, of a mechanical system, consisting of rigid bodies coupled by kinematic pairs or joints, is to use either Newton-Euler (NE) or Euler-Lagrange (EL) equations. While the NE equations are obtained from the free-body diagrams, the EL equations resulted from the kinetic and potential energy of the system. The former is not suitable for motion simulation, as it finds the internal forces and torques that do not affect the motion of the system. Alternatively, EL equations give independent set of equations that are good for motion simulation, however, require complex calculations for the partial derivatives. With the advent of digital computation, a series of new methods in the study of dynamic modeling of mechanical systems have been developed. Huston and Passerello (1974) introduced the first computer-oriented method to reduce the dimension of the unconstrained dynamical equations, namely, Newton-Euler equations of motion, by eliminating the constraint forces. What was basically used to reduce the dimension is an *orthogonal complement* of the velocity constraints of the mechanical system under study. An orthogonal complement is defined as the matrix whose columns span the null-space of the matrix of the velocity constraints, and, hence, the premultiplication of the transpose of it with the unconstrained dynamic equations of motion vanishes the constrained moments and forces. The said orthogonal complement is not unique. In some approaches, an orthogonal complement is found using numerical schemes which are of an intensive nature, requiring, for example, singular-value decomposition or eigenvalue computations (Wehage and Haug, 1982; Kamman and Huston, 1984). In Angeles and Lee (1988), Angeles and Ma (1988), and Saha and Angeles (1991), however, the complement is obtained naturally from the velocity constraint expressions without any complex computation. Therefore, the complement is called *natural orthogonal complement* (NOC). The NOC is the matrix that relates the angular and linear velocities of the rigid bodies in the system to the associated joint rates, as in Eq. (16).

The purpose of deriving a dynamic model here is to obtain inverse and forward dynamics algorithms required in control and simulation of the mechanical systems under study, respectively. While almost all proposed inverse dynamics algorithms for serial-chain mechanical systems, as shown in Fig. 1, are recursive of order n, $\mathcal{O}(n)$—n being the degrees-of-freedom of the system at hand—complexity, e.g., Hollerbach (1980), Luh, Walker and Paul (1980), Kane and Levinson (1983), Angeles et al. (1989), Sciavicco and Siciliano (1996), most of the traditional forward dynamics algorithms are of $\mathcal{O}(n^3)$ (Walker and Orin, 1982; Kane and Levinson, 1983; Angeles and Ma, 1988). Note here that in inverse dynamics the explicit derivation of the equations of motion in terms of the generalized coordinates is not required, e.g., in Sciavicco and Siciliano (1996), where the joint torques are calculated from the trajectory of the end-effector. Alternatively, explicit expressions for the matrices, particularly, the generalized inertia matrix associated with the equations of motion must be evaluated for forward dynamics, e.g., in Angeles and Ma (1988) and others, in which the joint accelerations are solved from the equations of motion. Conventionally, a numerical approach is taken to solve for the joint accelerations. For example, in Angeles and Ma (1988), (i) first, the elements of the inertia matrix are evaluated; (ii) then, the numerical decomposition of the matrix, namely, the Cholesky decomposition (Stewart, 1973), is performed; and (iii) finally, the joint accelerations are solved by backward and forward substitutions. Since the complexity of the Cholesky decomposition is of order n^3, the forward dynamics algorithm also requires $\mathcal{O}(n^3)$ computations. There is, however, an alternative approach to obtain a forward dynamics algorithm recursively, whose computational complexity is in the order n, i.e., $\mathcal{O}(n)$, e.g., Armstrong (1979),

[1] Presently (May 1999–Jan. 2000) at the Institute B of Mechanics, University of Stuttgart, Stuttgart, Germany as a Humbold Fellow.

Contributed by the Applied Mechanics Division of THE AMERICAN SOCIETY OF MECHANICAL ENGINEERS for publication in the ASME JOURNAL OF APPLIED MECHANICS.
Discussion on the paper should be addressed to the Technical Editor, Professor Lewis T. Wheeler, Department of Mechanical Engineering, University of Houston, Houston, TX 77204-4792, and will be accepted until four months after final publication of the paper itself in the ASME JOURNAL OF APPLIED MECHANICS.
Manuscript received by the ASME Applied Mechanics Division, July 14, 1998; final revision, June 17, 1999. Associate Technical Editor: N. C. Perkins.

 Copyright © 1999 by ASME

Downloaded 04 May 2010 to 171.66.16.27. Redistribution subject to ASME license or copyright; see http://www.asme.org/terms/Terms_Use.cfm

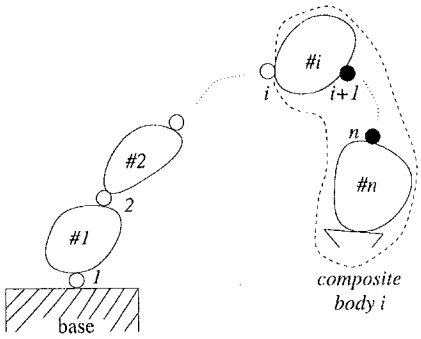


Fig. 1 An *n*-body serial manipulator

Featherstone (1983), Rodriguez (1987), Schiehlen (1991), Rodriguez and Kreutz-Delgado (1992), and Saha (1997). There is also a parallel $\mathcal{O}(\log N)$ algorithm proposed in Fijany et al. (1995) which requires a special computer hardware, namely, a parallel architecture. Because of the special hardware requirement the parallel algorithms will not be discussed further.

The algorithm by Armstrong (1979) was the first of its kind where the recursive solution to the equations of motion of an n-link manipulator mounted on a spacecraft is obtained. Featherstone (1983) has introduced the concept of *articulated body inertia* (ABI) which has been efficiently evaluated by McMillan and Orin (1995). The ABI is derived by extending the expressions for the equations of motion of a single body to a system of coupled bodies. Rodriguez (1987), on the other hand, presented a novel robot inverse and forward dynamics algorithms based on Kalman filtering and smoothing technique arising in the state estimation theory. The methodology has been used to solve several other dynamics problems as well, namely, by Rodriguez, Jain, and Kreutz-Delgado (1991), and Jain and Rodriguez (1995). Schiehlen (1991) and Saha (1997), however, have independently used the linear algebra approach to arrive at a recursive forward dynamics algorithm. It is interesting to note that, compared to the $\mathcal{O}(n^3)$ schemes, e.g., Angeles and Ma (1988), computational complexity of all the $\mathcal{O}(n)$ schemes, wherever known, are efficient when $n \geq 12$, as is evident from Table 2. The $\mathcal{O}(n)$ algorithms, however, calculate the joint accelerations that are smooth functions of time (Ascher et al., 1997). As a result, numerical integration is faster and, hence, the total time in simulation may be less while comparing with the $\mathcal{O}(n^3)$ scheme. Besides, $\mathcal{O}(n)$ algorithms provide physical interpretations of the parameters they calculate and the intermediate steps they follow. Thus, the recursive forward dynamics is becoming more and more popular.

In this paper, the NOC (Angeles and Lee, 1988) is taken one step further to *uniformly* develop a set of independent dynamic equations of motion from which both recursive inverse and forward dynamics algorithms can be written. Here, the NOC is expressed as a product of two matrices, one is a block triangular and the other one is a block diagonal. Hence, the term *decoupled* added to it. Unlike the NOC, its modified form, i.e., the DeNOC, allows one to write expressions of the elements of the matrices and vectors associated with the dynamic equations of motion in *analytical, recursive* form, as shown in Section 4. These characteristics were not so obvious with the earlier form of the NOC, e.g., in Saha and Angles (1991). Moreover, many of the physical interpretations obtained in this paper have corresponding interpretations in Featherstone (1983), Rodriguez (1987), Rodriguez and Kreutz-Delgado (1992), and others, as indicated after Eqs. (14), (17), and (50). The present approach provides an alternate approach to the development of a recursive forward dynamics algorithm, compared to others, e.g., Rodriguez (1987). The present approach is built upon basic mechanics and linear algebra theory. Hence, it is easy to comprehend, even by a fresh mechanical engineer without any knowledge of control theory. Moreover, there is equivalence of many steps and interpreted variables obtained from Gaussian elimination of the inertia matrix, as shown in Appendix B, and Kalman filtering (Rodriguez, 1987). As a result, it may be commented that they are equivalent under certain conditions. The real proof is, however, behind the scope of this paper.

The contributions of this paper are listed as follows.

1 A systematic *uniform* development of the dynamic model of a serial-chain mechanical system. Here the word, uniform, implies that *no* different sets of equations of motion are required to obtain inverse and forward dynamics algorithms, as in Sciavicco and Siciliano (1996) and others, where Newton-Euler equations of the motion of the uncoupled bodies are used to obtain a recursive inverse dynamics algorithm and the joint accelerations (forward dynamics) are computed from the independent set of equations.

2 Recursive expressions not only for the generalized inertia matrix (Saha, 1997), but also for the generalized matrix of convective inertia terms, and the generalized forces/torques, as shown in Section 4.

3 As a consequence of the above items, not only a forward dynamics algorithm (Saha, 1997) but also an inverse dynamics algorithm is possible from the same set of dynamics equations of motion.

4 Implementation of the above algorithms to a planar three-degrees-of-freedom manipulator and a six-degrees-of-freedom Stanford arm.

5 Physical interpretation of different terms obtained during the dynamic modeling, and correlation of those with the similar terms appeared in the literature, e.g., Featherstone (1983) and Rodriguez (1987) and Rodriguez and Kreutz-Delgado (1992).

The paper is organized as follows: Section 2 introduces some definitions required to derive the dynamic model given in Section 3. Section 4 shows how to derive the analytical expressions for the matrices and vectors associated with the equations of motion, whereas Section 5 gives the applications, namely, inverse and forward dynamics algorithms. The results of the algorithms with respect to two examples are provided in Section 6.

2 Some Definitions

Referring to Fig. 1, it is assumed that a serial multibody system, namely, the serial manipulator, has a fixed "base" and n moving rigid bodies, numbered #1, . . . , #n, coupled by n one-degree-of-freedom kinematic pairs or joints, say, a prismatic or a revolute, which are indicated in Fig. 1 as 1, . . . , n. The ith joint couples the ith body with that of the $(i-1)$st. Now, referring to the motion of the ith body, Fig. 2, the following terms are defined:

***t**$_i$ and **n**$_i$:* the six-dimensional vectors of *twist* and *wrench* of the ith link, i.e.,

$$\mathbf{t}_i \equiv \begin{bmatrix} \boldsymbol{\omega}_i \\ \mathbf{v}_i \end{bmatrix} \quad \text{and} \quad \mathbf{w}_i \equiv \begin{bmatrix} \mathbf{n}_i \\ \mathbf{f}_i \end{bmatrix} \tag{1}$$

where $\boldsymbol{\omega}_i$ and $\mathbf{v}_i$ are the three-dimensional vectors of angular velocity and the linear velocity of the mass center of the ith link, C_i, as shown in Fig. 2, respectively, whereas $\mathbf{n}_i$ and $\mathbf{f}_i$ are the three-dimensional vectors of the moment about C_i and the force at C_i, respectively.

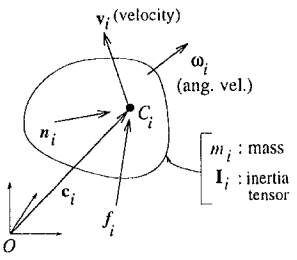


Fig. 2 Free-body diagram of the *i*th body

Downloaded 04 May 2010 to 171.66.16.27. Redistribution subject to ASME license or copyright; see http://www.asme.org/terms/Terms_Use.cfm

$\boldsymbol{\Omega}_i$ *and* $\mathbf{M}_i$*:* the 6×6 matrices of *angular velocity* and *mass* of the ith body, respectively, namely,

$$\boldsymbol{\Omega}_i \equiv \begin{bmatrix} \boldsymbol{\omega}_i \times \mathbf{1} & \mathbf{O} \\ \mathbf{O} & \boldsymbol{\omega}_i \times \mathbf{1} \end{bmatrix} \quad \text{and} \quad \mathbf{M}_i \equiv \begin{bmatrix} \mathbf{I}_i & \mathbf{O} \\ \mathbf{O} & m_i\mathbf{1} \end{bmatrix} \tag{2}$$

where $\boldsymbol{\omega}_i \times \mathbf{1}$ is the 3×3 cross-product tensor associated with vector $\boldsymbol{\omega}_i$, which when operates on any three-dimensional Cartesian vector, $\mathbf{x}$, results in a cross-product vector, i.e., $(\boldsymbol{\omega}_i \times \mathbf{1})\mathbf{x} \equiv \boldsymbol{\omega}_i \times \mathbf{x}$. Moreover, $\mathbf{I}_i$ and m_i are the 3×3 inertia tensor about the mass center, C_i, and the mass of the ith body, respectively. Furthermore, $\mathbf{1}$ and $\mathbf{O}$ are the 3×3 identity matrix and the matrix of zeros, respectively. Henceforth, the dimensions of $\mathbf{1}$ and $\mathbf{O}$ should be understood as of dimensions that are compatible with the dimensions of the matrix expressions where they appear.

t and w: the $6n$-dimensional vectors of generalized twist and wrench, respectively, i.e.,

$$\mathbf{t} \equiv [\mathbf{t}_1^T, \ldots, \mathbf{t}_n^T]^T \quad \text{and} \quad \mathbf{w} \equiv [\mathbf{w}_1^T, \ldots, \mathbf{w}_n^T]^T \tag{3}$$

where $\mathbf{t}_i$ and $\mathbf{w}_i$, for $i = 1, \ldots, n$, are defined in Eq. (1).

$\boldsymbol{\Omega}$ *and* $\mathbf{M}$*:* the $6n \times 6n$ matrices of generalized angular velocity and mass, respectively, namely,

$$\boldsymbol{\Omega} \equiv \text{diag}\,[\boldsymbol{\Omega}_1, \ldots, \boldsymbol{\Omega}_n] \quad \text{and} \quad \mathbf{M} \equiv \text{diag}\,[\mathbf{M}_1, \ldots, \mathbf{M}_n] \tag{4}$$

where $\boldsymbol{\Omega}_i$ and $\mathbf{M}_i$, for $i = 1, \ldots, n$, are given in Eq. (2).

$\dot{\boldsymbol{\theta}}$*:* the n-dimensional independent vector of joint rates, i.e.,

$$\dot{\boldsymbol{\theta}} \equiv [\dot{\theta}_1, \ldots, \dot{\theta}_n]^T \tag{5}$$

where θ_i is the displacement of the ith joint, as shown in Fig. 3.

3 Dynamic Modeling Using the DeNOC

For a serial-chain mechanical system shown in Fig. 1, the steps to obtain the dynamic equations of motion using the DeNOC matrices are given below:

1 Derivation of the Unconstrained Newton-Euler (NE) Equations of Motion:

(a) From the free-body diagram of the ith rigid body, Fig. 2, write the Newton-Euler equations of motion as

$$\mathbf{I}_i\dot{\boldsymbol{\omega}}_i + \boldsymbol{\omega}_i \times \mathbf{I}_i\boldsymbol{\omega}_i = \mathbf{n}_i \tag{6a}$$

$$m_i\dot{\mathbf{v}}_i = \mathbf{f}_i \tag{6b}$$

where $\mathbf{n}_i$ and $\mathbf{f}_i$ are the resultant moment about and force applied at the mass center, C_i, respectively. Using the definitions given in Eqs. (1) and (2), the above six scalar equations can be put in a compact form as

$$\mathbf{M}_i\dot{\mathbf{t}}_i + \dot{\mathbf{M}}_i\mathbf{t}_i = \mathbf{w}_i \tag{7}$$

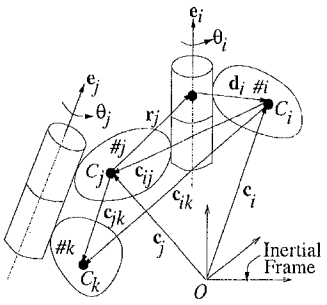


Fig. 3 A coupled system

where the six-dimensional *twist-rate* vector, $\dot{\mathbf{t}}_i$, and the 6×6 *mass-rate* matrix, $\dot{\mathbf{M}}_i$, are, respectively, the time derivative of $\mathbf{t}_i$ and $\mathbf{M}_i$, which are defined as

$$\dot{\mathbf{t}}_i \equiv \begin{bmatrix} \dot{\boldsymbol{\omega}}_i \\ \dot{\mathbf{v}}_i \end{bmatrix} \quad \text{and} \quad \dot{\mathbf{M}}_i \equiv \begin{bmatrix} \boldsymbol{\omega}_i \times \mathbf{I}_i & \mathbf{O} \\ O & \mathbf{O} \end{bmatrix}. \tag{8}$$

(b) Write Eq. (7) for $i = 1, \ldots, n$: This gives $6n$ uncoupled scalar equations for the whole system, which are put in the following form:

$$\mathbf{M}\dot{\mathbf{t}} + \dot{\mathbf{M}}\mathbf{t} = \mathbf{w} \tag{9}$$

where $\dot{\mathbf{t}}$ and $\dot{\mathbf{M}}$ are the time derivative of the generalized twist, $\mathbf{t}$, and generalized mass, $\mathbf{M}$, respectively, i.e.,

$$\dot{\mathbf{t}} \equiv [\dot{\mathbf{t}}_1^T, \ldots, \dot{\mathbf{t}}_n^T]^T \quad \text{and} \quad \dot{\mathbf{M}} \equiv \text{diag}\,[\dot{\mathbf{M}}_1, \ldots, \dot{\mathbf{M}}_n] \tag{10}$$

in which $\dot{\mathbf{t}}_i$ and $\dot{\mathbf{M}}_i$ appear in Eq. (8).

2 Derivation of Kinematic Constraints:

(a) In this step, motion constraints due to the kinematic pairs are derived. For example, velocity constraints between two links, $\#i$ and $\#j$, coupled by the ith revolute joint, as shown in Fig. 3, can be expressed as

$$\boldsymbol{\omega}_i = \boldsymbol{\omega}_j + \dot{\theta}_i\mathbf{e}_i \tag{11a}$$

$$\mathbf{v}_i = \mathbf{v}_j + \boldsymbol{\omega}_j \times \mathbf{r}_j + \boldsymbol{\omega}_i \times \mathbf{d}_i. \tag{11b}$$

The above six scalar equations are written in a compact form as

$$\mathbf{t}_i = \mathbf{B}_{ij}\mathbf{t}_j + \mathbf{p}_i\dot{\theta}_i \tag{12}$$

where the 6×6 matrix, $\mathbf{B}_{ij}$, and the six-dimensional vector, $\mathbf{p}_i$, are as follows:

$$\mathbf{B}_{ij} \equiv \begin{bmatrix} \mathbf{1} & \mathbf{O} \\ \mathbf{c}_{ij} \times \mathbf{1} & \mathbf{1} \end{bmatrix} \quad \text{and} \quad \mathbf{p}_i \equiv \begin{bmatrix} \mathbf{e}_i \\ \mathbf{e}_i \times \mathbf{d}_i \end{bmatrix} \tag{13}$$

$\mathbf{c}_{ij} \times \mathbf{1}$ being the cross-product tensor associated with vector $\mathbf{c}_{ij}$, defined similar to $\boldsymbol{\omega}_i \times \mathbf{1}$ of Eq. (2), i.e., $(\mathbf{c}_{ij} \times \mathbf{1})\mathbf{x} \equiv \mathbf{c}_{ij} \times \mathbf{x}$, for any arbitrary three-dimensional Cartesian vector $\mathbf{x}$. The vector, $\mathbf{c}_{ij}$, as shown in Fig. 3, is given by, $\mathbf{c}_{ij} \equiv -\mathbf{d}_i - \mathbf{r}_j$. It is interesting to note here that the matrix, $\mathbf{B}_{ij}$, and the vector, $\mathbf{p}_i$, have the following interpretations:

- For two rigidly connected moving bodies, $\#i$ and $\#j$, $\mathbf{B}_{ij}$, propagates the twist of $\#j$ to $\#i$. Hence, matrix $\mathbf{B}_{ij}$ is termed here as the *twist propagation matrix,* which has the following properties:

$$\mathbf{B}_{ij}\mathbf{B}_{jk} = \mathbf{B}_{ik}, \quad \mathbf{B}_{ii} = \mathbf{1}, \quad \text{and} \quad \mathbf{B}_{ij}^{-1} = \mathbf{B}_{ji}. \tag{14}$$

  Matrix $\mathbf{B}_{ij}$ is nothing but the *state transition* matrix of Rodriguez (1987).
- Vector, $\mathbf{p}_i$, on the other hand, takes into account the motion of the ith joint. Hence, $\mathbf{p}_i$ is termed as the *joint-rate propagation vector,* which is dependent on the type of joint. For example, the expression of $\mathbf{p}_i$ in Eq. (13) is for a revolute joint shown in Fig. 3, whereas for a prismatic joint vector $\mathbf{p}_i$ is given by

$$\mathbf{p}_i \equiv \begin{bmatrix} \mathbf{0} \\ \mathbf{e}_i \end{bmatrix}: \quad \text{for a prismatic joint} \tag{15}$$

  where $\mathbf{e}_i$ is the unit vector parallel to the axis of linear motion. Correspondingly, $\dot{\theta}_i$ of Eq. (12) would mean the linear joint rate. Other joints are not treated here because any other joint, e.g., spherical or screw, can be treated as combination of revolute or revolute and prismatic pairs, respectively.

Downloaded 04 May 2010 to 171.66.16.27. Redistribution subject to ASME license or copyright; see http://www.asme.org/terms/Terms_Use.cfm

(b) Write Eq. (12), for $i = 1, \ldots, n$, as

$$\mathbf{t} = \mathbf{N}\dot{\boldsymbol{\theta}}, \quad \text{where} \quad \mathbf{N} \equiv \mathbf{N}_l\mathbf{N}_d. \tag{16}$$

In Eq. (16), $\mathbf{N}$ is the $6n \times n$ NOC matrix, introduced in Angeles and Lee (1988), whereas its decoupled form, $\mathbf{N} \equiv \mathbf{N}_l\mathbf{N}_d$, is termed as the *decoupled* NOC (DeNOC) matrices (Saha, 1997). The $6n \times 6n$ lower block triangular matrix, $\mathbf{N}_l$, and the $6n \times n$ block diagonal matrix, $\mathbf{N}_d$, are given by

$$\mathbf{N}_l \equiv \begin{bmatrix} \mathbf{1} & \mathbf{O} & \cdots & \mathbf{O} \\ \mathbf{B}_{21} & \mathbf{1} & \cdots & \mathbf{O} \\ \vdots & \vdots & \ddots & \vdots \\ \mathbf{B}_{n1} & \mathbf{B}_{n2} & \cdots & \mathbf{1} \end{bmatrix} \quad \text{and}$$

$$\mathbf{N}_d \equiv \begin{bmatrix} \mathbf{p}_1 & \mathbf{0} & \cdots & \mathbf{0} \\ \mathbf{0} & \mathbf{p}_2 & \cdots & \mathbf{0} \\ \vdots & \vdots & \ddots & \vdots \\ \mathbf{0} & \mathbf{0} & \cdots & \mathbf{p}_n \end{bmatrix} \tag{17}$$

where the first two properties of the twist propagation matrix, $\mathbf{B}_{ij}$, given in Eq. (14) are used. Moreover, $\mathbf{O}$ and $\mathbf{0}$ are the 6×6 matrix and the six-dimensional vector of zeros, respectively. Matrices $\mathbf{N}_l$ and $\mathbf{N}_d$ are the *spatial operators* of Rodriguez and Kreutz-Delgado (1992), which are "anticausal" and "memory-less" nonrecursive, respectively.

3 Incorporation of the Kinematic Constraints Into the NE Equations of Motion: Premultiply $\mathbf{N}^T$ with the decoupled NE equations of motions, Eq. (9), i.e.,

$$\mathbf{N}^T(\mathbf{M}\dot{\mathbf{t}} + \dot{\mathbf{M}}\mathbf{t}) = \mathbf{N}^T(\mathbf{w}^E + \mathbf{w}^I) \tag{18}$$

where $\mathbf{w}$ is substituted as $\mathbf{w} \equiv \mathbf{w}^E + \mathbf{w}^I$—$\mathbf{w}^E$ and $\mathbf{w}^I$ are the generalized external and internal constraint wrenches, respectively. Since constraint moments and forces do not perform any work, $\mathbf{t}^T\mathbf{w}^I$ vanishes, i.e., $\mathbf{t}^T\mathbf{w}^I = \dot{\boldsymbol{\theta}}^T\mathbf{N}^T\mathbf{w}^I = \mathbf{0}$, which implies that, for independent $\dot{\boldsymbol{\theta}}$, $\mathbf{N}^T\mathbf{w}^I = \mathbf{0}$. Hence, Eq. (18) is rewritten as

$$\mathbf{N}^T(\mathbf{M}\dot{\mathbf{t}} + \dot{\mathbf{M}}\mathbf{t}) = \mathbf{N}^T\mathbf{w}^E. \tag{19}$$

Note that in order to eliminate the constraint wrench from the decoupled NE equations, Eq. (9), as done in Eq. (19), it is important to write the generalized twist, $\mathbf{t}$, as a linear transformation of the *independent* generalized speed, as in Eq. (16).

4 Constrained Euler-Lagrange (EL) Dynamic Equations of Motion: Substitute the expression of $\mathbf{t}$, Eq. (16), and its time derivative, i.e., $\dot{\mathbf{t}} = \mathbf{N}\ddot{\boldsymbol{\theta}} + \dot{\mathbf{N}}\dot{\boldsymbol{\theta}}$, into Eq. (19). The result is the following constrained dynamic equations of motion:

$$\mathbf{I}\ddot{\boldsymbol{\theta}} + \mathbf{C}\dot{\boldsymbol{\theta}} = \boldsymbol{\tau} \tag{20}$$

where

$\mathbf{I} \equiv \mathbf{N}^T\mathbf{M}\mathbf{N} \equiv \mathbf{N}_d^T\tilde{\mathbf{M}}\mathbf{N}_d$: the $n \times n$ generalized inertia matrix (*GIM*);

$\mathbf{C} \equiv \mathbf{N}^T(\mathbf{M}\dot{\mathbf{N}} + \dot{\mathbf{M}}\mathbf{N}) \equiv \mathbf{N}_d^T\tilde{\mathbf{M}}'\mathbf{N}_d$: the $n \times n$ matrix of convective inertia terms;

$\boldsymbol{\tau} \equiv \mathbf{N}^T\mathbf{w}^E \equiv \mathbf{N}_d^T\tilde{\mathbf{w}}^E$: the n-dimensional vector of generalized forces due to driving torques and those resulting from gravity and dissipation, etc.

The expressions for $\tilde{\mathbf{M}}$, $\tilde{\mathbf{M}}'$, and $\tilde{\mathbf{w}}^E$ are associated with the composite body of the system under study and derived in the next section, Section 4. Note that Eq. (20) is essentially the Euler-Lagrange equations of motion that has been arrived from the uncoupled Newton-Euler equations, e.g., Eq. (9). Moreover, the use of the NOC, $\mathbf{N}$, as introduced in Angeles and Lee (1988), does not allow further simplification of associated expressions of Eq. (20), i.e., matrices $\mathbf{I}$ and $\mathbf{C}$, and vector $\boldsymbol{\tau}$. Hence, a computer algorithm is required at this stage for dynamic analysis. Alternatively, the DeNOC matrices given in Eq. (16) allows one to write the analytical *recursive* expressions for each element of the matrices, $\mathbf{I}$, $\mathbf{C}$, and $\boldsymbol{\tau}$, as shown in the following section. These expressions lead to *recursive* inverse and forward dynamics algorithms, given in Sections 5.1 and 5.2, respectively, whose computational complexities are of order n, i.e., $\mathcal{O}(n)$, and provide many physical interpretations, e.g., after Eqs. (14), (17), (23*b*), and (50).

4 Analytical Expressions for I, C, and $\boldsymbol{\tau}$

The analytical expressions for the GIM, $\mathbf{I}$, the generalized matrix of convective inertia terms, $\mathbf{C}$, and the generalized vector of joint forces/torques, as given after Eq. (20), are derived next. These expressions provide the basis for *uniform* development of the *recursive* inverse and forward dynamics algorithms. That is, unlike other approaches, e.g., Sciavicco and Siciliano (1996) and others, where free-body diagrams and NE equations are used to develop inverse dynamics algorithm and the EL equations are used for forward dynamics, here only one set of equations, namely, Eqs. (20), (24), (29), and (30), are used for both the algorithms.

4.1 Derivation of the GIM, I. Substituting the expression for the NOC in terms of the DeNOC matrices, i.e., $\mathbf{N} \equiv \mathbf{N}_l\mathbf{N}_d$, as in Eq. (17), into that of matrix $\mathbf{I} \equiv \mathbf{N}^T\mathbf{M}\mathbf{N}$, as given after Eq. (20), one obtains

$$\mathbf{I} \equiv \mathbf{N}_d^T\tilde{\mathbf{M}}\mathbf{N}_d, \quad \text{where} \quad \tilde{\mathbf{M}} \equiv \mathbf{N}_l^T\mathbf{M}\mathbf{N}_l \tag{21}$$

in which the $6n \times 6n$ symmetric matrix, $\tilde{\mathbf{M}}$, is given by

$$\tilde{\mathbf{M}} \equiv \begin{bmatrix} \tilde{\mathbf{M}}_1 & \mathbf{B}_{21}^T\tilde{\mathbf{M}}_2 & \cdots & \mathbf{B}_{n1}^T\tilde{\mathbf{M}}_n \\ \tilde{\mathbf{M}}_2\mathbf{B}_{21} & \tilde{\mathbf{M}}_2 & \cdots & \mathbf{B}_{n2}^T\tilde{\mathbf{M}}_n \\ \vdots & \vdots & \ddots & \vdots \\ \tilde{\mathbf{M}}_n\mathbf{B}_{n1} & \tilde{\mathbf{M}}_n\mathbf{B}_{n2} & \cdots & \tilde{\mathbf{M}}_n \end{bmatrix} \tag{22}$$

where the 6×6 matrix, $\tilde{\mathbf{M}}_i$, for $i = 1, \ldots, n$, is defined as

$$\tilde{\mathbf{M}}_i \equiv \mathbf{M}_i + \sum_{k=i+1}^{n} \mathbf{B}_{ki}^T\mathbf{M}_k\mathbf{B}_{ki}. \tag{23a}$$

Note the summation over $k = i + 1, \ldots, n$ in Eq. (23*a*). An algorithm computing $\tilde{\mathbf{M}}_i$, for $i = 1, \ldots, n$, from Eq. (23*a*) will certainly require order n^2 computations. However, a close look to Eq. (23*a*) with the first two properties of $\mathbf{B}_{ij}$, Eq. (14), in mind reveals that the summation expression can be evaluated recursively, i.e., $\sum_{k=i+1}^{n} \mathbf{B}_{ki}^T\mathbf{M}_k\mathbf{B}_{ki} \equiv \mathbf{B}_{i+1,i}^T\tilde{\mathbf{M}}_{i+1}\mathbf{B}_{i+1,i}$, for $i = n, \ldots, 1$, with $\tilde{\mathbf{M}}_{n+1} \equiv \mathbf{O}$, because there is no $(n + 1)$st link in the system. Hence, Eq. (23*a*) has the following recursive relation:

$$\tilde{\mathbf{M}}_i = \mathbf{M}_i + \mathbf{B}_{i+1,i}^T\tilde{\mathbf{M}}_{i+1}\mathbf{B}_{i+1,i} \quad \text{where} \quad \tilde{\mathbf{M}}_n \equiv \mathbf{M}_n. \tag{23b}$$

The 6×6 matrix, $\tilde{\mathbf{M}}_i$, is the mass matrix of *composite body, i*, i.e., $\tilde{\mathbf{M}}_i$ represents the mass and inertia properties of the system comprising of $(n - i + 1)$ rigidly connected bodies, namely, bodies $\#i, \ldots, \#n$, as indicated in Fig. 1 by dotted line. The expressions for the elements of the GIM, $\mathbf{I}$ of Eq. (20), which is symmetric positive definite, are then given by

$$i_{ij} = i_{ji} = \mathbf{p}_i^T\tilde{\mathbf{M}}_i\mathbf{B}_{ij}\mathbf{p}_j \tag{24}$$

for $i = 1, \ldots, n$; $j = 1, \ldots, i$.

Downloaded 04 May 2010 to 171.66.16.27. Redistribution subject to ASME license or copyright; see http://www.asme.org/terms/Terms_Use.cfm

Table 1 Computational complexities in inverse dynamics

Algorithm	M	A	$n = 6$	
Hollerbach (1980)	$412n - 277$	$320n - 201$	$2195M$	$1719A$
Luh et al. (1980)	$150n - 48$	$131n + 48$	$852M$	$834A$
Walker and Orin (1982)	$137n - 22$	$101n - 11$	$800M$	$595A$
Proposed	$120n - 44$	$97n - 55$	$676M$	$527A$
Khalil et al. (1986)	$105n - 92$	$94n - 86$	$538M$	$478A$
Angeles et al. (1989)	$105n - 109$	$90n - 105$	$521M$	$435A$
Balafoutis et al. (1988)	$93n - 69$	$81n - 65$	$489M$	$421A$

M: Multiplication/Division; A: Addition/Subtraction

4.2 Derivation of C Matrix. Using the NOC and its time derivative in terms of the DeNOC matrices, i.e., $\mathbf{N} \equiv \mathbf{N}_l\mathbf{N}_d$, and $\dot{\mathbf{N}} \equiv \dot{\mathbf{N}}_l\mathbf{N}_d + \mathbf{N}_l\dot{\mathbf{N}}_d$, respectively, the generalized matrix of convective inertia terms, $\mathbf{C}[\equiv\mathbf{N}^T(\mathbf{M}\dot{\mathbf{N}} + \dot{\mathbf{M}}\mathbf{N})]$, as defined after Eq. (20), is obtained as

$$\mathbf{C} \equiv \mathbf{N}_d^T\tilde{\mathbf{M}}'\mathbf{N}_d, \quad \text{where} \quad \tilde{\mathbf{M}}' \equiv \mathbf{N}_l^T\mathbf{M}\dot{\mathbf{N}}_l + \tilde{\mathbf{M}}\boldsymbol{\Omega} + \tilde{\dot{\mathbf{M}}} \tag{25}$$

in which the following identities are used:

$$\dot{\mathbf{N}}_d \equiv \boldsymbol{\Omega}\mathbf{N}_d \quad \text{and} \quad \tilde{\dot{\mathbf{M}}} = \mathbf{N}_l^T\dot{\mathbf{M}}\mathbf{N}_l \tag{26}$$

where the $6n \times 6n$ matrix, $\boldsymbol{\Omega}$, is defined in Eq. (4). In Eq. (25), the multiplication of two block diagonal matrices, $\mathbf{M}$ and $\boldsymbol{\Omega}$, can be easily performed, whereas the expressions for the matrices, $\mathbf{N}_l^T\mathbf{M}\dot{\mathbf{N}}_l$ and $\tilde{\dot{\mathbf{M}}}$, are shown below:

$$\mathbf{N}_l^T\mathbf{M}\dot{\mathbf{N}}_l \equiv \begin{bmatrix} \mathbf{B}_{21}^T\tilde{\mathbf{H}}_{21} & \cdots & \mathbf{B}_{n1}^T\tilde{\mathbf{H}}_{n,n-1} & \mathbf{O} \\ \tilde{\mathbf{H}}_{21} & \cdots & \mathbf{B}_{n2}^T\tilde{\mathbf{H}}_{n,n-1} & \mathbf{O} \\ \vdots & \ddots & \vdots & \vdots \\ \tilde{\mathbf{H}}_{n-1,1} & \cdots & \mathbf{B}_{n2}^T\tilde{\mathbf{H}}_{n,n-1} & \mathbf{O} \end{bmatrix} \quad \text{and}$$

$$\tilde{\dot{\mathbf{M}}} \equiv \begin{bmatrix} \tilde{\dot{\mathbf{M}}}\tilde{\dot{\mathbf{M}}}_1 & \tilde{\dot{\mathbf{M}}}_2 & \cdots & \tilde{\dot{\mathbf{M}}}_n \\ \tilde{\dot{\mathbf{M}}}_2 & \tilde{\dot{\mathbf{M}}}_2 & \cdots & \tilde{\dot{\mathbf{M}}}_n \\ \vdots & \vdots & \ddots & \vdots \\ \tilde{\dot{\mathbf{M}}}_n & \tilde{\dot{\mathbf{M}}}_n & \cdots & \tilde{\dot{\mathbf{M}}}_n \end{bmatrix}, \tag{27}$$

the 6×6 matrices, $\tilde{\dot{\mathbf{M}}}_i$ and $\tilde{\mathbf{H}}_{ij}$, for $i = 1, \ldots, n$; $j = 1, \ldots, i - 1$, being obtained as

$$\tilde{\dot{\mathbf{M}}}_i = \dot{\mathbf{M}}_i + \tilde{\dot{\mathbf{M}}}_{i+1} \quad \text{and} \quad \tilde{\mathbf{H}}_{ij} \equiv \tilde{\mathbf{M}}_i\dot{\mathbf{B}}_{ij} + \mathbf{B}_{i+1,i}^T\tilde{\mathbf{H}}_{i+1,i} \tag{28}$$

in which $\tilde{\mathbf{M}}_{n+1} = \tilde{\mathbf{H}}_{n+1,n} = \mathbf{O}$. The individual element of the $n \times n$ matrix, $\mathbf{C}$, i.e., c_{ij}, for $i, j = 1, \ldots, n$ is given as

$$c_{ij} = \begin{cases} \mathbf{p}_i^T(\mathbf{B}_{ji}^T\tilde{\mathbf{M}}_j\boldsymbol{\Omega}_j + \mathbf{B}_{j+1,i}^T\tilde{\mathbf{H}}_{j+1,j} + \tilde{\dot{\mathbf{M}}}_j)\mathbf{p}_j & \text{if} \quad i \le j \\ \mathbf{p}_i^T(\tilde{\mathbf{M}}_i\mathbf{B}_{ij}\boldsymbol{\Omega}_j + \tilde{\mathbf{H}}_{ij} + \tilde{\dot{\mathbf{M}}}_i)\mathbf{p}_j & \text{otherwise.} \end{cases} \tag{29}$$

4.3 Derivation of $\boldsymbol{\tau}$ Vector. The generalized vector of forces and torques, $\boldsymbol{\tau}$, can be obtained from its expression after Eq. (20), i.e., for, $i = 1, \ldots, n$,

$$\tau_i = \mathbf{p}_i^T\tilde{\mathbf{w}}_i^E, \quad \text{where} \quad \tilde{\mathbf{w}}_i^E = \mathbf{w}_i^E + \mathbf{B}_{i+1,i}^T\tilde{\mathbf{w}}_{i+1}^E \tag{30}$$

in which $\tilde{\mathbf{w}}_i^E$ is the six-dimensional vector component of the $6n$-dimensional vector, $\tilde{\mathbf{w}}^E$, namely,

$$\tilde{\mathbf{w}}^E \equiv [(\tilde{\mathbf{w}}_1^E)^T, \ldots, (\tilde{\mathbf{w}}_n^E)^T]^T. \tag{31}$$

Note in Eq. (30) that in the absence of any external forces and moments on the end-effector, $\tilde{\mathbf{w}}_{n+1}^E = \mathbf{0}$.

5 Applications

A class of serial multibody systems are industrial manipulators. Suitable dynamic models of these manipulators are required mainly for their control and simulation purposes. Control involves *inverse dynamics,* whereas simulation requires *forward dynamics.* These algorithms are presented in the following subsections.

5.1 Inverse Dynamics Algorithm. The inverse dynamics problem is defined as, *given the motion of a manipulator, calculate the actuator forces/torques required to maintain the given motion.* Based on the dynamic equations of motion, Eq. (20) and the expressions for the elements of the associated matrices, $\mathbf{I}$, $\mathbf{C}$, and $\boldsymbol{\tau}$, Eqs. (24), (29), and (30), respectively, a recursive inverse dynamics algorithm is presented here for the following input: For $i = 1, \ldots, n$,

1 constant Denavit-Hartenberg (DH) parameters (Denavit and Hartenberg, 1955)—the DH parameters are also defined in Appendix A—of the system under study, i.e., a_i, b_i, and α_i, for a revolute pair, and a_i, b_i, and θ_i, for a prismatic pair.
2 time history of the *variable* DH parameter, i.e., θ_i, for a revolute pair, and b_i, for a prismatic joint, and their first and second time derivatives, i.e., $\dot{\theta}_i$, $\ddot{\theta}_i$, and $\dot{b}_i$, $\ddot{b}_i$.
3 mass of each body, m_i.
4 vector denoting the distance of the $(i + 1)$st joint from the ith mass center, C_i, in the $(i + 1)$st frame.
5 inertia tensor of the ith link about its mass center, C_i, in the $(i + 1)$st frame.

The inverse dynamics algorithm then calculates the joint forces/torques, i.e., τ_i, for $i = 1, \ldots, n$, in two recursive steps, as shown below:

Forward Recursion

$$\begin{aligned} \boldsymbol{\nu}_1 &= \mathbf{p}_1\dot{\theta}_1; & \boldsymbol{\xi}_1 &= \mathbf{p}_1\ddot{\theta}_1 + \boldsymbol{\Omega}_1\mathbf{p}_1\dot{\theta}_1 \\ \boldsymbol{\nu}_2 &= \mathbf{p}_2\dot{\theta}_2 + \boldsymbol{\nu}_1; & \boldsymbol{\xi}_2 &= \mathbf{p}_2\ddot{\theta}_2 + \boldsymbol{\Omega}_2\mathbf{p}_2\dot{\theta}_2 + \mathbf{B}_{21}\boldsymbol{\xi}_1 + \dot{\mathbf{B}}_{21}\boldsymbol{\nu}_1 \\ &\vdots & &\vdots \\ \boldsymbol{\nu}_n &= \mathbf{p}_n\dot{\theta}_n + \boldsymbol{\nu}_{n-1}; & \boldsymbol{\xi}_n &= \mathbf{p}_n\ddot{\theta}_n + \boldsymbol{\Omega}_n\mathbf{p}_n\dot{\theta}_n + \mathbf{B}_{n,n-1}\boldsymbol{\xi}_{n-1} \\ & & &\quad + \dot{\mathbf{B}}_{n,n-1}\boldsymbol{\nu}_{n-1} \end{aligned}$$

Backward Recursion

$$\begin{aligned} \boldsymbol{\gamma}_n &= \mathbf{M}_n\boldsymbol{\xi}_n + \dot{\mathbf{M}}_n\boldsymbol{\nu}_n; & \tau_n &= \mathbf{p}_n^T\boldsymbol{\gamma}_n \\ \boldsymbol{\gamma}_{n-1} &= \mathbf{M}_{n-1}\boldsymbol{\xi}_{n-1} + \dot{\mathbf{M}}_{n-1}\boldsymbol{\nu}_{n-1} + \mathbf{B}_{n,n-1}^T\boldsymbol{\gamma}_n; & \tau_{n-1} &= \mathbf{p}_{n-1}^T\boldsymbol{\gamma}_{n-1} \\ &\vdots & &\vdots \\ \boldsymbol{\gamma}_1 &= \mathbf{M}_1\boldsymbol{\xi}_1 + \dot{\mathbf{M}}_1\boldsymbol{\nu}_1 + \mathbf{B}_{21}^T\boldsymbol{\gamma}_2; & \tau_1 &= \mathbf{p}_1^T\boldsymbol{\gamma}_1 \end{aligned}$$

where $\boldsymbol{\nu}_i$, $\boldsymbol{\xi}_i$, and $\boldsymbol{\gamma}_i$ are the six-dimensional vectors. Note from the expression for τ_i above and that in Eq. (30), $\tilde{\mathbf{w}}_i^E \equiv \boldsymbol{\gamma}_i$, while $\tilde{\mathbf{w}}_{n+1}^E = \mathbf{0}$. This implies that, without any external forces/moments on the end-effector, only inertia forces, $\boldsymbol{\gamma}_i$, contribute to $\mathbf{w}_i^E$, and, hence, the required joint forces/torques are due to system motion only.

For an all revolute-joint serial manipulator, the computational complexity of the above algorithm is compared in Table 1 with

Table 2 Computational complexities in forward dynamics

Algorithm	M	A	$n = 6$	$n = 12$
Proposed	$201n - 335$	$193n - 361$	$871M\ 797A$	$2077M\ 1955A$
Featherstone (1983)	$199n - 198$	$174n - 173$	$996M\ 871A$	$2190M\ 1915A$
Walker and Orin (1982)	$\frac{1}{6}n^3 + 11\frac{1}{2}n^2 + 38\frac{1}{3}n - 47$	$\frac{1}{6}n^3 + 7n^2 + 38\frac{5}{6}n - 46$	$633M\ 480A$	$2357M\ 1716A$

M: Multiplication/Division; A: Addition/Subtraction

Downloaded 04 May 2010 to 171.66.16.27. Redistribution subject to ASME license or copyright; see http://www.asme.org/terms/Terms_Use.cfm

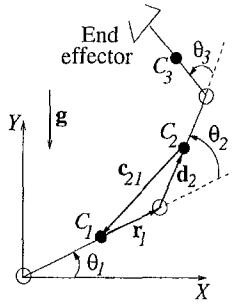


Fig. 4 A three-degrees-of-freedom manipulator

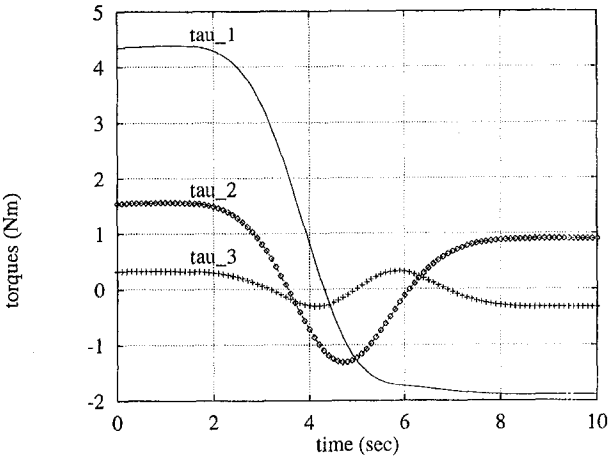


Fig. 5 Torques for three-degrees-of-freedom manipulator

some other existing algorithms. Even though the algorithm is not the best but it is very simple, as evident from the two-step algorithm where six-dimensional vectors are treated similar to those of three dimensional vectors. That is, if one knows $\boldsymbol{\nu}_1$ finding out $\boldsymbol{\nu}_2$ is very similar to the evaluation of the linear velocity of body 2 from the known linear velocity of body 1. A computer software called RIDIM (Recursive Inverse Dynamics of Industrial Manipulators) is developed in C++, which has the following features:

- RIDIM can handle manipulators with both revolute and prismatic pairs or joints;
- gravity is taken into account by providing negative acceleration due to the gravity, denoted by **g**, to the first body, #1 (Kane and Levinson, 1983), i.e., an additional term is added to $\boldsymbol{\xi}_1$ as

$$\boldsymbol{\xi}_1 = \mathbf{p}_1\ddot{\theta}_1 + \boldsymbol{\Omega}_1\mathbf{p}_1\dot{\theta}_1 + \boldsymbol{\rho} \quad \text{where} \quad \boldsymbol{\rho} \equiv [\mathbf{0}^T, -\mathbf{g}^T]^T. \tag{32}$$

The rest of the algorithm remains same.

The software is illustrated with two examples, as in Section 6.

5.2 Forward Dynamics Algorithm. Forward dynamics is defined as, *given the joint forces/torques, find the joint accelerations.* This step is required in simulation, where the joint accelerations, $\ddot{\boldsymbol{\theta}}$, are solved from the dynamic equations of motion, Eq. (20), and integrated numerically to obtain the joint velocities and positions, $\dot{\boldsymbol{\theta}}$ and $\boldsymbol{\theta}$, respectively, for a given set of initial conditions.

The required input for the forward dynamics algorithm are as follows: For $i = 1, \ldots, n$,

- inverse dynamics items, 1, and 3–5, as in Section 5.1.
- initial value for the *variable* DH parameter, i.e., θ_i, for a revolute pair, and b_i, for a prismatic pair, and their first time derivative, i.e., $\dot{\theta}_i$ and $\dot{b}_i$.
- time history of the input joint forces/torques, i.e., τ_i.
- each component of the six-dimensional vector, $\boldsymbol{\phi} \equiv \boldsymbol{\tau} - \mathbf{C}\dot{\boldsymbol{\theta}}$, i.e., ϕ_i, which is to be computed from any recursive inverse dynamics scheme, e.g., the one given in Section 5.1, while $\ddot{\boldsymbol{\theta}} = \mathbf{0}$ (Walker and Orin, 1982).

The forward dynamics algorithm, as proposed in Saha (1997), is presented here for the sake of completeness of this paper. The algorithm is based on the $\mathbf{UDU}^T$ decomposition of the generalized inertia matrix, $\mathbf{I}$ of Eq. (20), i.e., $\mathbf{I} \equiv \mathbf{UDU}^T$, as outlined in Appendix B. Substituting for $\mathbf{I}$, and, $\boldsymbol{\phi} \equiv \boldsymbol{\tau} - \mathbf{C}\dot{\boldsymbol{\theta}}$, in Eq. (20), one obtains

$$\mathbf{UDU}^T\ddot{\boldsymbol{\theta}} = \boldsymbol{\phi}. \tag{33}$$

A three-step recursive scheme is then used to calculate the joint accelerations from the above equations, i.e.,

1 Solution for $\hat{\boldsymbol{\tau}}$: The solution, $\hat{\boldsymbol{\tau}} = \mathbf{U}^{-1}\boldsymbol{\phi}$, is evaluated as

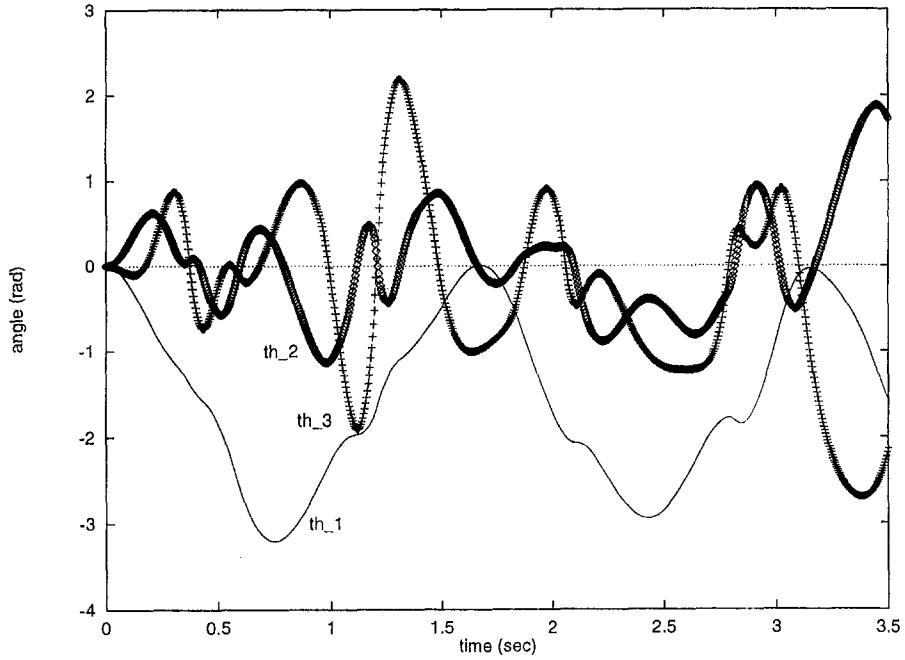


Fig. 6 Simulated joint angles of the planar manipulator

Downloaded 04 May 2010 to 171.66.16.27. Redistribution subject to ASME license or copyright; see http://www.asme.org/terms/Terms_Use.cfm

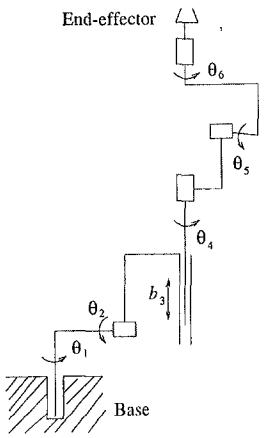


Fig. 7 The six-degrees-of-freedom Stanford arm

$$\hat{\tau}_i = \phi_i - \mathbf{p}_i^T \boldsymbol{\eta}_{i,i+1} \tag{34}$$

where $\hat{\tau}_n \equiv \phi_n$, and the six-dimensional vector, $\boldsymbol{\eta}_{i,i+1}$, is obtained as

$$\boldsymbol{\eta}_{i,i+1} \equiv \mathbf{B}_{i+1,i}^T \boldsymbol{\eta}_{i+1} \quad \text{and} \quad \boldsymbol{\eta}_{i+1} \equiv \boldsymbol{\psi}_{i+1} \hat{\tau}_{i-1} + \boldsymbol{\eta}_{i+1,i+2} \tag{35}$$

in which $\boldsymbol{\eta}_{n,n+1} = \mathbf{0}$. The new variable, $\boldsymbol{\psi}_{i+1}$, is the six-dimensional vector which is defined in Appendix B.

2 Solution for $\tilde{\tau}$: The solution of the equation, $\mathbf{D}\tilde{\tau} = \hat{\tau}$, involves the inverse of the diagonal matrix, $\mathbf{D}$ of Eq. (54), which is simple, namely, $\mathbf{D}^{-1}$ has only nonzero diagonal elements that are the reciprocal of the corresponding diagonal elements of $\mathbf{D}$. Thus, vector $\tilde{\tau}$ is obtained as follows: For $i = 1, \ldots, n$,

$$\tilde{\tau}_i = \hat{\tau}_i / \hat{m}_i.$$

The scalar, $\hat{m}_i$, is defined in Eq. (47).

3 Solution for $\ddot{\theta}$: In this step, $\ddot{\boldsymbol{\theta}} = \mathbf{U}^{-T}\tilde{\tau}$, is calculated, for $i = 2, \ldots, n$

$$\ddot{\theta}_i = \tilde{\tau}_i - \boldsymbol{\psi}_i^T \boldsymbol{\mu}_{i,i-1} \tag{36}$$

where $\ddot{\theta}_1 \equiv \tilde{\tau}_1$, and the six-dimensional vector, $\boldsymbol{\mu}_{i,i-1}$, is obtained from

$$\boldsymbol{\mu}_{i,i-1} \equiv \mathbf{B}_{i,i-1} \boldsymbol{\mu}_{i-1} \quad \text{and} \quad \boldsymbol{\mu}_{i-1} \equiv \mathbf{p}_{i-1} \ddot{\theta}_{i-1} + \boldsymbol{\mu}_{i-1,i-2} \tag{37}$$

in which $\boldsymbol{\mu}_{10} = \mathbf{0}$.

The complexity of the proposed forward dynamics algorithm is compared in Table 2 with some other algorithms. The complexity of the proposed algorithm is very similar to those of Featherstone (1983).

Based on the above algorithm, a simulation software, RFDSIM (Recursive Forward Dynamics and Simulation of Industrial Manipulators) is also developed in C++ in which the numerical integration scheme is based on the Runge-Kutta fifth/sixth-order method (Press et al., 1997).

6 Examples

For the illustration of the inverse and forward dynamics algorithms developed in Sections 5.1 and 5.2, respectively, two manipulators, namely, a three-degrees-of-freedom planar manipulator and a six-degrees-of-freedom Stanford arm, as shown in Figs. 4 and 7, respectively, are analyzed using RIDIM and RFDSIM software.

6.1 A Three-Degrees-of-Freedom Planar Manipulator. The manipulator under study is assumed to move in the X–Y plane, whereas the gravity is working in the negative Y direction, as indicated in Fig. 4. Let $\mathbf{i}$ and $\mathbf{j}$ be the two unit vectors parallel to the axes, X and Y, respectively, and $\mathbf{k} \equiv \mathbf{i} \times \mathbf{j}$. The expressions for the three joint torques, namely, τ_1, τ_2, and τ_3, are evaluated explicitly from the inverse dynamics algorithm given in Section 5.1, which exactly match with those reported in Angeles (1997). Moreover, RIDIM is used to find the joint torques for the following normal joint angle trajectories and their corresponding 1st and 2nd time derivatives:

$$\theta_i = \frac{1}{2}\left[\frac{2\pi}{T} t - \sin\left(\frac{2\pi}{T} t\right)\right] \tag{38}$$

with $T = 10.0$ sec. The joint torques obtained from RIDIM are plotted in Fig. 5, where "tau_1" "tau_2" and "tau_3" denote the joint torques, τ_1, τ_2, and τ_3, respectively. The plots are also verified with the plots obtained from the explicit expressions.

In order to test RFDSIM, free fall simulation, i.e., motion due to gravity only, without any external joint torque, of the manipulator is carried out with the initial conditions as $\theta_i(0) = \dot{\theta}_i(0) = 0$, for $i = 1, 2, 3$. The variations of the simulated joint angles are shown in Figs. 6, where "th_1," "th_2," and "th_3" represent θ_1, θ_2, and θ_3, respectively. Note from Fig. 4 that due to gravity the first joint angle, θ_1, will increase initially in the negative direction, as evident from Fig. 6. Moreover, the system under gravity behaves as a triple pendulum. These is evident from all the joint angle variations, namely, θ_1, θ_2, and θ_3 of Fig. 6.

6.2 A Stanford Arm. As a second example, a more general six-axis six-degrees-of-freedom manipulator, namely, the Stanford arm, as shown in Fig. 7, is taken whose Denavit-Hartenberg (DH) parameters, along with the mass and inertia properties are given in Table 3. The normal joint trajectory for the six joints are taken from Cyril (1988) as

$$\theta_i = \frac{1}{2}\left[\frac{2\pi}{T} t - \sin\left(\frac{2\pi}{T} t\right)\right] \quad \text{for} \quad i \neq 3 \tag{39a}$$

$$b_3 = \frac{1}{2}\left[\frac{2\pi}{T} t - \sin\left(\frac{2\pi}{T} t\right)\right] \tag{39b}$$

with $T = 10.0$ sec, $\theta_i(0) = 0$, for $i \neq 2, 3$, $\theta_2(0) = 90$ deg, $b_3(0) = 0$, and $\theta_i(T) = 60$ deg, for $i \neq 3$ and $b_3(T) = 0.1$ m. The joint torques are calculated from RIDIM and plotted in Figs.

Table 3 DH parameters, and mass and inertia properties of Stanford arm

Link	a_i (m)	b_i (m)	α_i (deg)	θ_i (deg)	m_i (kg)	r_x	r_y (m)	r_z	I_{xx}	I_{yy} (kg-m^2)	I_{zz}
1	0	.2	−90	θ_1 (0)	9	0	−.1	0	.01	.02	.01
2	0	.1	−90	θ_2 (90)	6	0	0	0	.05	.06	.01
3	0	b_3(0)	0	0	4	0	0	0	.4	.4	.01
4	0	.6	90	θ_4 (0)	1	0	−.1	0	.001	.001	.0005
5	0	0	−90	θ_5 (0)	.6	0	0	0	.0005	.0005	.0002
6	0	0	0	θ_6 (0)	.5	0	0	0	.003	.001	.002

Downloaded 04 May 2010 to 171.66.16.27. Redistribution subject to ASME license or copyright; see http://www.asme.org/terms/Terms_Use.cfm

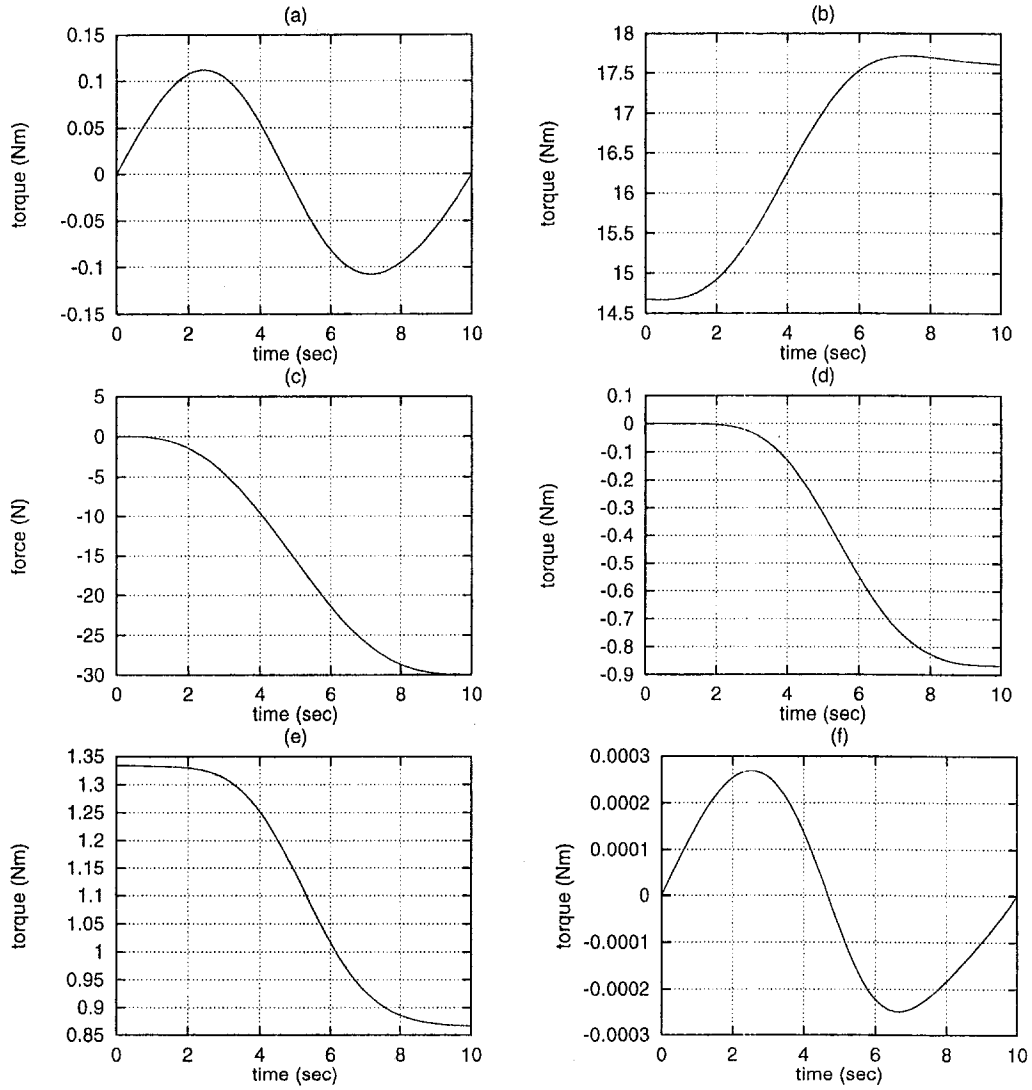


Fig. 8 Torques and force for the six-degrees-of-freedom Stanford arm at (*a*) Joint 1; (*b*) Joint 2; (*c*) Joint 3; (*d*) Joint 4; (*e*) Joint 5; (*f*) Joint 6

8(*a*)–(*f*), which exactly match with those reported in Cyril (1988) for the same arm.

Interpretations similar to the planar manipulator, as given in Section 6.1, can be provided for the Stanford arm also. For example, the motion of joint 3 should sharply increase once the joint 2 turns more than 90 deg, which are evident from Figs. 9(*c*) and (*b*), respectively.

7 Conclusions

A dynamic modeling methodology for serial multi-body mechanical systems is presented. The modeling is based on the Newton-Euler equations of motion and the DeNOC matrices associated with the kinematic constraints, namely, Eq. (16). The dynamic modeling using the DeNOC has the following features:

- physical interpretations of many terms, e.g., the mass matrix of a *composite body,* as defined after Eq. (23*b*), and others, as given after Eqs. (14), (17), and (50).
- unlike the original definition of the NOC (Angeles and Lee, 1988), the DeNOC provides recursive analytical expressions for the elements of the associated matrices, i.e., **I**, **C**, and $\boldsymbol{\tau}$, Eqs. (24), (29), and (30), respectively.
- due to the recursive expressions of the elements of matrices, **I**, **C**, and $\boldsymbol{\tau}$, recursive $\mathcal{O}(n)$ algorithms for inverse and forward dynamics are possible for a general n-axis industrial manipulator, as presented in Section 5.1 and 5.2.

The computational complexities for both the inverse and forward dynamics algorithms are computed and compared in Tables 1 and 2, respectively. The algorithms are not the best in terms of the complexities, however, provide simple algorithms, particularly, the inverse dynamics algorithm presented in Section 5.1. They are also developed uniformly from the same set of equations, namely, Eqs. (20), (24), (29), and (30), which is simple to implement. Two software, namely, RIDIM and RFDSIM are developed in C++, which are tested with respect to two manipulators, namely, a three-degrees-of-freedom planar manipulator and a six-degrees-of-freedom Stanford arm. The results from RIDIM are compared with those available in the literature for the same systems, namely, with Angeles (1997) for the three-degrees-of-freedom manipulator and with Cyril (1988) for the six-degrees-of-freedom Stanford arm, whereas the results of RFDSIM are interpreted intuitively.

Acknowledgment

A part of the research work reported in this paper was possible under the Department of Science and Technology, Government of India, Grant No. HR/OY/E-02/96. The author sincerely acknowledges the support.

References

Angeles, J., 1997, *Fundamentals of Robotic Mechanical Systems,* Springer-Verlag, New York.

Downloaded 04 May 2010 to 171.66.16.27. Redistribution subject to ASME license or copyright; see http://www.asme.org/terms/Terms_Use.cfm

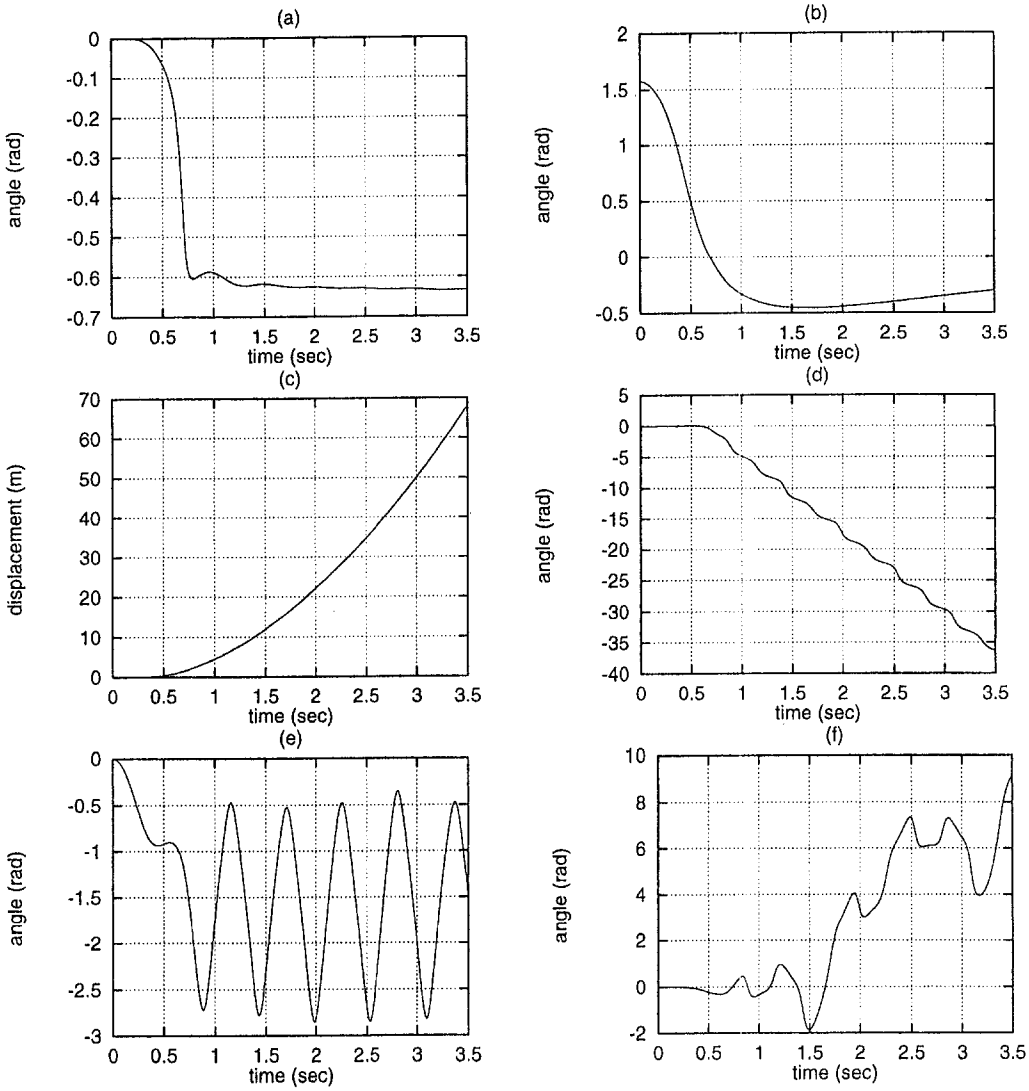


Fig. 9 Simulated joint angles and displacement for the six-degrees-of-freedom Stanford arm at (*a*) Joint 1; (*b*) Joint 2; (*c*) Joint 3; (*d*) Joint 4; (*e*) Joint 5; (*f*) Joint 6

Angeles, J., and Lee, S., 1988, "The Formulation of Dynamical Equations of Holonomic Mechanical Systems Using a Natural Orthogonal Complement," ASME JOURNAL OF APPLIED MECHANICS, Vol. 55, pp. 243–244.

Angeles, J., and Ma, O., 1988, "Dynamic Simulation of n-axis Serial Robotic Manipulators Using a Natural Orthogonal Complement," *Int. J. of Rob. Res.*, Vol. 7, No. 5, pp. 32–47.

Angeles, J., Ma, O., and Rojas, A., 1989, "An Algorithm for the Inverse Dynamics of n-Axis General Manipulator Using Kane's Formulation of Dynamical Equations," *Computers and Mathematics with Applications,* Vol. 17, No. 12, pp. 1545–1561.

Armstrong, W. W., 1979, "Recursive Solution to the Equations of Motion of an n-Link Manipulator," *Proc. of the 5th World Cong. on Th. of Mach. and Mech.*, Vol. 2, Montreal, Canada, ASME, New York, pp. 1343–1346.

Ascher, U. M., Pai, D. K., and Cloutier, B. P., 1997, "Forward Dynamics, Elimination Methods, and Formulation Stiffness in Robot Simulation," *Int. J. of Rob. Res.*, Vol. 16, No. 6, pp. 749–758.

Cyril, X., 1988, "Dynamics of Flexible-Link Manipulators," Ph.D. thesis, McGill University, Canada.

Denavit, J., and Hartenberg, R. S., 1955, "A Kinematic Notation for Lower-Pair Mechanisms Based on Matrices," ASME JOURNAL OF APPLIED MECHANICS, Vol. 77, pp. 215–221.

Featherstone, R., 1983, "The Calculation of Robot Dynamics Using Articulated-Body Inertias," *Int. J. of Rob. Res.*, Vol. 2, No. 1, pp. 13–30.

Fijany, A., Sharf, I., and D'Eleuterio, M. T. D., 1995, "Parallel $\mathcal{O}(\log N)$ Algorithms for Computation of Manipulator Forward Dynamics," *IEEE Trans. on R&A,* Vol. 11, No. 3.

Hollerbach, J. M., 1980, "A Recursive Lagrangian Formulation of Manipulator Dynamics and a Comparative Study of Dynamics Formulation Complexity," *IEEE Trans. on Sys., Man, and Cybernatics,* Vol. SMC-10, pp. 730–736.

Huston, H., and Passerello, C. E., 1974, "On Constraint Equations—A New Approach," ASME JOURNAL OF APPLIED MECHANICS, Vol. 41, pp. 1130–1131.

Jain, A., and Rodriguez, G., 1995, "Diagonalized Lagrangian Robot Dynamics," *IEEE Trans. on R&A,* Vol. 11, No. 4, pp. 571–584.

Kamman, J. W., and Huston, R. L., 1984, "Dynamics of Constrained Multibody Systems," ASME JOURNAL OF APPLIED MECHANICS, Vol. 51, pp. 899–903.

Kane, T. R., and Levinson, D. A., 1983, "The Use of Kane's Dynamical Equations for Robotics," *Int. J. of Rob. Res.*, Vol. 2, No. 3, pp. 3–21.

Lilly, K. W., and Orin, D. E., 1990, "Efficient $\mathcal{O}(n)$ Computation of the Operational Space Inertia Matrix," *Proc. of the IEEE Conf. on R&A,* Vol. 2, Cincinnati, OH, May 13–18, pp. 1014–1019.

Luh, J. Y. S., Walker, M. W., and Paul, R. P. C., 1980, "On-Line Computational Scheme for Mechanical Manipulators," ASME *Journal of Dynamic Systems, Measurement and Control,* Vol. 102, pp. 69–76.

McMillan, S., and Orin, D. E., 1995, "Efficient Computation of Articulated-Body Inertias Using Successive Axial Screws," *IEEE Trans. on R&A,* Vol. 11, No. 4, pp. 606–611.

Press, W. H., Teukolsky, S. A., Vellerling, W. T., and Flannery, B. P., 1997, *Numerical Recipes in C,* 2nd Ed., Cambridge University Press, New Delhi.

Rodriguez, G., 1987, "Kalman Filtering, Smoothing, and Recursive Robot Arm Forward and Inverse Dynamics," *IEEE Trans. on R&A,* Vol. RA-3, No. 6, pp. 624–639.

Rodriguez, G., Jain, A., and Kreutz-Delgado, K., 1991, "A Spatial Operator Algebra for Manipulation Modeling and Control," *Int. J. of Rob. Res.*, Vol. 10, No. 4, pp. 371–381.

Rodriguez, G., and Kreutz-Delgado, K., 1992, "Spatial Operator Factorization and Inversion of the Manipulator Mass Matrix," *IEEE Trans. on R&A,* Vol. 8, No. 1, pp. 65–76.

Saha, S. K., and Angeles, J., 1991, "Dynamics of Nonholonomic Mechanical Systems Using a Natural Orthogonal Complement," ASME JOURNAL OF APPLIED MECHANICS, Vol. 58, pp. 238–243.

Downloaded 04 May 2010 to 171.66.16.27. Redistribution subject to ASME license or copyright; see http://www.asme.org/terms/Terms_Use.cfm

Saha, S. K., 1997, "A Decomposition of the Manipulator Inertia Matrix," *IEEE Trans. on R&A*, Vol. 13, No. 2, pp. 301–304.

Schiehlen, W., 1991, "Computational Aspects in Multibody System Dynamics," *Computer Methods in Applied Mechanics and Engineering*, Vol. 90, No. 1–3, pp. 569–582.

Sciavicco, L., and Siciliano, B., 1996, *Modeling and Control of Robot Manipulators*, McGraw-Hill, New York.

Stewart, G. E., 1973, *Introduction to Matrix Computations*, Academic Press, San Diego, CA.

Walker, M. W., and Orin, D. E., 1982, "Efficient Dynamic Computer Simulation of Robotic Mechanisms," ASME *Journal of Dynamic Systems, Measurement and Control*, Vol. 104, pp. 205–211.

Wehage, R. A., and Haug, E. J., 1982, "Generalized Coordinate Partitioning for Dimension Reduction in Analysis of Constrained Dynamic Systems," ASME *Journal of Mechanical Design*, Vol. 104, pp. 247–255.

APPENDIX A

Denavit-Hartenberg Nomenclature

In order to describe the Denavit-Hartenberg (DH) nomenclatures (Denavit and Hartenberg, 1955) that is followed here, note that the manipulator under study consists of $n + 1$ links, namely, a "base" and n links, denoted by #1, . . . , #n, coupled by n pairs numbered as 1, . . . , n, respectively. As shown in Fig. 1, ith pair couples the $(i - 1)$st and the ith links. Moreover, a coordinate system X_i, Y_i, Z_i is attached to the $(i - 1)$st link.

Then, for the first n frames, DH parameters are defined according to the following rules: Referring to Fig. 10,

1 Z_i is the axis of the ith pair. Its positive direction can be chosen arbitrarily.
2 X_i is defined as the common perpendicular to Z_{i-1} and Z_i, directed from the former to the latter. The origin of the ith frame, O_i, is the point where X_i intersects Z_i. If these two axes intersect, the positive direction of X_i is chosen arbitrary. The origin, O_i, is coincides with the origin of the $(i - 1)$st frame, O_{i-1}.
3 the distance between Z_i and Z_{i+1} is defined as a_i, which is *non-negative.*
4 the Z_i coordinate of the intersection of the X_{i+1} axis with Z_i is defined as b_i, which thus can be either positive or negative. For a prismatic joint, b_i is variable.
5 the angle between Z_i and Z_{i+1} is defined as α_i, and is measured about the positive direction of X_{i+1}, and
6 the angle between X_i and X_{i+1} is defined as θ_i, and is measured about the positive direction of Z_i. For a revolute joint, θ_i is variable.

Since no $(n + 1)$st link exists the above definitions do not apply to the $(n + 1)$st frame and it can be chosen at will.

APPENDIX B

Decomposition of the GIM, I

In order to obtain the $\mathbf{UDU}^T$ decomposition of the GIM, **I** of Eq. (20)—the elements of which are given by Eq. (24)—the rules of the Gaussian elimination (GE) (Stewart, 1973) are applied on these elements for the Reverse Gaussian Elimination (RGE), as proposed in Saha (1997). The scheme is reproduced here for the completeness of the paper.

B.1 RGE of the GIM, I. Conventionally, the GE (Stewart, 1973) begins from the first column of the matrix under interest. In the proposed elimination, it is assumed that the GE of matrix **I**, Eq. (20), whose elements are given by Eq. (24), starts from the nth column. This is to obtain recursive relations starting from the nth body. Thus, the RGE name is used. In RGE, after the annihilation of the first $(n - 1)$ elements of the nth column, the modified inertia matrix, denoted by $\mathbf{L}_n$, is expressed as

$$\mathbf{L}_n \equiv \begin{bmatrix} i_{11}^{(n)} & & \text{sym} & 0 \\ \vdots & \ddots & & 0 \\ i_{n-1,1}^{(n)} & \cdots & i_{n-1,n-1}^{(n)} & 0 \\ i_{n1} & \cdots & i_{n,n-1} & i_{nn} \end{bmatrix} \tag{40}$$

where i_{nn} is the *pivot* (Stewart, 1973) and $i_{ij}^{(n)}$ are the modified elements of **I**, whereas "sym" denotes the symmetric elements of the $(n - 1) \times (n - 1)$ matrix, resulting from the deletion of the nth row and column of matrix $\mathbf{L}_n$. Equation (40) is realized by premultiplying matrix **I** with the *elementary upper triangular matrix* (EUTM) of order n and index n, as done in GE with *elementary lower triangular matrix* (ELTM) (Stewart, 1973). An EUTM of order n and index k, denoted by $\mathbf{E}_k$, is defined as

$$\mathbf{E}_k \equiv \mathbf{1} - \boldsymbol{\alpha}_k \boldsymbol{\lambda}_k^T \tag{41}$$

where **1** is the $n \times n$ identity matrix and the n-dimensional vectors, $\boldsymbol{\alpha}_k$ and $\boldsymbol{\lambda}_k$, are defined by

$$\boldsymbol{\alpha}_k \equiv [\alpha_{1k}, \ldots, \alpha_{k-1,k}, 0, \ldots, 0]^T \tag{42}$$

$$\boldsymbol{\lambda}_k \equiv [0, \ldots, 0, 1, \ldots, 0]^T. \tag{43}$$

From Eqs. (42) and (43), the EUTM, $\mathbf{E}_k$, Eq. (41), has the following structure:

$$\mathbf{E}_k \equiv \begin{bmatrix} 1 & 0 & \cdots & -\alpha_{1k} & \cdots & 0 \\ & \ddots & \vdots & \vdots & \vdots & \vdots \\ & & 1 & -\alpha_{k-1,k} & \cdots & 0 \\ & & & 1 & \cdots & 0 \\ & & 0's & & \ddots & \vdots \\ & & & & & 1 \end{bmatrix} \tag{44}$$

where "$0's$" imply zeros. Moreover, in the RGE, the modified matrix after the annihilation of the first k–1 elements of the kth column is expressed as

$$\mathbf{L}_k = \mathbf{E}_k \mathbf{L}_{k+1} \tag{45}$$

Note here that, if $k = n$ and $\mathbf{L}_{n+1} \equiv \mathbf{I}$, and the matrix, $\mathbf{L}_n$ of Eq. (40), follows from Eq. (45). Furthermore, the elements of $\mathbf{E}_k$ and $\mathbf{L}_k$, α_{ik} and $i_{ij}^{(k)}$, respectively, are computed from the following scheme:

- For $k = n, \ldots, 2$; Do $i = k - 1, \ldots, 1$; Do $j = i, \ldots, 1$

$$\alpha_{ik} = \mathbf{p}_i^T \boldsymbol{\psi}_{ik} \quad \text{and} \quad i_{ij}^{(k)} = \mathbf{p}_i^T \hat{\mathbf{M}}_{ik} \mathbf{B}_{ij} \mathbf{p}_j \tag{46}$$

  end do j; end do i; end for k.

In Eq. (46), matrix $\mathbf{B}_{ij}$, and vectors $\mathbf{p}_i$ and $\mathbf{p}_j$ are defined in Eq. (13), whereas the six-dimensional vector $\boldsymbol{\psi}_{ik}$ and the terms associated to it are given as

$$\hat{\boldsymbol{\psi}}_k \equiv \hat{\mathbf{M}}_k \mathbf{p}_k, \quad \hat{\boldsymbol{\psi}}_{ik} \equiv \mathbf{B}_{ki}^T \hat{\boldsymbol{\psi}}_k, \quad \hat{m}_k \equiv \mathbf{p}_k^T \hat{\boldsymbol{\psi}}_k, \tag{47}$$

$$\boldsymbol{\psi}_k \equiv \frac{\hat{\boldsymbol{\psi}}_k}{\hat{m}_k}, \quad \text{and} \quad \boldsymbol{\psi}_{ik} \equiv \frac{\hat{\boldsymbol{\psi}}_{ik}}{\hat{m}_k}. \tag{48}$$

In Eq. (47), $\hat{\mathbf{M}}_k \equiv \hat{\mathbf{M}}_{k,k+1}$, which is used to simplify the notation. The 6×6 matrix, $\hat{\mathbf{M}}_{ik}$ of Eq. (46) and $\hat{\mathbf{M}}_k$ ($\equiv \hat{\mathbf{M}}_{k,k+1}$) of Eq. (47), are evaluated from the following relation:

$$\hat{\mathbf{M}}_{ik} \equiv \tilde{\mathbf{M}}_i - \boldsymbol{\Psi}_{ik}, \quad \text{where} \quad \boldsymbol{\Psi}_{ik} \equiv \sum_{l=k}^{n} \hat{\boldsymbol{\psi}}_{il} \boldsymbol{\psi}_{il}^T \tag{49}$$

and $\tilde{\mathbf{M}}_i$ is given in Eq. (23a). Note that, the 6×6 matrix, $\boldsymbol{\Psi}_{ik}$, has a recursive relation, whose substitution, along with that of $\tilde{\mathbf{M}}_i$, Eq.

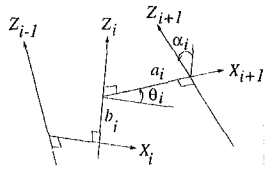


Fig. 10 Denavit-Hartenberg nomenclature

Downloaded 04 May 2010 to 171.66.16.27. Redistribution subject to ASME license or copyright; see http://www.asme.org/terms/Terms_Use.cfm

(23*b*), into the expression of $\hat{\mathbf{M}}_{ik}$, Eq. (49), leads to a recursive equation, i.e.,

$$\hat{\mathbf{M}}_{ik} = \mathbf{M}_i + \mathbf{B}_{i+1,i}^T \hat{\mathbf{M}}_{i+1,k} \mathbf{B}_{i+1,i} \quad \text{and} \quad \hat{\mathbf{M}}_{kk} = \hat{\mathbf{M}}_k - \hat{m}_k \boldsymbol{\psi}_k \boldsymbol{\psi}_k^T \quad (50)$$

where $k = n, \ldots, 2$; $i = k - 1, \ldots, 1$. Moreover, for $i = k - 1$, $\hat{\mathbf{M}}_{i+1,k} \equiv \hat{\mathbf{M}}_{kk}$, and $\hat{\mathbf{M}}_n \equiv \mathbf{M}_n$.

Note that, in contrast to the definition of $\tilde{\mathbf{M}}_i$ associated to the *composite body, i*, Eq. (23*a*), the matrix, $\hat{\mathbf{M}}_i$, as in Eq. (50) for $k = i$, has the following interpretation: It represents the mass and inertia properties of the *articulated body i*, which is defined as the system consisting of bodies #*i*, . . . , #*n* that are coupled by joints $i + 1, \ldots, n$, i.e., replace the fixed joints of the *i*th composite body, as shown in Fig. 1 by the dotted line, by a kinematic pair, say, a revolute joint. Here, the matrix, $\hat{\mathbf{M}}_i$, incorporates the effects of joints into the rigid *composite system i*, resulting $\tilde{\mathbf{M}}_i$ of Eq. (23*a*). In fact, comparison of the expressions for $\tilde{\mathbf{M}}_i$ and $\hat{\mathbf{M}}_i$ ($\equiv \hat{\mathbf{M}}_{i,i+1}$), as in Eqs. (23*b*) and can be obtained from (49), respectively, show that the 6×6 matrix, $\boldsymbol{\Psi}_{i,i+1}$, causes this change. This could have prompted Lilly and Orin (1990) to name the matrix as the *articulation transformation* matrix. Matrix, $\hat{\mathbf{M}}_i$ is also termed as the *articulated-body inertia of link i* (Featherstone, 1983), and the *state estimation error covariance* (Rodriguez, 1987; Rodriguez and Kreutz-Delgado, 1992) that satisfies the discrete Riccati equations. Thus, it is commented that a correlation exists between the Gaussian elimination technique and the Kalman filtering approach, which can be exploited for the deeper understanding of the dynamics characteristics of a complex mechanical system. Finally, the scalar, $\hat{m}_i$, is interpreted as the moment of inertia of the *articulated body, i*, about the axis of rotation of the *i*th joint.

B.2 UDU^T Decomposition. The scheme to obtain the **UDU**^{T} are then given in the following steps:

1 The RGE of **I**, whose elements are given by Eq. (24), can be expressed as

$$\mathbf{EI} = \mathbf{L}_2, \quad \text{where} \quad \mathbf{E} \equiv \mathbf{E}_2 \ldots \mathbf{E}_n \quad (51)$$

in which the $n \times n$ matrix, $\mathbf{E}_k$, for $k = n, \ldots, 2$, is the EUTM and **E** and $\mathbf{L}_2$, respectively, are the $n \times n$ upper and lower triangular matrices.

2 An essential property of the EUTM, $\mathbf{E}_K$, similar to the ELTM (Stewart, 1973), is

$$\mathbf{E}_k^{-1} \equiv (\mathbf{1} - \boldsymbol{\alpha}_k \boldsymbol{\lambda}_k^T)^{-1} = \mathbf{1} + \boldsymbol{\alpha}_k \boldsymbol{\lambda}_k^T \quad (52)$$

where $\boldsymbol{\alpha}_k$ and $\boldsymbol{\lambda}_k$ are defined in Eqs. (42) and (43), respectively. Using Eq. (52), the GIM, **I**, is written from Eq. (51) as

$$\mathbf{I} = \mathbf{UL}_2, \quad \text{where} \quad \mathbf{U} \equiv \mathbf{E}^{-1}. \quad (53)$$

In Eq. (53), **U** and $\mathbf{L}_2$ are the $n \times n$ upper and lower triangular matrices, respectively. Moreover, from the inverse of the EUTM, Eq. (52), it is clear that the diagonal elements of **U** are unity and the above-diagonal elements are the components of the vector, $\boldsymbol{\alpha}_k$, for $k = 2, \ldots, n$, that are evaluated in Eq. (46).

3 Since the factorization, given by Eq. (53) is not unique (Stewart, 1973), a unique decomposition is obtained by normalizing the elements of $\mathbf{L}_2$ as

$$\mathbf{L}_2 = \mathbf{DL}, \quad \text{where} \quad \mathbf{D} \equiv \text{diag}\,[\hat{m}_1, \ldots, \hat{m}_n] \quad (54)$$

D being the $n \times n$ diagonal matrix, whose non zero elements are those of the matrix, $\mathbf{L}_2$, as calculated in Eq. (47). Hence, the diagonal elements of matrix **L** are unity.

4 Since, for the SPD matrix, **I**, $\mathbf{L} \equiv \mathbf{U}^T$ (Stewart, 1973), the desired decomposition of the manipulator GIM, **I** of Eq. (20), is given as

$$\mathbf{I} = \mathbf{UDU}^T \quad (55)$$

where the elements of the matrices, **U** and **D**, are evaluated using Eqs. (46)–(50).

Downloaded 04 May 2010 to 171.66.16.27. Redistribution subject to ASME license or copyright; see http://www.asme.org/terms/Terms_Use.cfm

B. Hu

P. Eberhard

Institute B of Mechanics,
University of Stuttgart,
Pfaffenwaldring 9,
70550 Stuttgart, Germany
e-mail: [hbi,pe]@mechb.uni-stuttgart.de

Response Bounds for Linear Damped Systems

In this paper response bounds of linear damped systems are reviewed and new response bounds are presented for free vibrations and forced vibrations under impulsive, step, and harmonic excitation. In comparison to the response bounds available in the literature, the ones presented here are not only closer to the exact responses, but are also simpler to compute. Previous bounds are given only on the Euclidean norm of the state vector or the displacement vector. Here, the response bounds are also given on individual coordinates, information which is more meaningful in engineering.

1 Introduction

Responses of linear damped systems are available from the solution of differential equations. However, for large structural systems, which are usually modeled by the finite element method, calculating dynamic responses sometimes requires too much computation time. On the other hand, knowing the exact response of every coordinate is not always necessary. Therefore, simple response bounds are of great interest, both from a mathematical point of view and from an engineering point of view. For classically damped systems, for which modal analysis can be used, response bounds are readily obtained from the individual modes. However, for nonclassically damped systems, they are far more difficult to derive (Nicholson, 1987a).

Response bounds of linear damped systems were first investigated for the Euclidean norm of the state vector. Plaut and Infante (1972) gave response bounds based on the solution of a Ljapunov matrix equation. Nicholson (1987a) provided response bounds in terms of eigenvalues of modified damping and stiffness matrices. In contrast to the frequently used state vector, for free vibrations Yae and Inman (1987) presented response bounds on the Euclidean norm of the displacement vector using eigenfrequencies and the diagonal elements of the modal damping matrix. For steady-state responses of linear damped systems excited by harmonic excitations, bounds were given for the maximum amplitudes on the Euclidean norm of the displacement vector. We call these bounds preferably frequency response bounds since these bounds are time-independent. Results about frequency response bounds were given by Müller (1979), Nicholson (1980), Nicholson and Inman (1983), Yae and Inman (1987), and Hu and Schiehlen (1996a).

Instead of response bounds, also amplitude bounds were investigated, which are time-independent and limit the maximum peak values of vibration responses. For classically damped systems, Müller and Schiehlen (1985) have given amplitude bounds for normal coordinates. Thomson (1993) presented an approach to calculate approximate amplitude bounds for original physical coordinates using the maximum amplitude of the first mode response supplemented by the square root of the sum of squares of peaks for high modes. For nonclassically damped systems, the authors (Schiehlen and Hu, 1995, 1996; Hu and Schiehlen, 1996b) have presented amplitude bound for free vibrations and forced vibrations as well as for both vibrations together. In this paper, we use some previous results about amplitude bounds to derive time-decaying response bounds for general linear damped systems which may be nonclassically or classically damped systems. Three kinds of response bounds, i.e. bounds on the Euclidean norm of the state vector, bounds on the Euclidean norm of the displacement vector, and bounds for individual coordinates will be discussed in the following.

2 Background

The equations describing the vibration of an n-degree-of-freedom linear system can be written as

$$\mathbf{M}\ddot{\mathbf{y}} + \mathbf{D}\dot{\mathbf{y}} + \mathbf{K}\mathbf{y} = \mathbf{f}(t), \quad \mathbf{y}(0) = \mathbf{y}_0, \quad \dot{\mathbf{y}}(0) = \dot{\mathbf{y}}_0 \tag{1}$$

with the mass matrix $\mathbf{M} \in \mathbb{R}^{n\times n}$, the damping matrix $\mathbf{D} \in \mathbb{R}^{n\times n}$ and the stiffness matrix $\mathbf{K} \in \mathbb{R}^{n\times n}$. As usual, it may be assumed that the matrices $\mathbf{M}$ and $\mathbf{K}$ are symmetric and positive definite, the matrix $\mathbf{D}$ is positive semi-definite. The displacement $\mathbf{y}(t)$ is an n-dimensional vector. The initial time is, without loss of generality, chosen to be zero. The vectors $\mathbf{y}_0$ and $\dot{\mathbf{y}}_0$ correspond to the initial displacements and the initial velocities, respectively. The vector function $\mathbf{f}(t)$ represents an external excitation. Usually, three special kinds of excitations are considered:

- impulsive excitation

$$\mathbf{f}(t) = \mathbf{b}\delta(t) \tag{2}$$

where $\delta(t)$ is the Dirac function,

- step excitation

$$\mathbf{f}(t) = \mathbf{b}H(t) \tag{3}$$

where $H(t)$ is the Heaviside function, and

- harmonic excitation

$$\mathbf{f}(t) = \mathbf{b}\cos(\omega t + \varphi). \tag{4}$$

The vector $\mathbf{b} \in \mathbb{R}^n$ is constant.

Equation (1) is often transformed into a more convenient form by the substitution

$$\mathbf{q}(t) = \mathbf{M}^{1/2}\mathbf{y}(t), \quad \mathbf{y}(t) = \mathbf{M}^{-1/2}\mathbf{q}(t). \tag{5}$$

Premultiplication of Eq. (1) by $\mathbf{M}^{-1/2}$ yields

$$\ddot{\mathbf{q}} + \mathbf{D}^*\dot{\mathbf{q}} + \mathbf{K}^*\mathbf{q} = \mathbf{M}^{-1/2}\mathbf{f}(t),$$
$$\mathbf{q}(0) = \mathbf{M}^{1/2}\mathbf{y}_0, \quad \dot{\mathbf{q}}(0) = \mathbf{M}^{1/2}\dot{\mathbf{y}}_0 \tag{6}$$

where the new damping matrix $\mathbf{D}^*$ and the new stiffness matrix $\mathbf{K}^*$ read as

$$\mathbf{D}^* = \mathbf{M}^{-1/2}\mathbf{D}\mathbf{M}^{-1/2}, \quad \mathbf{K}^* = \mathbf{M}^{-1/2}\mathbf{K}\mathbf{M}^{-1/2}. \tag{7}$$

The response bounds available in the literature were usually given for the equations of motion in form (6). However, it should be noted that for this transformation the eigenvectors and the eigen-

Contributed by the Applied Mechanics Division of THE AMERICAN SOCIETY OF MECHANICAL ENGINEERS for publication in the ASME JOURNAL OF APPLIED MECHANICS.

Discussion on the paper should be addressed to the Technical Editor, Professor Lewis T. Wheeler, Department of Mechanical Engineering, University of Houston, Houston, TX 77204-4792, and will be accepted until four months after final publication of the paper itself in the ASME JOURNAL OF APPLIED MECHANICS.

Manuscript received by the ASME Applied Mechanics Division, Aug. 24, 1998; final revision, Jan. 19, 1998. Associate Technical Editor: A. A. Ferri.

 Copyright © 1999 by ASME

Downloaded 04 May 2010 to 171.66.16.27. Redistribution subject to ASME license or copyright; see http://www.asme.org/terms/Terms_Use.cfm

values of the mass matrix $\mathbf{M}$ must be calculated so that the matrix $\mathbf{M}^{-1/2}$ is computable.

The Eq. (1) can also be reformulated in state space form

$$\dot{\mathbf{x}} = \mathbf{A}\mathbf{x} + \mathbf{f}_x(t) \tag{8}$$

where the state vector $\mathbf{x}$, the system matrix $\mathbf{A}$, and the excitation vector $\mathbf{f}_x(t)$ read as

$$\mathbf{x} = \begin{bmatrix} \mathbf{y} \\ \dot{\mathbf{y}} \end{bmatrix}, \ \mathbf{A} = \begin{bmatrix} \mathbf{0} & \mathbf{I} \\ -\mathbf{M}^{-1}\mathbf{K} & -\mathbf{M}^{-1}\mathbf{D} \end{bmatrix},$$

$$\mathbf{f}_x(t) = \begin{bmatrix} \mathbf{0} \\ \mathbf{M}^{-1}\mathbf{f}(t) \end{bmatrix}. \tag{9}$$

The matrix $\mathbf{I}$ denotes the identity matrix. We use the symbol $\|\bullet\|$ for the Euclidean norm of a vector $\bullet$ or a matrix $\bullet$. Response bounds may be determined, e.g., on the Euclidean norm of the state vector, $\|\mathbf{x}(t)\|$, or on the Euclidean norm of the displacement vector, $\|\mathbf{y}(t)\|$, or even for individual components of the state vector, $|x_i(t)|$.

The first response bound for $\|\mathbf{x}(t)\|$ (see Plaut and Infante, 1972) follows to be

$$\|\mathbf{x}(t)\| \le e^{\lambda t}\|\mathbf{x}(0)\| + \int_0^t e^{\lambda(t-\tau)}\|\mathbf{f}_x(\tau)\|d\tau \tag{10}$$

where λ is the maximum eigenvalue of the symmetric matrix $\mathbf{A}_{\text{sym}} := (\mathbf{A} + \mathbf{A}^T)/2$. The response bounds given by Eq. (10) are usually not sharp and the computation of the maximum eigenvalue λ of the matrix $\mathbf{A}_{\text{sym}} \in \mathbb{R}^{2n\times 2n}$ is very time-consuming. Later, Nicholson (1987a) derived response bounds for forced vibrations of a system (6),

$$\|\mathbf{x}(t)\| \le \|\mathbf{X}^{-1}\| \int_0^t e^{-s(t-\tau)}\|\mathbf{M}^{-1/2}\mathbf{f}(\tau)\|d\tau \tag{11}$$

where the matrix $\mathbf{X}$ is computed as

$$\mathbf{X} = \begin{bmatrix} \mathbf{I} & z\mathbf{I} \\ \mathbf{0} & [\mathbf{K}^* - z(\mathbf{D}^* - z\mathbf{I})]^{1/2} \end{bmatrix}. \tag{12}$$

The parameter z in the matrix $\mathbf{X}$ satisfies the relation

$$z \le \min\{\lambda_m(\mathbf{D}^*), z^*\} \tag{13}$$

where

$$z^* = \begin{cases} \lambda_m(\mathbf{D}^*) & \text{if } \lambda_M^2(\mathbf{D}^*) < 4\lambda_m(\mathbf{K}^*), \\ \frac{1}{2}(\lambda_M(\mathbf{D}^*) - \sqrt{\lambda_M^2(\mathbf{D}^*) - 4\lambda_m(\mathbf{K}^*)}) & \text{otherwise.} \end{cases} \tag{14}$$

Here λ_m and λ_M denote the minimum and maximum eigenvalue of a matrix. The quantity s in Eq. (11) is calculated from

$$s = \min\{\lambda_m(\mathbf{D}^*) - z, z\}. \tag{15}$$

Using Eq. (11), Nicholson (1987a) stated that for an impulsive response $\mathbf{x}_\delta(t)$ under the excitation (2), the norm of the state vector $\mathbf{x}_\delta$ is bounded by

$$\|\mathbf{x}_\delta(t)\| \le e^{-st}\|\mathbf{X}^{-1}\|\|\mathbf{M}^{-1/2}\mathbf{b}\| \tag{16}$$

and for a step response $\mathbf{x}_s(t)$ under the excitation (3), the relative overshoot is defined

$$m(t) := \frac{\|\mathbf{x}_s(t) - \mathbf{x}_s^*\|}{\|\mathbf{x}_s^*\|} \le e^{-st}\|\mathbf{X}^{-1}\|\|\mathbf{X}\| \tag{17}$$

where the vector $\mathbf{x}_s^*$ is the steady-state response of the step excitation (3) and equal to $[(\mathbf{K}^{-1}\mathbf{b})^T\mathbf{0}^T]^T$. The response bounds for $\|\mathbf{x}(t)\|$ presented in (Nicholson, 1987a) are expressed in terms of eigenvalues of some $n \times n$-matrices. Compared to the response bounds given in Eq. (10), they take less evaluation time.

The best response bounds on the Euclidean norm of the displacement vector for underdamped systems (see also Inman and Andry, 1980) were given in Yae and Inman (1987). The computation of their response bounds for a system (6) first requires the computation of an orthogonal matrix $\mathbf{P}$, which makes the matrix $\mathbf{\Lambda}_K := \mathbf{P}^T\mathbf{K}^*\mathbf{P}$ diagonal. Then, the matrix $\mathbf{P}^T\mathbf{D}^*\mathbf{P}$ can be expressed as the sum of a diagonal matrix $\mathbf{\Lambda}_C$ and a remainder matrix $\mathbf{C}_1$, i.e.,

$$\mathbf{P}^T\mathbf{D}^*\mathbf{P} := \mathbf{\Lambda}_C + \mathbf{C}_1. \tag{18}$$

With another diagonal matrix

$$\mathbf{\Lambda}_D := (4\mathbf{\Lambda}_K - \mathbf{\Lambda}_C^2)^{1/2}, \tag{19}$$

and two parameters

$$\alpha := \|\mathbf{q}(0)\| + \|(4\mathbf{K} - \mathbf{D}^2)^{-1/2}[2\dot{\mathbf{q}}(0) + \mathbf{D}\mathbf{q}(0)]\|, \tag{20}$$

$$\beta := \|[\mathbf{I} + (\mathbf{\Lambda}_D^{-1}\mathbf{\Lambda}_C)^2]^{1/2}\|, \tag{21}$$

the response bounds for free vibration follows:

$$\|\mathbf{q}(t)\| \le \alpha \exp([-\lambda_m(\mathbf{\Lambda}_C)/2 + \beta\|\mathbf{C}_1\|]t). \tag{22}$$

The frequency bound for steady-state responses under harmonic excitations reads

$$\|\mathbf{q}(t)\| \le \frac{2\|\mathbf{M}^{-1/2}\mathbf{b}\|}{\lambda_m(\mathbf{\Lambda}_C\mathbf{\Lambda}_D)} \exp\left(\frac{\beta\|\mathbf{C}_1\|}{\lambda_m(\mathbf{\Lambda}_C)}\right). \tag{23}$$

Yae and Inman (1987) showed that these bounds are sharp for classically damped systems, but not sharp for nonclassically damped systems.

Amplitude bounds for free vibrations were discussed by Schiehlen and Hu (1995). To prepare the derivation of new response bounds, we restate some previous results here. For systems of type (1), the energy function reads as

$$E(t) := \tfrac{1}{2}\dot{\mathbf{y}}^T(t)\mathbf{M}\dot{\mathbf{y}}(t) + \tfrac{1}{2}\mathbf{y}^T(t)\mathbf{K}\mathbf{y}(t) \tag{24}$$

and the initial energy is

$$E_0 := E(0) = \tfrac{1}{2}\dot{\mathbf{y}}_0^T\mathbf{M}\dot{\mathbf{y}}_0 + \tfrac{1}{2}\mathbf{y}_0^T\mathbf{K}\mathbf{y}_0. \tag{25}$$

For free vibrations, i.e., for $\mathbf{f}(t) = \mathbf{0}$, there cannot be an increase in energy with time

$$E(t) \le E_0. \tag{26}$$

From Eq. (26), we derive two inequalities

$$\lambda_m(\mathbf{K})\|\mathbf{y}(t)\|^2 \le \mathbf{y}^T\mathbf{K}\mathbf{y}(t) \le 2E(t) \le 2E_0, \tag{27}$$

$$\lambda_m(\mathbf{M})\|\dot{\mathbf{y}}(t)\|^2 \le \dot{\mathbf{y}}^T\mathbf{M}\dot{\mathbf{y}}(t) \le 2E(t) \le 2E_0. \tag{28}$$

Hence, simple amplitude bounds for $\|\mathbf{y}(t)\|$ and $\|\dot{\mathbf{y}}(t)\|$ can be given:

$$\max_t \|\mathbf{y}(t)\| \le \sqrt{2\lambda_m^{-1}(\mathbf{K})E_0} \quad \text{and}$$

$$\max_t \|\dot{\mathbf{y}}(t)\| \le \sqrt{2\lambda_m^{-1}(\mathbf{M})E_0}. \tag{29}$$

Moreover, suppose M_{ii}^{-1} and K_{ii}^{-1} are the diagonal elements of the matrices $\mathbf{M}^{-1}$ and $\mathbf{K}^{-1}$, respectively, then there exist simple amplitude bounds for every individual coordinate (see Schiehlen and Hu, 1995).

$$\max_t |y_i(t)| \le \sqrt{2K_{ii}^{-1}E_0} \quad \text{and}$$

$$\max_t |\dot{y}_i(t)| \le \sqrt{2M_{ii}^{-1}E_0}. \tag{30}$$

Downloaded 04 May 2010 to 171.66.16.27. Redistribution subject to ASME license or copyright; see http://www.asme.org/terms/Terms_Use.cfm

3 Derivation of Response Bounds

If the excitation $\mathbf{f}(t)$ is not vanishing, then the linear differential Eq. (1) is called inhomogeneous. Usually, a particular solution $\mathbf{y}_p(t)$ is quite simple to obtain, for example, for a step excitation (2) we get

$$\mathbf{y}_p = \mathbf{K}^{-1}\mathbf{b} \tag{31}$$

and for a harmonic excitation (3) it follows

$$\mathbf{y}_p(t) = \begin{bmatrix} a_1 \cos(\omega t + \varphi + \varphi_1) \\ a_2 \cos(\omega t + \varphi + \varphi_2) \\ \vdots \\ a_n \cos(\omega t + \varphi + \varphi_n) \end{bmatrix} \tag{32}$$

where

$$\begin{bmatrix} a_1 e^{j\varphi_1} \\ a_2 e^{j\varphi_2} \\ \vdots \\ a_n e^{j\varphi_n} \end{bmatrix} = [-\omega^2\mathbf{M} + j\omega\mathbf{D} + \mathbf{K}]^{-1}\mathbf{b}, \quad j = \sqrt{-1}. \tag{33}$$

These particular solutions are also the steady-state responses of the system. If we introduce a new set of coordinates

$$\Delta\mathbf{y}(t) = \mathbf{y}(t) - \mathbf{y}_p(t) \tag{34}$$

which satisfy the homogeneous differential equation

$$\mathbf{M}\Delta\ddot{\mathbf{y}}(t) + \mathbf{D}\Delta\dot{\mathbf{y}}(t) + \mathbf{K}\Delta\mathbf{y}(t) = \mathbf{0} \tag{35}$$

with initial conditions

$$\Delta\mathbf{y}(0) = \mathbf{y}_0 - \mathbf{y}_p(0), \quad \Delta\dot{\mathbf{y}}(0) = \dot{\mathbf{y}}_0 - \dot{\mathbf{y}}_p(0), \tag{36}$$

then, the response $\Delta\mathbf{y}(t)$ can be computed as a free vibration. Due to Eq. (34), it follows from the triangle inequality for the response

$$\|\mathbf{y}(t)\| \le \|\mathbf{y}_p(t)\| + \|\Delta\mathbf{y}(t)\|,$$
$$\|\dot{\mathbf{y}}(t)\| \le \|\dot{\mathbf{y}}_p(t)\| + \|\Delta\dot{\mathbf{y}}(t)\|. \tag{37}$$

The norms $\|\mathbf{y}_p(t)\|$ and $\|\dot{\mathbf{y}}_p(t)\|$ are simple to compute, while the computation of the norms $\|\Delta\mathbf{y}(t)\|$ and $\|\Delta\dot{\mathbf{y}}(t)\|$ is very time-consuming for large systems. Therefore, simple response bounds for free vibrations $\Delta\mathbf{y}(t)$ are desirable.

Now we discuss response bounds for free vibrations. Letting $\mathbf{f}(t) = \mathbf{0}$ and performing the transformation

$$\mathbf{y}^*(t) = e^{dt}\mathbf{y}(t) \tag{38}$$

for Eq. (1), we get a homogeneous differential equation for $\mathbf{y}^*(t)$,

$$\mathbf{M}\ddot{\mathbf{y}}^* + \mathbf{D}'\dot{\mathbf{y}}^* + \mathbf{K}'\mathbf{y}^* = \mathbf{0}, \tag{39}$$

where the matrices $\mathbf{D}'$ and $\mathbf{K}'$ are computed as

$$\mathbf{D}' = \mathbf{D} - 2d\mathbf{M}, \quad \mathbf{K}' = \mathbf{K} - d\mathbf{D} + d^2\mathbf{M}. \tag{40}$$

The initial conditions for $\mathbf{y}^*(t)$ are

$$\mathbf{y}^*(0) = \mathbf{y}(0) = \mathbf{y}_0,$$
$$\dot{\mathbf{y}}^*(0) = \dot{\mathbf{y}}(0) + d\mathbf{y}(0) = \dot{\mathbf{y}}_0 + d\mathbf{y}_0. \tag{41}$$

The parameter d is chosen such that the matrices $\mathbf{D}'$ and $\mathbf{K}'$ are positive definite. According to some investigations about the eigenvalue bounds of system (1) (see Nicholson, 1987b, 1996; Hu and Schiehlen, 1996a), the real part of the eigenvalues of the system is smaller than $(-\mu)$, where μ is defined to be

$$\mu = \begin{cases} \lambda_m(\mathbf{D}^*)/2 & \text{for } \lambda_M^2(\mathbf{D}^*) \le 4\lambda_m(\mathbf{K}^*), \\ \min\{\frac{1}{2}(\lambda_M(\mathbf{D}^*) - \sqrt{\lambda_M^2(\mathbf{D}^*) - 4\lambda_m(\mathbf{K}^*)}), \frac{1}{2}\lambda_m(\mathbf{D}^*)\} & \text{otherwise.} \end{cases} \tag{42}$$

For an oscillatory system, i.e., all its eigenvalues have nonzero imaginary parts (for example, in an underdamped system), the quantity u can be set equal to $\lambda_m(\mathbf{D}^*)/2$. We may set d to an arbitrary value within the interval $[0, \mu]$. Since $d \le \mu \le \lambda_m(\mathbf{D}^*)/2$, the matrix $\mathbf{D}'$ certainly is positive semidefinite. If the system matrix $\mathbf{A}$ as usual is diagonalizable with a similarity transformation, then the response $\mathbf{y}^*(t)$ is bounded and the system (39) is stable. According to a theorem from Müller (1977), if the mass matrix $\mathbf{M}$ is positive definite and the damping matrix $\mathbf{D}'$ is positive semidefinite, then the stiffness matrix $\mathbf{K}'$ must be positive definite for a stable system. Its eigenvalues and the diagonal elements of its inverse matrix also are positive.

From Eq. (38), we obtain

$$\mathbf{y}(t) = e^{-dt}\mathbf{y}^*(t) \quad \text{and} \quad \dot{\mathbf{y}}(t) = e^{-dt}[\dot{\mathbf{y}}^*(t) - d\mathbf{y}^*(t)]. \tag{43}$$

Denoting an initial energy for $\mathbf{y}^*$,

$$E_0^* = \tfrac{1}{2}\dot{\mathbf{y}}^{*T}(0)\mathbf{M}\dot{\mathbf{y}}^*(0) + \tfrac{1}{2}\mathbf{y}^{*T}(0)\mathbf{K}'\mathbf{y}^*(0)$$
$$= E_0 + d^2\mathbf{y}_0^T\mathbf{M}\mathbf{y}_0 + d\mathbf{y}_0^T\mathbf{M}\dot{\mathbf{y}}_0 - d\mathbf{y}_0^T\mathbf{D}\mathbf{y}_0/2 \tag{44}$$

and using Eqs. (29) and (43), the response bounds are

$$\|\mathbf{y}(t)\| \le e^{-dt}\|\mathbf{y}^*(t)\| \le e^{-dt}\sqrt{2\lambda_m^{-1}(\mathbf{K}')E_0^*}, \tag{45}$$

$$\|\dot{\mathbf{y}}(t)\| \le e^{-dt}(\|\dot{\mathbf{y}}^*(t)\| + d\|\mathbf{y}^*(t)\|)$$
$$\le e^{-dt}(\sqrt{2\lambda_m^{-1}(\mathbf{M})E_0^*} + d\sqrt{2\lambda_m^{-1}(\mathbf{K}')E_0^*}). \tag{46}$$

The response bound for $\|\mathbf{x}(t)\|$ follows directly:

$$\|\mathbf{x}(t)\| \le \sqrt{\|\mathbf{y}(t)\|^2 + \|\dot{\mathbf{y}}(t)\|^2}$$
$$\le e^{-dt}\sqrt{\|\mathbf{y}^*(t)\|^2 + (\|\dot{\mathbf{y}}^*(t)\| + d\|\mathbf{y}^*(t)\|)^2}$$
$$\le e^{-dt}\sqrt{2E_0^*[\lambda_m^{-1}(\mathbf{K}') + (\sqrt{\lambda_m^{-1}(\mathbf{M})} + d\sqrt{\lambda_m^{-1}(\mathbf{K}')})^2]}. \tag{47}$$

Moreover, response bounds for individual coordinates can be derived from Eq. (30)

$$|y_i(t)| \le e^{-dt}\sqrt{2K_{ii}'^{-1}E_0^*} \text{ and}$$
$$|\dot{y}_i(t)| \le e^{-dt}(\sqrt{2M_{ii}^{-1}E_0^*} + d\sqrt{2K_{ii}'^{-1}E_0^*}). \tag{48}$$

These bounds are valid for an arbitrary value $d \in [0, \mu]$. We suggest the use of $d = 0$ for small t and $d = \mu$ for large t. Combining Eqs. (29)–(30) and (45)–(48) and setting d to μ, we can now state new response bounds for free vibrations.

THEOREM 1: *For a system (1) with $\mathbf{f}(t) = \mathbf{0}$, if M_{ii}^{-1} and $K_{ii}'^{-1}$ are the ith diagonal elements of the matrices $\mathbf{M}^{-1}$ and $\mathbf{K}'^{-1}$, respectively, and the matrix $\mathbf{K}'$ is defined as in Eq. (40), where d is set to μ given by Eq. (42), then the following inequalities hold true:*

$$\|\mathbf{y}(t)\| \le \min\{\sqrt{2\lambda_m^{-1}(\mathbf{K})E_0}, e^{-\mu t}\sqrt{2\lambda_m^{-1}(\mathbf{K}')E_0^*}\}, \tag{49}$$

$$\|\dot{\mathbf{y}}(t)\| \le \min\{\sqrt{2\lambda_m^{-1}(\mathbf{M})E_0}, e^{-\mu t}(\sqrt{2\lambda_m^{-1}(\mathbf{M})E_0^*} + \mu\sqrt{2\lambda_m^{-1}(\mathbf{K}')E_0^*})\}, \tag{50}$$

$$|y_i(t)| \le \min\{\sqrt{2K_{ii}^{-1}E_0}, e^{-\mu t}\sqrt{2K_{ii}'^{-1}E_0^*}\}, \tag{51}$$

$$|\dot{y}_i(t)| \le \min\{\sqrt{2M_{ii}^{-1}E_0}, e^{-\mu t}(\sqrt{2M_{ii}^{-1}E_0^*} + \mu\sqrt{2K_{ii}'^{-1}E_0^*})\}. \tag{52}$$

These bounds are easy to compute. For the computation of the decaying coefficient μ, instead of computing $\mathbf{M}^{-1/2}$, the Cholesky decomposition of the mass matrix $\mathbf{M} = \mathbf{L}^T\mathbf{L}$ is preferable, where matrix $\mathbf{L}$ is a left triangular matrix. The eigenvalues of the matrices $\mathbf{M}^{-1/2}\mathbf{D}\mathbf{M}^{-1/2}$ and $\mathbf{L}^{-T}\mathbf{D}\mathbf{L}^{-1}$ are the same. Hence, we can use this property to compute the extreme eigenvalues appearing in Eq. (42),

Downloaded 04 May 2010 to 171.66.16.27. Redistribution subject to ASME license or copyright; see http://www.asme.org/terms/Terms_Use.cfm

$$\lambda_m(\mathbf{D}^*) = \lambda_m(\mathbf{L}^{-T}\mathbf{D}\mathbf{L}^{-1}), \quad (53)$$

$$\lambda_M(\mathbf{D}^*) = \lambda_M(\mathbf{L}^{-T}\mathbf{D}\mathbf{L}^{-1}), \quad (54)$$

$$\lambda_m(\mathbf{K}^*) = \lambda_m(\mathbf{L}^{-T}\mathbf{K}\mathbf{L}^{-1}). \quad (55)$$

For oscillatory systems, only the minimum eigenvalue of the matrix $\mathbf{L}^{-T}\mathbf{D}\mathbf{L}^{-1}$ is required for the computation of μ.

Further, we discuss an impulsive response $\mathbf{y}_\delta(t)$ of a system (1) for an excitation (2). The initial conditions $\mathbf{y}_0$ and $\dot{\mathbf{y}}_0$ are set to zero. The impulsive response $\mathbf{y}_\delta(t)$ for $t > 0$ is equivalent to a free vibration with changed initial conditions as described by the equations

$$\mathbf{M}\ddot{\mathbf{y}}_\delta + \mathbf{D}\dot{\mathbf{y}}_\delta + \mathbf{K}\mathbf{y}_\delta = \mathbf{0}, \quad \mathbf{y}_\delta(0) = \mathbf{0}, \quad \dot{\mathbf{y}}_\delta(0) = \mathbf{M}^{-1}\mathbf{b}. \quad (56)$$

In this case, the initial energy is simply

$$E_0 = E_0^* = \tfrac{1}{2}\mathbf{b}^T\mathbf{M}^{-1}\mathbf{b}. \quad (57)$$

Using Theorem 1, the response bounds for the impulsive response $\mathbf{y}_\delta(t)$ are

$$\|\mathbf{y}_\delta(t)\| \le \min\{\sqrt{\lambda_m^{-1}(\mathbf{K})}, e^{-\mu t}\sqrt{\lambda_m^{-1}(\mathbf{K}')}\}\sqrt{\mathbf{b}^T\mathbf{M}^{-1}\mathbf{b}}, \quad (58)$$

$$\|\dot{\mathbf{y}}_\delta(t)\| \le \min\{\sqrt{\lambda_m^{-1}(\mathbf{M})}, e^{-\mu t}(\sqrt{\lambda_m^{-1}(\mathbf{M})} + \mu\sqrt{\lambda_m^{-1}(\mathbf{K}')})\}\sqrt{\mathbf{b}^T\mathbf{M}^{-1}\mathbf{b}}, \quad (59)$$

$$|y_{\delta_i}(t)| \le \min\{\sqrt{K_{ii}^{-1}}, e^{-\mu t}\sqrt{K_{ii}'^{-1}}\}\sqrt{\mathbf{b}^T\mathbf{M}^{-1}\mathbf{b}}, \quad (60)$$

$$|\dot{y}_{\delta_i}(t)| \le \min\{\sqrt{M_{ii}^{-1}}, e^{-\mu t}(\sqrt{M_{ii}^{-1}} + \mu\sqrt{K_{ii}'^{-1}})\}\sqrt{\mathbf{b}^T\mathbf{M}^{-1}\mathbf{b}}. \quad (61)$$

For a general transient excitation $\mathbf{b}f(t)$ with a scalar time function $f(t)$ and initial conditions equal to zero, according to linear system theory, the responses read as

$$\mathbf{y}(t) = \int_0^t \mathbf{y}_\delta(t-\tau)f(\tau)d\tau \quad \text{and}$$

$$\dot{\mathbf{y}}(t) = \int_0^t \dot{\mathbf{y}}_\delta(t-\tau)f(\tau)d\tau. \quad (62)$$

Using Eqs. (58)–(62), we can also give response bounds for a transient excitation, for example,

$$\|\mathbf{y}(t)\| \le \int_0^t \|\mathbf{y}_\delta(t-\tau)\|\,|f(\tau)|d\tau$$

$$\le \sqrt{\lambda_m^{-1}(\mathbf{K}')\mathbf{b}^T\mathbf{M}^{-1}\mathbf{b}}\int_0^t e^{-\mu(t-\tau)}|f(\tau)|d\tau. \quad (63)$$

Furthermore, using Theorem 1, we can derive response bounds for $\Delta\mathbf{y}$ as defined in Eq. (34), where E_0 must be substituted with $E_p(0)$ and E_0^* with $E_p^*(0)$. The two kinds of initial energy $E_p(0)$ and $E_p^*(0)$ read as

$$E_p(0) = \tfrac{1}{2}\Delta\dot{\mathbf{y}}^T(0)\mathbf{M}\Delta\dot{\mathbf{y}}(0) + \tfrac{1}{2}\Delta\mathbf{y}^T(0)\mathbf{K}\Delta\mathbf{y}(0), \quad (64)$$

$$E_p^*(0) = \tfrac{1}{2}[\Delta\dot{\mathbf{y}}(0) + \mu\Delta\mathbf{y}(0)]^T\mathbf{M}[\Delta\dot{\mathbf{y}}(0) + \mu\Delta\mathbf{y}(0)] + \tfrac{1}{2}\Delta\mathbf{y}^T(0)\mathbf{K}'\Delta\mathbf{y}(0). \quad (65)$$

Then, using Eq. (37), we can state some response bounds for the response $\mathbf{y}(t)$. For simplicity, we discuss here only step responses $\mathbf{y}_s(t)$ and harmonic responses $\mathbf{y}_h(t)$ with vanishing initial conditions $\mathbf{y}_0 = \dot{\mathbf{y}}_0 = \mathbf{0}$.

For a step excitation (3), the two initial energy values are

$$E_p(0) = \tfrac{1}{2}\mathbf{b}^T\mathbf{K}^{-1}\mathbf{b} =: E_s(0), \quad (66)$$

$$E_p^*(0) = \tfrac{1}{2}\mathbf{b}^T\mathbf{K}^{-1}(\mu^2\mathbf{M} + \mathbf{K}')\mathbf{K}^{-1}\mathbf{b} =: E_s^*(0) \quad (67)$$

following from Eqs. (31), (64), and (65). Hence, the response bounds for the step response $\mathbf{y}_s(t)$ are

$$\|\mathbf{y}_s(t)\| \le |\mathbf{K}^{-1}\mathbf{b}| + \min\{\sqrt{2\lambda_m^{-1}(\mathbf{K})E_s(0)}, e^{-\mu t}\sqrt{2\lambda_m(\mathbf{K}')E_s^*(0)}\}, \quad (68)$$

$$\|\dot{\mathbf{y}}_s(t)\| \le \min\{\sqrt{2\lambda_m^{-1}(\mathbf{M})E_s(0)}, e^{-\mu t}(\sqrt{2\lambda_m^{-1}(\mathbf{M})E_s^*(0)} + \mu\sqrt{2\lambda_m(\mathbf{K}')E_s^*(0)})\}, \quad (69)$$

$$|y_{s_i}(t)| \le |(\mathbf{K}^{-1}\mathbf{b})_i| + \min\{\sqrt{2K_{ii}^{-1}E_s(0)}, e^{-\mu t}\sqrt{2K_{ii}'^{-1}E_s^*(0)}\}, \quad (70)$$

$$|\dot{y}_{s_i}(t)| \le \min\{\sqrt{2M_{ii}^{-1}E_s(0)}, e^{-\mu t}(\sqrt{2M_{ii}^{-1}E_s^*(0)} + \mu\sqrt{2K_{ii}'^{-1}E_s^*(0)})\}. \quad (71)$$

Moreover, we can easily get a response bound for $\|\mathbf{x}_s(t)\|$ from Eqs. (68) and (69). It turns out that for the relative overshoot, we get

$$m(t) \le \min\{\alpha_1, \alpha_2 e^{-\mu t}\}/\|\mathbf{K}^{-1}\mathbf{b}\| \quad (72)$$

where α_1 and α_2 read as

$$\alpha_1 = \sqrt{2[\lambda_m^{-1}(\mathbf{K}) + \lambda_m^{-1}(\mathbf{M})]E_s(0)}, \quad (73)$$

$$\alpha_2 = \sqrt{2[\lambda_m^{-1}(\mathbf{K}') + (\sqrt{\lambda_m^{-1}(\mathbf{M})} + \mu\sqrt{\lambda_m^{-1}(\mathbf{K}')})^2]E_s^*(0)}. \quad (74)$$

Compared to the bounds (17) given by Nicholson (1987a), the bound (72) for the overshoot is easier to compute and also sharper since $\mu \ge s$ and the condition number of the matrix $\mathbf{X}$ is usually large.

For a harmonic excitation (4), we have due to Eq. (32),

$$\mathbf{y}_p(0) = \begin{bmatrix} a_1\cos(\varphi+\varphi_1) \\ a_2\cos(\varphi+\varphi_2) \\ \vdots \\ a_n\cos(\varphi+\varphi_n) \end{bmatrix} \quad \text{and}$$

$$\dot{\mathbf{y}}_p(0) = -\omega\begin{bmatrix} a_1\sin(\varphi+\varphi_1) \\ a_2\sin(\varphi+\varphi_2) \\ \vdots \\ a_n\sin(\varphi+\varphi_n) \end{bmatrix}. \quad (75)$$

The initial energy values are

$$E_p(0) = \tfrac{1}{2}\dot{\mathbf{y}}_p^T(0)\mathbf{M}\dot{\mathbf{y}}_p(0) + \tfrac{1}{2}\mathbf{y}_p^T(0)\mathbf{K}\mathbf{y}_p(0) =: E_h(0), \quad (76)$$

$$E_p^*(0) = \tfrac{1}{2}[\dot{\mathbf{y}}_p(0) + \mu\mathbf{y}_p(0)]^T\mathbf{M}[\dot{\mathbf{y}}_p(0) + \mu\mathbf{y}_p(0)] + \tfrac{1}{2}\mathbf{y}_p^T(0)\mathbf{K}'\mathbf{y}_p(0) =: E_h^*(0). \quad (77)$$

Using Theorem 1 yields response bounds for the harmonic response $\mathbf{y}_h(t)$

$$\|\mathbf{y}_h(t)\| \le \|\mathbf{y}_p(t)\| + \min\{\sqrt{2\lambda_m^{-1}(\mathbf{K})E_h(0)}, e^{-\mu t}\sqrt{2\lambda_m(\mathbf{K}')E_h^*(0)}\}, \quad (78)$$

$$\|\dot{\mathbf{y}}_h(t)\| \le \|\dot{\mathbf{y}}_p(t)\| + \min\{\sqrt{2\lambda_m^{-1}(\mathbf{M})E_h(0)}, e^{-\mu t}(\sqrt{\lambda_m^{-1}(\mathbf{M})} + \mu\sqrt{\lambda_m(\mathbf{K}')})\sqrt{2E_h^*(0)}\}, \quad (79)$$

$$|y_{h_i}(t)| \le |y_{p_i}(t)| + \min\{\sqrt{2K_{ii}^{-1}E_h(0)}, e^{-\mu t}\sqrt{2K_{ii}'^{-1}E_h^*(0)}\}, \quad (80)$$

$$|\dot{y}_{h_i}(t)| \le |\dot{y}_{p_i}(t)| + \min\{\sqrt{2M_{ii}^{-1}E_h(0)}, e^{-\mu t}(\sqrt{M_{ii}^{-1}} + \mu\sqrt{K_{ii}'^{-1}})\sqrt{2E_h^*(0)}\} \quad (81)$$

Downloaded 04 May 2010 to 171.66.16.27. Redistribution subject to ASME license or copyright; see http://www.asme.org/terms/Terms_Use.cfm

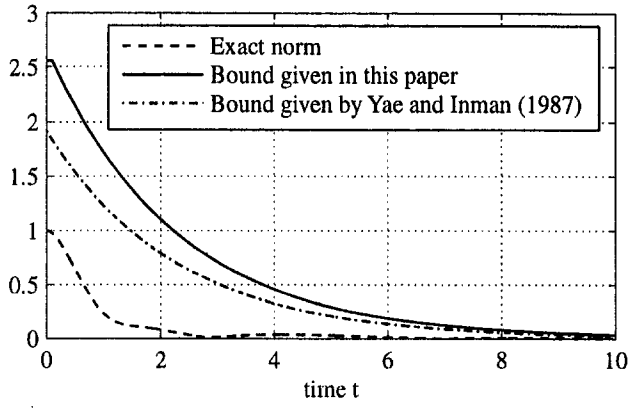


Fig. 1 Response bounds on the norm $\|\mathbf{y}(t)\|$ for the initial conditions $y_1(0) = 1$, $y_2(0) = \dot{y}_1(0) = \dot{y}_2(0) = 0$

where the steady-state response $\mathbf{y}_p(t)$ is given in Eq. (32). Furthermore, if we want to avoid the computation of $\mathbf{y}_p(t)$, some frequency response bounds can be used. Investigations of frequency response bounds can be found in Müller (1979), Nicholson (1980), Nicholson and Inman (1983), Yae and Inman (1987), and Hu and Schiehlen (1996a). If we use a frequency response bound α_p, i.e.,

$$\|\mathbf{y}_p(t)\|/\|\mathbf{b}\| \le \alpha_p, \tag{82}$$

then the two initial energy values $E_h(0)$ and $E_h^*(0)$ defined in Eqs. (76) and (77) are bounded:

$$E_h(0) \le \frac{\alpha_p^2}{2}[\omega^2\lambda_M(\mathbf{M}) + \lambda_M(\mathbf{K})]\|\mathbf{b}\|^2, \tag{83}$$

$$E_h^*(0) \le \frac{\alpha_p^2}{2}[(\omega + \mu)^2\lambda_M(\mathbf{M}) + \lambda_M(\mathbf{K}')]\|\mathbf{b}\|^2. \tag{84}$$

Using Theorem 1 and Eqs. (83) and (84) yields a response bound for $\mathbf{y}_h(t)$:

$$\|\mathbf{y}_h(t)\| \le \alpha_p\|\mathbf{b}\|(1 + \min\{\alpha_3, \alpha_4 e^{-\mu t}\}) \tag{85}$$

where α_3 and α_4 read as

$$\alpha_3 = \sqrt{\lambda_m^{-1}(\mathbf{K})[\omega^2\lambda_M(\mathbf{M}) + \lambda_M(\mathbf{K})]}, \tag{86}$$

$$\alpha_4 = \sqrt{\lambda_m^{-1}(\mathbf{K}')[(\omega + \mu)^2\lambda_M(\mathbf{M}) + \lambda_M(\mathbf{K}')]}. \tag{87}$$

For the frequency response bounds α_p, two simple bounds which are given in Hu and Schiehlen (1996a) may be used. The first frequency response bound reads as

$$\alpha_p = \frac{1}{\omega\lambda_m(\mathbf{D})} \tag{88}$$

which depends on the excitation frequency ω. The other one reads as

$$\alpha_p = \max\left\{\frac{1}{\sqrt{2}d_0}, 1\right\}\frac{\lambda_M(\mathbf{D})}{\lambda_m(\mathbf{D})\lambda_m(\mathbf{K})} \tag{89}$$

where the parameter d_0 is

$$d_0 = \frac{\lambda_m(\mathbf{D})}{2\sqrt{\lambda_M(\mathbf{M})\lambda_M(\mathbf{K})}}. \tag{90}$$

This frequency response bound is independent of the excitation frequency ω. Moreover, if a system is classically damped or weakly coupled, i.e., the matrix norm $\|\mathbf{C}_1\|$ defined in Eq. (18) is close to zero, the inequality (23) given by Yae and Inman (1987) may also be used for the computation of α_p.

4 Comparisons for Several Examples

In this section some examples discussed by Yae and Inman (1987) as well as Nicholson (1987a) are chosen to provide a comparison between the bounds given here and ones developed by other authors. Though a great advantage of response bounds is the saving in computation time for large-scale systems, the examples here are of low order for the convenience of presentation. The systems under consideration are of the type described in Eq. (1). Three kinds of responses, free-vibration responses, step responses, and harmonic responses, are discussed. Impulsive responses are not separately considered here, since they are only special cases of free-vibration responses for modified initial conditions.

4.1 Free-Vibration Response. For free-vibration response, the excitation $\mathbf{f}(t)$ vanishes for all times. In the first case, a classically damped system given in (Yae and Inman, 1987) is investigated. The matrices appearing in Eq. (1) are for this system

$$\mathbf{M} = \mathbf{I}, \quad \mathbf{K} = \begin{bmatrix} 5 & -1 \\ -1 & 1 \end{bmatrix} \quad \text{and} \quad \mathbf{D} = (\mathbf{M} + \mathbf{K})/2. \tag{91}$$

The response bounds given by Yae and Inman (1987) and the ones presented in this paper are shown in Figs. 1 and 2 for different initial conditions. Compared to the exact responses, both bounds show a similar sharpness and it is in general impossible to predict which bound is sharper.

In the second case, the system, given also in Yae and Inman (1987), is described by

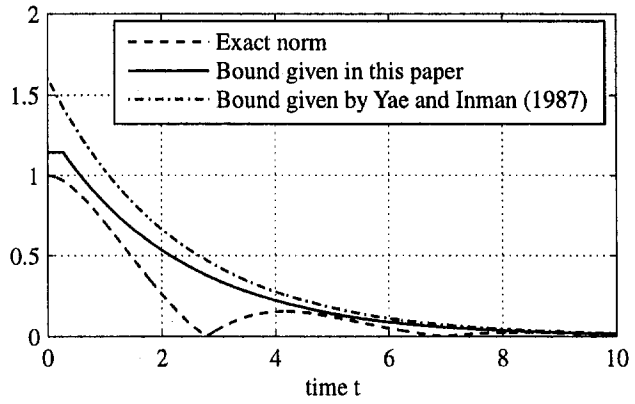


Fig. 2 Response bounds on the norm $\|\mathbf{y}(t)\|$ for the initial conditions $y_2(0) = 1$, $y_1(0) = \dot{y}_1(0) = \dot{y}_2(0) = 0$

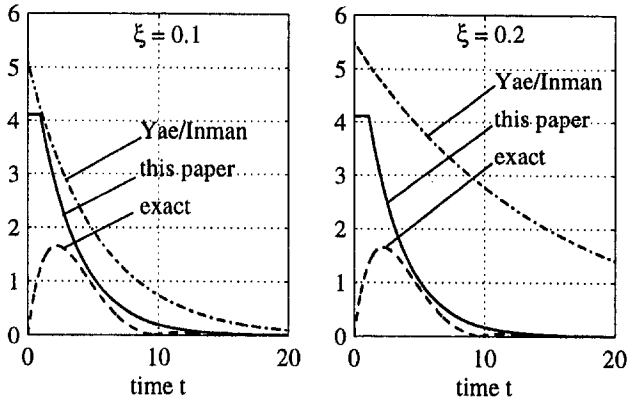


Fig. 3 Response bounds on the norm $\|\mathbf{y}(t)\|$ of a nonclassically damped system for different ξ

Downloaded 04 May 2010 to 171.66.16.27. Redistribution subject to ASME license or copyright; see http://www.asme.org/terms/Terms_Use.cfm

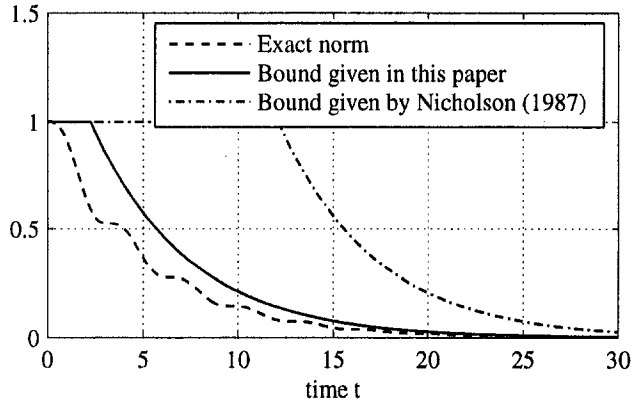


Fig. 4 Exact relative overshoot $m(t)$ and its bounds

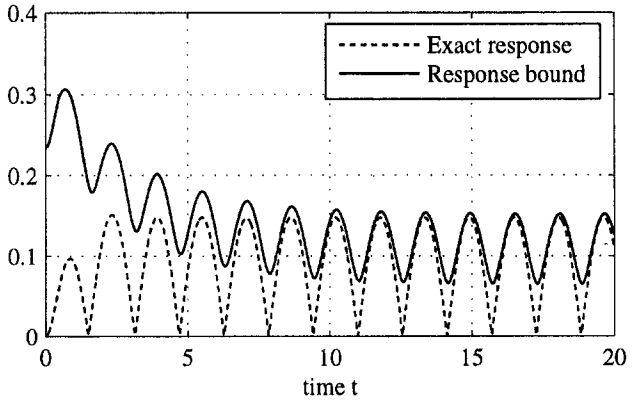


Fig. 6 Exact response $|y_1(t)|$ and its bound

$$\mathbf{M} = \mathbf{I}, \quad \mathbf{K} = \begin{bmatrix} 5 & -1.5 & 0 & 0 \\ -1.5 & 3 & -1.5 & 0 \\ 0 & -1.5 & 3 & -1.5 \\ 0 & 0 & -1.5 & 1.5 \end{bmatrix},$$

$$\mathbf{D} = \frac{\mathbf{M} + \mathbf{K}}{2} + \xi \begin{bmatrix} 1 & 0 & 0 & 0 \\ 0 & 0 & 0 & 0 \\ 0 & 0 & 0 & 0 \\ 0 & 0 & 0 & 1 \end{bmatrix} \tag{92}$$

where ξ is introduced to describe a nonclassically damped system. For the initial conditions

$$\mathbf{y}(0) = \mathbf{0}, \quad \dot{y}_1(0) = \dot{y}_2(0) = \dot{y}_3(0) = \dot{y}_4(0) = 1, \tag{93}$$

Figure 3 shows that the response bounds presented in this paper are much sharper than the bounds given by Yae and Inman (1987). Moreover, also bounds for individual coordinates are developed in this paper.

4.2 Step Response. For a step excitation (3), Nicholson (1987a) presented a response bound on the norm of the state vector $\|\mathbf{x}(t)\|$. Using a system investigated by him,

$$\mathbf{M} = \mathbf{I}, \ \mathbf{D} = \begin{bmatrix} 0.4 & 0.01 \\ 0.01 & 4 \end{bmatrix},$$

$$\mathbf{K} = \begin{bmatrix} 1 & 0 \\ 0 & 100 \end{bmatrix}, \quad \mathbf{b} = \begin{bmatrix} 1 \\ 1 \end{bmatrix}, \tag{94}$$

we compare the different bounds for the relative overshoot $m(t)$.

The steady-state response of this system is $\mathbf{x}_s^* = [1, 0.01, 0, 0]^T$. Nicholson (1987a) stated without proof that the relative overshoot $m(t)$ for an underdamped system will never exceed a value of one. Suppose this statement is true, then both bounds (17) and (72) can also be limited by a value of one. The exact overshoot $m(t)$ and the bound (17) given by Nicholson (1987a) and the bound (72) presented in this paper are shown in Fig. 4. It is shown clearly that the bound presented in this paper is much sharper.

4.3 Harmonic Response. For harmonic responses, there exist some frequency bounds for steady-state responses in the literature. However, time-decaying response bounds for transient harmonic responses are not described yet. In this paper, response bounds for transient harmonic responses are presented. For the system specified by Eq. (92) with

$$\xi = 0.2, \quad \mathbf{b} = [1, 0, 0, 0]^T, \quad \omega = 2 \quad \text{and} \quad \varphi = 0, \tag{95}$$

Figure 5 shows the exact response norm $\|\mathbf{y}(t)\|$ and the computed response bound. Moreover, response bounds for individual coordinates can be computed. As an example, Fig. 6 shows the exact response $|y_1(t)|$ and its response bounds. It is shown that the developed response bounds are very close to the exact responses.

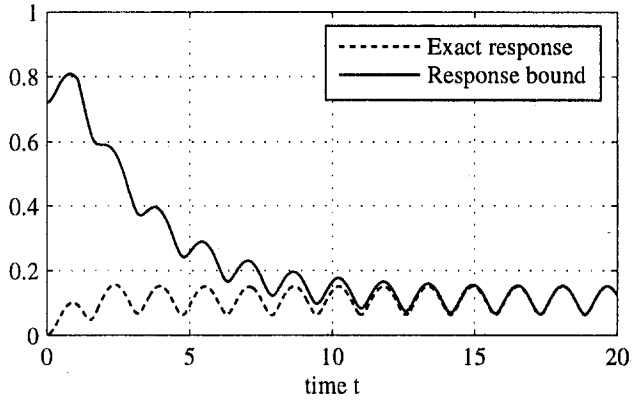


Fig. 5 Exact response norm $\|\mathbf{y}(t)\|$ and its bound

5 Conclusion

In this paper, first some published results for the computation of response bounds are considered. Then, for general linear damped systems (classically damped or nonclassically damped, underdamped or overdamped), simple response bounds for the free-vibration response, step response, and harmonic response are presented. Compared with previous response bounds, the bounds given in this paper depend only on some extreme eigenvalues and are simpler to compute. Some examples show that the bounds given here are even sharper than some previously presented bounds.

In addition to the response bounds on the norm of the state vector $\mathbf{x}$ or the displacement vector $\mathbf{y}$, also response bounds for individual coordinates, e.g., for a displacement coordinate y_i or for a velocity coordinate $\dot{y}_i$, are presented in this paper. This provides a possibility to separately investigate the vibration level of interested coordinates. Moreover, these bounds also have a simple relation to physical parameters and their calculation leads to significant savings in computation time compared to the computation of detailed solutions. These improvements will be useful, e.g., in design and automatic control.

Acknowledgment

The first author acknowledges the support of the German Research Foundation (DFG), SFB 404, Project B1.

References

Hu, B., and Schiehlen, W., 1996a, "Eigenvalue, Frequency Response and Variance Bounds of Linear Damped Systems," *Eur. J. Mech., A/Solids*, Vol. 15, pp. 617–646.

Hu, B., and Schiehlen, W., 1996b, "Amplitude Bounds of Linear Forced Vibrations," *Archive of Applied Mechanics*, Vol. 66, pp. 357–368.

Downloaded 04 May 2010 to 171.66.16.27. Redistribution subject to ASME license or copyright; see http://www.asme.org/terms/Terms_Use.cfm

Inman, D. J., and Andry, A. N., 1980, "Some Results on the Nature of Eigenvalues of Discrete Damped Linear Systems," ASME JOURNAL OF APPLIED MECHANICS, Vol. 47, pp. 927–930.

Müller, P. C., 1977, *Stabilität und Matrizen,* Springer, Berlin, pp. 171–172.

Müller, P. C., 1979, "Remarks on Vibrations of Damped Linear Systems," *Mech. Res. Comm.,* Vol. 6, pp. 7–15.

Müller, P. C., and Schiehlen, W. O., 1985, *Linear Vibrations,* Martinus Nijhoff, Dordrecht, The Netherlands, p. 136.

Nicholson, D. W., 1980, "Bounds on the Forced Responses of a Damped Linear System," *Mech. Res. Comm.,* Vol. 7, pp. 305–308.

Nicholson, D. W., 1987a, "Response Bounds for Nonclassically Damped Mechanical Systems Under Transient Loads," ASME JOURNAL OF APPLIED MECHANICS, Vol. 54, pp. 430–433.

Nicholson, D. W., 1987b, "Eigenvalue Bounds for Linear Mechanical Systems With Nonmodal Damping," *Mech. Res. Commun.,* Vol. 14, pp. 115–122.

Nicholson, D. W., and Inman, D. J., 1983, "Stable Response of Damped Linear Systems," *The Shock and Vibration Digest,* Vol. 15, pp. 19–25.

Nicholson, D. W., and Lin, B., 1996, "Stable Response of Non-Classically Damped Mechanical Systems—II," ASME *Appl. Mech. Rev.,* Vol. 49, No. 10, pp. S49–S54.

Plaut, R. H., and Infante, E. F., 1972, "Bounds on Motions of System Lumped and Continuous Dynamic Systems," ASME JOURNAL OF APPLIED MECHANICS, Vol. 39, pp. 251–256.

Schiehlen, W., and Hu, B., 1995, "Amplitude Bounds of Linear Free Vibrations," ASME JOURNAL OF APPLIED MECHANICS, Vol. 62, pp. 231–233.

Schiehlen, W., and Hu, B., 1996, "Amplitude Bounds of Linear Vibration Responses," *Z. angew. Math. Mech.,* Vol. 76, pp. 453–454.

Thomson, W. T., 1993, *Theory of Vibration with Applications,* Chapman and Hall, London, pp. 192–195.

Yae, K. H., and Inman, D. J., 1987, "Response Bounds for Linear Underdamped Systems," ASME JOURNAL OF APPLIED MECHANICS, Vol. 54, pp. 419–423.

Downloaded 04 May 2010 to 171.66.16.27. Redistribution subject to ASME license or copyright; see http://www.asme.org/terms/Terms_Use.cfm

Transverse Normal Stress Effects in Multilayered Plates

E. Carrera
Research Professor,
Department of Aerospace Engineering,
Politecnico di Torino,
Corso Duca degli Abrussi 24,
10129 Torino, Italy
e-mail: carrera@polito.it

An evaluation of transverse normal stress σ_{zz} effects in multilayered plate modeling is given in this paper. Mixed theories with continuous interlaminar transverse shear and normal stresses have been formulated on the basis of Reissner's theorem (Reissner, 1984). The case in which the number of the displacement variables preserves independence by the number of constitutive layers, N_l, has been investigated. Classical models based on standard displacement formulations have been discussed for comparison purposes. The analysis of transverse stress effects has been conducted by allowing a constant, linear, and higher-order distribution of the transverse displacement components in the plate thickness directions. Related two-dimensional models are compared for the static response of symmetrically and unsymmetrically layered, simply supported plates made of isotropic as well as orthotropic layers. The conducted numerical investigation and comparison with available results have above all led to the following conclusions. The possibility of including σ_{zz} makes the used mixed theories more attractive that other available modelings. σ_{zz} plays a fundamental role in thick laminate plates analysis. Such a role increases in transversely anisotropic multilayered plate analysis. With an increase of the plate thickness, a very accurate description of σ_{zz} requires modelings whose number of independent variables depends on N_l.

1 Introduction

Elasticity solutions on layered plates (Pagano, 1969; Noor and Burton, 1989) and shells (Ren, 1987; Varadan and Bhaskar, 1991) indicate a number of requirements to accurately describe their elastodynamic response. Among these, the fulfillment of interlaminar continuity of the transverse stresses (shear and normal components), as well as the so-called zigzag form of the displacement field in the thickness direction, are necessary requirements. Very accurate analyses which consider each layer individually *layer-wise models* (LWM) (or multilayers or individual single-layer models) have confirmed these conclusions for the static (Srinivas, 1973; Mau, 1973; Toledano and Murakami, 1987a; Robbins and Reddy, 1993; Carrera, 1998a) and dynamic (Cheung and Wu, 1972; Barbero, Reddy, and Teply, 1990; Cho, Bert, and Striz, 1991; Carrera, 1998b, c) analysis of plate and shell structures. Herein attention is focused on the so-called *equivalent single-layer models* (ESLM). In such a case the number of resulting variables is independent of the number of N_l layers. The work by Hildebrand, Reissner, and Thomas (1940) and by Lo, Christensen, and Wu (1977) are examples of analyses in which higher-order displacement models have been employed. An interesting survey on this subject has been given by Reissner (1985). More recent studies on so-called p-extension, which are mainly oriented to finite element applications, have been probed by Szabo and Sahrmann (1988) and Surana and Sorem (1991). These types of classical theories do not include interlaminar continuity for the transverse shear and normal stresses nor allow the zigzag form for the displacement variables. The intrinsic coupling experienced by orthotropic material between in-plane σ_{xx}, σ_{yy} and out-of-plane σ_{zz} stresses makes the a priori fulfillment of σ_{zz} interlaminar equilibria diffult. Transverse normal stress has, in fact, been discarded in most of the available ESLM analyses. Interlaminar equilibria is usually restricted to the transverse shear components while the zigzag form appears only in the two in-plane components of the displacement. Among these analyses one can mention the early works by Ambartsumian (1968), Whitney (1969), and Rath and Das (1973), which have been more recently revised and extended by Bhashar and Varadan (1989), Di Sciuva (1993), Cho and Parmerter (1993), Soldatos and Timarci (1993), and Idlbi, Karama, and Touratier (1997). A different approach was introduced by Ren (1986) who extended an early theory by Lekhnitskii (1935) to plates that had been presented for beams; the resulting model showed the same restrictions as the previously mentioned analyses. To overcome these restrictions, Reissner proposed a mixed variational theorem RMVT which permits one to assume two independent interlaminar continuous fields for the displacements and transverse stresses (including σ_{zz} components). Similar conclusions were achieved as can be seen in Russian literature (see the very interesting and exhaustive overview presented by Grigolyuk and Kulikov (1988)). A complete discussion on the use of RMVT has recently been presented by the Author (Carrera, 1995, 1997). As far as ESLM is concerned, RMVT was employed by Murakami (1986) and Toledano and Murakami (1987b). σ_{zz} was discarded by Murakami (1986) but retained by Toledano and Murakami (1987b). Extensions to the shells of Murakami's theory were developed by Bhaskar and Varadan (1992) and Jing and Tzeng (1993).

To the best of the author's knowledge there is no available study in which the effects of normal stress σ_{zz} (both interlaminar continuity and zigzag form of transverse displacement u_z) are considered in the framework of ESL analyses. Such a study could establish the limitations of those modelings in which the σ_{zz} stress is neglected. The focus of the current work is directed towards removing this lack.

It would appear clear from the above-mentioned literature that such an aim could be reached in the framework of Reissner's mixed theorem applications. RMVT is therefore applied in the present work. Attention has herein been restricted to plate geometries. The classical model based on the standard displacement formulation is also derived. An analysis of transverse stress effects has been conducted by allowing different polynomials order N in the assumed expansions of displacement and/or stress unknowns. A layer-wise model which has been shown (Carrera, 1998a, b, c) to give a quasi-three-dimensional description of multilayered

Contributed by the Applied Mechanics Division of THE AMERICAN SOCIETY OF MECHANICAL ENGINEERS for publication in the ASME JOURNAL OF APPLIED MECHANICS.
Discussion on the paper should be addressed to the Technical Editor, Professor Lewis T. Wheeler, Department of Mechanical Engineering, University of Houston, Houston, TX 77204-4792, and will be accepted until four months after final publication of the paper itself in the ASME JOURNAL OF APPLIED MECHANICS.
Manuscript received by the ASME Applied Mechanics Division, July 24, 1998; final revision, Mar. 5, 1999. Associate Technical Editor: W. K. Liu.

 Copyright © 1999 by ASME

Downloaded 04 May 2010 to 171.66.16.27. Redistribution subject to ASME license or copyright; see http://www.asme.org/terms/Terms_Use.cfm

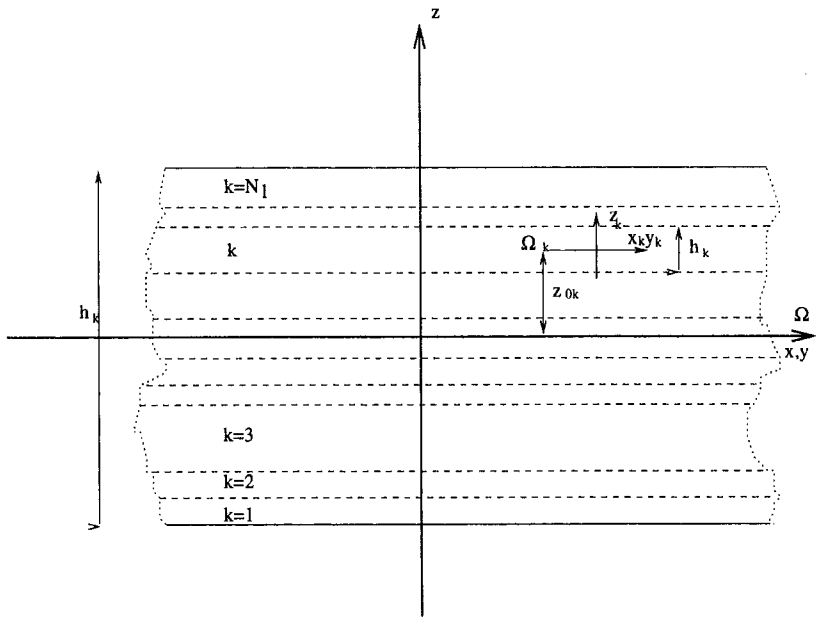


Fig. 1 Multilayered plate

structures is also introduced. This model has herein been used as a reference solution to assess simplified ESL analyses. All these models in this paper are written in a unified manner by referring to techniques developed by the author in earlier works.

2 Preliminary

The geometry and coordinate system of the laminated plates of N_l layers are shown in Fig. 1. The integer k, which is extensively used as both subscripts or superscripts, denotes the layer number that starts from the plate bottom. x and y are the plate middle surface Ω^k coordinates. Γ^k is the layer boundary on Ω^k. z and z_k are the plate and layer thickness coordinates; h and h_k denote the plate and layer thickness, respectively. $\zeta_k = 2z_k/h_k$ is the nondimensioned local plate coordinate; A_k denotes the k-layer thickness domain. Symbols that are not affected by the k subscript/superscripts refer to the whole plate.

The lamina are considered to be homogeneous and to operate in the linear elastic range. Stiffness coefficients are employed in standard form of the Hooke's law for the anisotropic k-lamina. This reads $\sigma_i = \tilde{C}_{ij}\epsilon_j$ where the subindices i and j, ranging from 1 to 6, stand for the index couples 11, 22, 33, 13, 23, and 12, respectively. The material is assumed to be orthotropic as specified by $\tilde{C}_{14} = \tilde{C}_{24} = \tilde{C}_{34} = \tilde{C}_{64} = \tilde{C}_{15} = \tilde{C}_{25} = \tilde{C}_{35} = \tilde{C}_{65} = 0$. This implies that σ^k_{xz} and σ^k_{yz} depend only on ϵ^k_{xz} and ϵ^k_{yz}. In matrix form

$$\boldsymbol{\sigma}^k_{pH_d} = \tilde{\mathbf{C}}^k_{pp}\boldsymbol{\epsilon}^k_{pG} + \tilde{\mathbf{C}}^k_{pn}\boldsymbol{\epsilon}^k_{nG}$$

$$\boldsymbol{\sigma}^k_{nH} = \tilde{\mathbf{C}}^k_{np}\boldsymbol{\epsilon}^k_{pG} + \tilde{\mathbf{C}}^k_{nn}\boldsymbol{\epsilon}^k_{nG} \tag{1}$$

where

$$\tilde{\mathbf{C}}^k_{pp} = \begin{bmatrix} \tilde{C}^k_{11} & \tilde{C}^k_{12} & \tilde{C}^k_{16} \\ \tilde{C}^k_{12} & \tilde{C}^k_{22} & \tilde{C}^k_{26} \\ \tilde{C}^k_{16} & \tilde{C}^k_{26} & \tilde{C}^k_{66} \end{bmatrix}, \quad \tilde{\mathbf{C}}^k_{pn} = \tilde{\mathbf{C}}^{k^T}_{np} = \begin{bmatrix} 0 & 0 & \tilde{C}^k_{13} \\ 0 & 0 & \tilde{C}^k_{23} \\ 0 & 0 & \tilde{C}^k_{36} \end{bmatrix},$$

$$\tilde{\mathbf{C}}^k_{nn} = \begin{bmatrix} \tilde{C}^k_{44} & \tilde{C}^k_{45} & 0 \\ \tilde{C}^k_{45} & \tilde{C}^k_{55} & 0 \\ 0 & 0 & \tilde{C}^k_{66} \end{bmatrix}.$$

Boldface letters denote arrays. The superscript T signifies array transposition. The subscripts n and p denote transverse (out-of-plane, normal) and in-plane values, respectively. Therefore

$$\boldsymbol{\sigma}^k_p = \{\sigma^k_{xx}, \sigma^k_{yy}, \sigma^k_{xy}\}, \quad \boldsymbol{\sigma}^k_n = \{\sigma^k_{xz}, \sigma^k_{yz}, \sigma^k_{zz}\}$$

$$\boldsymbol{\epsilon}^k_p = \{\epsilon^k_{xx}, \epsilon^k_{yy}, \epsilon^k_{xy}\}, \quad \boldsymbol{\epsilon}^k_n = \{\epsilon^k_{xz}, \epsilon^k_{yz}, \epsilon^k_{zz}\}.$$

It should be noticed that σ_{zz} couples the in-plane and out-of-plane stress and strain components. Subscript H denotes stresses evaluated with Hooke's law while subscript G denotes the strain from the geometrical relation Eq. (3). Further subscript d signifies values employed in the displacement formulation. Equation (1) is used in conjunction with a standard displacement formulation, while, for the adopted mixed solution procedure, the stress-strain relationships are conveniently put in the following mixed form:

$$\boldsymbol{\sigma}^k_{pH} = \mathbf{C}^k_{pp}\boldsymbol{\epsilon}^k_{pG} + \mathbf{C}^k_{pn}\boldsymbol{\sigma}^k_{nM}$$

$$\boldsymbol{\epsilon}^k_{nH} = \mathbf{C}^k_{np}\boldsymbol{\epsilon}^k_{pG} + \mathbf{C}^k_{nn}\boldsymbol{\sigma}^k_{nM} \tag{2}$$

where both stiffness and compliance coefficients are employed. The subscript M states that the transverse stresses are those of the assumed model in Eq. (14) (see the next sections). The relation between the arrays of coefficients in the two forms of Hooke's law is simply found:

$$\mathbf{C}^k_{pp} = \tilde{\mathbf{C}}^k_{pp} - \tilde{\mathbf{C}}^k_{pn}\tilde{\mathbf{C}}^{k^{-1}}_{nn}\tilde{\mathbf{C}}^k_{np}, \quad \mathbf{C}^k_{pn} = \tilde{\mathbf{C}}^k_{pn}\tilde{\mathbf{C}}^{k^{-1}}_{nn}$$

$$\mathbf{C}^k_{np} = -\tilde{\mathbf{C}}^{k^{-1}}_{nn}\tilde{\mathbf{C}}^k_{np}, \quad \mathbf{C}^k_{nn} = \tilde{\mathbf{C}}^{k^{-1}}_{nn}.$$

Superscript -1 denotes an inversion of the array.

The strain components $\boldsymbol{\epsilon}^k_p$, $\boldsymbol{\epsilon}^k_n$ are linearly related to the displacements $\mathbf{u}^k(\{u^k_x, u^k_y, u^k_z\})$, according to the following geometrical relations:

$$\boldsymbol{\epsilon}^k_{pG} = \mathbf{D}_p\mathbf{u}^k, \quad \boldsymbol{\epsilon}^k_{nG} = \mathbf{D}_n\mathbf{u}^k. \tag{3}$$

$\mathbf{D}_p$ and $\mathbf{D}_n$ denotes in-plane and out-of-plane differential operators

$$\mathbf{D}_p = \begin{bmatrix} \partial_x & 0 & 0 \\ 0 & \partial_y & 0 \\ \partial_y & \partial_x & 0 \end{bmatrix}; \quad \mathbf{D}_n = \begin{bmatrix} \partial_z & 0 & \partial_x \\ 0 & \partial_z & \partial_y \\ 0 & 0 & \partial_z \end{bmatrix}.$$

3 Displacement and Stress Assumption

3.1 Classical Models. First, classical models are considered. As usual, the displacement variables are expressed in Taylor series

Downloaded 04 May 2010 to 171.66.16.27. Redistribution subject to ASME license or copyright; see http://www.asme.org/terms/Terms_Use.cfm

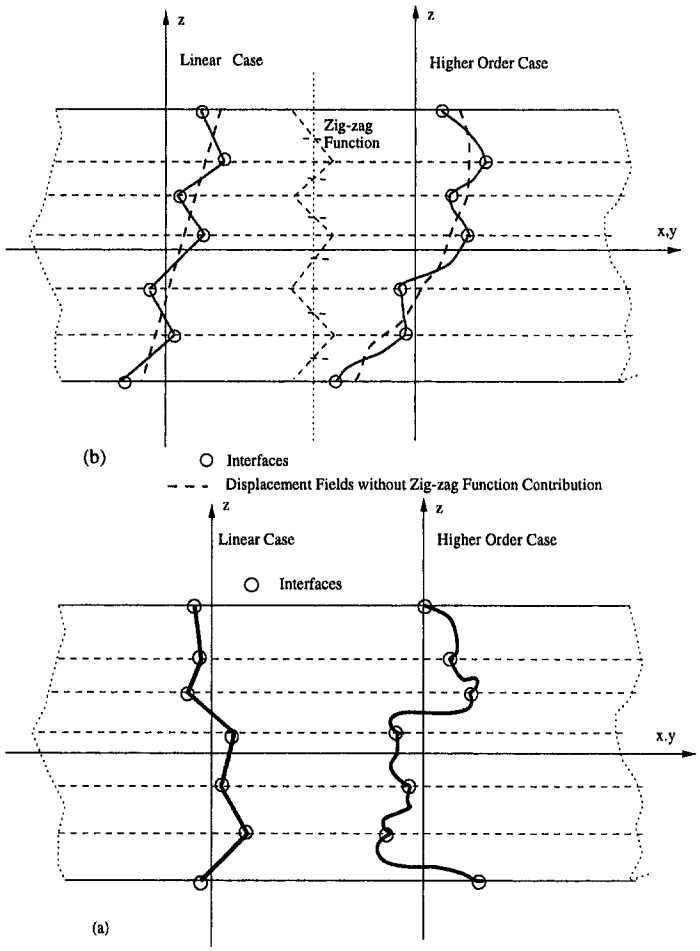


Fig. 2 Displacement and stress fields assumed for the employed models

in terms of unknown variables which are defined on the plate reference surface Ω,

$$\mathbf{u} = \mathbf{u}_0 + z^r \mathbf{u}_r, \quad r = 1, 2, \ldots, N. \tag{4}$$

N is a free parameter of the model. Different values for different modelings and different displacement and stress components are assumed. The repeated r indexes are summed over their ranges. Subscript 0 denotes displacement values with correspondence to the plate reference surface Ω. Linear and higher-order distributions in the z-direction are introduced by the r-polynomials. The assumed models can be written with the same notations that will be adopted for the layer-wise stress model Eq. (9). Equation (4) is therefore rewritten

$$\mathbf{u} = F_t \mathbf{u}_t + F_b \mathbf{u}_b + F_r \mathbf{u}_r = F_\tau \mathbf{u}_\tau, \quad \tau = t, b, r, \quad r = 1, 2, \ldots, N-1. \tag{5}$$

Subscript b denotes values related to the plate reference surface $\Omega(\mathbf{u}_b = \mathbf{u}_0)$ while subscript t refers to the highest term $(\mathbf{u}_t = \mathbf{u}_N)$. The F_τ functions assume the following explicit form

$$F_b = 1, \quad F_t = z^N, \quad F_r = z^r, \quad r = 1, 2, \ldots, N-1. \tag{6}$$

Transverse stress σ_{zz} and strain ϵ_{zz} effects are discarded by forcing a constant $(N = 0)$ distribution for the u_z-expansion.

3.2 Mixed Models. The zigzag form of the displacement fields can be reproduced in Eq. (4) by employing the Murakami idea (Murakami, 1986). In the framework of the ESL description and according to Murakami (1986), a zigzag term can be introduced into Eq. (4) (see Fig. 2):

$$\mathbf{u}^k = \mathbf{u}_0 + (-1)^k \zeta_k \mathbf{u}_Z + z^r \mathbf{u}_r, \quad r = 1, 2, \ldots, N. \tag{7}$$

Subscript Z refers to the introduced zigzag term. With unified notations Eq. (8) becomes

$$\mathbf{u}^k = F_t \mathbf{u}_t + F_b \mathbf{u}_b + F_r \mathbf{u}_r = F_\tau \mathbf{u}_\tau, \quad \tau = t, b, r, \quad r = 1, 2, \ldots, N. \tag{8}$$

Subscript t refers to the introduced zigzag term $(\mathbf{u}_t = \mathbf{u}_Z,\ F_t = (-1)^k \zeta_k)$. The F_t functions assume the following explicit form. It should be noticed that F_t assumes the values ± 1 in correspondence to the bottom and the top interface of the k-layer (see Fig. 2).

The thickness expansion used for displacement variables in Eq. (8) is not suitable for the transverse stress cases. For instance, homogeneous top-bottom plate surface conditions cannot be imposed. Transverse stresses are therefore herein described by means of the layer-wise description (Murakami, 1986; Toledano-Murakami, 1987b; Carrera, 1995, 1998a)

$$\boldsymbol{\sigma}^k_{nM} = F_t \boldsymbol{\sigma}^k_{nt} + F_b \boldsymbol{\sigma}^k_{nb} + F_r \boldsymbol{\sigma}^k_{nr} = F_\tau \boldsymbol{\sigma}^k_{n\tau}, \quad \tau = t, b, r, \quad r = 2, 3, \ldots, N; \quad k = 1, 2, \ldots, N_l. \tag{9}$$

In contrast to in Eq. (8), it is now intended that the subscripts t and b denote values related to the layer top and bottom surface, respectively. They consist of the linear part of the expansion. The thickness functions $F_\tau(\zeta_k)$ have now been defined at the k-layer level,

$$F_t = \frac{P_0 + P_1}{2}, \quad F_b = \frac{P_0 - P_1}{2},$$

Downloaded 04 May 2010 to 171.66.16.27. Redistribution subject to ASME license or copyright; see http://www.asme.org/terms/Terms_Use.cfm

$$F_r = P_r - P_{r-2}, \quad r = 2, 3, \ldots, N, \tag{10}$$

in which $P_j = P_j(\zeta_k)$ is the Legendre polynomial of the j-order defined in the ζ_k-domain: $-1 \le \zeta_k \le 1$. The parabolic, cubic, and fourth-order stress field Eq. (9) will be associated to linear, parabolic, and cubic displacement field Eq. (8), respectively, in the numerical investigations. The related polynomials are

$$P_0 = 1, \quad P_1 = \zeta_k, \quad P_2 = (3\zeta_k^2 - 1)/2,$$

$$P_3 = \frac{5\zeta_k^3}{2} - \frac{3\zeta_k}{2}, \quad P_4 = \frac{35\zeta_k^4}{8} - \frac{15\zeta_k^2}{4} + \frac{3}{8}.$$

The chosen functions have the following properties:

$$\zeta_k = \begin{cases} 1: & F_t = 1; \quad F_b = 0; \quad F_r = 0 \\ -1: & F_t = 0; \quad F_b = 1; \quad F_r = 0. \end{cases} \tag{11}$$

The top and bottom values have been used as unknown variables. The interlaminar transverse shear and normal stress continuity can therefore be easily linked:

$$\boldsymbol{\sigma}_{nt}^k = \boldsymbol{\sigma}_{nb}^{(k+1)}, \quad k = 1, \quad N_l - 1. \tag{12}$$

In those cases in which the top/bottom-shell stress values are prescribed (zero or imposed values), the following additional equilibrium conditions must be accounted for,

$$\boldsymbol{\sigma}_{nb}^1 = \bar{\boldsymbol{\sigma}}_{nb}, \quad \boldsymbol{\sigma}_{nt}^{N_l} = \bar{\boldsymbol{\sigma}}_{nt}, \tag{13}$$

where the overbar is the imposed values in correspondence to the plate boundary surfaces. Examples of linear and higher-order fields have been plotted in Fig. 2. The stress variables could be eliminated by employing the *weak form of Hooke's law* proposed in (Carrera, 1996).

3.3 Layer-Wise Mixed Model. According to Carrera (1995, 1998a) two independent layer-wise fields are assumed for both displacement and stress variables as in Eq. (9),

$$\begin{aligned} &\mathbf{u}^k = F_t\mathbf{u}_t^k + F_b\mathbf{u}_b^k + F_r\mathbf{u}_r^k = F_\tau\mathbf{u}_\tau^k && \tau = t, b, r \\ &&& r = 2, 3, \ldots, N \\ &\boldsymbol{\sigma}_{nM}^k = F_t\boldsymbol{\sigma}_{nt}^k + F_b\boldsymbol{\sigma}_{nb}^k + F_r\boldsymbol{\sigma}_{nr}^k = F_\tau\boldsymbol{\sigma}_{n\tau}^k && k = 1, 2, \ldots, N_l. \end{aligned} \tag{14}$$

In addition to Eq. (12) the compatibility of the displacement reads

$$\mathbf{u}_t^k = \mathbf{u}_b^{(k+1)}, \quad k = 1, \quad N_l - 1. \tag{15}$$

4 Governing Equations

In order to write all the models mentioned in the previous section it is convenient to refer to all the stress and displacement variables at the k-layer level, i.e., to use a layer-wise description. ESL cases are achieved by writing the governing equations at the multilayered plate level.

The displacement approach is formulated in terms of $\mathbf{u}^k$ by variatianally imposing the equilibrium via the principle of virtual displacements. In the static case this establishes

$$\sum_{k=1}^{N_l} \int_{\Omega^k} \int_{A_k} (\delta\boldsymbol{\epsilon}_{pG}^{kT}\boldsymbol{\sigma}_{pH_d}^k + \delta\boldsymbol{\epsilon}_{nG}^{kT}\boldsymbol{\sigma}_{nH_d}^k) d\Omega^k dz = \delta L^e \tag{16}$$

where δ signifies virtual variations. The variation of the internal work has been split into in-plane and out-of-plane parts and involves the stress obtained from Hooke's Law and the strain from the geometrical relations. δL_e is the virtual variation of the work done by the external layer-forces $\mathbf{p}^k(\{p_x^k, p_y^k, p_z^k\})$.

In the mixed case, the equilibrium and compatibility are both formulated in terms of the $\mathbf{u}^k$ and $\boldsymbol{\sigma}_n^k$ unknowns via Reissner's mixed variational theorem (Reissner, 1984, 1986),

$$\sum_{k=1}^{N_l} \int_{\Omega^k} \int_{A_k} (\delta\boldsymbol{\epsilon}_{pG}^{kT}\boldsymbol{\sigma}_{pH}^k + \delta\boldsymbol{\epsilon}_{nG}^{kT}\boldsymbol{\sigma}_{nM}^k + \delta\boldsymbol{\sigma}_{nM}^{kT}(\boldsymbol{\epsilon}_{nG}^k - \boldsymbol{\epsilon}_{nH}^k)) d\Omega^k dz = \delta L^e. \tag{17}$$

The L.H.S. includes the variations of the internal work in the plate: the first two terms come from the displacement formulation, they lead to variatianally consistent equilibrium conditions; the third "mixed" term variationally enforces the compatibility of the transverse strains components.

Upon substitution of Eqs. (1), (2), and (3), as well as of the requested assumed model Eqs. (4)–(14) and by integrating by parts, the two previous variational equations lead to governing differential equations. These equations were written in Carrera (1998b) in terms of stress and strain resultants; details on the treatment of the variational equations were also reported in this work. For the sake of conciseness, the governing equations have herein been expressed in terms of the introduced stress and displacement variables.

The displacement formulation yields to the following equilibrium conditions:

$$\delta\mathbf{u}_\tau^k: \quad \mathbf{K}_d^{k\tau s}\mathbf{u}_s^k = \mathbf{p}_\tau^k. \tag{18}$$

The related boundary conditions are

$$\mathbf{u}_\tau^k = \bar{\mathbf{u}}_\tau^k \quad \text{or} \quad \boldsymbol{\Pi}_d^{k\tau s}\mathbf{u}_s^k = \boldsymbol{\Pi}_d^{k\tau s}\bar{\mathbf{u}}_s^k \tag{19}$$

while the mixed case leads to the following set of equilibrium and constitutive equations

$$\begin{aligned} &\delta\mathbf{u}_\tau^k: \quad \mathbf{K}_{uu}^{k\tau s}\mathbf{u}_s^k + \mathbf{K}_{u\sigma}^{k\tau s}\boldsymbol{\sigma}_{ns}^k = \mathbf{p}_\tau^k \\ &\delta\boldsymbol{\sigma}_{n\tau}^k: \quad \mathbf{K}_{\sigma u}^{k\tau s}\mathbf{u}_s^k + \mathbf{K}_{\sigma\sigma}^{k\tau s}\boldsymbol{\sigma}_{ns}^k = 0 \end{aligned} \tag{20}$$

and to the boundary conditions

$$\mathbf{u}_\tau^k = \bar{\mathbf{u}}_\tau^k \quad \text{or} \quad \boldsymbol{\Pi}_u^{k\tau s}\mathbf{u}_s^k + \boldsymbol{\Pi}_\sigma^{k\tau s}\boldsymbol{\sigma}_{ns}^k = \boldsymbol{\Pi}_u^{k\tau s}\bar{\mathbf{u}}_s^k + \boldsymbol{\Pi}_\sigma^{k\tau s}\bar{\boldsymbol{\sigma}}_{ns}^k. \tag{21}$$

The further subscript/superscript $s = t, b, r$ has been introduced in order to distinguish the terms related to the introduced variables from those related to their variations. In explicit form

$$\begin{aligned} \mathbf{K}_d^{k\tau s} &= -\mathbf{D}_p^T(\tilde{\mathbf{Z}}_{pp}^{k\tau s}\mathbf{D}_p + \tilde{\mathbf{Z}}_{pn}^{k\tau s}\mathbf{D}_{n\Omega} + \tilde{\mathbf{Z}}_{pn}^{k\tau s_z}\mathbf{D}_{n\Omega}) - \mathbf{D}_{n\Omega}^T(\tilde{\mathbf{Z}}_{np}^{k\tau s}\mathbf{D}_p \\ &\quad + \tilde{\mathbf{Z}}_{nn}^{k\tau s}\mathbf{D}_{n\Omega} + \tilde{\mathbf{Z}}_{nn}^{k\tau s_z}) + \tilde{\mathbf{Z}}_{np}^{k\tau_z s}\mathbf{D}_p + \tilde{\mathbf{Z}}_{nn}^{k\tau_z s}\mathbf{D}_{n\Omega} + \tilde{\mathbf{Z}}_{nn}^{k\tau_z s_z} \\ \boldsymbol{\Pi}_d^{k\tau s} &= \mathbf{I}_p^T(\tilde{\mathbf{Z}}_{pp}^{k\tau s}\mathbf{D}_p + \tilde{\mathbf{Z}}_{pn}^{k\tau s}\mathbf{D}_{n\Omega} + \tilde{\mathbf{Z}}_{pn}^{k\tau s_z}\mathbf{D}_{n\Omega}) \\ &\quad + \mathbf{I}_{n\Omega}^T(\tilde{\mathbf{Z}}_{np}^{k\tau s}\mathbf{D}_p + \tilde{\mathbf{Z}}_{nn}^{k\tau s}\mathbf{D}_{n\Omega} + \tilde{\mathbf{Z}}_{nn}^{k\tau s_z}) \\ \mathbf{K}_{uu}^{k\tau s} &= -\mathbf{D}_p^T\mathbf{Z}_{pp}^{k\tau s}\mathbf{D}_p \quad \mathbf{K}_{u\sigma}^{k\tau s} = -\mathbf{D}_p^T\mathbf{Z}_{pn}^{k\tau s} + E_{\tau_z s}\mathbf{I} - E_{\tau s}\mathbf{D}_{n\Omega}^T \\ \mathbf{K}_{\sigma u}^{k\tau s} &= E_{\tau s}\mathbf{D}_{n\Omega} + E_{\tau s_z}\mathbf{I} - \mathbf{Z}_{np}^{k\tau s}\mathbf{D}_p \quad \mathbf{K}_{\sigma\sigma}^{k\tau s} = -\mathbf{Z}_{nn}^{k\tau s} \\ \boldsymbol{\Pi}_u^{k\tau s} &= \mathbf{I}_p^T\mathbf{Z}_{pp}^{k\tau s}\mathbf{D}_p \quad \boldsymbol{\Pi}_\sigma^{k\tau s} = \mathbf{Z}_{pn}^{k\tau s} + E_{\tau s}\mathbf{I}_{n\Omega}^T \end{aligned} \tag{22}$$

where

$$\mathbf{D}_{n\Omega} = \begin{bmatrix} 0 & 0 & \partial_x \\ 0 & 0 & \partial_y \\ 0 & 0 & 0 \end{bmatrix}; \quad \mathbf{I} = \begin{bmatrix} 1 & 0 & 0 \\ 0 & 1 & 0 \\ 0 & 0 & 1 \end{bmatrix};$$

$$\mathbf{I}_p = \begin{bmatrix} 1 & 0 & 0 \\ 0 & 1 & 0 \\ 1 & 1 & 0 \end{bmatrix}; \quad \mathbf{I}_{n\Omega} = \begin{bmatrix} 0 & 0 & 1 \\ 0 & 0 & 1 \\ 0 & 0 & 0 \end{bmatrix}.$$

The integration in the thickness coordinate has been a priori carried out as usual in two-dimensional modelings: The following layer-stiffnesses and integrals have been introduced:

Downloaded 04 May 2010 to 171.66.16.27. Redistribution subject to ASME license or copyright; see http://www.asme.org/terms/Terms_Use.cfm

$$(\tilde{\mathbf{Z}}^{k\tau s}_{pp}, \tilde{\mathbf{Z}}^{k\tau s}_{pn}, \tilde{\mathbf{Z}}^{k\tau s}_{np}, \tilde{\mathbf{Z}}^{k\tau s}_{nn}, \mathbf{Z}^{k\tau s}_{pp}, \mathbf{Z}^{k\tau s}_{pn}, \mathbf{Z}^{k\tau s}_{np}, \mathbf{Z}^{k\tau s}_{nn}) = (\tilde{\mathbf{C}}^{k}_{pp}, \tilde{\mathbf{C}}^{k}_{pn}, \tilde{\mathbf{C}}^{k}_{np}, \tilde{\mathbf{C}}^{k}_{nn}, \mathbf{C}^{k}_{pp}, \mathbf{C}^{k}_{pn}, \mathbf{C}^{k}_{np}, \mathbf{C}^{k}_{nn}) E_{\tau s}$$

$$(\tilde{\mathbf{Z}}^{k\tau s_z}_{pn}, \tilde{\mathbf{Z}}^{k\tau_z s}_{np}, \tilde{\mathbf{Z}}^{k\tau s_z}_{nn}, \tilde{\mathbf{Z}}^{k\tau_z s}_{nn}, \tilde{\mathbf{Z}}^{k\tau_z s_z}_{nn}) = (\tilde{\mathbf{C}}^{k}_{pn} E_{\tau s_z}, \tilde{\mathbf{C}}^{k}_{np} E_{\tau_z s}, \tilde{\mathbf{C}}^{k}_{nn} E_{\tau s_z}, \tilde{\mathbf{C}}^{k}_{nn} E_{\tau_z s}, \tilde{\mathbf{C}}^{k}_{nn} E_{\tau_z s_z})$$

$$(E^{k}_{\tau s}, E_{\tau_z s}, E_{\tau s_z}, E^{k}_{\tau_z s_z}) = \int_{A_k} (F_\tau F_s, F_{\tau_z} F_s, F_\tau F_{s_z}, F_{\tau_z} F_{s_z}) dz. \quad (23)$$

Explicit forms of the governing equations for each layer can be written by expanding the introduced subscripts and superscripts in the previous arrays as follows:

$$k = 1, 2, \ldots, N_l; \quad \tau = t, r, b, \quad s = t, r, b, \quad (r = 2, \ldots, N).$$

4.1 Assembly From Layer to Multilayered Plate Level. In the previous sections mixed and standard displacement formulations have been written for the N_l independent layers. Multilayered equations can be written according to the usual variational statements: Stiffness and/or compliances related to the same variables are accumulated in this process. Interlaminar continuity conditions are imposed at this stage. Details on this procedure can be found in the already mentioned papers (Carrera, 1995, 1998a). Multilayered arrays are introduced. The equilibrium and boundary conditions for the displacement formulation take on the following form:

$$\mathbf{K}_d \mathbf{u} = \mathbf{p}$$

$$\mathbf{u} = \bar{\mathbf{u}} \quad \text{or} \quad \mathbf{\Pi}_d \mathbf{u} = \mathbf{\Pi}_d \bar{\mathbf{u}} \quad (24)$$

while for the mixed case, one has

$$\mathbf{K}_{uu}\mathbf{u} + \mathbf{K}_{u\sigma}\boldsymbol{\sigma}_n = \mathbf{p} + \mathbf{p}_u^{1N_l}$$

$$\mathbf{K}_{\sigma u}\mathbf{u} + \mathbf{K}_{\sigma\sigma}\boldsymbol{\sigma}_n = \mathbf{p}_\sigma^{1N_l} \quad (25)$$

with boundary conditions

$$\mathbf{u} = \bar{\mathbf{u}} \quad \text{or} \quad \mathbf{\Pi}_u \mathbf{u} + \mathbf{\Pi}_\sigma \boldsymbol{\sigma}_n = \mathbf{\Pi}_u \bar{\mathbf{u}} + \mathbf{\Pi}_\sigma \bar{\boldsymbol{\sigma}}_n. \quad (26)$$

$\mathbf{p}_u^{1N_l}$ and $\mathbf{p}_\sigma^{1N_l}$ are the arrays obtained from the transverse stress values imposed at the top/bottom of the plate.

4.2 Closed-Form Solutions for Cross-Ply Laminated Plates. The boundary value problem governed by Eqs. (24), (25), and (26) in the most general case of geometry, boundary conditions and layouts, could be solved by implementing only approximated solution procedures. The particular case in which the material has the properties $\tilde{C}_{16} = \tilde{C}_{26} = \tilde{C}_{36} = \tilde{C}_{45} = 0$, has here been considered, for which Navier-type closed-form solutions can be found by assuming the following harmonic forms for the applied loadings and unknown variables,

$$(u^k_{x_\tau}, \sigma^k_{xz_\tau}, p^k_{x_\tau}) = \sum_{m,n} (U^k_x, S^k_{xz_\tau}, P^k_{x_\tau}) \cos\frac{m\pi x}{a} \sin\frac{n\pi y}{b}$$

$$(u^k_{y_\tau}, \sigma^k_{yz_\tau}, p^k_{y_\tau}) = \sum_{m,n} (U^k_y, S^k_{yz_\tau}, P^k_{y_\tau}) \sin\frac{m\pi x}{a} \cos\frac{n\pi y}{b}$$

$$(u^k_{z_\tau}, \sigma^k_{zz_\tau}, p^k_{z_\tau}) = \sum_{m,n} (U^k_z, S^k_{zz_\tau}, P^k_{z_\tau}) \sin\frac{m\pi x}{a} \sin\frac{n\pi y}{b}. \quad (27)$$

a and b are the plate lengths in the x and y directions, respectively, while m and n are the correspondent wave numbers. Capital letters in the R.H.S. are correspondent maximum amplitudes. On substitution of Eqn. (27), the governing equations assume the form of a linear system of algebraic equations. This procedure has been coded for the different case theories and results are discussed in the next section.

Table 1 List of the acronyms used to denote plate theories

— Theories from literature	
Exact	Three dimensional solution after Pagano (1969)
C&P1, C&P3	Linear and cubic case after Cho and Parmerter (1993)
D&S1, D&S3	Linear and cubic case after Di Sciuva (1993)
IK&T	Idlbi, Karama and Touratier (1997)
LC&W	Lo, Christiansen and Wu (1977)
T&M1,T&M3	Murakami (1986) and Toledano and Murakami (1987b)
Ren	Ren (1986)
— Present Theories	
D1i,D2i,D3i**	Classical models in Eqns.(4)
D1d,D2d,D3d*	Classical models discarding σ_{zz}
D3Zi	Classical models using Eqns.(8) instead of Eqns.(4)
LW4	Mixed layer-wise model Eqn.(14) relate to N=4
M1i,M2i,M3i	Mixed models in Eqn.(8), Eqn.(9)
M1d,M2d,M3d	Mixed models discarding σ_{zz}
M3ia***	M3i-case discarding zigzag $(-1)^k u_{Z_z}$ term.

* suffixes 1,2,3 denote linear, parabolic and cubic u-fields, respectively, while d signifies that σ_{zz} has been discarded.
** suffix i denotes results including σ_{zz}.
*** suffix a refers to analyses discarding the zigzag terms in u_z of Eqn.(8).

5 Results and Discussion

Simply supported plates bent by a transverse bi-sinusoidal distribution of normal pressure $p^{N_l}_{z_t}$ applied to the top surface of the whole plate have been considered. Two loading cases $m = 1$, $n = 0$ (cylindrical bending) and $m = n = 1$ have been considered. Several particular case theories related to different N-orders of the expansion in the introduced displacement and stress fields have been considered. The treated subcases are described in Table 1 where the used acronyms are listed. Through the thickness distribution of in-plane and transverse stress and displacement amplitudes have been analyzed. The following nondimensioned parameters have been introduced:

$$\bar{S}_{xz} = S_{xz}/(p^{N_l}_{z_t} a/h), \quad \bar{S}_{zz} = S_{zz}/p^{N_l}_{z_t},$$

$$\bar{U}_x = U_x E_T/(p^{N_l}_{z_t}(a/h)^3), \quad \bar{U}_z = U_z \times 100 E_T h^3/(p^{N_l}_{z_t} a^4)$$

Thin and thick as well as square and rectangular plate geometries have been analyzed. Cross-ply, symmetrically ($N_l = 3, 9$) and unsymmetrically ($N_l = 4$) laminated plates are considered in Tables 2–4 and Figs. 2–8. The mechanical data of the lamina are those used by Pagano (1969): $E_L = 25 \times 10^6$ psi, $E_T = 1 \times 10^6$ psi, $G_{LT} = 0.5 \times 10^6$ psi, $G_{TT} = 0.2 \times 10^6$ psi, $\nu_{LT} = \nu_{TT} = .25$; where, following the usual notation (Reddy, 1997), L signifies

Table 2 Maximum transverse displacement $\bar{U}_z$ ($z = 0$) of thick plate in cylindrical bending. Comparison of present analyses to exact solutions and to available mixed results.

	a/h=4		a/h=6	
	N_l=3	N_l=4	N_l=3	N_l=4
Exact	2.887	4.181	1.635	2.556
T&M3	2.881	4.105	1.634	2.519
C&P3	-	4.083	-	2.501
T&M1	2.907	3.316	1.636	2.107
C&P1	-	3.316	-	2.107
LC&W	2.687	3.587	1.514	2.242
Present Analysis				
LW4	2.887	4.181	1.625	2.556
—σ_{zz} included				
M3i	2.881	4.102	1.634	2.514
M2i	2.831	3.478	1.602	2.195
M1i	2.904	3.300	1.634	2.095
—σ_{zz} discarded				
M3d	2.898	4.124	1.637	2.516
M2d	2.848	3.488	1.605	2.195
M1d	2.904	3.306	1.634	2.098

Downloaded 04 May 2010 to 171.66.16.27. Redistribution subject to ASME license or copyright; see http://www.asme.org/terms/Terms_Use.cfm

Table 3 Influence of thickness ration on $\bar{U}_z$ ($z = 0$) and $\bar{S}_{xz}$ ($z = 0$ unless denoted). Rectangular ($b = 3a$) three-layered plates.

	$\bar{U}_z$			$\bar{S}_{xz}$			
a/h	4	10	20	4	z	10	20
Exact	2.820	.919	.610	.387	-	.420	.434
IK&TC	2.729	.918	.609	.378	-	.441	.451
D&S1	2.717	.881	.599	.366	-	.419	-
D&S3	2.757	.919	.610	.329	-	.420	-
Ren	2.80	.920	-	.317	-	.415	-
	Present Analysis						
LW4	2.821	.919	.610	.387	-.23	.420	.434
	—σ_{zz} included						
M3i	2.815	.919	.609	.385	-.23	.420	.434
M3ia	2.815	.919	.609	.388	-.23	.420	.434
M2i	2.767	.906	.606	.393	-.23	.421	.435
M1i	2.839	.915	.606	.399	-.23	.420	.434
D3Zi	2.811	.919	.610	.389	.27	.420	.434
D3i	2.625	.867	.596	.378	-.17	.427	.436
	—σ_{zz} discarded						
M3d	2.832	.918	.607	.386	±.27	.420	.434
M2d	2.784	.904	.604	.393	±.23	.421	.435
M1d	2.839	.915	.606	.394	±.23	.420	.434
D3Zd	2.828	.918	.607	.348	±.27	.420	.434
D3d	2.644	.866	.593	.377	0	.427	.436

the fiber direction, T the transverse direction, and ν_{LT} is the major Poisson ratio.

Tables 2 and 3 compare present analysis to available results. A good agreement with the mixed models by Murakami (1986) and Toledano and Murakami (1987b) has been found. The LW4 analysis matches the exact solution with excellent accuracy. Such a result confirms (Carrera, 1998a, b, c) the reliability of layer-wise mixed models to give a three-dimensional description of stress and displacement fields in laminated plates. LW4 analysis has in fact been taken as a reference solutions in Table 4 and Figs. 3–12. The improvements introduced by taking σ_{zz} effects into account are evident for the thick plate cases. Higher-order mixed models lead to the best description. A comparison with the other models of Table 3 (C&P1, C&P3, D&S1, D&S3, IK&T which allow interlaminar continuous transverse shear stresses) reveals that the extension of such a continuity to σ_{zz} permits one to conclude that the M3i-model leads to the best ESL results. These comments are further confirmed by comparing the M3d, M2d, M1d to M3i, M2i, M1i analysis. Nevertheless, D3Zi results show that the classical displacement formulation can be greatly improved by introducing a zigzag functions $(-1)^k \mathbf{u}_z$ into Eq. (4).

Table 4 Influence of thickness ratio on $\bar{U}_z$ ($z = 0$). Same data of Table 2 (three-layer case).

a/h	2.5	5	10	100
LW4	5.963	2.091	.9316	.5140
	—σ_{zz} included			
M3i	5.912	2.089	.9180	.5140
M3ia	5.912	2.089	.9180	.5140
M2i	5.876	2.045	.9180	.5140
M1i	6.099	2.094	.9284	.5138
D3Zi	5.874	2.087	.9316	.5116
D3i	5.644	1.935	.8793	.5122
	—σ_{zz} discarded			
M3d	6.015	2.096	.9309	.5118
M2d	5.982	2.056	.9172	.5117
M1d	6.099	2.094	.9281	.5118
D3Zd	5.978	2.094	.9308	.5118
D3d	5.755	1.943	.8786	.5112

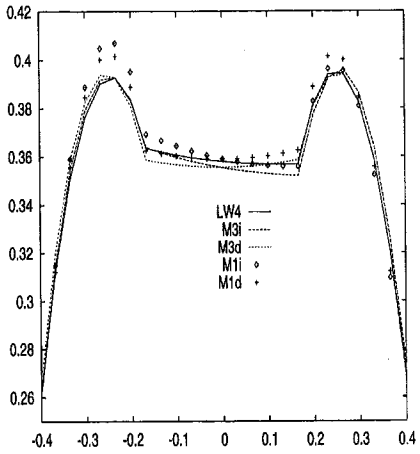


Fig. 3 $\bar{S}_{xz}$ versus z: asymmetry introduced by σ_{zz} effects. Data of Table 2 (three-layers case, $a/h = 4$).

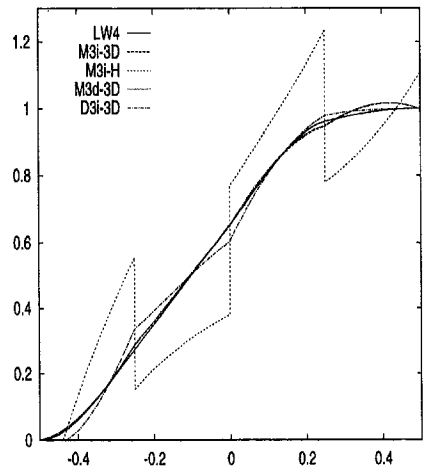


Fig. 4 $\bar{S}_{xz}$ versus z. Data of Table 2 (four-layers case, $a/h = 4$).

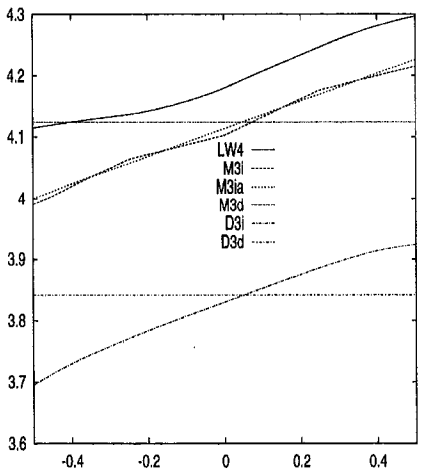


Fig. 5 $\bar{U}_z$ versus z. Data of Table 2 (four-layers case, $a/h = 4$).

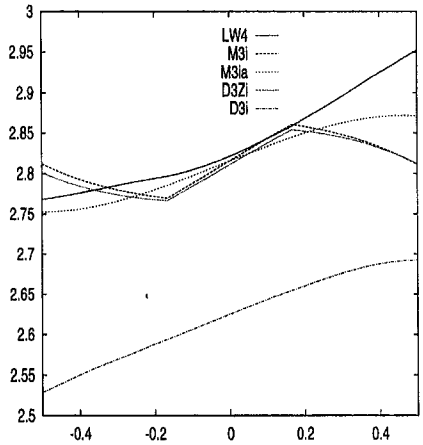


Fig. 6 $\bar{U}_z$ versus z. Data of Table 3 ($a/h = 4$).

Downloaded 04 May 2010 to 171.66.16.27. Redistribution subject to ASME license or copyright; see http://www.asme.org/terms/Terms_Use.cfm

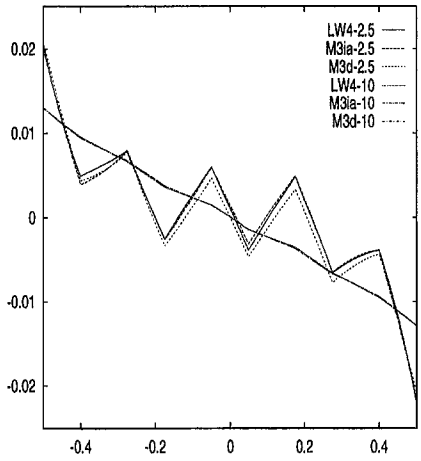


Fig. 7 $\bar{U}_z$ **versus** z**. Data of Table 2 (nine-layers case,** $a/h = 2.5, 10$**).**

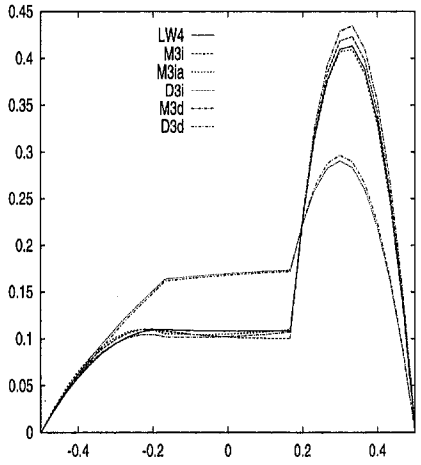


Fig. 10 $\bar{S}_{xz}$ **versus** z**. Square plate made of isotropic layers (Unsymmetrically laminated case,** $a/h = 4$**).**

Figure 3 makes a fundamental limitation of each laminated theory which neglected σ_{zz} evident. The top part of the diagram has been plotted. As confirmed in Table 3 ($a/h = 4$ case) and the plate being loaded at the top surface, σ_{zz} enforces a nonsymmetrical distribution of $\bar{S}_{xz}$ versus z for LW4, M3i, and M1i analyses. On the other hand, M3d and M1d analysis as well as any other plate theories in which σ_{zz} is discarded, cannot improve the transverse stress fields in the whole thickness. The plate being symmetrically laminated, M3d and M1d analyses in fact *tragically* lead to a symmetrical distribution of $\bar{S}_{xz}$ versus z: They cannot, therefore, in any case furnish the nonsymmetrical distribution of the LW4 analysis. Nevertheless, M3i results are very close to LW4 analysis.

Figure 4 shows that Hooke's law (suffix-H) leads to interlaminar discontinuous transverse normal stresses. σ_{zz} is therefore calculated via integration of the three dimensional equilibrium equa-

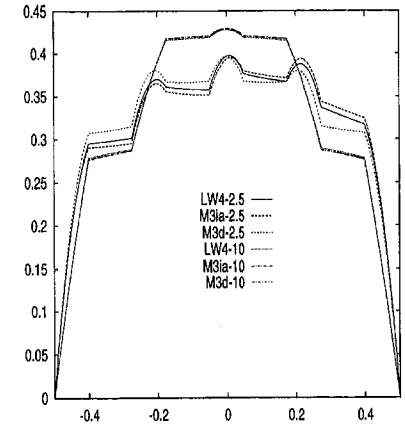


Fig. 8 $\bar{S}_{xz}$ **versus** z**. Data of Table 2 (nine-layers case,** $a/h = 2.5, 100$**).**

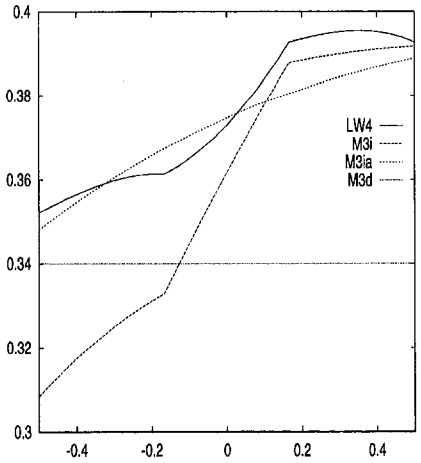


Fig. 11 $\bar{U}_z$ **versus** z**. Square plate made of isotropic layers (Unsymmetrically laminated case,** $a/h = 4$**).**

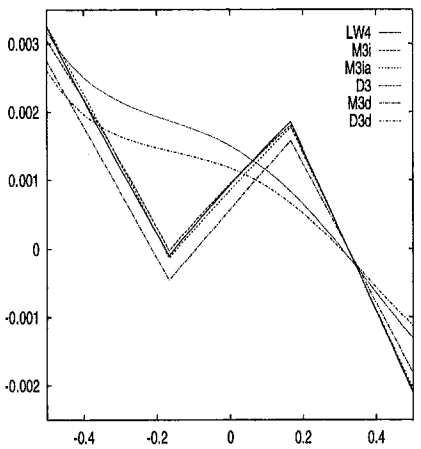


Fig. 9 $\bar{U}_x$ **versus** z**. Square plate made of isotropic layers (Unsymmetrically laminated case,** $a/h = 4$**).**

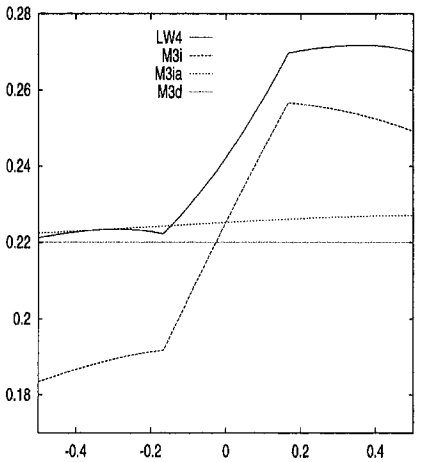


Fig. 12 $\bar{U}_z$ **versus** z**. Square plate made of isotropic layers (Symmetrically laminated case,** $a/h = 4$**).**

Downloaded 04 May 2010 to 171.66.16.27. Redistribution subject to ASME license or copyright; see http://www.asme.org/terms/Terms_Use.cfm

tions, related results are depicted by suffix-3D.[1] The superiority has to be registered of modeling including σ_{zz} as well as of referring to the mixed approach with respect to the displacement one. Major differences for the different theories, with respect to those in the previous tables, can be observed in Figs. 5 and 6 where $\bar{U}_z$ versus z has been plotted for a three and a four-layered plate, respectively. It should be noticed that the laminated plates being transversely isotropic (i.e., $E_z = E_T$ does not vary in the thickness direction) the zigzag terms u_{Z_t} of Eq. (8) could introduce an unmotivated constraint. The zigzag form has infact barely been exhibited by the LW4 analysis and better results have been obtained by the M3ia analysis.

The results on the thickness ratio effects are given in Table 4 and Figs. 7 and 8. Unrealistic symmetric distributions of and transverse shear stress discussed in Fig. 3, for those analyses which neglect σ_{zz}, can be confirmed for the case of Fig. 8 and extended to the in-plane displacement diagram of Fig. 7. It should be noticed that the maximum values $(S_{xz}/p_{zt}^{N_l})_{\max} \approx .4 \times 2.5 \approx 1.$ is almost coincident to the maximum σ_{zz} value $(S_{zz}/p_{zt}^{N_l})_{\max} = 1.$ for the thicker plate case: This is the simple reason why σ_{zz} cannot be neglected in thick plate analysis. Symmetry is reached for thinner plates. The superiority of modelings which include σ_{zz} as well as the convenience of referring to mixed descriptions has been confirmed.

A multilayered plate with nonconstant distribution of Young modulus E_z in the thickness direction has been considered in Figs. 9–12. A three-layered thick plate constituted by isotropic ($\nu = .3$) layers has been investigated. Figures 9–11 consider unsymmetrically laminated plates with $E^1/E^2 = 10$; $E^3/E^2 = 100$ where E^k ($k = 1, 2, 3$) are the Young moduli of the three layers. Fig. 12 considers a symmetrically laminated plate $E^1/E^2 = E^3/E^2 = 100$. The E^2 modulus has been used in the considered nondimensioned amplitudes. The superiority of the mixed cases over the displacement ones is evident. Nevertheless, for such a transversely anisotropic plate and in contrast to what has been written for the case of Figs. 5 and 6, the LW4 analysis of Figs. 9 and 12 shows an evident zigzag form for $\bar{U}_z$. Therefore, better results are obtained with the M3i analysis than with the M3ia ones. On the other hand the differences between M3i and LW4 analyses are larger than those experienced for the treated cross-ply plates. Such a conclusion draws attention to the fundamental limitation of two-dimensional modelings which preserve the number of the variables independent from the numbers of layers: They cannot accurately describe σ_{zz} and the related effects of thick structures even though mixed models are implemented. That is, a layer-wise description is required for this purpose.

6 Conclusions

This paper has evaluated the effects of transverse normal stress in two-dimensional modeling of multilayered plates which preserve the number of the unknown variables to be independent from the number of layers. Mixed formulations have been used for this purpose. A comparison with the classical displacement formulation has also been considered. From the conducted investigation the following main remarks can be made.

1 The a priori fulfillment of the interlaminar continuity for σ_{zz} makes mixed models more attractive than other available models which violate such a continuity.
2 Thick plate analysis has shown that refinements of existing theories can be meaningless unless both interlaminar continuous transverse shear and normal stresses are taken into account in a refined theory.
3 The number of the independent variables should be conveniently taken dependent on N_l in very thick plate analysis. Such a requirement becomes mandatory for the case of transversely anisotropic multilayered plates.

The conclusions reached in this paper have been restricted to bended, simply supported orthotropic plates. Additional investigations should be addressed to different geometries, boundary conditions, as well as multilayered lay-outs. Finite element method could be conveniently used to these aims. Works in this direction are in progress and results could be proposed in future works. However, the proposed closed-form results could be used as reference solution to assess approximated analyses.

[1] Even though the mixed models furnish σ_{zz} a priori, its a posteriori evaluation has been preferred for two reasons: (1) to compare consistent results (classical formulation do not permit a priori evaluations); (2) the integration of three-dimensional equilibrium equations leads to better results (Bhaskar and Varadan, 1992; Carrera, 1996).

Acknowledgments

The author is deeply indebted to the late Prof. Eric Reissner for his encouragement to work on the subject of this paper. Further acknowledgments are directed to the late Prof. Placido Cicala for the many suggestions and criticisms given during the review process of the paper (Carrera, 1995).

References

Ambartsumian, S. A., 1968, "On General Theory of Anisotropic Shells," *PMM*, Vol. 22, No. 2, pp. 226–237.

Barbero, E. J., Reddy, J. N., and Teply, J. L., 1990, "General Two-Dimensional Theory of laminated Cylindrical Shells," *American Institute of Aeronautics and Astronautics Journal*, Vol. 28, pp. 544–553.

Bhashar, B., and Varadan, T. K., 1989, "Refinement of Higher-Order Laminated Plate Theories," *American Institute of Aeronautics and Astronautics Journal*, Vol. 27, pp. 1830–1831.

Bhaskar, K., and Varadan, T. K., 1992, "Reissner's New Mixed Variational Principle Applied to Laminated Cylindrical Shells," ASME *Journal of Pressure Vessel Technology*, Vol. 114, pp. 115–119.

Carrera, E., 1995, "A Class of Two Dimensional Theories for Multilayered Plates Analysis," *Atti Accademia delle Scienze di Torino, Mem Sci. Fis.*, Vol. 19–20, pp. 49–87.

Carrera, E., 1996, "C^0 Reissner-Mindlin Multilayered Plate Elements Including Zig-Zag and Interlaminar Stresses Continuity," *International Journal for Numerical Methods in Engineering*, Vol. 39, pp. 1797–1820.

Carrera, E., 1997, "C_z^0-Requirements: Models for the Two-Dimensional Analysis of Multilayered Structures," *Composite Structures*, Vol. 37, pp. 373–383.

Carrera, E., 1998a, "Evaluation of Layer-Wise Mixed Theories for Laminated Plates Analysis," *American Institute of Aeronautics and Astronautics Journal*, Vol. 36, pp. 830–839.

Carrera, E., 1998b, "Layer-Wise Mixed Models for Accurate Vibration Analysis of Multilayered Plates," ASME Journal of Applied Mechanics, Vol. 65, pp. 820–828.

Carrera, E., 1998c, "A Reissner's Mixed Variational Theorem Applied to Vibrational Analysis of Multilayered Shell," ASME Journal of Applied Mechanics, Vol. 66, pp. 69–78.

Cho, K. N., Bert, C. W., and Striz, A. G., 1991, "Free Vibrations of Laminated Rectangular Plates Analyzed by Higher Order Individual-Layer Theory," *Journal of Sound and Vibration*, Vol. 145, pp. 429–442.

Cheung, Y. K., and Wu, C. I., 1972, "Free Vibrations of Thick, Layered Cylinders Having Finite Length With Various Boundary Conditions," *Journal of Sound and Vibration*, Vol. 24, pp. 189–200.

Cho, M., and Parmerter, R. R., 1993, "Efficient Higher Order Composite Plate Theory for General Lamination Configurations," *American Institute of Aeronautics and Astronautics Journal*, Vol. 31, pp. 1299–1305.

Di Sciuva, M., 1993, "A General Quadrilater Multilayered Plate Element With Continuous Interlaminar Stresses," *Composite Structures*, Vol. 47, pp. 91–105.

Grigolyuk, E. I., and Kulikov, G. M., 1988, "General Direction of the Development of the Theory of Shells," *Mekhanica Kompozitnykh Materialov*, No. 2, pp. 287–298.

Hildebrand, F. B., Reissner, E., and Thomas, G. B., 1940, "Notes on the Foundations of the Theory of Small Displacement of Orthotropic Shells," NACA TN-1833, Washington, DC.

Idlbi, A., Karama, M., and Touratier, M., 1997, "Comparison of Various Laminated Plate Theories," *Composite Structures*, Vol. 37, pp. 173–184.

Jing, H., and Tzeng, K., 1993, "Refined Shear Deformation Theory of Laminated Shells," *American Institute of Aeronautics and Astronautics Journal*, Vol. 31, pp. 765–773.

Lekhnitskii, S. G., 1935, "Strength Calculation of Composite Beams," *Vestnik inzhen. i tekhnikov*, No. 9.

Lo, K. H., Christensen, R. M., and Wu, E. M., 1977, "A Higher-Order Theory of Plate Deformation, Part 2: Laminated Plates," ASME Journal of Applied Mechanics, Vol. 44, pp. 669–676.

Murakami, H., 1986, "Laminated Composite Plate Theory With Improved In-Plane Response," ASME Journal of Applied Mechanics, Vol. 53, pp. 661–666.

Noor, A. K., and Burton, W. S., 1989, "Stress and Free Vibration Analyses of Multilayered Composite Plates," *Composite Structures*, Vol. 11, pp. 183–204.

Pagano, N. J., 1969, "Exact Solutions for Composite Laminates in Cylindrical Bending," *Journal of Composite Materials*, Vol. 3, pp. 398–411.

Rath, B. K., and Das, Y. C., 1973, "Vibration of Layered Shells," *Journal of Sound and Vibration*, Vol. 28, pp. 737–757.

Downloaded 04 May 2010 to 171.66.16.27. Redistribution subject to ASME license or copyright; see http://www.asme.org/terms/Terms_Use.cfm

Reddy, J. N., 1997, *Mechanics of Laminated Composite Plates, Theory and Analysis,* CRC Press, Boca Raton, FL.

Reissner, E., 1984, "On a Certain Mixed Variational Theory and a Proposed Applications," *International Journal for Numerical Methods in Engineering,* Vol. 20, pp. 1366–1368.

Reissner, E., 1985, "Reflections on the Theory of Elastic Plates," Applied Mechanics Review, Vol. 38, pp. 1433–1464.

Reissner, E., 1986, "On a Mixed Variational Theorem and on a Shear Deformable Plate Theory," *International Journal for Numerical Methods in Engineering,* Vol. 23, pp. 193–198.

Ren, J. G., 1986, "A New Theory for Laminated Plates," *Composite Science and Technology,* Vol. 26, pp. 225–239.

Ren, J. G., 1987, "Exact Solutions for Laminated Cylindrical Shells in Cylindrical Bending," *Composite Science and Technology,* Vol. 29, pp. 169–187.

Robbins, D. H., Jr., and Reddy, J. N., 1993, "Modeling of Thick Composites Using a Layer-Wise Theory," *International Journal of Numerical Methods in Engineering,* Vol. 36, pp. 655–677.

Soldatos, K. P., and Timarci, T., 1993, "A Unified Formulation of Laminated Composites, Shear Deformable, Five-Degrees-of-Freedom Cylindrical Shell Theories," *Composite Structures,* Vol. 25, pp. 165–171.

Srinivas, S., 1973, "A Refined Analysis of Composite Laminates," *Journal of Sound and Vibration,* Vol. 30, pp. 495–50.

Szabo, B., and Sahrmann, A., 1988, "Hierarchic Plate and Shell Models Based on *p*-Extension," *International Journal for Numerical Methods in Engineering,* Vol. 8, pp. 495–450.

Surana, S. K., and Sorem, R. M., 1991, "Completely Hierarchical *p*-Version Curved Shell Elements for Laminated Composite Plates and Shells," *Computational Mechanics,* pp. 237–251.

Toledano, A., and Murakami, H., 1987a, "A Composite Plate Theory for Arbitrary Laminated Configurations," ASME JOURNAL OF APPLIED MECHANICS, Vol. 54, pp. 181–189.

Toledano, A., and Murakami, H., 1987b, "A Higher-Order Laminated Plate Theory with Improved In-Plane Responses," *International Journal of Solids and Structures,* Vol. 23, pp. 111–131.

Varadan, T. K., and Bhaskar, K., 1991, "Bending of Laminated Orthotropic Cylindrical Shells—An Elasticity Approach," *Composite Structures,* Vol. 17, pp. 141–156.

Whitney, J. M., 1969, "The Effects of Transverse Shear Deformation on the Bending of Laminated Plates," *Journal of Composite Materials,* Vol. 3, pp. 534–547.

Downloaded 04 May 2010 to 171.66.16.27. Redistribution subject to ASME license or copyright; see http://www.asme.org/terms/Terms_Use.cfm

Journal of Applied Mechanics

Brief Notes

A Brief Note is a short paper that presents a specific solution of technical interest in mechanics but which does not necessarily contain new general methods or results. A Brief Note should not exceed 1500 words *or equivalent* (a typical one-column figure or table is equivalent to 250 words; a one line equation to 30 words). Brief Notes will be subject to the usual review procedures prior to publication. After approval such Notes will be published as soon as possible. The Notes should be submitted to the Technical Editor of the JOURNAL OF APPLIED MECHANICS. Discussions on the Brief Notes should be addressed to the Editorial Department, ASME, United Engineering Center, 345 East 47th Street, New York, N. Y. 10017, or to the Technical Editor of the JOURNAL OF APPLIED MECHANICS. Discussions on Brief Notes appearing in this issue will be accepted until two months after publication. Readers who need more time to prepare a Discussion should request an extension of the deadline from the Editorial Department.

Applying the Lagrange Method to Solve Problems of Control Constraints

A. Rosen[1]

1 Introduction

The use of Lagrange multipliers is a well-known approach to obtain the equations of motion of constrained dynamic systems, within the framework of the standard Lagrange method. Yet, this approach is confined to a limited class of constraints and cannot be applied to others. One of the problematic cases includes control (servo) constraints. Control constraints are associated with mechanisms that make use of auxiliary energy sources that are automatically regulated so as to realize a specified condition (constraint) at each instant of time. This condition is expressed by a constraint equation that may either be holonomic or nonholonomic. In certain cases control constraints may include few constraint equations that include highly nonlinear effects.

For years researchers tried to overcome this weakness of the standard Lagrange method. To the best of the author's knowledge the only textbook in English that describes a special method to deal with control constraints is the translation from French of Cabannes' book (1968). Possible reasons that this method, which has been known for many decades (see, for example, Levi-Civita, 1926), has not been described in other English textbooks on analytical dynamics that were published during the years, are as follows:

(a) The application of the method is not straightforward, but rather indirect and slippery, even for simple problems. The main difficulty involves the stage of converting the control constraints (Eq. (7.2.4-2) of Cabannes, 1968) into the linear differential relations that are included in the set of Lagrange equations (Eq. (7.2.4-6) of Cabannes, 1968). Even the number of relations is not known in advance and is not necessarily equal to the number of constraint equations.

(b) The control constraints are assumed to be linear with respect to the generalized velocities and independent of accelerations. Since many control systems are based on feedback from accelerometers (angular and linear), this method cannot be applied in many important problems.

(c) In many cases the physical meaning of the constraint disappears, in contrast to Newton's approach (see the example in what follows).

Recently, a new formulation of the Lagrange method for constrained dynamics was presented (Rosen and Edelstein, 1997a, b, 1998). It represents a consistent variational approach and offers a unified approach to holonomic and nonholonomic constraints. This new formulation offers a straightforward direct solution of the problem of control constraints, it preserves the direct physical interpretation of the constraints, and can deal with constraints that are nonlinear in the velocities and dependent on accelerations as well. The use of the new formulation will be shown by its application to solve a problem that appears in Cabannes' book (1976).

2 Description of the Problem

In a fixed vertical plane, a circular disk Σ_1 is free to rotate about its center O. A plate Σ is pin-jointed at a point A on Σ_1, Fig. 1. We wish to study the motion of the system, given that a motor acts on the disk Σ_1 to keep the angle $(\mathbf{OA}, \mathbf{AG}) = \pi/2$, where G designates the center of mass of the plate Σ.

Let us put $OA = R$, $AG = a$, and denote M the mass of the plate Σ and by Mk^2 its moment of inertia about the point G. With the axis Ox directed in the vertically descending direction, let us put $\alpha = (\mathbf{Ox}, \mathbf{OA})$ and $\beta = (\mathbf{Ox}, \mathbf{AG})$. The moment of inertia of the disk Σ_1 about the point O, is I_1.

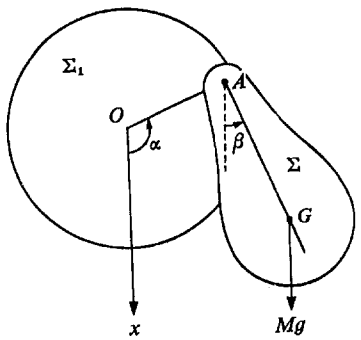


Fig. 1 Description of the problem

[1] Professor, Faculty of Aerospace Engineering, Technion-Israel Institute of Technology, Haifa 32000, Israel. Mem. ASME.

Contributed by the Applied Mechanics Division of THE AMERICAN SOCIETY OF MECHANICAL ENGINEERS for publication in the ASME JOURNAL OF APPLIED MECHANICS. Manuscript received by the ASME Applied Mechanics Division, Sept. 30, 1998; final revision, June 17, 1999. Associate Technical Editor: N. C. Perkins.

 Copyright © 1999 by ASME

Downloaded 04 May 2010 to 171.66.16.27. Redistribution subject to ASME license or copyright; see http://www.asme.org/terms/Terms_Use.cfm

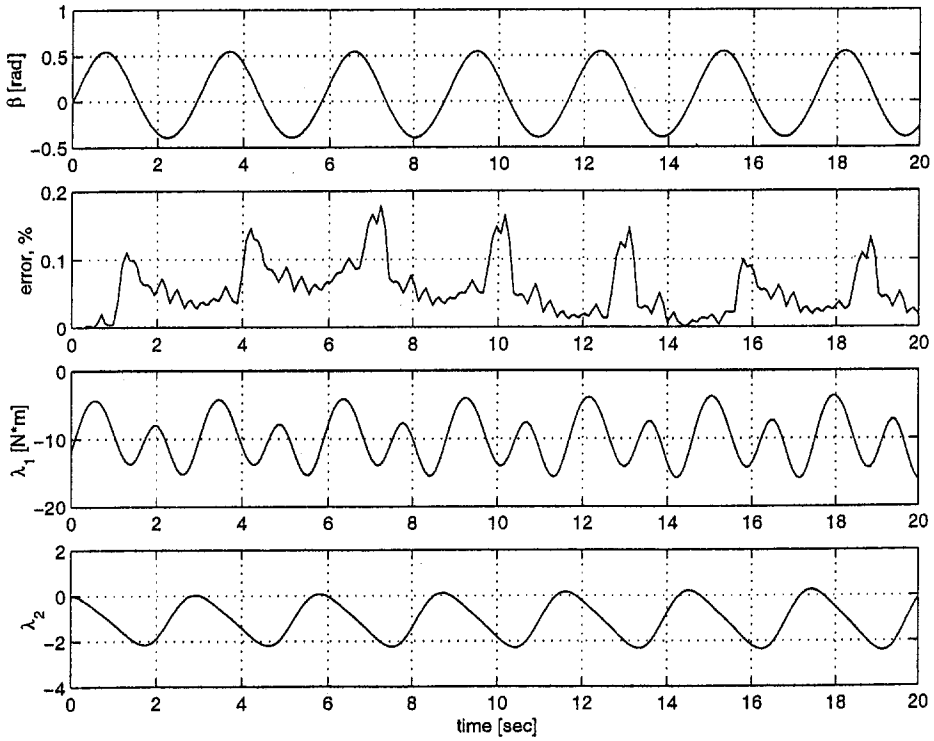


Fig. 2 Results [$M = I_1 = R = a = k = \dot{\beta}_0 = 1$; $\beta_0 = (\lambda_2)_0 = (\dot{\lambda}_2)_0 = 0$]

3 Solution

Although not indicated by Cabannes, the solution of this problem is solely defined by the constraints equation. In fact a student, after finishing his basic course in dynamics, can easily solve this problem using Newton's approach. A straightforward simple calculation will lead him to the expression for the moment M_A that is applied by disk Σ_1 on the plate Σ (positive in the counterclockwise direction):

$$M_A = M[a \cdot R \cdot \cos(\alpha - \beta) \cdot \ddot{\alpha} + (a^2 + k^2) \cdot \ddot{\beta} - a \cdot R \cdot \sin(\alpha - \beta) \cdot \dot{\alpha}^2] + M \cdot g \cdot a \cdot \sin\beta. \quad (1)$$

According to the conditions of the present problem,

$$\alpha - \beta = \frac{\pi}{2}. \quad (2)$$

For the case of a pin-joint at A, M_A should become zero, thus Eqs. (1) and (2) result in the following equation for β:

$$(a^2 + k^2)\ddot{\beta} - R \cdot a \cdot \dot{\beta}^2 + g \cdot a \cdot \sin\beta = 0. \quad (3)$$

The solution of the last equation (see Cabannes, 1976) defines β as a function of time, presenting the solution to the problem.

The method presented by Cabannes lacks the direct physical interpretation of Newton's approach. It is based on an examination of the virtual power that acts on the plate, leading to the conclusion that the Lagrange equation corresponding to β should not contain any multiplier.

The solution of the problem using the new formulation of Lagrange method preserves the clear physical interpretation of Newton's method and, unlike Cabannes' method, is straightforward and direct. The derivations can be simplified significantly if it is a priori assumed that the angle $(\mathbf{OA}, \mathbf{AG}) = \pi/2$, while writing down the expression for the kinetic energy and the potential of the gravity forces. Nevertheless, this condition will not be applied a priori in order to present the easy and direct application, as well as the clear interpretation of the new formulation.

The kinetic energy of the entire system, T, is

$$T = \frac{1}{2} I_1 \cdot \dot{\alpha}^2 + \frac{1}{2} M[R^2 \cdot \dot{\alpha}^2 + a^2 \cdot \dot{\beta}^2 + 2 \cdot R \cdot a \cdot \cos(\alpha - \beta) \cdot \dot{\alpha} \cdot \dot{\beta} + k^2 \cdot \dot{\beta}^2]. \quad (4)$$

The potential of the gravity forces is

$$V = -(R \cdot \cos\alpha + a \cdot \cos\beta) \cdot M \cdot g. \quad (5)$$

The two constraint equations are

$$\alpha - \beta - \frac{\pi}{2} = 0 \quad (6a)$$

$$M_A = 0. \quad (6b)$$

The expression for M_A is given by Eq. (1).

The modified Lagrangian includes two constraints and is (Rosen and Edelstein, 1997a, b)

$$L_d = T - V - \lambda_1\left(\alpha - \beta - \frac{\pi}{2}\right) - \lambda_2 M_A. \quad (7)$$

There are four unknowns (α, β, λ_1, and λ_2). The four equations that govern the motion are obtained after the application of a direct variational approach (see Rosen and Edelstein, 1997a, b):

$$-\frac{d^2}{dt^2}\left(\frac{\partial Ld}{\partial \ddot{\alpha}}\right) + \frac{d}{dt}\left(\frac{\partial Ld}{\partial \dot{\alpha}}\right) - \frac{\partial Ld}{\partial \alpha} = 0 \quad (8a)$$

$$-\frac{d^2}{dt^2}\left(\frac{\partial Ld}{\partial \ddot{\beta}}\right) + \frac{d}{dt}\left(\frac{\partial Ld}{\partial \dot{\beta}}\right) - \frac{\partial Ld}{\partial \beta} = 0 \quad (8b)$$

$$\alpha - \beta - \frac{\pi}{2} = 0 \quad (8c)$$

$$M_A = 0. \quad (8d)$$

It is easy to see that the last two equations give Eq. (3) that is solved for β. Then α is obtained from Eq. (8c).

Downloaded 04 May 2010 to 171.66.16.27. Redistribution subject to ASME license or copyright; see http://www.asme.org/terms/Terms_Use.cfm

The first two equations are used to find λ_1 and λ_2. If Eq. (8c) is applied, then these two equations become

$$(I_1 + M \cdot R^2)\ddot{\beta} + M \cdot R \cdot a \cdot \dot{\beta}^2 + M \cdot R \cdot g \cdot \cos\beta + \lambda_1 + 2 \cdot M \cdot R \cdot a \cdot \dot{\beta} \cdot \dot{\lambda}_2 + M \cdot R \cdot a \cdot \ddot{\beta} \cdot \lambda_2 = 0 \quad (9a)$$

$$M(a^2 + k^2)\ddot{\beta} - M \cdot R \cdot a \cdot \dot{\beta}^2 + M \cdot a \cdot g \cdot \sin\beta - \lambda_1 + M(a^2 + k^2)\ddot{\lambda}_2 + M \cdot R \cdot a \cdot \ddot{\beta} \cdot \lambda_2 + M \cdot a \cdot g \cdot \cos\beta \cdot \lambda_2 = 0. \quad (9b)$$

λ_1 disappears after adding the last two equations, and the equation of motion of the entire system (the attached disk and plate) is obtained:

$$[I_1 + M(R^2 + a^2 + k^2)]\ddot{\beta} + M \cdot g(R \cdot \cos\beta + a \cdot \sin\beta) + M(a^2 + k^2)\ddot{\lambda}_2 + 2 \cdot M \cdot R \cdot a(\dot{\beta} \cdot \dot{\lambda}_2 + \ddot{\beta} \cdot \lambda_2) + M \cdot g \cdot a \cdot \cos\beta \cdot \lambda_2 = 0. \quad (10)$$

The first term in the last equation presents the inertial moment (of the entire system) about the point O (positive in the counterclockwise direction). The second term is the contribution of gravity to the moment about the same point. The last three terms represent the moment that is applied by the motor on disk Σ_1 (the control moment), M_e:

$$M_e = -M(a^2 + k^2)\ddot{\lambda}_2 - 2 \cdot M \cdot R \cdot a(\dot{\beta} \cdot \dot{\lambda}_2 + \ddot{\beta} \cdot \lambda_2) - M \cdot g \cdot a \cdot \cos\beta \cdot \lambda_2. \quad (11)$$

The fact that the new formulation of Lagrange method offers a unified approach to all kinds of constraints is shown again if one drops all the terms that include λ_2 and its derivatives in Eq. (10). This means that the condition of a pin-joint at A is dropped and instead a rigid joint is considered. Then Eq. (10) converges to the well-known equation of vibrations of the entire system about point O, under the influence of gravity (a physical pendulum).

Cabannes gives an analytic solution of Eq. (3). For the case where the initial conditions are $\beta = \beta_0 = 0$ and $\dot{\beta} = \dot{\beta}_0$, this solution is

$$\dot{\beta}^2 - \left(\dot{\beta}_0^2 - \frac{g}{R}\frac{m}{1 + m^2}\right)e^{m\beta} - \frac{mg}{R(1 + m^2)}(\cos\beta + m \sin\beta) = 0 \quad (12)$$

where

$$m = \frac{2Ra}{a^2 + k^2}. \quad (13)$$

In Fig. 2 results for the case

$$M = I_1 = R = a = k = \dot{\beta}_0 = 1; \quad \beta_0 = (\lambda_2)_0 = (\dot{\lambda}_2)_0 = 0$$

are presented. These results were obtained by direct numerical integration of Eqs. (3) and (10), while Eq. (9) was used to solve for λ_1. β, λ_1, and λ_2 exhibit a periodic behavior that is different for each unknown. In order to verify the accuracy of the numerical integration the values of $\dot{\beta}$ and β, at any moment, were substituted into the left side of Eq. (12) and the result divided by $\dot{\beta}^2$. The absolute value of this relative error (in percents) is also shown and indicates that the numerical integration is associated with relatively small errors.

4 Conclusions

Recently a new formulation of the Lagrange method was presented by Rosen and Edelstein. This formulation offers a unified approach of dealing with holonomic or nonholonomic constraints that is correct from a variational mathematical point of view for both kinds of constraints.

The use of the new formulation to solve problems of control constraints has been presented in this note. The advantages of the new formulation are the following:

(a) It is straightforward and easy to apply. Thus, the new formulation is suitable for a general purpose computer code.

(b) There is a unified approach to all the kinds of constraints, holonomic or nonholonomic.

(c) It is possible to deal with constraints that include accelerations and nonlinear expressions of the velocities.

(d) There is a clear direct physical interpretation of the constraints, similar to that offered by Newton's method.

References

Cabannes, H., 1968, *General Mechanics*, Blaisdell Publishing Co. translation from French by S. P. Sutera.

Levi-Civita, T., 1926, *Meccanica Razionale*, Vol. II, Bologna, Nicola Zanichelli, pp. 303–306.

Rosen, A., and Edelstein, E., 1997a, "Investigations of a New Formulation of the Lagrange Method for Constrained Dynamic Systems," ASME JOURNAL OF APPLIED MECHANICS, Vol. 64, pp. 116–122.

Rosen, A., and Edelstein, E., 1997b, Reply to a discussion by Professor P. Hagedorn of the paper "Investigation of a New Formulation of the Lagrange Method for Constrained Dynamic Systems," ASME JOURNAL OF APPLIED MECHANICS, Vol. 64, pp. 1025–1027.

Rosen, A., and Edelstein, E., 1998, "A New Examination of the Problem of Constrained Dynamics," *Proceedings of the 38th Israel Ann. Conf. on Aerospace Sciences*, Feb. 25–26, pp. 186–197.

Steady-State Deflection of a Circular Plate Rotating Near Its Critical Speed

Jen-San Chen[1]

The steady-state response of a disk spinning near its critical speed and under space-fixed time-invariant load is analyzed by using von Karman's nonlinear plate model. It is found that as the disk rotates beyond a modified critical speed there exist three steady-state deflections, among which only one is in the same direction as the applied load and is stable in the presence of space-fixed damping.

Introduction

Conventional linearized plate theory predicts that the steady-state deflection of a spinning disk under space-fixed time-invariant load approaches infinity as the rotation speed approaches the critical speed. This conclusion contradicts experimental result that shows the existence of finite steady-state deflection even at the critical speed (Tobias and Arnold, 1957). In order to capture the physical essence of critical speed resonance, Raman and Mote (1999) recently adopted von Karman's plate model (Nowinski, 1964) to study the nonlinear oscillations of a disk spinning near its critical speed and subject to rotating damping. Since their analysis is performed in a rotating frame, the forcing terms are time-dependent and averaging technique has to be used. In many spinning disk applications, however, the external damping is space-fixed, such as the damping in circular saw guides and disk drive

[1] Associate Professor, Department of Mechanical Engineering, National Taiwan University, Taipei Taiwan 10617, R.O.C.

Contributed by the Applied Mechanics Division of THE AMERICAN SOCIETY OF MECHANICAL ENGINEERS for publication in the ASME JOURNAL OF APPLIED MECHANICS. Manuscript received by the ASME Applied Mechanics Division, Dec. 18, 1998; final revision, May 4, 1999. Associate Technical Editor: N. C. Perkins.

Downloaded 04 May 2010 to 171.66.16.27. Redistribution subject to ASME license or copyright; see http://www.asme.org/terms/Terms_Use.cfm

The first two equations are used to find λ_1 and λ_2. If Eq. (8c) is applied, then these two equations become

$$(I_1 + M \cdot R^2)\ddot{\beta} + M \cdot R \cdot a \cdot \dot{\beta}^2 + M \cdot R \cdot g \cdot \cos\beta + \lambda_1 + 2 \cdot M \cdot R \cdot a \cdot \dot{\beta} \cdot \dot{\lambda}_2 + M \cdot R \cdot a \cdot \ddot{\beta} \cdot \lambda_2 = 0 \quad (9a)$$

$$M(a^2 + k^2)\ddot{\beta} - M \cdot R \cdot a \cdot \dot{\beta}^2 + M \cdot a \cdot g \cdot \sin\beta - \lambda_1 + M(a^2 + k^2)\ddot{\lambda}_2 + M \cdot R \cdot a \cdot \ddot{\beta} \cdot \lambda_2 + M \cdot a \cdot g \cdot \cos\beta \cdot \lambda_2 = 0. \quad (9b)$$

λ_1 disappears after adding the last two equations, and the equation of motion of the entire system (the attached disk and plate) is obtained:

$$[I_1 + M(R^2 + a^2 + k^2)]\ddot{\beta} + M \cdot g(R \cdot \cos\beta + a \cdot \sin\beta) + M(a^2 + k^2)\ddot{\lambda}_2 + 2 \cdot M \cdot R \cdot a(\dot{\beta} \cdot \dot{\lambda}_2 + \ddot{\beta} \cdot \lambda_2) + M \cdot g \cdot a \cdot \cos\beta \cdot \lambda_2 = 0. \quad (10)$$

The first term in the last equation presents the inertial moment (of the entire system) about the point O (positive in the counterclockwise direction). The second term is the contribution of gravity to the moment about the same point. The last three terms represent the moment that is applied by the motor on disk Σ_1 (the control moment), M_e:

$$M_e = -M(a^2 + k^2)\ddot{\lambda}_2 - 2 \cdot M \cdot R \cdot a(\dot{\beta} \cdot \dot{\lambda}_2 + \ddot{\beta} \cdot \lambda_2) - M \cdot g \cdot a \cdot \cos\beta \cdot \lambda_2. \quad (11)$$

The fact that the new formulation of Lagrange method offers a unified approach to all kinds of constraints is shown again if one drops all the terms that include λ_2 and its derivatives in Eq. (10). This means that the condition of a pin-joint at A is dropped and instead a rigid joint is considered. Then Eq. (10) converges to the well-known equation of vibrations of the entire system about point O, under the influence of gravity (a physical pendulum).

Cabannes gives an analytic solution of Eq. (3). For the case where the initial conditions are $\beta = \beta_0 = 0$ and $\dot{\beta} = \dot{\beta}_0$, this solution is

$$\dot{\beta}^2 - \left(\dot{\beta}_0^2 - \frac{g}{R}\frac{m}{1 + m^2}\right)e^{m\beta} - \frac{mg}{R(1 + m^2)}(\cos\beta + m \sin\beta) = 0 \quad (12)$$

where

$$m = \frac{2Ra}{a^2 + k^2}. \quad (13)$$

In Fig. 2 results for the case

$$M = I_1 = R = a = k = \dot{\beta}_0 = 1; \quad \beta_0 = (\lambda_2)_0 = (\dot{\lambda}_2)_0 = 0$$

are presented. These results were obtained by direct numerical integration of Eqs. (3) and (10), while Eq. (9) was used to solve for λ_1. β, λ_1, and λ_2 exhibit a periodic behavior that is different for each unknown. In order to verify the accuracy of the numerical integration the values of $\dot{\beta}$ and β, at any moment, were substituted into the left side of Eq. (12) and the result divided by $\dot{\beta}^2$. The absolute value of this relative error (in percents) is also shown and indicates that the numerical integration is associated with relatively small errors.

4 Conclusions

Recently a new formulation of the Lagrange method was presented by Rosen and Edelstein. This formulation offers a unified approach of dealing with holonomic or nonholonomic constraints that is correct from a variational mathematical point of view for both kinds of constraints.

The use of the new formulation to solve problems of control constraints has been presented in this note. The advantages of the new formulation are the following:

(a) It is straightforward and easy to apply. Thus, the new formulation is suitable for a general purpose computer code.

(b) There is a unified approach to all the kinds of constraints, holonomic or nonholonomic.

(c) It is possible to deal with constraints that include accelerations and nonlinear expressions of the velocities.

(d) There is a clear direct physical interpretation of the constraints, similar to that offered by Newton's method.

References

Cabannes, H., 1968, *General Mechanics*, Blaisdell Publishing Co. translation from French by S. P. Sutera.

Levi-Civita, T., 1926, *Meccanica Razionale*, Vol. II, Bologna, Nicola Zanichelli, pp. 303–306.

Rosen, A., and Edelstein, E., 1997a, "Investigations of a New Formulation of the Lagrange Method for Constrained Dynamic Systems," ASME JOURNAL OF APPLIED MECHANICS, Vol. 64, pp. 116–122.

Rosen, A., and Edelstein, E., 1997b, Reply to a discussion by Professor P. Hagedorn of the paper "Investigation of a New Formulation of the Lagrange Method for Constrained Dynamic Systems," ASME JOURNAL OF APPLIED MECHANICS, Vol. 64, pp. 1025–1027.

Rosen, A., and Edelstein, E., 1998, "A New Examination of the Problem of Constrained Dynamics," *Proceedings of the 38th Israel Ann. Conf. on Aerospace Sciences*, Feb. 25–26, pp. 186–197.

Steady-State Deflection of a Circular Plate Rotating Near Its Critical Speed

Jen-San Chen[1]

The steady-state response of a disk spinning near its critical speed and under space-fixed time-invariant load is analyzed by using von Karman's nonlinear plate model. It is found that as the disk rotates beyond a modified critical speed there exist three steady-state deflections, among which only one is in the same direction as the applied load and is stable in the presence of space-fixed damping.

Introduction

Conventional linearized plate theory predicts that the steady-state deflection of a spinning disk under space-fixed time-invariant load approaches infinity as the rotation speed approaches the critical speed. This conclusion contradicts experimental result that shows the existence of finite steady-state deflection even at the critical speed (Tobias and Arnold, 1957). In order to capture the physical essence of critical speed resonance, Raman and Mote (1999) recently adopted von Karman's plate model (Nowinski, 1964) to study the nonlinear oscillations of a disk spinning near its critical speed and subject to rotating damping. Since their analysis is performed in a rotating frame, the forcing terms are time-dependent and averaging technique has to be used. In many spinning disk applications, however, the external damping is space-fixed, such as the damping in circular saw guides and disk drive

[1] Associate Professor, Department of Mechanical Engineering, National Taiwan University, Taipei Taiwan 10617, R.O.C.

Contributed by the Applied Mechanics Division of THE AMERICAN SOCIETY OF MECHANICAL ENGINEERS for publication in the ASME JOURNAL OF APPLIED MECHANICS. Manuscript received by the ASME Applied Mechanics Division, Dec. 18, 1998; final revision, May 4, 1999. Associate Technical Editor: N. C. Perkins.

Downloaded 04 May 2010 to 171.66.16.27. Redistribution subject to ASME license or copyright; see http://www.asme.org/terms/Terms_Use.cfm

head-suspensions. In this note we study critical speed resonance in a space-fixed frame with emphasis on the effects of space-fixed damping on the stability of steady-state deflections. In the present formulation the forcing terms are time-invariant and no perturbation techniques are needed.

Equations of Motion

The dimensionless equations of motion of a disk spinning with constant speed Ω with respect to a space-fixed frame (r, θ) can be written as

$$w_{,tt} + 2\Omega w_{,t\theta} + \Omega^2 w_{,\theta\theta} + c_f w_{,t} + \nabla^4 w - r^{-1}(\sigma_r r w_{,r})_{,r} - r^{-2}\sigma_\theta w_{,\theta\theta} = w_{,rr}(r^{-1}\phi_{,r} + r^{-2}\phi_{,\theta\theta}) + (r^{-1}w_{,r} + r^{-2}w_{,\theta\theta})\phi_{,rr} - 2(r^{-1}w_{,\theta})_{,r}(r^{-1}\phi_{,\theta})_{,r} + q(r, \theta) \quad (1)$$

$$\nabla^4\phi = -\epsilon[w_{,rr}(r^{-1}w_{,r} + r^{-2}w_{,\theta\theta}) + 2r^{-3}w_{,r\theta}w_{,\theta} - r^{-2}(w_{,r\theta})^2 - r^{-4}(w_{,\theta})^2]. \quad (2)$$

w and ϕ are transverse displacement and stress function, respectively. The relations between dimensionless quantities and physical quantities (with asterisks) are

$$t = \frac{t^*}{b^2}\sqrt{\frac{D}{\rho h}}, \quad \Omega = \Omega^* b^2\sqrt{\frac{\rho h}{D}}, \quad r = \frac{r^*}{b},$$

$$w = w^*\sqrt{\frac{b}{h^3}}, \quad \phi = \phi^*\frac{h}{D}$$

$$q = q^*\sqrt{\frac{b^9}{D^2h^3}}, \quad c_f = c_f^*\frac{b^2}{\sqrt{\rho h D}}, \quad \epsilon = 12(1-\nu^2)\frac{h}{b}, \quad \eta = \frac{a}{b}.$$

The parameters ρ, h, E, ν, and D are the mass density, thickness, Young's modulus, Poisson ratio, and flexural rigidity of the disk, respectively. c_f^* represents a space-fixed homogeneous damping. $q^*(r^*, \theta)$ is the space-fixed time-invariant loading. The disk is assumed to be "partially clamped" at the inner radius $r^* = a$, and is free at the outer radius $r^* = b$ (Benson and Bogy, 1978). σ_r and σ_θ in Eq. (1) are dimensionless stresses due to centrifugal effect. In the special case when $\epsilon = 0$, the solution ϕ in Eq. (2) is identically zero, and as a consequence Eq. (1) reduces to

$$w_{,tt} + 2\Omega w_{,t\theta} + \Omega^2 w_{,\theta\theta} + c_f w_{,t} + \nabla^4 w - r^{-1}(\sigma_r r w_{,r})_{,r} - r^{-2}\sigma_\theta w_{,\theta\theta} = q. \quad (3)$$

Equation (3) is the conventional equation used in the literature without considering von Karman's effect. The natural frequency and the orthonormal eigenfunction of a freely spinning disk (i.e., $c_f = 0$, $q = 0$) are denoted by ω_{mn} and $w_{mn} = R_{mn}(r)e^{in\theta}$, respectively.

Steady-State Deflection Near Critical Speed

We assume that when the disk rotates near its critical speed Ω_c of mode w_{mn}, the solution w of Eqs. (1) and (2) can be approximated by a two-mode expansion,

$$w(r, \theta, t) = c_{mn}(t)w_{mn} + \bar{c}_{mn}(t)\bar{w}_{mn}. \quad (4)$$

Both $c_{mn}(t)$ and $w_{mn}(r, \theta)$ in Eq. (4) are complex functions. In order to solve ϕ in Eq. (2) we introduce a set of eigenfunctions ϕ_{mn} satisfying the following differential equation:

$$\nabla^4\phi_{mn} - \beta_{mn}^4\phi_{mn} = 0. \quad (5)$$

ϕ_{mn} satisfy the same boundary conditions as ϕ does. After expressing ϕ in terms of eigenfunctions series ϕ_{mn} and following Galerkin's procedure, we can discretize Eqs. (1) and (2) into

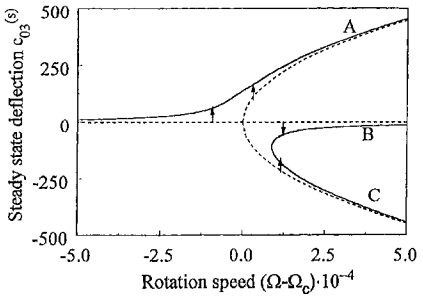


Fig. 1 Steady-state deflection $c_{03}^{(s)}$ near the critical speed

$$\ddot{c}_{mn} + (2in\Omega + c_f)\dot{c}_{mn} + \kappa_{mn}c_{mn} + \epsilon\gamma|c_{mn}|^2c_{mn} - q_{mn} = 0 \quad (6)$$

where

$$q_{mn} = \int_{\theta=0}^{2\pi}\int_{r=\eta}^{1} q(r, \theta)R_{mn}(r)e^{-in\theta}r\,dr\,d\theta \quad (7)$$

$$\kappa_{mn} = \omega_{mn}(\omega_{mn} + 2n\Omega). \quad (8)$$

Constant γ can be obtained via numerical integration involving eigenfunctions w_{mn} and ϕ_{mn}. It is noted that for a reflected wave the integer n is considered as positive, while the natural frequency ω_{mn} is considered as negative. Therefore κ_{mn} is positive in the subcritical speed range, and is negative in the supercritical speed range. $|c_{mn}|$ represents the absolute value of complex number c_{mn}. The steady-state solutions $c_{mn}^{(s)}$ satisfy the equation

$$\kappa_{mn}c_{mn}^{(s)} + \epsilon\gamma|c_{mn}^{(s)}|^2c_{mn}^{(s)} - q_{mn} = 0. \quad (9)$$

It is noted that this cubic equation allows only real roots. In the special case of a freely spinning disk when $q_{mn} = 0$, there is one trivial steady-state solution $c_{mn}^{(s)} = 0$ in the subcritical speed range $\Omega < \Omega_c$. On the other hand, in the supercritical speed range $\Omega > \Omega_c$, there are three real roots, i.e., $c_{mn}^{(s)} = 0$ and $c_{mn}^{(s)} = \pm\sqrt{-\kappa_{mn}/\epsilon\gamma}$. The dashed lines in Fig. 1 represent the steady-state deflections $c_{03}^{(s)}$ of a disk with clamping ratio $\eta = 0.5$ and Poisson ratio $\nu = 0.27$. The critical speed Ω_c of mode w_{03} is 8.75. The dimensionless thickness ϵ is taken to be 10^{-6} and the constant γ is calculated as 0.393.

In the case of a loaded disk with $q_{mn} > 0$, we can show that there is a modified critical speed $\Omega_c^* > \Omega_c$,

$$\Omega_c^* = \Omega_c + \frac{3}{2n^2\Omega_c}\left(\frac{\epsilon\gamma q_{mn}^2}{4}\right)^{1/3}. \quad (10)$$

When $\Omega < \Omega_c^*$ there is only one positive real root. On the other hand, there are three distinct real roots as $\Omega > \Omega_c^*$. The solid lines in Fig. 1 represent the steady-state solution $c_{03}^{(s)}$ when $q_{03} = 1$. The deflection A is always in the same direction as the applied load, while the deflections B and C are in the opposite direction. The small arrows in Fig. 1 indicate the deflection change from freely spinning disk to loaded disk.

Stability Analysis of Steady-State Solutions

In order to investigate the stability of the steady-state solutions, we express the solution c_{mn} in Eq. (6) as

$$c_{mn}(t) = c_{mn}^{(s)} + \hat{c}(t). \quad (11)$$

After substituting Eq. (11) into Eq. (6), using Eq. (9) and linearizing with respect to $\hat{c}$, we obtain the following equation:

$$\ddot{\hat{c}} + (2in\Omega + c_f)\dot{\hat{c}} + \kappa_{mn}\hat{c} + \epsilon\gamma(c_{mn}^{(s)})^2(2\hat{c} + \bar{\hat{c}}) = 0. \quad (12)$$

The eigenvalue λ of Eq. (12) can be obtained by solving the following quartic equation:

Downloaded 04 May 2010 to 171.66.16.27. Redistribution subject to ASME license or copyright; see http://www.asme.org/terms/Terms_Use.cfm

$$\lambda^4 + 2c_f\lambda^3 + [2\kappa_{mn} + 4\epsilon\gamma(c_{mn}^{(s)})^2 + c_f^2 + 4n^2\Omega^2]\lambda^2 + 2c_f[\kappa_{mn} + 2\epsilon\gamma(c_{mn}^{(s)})^2]\lambda + [\kappa_{mn} + 3\epsilon\gamma(c_{mn}^{(s)})^2][\kappa_{mn} + \epsilon\gamma(c_{mn}^{(s)})^2] = 0. \quad (13)$$

The steady-state solution is unstable when the real part of any of the four eigenvalues λ's is positive.

First of all we consider the deflections of the freely spinning disk with $c_f = 0$. For the trivial deflection $c_{mn}^{(s)} = 0$, the square of the eigenvalues solved from Eq. (13) are $\lambda^2 = -\omega_{mn}^2$ and $-(\omega_{mn} + 2n\Omega)^2$. For the nontrivial solutions $c_{mn}^{(s)} = \pm\sqrt{-\kappa_{mn}/\epsilon\gamma}$, $\lambda^2 = 0$ and $2\kappa_{mn} - 4n^2\Omega^2$. Therefore, the steady-state solutions of a freely spinning disk are neutrally stable to the first order of the stability analysis.

For the case of a loaded disk, it is difficult to express λ^2 in terms of physical parameters explicitly. However, we can study how λ^2 varies as q_{mn} increases from zero by differentiating Eq. (13) with respect to q_{mn} to obtain the first-order derivative $[\partial(\lambda^2)/\partial q_{mn}]|_{q_{mn}=0}$. For the trivial solution $c_{mn}^{(s)} = 0$, we can show that the derivatives for $\lambda^2 = -\omega_{mn}^2$ and $-(\omega_{mn} + 2n\Omega)^2$ are zero. Therefore, deflection B remains neutrally stable when the space-fixed load is present.

For the nontrivial deflections $c_{mn}^{(s)} = \pm\sqrt{-\kappa_{mn}/\epsilon\gamma}$ in the supercritical speed range, the derivative for $\lambda^2 = 0$ is

$$\left.\frac{\partial(\lambda^2)}{\partial q_{mn}}\right|_{q_{mn}=0,\lambda^2=0} = \mp\frac{1}{2n^2\Omega^2 - \kappa_{mn}}\sqrt{\frac{-\kappa_{mn}}{\epsilon\gamma}}. \quad (14)$$

From Eq. (14) we can predict that λ^2 is negative for deflection A, and positive for deflection C. As a consequence, the steady-state deflection C of the loaded disk is unstable, and deflection A remains neutrally stable.

Space-Fixed Damping Effects

We next study the behavior of the eigenvalues when space-fixed damping is present. To do so, we differentiate Eq. (13) with respect to c_f and calculate the derivative at $c_f = 0$ and $q_{mn} = 0$. For the trivial solution $c_{mn}^{(s)} = 0$ the derivative of eigenvalue $\pm\omega_{mn}$ is

$$\left.\frac{\partial\lambda}{\partial c_f}\right|_{c_f=0,\lambda=\pm i\omega_{mn}} = \frac{-\omega_{mn}}{4n\Omega}. \quad (15)$$

In the supercritical speed range, the right-hand side of Eq. (15) is positive real. We therefore conclude that deflection B of the loaded disk is unstable in the presence of c_f.

For the negative deflection of the freely spinning disk, we first observe that c_f has no effect on the degenerate eigenvalues $\lambda = 0$. However, we have shown in the preceding section that applied load tends to drive one of these two degenerate eigenvalues to positive real for deflection C. Therefore, we conclude that deflection C of the loaded disk is also unstable when external damping c_f is present.

For the positive deflection of the freely spinning disk, applied load tends to drive the degenerate eigenvalues $\lambda = 0$ to purely imaginary, while c_f has no effect on these two eigenvalues. Therefore, deflection A is neutrally stable to the first order of the stability analysis. However, if we approximate λ of the undamped loaded disk by Eq. (14), then we obtain an estimate of the eigenvalue change of the loaded disk as

$$\left.\frac{\partial\lambda}{\partial c_f}\right|_{c_f=0} = \frac{\kappa_{mn}\sqrt{\epsilon\gamma}(2n^2\Omega^2 - \kappa_{mn}) - q_{mn}\sqrt{-\kappa_{mn}}}{2\sqrt{\epsilon\gamma}\,(2n^2\Omega^2 - \kappa_{mn})^2 - 2q_{mn}\sqrt{-\kappa_{mn}}}. \quad (16)$$

The right-hand side of Eq. (16) is negative for small q_{mn}. Therefore, c_f drives the eigenvalues from 0 to negative real. On the other hand, the derivative of the eigenvalues $\lambda = \pm i\sqrt{4n^2\Omega^2 - 2\kappa_{mn}}$ can be calculated as

$$\left.\frac{\partial\lambda}{\partial c_f}\right|_{c_f=0} = -1 + \frac{\kappa_{mn}}{4n^2\Omega^2 - 2\kappa_{mn}}. \quad (17)$$

The right-hand side of Eq. (17) is always negative. Therefore, we conclude that deflection A of the loaded disk is stabilized by the external damping.

References

Benson, R. C., and Bogy, D. B., 1978, "Deflection of a Very Flexible Spinning Disk Due to a Stationary Transverse Load," ASME JOURNAL OF APPLIED MECHANICS, Vol. 45, pp. 636–642.

Nowinski, J. L., 1964, "Nonlinear Transverse Vibrations of a Spinning Disk," ASME JOURNAL OF APPLIED MECHANICS, Vol. 31, pp. 72–78.

Raman, A., and Mote, Jr., C. D., 1999, "Non-linear Oscillations of Circular Plates Near a Critical Speed Resonance," *International Journal of Non-Linear Mechanics*, Vol. 34, pp. 139–157.

Tobias, S. A., and Arnold, R. N., 1957, "The Influence of Dynamical Imperfection on the Vibration of Rotating Disks," *Proceedings of the Institution of Mechanical Engineers*, Vol. 171, pp. 669–690.

Maximizing the Natural Frequencies and Transverse Stiffness of Centrally Clamped, Circular Disks by Thickening the Clamped Part of the Disk

A. A. Renshaw[1]

The natural frequencies and transverse stiffness of centrally clamped, circular disks are computed taking into account the flexibility of the central clamp and the thickness of the clamped part of the disk. When compared to experimental vibration data, these predictions are more accurate than the traditional, perfect clamping predictions, particularly for zero and one-nodal-diameter vibration modes. The reduction in natural frequency or transverse stiffness caused by clamping flexibility can be mitigated either by increasing the clamping stiffness or by increasing the hub thickness, defined here as the thickness of the disk sandwiched by the central clamp. A design study of these two alternatives for both stationary and rotating disks shows that increasing the hub thickness is often a more attractive design alternative.

1 Introduction

For the past decade, an interesting, industrial circular saw design has existed in which the hub thickness of the saw, defined here as the thickness of the part of the saw that is sandwiched between the thick clamping collars, is two to four times thicker than the exposed part of the saw (Bird, 1990). The origins of this design are unclear, although they may lie in the designs of unclamped, "free-floating" circular saws (Mote, 1977; Renshaw and Mote, 1996). The inventor of the design claims that increased hub thickness raises the critical speed of the saw *even for centrally clamped saws.* What is interesting about this claim is that the hub thickness is irrelevant in the traditional model of a centrally clamped saw.

[1] Department of Mechanical Engineering, Columbia University, M/C 4703, New York, NY 10027. Mem. ASME.

Contributed by the Applied Mechanics Division of THE AMERICAN SOCIETY OF MECHANICAL ENGINEERS for publication in the ASME JOURNAL OF APPLIED MECHANICS. Manuscript received by the ASME Applied Mechanics Division, Feb. 10, 1999; final revision, May 4, 1999. Associate Technical Editor: N. C. Perkins.

Downloaded 04 May 2010 to 171.66.16.27. Redistribution subject to ASME license or copyright; see http://www.asme.org/terms/Terms_Use.cfm

$$\lambda^4 + 2c_f\lambda^3 + [2\kappa_{mn} + 4\epsilon\gamma(c_{mn}^{(s)})^2 + c_f^2 + 4n^2\Omega^2]\lambda^2 + 2c_f[\kappa_{mn} + 2\epsilon\gamma(c_{mn}^{(s)})^2]\lambda + [\kappa_{mn} + 3\epsilon\gamma(c_{mn}^{(s)})^2][\kappa_{mn} + \epsilon\gamma(c_{mn}^{(s)})^2] = 0. \quad (13)$$

The steady-state solution is unstable when the real part of any of the four eigenvalues λ's is positive.

First of all we consider the deflections of the freely spinning disk with $c_f = 0$. For the trivial deflection $c_{mn}^{(s)} = 0$, the square of the eigenvalues solved from Eq. (13) are $\lambda^2 = -\omega_{mn}^2$ and $-(\omega_{mn} + 2n\Omega)^2$. For the nontrivial solutions $c_{mn}^{(s)} = \pm\sqrt{-\kappa_{mn}/\epsilon\gamma}$, $\lambda^2 = 0$ and $2\kappa_{mn} - 4n^2\Omega^2$. Therefore, the steady-state solutions of a freely spinning disk are neutrally stable to the first order of the stability analysis.

For the case of a loaded disk, it is difficult to express λ^2 in terms of physical parameters explicitly. However, we can study how λ^2 varies as q_{mn} increases from zero by differentiating Eq. (13) with respect to q_{mn} to obtain the first-order derivative $[\partial(\lambda^2)/\partial q_{mn}]|_{q_{mn}=0}$. For the trivial solution $c_{mn}^{(s)} = 0$, we can show that the derivatives for $\lambda^2 = -\omega_{mn}^2$ and $-(\omega_{mn} + 2n\Omega)^2$ are zero. Therefore, deflection B remains neutrally stable when the space-fixed load is present.

For the nontrivial deflections $c_{mn}^{(s)} = \pm\sqrt{-\kappa_{mn}/\epsilon\gamma}$ in the supercritical speed range, the derivative for $\lambda^2 = 0$ is

$$\left.\frac{\partial(\lambda^2)}{\partial q_{mn}}\right|_{q_{mn}=0,\lambda^2=0} = \mp\frac{1}{2n^2\Omega^2 - \kappa_{mn}}\sqrt{\frac{-\kappa_{mn}}{\epsilon\gamma}}. \quad (14)$$

From Eq. (14) we can predict that λ^2 is negative for deflection A, and positive for deflection C. As a consequence, the steady-state deflection C of the loaded disk is unstable, and deflection A remains neutrally stable.

Space-Fixed Damping Effects

We next study the behavior of the eigenvalues when space-fixed damping is present. To do so, we differentiate Eq. (13) with respect to c_f and calculate the derivative at $c_f = 0$ and $q_{mn} = 0$. For the trivial solution $c_{mn}^{(s)} = 0$ the derivative of eigenvalue $\pm\omega_{mn}$ is

$$\left.\frac{\partial\lambda}{\partial c_f}\right|_{c_f=0,\lambda=\pm i\omega_{mn}} = \frac{-\omega_{mn}}{4n\Omega}. \quad (15)$$

In the supercritical speed range, the right-hand side of Eq. (15) is positive real. We therefore conclude that deflection B of the loaded disk is unstable in the presence of c_f.

For the negative deflection of the freely spinning disk, we first observe that c_f has no effect on the degenerate eigenvalues $\lambda = 0$. However, we have shown in the preceding section that applied load tends to drive one of these two degenerate eigenvalues to positive real for deflection C. Therefore, we conclude that deflection C of the loaded disk is also unstable when external damping c_f is present.

For the positive deflection of the freely spinning disk, applied load tends to drive the degenerate eigenvalues $\lambda = 0$ to purely imaginary, while c_f has no effect on these two eigenvalues. Therefore, deflection A is neutrally stable to the first order of the stability analysis. However, if we approximate λ of the undamped loaded disk by Eq. (14), then we obtain an estimate of the eigenvalue change of the loaded disk as

$$\left.\frac{\partial\lambda}{\partial c_f}\right|_{c_f=0} = \frac{\kappa_{mn}\sqrt{\epsilon\gamma}(2n^2\Omega^2 - \kappa_{mn}) - q_{mn}\sqrt{-\kappa_{mn}}}{2\sqrt{\epsilon\gamma}\,(2n^2\Omega^2 - \kappa_{mn})^2 - 2q_{mn}\sqrt{-\kappa_{mn}}}. \quad (16)$$

The right-hand side of Eq. (16) is negative for small q_{mn}. Therefore, c_f drives the eigenvalues from 0 to negative real. On the other hand, the derivative of the eigenvalues $\lambda = \pm i\sqrt{4n^2\Omega^2 - 2\kappa_{mn}}$ can be calculated as

$$\left.\frac{\partial\lambda}{\partial c_f}\right|_{c_f=0} = -1 + \frac{\kappa_{mn}}{4n^2\Omega^2 - 2\kappa_{mn}}. \quad (17)$$

The right-hand side of Eq. (17) is always negative. Therefore, we conclude that deflection A of the loaded disk is stabilized by the external damping.

References

Benson, R. C., and Bogy, D. B., 1978, "Deflection of a Very Flexible Spinning Disk Due to a Stationary Transverse Load," ASME JOURNAL OF APPLIED MECHANICS, Vol. 45, pp. 636–642.

Nowinski, J. L., 1964, "Nonlinear Transverse Vibrations of a Spinning Disk," ASME JOURNAL OF APPLIED MECHANICS, Vol. 31, pp. 72–78.

Raman, A., and Mote, Jr., C. D., 1999, "Non-linear Oscillations of Circular Plates Near a Critical Speed Resonance," *International Journal of Non-Linear Mechanics*, Vol. 34, pp. 139–157.

Tobias, S. A., and Arnold, R. N., 1957, "The Influence of Dynamical Imperfection on the Vibration of Rotating Disks," *Proceedings of the Institution of Mechanical Engineers*, Vol. 171, pp. 669–690.

Maximizing the Natural Frequencies and Transverse Stiffness of Centrally Clamped, Circular Disks by Thickening the Clamped Part of the Disk

A. A. Renshaw[1]

The natural frequencies and transverse stiffness of centrally clamped, circular disks are computed taking into account the flexibility of the central clamp and the thickness of the clamped part of the disk. When compared to experimental vibration data, these predictions are more accurate than the traditional, perfect clamping predictions, particularly for zero and one-nodal-diameter vibration modes. The reduction in natural frequency or transverse stiffness caused by clamping flexibility can be mitigated either by increasing the clamping stiffness or by increasing the hub thickness, defined here as the thickness of the disk sandwiched by the central clamp. A design study of these two alternatives for both stationary and rotating disks shows that increasing the hub thickness is often a more attractive design alternative.

1 Introduction

For the past decade, an interesting, industrial circular saw design has existed in which the hub thickness of the saw, defined here as the thickness of the part of the saw that is sandwiched between the thick clamping collars, is two to four times thicker than the exposed part of the saw (Bird, 1990). The origins of this design are unclear, although they may lie in the designs of unclamped, "free-floating" circular saws (Mote, 1977; Renshaw and Mote, 1996). The inventor of the design claims that increased hub thickness raises the critical speed of the saw *even for centrally clamped saws.* What is interesting about this claim is that the hub thickness is irrelevant in the traditional model of a centrally clamped saw.

[1] Department of Mechanical Engineering, Columbia University, M/C 4703, New York, NY 10027. Mem. ASME.

Contributed by the Applied Mechanics Division of THE AMERICAN SOCIETY OF MECHANICAL ENGINEERS for publication in the ASME JOURNAL OF APPLIED MECHANICS. Manuscript received by the ASME Applied Mechanics Division, Feb. 10, 1999; final revision, May 4, 1999. Associate Technical Editor: N. C. Perkins.

Downloaded 04 May 2010 to 171.66.16.27. Redistribution subject to ASME license or copyright; see http://www.asme.org/terms/Terms_Use.cfm

Since the stiffness of the clamping collars is normally four to five orders of magnitude greater than the stiffness of the saw, it is customary to assume that the clamping collars prohibit any significant motion of the hub. When deflection of the hub of the saw is not included in the model, the hub thickness becomes irrelevant.

The purpose of this brief note is to investigate the effect of clamp flexibility and hub thickness in the design of centrally clamped, circular disks in order to analytically assess the significance of these effects and determine the potential benefits of thick-hub designs. Such a study may not only explain the rationale behind existing thick-hub saws, but may also suggest improved designs for other circular disk technologies such as magnetic computer memory disks. Although an extensive literature exists on clamped, circular rotating disks (e.g., Lamb and Southwell, 1921; Mote, 1965; Iwan and Moeller, 1976; Benson and Bogy, 1978), to the author's knowledge, the effect of clamp flexibility has not been previously investigated.

In the present study, the natural frequencies and transverse stiffness of centrally clamped, circular disks are computed taking into account the flexibility of the central clamp and the thickness of the clamped part of the disk. When compared to experimental vibration data, these predictions are more accurate than the traditional, perfect clamping predictions, particularly for zero and one-nodal-diameter vibration modes. The reduction in natural frequency or transverse stiffness caused by clamping flexibility can be mitigated either by increasing the clamping stiffness or by increasing the hub thickness, defined here as the thickness of the disk sandwiched by the central clamp. A design study of these two alternatives for both stationary and rotating disks shows that increasing the hub thickness is often a more attractive design alternative.

2 Modeling

A thin, axisymmetric, circular disk of outer radius R_o, density ρ, Young's modulus E, and Poisson's ratio ν, spins about its axis of symmetry at a constant angular speed Ω'. Polar coordinates (R, θ) are fixed in the stationary frame of reference with the center of the disk at the origin. The disk is concentrically mounted on a thick, annular clamping ring that is rigidly attached to a central rotating spindle. The disk is then sandwiched between this thick annular clamping ring and a mating annular clamping ring, and the assembly is firmly bolted together so that the disk is held in place by a transverse, normal clamping pressure between radii $R = R_{ci}$ and $R = R_{co}$. The disk is of two different uniform thicknesses

$$H = \begin{cases} H_c & R_{ci} \le R < R_{co} \\ H_o & R_{co} < R \le R_o \end{cases}. \tag{1}$$

We model the central clamping in two different ways. In the first model, herein referred to as *perfect clamping,* we assume that the thick clamping rings and bolts are rigid and the disk is unable to deform in the region $R_{ci} \le R \le R_{co}$. In the second model, herein referred to as *flexible clamping,* we assume that the stiffness of transverse clamping, K_c, is determined by the stiffness of the clamping bolts which are modeled as a uniform elastic foundation of stiffness $K_c/\pi(R_{co}^2 - R_{ci}^2)$ in the annulus $R_{ci} \le R \le R_{co}$. K_c is zero for $R_{co} < R \le R_o$. The perfect clamping model is an idealization of the flexible clamping model in the limit $K_c \to \infty$.

The axisymmetric steady-state in-plane radial displacement of the disk is $u'(R)$, and the axisymmetric radial and hoop stresses in the disk are σ_r' and σ_θ', respectively. The transverse displacement of the disk is $w'(t', R, \theta)$ where t' is time. The disk is loaded transversely by the force per unit area $F(R, \theta, t')$.

Dimensionless variables are defined as follows:

$$r = R/R_o \quad w = W/H_o \quad t = t'\sqrt{D_o/\rho H_o R_o^4}$$

$$u = u'R_o/H_o^2 \quad \sigma = \sigma' H_o R_o^2/D \quad f = FR_o^4/D_o H_o \tag{2}$$

where subscripts have been omitted for brevity and $D_o = EH_o^3/12(1 - \nu^2)$. Dimensionless parameters describing the system are

$$\Omega = \Omega'\sqrt{\rho H_o R_o^4/D_o} \quad c_i = R_{ci}/R_o \quad c_o = R_{co}/R_o$$

$$k_c = K_c R_o^2/D_o \quad A_c = \pi(c_o^2 - c_i^2) \tag{3}$$

and the dimensionless thickness is

$$h = \begin{cases} h_c \equiv H_c/H_o & c_i \le r < c_o \\ 1 & c_o < r \le 1 \end{cases}. \tag{4}$$

h_c is referred to as the hub thickness of the disk.

The standard Kirchhoff plate model with in-plane stresses is

Table 1 Comparison of the natural frequency predictions of the perfect clamping and flexible clamping models with the experimental measurements of D'Angelo and Mote (1993). Mode (*m*, *n*) corresponds to *m* nodal circles and *n* nodal diameters.

	EXP.	PERFECT CLAMPING		FLEXIBLE CLAMPING $K_c = 2 \times 10^9$ N/m		FLEXIBLE CLAMPING $K_c = 0.9 \times 10^9$ N/m	
Mode (m,n)	Freq. (Hz)	Freq. (Hz)	% Error	Freq. (Hz)	% Error	Freq. (Hz)	% Error
(0,1)	37.19	39.63	6.56%	38.19	2.69%	37.73	1.45%
(0,0)	38.40	40.29	4.92%	39.01	1.59%	38.60	0.52%
(0,2)	47.10	48.13	2.19%	46.79	-0.66%	46.37	-1.55%
(0,3)	79.78	80.34	0.70%	79.62	-0.20%	79.40	-0.48%
(0,4)	133.08	133.61	0.40%	133.32	0.18%	133.24	0.12%
(0,5)	202.18	203.13	0.47%	203.04	0.43%	203.01	0.41%
(1,0)	250.36	257.75	2.95%	248.96	-0.56%	246.15	-1.68%
(1,1)	262.38	269.96	2.89%	261.32	-0.40%	258.56	-1.46%
(0,6)	285.71	286.89	0.41%	286.86	0.40%	286.85	0.40%
(1,2)	304.79	308.21	1.12%	300.22	-1.50%	297.68	-2.33%
(1,3)	374.92	375.47	0.15%	368.90	-1.61%	366.84	-2.16%
(0,7)	382.90	384.14	0.32%	384.13	0.32%	384.13	0.32%
(1,4)	475.09	472.77	-0.49%	468.18	-1.45%	466.77	-1.75%
(0,8)	493.36	494.59	0.25%	494.59	0.25%	494.59	0.25%
(1,5)	601.84	597.90	-0.65%	595.22	-1.10%	594.43	-1.23%
(0,9)	616.66	618.10	0.23%	618.10	0.23%	618.10	0.23%
(0,10)	753.24	754.58	0.18%	754.58	0.18%	754.58	0.18%
(0,11)	902.93	903.94	0.11%	903.94	0.11%	903.94	0.11%
(1,7)	920.37	915.29	-0.55%	914.74	-0.61%	914.59	-0.63%
(0,12)	1065.90	1066.15	0.02%	1066.15	0.02%	1066.15	0.02%
(0,13)	1241.00	1241.14	0.01%	1241.14	0.01%	1241.14	0.01%
(0,14)	1429.00	1428.88	-0.01%	1428.88	-0.01%	1428.88	-0.01%
STANDARD DEV. OF ERRORS:			1.83%		0.97%		1.02%

Downloaded 04 May 2010 to 171.66.16.27. Redistribution subject to ASME license or copyright; see http://www.asme.org/terms/Terms_Use.cfm

Table 2 Comparison of the natural frequency predictions of the perfect clamping and flexible clamping models for a typical 3.5-in. hard disk drive. $K_c = 1.3 \times 10^9$ N/m. Mode (m, n) corresponds to m nodal circles and n nodal diameters.

NATURAL FREQUENCIES

Mode (m,n)	PERFECT CLAMPING Freq. (Hz)	PERFECT CLAMPING Freq. (D'less)	FLEXIBLE CLAMPING Freq. (Hz)	FLEXIBLE CLAMPING Freq. (D'less)	Percent Reduction
(0,0)	1158	8.1749	1108	7.1111	-13.01%
(0,1)	1160	8.1883	996	7.0312	-14.13%
(0,2)	1342	9.4730	1182	8.3441	-11.92%
(0,3)	2003	14.1378	1898	13.3966	-5.24%
(0,4)	3168	22.3571	3114	21.9759	-1.71%

TRANSVERSE STIFFNESS

K_t (kN/m)	k_t (D'less)	K_t (kN/m)	k_t (D'less)	Percent Reduction
66.35	10.1939	55.69	8.5565	-16.06%

used to determine the natural frequencies and transverse stiffness of the disk (Mote, 1965; Iwan and Moeller, 1976; Renshaw, D'Angelo III, and Mote, 1994). This model requires solving two problems, the first for u, the second for w. For the problem for u, which decouples from the problem for w, we assume that the clamping does not restrict the in-plane motion of the disk. As a result, the stress-free boundary conditions

$$\sigma_r(c_i) = \sigma_r(1) = 0 \tag{5}$$

are used. Note that these boundary condition only affect the results for rotating disks. In stationary disks $u = \sigma_r = \sigma_\theta = 0$.

The boundary conditions for the problem for w divide into two cases. For *perfect clamping,* the boundary conditions

$$w(c_o) = w_{,r}(c_o) = 0 \tag{6}$$

and vanishing moment and shear forces at $r = 1$ are used. It is assumed that $w \equiv 0$ for $c_i \le r \le c_o$. For *flexible clamping,* we assume that the moment and shear forces vanish at $r = c_i$ and $r = 1$.

The transverse stiffness of the disk is derived from the solution of the steady-state deflection of the disk under a concentrated point load at its edge, i.e.,

$$f = \delta(r - 1)\delta(\theta)/r \quad w = \hat{w}(r, \theta) \tag{7}$$

where $\delta(\ )$ is the Dirac function. We define the *transverse* stiffness of the disk as

$$k_t = 1/\hat{w}(1, 0). \tag{8}$$

For realistic configurations, we anticipate that $k_t \ll k_c$, and, in fact, k_t is typically several orders of magnitude less than k_c.

The finite element method with the three-node element described by (Chen and Ren, 1998) is used, with quadratic trial functions for u and quintic trial functions for w. Since this element converges rapidly, only five elements are used in $c_i \le r \le c_o$ and ten elements are used in $c_o \le r \le 1$. This mesh gives natural frequencies that are within one percent of those with twice as many elements.

3 Model Verification

We first compare the model predictions with the natural frequencies experimentally measured in (D'Angelo III and Mote, 1993). In this work, the lowest 22 natural frequencies of a stationary steel disk with $R_o = 178$ mm and $H_o = H_c = 0.775$ mm were measured with high accuracy. The disk had a central hole at radius $R = 31.75$ mm, and was transversely clamped between $R = 37.45$ mm and $R = 53.35$ mm. We use $E = 207$ GPa (D'Angelo III and Mote (1993) used 200 GPa), $\rho = 7840$ kg/m^3, and $\nu = 0.30$. $c_i = 0.21$ and $c_o = 0.30$.

The clamping collars were held in place by six $\frac{1}{4}$-inch cap screws for which the effective cross-sectional area is 24 mm^2 (Juvinal, 1983). From the description provided in (D'Angelo III and Mote, 1993), it is not clear how long the unthreaded lengths of the screws were: the description only places the length between 15 mm and 34 mm. We report results for both 15 mm, which gives us the highest possible stiffness, and 34 mm. For 15 mm, the stiffness of the collar can be estimated as (Juvinal, 1983)

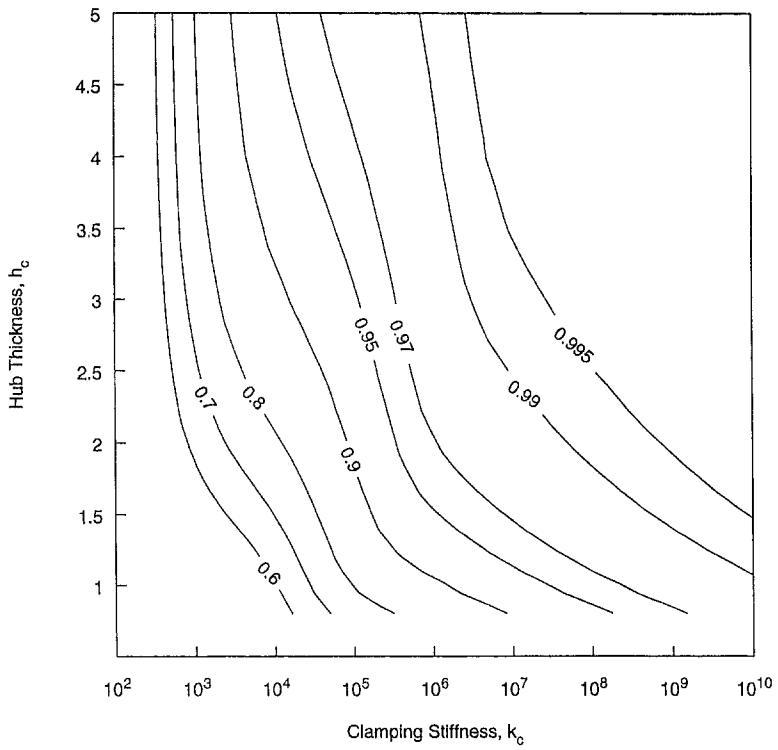


Fig. 1 Contour plot of the reduction ratio of transverse stiffness for $\Omega = 0$

Downloaded 04 May 2010 to 171.66.16.27. Redistribution subject to ASME license or copyright; see http://www.asme.org/terms/Terms_Use.cfm

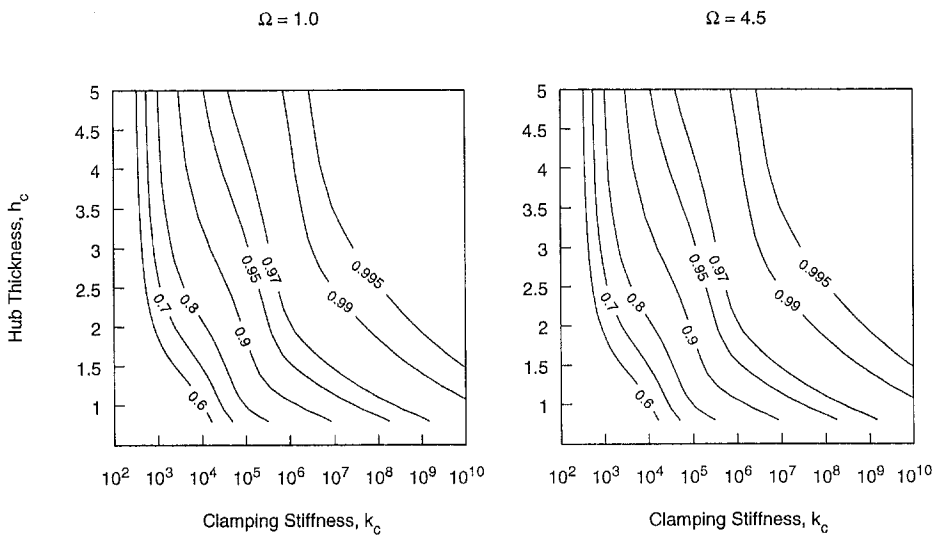


Fig. 2 Contour plots of the reduction ratio of transverse stiffness for Ω = 1.0 and Ω = 4.5

$$K_c = \frac{NAE}{L} = \frac{(6)(24\ \text{mm}^2)(207 \times 10^3\ \text{N/mm}^2)}{(15\ \text{mm})} \sim 2 \times 10^9\ \text{N/m} \quad (9)$$

or, in dimensionless terms, $k_c = 7.2 \times 10^6$. For 34 mm, $K_c \sim 0.9 \times 10^9$ N/m. Table 1 compares the experimental natural frequency measurements of the disk to the frequencies computed with the perfect clamping and flexible clamping models. The flexible clamping model reduces the standard deviation of the errors (0.97 percent for 15 mm; 1.02 percent for 34 mm) from its value for the perfect clamping model (1.83 percent). Most of this error reduction occurs in modes with zero to five nodal diameters and, in particular, in the zero and one-nodal-diameter modes. For example, the zero-nodal circle, one-nodal-diameter mode error is reduced from 6.56 percent to either 2.69 percent or 1.45 percent by incorporating clamp flexibility, while the zero-nodal circle, zero-nodal-diameter mode error is reduced from 4.92 percent to either 1.59 percent or 0.52 percent, depending on clamping stiffness. The measurements of these two frequencies have the largest errors in either model and are the most sensitive to clamping flexibility. Modes with six or more nodal diameters are not significantly changed by the clamp flexibility. From these results we conclude that the effects of clamping flexibility are experimentally observable and analytically predictable.

4 Design Study: k_c Versus h_c

We adopt the geometry of a typical 3.5-inch hard disk drive and perform a design study on the effect of clamping stiffness k_c and hub thickness h_c on the natural frequencies and transverse stiffness (k_t) of the disk. We consider a single aluminum disk with R_o = 47.5 mm and H_o = 1.3 mm. E = 72 GPa, ρ = 2800 kg/m^3, and ν = 0.32. The clamping collar begins at the central hole in the disk at R_{ci} = 12.5 mm and extends to R_{co} = 17.5 mm. Hence c_i = 0.26 and c_o = 0.37. The clamping is provided by four steel screws of diameter 2 mm and length 2 mm. This gives $K_c \sim 1.3 \times 10^9$ N/m or, in dimensionless numbers, $k_c \sim 2.0 \times 10^5$.

Table 2 lists dimensional and dimensionless predictions of the transverse stiffness and the five lowest natural frequencies of this disk for Ω = 0 using both the perfect and flexible clamping models. Even though the clamping stiffness k_c is five orders of magnitude greater than the transverse stiffness of the disk k_t, the clamp flexibility is sufficient to significantly reduce the lowest natural frequencies and the transverse stiffness of the disk. In this case, the first three natural frequencies are reduced more than ten percent due to clamp flexibility while the transverse stiffness is reduced 16 percent. Reductions in natural frequency and stiffness of this magnitude can be significant in disk drive design.

We define the *reduction ratio* of either the transverse stiffness or natural frequencies of the disk as the ratio of the prediction using the flexible clamping model to the prediction using the perfect clamping model.

Figure 1 presents a contour plot of the reduction ratio of the transverse stiffness k_t over the ranges $10^2 \le k_c \le 10^{10}$ and $0.8 \le h_c \le 5$ with Ω = 0. Contour plots of the reduction ratio of the natural frequencies are similar to Fig. 1. For a disk of uniform thickness (h_c = 1), $k_c \sim 10^6$ leads to about a ten percent reduction in stiffness and frequency when compared to perfect clamping; $k_c \sim 10^8$ produces a five percent reduction; and $k_c \sim 10^{10}$ produces a one percent reduction. However, increasing h_c to more than one substantially improves these numbers (i.e., lessens the reductions in stiffness). For example, when $h_c = 2$, $k_c \sim 10^6$ has only a three percent reduction from perfect clamping; $k_c \sim 10^8$ has less than a one percent reduction. Further increases in h_c lead to even less reductions, although at a slower rate once $h_c > 3$.

Mechanical designers can increase the natural frequencies and transverse stiffness of a disk by either increasing k_c or h_c. The results presented here illustrate that, in many cases, increasing h_c is a more practical alternative k_c. For example, in a typical 3.5-inch hard disk drive, the disks are separated by spacers that are 4.5 mm thick, i.e., more than three times the disk thickness. Hence h_c can be increased without interfering with the rest of the disk drive operation or design. However, increasing k_c, which can be done by adding more bolts or reducing their lengths, can be geometrically difficult. For instance, the circumference of the bolt circle in a 3.5-inch disk drive is only about 63 mm. As a result, only about 30 bolts can physically fit in the clamp, and, even if one did insert 30 clamping bolts, it would only increase the clamping stiffness by a factor of 7.5. The resulting increase in k_t such a design change would cause would be modest.

Similar results are obtained for rotating disks. Figure 2 show contour plots of the transverse stiffness reduction ratio for the same disk rotating at Ω = 1 (19 percent of critical speed; typical of disk drive applications) and Ω = 4.5 (85 percent of critical speed; typical of sawing applications). Once again, a similar design tradeoff is illustrated between the two possible methods of increasing k_t. Increasing k_c and h_c will increase k_t, but increasing h_c appears to be a more attractive alternative.

Acknowledgment

The author thanks Warren M. Bird for his comments and insights on thick-hub circular saw designs.

Downloaded 04 May 2010 to 171.66.16.27. Redistribution subject to ASME license or copyright; see http://www.asme.org/terms/Terms_Use.cfm

References

Benson, R. C., and Bogy, D. B., 1978, "Deflection of a Very Flexible Spinning Disk Due to a Stationary Transverse Load," ASME JOURNAL OF APPLIED MECHANICS, Vol. 45, pp. 636–642.

Bird, W. M., 1990, "Rotating Saw Blade Having Improved Critical Vibrational Speed," U.S. Patent Number 4,979,417.

Chen, D.-Y., and Ren, B.-S., 1998, "Finite Element Analysis of the Lateral Vibration of Thin Annular and Circular Plates With Variable Thickness," ASME *Journal of Vibration and Acoustics,* Vol. 120, pp. 747–752.

D'Angelo III, C., and Mote, Jr., C. D., 1993, "Natural Frequencies of a Thin Disk, Clamped by Thick Collars With Friction at the Contacting Surfaces, Spinning at High Rotation Speed," *Journal of Sound and Vibration,* Vol. 168, pp. 1–14.

Iwan, W. D., and Moeller, T. L., 1976, "The Stability of a Spinning Elastic Disk With a Transverse Load System," ASME JOURNAL OF APPLIED MECHANICS, Vol. 43, pp. 485–490.

Juvinal, R. C., 1983, *Fundamentals of Machine Component Design,* John Wiley and Sons, New York.

Lamb, H., and Southwell, R. V., 1921, "The Vibrations of a Spinning Disk," *Proceedings of the Royal Society of London,* Vol. A99, pp. 272–280.

Mote, Jr., C. D., 1965, "Free Vibration of Initially Stressed Circular Disks," ASME *Journal of Engineering for Industry,* Vol. 87, pp. 258–264.

Mote, Jr., C. D., 1977, "Moving-Load Stability of a Circular Plate on a Floating Central Collar," *Journal of the Acoustical Society of America,* Vol. 61, No. 2, pp. 439–447.

Renshaw, A. A., D'Angelo III, C., and Mote, Jr., C. D., 1994, "Aerodynamically Excited Vibration of a Rotating Disk," *Journal of Sound and Vibration,* Vol. 177, No. 5, pp. 577–590.

Renshaw, A. A., and Mote, Jr., C. D., 1996, "Local Stability of Gyroscopic Systems Near Vanishing Eigenvalues," ASME JOURNAL OF APPLIED MECHANICS, Vol. 63, pp. 116–120.

Magnetohydrodynamic Squeeze Film Characteristics Between Parallel Circular Plates Containing a Single Central Air Bubble in the Inertial Flow Regime

R. Usha[1] and P. Vimala[1]

In this paper, the magnetic effects on the Newtonian squeeze film between two circular parallel plates, containing a single central air bubble of cylindrical shape are theoretically investigated. A uniform magnetic field is applied perpendicular to the circular plates, which are in sinusoidal relative motion, and fluid film inertia effects are included in the analysis. Assuming an ideal gas under isothermal condition for an air bubble, a nonlinear differential equation for the bubble radius is obtained by approximating the momentum equation governing the magnetohydrodynamic squeeze film by the mean value averaged across the film thickness. Approximate analytical solutions for the air bubble radius, pressure distribution, and squeeze film force are determined by a perturbation method for small amplitude of sinusoidal motion and are compared with the numerical solution obtained by solving the nonlinear differential equation. The combined effects of air bubble, fluid film inertia, and magnetic field on the squeeze film force are analyzed.

1 Introduction

Owing to the increasing importance in many industrial applications in recent years, the magnetohydrodynamic lubrication phenomena has received considerable attention. The increased use of liquid-metal lubricants in high-temperature bearings and the use of low-viscosity lubricants to reduce the energy losses have motivated the investigations of the magnetohydrodynamic effects and inertial effects in lubrication (Hughes and Elco, 1962; Kuzma, Maki, and Donnelley, 1964; Kamiyama, 1969; Hamza, 1988, 1989). The investigations by Saki et al. (1975a, b) have motivated Haber and Etsion (1985) and Hashimoto (1995) to study the squeeze film characteristics between parallel circular plates containing a single central air bubble in the inertial flow regime. In this note the combined effects of magnetic field, air bubble, and fluid film inertia on the Newtonian squeeze film between two parallel circular plates which are in relative sinusoidal motion have been analyzed.

2 Formulation Based on Modified Lubrication Theory

We consider axially symmetric radial flow of an electrically conducting lubricant fluid between two parallel circular plates, which at time t, are separated a distance $h(t)$ apart and a uniform magnetic field B_o is applied perpendicular to the two plates (Fig. 1). The plates are made of nonconducting material. There is no applied electric field and the induced magnetic field is neglected. Applying the hydrodynamic lubrication assumptions for thin films, the governing equation of motion in the radial direction and the equation of continuity are

$$\rho\left(\frac{\partial u}{\partial t} + u\frac{\partial u}{\partial r} + w\frac{\partial u}{\partial z}\right) = -\frac{\partial p}{\partial r} + \mu\frac{\partial^2 u}{\partial z^2} - \sigma u B_o^2 \quad (1)$$

$$\frac{1}{r}\frac{\partial (ru)}{\partial r} + \frac{\partial w}{\partial z} = 0 \quad (2)$$

where u, w denote velocity components in the r and z increasing directions, respectively; σ denotes the fluid electrical conductivity; and μ the coefficient of viscosity. Assuming that the fluid film contains a large amount of air as a single central air bubble of cylindrical shape, the equation for the squeeze motion is given by

$$2\pi r\int_0^{h(t)} u\,dz = \pi\left[\frac{\partial}{\partial t}(a^2 h) - r^2\frac{\partial h}{\partial t}\right]. \quad (3)$$

The boundary conditions are

$$u(r, 0, t) = u(r, h, t) = 0;$$

$$w(r, 0, t) = 0, \quad w(r, h, t) = \frac{\partial h}{\partial t}. \quad (4)$$

The boundary condition for film pressure, considering the entrance pressure drop at the disk edge, is given by

$$p(r_a, t) = p_a - j\frac{C_e \rho r_a^2}{8h^2}\left(\frac{\partial h}{\partial t}\right)^2,$$

$$j = 0 \quad \text{for} \quad \frac{\partial h}{\partial t} < 0, \quad j = 1 \quad \text{for} \quad \frac{\partial h}{\partial t} > 0 \quad (5)$$

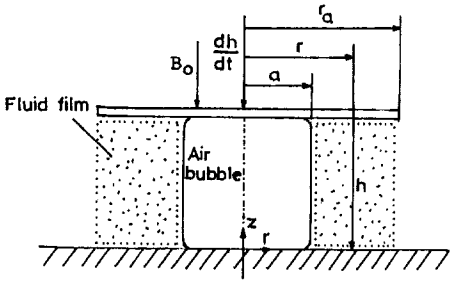


Fig. 1 Squeeze film between two parallel circular plates containing a central air bubble in the presence of a magnetic field

[1] Department of Mathematics, Indian Institute of Technology, Madras 600 036, India.

Contributed by the Applied Mechanics Division of THE AMERICAN SOCIETY OF MECHANICAL ENGINEERS for publication in the ASME JOURNAL OF APPLIED MECHANICS. Manuscript received by the ASME Applied Mechanics Division, Aug. 28, 1997; final revision, May 18, 1999. Associate Technical Editor: D. A. Siginer.

Downloaded 04 May 2010 to 171.66.16.27. Redistribution subject to ASME license or copyright; see http://www.asme.org/terms/Terms_Use.cfm

References

Benson, R. C., and Bogy, D. B., 1978, "Deflection of a Very Flexible Spinning Disk Due to a Stationary Transverse Load," ASME JOURNAL OF APPLIED MECHANICS, Vol. 45, pp. 636–642.

Bird, W. M., 1990, "Rotating Saw Blade Having Improved Critical Vibrational Speed," U.S. Patent Number 4,979,417.

Chen, D.-Y., and Ren, B.-S., 1998, "Finite Element Analysis of the Lateral Vibration of Thin Annular and Circular Plates With Variable Thickness," ASME *Journal of Vibration and Acoustics,* Vol. 120, pp. 747–752.

D'Angelo III, C., and Mote, Jr., C. D., 1993, "Natural Frequencies of a Thin Disk, Clamped by Thick Collars With Friction at the Contacting Surfaces, Spinning at High Rotation Speed," *Journal of Sound and Vibration,* Vol. 168, pp. 1–14.

Iwan, W. D., and Moeller, T. L., 1976, "The Stability of a Spinning Elastic Disk With a Transverse Load System," ASME JOURNAL OF APPLIED MECHANICS, Vol. 43, pp. 485–490.

Juvinal, R. C., 1983, *Fundamentals of Machine Component Design,* John Wiley and Sons, New York.

Lamb, H., and Southwell, R. V., 1921, "The Vibrations of a Spinning Disk," *Proceedings of the Royal Society of London,* Vol. A99, pp. 272–280.

Mote, Jr., C. D., 1965, "Free Vibration of Initially Stressed Circular Disks," ASME *Journal of Engineering for Industry,* Vol. 87, pp. 258–264.

Mote, Jr., C. D., 1977, "Moving-Load Stability of a Circular Plate on a Floating Central Collar," *Journal of the Acoustical Society of America,* Vol. 61, No. 2, pp. 439–447.

Renshaw, A. A., D'Angelo III, C., and Mote, Jr., C. D., 1994, "Aerodynamically Excited Vibration of a Rotating Disk," *Journal of Sound and Vibration,* Vol. 177, No. 5, pp. 577–590.

Renshaw, A. A., and Mote, Jr., C. D., 1996, "Local Stability of Gyroscopic Systems Near Vanishing Eigenvalues," ASME JOURNAL OF APPLIED MECHANICS, Vol. 63, pp. 116–120.

Magnetohydrodynamic Squeeze Film Characteristics Between Parallel Circular Plates Containing a Single Central Air Bubble in the Inertial Flow Regime

R. Usha[1] and P. Vimala[1]

In this paper, the magnetic effects on the Newtonian squeeze film between two circular parallel plates, containing a single central air bubble of cylindrical shape are theoretically investigated. A uniform magnetic field is applied perpendicular to the circular plates, which are in sinusoidal relative motion, and fluid film inertia effects are included in the analysis. Assuming an ideal gas under isothermal condition for an air bubble, a nonlinear differential equation for the bubble radius is obtained by approximating the momentum equation governing the magnetohydrodynamic squeeze film by the mean value averaged across the film thickness. Approximate analytical solutions for the air bubble radius, pressure distribution, and squeeze film force are determined by a perturbation method for small amplitude of sinusoidal motion and are compared with the numerical solution obtained by solving the nonlinear differential equation. The combined effects of air bubble, fluid film inertia, and magnetic field on the squeeze film force are analyzed.

1 Introduction

Owing to the increasing importance in many industrial applications in recent years, the magnetohydrodynamic lubrication phenomena has received considerable attention. The increased use of liquid-metal lubricants in high-temperature bearings and the use of low-viscosity lubricants to reduce the energy losses have motivated the investigations of the magnetohydrodynamic effects and inertial effects in lubrication (Hughes and Elco, 1962; Kuzma, Maki, and Donnelley, 1964; Kamiyama, 1969; Hamza, 1988, 1989). The investigations by Saki et al. (1975a, b) have motivated Haber and Etsion (1985) and Hashimoto (1995) to study the squeeze film characteristics between parallel circular plates containing a single central air bubble in the inertial flow regime. In this note the combined effects of magnetic field, air bubble, and fluid film inertia on the Newtonian squeeze film between two parallel circular plates which are in relative sinusoidal motion have been analyzed.

2 Formulation Based on Modified Lubrication Theory

We consider axially symmetric radial flow of an electrically conducting lubricant fluid between two parallel circular plates, which at time t, are separated a distance $h(t)$ apart and a uniform magnetic field B_o is applied perpendicular to the two plates (Fig. 1). The plates are made of nonconducting material. There is no applied electric field and the induced magnetic field is neglected. Applying the hydrodynamic lubrication assumptions for thin films, the governing equation of motion in the radial direction and the equation of continuity are

$$\rho\left(\frac{\partial u}{\partial t} + u\frac{\partial u}{\partial r} + w\frac{\partial u}{\partial z}\right) = -\frac{\partial p}{\partial r} + \mu\frac{\partial^2 u}{\partial z^2} - \sigma u B_o^2 \quad (1)$$

$$\frac{1}{r}\frac{\partial (ru)}{\partial r} + \frac{\partial w}{\partial z} = 0 \quad (2)$$

where u, w denote velocity components in the r and z increasing directions, respectively; σ denotes the fluid electrical conductivity; and μ the coefficient of viscosity. Assuming that the fluid film contains a large amount of air as a single central air bubble of cylindrical shape, the equation for the squeeze motion is given by

$$2\pi r\int_0^{h(t)} u\,dz = \pi\left[\frac{\partial}{\partial t}(a^2 h) - r^2\frac{\partial h}{\partial t}\right]. \quad (3)$$

The boundary conditions are

$$u(r, 0, t) = u(r, h, t) = 0;$$

$$w(r, 0, t) = 0, \quad w(r, h, t) = \frac{\partial h}{\partial t}. \quad (4)$$

The boundary condition for film pressure, considering the entrance pressure drop at the disk edge, is given by

$$p(r_a, t) = p_a - j\frac{C_e \rho r_a^2}{8h^2}\left(\frac{\partial h}{\partial t}\right)^2,$$

$$j = 0 \quad \text{for} \quad \frac{\partial h}{\partial t} < 0, \quad j = 1 \quad \text{for} \quad \frac{\partial h}{\partial t} > 0 \quad (5)$$

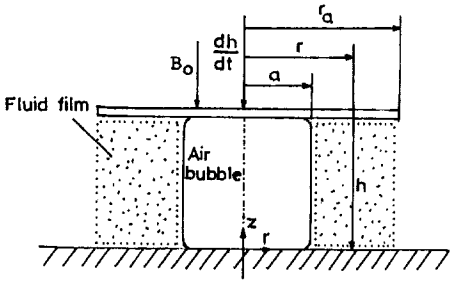


Fig. 1 Squeeze film between two parallel circular plates containing a central air bubble in the presence of a magnetic field

[1] Department of Mathematics, Indian Institute of Technology, Madras 600 036, India.

Contributed by the Applied Mechanics Division of THE AMERICAN SOCIETY OF MECHANICAL ENGINEERS for publication in the ASME JOURNAL OF APPLIED MECHANICS. Manuscript received by the ASME Applied Mechanics Division, Aug. 28, 1997; final revision, May 18, 1999. Associate Technical Editor: D. A. Siginer.

Downloaded 04 May 2010 to 171.66.16.27. Redistribution subject to ASME license or copyright; see http://www.asme.org/terms/Terms_Use.cfm

where C_e is the pressure loss coefficient and ρ is the density of fluid. As the film thickness is very small when compared with other lengths in the squeeze film, we assume that the inertia force and the magnetic force are constants over the film thickness. The inertia terms and the magnetic terms in the momentum Eq. (1) are approximated by the mean value averaged across the film thickness (Hashimoto and Wada, 1986) and Eq. (1) on using (4) gives

$$\frac{\rho}{h(t)}\left[\frac{\partial}{\partial t}\int_0^{h(t)} u dz + \left(\frac{\partial}{\partial r}+\frac{1}{r}\right)\int_0^{h(t)} u^2 dz\right] + \frac{\sigma B_o^2}{h(t)}\int_0^{h(t)} u dz = -\frac{\partial p}{\partial r} + \mu\frac{\partial^2 u}{\partial z^2}. \quad (6)$$

Introducing the equivalent pressure gradient f_e in (6) as

$$f_e = \frac{\rho}{h(t)}\left[\frac{\partial}{\partial t}\int_0^{h(t)} u dz + \left(\frac{\partial}{\partial r}+\frac{1}{r}\right)\int_0^{h(t)} u^2 dz\right] + \frac{\sigma B_o^2}{h(t)}\int_0^{h(t)} u dz + \frac{\partial p}{\partial r} \quad (7)$$

and integrating the resulting equation and using (3), we obtain

$$u = \frac{f_e}{2\mu} z(z-h); \quad f_e = -\frac{6\mu}{rh^3}\left[(a^2-r^2)\frac{\partial h}{\partial t} + 2ah\frac{\partial a}{\partial t}\right]. \quad (8)$$

The squeeze film pressure is obtained by integrating Eq. (7) with respect to r, using Eqs. (5) and (8) and is given by

$$p = \left(-\frac{6\mu}{h^3}-\frac{\sigma B_o^2}{2h}\right)\left[\left(a^2 g_1 - \frac{g_2}{2}\right)\frac{\partial h}{\partial t} + 2ahg_1\frac{\partial a}{\partial t}\right] - \frac{\rho}{h}\left[\frac{1}{2}\left(a^2 g_1 - \frac{g_2}{2}\right)\frac{\partial^2 h}{\partial t^2} + g_1\left\{2a\frac{\partial a}{\partial t}\frac{\partial h}{\partial t} + ah\frac{\partial^2 a}{\partial t^2} + h\left(\frac{\partial a}{\partial t}\right)^2\right\} - \frac{3}{10h}\left\{\left(-\frac{a^4 g_3}{2} + 2a^2 g_1 - \frac{3g_2}{2}\right)\left(\frac{\partial h}{\partial t}\right)^2 + 4ah\frac{\partial a}{\partial t}\frac{\partial h}{\partial t}\left(-\frac{a^2 g_3}{2} + g_1\right) - 2a^2 h^2\left(\frac{\partial a}{\partial t}\right)^2 g_3\right\}\right] + p_a - j\frac{C_e\rho r_a^2}{8h^2}\left(\frac{\partial h}{\partial t}\right)^2 \quad (9)$$

where

$$g_1 = \ln\left(\frac{r}{r_a}\right), \quad g_2 = r^2 - r_a^2, \quad g_3 = \frac{1}{r^2} - \frac{1}{r_a^2}. \quad (10)$$

The assumption of ideal gas under isothermal condition for an air bubble yields the air bubble pressure as

$$p_b = \frac{h_o a_o^2}{ha^2} p_a, \quad h(0) = h_0, \quad a(0) = a_0. \quad (11)$$

The nonlinear differential equation for the air bubble radius $a(t)$ is obtained using (9), (11), and $p|_{r=a} = p_b$ as

$$p_a\left(1 - \frac{h_o a_o^2}{ha^2}\right) - j\frac{C_e\rho r_a^2}{8h^2}\left(\frac{\partial h}{\partial t}\right)^2 - \left(\frac{6\mu}{h^3}+\frac{\sigma B_o^2}{2h}\right)\left[\left(a^2 g_{1a} - \frac{g_{2a}}{2}\right)\frac{\partial h}{\partial t} + 2ahg_{1a}\frac{\partial a}{\partial t}\right] - \frac{\rho}{h}\left[\frac{1}{2}\left(a^2 g_{1a} - \frac{g_{2a}}{2}\right)\frac{\partial^2 h}{\partial t^2} + g_{1a}\left(2a\frac{\partial a}{\partial t}\frac{\partial h}{\partial t} + ah\frac{\partial^2 a}{\partial t^2} + h\left(\frac{\partial a}{\partial t}\right)^2\right)\right] + \frac{3\rho}{10h^2}\left[\left(-\frac{a^4 g_{3a}}{2} + 2a^2 g_{1a} - \frac{3g_{2a}}{2}\right)\left(\frac{\partial h}{\partial t}\right)^2 + 4ah\frac{\partial a}{\partial t}\frac{\partial h}{\partial t}\left(-\frac{a^2 g_{3a}}{2} + g_{1a}\right)\right] - \frac{3\rho}{10h^2}\left[2a^2 h^2\left(\frac{\partial a}{\partial t}\right)^2 g_{3a}\right] = 0 \quad (12)$$

where $g_{1a} = g_1|_{r=a}$, $g_{2a} = g_2|_{r=a}$, $g_{3a} = g_3|_{r=a}$. The squeeze film force is obtained by integrating the film pressure and is given by

$$f = 2\pi\left[\int_0^a (p_b - p_a) r dr + \int_a^{r_a} (p - p_a) r dr\right]. \quad (13)$$

3 Solution of Sinusoidal Squeeze Motion

The solution of the modified lubrication equations for the magnetohydrodynamic squeeze film is obtained by taking the film thickness under the sinusoidal squeeze motion as

$$h(t) = h_o + e\sin\omega t. \quad (14)$$

Introducing the following nondimensional quantities

$$F = \frac{f}{\pi r_a^2 p_a}, \quad H = \frac{h}{h_o}, \quad T = \omega t, \quad P = \frac{p}{p_a}, \quad R = \frac{r}{r_a}, \quad \mathrm{Re}^* = \frac{\rho h_o^2 \omega}{\mu},$$

$$M = \left(\frac{\sigma}{\mu}\right)^{1/2} H h_o B_o, \quad S = \frac{\mu\omega^2 r_a^2}{p_a h_o^2}, \quad \alpha = \frac{a}{r_a}, \quad \epsilon = \frac{e}{h_o}. \quad (15)$$

Equations for squeeze film pressure, air bubble radius and squeeze film force are obtained from (9), (11), (12), and (13). Using the nondimensional form of Eq. (12) and the initial conditions $\alpha\,(T = 0) = \alpha_0$, $\dot{\alpha}\,(T = 0) = 0$, the approximate analytical solution for $\alpha(T)$ is obtained using a perturbation technique for small amplitude of sinusoidal squeeze motion. The air bubble radius is expanded when $\epsilon \ll 1$ as $\alpha = \alpha_0 + \epsilon\alpha_1 + \epsilon^2\alpha_2 + \ldots$ and the dimensionless squeeze film force is obtained from Eq. (13).

4 Results and Discussion

The differential equation for the dimensionless air bubble radius $\alpha(T)$ is solved numerically by Runge Kutta Gill method. The numerical solutions become fully developed with the fifth period of sinusoidal squeeze motion and the solutions of the fifth period are presented. The numerical solutions (nonlinear solutions) and the analytical solutions (linearized solutions) are represented by the solid lines and broken lines, respectively.

The relation between the dimensionless squeeze film force F and the variation of film thickness $\Delta H/\epsilon\,(= \sin T)$ for the squeeze Sommerfeld number of $S = 1$ and $S = 10$ is presented in Fig. 2. It is observed that the squeeze film force varies on the elliptical trajectories when $\mathrm{Re}^* = 0$ and the influence of initial air bubble radius on the trajectories is not significant and the influence of initial air bubble radius is well pronounced as the squeeze Reynolds number Re^* and Hartmann number M increase.

Figure 3 presents the effects of fluid inertia and magnetic forces on the maximum squeeze film force. It is observed that

(i) squeeze film force increases with increase in M, for a fixed value of Re^* and a fixed value of initial air bubble radius,
(ii) squeeze film force increases with decrease in the initial air bubble radius for all values of M,
(iii) the effects of fluid inertia on the squeeze film force are larger as the squeeze Sommerfeld number increases and it is further enhanced by the presence of the magnetic field,

Downloaded 04 May 2010 to 171.66.16.27. Redistribution subject to ASME license or copyright; see http://www.asme.org/terms/Terms_Use.cfm

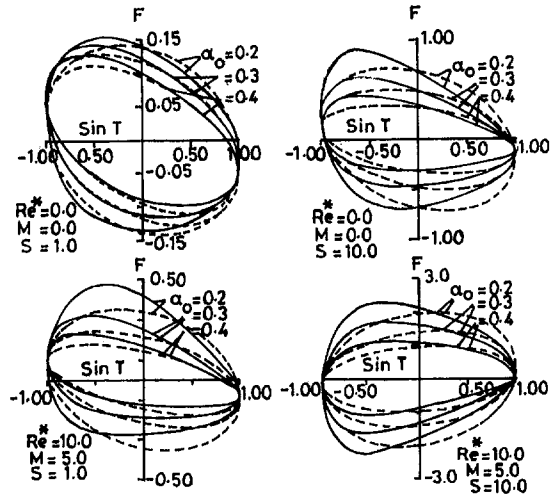


Fig. 2 Relation between squeeze film force and film thickness for ϵ = 0.1

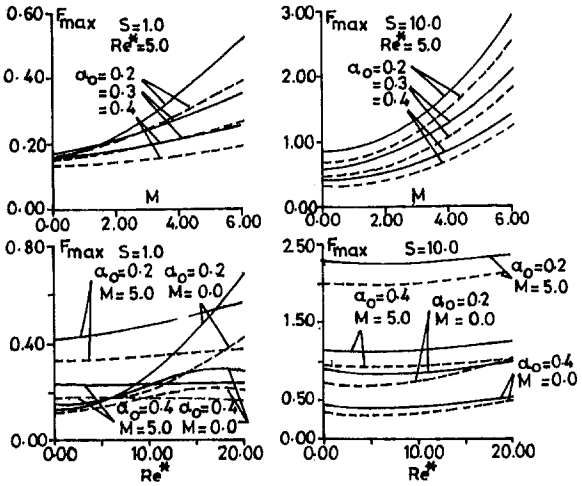


Fig. 3 The effects of magnetic field and inertia forces on the maximum variation of squeeze film force for ϵ = 0.1

(iv) the effects of fluid inertia on the squeeze film forces are larger as the initial air bubble radius decreases and it is further enhanced by the presence of the magnetic field,

(v) the squeeze film force is strongly dependent on the magnitude of initial air bubble radius, squeeze Reynolds number, squeeze Sommerfeld number and the Hartmann number.

The present results for Re* = 0 and M = 0 agree with the results obtained by Haber and Etsion (1985), in which fluid inertia effects and magnetic force effects have been neglected.

Acknowledgment

The authors wish to thank Prof. Dennis Siginer, Associate Editor, for his valuable suggestions and Prof. L. T. Wheeler, Technical Editor, and the referee for their encouraging comments.

References

Haber, S., and Etsion, I., 1985, "Analysis of an Oscillatory Oil Squeeze Film Containing a Central Gas Bubble," *ASLE Trans.*, Vol. 23, No. 2, pp. 253–260.

Hamza, E. A., 1989, "A Similar Flow Between Two Disks in the Presence of a Magnetic Field," ASME JOURNAL OF APPLIED MECHANICS, Vol. 56, pp. 218–221.

Hamza, E. A., 1988, "The Magnetohydrodynamic Squeeze Film," ASME *Journal of Tribology*, Vol. 110, No. 2, pp. 375–377.

Hashimoto, H., 1995, "Squeeze Film Characteristics Between Parallel Circular Plates Containing a Single Central Air Bubble in the Inertial Flow Regime," ASME *Journal of Tribology*, Vol. 117, pp. 513–518.

Hughes, W. F., and Elco, R. A., 1962, "Magnetohydrodynamic Lubrication Flow Between Parallel Rotating Disks," *J. Fluid Mech.*, Vol. 13, pp. 21–32.

Kamiyama, S., 1969, "Inertia Effects in MHD Hydrostatic Thrust Bearing," ASME *Journal of Lubrication Technology*, Vol. 91, pp. 589–596.

Kuzma, D. C., Maki, E. R., and Donnelley, R. J., 1964, "The Magnetohydrodynamic Squeeze Film," *J. Fluid Mech.*, Vol. 19, pp. 395–400.

Saki, K., Hirano, F., Sakai, T., and Shimogawa, T., 1975a, "The Behaviour of Oil Film Between the Static and the Vibrating Plate (1st Report)," *J. JSLE*, Vol. 20, No. 8, pp. 582–592.

Saki, K., Hirano, F., and Sakai, T., 1975b, "The Behaviour of Oil Film Between the Static and the Vibrating Plate (2nd Report)," *J. JSLE*, Vol. 20, No. 8, pp. 560–566.

Generation (or Degeneration) of a Separation Bubble in a Liquid-Filled Cylinder Through Spin-Up (or Spin-Down) Process

S. Bhattacharyya[1,2] and A. Pal[1]

The present study deals with the spin-up and spin-down of viscous incompressible fluid confined in a cylindrical enclosure. The spin-up (or spin-down) is developed by increasing (or decreasing) abruptly the angular velocity of the upper endwall where initial steady flow is either due to uniform rotation of the lower endwall or due to rotation of both end walls in the same direction with small rotation ratio of the top-bottom endwalls. We have seen numerically that through spin-up, an on-axis separation bubble can be generated (vortex breakdown) in a flow when the Reynolds number is much lower than the critical value of the Reynolds number $(Re)_c$ for the onset of vortex breakdown. At the ultimate steady state the separation bubble appears and a waviness in the stream surfaces in the vicinity of the lower endwall is found. The spin-down process acts in the opposite way. We found that for the flow with Reynolds number above the critical value $(Re)_c$, the vortex breakdown can be prevented through spin-down and the ultimate steady-state flow is also free from it.

1 Introduction

Vortex breakdown is the term used to describe a phenomena in which sudden changes are observed in the structure of a vortex core embedded in a flow field with a velocity gradient along the axis of the vortex. Among these abrupt changes is the appearance of an on-axis stagnation point that is followed by either a separation bubble within the vortex or a spiraling of the vortex core. Vortex breakdown phenomena in a liquid-filled cylindrical enclosure with one endwall in uniform rotation was studied experimentally by Escudier (1984). A noteworthy feature of the separation bubbles in closed cylindrical geometry, as observed by Escudier (1984), was that these flows are axisymmetric. Various aspects of vortex breakdown in a cylindrical enclosure were investigated numerically as well as experimentally in recent years by several authors, namely Lopez (1990, 1995), Valentine and Jahnke (1994), Gelfgat et al. (1996), Watson and Neitzel (1996), and Spohn et al.

[1] Department of Mathematics, Indian Institute of Technology, Kharagpur 721 302, India.

[2] e-mail: somnath@maths.iitkgp.ernet.in.

Contributed by the Applied Mechanics Division of THE AMERICAN SOCIETY OF MECHANICAL ENGINEERS for publication in the ASME JOURNAL OF APPLIED MECHANICS. Manuscript received by the ASME Applied Mechanics Division, Sept. 30, 1997; final revision, May 10, 1999. Associate Technical Editor: D. A. Signier.

Downloaded 04 May 2010 to 171.66.16.27. Redistribution subject to ASME license or copyright; see http://www.asme.org/terms/Terms_Use.cfm

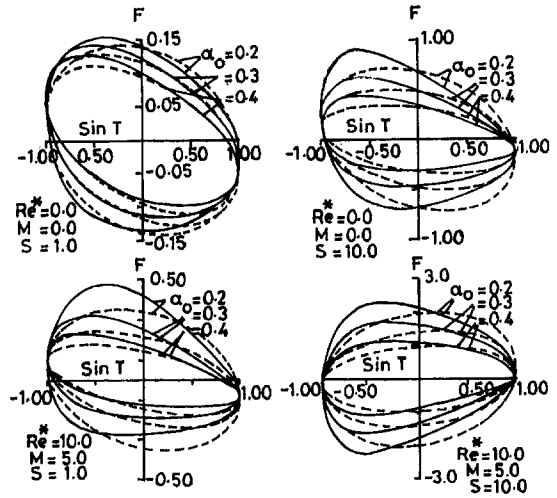


Fig. 2 Relation between squeeze film force and film thickness for ϵ = 0.1

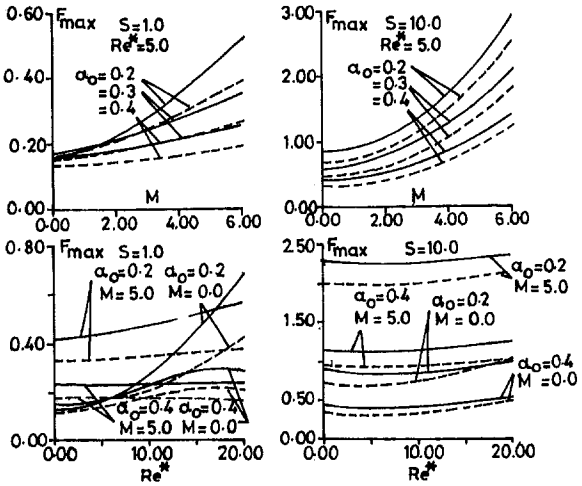


Fig. 3 The effects of magnetic field and inertia forces on the maximum variation of squeeze film force for ϵ = 0.1

(iv) the effects of fluid inertia on the squeeze film forces are larger as the initial air bubble radius decreases and it is further enhanced by the presence of the magnetic field,

(v) the squeeze film force is strongly dependent on the magnitude of initial air bubble radius, squeeze Reynolds number, squeeze Sommerfeld number and the Hartmann number.

The present results for Re* = 0 and M = 0 agree with the results obtained by Haber and Etsion (1985), in which fluid inertia effects and magnetic force effects have been neglected.

Acknowledgment

The authors wish to thank Prof. Dennis Siginer, Associate Editor, for his valuable suggestions and Prof. L. T. Wheeler, Technical Editor, and the referee for their encouraging comments.

References

Haber, S., and Etsion, I., 1985, "Analysis of an Oscillatory Oil Squeeze Film Containing a Central Gas Bubble," *ASLE Trans.*, Vol. 23, No. 2, pp. 253–260.

Hamza, E. A., 1989, "A Similar Flow Between Two Disks in the Presence of a Magnetic Field," ASME JOURNAL OF APPLIED MECHANICS, Vol. 56, pp. 218–221.

Hamza, E. A., 1988, "The Magnetohydrodynamic Squeeze Film," ASME *Journal of Tribology*, Vol. 110, No. 2, pp. 375–377.

Hashimoto, H., 1995, "Squeeze Film Characteristics Between Parallel Circular Plates Containing a Single Central Air Bubble in the Inertial Flow Regime," ASME *Journal of Tribology*, Vol. 117, pp. 513–518.

Hughes, W. F., and Elco, R. A., 1962, "Magnetohydrodynamic Lubrication Flow Between Parallel Rotating Disks," *J. Fluid Mech.*, Vol. 13, pp. 21–32.

Kamiyama, S., 1969, "Inertia Effects in MHD Hydrostatic Thrust Bearing," ASME *Journal of Lubrication Technology*, Vol. 91, pp. 589–596.

Kuzma, D. C., Maki, E. R., and Donnelley, R. J., 1964, "The Magnetohydrodynamic Squeeze Film," *J. Fluid Mech.*, Vol. 19, pp. 395–400.

Saki, K., Hirano, F., Sakai, T., and Shimogawa, T., 1975a, "The Behaviour of Oil Film Between the Static and the Vibrating Plate (1st Report)," *J. JSLE*, Vol. 20, No. 8, pp. 582–592.

Saki, K., Hirano, F., and Sakai, T., 1975b, "The Behaviour of Oil Film Between the Static and the Vibrating Plate (2nd Report)," *J. JSLE*, Vol. 20, No. 8, pp. 560–566.

Generation (or Degeneration) of a Separation Bubble in a Liquid-Filled Cylinder Through Spin-Up (or Spin-Down) Process

S. Bhattacharyya[1,2] and A. Pal[1]

The present study deals with the spin-up and spin-down of viscous incompressible fluid confined in a cylindrical enclosure. The spin-up (or spin-down) is developed by increasing (or decreasing) abruptly the angular velocity of the upper endwall where initial steady flow is either due to uniform rotation of the lower endwall or due to rotation of both end walls in the same direction with small rotation ratio of the top-bottom endwalls. We have seen numerically that through spin-up, an on-axis separation bubble can be generated (vortex breakdown) in a flow when the Reynolds number is much lower than the critical value of the Reynolds number $(Re)_c$ for the onset of vortex breakdown. At the ultimate steady state the separation bubble appears and a waviness in the stream surfaces in the vicinity of the lower endwall is found. The spin-down process acts in the opposite way. We found that for the flow with Reynolds number above the critical value $(Re)_c$, the vortex breakdown can be prevented through spin-down and the ultimate steady-state flow is also free from it.

1 Introduction

Vortex breakdown is the term used to describe a phenomena in which sudden changes are observed in the structure of a vortex core embedded in a flow field with a velocity gradient along the axis of the vortex. Among these abrupt changes is the appearance of an on-axis stagnation point that is followed by either a separation bubble within the vortex or a spiraling of the vortex core. Vortex breakdown phenomena in a liquid-filled cylindrical enclosure with one endwall in uniform rotation was studied experimentally by Escudier (1984). A noteworthy feature of the separation bubbles in closed cylindrical geometry, as observed by Escudier (1984), was that these flows are axisymmetric. Various aspects of vortex breakdown in a cylindrical enclosure were investigated numerically as well as experimentally in recent years by several authors, namely Lopez (1990, 1995), Valentine and Jahnke (1994), Gelfgat et al. (1996), Watson and Neitzel (1996), and Spohn et al.

[1] Department of Mathematics, Indian Institute of Technology, Kharagpur 721 302, India.

[2] e-mail: somnath@maths.iitkgp.ernet.in.

Contributed by the Applied Mechanics Division of THE AMERICAN SOCIETY OF MECHANICAL ENGINEERS for publication in the ASME JOURNAL OF APPLIED MECHANICS. Manuscript received by the ASME Applied Mechanics Division, Sept. 30, 1997; final revision, May 10, 1999. Associate Technical Editor: D. A. Signier.

Downloaded 04 May 2010 to 171.66.16.27. Redistribution subject to ASME license or copyright; see http://www.asme.org/terms/Terms_Use.cfm

(1998). The physical mechanism of the vortex breakdown process was investigated theoretically by Brown and Lopez (1990).

In this note we made a numerical study on two cases of transient flow in a liquid-filled cylindrical enclosure. The initial flow is considered to be either due to rotation of the lower endwall or due to corotation of the top-bottom endwall with a small rotation ratio. In the spin-up case (Case I) the top endwall is set to rotate impulsively with smaller angular velocity in the same direction as that of the lower endwall and in the spin-down case (Case II) the top endwall is brought to rest abruptly when it was in corotation with the lower endwall with small rotation ratio. The unsteady axisymmetric Navier-Stokes equations describing the flow from initial steady state to the terminal steady are solved numerically.

Neitzel and Davies (1981) studied numerically the nonlinear spin-down problem in a cylinder which was initially in rigid-body rotation and was suddenly brought to rest. Subsequently, Valentine and Miller (1994) investigated the spin-down problem and found that vortex breakdown occurs in the transient phase.

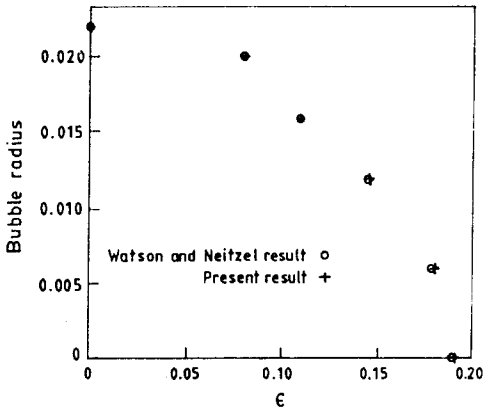


Fig. 1 Comparison of bubble radius with Watson and Neitzel for various values of the top-bottom endwall rotation ratio when $A = 1.5$ and Re = 1500

2 Formulation of the Problem

An incompressible viscous fluid completely fills a cylinder of radius R and height H. Cylindrical polar coordinates (r, θ, z) are used such that the z-axis is chosen as the axis of the cylinder and the bottom endwall lies on the plane $z = 0$. The governing equations are the axisymmetric Navier-Stokes equations, together with the continuity equation and appropriate boundary and initial conditions. The velocity components are scaled by $1/R\Omega$, where Ω is the angular velocity of the lower end wall. Introducing the stream function ψ, the nondimensional velocity vector is $q = (u, v, w) = (1/r\ \partial\psi/\partial z,\ \Gamma/r,\ -1/r\ \partial\psi/\partial r)$ and the azimuthal component of vorticity ζ is given by

$$\zeta = \frac{1}{r}\left(\frac{\partial^2\psi}{\partial r^2} - \frac{1}{r}\frac{\partial\psi}{\partial r} + \frac{\partial^2\psi}{\partial z^2}\right). \tag{1}$$

The nondimensional axisymmetric Navier-Stokes equations are

$$\frac{\partial\zeta}{\partial t} + u\frac{\partial\zeta}{\partial r} + w\frac{\partial\zeta}{\partial z} - \frac{u\zeta}{r} - \frac{2\Gamma}{r^3}\frac{\partial\Gamma}{\partial z} = \mathrm{Re}^{-1}\left(\frac{\partial^2\zeta}{\partial r^2} + \frac{1}{r}\frac{\partial\zeta}{\partial r} - \frac{\zeta}{r^2} + \frac{\partial^2\zeta}{\partial z^2}\right) \tag{2}$$

$$\frac{\partial\Gamma}{\partial t} + u\frac{\partial\Gamma}{\partial r} + w\frac{\partial\Gamma}{\partial z} = \mathrm{Re}^{-1}\left(\frac{\partial^2\Gamma}{\partial r^2} - \frac{1}{r}\frac{\partial\Gamma}{\partial r} + \frac{\partial^2\Gamma}{\partial z^2}\right). \tag{3}$$

The boundary conditions are

$$\psi = 0, \quad \partial\psi/\partial r = 0, \quad \partial\psi/\partial z = 0, \quad v = r,$$

$$\zeta = 1/r(\partial^2\psi/\partial z^2) \quad \text{at } z = 0, \quad 0 \le r \le 1$$

$$\psi = 0, \quad \partial\psi/\partial r = 0, \quad \partial\psi/\partial z = 0, \quad v = \epsilon r,$$

$$\zeta = 1/r(\partial^2\psi/\partial z^2) \quad \text{at } z = 1, \quad 0 \le r \le 1$$

$$\psi = 0, \quad v = 0, \quad \zeta = 0 \quad \text{at } r = 0, \quad 0 \le z \le A$$

$$\psi = 0, \quad v = 0, \quad \zeta = 1/r(\partial^2\psi/\partial r^2) \quad \text{at } r = 1, \quad 0 \le z \le A. \tag{4}$$

Here ν is the kinematic viscosity, $1/\Omega$ is the time scale and $1/R$ is the length scale. The flow is characterized by three dimensionless parameters: the aspect ratio $A = H/R$, the Reynolds number $\mathrm{Re} = \Omega r^2/\nu$, and ϵ is the top-bottom endwall rotation ratio. At the initial steady state ($t = 0$) for Case I (spin-up) we choose $\epsilon = 0$ and for Case II (spin-down), $\epsilon > 0$. For $t > 0$, $\epsilon > 0$ when we considered Case I and for Case II, $\epsilon = 0$.

The set of coupled nonlinear partial differential Eqs. (1)–(3) are solved iteratively. A time marching method, namely, the alternating direction implicit scheme (ADI), is used for discretizing the time derivatives in the azimuthal vorticity transport Eq. (2) and the angular momentum Eq. (3). We have used an upwind difference scheme to discretize the convective terms and central differences in the diffusive terms. The Poisson's Eqs. (1) for the stream function are solved at every iteration using a fourth-order accurate compact difference scheme (Bhattacharyya et al., 1996). The solution for the initial steady state for both the cases are obtained in a similar way. The grid dependency tests were carried out using different uniform grid sizes. We found 100×100 grid size produces an optimal grid independent solution. At the early stage of the spin-up and spin-down we have taken the grid size in the temporal direction $\delta t = 0.0001$ which has been increased as time progresses.

3 Results and Discussion

In order to test the accuracy of our numerical method, we have compared our steady-state results for the stream function and azimuthal vorticity contours with those of Valentine and Jahnke (1994) for $\mathrm{Re} = 1854$ and $A = 1.5$ when the flow due to rotation of the top endwall are considered and found them in excellent agreement (not presented here). The separation bubble for $\mathrm{Re} = 1854$, $A = 1.5$ appears between $z = 0.35$ and $z = 0.4$, and the region about the axis of rotation where the azimuthal vorticity is negative is included between $z = 0.19$ and $z = 0.9$, which is identical with the results of Valentine and Jahnke. The separation bubble radius (which is determined numerically by locating the maximum radius at which a value of $\psi = 0$ is found) of our computation are also compared with Watson and Neitzel (1996) for $\mathrm{Re} = 1500$, $A = 1.5$ and at different values of the top-bottom endwall rotation ratio. An excellent agreement with our results are found (Fig. 1).

We considered for the spin-up case (Case I) the initial steady-state flow due to uniform rotation of the lower endwall with stationary top endwall and side wall for $\mathrm{Re} = 1300$. The value of the Reynolds number considered here is much less than the critical value of the Reynolds number $(\mathrm{Re})_c$ (=1600), the minimum value of the Reynolds number for the onset of vortex breakdown. We found that the curvature of the stream surfaces does not change sign and the secondary flow is a simple overturning motion.

The initial flow due to the rotation of the lower end wall is perturbed by rotating abruptly the upper end wall with a small top-bottom rotation ratio $\epsilon = 0.1$. Due to this abrupt change a transient flow develops. We find numerically that at a nondimensional time $t = 2.1$ a single separation bubble appears on the axis of rotation ($r = 0$). The stagnation points on the axis of rotation making the leading and trailing edges of the separation bubbles are found at $z = 0.4$ and $z = 0.5$, respectively. The separation bubble radius r_b is 0.075. In subsequent time during the spin-up process the separation bubble increases in size. At $t = 2.5$ the two

Downloaded 04 May 2010 to 171.66.16.27. Redistribution subject to ASME license or copyright; see http://www.asme.org/terms/Terms_Use.cfm

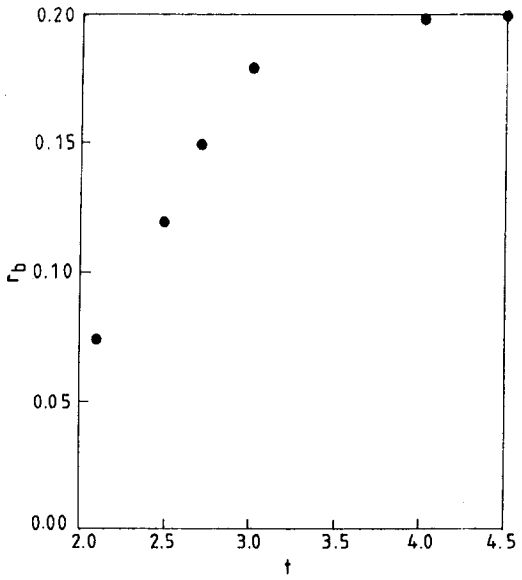


Fig. 2 Variation of separation bubble radius r_b with time during the spin-up process

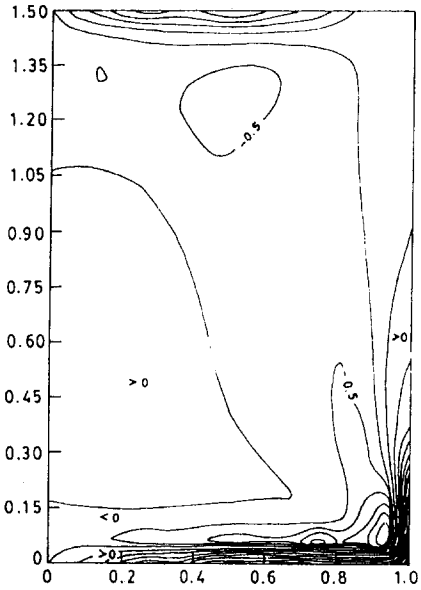


Fig. 4 Contour plots of the azimuthal component of vorticity ζ during the spin-up process when A = 1.5 and Re = 1300 at t = 4, $-3.0582 < \zeta < 7.122$, $\delta\zeta$ = 0.5, ϵ = 0.1

stagnation points forming the leading and trailing edge of the bubble are located at $z = 0.35$ and $z = 0.75$ on the axis of rotation $r = 0$ and the separation bubble radius $r_b = 0.12$.

Figure 2 shows the variation of separation bubble radius with time during the spin-up process. The vortex breakdown phenomena at Re = 1300 ($<(\mathrm{Re})_c$) takes place from the nondimensional time $t = 2.1$. The separation bubble radius increases its size with the increase of time during the spin-up process. The numerical results show that the spin-up process ends and the flow reaches the new steady state at the nondimensional time $t = 4$.

Figure 3 describes the streamline pattern at the terminal steady state ($t = 4$). The separation bubble occurs between $z = 0.25$ and $z = 0.75$ on the axis of rotation $r = 0$. The divergence in the streamlines in the axial direction near the lower Ekman layer is evident from the figure. This divergence of stream tube in the interior of the vortex flow causes the production of azimuthal component of vorticity with opposite sign.

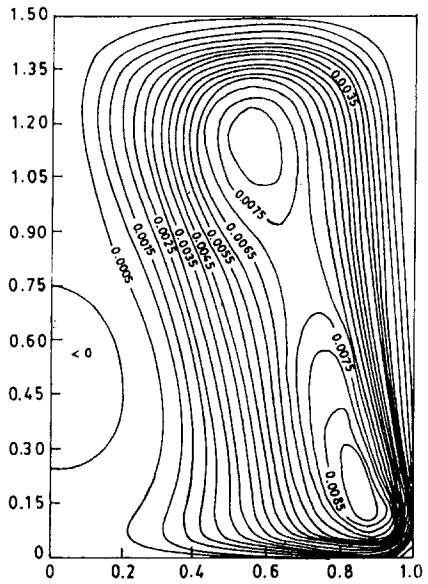


Fig. 3 Contour plots of the streamline ψ, $-6.8407 \times 10^{-5} < \psi < 0.0095$, $\delta\psi$ = 0.0015 at the terminal steady state when ϵ = 0.1 (spin-up), t = 4, A = 1.5, and Re = 1300

The azimuthal component of vorticity ζ plays an important role in the vortex breakdown. Externally imposed rotation of the lower endwall imparts a vertical component of vorticity to the flow. The production of the azimuthal component of vorticity can be through an axial gradient of the swirl velocity. In a flow with an axial gradient of the swirl velocity, the head of the material line element will travel in the azimuthal direction at a different speed than its tail. The result will be tilting of the material line in the azimuthal direction. Thus the axial swirl velocity gradient produces an azimuthal component of vorticity. We found that the azimuthal vorticity is positive in the boundary layer regions which is consistent with a deceleration of the meridional flow in the boundary layers. In the interior region of the cylinder ζ is negative except in a closed region around the axis of rotation where it is positive. In the core of the vortex a local production of radial velocity induces a divergence in the stream surfaces. The divergence in the stream surfaces causes the production of a positive component of azimuthal vorticity. This locally increased positive azimuthal vorticity becomes large enough beyond certain value of Reynolds num-

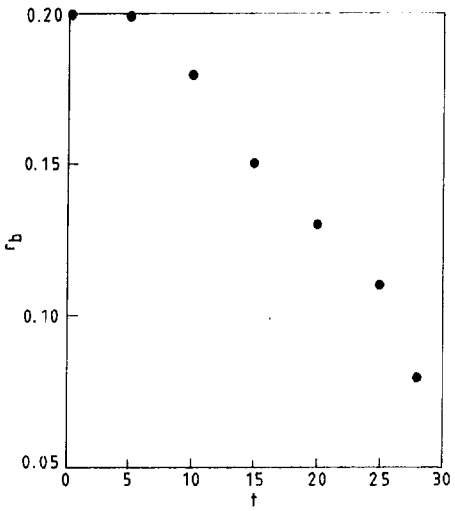


Fig. 5 Variation of separation bubble radius r_b with time during the spin-down process

Downloaded 04 May 2010 to 171.66.16.27. Redistribution subject to ASME license or copyright; see http://www.asme.org/terms/Terms_Use.cfm

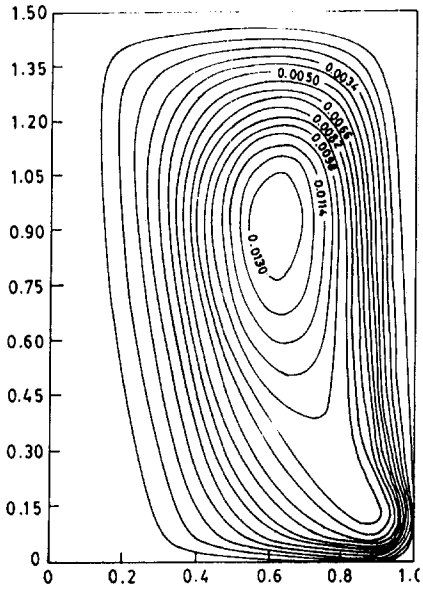


Fig. 6 Contour plots of the streamline ψ, $0 < \psi < 0.0144$, $\delta\psi = 0.002$ at the terminal steady state $t = 30$ when $\epsilon = 0.0$ (spin-down), $A = 1.5$ and Re = 1300

ber so as to halt the inward meridional flow provided by the Ekman layer pumping on the rotating endwall. This ultimately causes stagnation on the symmetry plane and the formation of a recirculation zone (separation bubble). During the spin-up process the region of positive azimuthal vorticity around the axis of rotation increases and this region always includes the region of recirculation. Figure 4 shows the azimuthal vorticity contours at the terminal steady state in the spin-up process. The positive region of ζ around the axis of rotation is included between the plane $z = 0.15$ and $z = 1.05$, which includes the region of the separation bubble.

In the initial steady-state flow for Case I the axial velocity w on the axis of rotation is predominantly inward. An axial flow reversal on the axis of rotation takes place from the nondimensional time $t = 2.1$ during the spin-up process. In subsequent time this region of reversed axial flow increases. At time $t = 2.1$, axial flow reversal on $r = 0$ takes place between $z = 0.4$ and $z = 0.5$ and at a nondimensional time $t = 4$ it takes place between $z = 0.25$ and $z = 0.75$. At the terminal steady state ($t = 4$) the axial flow reversal in the core of the vortex flow takes place in the vicinity of the lower endwall.

The spin-down process (Case II) is illustrated in Figs. 5 and 6. The initial steady flow is considered due to uniform corotation of the top and bottom endwall with angular velocity ratio $\epsilon = 0.1$ at the Reynolds number Re = 1300. In the initial steady-state flow vortex breakdown occurs and a separation bubble appears between $z = 0.25$ and $z = 0.75$. The divergence in the streamlines in the vortex core are found in the vicinity of the lower endwall. As time progresses in the spin-down process the separation bubble reduces in size and moves towards the stationary upper endwall. At a nondimensional time $t = 25$, the separation bubble appears between $z = 0.85$ and $z = 0.95$. From Fig. 5 it is evident that the bubble radius decreases with time and it disappear at the ultimate steady state. We have seen numerically that the flow reaches the ultimate steady state after a nondimensional time $t = 30$. The streamlines for the terminal steady state ($t = 30$) are shown in Fig. 6. The separation bubble disappeared and the streamlines are monotonic describing a steady secondary flow due to uniform rotation of the lower endwall.

The axial flow reversal on the axis of rotation ($r = 0$) occurs between $z = 0.25$ and $z = 0.75$ at the initial steady state of the spin-down. During the spin-down process the region of axial flow reversal reduces and moves towards the upper endwall. At the terminal steady state no axial flow reversal occurs in the interior region.

References

Bhattacharyya, S., Pal, A., and Nath, G., 1996, "Unsteady Flow and Heat Transfer Between Rotating Co-axial Disks," *Numerical Heat Transfer,* Part A, Vol. 30, p. 519.

Brown, G. L., and Lozez, J. M., 1990, "Axisymmetric Vortex Breakdown, Part 2. Physical Mechanism," *Journal of Fluid Mechanics,* Vol. 221, p. 553.

Escudier, M. P., 1984, "Observation of the Flow Produced in a Cylindrical Container by a Rotating Endwall," *Experiments in Fluids,* Vol. 2, p. 189.

Gelfgat, A. Y., Bar-Yoseph, P. Z., and Solan, A., 1996, "Stability of Combined Swirling Flow With and Without Vortex Breakdown," *Journal of Fluid Mechanics,* Vol. 311, p. 1.

Lopez, J. M., 1990, "Axisymmetric Vortex Breakdown, Part I. Confined Swirling Flow," *Journal of Fluid Mechanics,* Vol. 221, p. 533.

Lopez, J. M., 1995, "Unsteady Swirling Flow in an Enclosed Cylinder With Reflectional Symmetry," *Physics of Fluids,* Vol. 7, p. 2700.

Neitzel, G. P., and Davis, S. H., 1981, "Centrifugal Instabilities During Spin Down to Rest in Finite Cylinders," *Journal of Fluid Mechanics,* Vol. 102, p. 329.

Spohn, A., Mory, M., and Hopfinger, E. J., 1998, "Experiments on Vortex Breakdown in a Confined Flow Generated by a Rotating Disc," *Journal of Fluid Mechanics,* Vol. 370, p. 73.

Valentine, D. T., and Jahnke, C. C., 1994, "Flows Induced in a Cylinder With Both End Walls Rotating," *Physics of Fluids,* Vol. 6, p. 2702.

Valentine, D. T., and Miller, K. D., 1994, "Generation of Ring Vortices in Axisymmetric Spin-Down: A Numerical Investigation," *Physics of Fluids,* Vol. 6, p. 1535.

Watson, J. P., and Neitzel, G. P., 1996, "Numerical Evaluation of a Vortex Breakdown Criterion," *Physics of Fluids,* Vol. 8, p. 3063.

A Condition of the Existence of a Conductive Liquid Meniscus in an External Electric Field

A. F. Spivak[1] and Y. A. Dzenis[1]

Introduction

An emerging technology of manufacturing of thin polymer fibers by electrospinning is addressed. The method is based on the principle of spinning polymer solutions in high-voltage electric fields. It consists of the ejection, from the top of a capillary tube, of a charged jet which is elongated and accelerated by an external field. The method has been recently studied experimentally by Reneker and Chun (1996). The motion of jets in electric fields is important for many technical applications and has been considered by a number of authors. Excellent reviews on this topic can be found in papers by Clopeau and Prunet-Foch (1994) and Saville (1997). However, the problem of jet initiation has not yet been sufficiently studied.

Jet initiation is related to the existence of a liquid meniscus in an external electric field. In weak fields, the liquid is held at the end of a capillary tube by surface tension. The meniscus shape is defined by the balance of hydrostatic pressure, electric forces, and surface tension. When the electric field increases, the meniscus elongates until, at some critical value of field, surface tension can no longer balance hydrostatic pressure and electric forces, and a thin jet ejects from the meniscus apex. The value of the electric field at which a finite meniscus ceases to exist determines the jet initiation threshold. The general problem of meniscus formation is a coupled problem of electromechanics. The meniscus shape is defined by the force equilibrium, while the forces in the meniscus, in turn, depend on its shape. The problem complexity is further enhanced by the fact that meniscus volume is also unknown as the fluid is pulled from the capillary tube by the electric field. There-

[1] Department of Engineering Mechanics, Center for Materials Research and Analysis, University of Nebraska-Lincoln, NE 68588-0347.

Contributed by the Applied Mechanics Division of THE AMERICAN SOCIETY OF MECHANICAL ENGINEERS for publication in the ASME JOURNAL OF APPLIED MECHANICS. Manuscript received by the ASME Applied Mechanics Division, Nov. 3, 1997; final revision, June 4, 1999. Associate Technical Editor: D. A. Siginer.

Downloaded 04 May 2010 to 171.66.16.27. Redistribution subject to ASME license or copyright; see http://www.asme.org/terms/Terms_Use.cfm

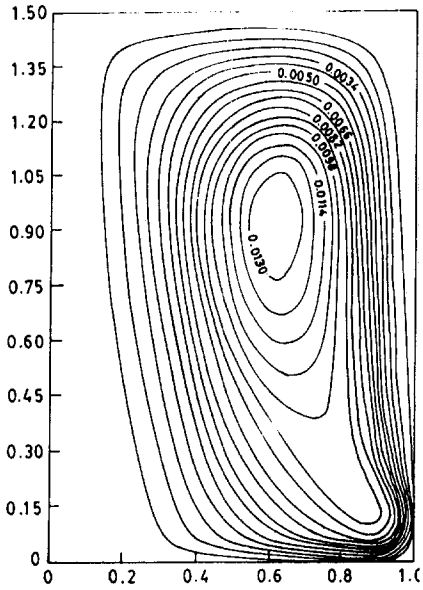


Fig. 6 Contour plots of the streamline ψ, $0 < \psi < 0.0144$, $\delta\psi = 0.002$ at the terminal steady state $t = 30$ when $\epsilon = 0.0$ (spin-down), $A = 1.5$ and Re = 1300

ber so as to halt the inward meridional flow provided by the Ekman layer pumping on the rotating endwall. This ultimately causes stagnation on the symmetry plane and the formation of a recirculation zone (separation bubble). During the spin-up process the region of positive azimuthal vorticity around the axis of rotation increases and this region always includes the region of recirculation. Figure 4 shows the azimuthal vorticity contours at the terminal steady state in the spin-up process. The positive region of ζ around the axis of rotation is included between the plane $z = 0.15$ and $z = 1.05$, which includes the region of the separation bubble.

In the initial steady-state flow for Case I the axial velocity w on the axis of rotation is predominantly inward. An axial flow reversal on the axis of rotation takes place from the nondimensional time $t = 2.1$ during the spin-up process. In subsequent time this region of reversed axial flow increases. At time $t = 2.1$, axial flow reversal on $r = 0$ takes place between $z = 0.4$ and $z = 0.5$ and at a nondimensional time $t = 4$ it takes place between $z = 0.25$ and $z = 0.75$. At the terminal steady state ($t = 4$) the axial flow reversal in the core of the vortex flow takes place in the vicinity of the lower endwall.

The spin-down process (Case II) is illustrated in Figs. 5 and 6. The initial steady flow is considered due to uniform corotation of the top and bottom endwall with angular velocity ratio $\epsilon = 0.1$ at the Reynolds number Re = 1300. In the initial steady-state flow vortex breakdown occurs and a separation bubble appears between $z = 0.25$ and $z = 0.75$. The divergence in the streamlines in the vortex core are found in the vicinity of the lower endwall. As time progresses in the spin-down process the separation bubble reduces in size and moves towards the stationary upper endwall. At a nondimensional time $t = 25$, the separation bubble appears between $z = 0.85$ and $z = 0.95$. From Fig. 5 it is evident that the bubble radius decreases with time and it disappear at the ultimate steady state. We have seen numerically that the flow reaches the ultimate steady state after a nondimensional time $t = 30$. The streamlines for the terminal steady state ($t = 30$) are shown in Fig. 6. The separation bubble disappeared and the streamlines are monotonic describing a steady secondary flow due to uniform rotation of the lower endwall.

The axial flow reversal on the axis of rotation ($r = 0$) occurs between $z = 0.25$ and $z = 0.75$ at the initial steady state of the spin-down. During the spin-down process the region of axial flow reversal reduces and moves towards the upper endwall. At the terminal steady state no axial flow reversal occurs in the interior region.

References

Bhattacharyya, S., Pal, A., and Nath, G., 1996, "Unsteady Flow and Heat Transfer Between Rotating Co-axial Disks," *Numerical Heat Transfer,* Part A, Vol. 30, p. 519.

Brown, G. L., and Lozez, J. M., 1990, "Axisymmetric Vortex Breakdown, Part 2. Physical Mechanism," *Journal of Fluid Mechanics,* Vol. 221, p. 553.

Escudier, M. P., 1984, "Observation of the Flow Produced in a Cylindrical Container by a Rotating Endwall," *Experiments in Fluids,* Vol. 2, p. 189.

Gelfgat, A. Y., Bar-Yoseph, P. Z., and Solan, A., 1996, "Stability of Combined Swirling Flow With and Without Vortex Breakdown," *Journal of Fluid Mechanics,* Vol. 311, p. 1.

Lopez, J. M., 1990, "Axisymmetric Vortex Breakdown, Part I. Confined Swirling Flow," *Journal of Fluid Mechanics,* Vol. 221, p. 533.

Lopez, J. M., 1995, "Unsteady Swirling Flow in an Enclosed Cylinder With Reflectional Symmetry," *Physics of Fluids,* Vol. 7, p. 2700.

Neitzel, G. P., and Davis, S. H., 1981, "Centrifugal Instabilities During Spin Down to Rest in Finite Cylinders," *Journal of Fluid Mechanics,* Vol. 102, p. 329.

Spohn, A., Mory, M., and Hopfinger, E. J., 1998, "Experiments on Vortex Breakdown in a Confined Flow Generated by a Rotating Disc," *Journal of Fluid Mechanics,* Vol. 370, p. 73.

Valentine, D. T., and Jahnke, C. C., 1994, "Flows Induced in a Cylinder With Both End Walls Rotating," *Physics of Fluids,* Vol. 6, p. 2702.

Valentine, D. T., and Miller, K. D., 1994, "Generation of Ring Vortices in Axisymmetric Spin-Down: A Numerical Investigation," *Physics of Fluids,* Vol. 6, p. 1535.

Watson, J. P., and Neitzel, G. P., 1996, "Numerical Evaluation of a Vortex Breakdown Criterion," *Physics of Fluids,* Vol. 8, p. 3063.

A Condition of the Existence of a Conductive Liquid Meniscus in an External Electric Field

A. F. Spivak[1] and Y. A. Dzenis[1]

Introduction

An emerging technology of manufacturing of thin polymer fibers by electrospinning is addressed. The method is based on the principle of spinning polymer solutions in high-voltage electric fields. It consists of the ejection, from the top of a capillary tube, of a charged jet which is elongated and accelerated by an external field. The method has been recently studied experimentally by Reneker and Chun (1996). The motion of jets in electric fields is important for many technical applications and has been considered by a number of authors. Excellent reviews on this topic can be found in papers by Clopeau and Prunet-Foch (1994) and Saville (1997). However, the problem of jet initiation has not yet been sufficiently studied.

Jet initiation is related to the existence of a liquid meniscus in an external electric field. In weak fields, the liquid is held at the end of a capillary tube by surface tension. The meniscus shape is defined by the balance of hydrostatic pressure, electric forces, and surface tension. When the electric field increases, the meniscus elongates until, at some critical value of field, surface tension can no longer balance hydrostatic pressure and electric forces, and a thin jet ejects from the meniscus apex. The value of the electric field at which a finite meniscus ceases to exist determines the jet initiation threshold. The general problem of meniscus formation is a coupled problem of electromechanics. The meniscus shape is defined by the force equilibrium, while the forces in the meniscus, in turn, depend on its shape. The problem complexity is further enhanced by the fact that meniscus volume is also unknown as the fluid is pulled from the capillary tube by the electric field. There-

[1] Department of Engineering Mechanics, Center for Materials Research and Analysis, University of Nebraska-Lincoln, NE 68588-0347.

Contributed by the Applied Mechanics Division of THE AMERICAN SOCIETY OF MECHANICAL ENGINEERS for publication in the ASME JOURNAL OF APPLIED MECHANICS. Manuscript received by the ASME Applied Mechanics Division, Nov. 3, 1997; final revision, June 4, 1999. Associate Technical Editor: D. A. Siginer.

Downloaded 04 May 2010 to 171.66.16.27. Redistribution subject to ASME license or copyright; see http://www.asme.org/terms/Terms_Use.cfm

fore, energy minimization approaches used, for example, in modeling atomization of liquids, cannot be applied.

An infinite charged conductive meniscus has been analyzed by Taylor (1964). The conical shape of the meniscus has been assumed. The cone semi-vertical angle has been calculated from the condition of equipotentiality of the surface of the conductive meniscus. Only the meniscus own electric field was taken into account. Influences of external electric field and hydrostatic pressure on the meniscus shape and charge redistribution have not been considered.

The Taylor's model cannot be used for the analysis of jet initiation that usually occurs at the meniscus apex, where the charge density and the electric stresses are maximum. In this model, the electric stress tensor on the cone surface, $\hat{\tau}_m \sim R^{-1}\hat{I}$, where $\hat{I}$ is the unit tensor and R is the distance from the cone apex, is singular at the apex, $R = 0$. Jets emanate from the meniscus apex when electric forces at the apex can be no longer balanced by surface tension. An approach to jet initiation analysis, based on electromechanics analysis of the meniscus apex, is proposed in this paper.

Governing Equations

Consider a meniscus of a charged conductive liquid held by surface tension at the end of a capillary tube in a constant external electric field, **E**. Assume zero bulk forces in the liquid. Therefore, the hydrostatic pressure, p, is constant inside the meniscus and can be considered an external parameter of problem. Assume that the dielectric permeability of a medium surrounding the meniscus is that of vacuum, ϵ_0. Then, the electrostatic field potential, ϕ, outside the meniscus is described by the following equation:

$$\Delta\phi = 0. \tag{1}$$

At a sufficient distance from the tube, the total potential, ϕ, can be represented by superposition of the potential of the external field, $\phi^{ext} = -\mathbf{E}\cdot\mathbf{r}$, where $\mathbf{r}$ is the position vector, and the potential of the induced charges on the meniscus, $\tilde{\phi}$. The electrostatic boundary condition on the meniscus surface is the Dirichlet's condition $\phi|_S = \phi_0$, $\phi_0 = \text{const}$. The meniscus shape is defined by the following force balance equation:

$$(p\hat{I} + \hat{\tau}_m)|_S\mathbf{n} = \sigma(k_n + k_t)\mathbf{n} \tag{2}$$

where $\hat{\tau}_m = \epsilon_0(\nabla\phi \otimes \nabla\phi) - \epsilon_0/2\,(\nabla\phi\cdot\nabla\phi)\hat{I}$ is the Maxwell's stress tensor describing the interaction of the electric field with charges induced on the meniscus surface, $\mathbf{n}$ is the unit normal vector external to the surface, σ is the surface tension coefficient, and k_n, k_t are the principal curvatures of the surface. The coupled electromechanical problem (1)–(2) is not amenable for the analysis without further assumptions on the meniscus shape.

Assume the axial symmetry of the capillary tube with the axis of symmetry parallel to the direction of the external field. Then, the meniscus surface is a figure of revolution that can be described, in cylindrical coordinates, by an equation $z = F_S(r)$. Near meniscus apex, a function $F_S(r)$ can be expanded in Taylor series $F_S(r) = F_{S|r=0} + (r^2/2\zeta) + O(r^3)$, where ξ is the apex curvature radius, $\xi^{-1} = (d^2/dr^2)F_{S|r=0}$. The following condition should be satisfied at the apex in order to avoid singularity: $(d/dr)F_{S|r=0} = 0$. As a result, the meniscus shape near apex can be approximated by the paraboloid of revolution: $z = (r^2/2\xi) - (\xi/2)$, where the apex curvature radius, ξ, is a parameter. This approximation is used to solve the problem (1)–(2) exactly, near the apex. The electric field and hydrostatic pressure are external parameters of the problem. To solve the problem, one has to find ϕ, ξ as functions of the external parameters.

Exact Solution at Apex

The total electric field potential near paraboloid can be obtained by solving Eq. (1) in parabolic coordinates (α, β, φ). Transformation from parabolic to Cartesian coordinates is defined by the following equations: $x = \xi\alpha\beta\cos(\varphi)$, $y = \xi\alpha\beta\sin(\varphi)$, $z = \xi(\beta^2 - \alpha^2)/2$. In parabolic coordinates, the meniscus surface near apex is approximated by a paraboloid described by the equation $\alpha = 1$; the apex curvature radius ξ is an unknown parameter. Zero-order Hankel transformation, $\hat{\Re}_0[f(\varsigma);\ s] = \int_0^\infty f(\varsigma)J_0(s\varsigma)\varsigma d\varsigma$, where $J_0(x)$ is the zero-order Bessel function, is applied to reduce the Laplace Eq. (1) to a modified zero-order Bessel equation. The boundary conditions are applied to define the coefficients of the general solution in terms of modified Bessel functions. As a result, the following solution of the electrostatic problem is obtained:

$$\phi(\alpha, \beta) = \phi_0; \quad \alpha < 1; \quad \beta \geq 0$$

$$\phi(\alpha, \beta) = \hat{\Re}_0[B(s)K_0(s\alpha);\ \beta] - \eta(\beta^2 - \alpha^2) + \tilde{\phi}_0 \qquad \alpha \geq 1; \quad \beta \geq 0 \tag{3}$$

where $\eta = (E\xi)/2$, E is the external electric field value, $K_0(x)$ is zero-order modified Bessel function, and $B(s)$, $\tilde{\phi}_0$ are constants. The Hankel's transformation integral, Eq. (3), can be expanded in zero-order Bessel function series as

$$\phi(\alpha, \beta) = \sum_{m=1}^{\infty} B_m K_0(\mu_m\alpha)J_0(\mu_m\beta) - \eta(\beta^2 - \alpha^2) + \tilde{\phi}_0 \qquad \alpha \geq 1 \quad 0 \leq \beta \leq 1 \tag{4}$$

where $B_m = [\eta(\chi_{2,m} - \chi_{0,m}) - \delta\phi\chi_{0,m}]/K_0(\mu_m)$, parameters $\mu_n \in \Im$ are zeroes of the zero-order Bessel function $\Im = \{\mu_n,\ n = 1, 2, \ldots;\ J_0(\mu_n) = 0,\ \mu_n < \mu_{n+1}\}$, parameters $\chi_{n,m}$ are

$$\chi_{0,m} = \frac{2}{\mu_m J_1(\mu_m)};$$

$$\chi_{2,m} = \frac{2}{[\mu_m J_1(\mu_m)]^2}\left(2J_0(\mu_m) + \left(\mu_m - \frac{4}{\mu_m}\right)J_1(\mu_m)\right)$$

and $\delta\phi$ is the difference between the potential of the external electric field at the meniscus apex and the potential of the meniscus: $\delta\phi = \phi^{ext}|_{\alpha=0,\beta=0} - \phi_0$. The unknown shape parameter, ξ is a solution of the force balance Eq. (2) with the potential defined by Eq. (4):

$$p = 2\sigma H(\xi, \beta) - \left.\frac{\epsilon_0(\nabla\phi\cdot\nabla\phi)}{2}\right|_S \tag{5}$$

where the local mean curvature of the surface is $H(\xi, \beta) = (2 + \beta^2)/(2\xi(1 + \beta^2)^{3/2})$. For small $\beta \ll 1$, Eq. (5) reduces to

$$\frac{p}{\epsilon_0 E^2} = \chi - (\psi_1\gamma^{-1}\chi + \psi_0)^2 \tag{6}$$

where $\chi = 2\sigma/(\xi\epsilon_0 E^2)$ is the dimensionless surface tension pressure, $\gamma = \sigma/(\epsilon_0 E\delta\phi)$ is the dimensionless parameter describing external electric conditions, and constants, ψ_0 and ψ_1, are defined by the following equations:

$$\psi_1 = \frac{1}{2\sqrt{2\pi}}\sum_{m=1}^{\infty}\frac{K_1(\mu_m)}{K_0(\mu_m)J_1(\mu_m)} \approx 0.243835;$$

$$\psi_0 = \frac{1}{2\sqrt{2\pi}}\left(1 - \sum_{m=1}^{\infty}\frac{\mu_m K_1(\mu_m)(\chi_{2,m} - \chi_{0,m})}{2K_0(\mu_m)}\right) \approx 0.458689.$$

Condition of Meniscus Existence

Equation (6) defines a three-dimensional surface in the parametric space (P, γ, χ), where $P = p/(\epsilon_0 E^2)$ is the dimensionless hydrostatic pressure. A cross section of this surface by the plane $P = 0$ defines the critical curve $\gamma = \gamma(\chi)$ in a two-dimensional

Downloaded 04 May 2010 to 171.66.16.27. Redistribution subject to ASME license or copyright; see http://www.asme.org/terms/Terms_Use.cfm

parametric space (γ, χ). Inequality $P \geq 0$ defines the parametric area in this space where the meniscus can exist. The necessary condition on the meniscus existence is $\gamma \geq 4\psi_0\psi_1 \approx 0.447378$. This condition can be rewritten as $\sigma \geq 0.447378 \cdot \delta\phi\epsilon_0 E$ that defines the maximum value of the external electric field.

Acknowledgment

The support of this work by the National Science Foundation under grant number DMI-9523022 is gratefully acknowledged.

References

Cloupeau, M., and Prunet-Foch, B., 1994, "Electrohydrodynamic Spraying Functioning Modes: A Critical Review," *Journal of Aerosol Science,* Vol. 25, pp. 1021–1036.

Reneker, D., and Chun, I., 1996, "Nanometer Diameter Fibers of Polymer, Produced by Electrospinning," *Nanotechnology,* Vol. 7, pp. 216–223.

Saville, D. A., 1997, "Electrohydrodynamics: The Taylor-Melcher Leaky Dielectric Model," *Annual Review of Fluid Mechanics,* Vol. 29, pp. 27–64.

Taylor, G., 1964, "Disintegration of Water Drops in an Electric Field," *Proceedings of the Royal Society, London,* Vol. A280, pp. 383–397.

An Approximate Analytic Solution of the One-Dimensional Foil Bearing Problem

A. A. Renshaw[1]

Approximate solutions are found to the one-dimensional steady-state foil bearing problem in which a longitudinally translating, flexible tensioned sheet of material rides on a thin film of entrained air as it wraps around a fixed cylinder. The approximate solutions use the first few terms of a scaled, exponential power series and minimize the squared residual in the governing differential equation. The solutions are simple, compare well with more exact solutions, and provide excellent starting points for more sophisticated, iterative solution algorithms.

1 Introduction

The foil bearing problem is a classical elastohydrodynamic lubrication problem describing the behavior of a longitudinally translating, flexible tensioned sheet of material that rides on a thin film of entrained air as it wraps around a fixed cylinder. These bearings are useful in both magnetic recording devices and paper and web handling devices that need to position the moving sheet of material as close as possible to a recording, drying, or control surface without physical contact. The one-dimensional version of this problem was proposed and approximately solved by Blok and van Rossum (1953). His results were subsequently improved and extended by Baumeister (1963), Langlois (1963), and Eshel and Elrod (1965).

Since these early results, foil bearing research has focused extensively on developing efficient numerical algorithms for solving the foil bearing problem in either one (Stahl et al., 1974; Lacey and Talke, 1990; Wickert, 1993; Lakshmikumaran and Wickert, 1996) or two dimensions (Ono et al., 1991; Moes, 1991; Sakai et al., 1996). Since the governing equations are nonlinear, these algorithms are all iterative, and, accordingly, their performance depends crucially on their initial values. Some algorithms have been designed to converge from poor initial guesses, while others require numerical damping in order to overcome numerical stiffness or avoid unphysical results such as negative film thickness. The existence of good initial guesses in the form of simple analytical expressions could help standardize convergence results, reduce the required number of iterations, and minimize the need for numerical damping.

In this brief note, we derive a simple approximate analytic solution to the one-dimensional foil bearing problem using the first few terms of a scaled exponential power series. Because of their rapid convergence in nonlinear boundary value problems, these series have been used to derive approximate analytical solutions to several classical fluid dynamics problems including the flow around an infinite, rotating disk, two-dimensional hydrodynamic flows with suction, and the Falkner-Skan equation (Dey, 1989; Ariel, 1994a, b, 1996). The crucial feature of this solution technique is the rescaling of the independent variable which dramatically increases the accuracy of the first few terms of the series at the cost of rendering the least squares minimization problem nonlinear. Rayleigh (1945) used a similar exponential rescaling to improve one-term estimates of fundamental vibration frequencies using the Rayleigh Quotient.

For the one-dimensional foil bearing problem, the solution can be found numerically to any desired accuracy (Eshel and Elrod, 1965; Stahl et al., 1974; Lacey and Talke, 1990; Wickert, 1993). Consequently, while the accuracy of the approximate solution obtained here is good, it does not compete with those numerical techniques, nor does it offer any new insight into foil bearing mechanics. However, the accuracy of the approximate solution is unusually good considering its extreme simplicity, and the solution can be easily used as the starting point for more sophisticated, iterative algorithms. The results also demonstrate the effectiveness and elegance of scaled exponential trial functions for approximate solutions of nonlinear boundary value problems.

2 Model

A tape of constant linear density ρ, tension σ, and width W, travels longitudinally at speed V and partially wraps around a cylinder of radius R as shown in Fig. 1. A thin film of air of viscosity μ and pressure P is entrained by the moving tape and supports the tape as it wraps around the cylinder so that the tape does not make direct contact with the cylinder. Over most of the wrap area, the film thickness and air pressure difference from ambient are constants, denoted $\bar{H}$ and $\bar{P} = (\sigma - \rho V^2)/WR$. $\bar{H}$ is to be found as part of the problem.

The tape motion is modeled as an axially moving string (Wickert, 1993) and the pressure in the air film by the incompressible, isothermal Reynolds equation (Szeri, 1980). Let $U(X)$ be the transverse deflection of the tape measured relative to the Cartesian

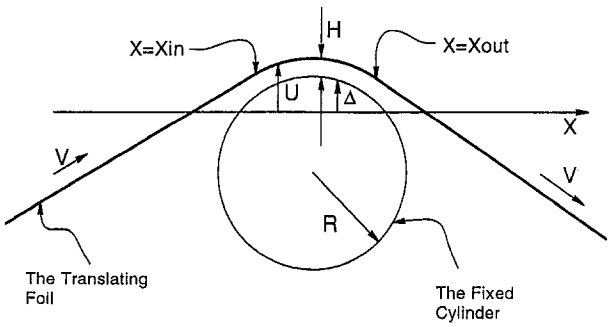


Fig. 1 Schematic of the foil bearing problem

[1] Department of Mechanical Engineering, Columbia University, M/C 4703, New York, NY 10027. Mem. ASME.

Contributed by the Applied Mechanics Division of THE AMERICAN SOCIETY OF MECHANICAL ENGINEERS for publication in the ASME JOURNAL OF APPLIED MECHANICS. Manuscript received by the ASME Applied Mechanics Division, Apr. 14, 1998; final revision, Aug. 16, 1999. Associate Technical Editor: D. A. Siginer.

Downloaded 04 May 2010 to 171.66.16.27. Redistribution subject to ASME license or copyright; see http://www.asme.org/terms/Terms_Use.cfm

parametric space (γ, χ). Inequality $P \geq 0$ defines the parametric area in this space where the meniscus can exist. The necessary condition on the meniscus existence is $\gamma \geq 4\psi_0\psi_1 \approx 0.447378$. This condition can be rewritten as $\sigma \geq 0.447378 \cdot \delta\phi\epsilon_0 E$ that defines the maximum value of the external electric field.

Acknowledgment

The support of this work by the National Science Foundation under grant number DMI-9523022 is gratefully acknowledged.

References

Cloupeau, M., and Prunet-Foch, B., 1994, "Electrohydrodynamic Spraying Functioning Modes: A Critical Review," *Journal of Aerosol Science,* Vol. 25, pp. 1021–1036.

Reneker, D., and Chun, I., 1996, "Nanometer Diameter Fibers of Polymer, Produced by Electrospinning," *Nanotechnology,* Vol. 7, pp. 216–223.

Saville, D. A., 1997, "Electrohydrodynamics: The Taylor-Melcher Leaky Dielectric Model," *Annual Review of Fluid Mechanics,* Vol. 29, pp. 27–64.

Taylor, G., 1964, "Disintegration of Water Drops in an Electric Field," *Proceedings of the Royal Society, London,* Vol. A280, pp. 383–397.

An Approximate Analytic Solution of the One-Dimensional Foil Bearing Problem

A. A. Renshaw[1]

Approximate solutions are found to the one-dimensional steady-state foil bearing problem in which a longitudinally translating, flexible tensioned sheet of material rides on a thin film of entrained air as it wraps around a fixed cylinder. The approximate solutions use the first few terms of a scaled, exponential power series and minimize the squared residual in the governing differential equation. The solutions are simple, compare well with more exact solutions, and provide excellent starting points for more sophisticated, iterative solution algorithms.

1 Introduction

The foil bearing problem is a classical elastohydrodynamic lubrication problem describing the behavior of a longitudinally translating, flexible tensioned sheet of material that rides on a thin film of entrained air as it wraps around a fixed cylinder. These bearings are useful in both magnetic recording devices and paper and web handling devices that need to position the moving sheet of material as close as possible to a recording, drying, or control surface without physical contact. The one-dimensional version of this problem was proposed and approximately solved by Blok and van Rossum (1953). His results were subsequently improved and extended by Baumeister (1963), Langlois (1963), and Eshel and Elrod (1965).

Since these early results, foil bearing research has focused extensively on developing efficient numerical algorithms for solving the foil bearing problem in either one (Stahl et al., 1974; Lacey and Talke, 1990; Wickert, 1993; Lakshmikumaran and Wickert, 1996) or two dimensions (Ono et al., 1991; Moes, 1991; Sakai et al., 1996). Since the governing equations are nonlinear, these algorithms are all iterative, and, accordingly, their performance depends crucially on their initial values. Some algorithms have been designed to converge from poor initial guesses, while others require numerical damping in order to overcome numerical stiffness or avoid unphysical results such as negative film thickness. The existence of good initial guesses in the form of simple analytical expressions could help standardize convergence results, reduce the required number of iterations, and minimize the need for numerical damping.

In this brief note, we derive a simple approximate analytic solution to the one-dimensional foil bearing problem using the first few terms of a scaled exponential power series. Because of their rapid convergence in nonlinear boundary value problems, these series have been used to derive approximate analytical solutions to several classical fluid dynamics problems including the flow around an infinite, rotating disk, two-dimensional hydrodynamic flows with suction, and the Falkner-Skan equation (Dey, 1989; Ariel, 1994a, b, 1996). The crucial feature of this solution technique is the rescaling of the independent variable which dramatically increases the accuracy of the first few terms of the series at the cost of rendering the least squares minimization problem nonlinear. Rayleigh (1945) used a similar exponential rescaling to improve one-term estimates of fundamental vibration frequencies using the Rayleigh Quotient.

For the one-dimensional foil bearing problem, the solution can be found numerically to any desired accuracy (Eshel and Elrod, 1965; Stahl et al., 1974; Lacey and Talke, 1990; Wickert, 1993). Consequently, while the accuracy of the approximate solution obtained here is good, it does not compete with those numerical techniques, nor does it offer any new insight into foil bearing mechanics. However, the accuracy of the approximate solution is unusually good considering its extreme simplicity, and the solution can be easily used as the starting point for more sophisticated, iterative algorithms. The results also demonstrate the effectiveness and elegance of scaled exponential trial functions for approximate solutions of nonlinear boundary value problems.

2 Model

A tape of constant linear density ρ, tension σ, and width W, travels longitudinally at speed V and partially wraps around a cylinder of radius R as shown in Fig. 1. A thin film of air of viscosity μ and pressure P is entrained by the moving tape and supports the tape as it wraps around the cylinder so that the tape does not make direct contact with the cylinder. Over most of the wrap area, the film thickness and air pressure difference from ambient are constants, denoted $\bar{H}$ and $\bar{P} = (\sigma - \rho V^2)/WR$. $\bar{H}$ is to be found as part of the problem.

The tape motion is modeled as an axially moving string (Wickert, 1993) and the pressure in the air film by the incompressible, isothermal Reynolds equation (Szeri, 1980). Let $U(X)$ be the transverse deflection of the tape measured relative to the Cartesian

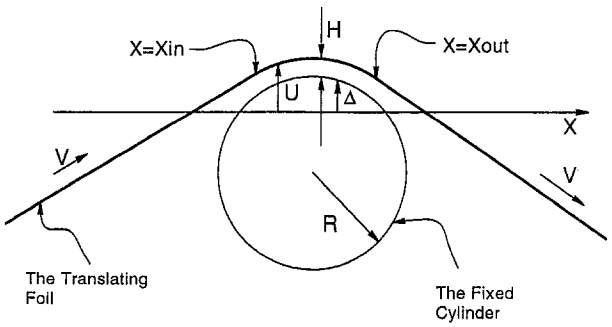


Fig. 1 Schematic of the foil bearing problem

[1] Department of Mechanical Engineering, Columbia University, M/C 4703, New York, NY 10027. Mem. ASME.

Contributed by the Applied Mechanics Division of THE AMERICAN SOCIETY OF MECHANICAL ENGINEERS for publication in the ASME JOURNAL OF APPLIED MECHANICS. Manuscript received by the ASME Applied Mechanics Division, Apr. 14, 1998; final revision, Aug. 16, 1999. Associate Technical Editor: D. A. Siginer.

Downloaded 04 May 2010 to 171.66.16.27. Redistribution subject to ASME license or copyright; see http://www.asme.org/terms/Terms_Use.cfm

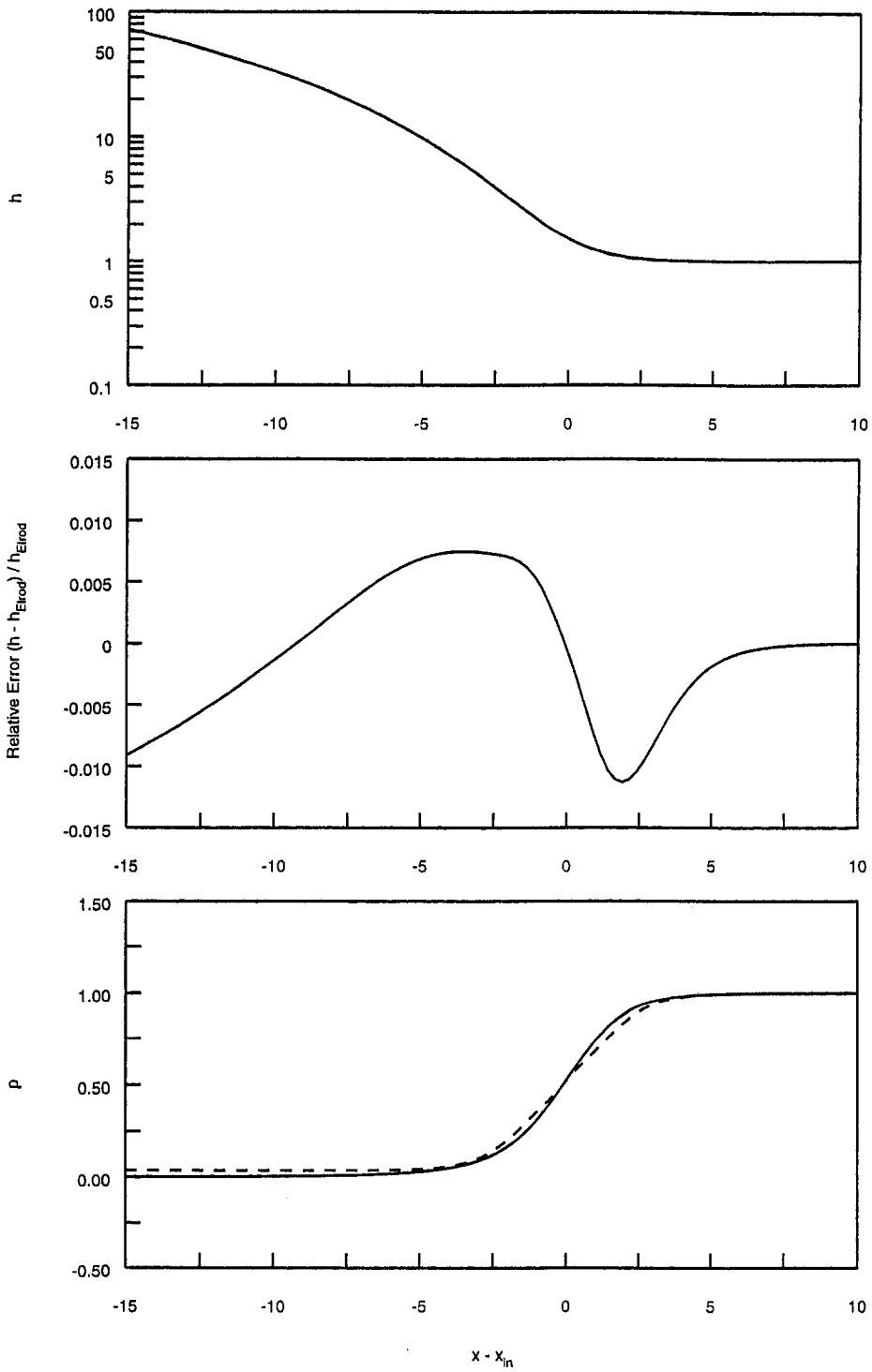


Fig. 2 Approximate inlet solutions for *h* and *p* (dashed line) compared with the solution from Eshel and Elrod (solid). The relative error in *h* is also shown. The two solutions for *h* are indistinguishable.

X-axis, $\Delta(X)$ be the transverse profile of the cylinder, and $H = U - \Delta$ be the air film thickness. The governing equations are

$$(\rho V^2 - \sigma)U'' = PW \tag{1}$$

$$(H^3P')' = 6\mu VH' \tag{2}$$

where a prime indicates differentiation with respect to X. Define the dimensionless parameters

$$\epsilon^3 = 6\mu VW/(\sigma - \rho V^2) \quad \epsilon^2\bar{h} = \bar{H}/R \tag{3}$$

and dimensionless variables

$$x/\epsilon = X/\bar{H} \quad u = U/\bar{H} \quad h = H/\bar{H} \quad \delta = \Delta/\bar{H} \quad p = P/\bar{P}. \tag{4}$$

Equations (1) and (2) can then be simplified and integrated to give the foil bearing equation (Baumeister, 1963; Eshel and Elrod, 1965)

$$h''' + \delta''' = (1 - h)/h^3 \tag{5}$$

where the prime has been redefined to indicate differentiation with respect to x, the pressure is

Downloaded 04 May 2010 to 171.66.16.27. Redistribution subject to ASME license or copyright; see http://www.asme.org/terms/Terms_Use.cfm

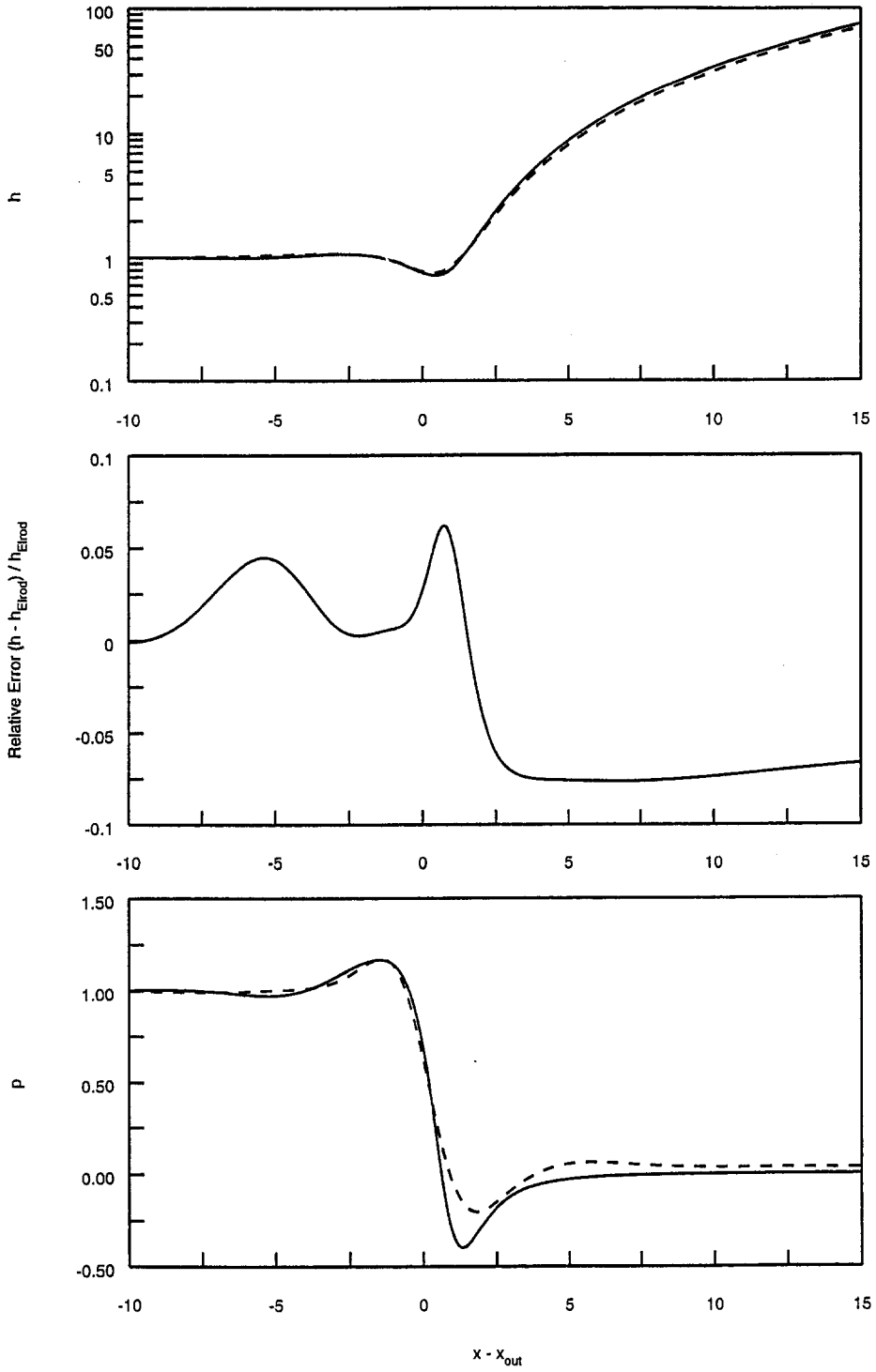


Fig. 3 Approximate outlet solutions for h and p (dashed line) compared with the solution from Eshel and Elrod (solid). The relative error in h is also shown.

$$p = -(\delta'' + h'')/\bar{h} \tag{6}$$

and $h \sim 1$ over the central portion of the cylinder.

In the classical derivation, it is assumed that the profile of the cylinder is quadratic so that $\delta'' = -\bar{h}$ and $\delta''' = 0$. When (5) is linearized about $h = 1$ under these assumptions, (5) becomes (Eshel and Elrod, 1965)

$$h''' + h = 1 \tag{7}$$

which has the general solution

$$h = 1 + ae^{-x} + be^{x/2} \sin\left(\sqrt{3}x/2 + c\right) \tag{8}$$

for constants a, b, and c. The geometry of the problem and the exponential exponents present in (8) suggest writing the solution to the general problem as the superposition of two distinct problems, the inlet problem defining the tape deflection from far to the left of the cylinder until it wraps over the cylinder with $h = 1$, and the outlet problem defining the tape deflection from where it wraps over the cylinder with $h = 1$ until far to the right of the cylinder.

Downloaded 04 May 2010 to 171.66.16.27. Redistribution subject to ASME license or copyright; see http://www.asme.org/terms/Terms_Use.cfm

For the inlet problem, it is assumed that far to the left of the cylinder, the tape displacement is linear in x. Let $x = x_{in}$ be the point of tangency of this linear deflection with the cylinder. Then far to the left of the cylinder,

$$\delta = \delta_{in} + (x - x_{in})\delta'_{in} - \bar{h}(x - x_{in})^2/2 \tag{9}$$

$$u = 1 + \delta_{in} + (x - x_{in})\delta'_{in}. \tag{10}$$

Consequently, the boundary conditions for the inlet problem are defined as

$$h = 1 + \bar{h}(x - x_{in})^2/2 \quad x \to -\infty \tag{11}$$

$$h = 1 + O(e^{-x}) \quad x \to +\infty. \tag{12}$$

Similarly, for the outlet problem, the boundary conditions are

$$h = 1 + O(e^{x/2} \sin(\sqrt{3}x/2 + c)) \quad \text{as} \quad x \to -\infty \tag{13}$$

$$h = 1 + \bar{h}(x - x_{out})^2/2 \quad x \to +\infty \tag{14}$$

where x_{out} is the point of tangency of the linear tape deflection far to the right of the cylinder with the cylinder. The general solution is then the sum of the inlet and outlet solutions minus one.

3 Approximate Analytic Solution

The approximate solution technique to be investigated here begins with the assumption of an exponential power series solution with an undetermined scaling constant. For problems whose domain is $0 \le z < \infty$, the trial functions are normally $e^{-m\alpha z}$ where α is the scaling constant to be determined by the analysis and m is a positive integer (Ariel, 1996). In our problem, the domain is $-\infty < z < \infty$ so the most convenient trial functions are

$$\tanh(m\alpha z) = \pm 1 \mp 2e^{\mp 2m\alpha z} \pm 2e^{\mp 4m\alpha z} \mp \ldots \quad z \to \pm\infty \tag{15}$$

$$\operatorname{sech}(m\alpha z) = 2e^{\mp m\alpha z} - 2e^{\mp 3m\alpha z} + 2e^{\mp 5m\alpha z} - \ldots \quad z \to \pm\infty. \tag{16}$$

The approximate solution is constructed using the simplest linear combinations of these trial functions that satisfy the boundary conditions. Because there are two forms of trial functions, the "simplest" linear combination is nonunique. We use the simplest and best performing linear combination. The coefficients of the linear combinations and α are determined by numerically minimizing the integral

$$J = \int_{-\infty}^{\infty} [h''' - (1 - h)/h^3]^2 dx \tag{17}$$

which minimizes the error in (5) in the least squared sense.

For convenience, we define α as

$$\alpha = 2/\sqrt{\bar{h}}, \tag{18}$$

which replaces $\bar{h}$ as an unknown to be determined. For the inlet problem let z be

$$z = (x - x_{in})/\alpha. \tag{19}$$

A simple linear combination of (15) and (16) satisfying (11) and (12) is

$$h = 1 + c_1[1 - \tanh(\alpha z/2)] + (z^2 + c_2)[1 - \tanh(\alpha z)] \tag{20}$$

where α, c_1, and c_2 are constants to be determined. Numerical minimization of J gives

$$\alpha = 2.542 \quad c_1 = 0.1522 \quad c_2 = 0.3681 \quad J = 0.0006122. \tag{21}$$

For this solution,

$$\bar{h} = 4/\alpha^2 = 0.6190. \tag{22}$$

Using a numerical integration technique, Eshel and Elrod (1965) found $\bar{h} = 0.6430$ which is only four percent greater.

For the outlet solution, α is considered known from having first solved the inlet problem. For the outlet solution let

$$z = (x - x_{out})/\alpha. \tag{23}$$

A simple linear combination of (15) and (16) satisfying (13) and (14) is

$$h = 1 + [d_1 \sin(\sqrt{3}\alpha z/2) + d_2 \cos(\sqrt{3}\alpha z/2)] \operatorname{sech}(\alpha z/2) + [z^2 + d_3][1 + \tanh(\alpha z/2)] \tag{24}$$

where d_1, d_2, and d_3 are to be determined. Numerical minimization of J using $\alpha = 2.542$ gives

$$d_1 = 0.03935 \quad d_2 = 0.06538 \quad d_3 = -0.2971 \quad J = 0.04185.$$

The minimum film thickness of the approximate solution is $h_{min} = 0.7531$. In Eshel and Elrod's solution $h_{min} = 0.716$, five percent lower.

Figures 2 and 3 show the approximate solutions for h and p for the inlet and outlet problems, respectively, compared to the numerically integrated solutions of Eshel and Elrod (1965). Also shown are the relative errors in h when compared to the numerically integrated values.

The approximate inlet solution is excellent. The relative error in h is well distributed between ± 1.2 percent and the two h's are indistinguishable. The error in p is somewhat higher, as expected from the differentiation, but has a maximum absolute difference of 0.06. The approximate outlet solution is good. The relative error in h is between ± 7.6 percent and the maximum absolute error in p is 0.27. Overall, the performance of the approximate solution is quite good, especially in light of the analytic simplicity of the solution.

References

Ariel, P. D., 1994a, "Hiemenz Flow in Hydrodynamics," *Acta Mechanica,* Vol. 103, pp. 31–43.

Ariel, P. D., 1994b, "Stagnation Point Flow With Suction—An Approximate Solution," ASME JOURNAL OF APPLIED MECHANICS, Vol. 61, pp. 976–978.

Ariel, P. D., 1996, "The Flow Near a Rotating Disk: An Approximate Solution," ASME JOURNAL OF APPLIED MECHANICS, Vol. 63, pp. 436–438.

Baumeister, H. K., 1963, "Nominal Clearance of the Foil Bearing," *IBM Journal of Research and Development,* Vol. 7, No. 2, Apr., pp. 153–154.

Blok, H., and van Rossum, J. J., 1953, "The Foil Bearing—A New Departure in Hydrodynamic Lubrication," *Lubrication Engineering,* Vol. 9, No. 6, December, pp. 316–320.

Dey, J., 1989, "A Simple Technique for Approximate Solution of the Falkner-Skan Equation," *Acta Mechanica,* Vol. 77, pp. 299–305.

Eshel, A., and Elrod, Jr., H. G., 1965, "The Theory of the Infinitely Wide, Perfectly Flexible, Self-Acting Foil Bearing," *Journal of Basic Engineering,* Vol. 87, pp. 831–836.

Lacey, C. A., and Talke, F. E., 1990, "A Tightly Coupled Numerical Foil Bearing Solution," *IEEE Transactions on Magnetics,* Vol. 26, pp. 3039–3043.

Lakshmikumaran, A. V., and Wickert, J. A., 1996, "On the Vibration of Coupled Traveling String and Air Bearing Systems," *Journal of Vibration and Acoustics,* Vol. 188, pp. 398–405.

Langlois, W. E., 1963, "The Lightly Loaded Foil Bearing at Zero Angle of Wrap," *IBM Journal of Research and Development,* Vol. 7, No. 2, Apr., pp. 112–116.

Moes, H., 1991, "The Air Gap Between Tape and Drum in a Video Recorder," *Journal of Magnetism and Magnetic Materials,* Vol. 95, pp. 1–13.

Ono, K., Kodama, N., and Michimura, S., 1991, "A New Numerical Analysis Method for Two-Dimensional Foil-Bearing Problems Based on Inverse Analysis Concept," *JSME International,* Series III, Vol. 34, No. 1, pp. 82–90.

Rayleigh, J. W. S., 1945, *The Theory of Sound,* Dover Publications, New York.

Sakai, K., Nagawa, Y., Okuyama, K., and Terayama, T., 1996, "Thin Spacing Analysis for Head-Tape Interface," ASME *Journal of Tribology,* Vol. 119, pp. 800–812.

Stahl, K. J., White, J. W., and Deckert, K. L., 1974, "Dynamic Response of Self-Acting Foil Bearings," *IBM Journal of Research and Development,* Vol. 18, pp. 513–520.

Szeri, A. Z., ed., 1980, *Tribology: Friction, Lubrication, and Wear,* McGraw-Hill, New York.

Downloaded 04 May 2010 to 171.66.16.27. Redistribution subject to ASME license or copyright; see http://www.asme.org/terms/Terms_Use.cfm

Wickert, J. A., 1993, "Free Linear Vibration of Self-Pressurized Foil Bearings," ASME *Journal of Vibration and Acoustics,* Vol. 115, pp. 145–151.

The Nonlinear Sloshing of Liquid in Tank With Pitching

L. Yin,[1] B. Wang,[1] X. Ma,[2] and J. Zou[1]

In this paper, a method used to analyze the sloshing of liquid in a tank subjected to forced pitching and (or) yawing oscillation is presented. First, a variational principle for a liquid in a container under pitching and (or) yawing oscillation is proposed. Based on the preceding variational principle and new Lagrangian, the nonlinear sloshing of liquid in a circle cylindrical tank under pitching excitation is studied analytically for the first time.

1 Introduction

Since analysis of sloshing can be applied to the design of spacecraft or to the earthquake resistant underground tank, sloshing has been widely studied. The liquid sloshing is one of the most difficult mathematical problems to be solved numerically as well as analytically, because the kinematic and dynamic boundary condition (Bernoulli's equation) at the free surface is nonlinear and the position of the free surface is time-dependent, not known a prior. Therefore, most of studies which have been conducted so far were based on the linear theory where the amplitude of liquid motions is far less than the characteristic length of the container, and the frequency of excitation is far away from the natural frequencies for the liquid inside the tank. Linearized theory of sloshing seems now well established, and it has been used widely as a practical technique (cf. Abramson, 1966; Buseck and Benaroya, 1993).

Among a few existing theoretical studies of finite amplitude liquid sloshing, most of them are conducted to nonlinear free oscillation of liquid and nonlinear forced oscillation of liquid at the case of horizontal or vertical translation of container (cf. Hutton, 1963; Miles, 1976). There are few studies dealing with the nonlinear oscillation of the liquid in a container subjected to forced pitching oscillation (cf. Faltinsen, 1974; Nakayama and Washizu, 1980), but these studies only focus on two-dimensional sloshing of liquid in a rectangular tank.

First, we establish the nonlinear initial-boundary partial differential equation system for the sloshing of liquid in a container subjected to forced pitching and (or) yawing oscillation. Then, a variational principle for a liquid in a container subjected to forced pitching and (or) yawing oscillation is proposed. Based on the preceding variational principle and new Lagrangian, the nonlinear sloshing of liquid in a three-dimensional, circle cylindrical, rigid open tank under pitching excitation is studied analytically for the first time.

2 A Variational Principle for Liquid Sloshing

2.1 Governing Equations. In the present context, we consider that container is forced to pitch and (or) yaw with an angular velocity vector $\mathbf{\Omega}(t)$. Figure 1 shows a three-dimensional cylindrical container in motion. A Cartesian coordinate system, O-XYZ, is an inertial system. Z-axis is directed upward, namely, in the opposite direction to the gravity. Another Cartesian coordinate system, o-xyz, is fixed to the container in such a manner that x-axis is parallel to the undisturbed free surface and the z-axis is in coincidence with the center line of the container. The distance between the undisturbed free surface and the x-axis is denoted by e, which is taken positive when the free surface is above the x-axis. h is the depth of liquid. The origin o is taken as the center of rotation. $\alpha_x(t)$ and $\alpha_y(t)$ is the angular of inclination of container at the time t.

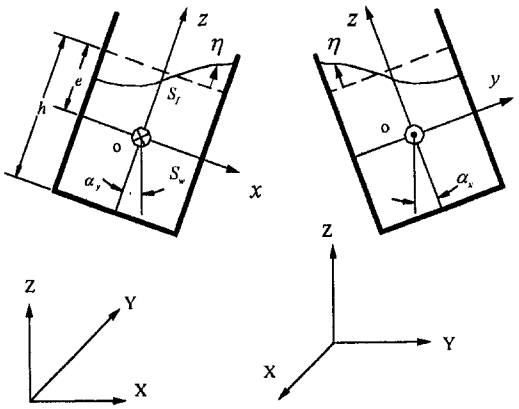


Fig. 1 A container under pitching and yawing excitation

It is assumed that the liquid is invisid and incompressible, and the flow is irrotational. The sloshing of liquid in container undergoing pitching and (or) yawing motion can be reduced to the following nonlinear, initial boundary value problem:

$$\nabla^2\Phi = 0 \quad \text{in } V \tag{1}$$

$$\frac{\partial\Phi}{\partial t} + \frac{1}{2}(\nabla\Phi)^2 - (\mathbf{\Omega}\times\mathbf{r})\cdot\nabla\Phi - \mathbf{g}\cdot\mathbf{r} = 0 \quad \text{on } S_f \tag{2}$$

$$\frac{\partial\eta}{\partial t} = (\nabla\Phi - \mathbf{\Omega}\times\mathbf{r})\cdot\nabla F \quad \text{on } S_f \tag{3}$$

$$\frac{\partial\Phi}{\partial n} = (\mathbf{\Omega}\times\mathbf{r})\cdot\mathbf{n} \quad \text{on } S_w \tag{4}$$

where V is the liquid region, $\mathbf{g}$ is the vector of gravity in the coordinate system o-xyz, $\mathbf{r}$ is the position vector of the liquid particle, $\mathbf{n}$ is the unit normal drawn outwardly on the wetted wall S_w, and $F = z - [\eta(x, y, t) + e]$ is the equation of the free surface. $\eta(x, y, t)$ is the height of the free surface measured from the undisturbed free surface. Up to now, the problem we are concerned with is expressed by Eqs. (1), (2), (3), and (4).

2.2 A Variational Principle. In the light of the ideas suggested by Luke, the expression of the pressure for a liquid in a container subjected to forced pitching and (or) yawing oscillation is used as the Lagrangian. Then, the variational principles is

$$\delta J = \delta\int_{t_1}^{t_2} L(\Phi, \eta)\cdot dt \tag{5}$$

where

$$L(\Phi, \eta) = -\iint\left\{\int_{-(h-e)}^{(\eta+e)}\left[\frac{\partial\Phi}{\partial t} + \frac{1}{2}(\nabla\Phi)^2 - (\mathbf{\Omega}\times\mathbf{r})\cdot\nabla\Phi - \mathbf{g}\cdot\mathbf{r}\right]dz\right\}dS \tag{6}$$

[1] Department of Astronautic and Mechanics, Harbin Institute of Technology, Harbin 150001, P. R. China.
[2] The Chinese Academy of Space Technology.

Contributed by the Applied Mechanics Division of THE AMERICAN SOCIETY OF MECHANICAL ENGINEERS for publication in the ASME JOURNAL OF APPLIED MECHANICS. Manuscript received by the ASME Applied Mechanics Division, July 9, 1998; final revision, July 8, 1999. Associate Technical Editor: D. A. Signier.

Downloaded 04 May 2010 to 171.66.16.27. Redistribution subject to ASME license or copyright; see http://www.asme.org/terms/Terms_Use.cfm

Wickert, J. A., 1993, "Free Linear Vibration of Self-Pressurized Foil Bearings," ASME *Journal of Vibration and Acoustics,* Vol. 115, pp. 145–151.

The Nonlinear Sloshing of Liquid in Tank With Pitching

L. Yin,[1] B. Wang,[1] X. Ma,[2] and J. Zou[1]

In this paper, a method used to analyze the sloshing of liquid in a tank subjected to forced pitching and (or) yawing oscillation is presented. First, a variational principle for a liquid in a container under pitching and (or) yawing oscillation is proposed. Based on the preceding variational principle and new Lagrangian, the nonlinear sloshing of liquid in a circle cylindrical tank under pitching excitation is studied analytically for the first time.

1 Introduction

Since analysis of sloshing can be applied to the design of spacecraft or to the earthquake resistant underground tank, sloshing has been widely studied. The liquid sloshing is one of the most difficult mathematical problems to be solved numerically as well as analytically, because the kinematic and dynamic boundary condition (Bernoulli's equation) at the free surface is nonlinear and the position of the free surface is time-dependent, not known a prior. Therefore, most of studies which have been conducted so far were based on the linear theory where the amplitude of liquid motions is far less than the characteristic length of the container, and the frequency of excitation is far away from the natural frequencies for the liquid inside the tank. Linearized theory of sloshing seems now well established, and it has been used widely as a practical technique (cf. Abramson, 1966; Buseck and Benaroya, 1993).

Among a few existing theoretical studies of finite amplitude liquid sloshing, most of them are conducted to nonlinear free oscillation of liquid and nonlinear forced oscillation of liquid at the case of horizontal or vertical translation of container (cf. Hutton, 1963; Miles, 1976). There are few studies dealing with the nonlinear oscillation of the liquid in a container subjected to forced pitching oscillation (cf. Faltinsen, 1974; Nakayama and Washizu, 1980), but these studies only focus on two-dimensional sloshing of liquid in a rectangular tank.

First, we establish the nonlinear initial-boundary partial differential equation system for the sloshing of liquid in a container subjected to forced pitching and (or) yawing oscillation. Then, a variational principle for a liquid in a container subjected to forced pitching and (or) yawing oscillation is proposed. Based on the preceding variational principle and new Lagrangian, the nonlinear sloshing of liquid in a three-dimensional, circle cylindrical, rigid open tank under pitching excitation is studied analytically for the first time.

2 A Variational Principle for Liquid Sloshing

2.1 Governing Equations. In the present context, we consider that container is forced to pitch and (or) yaw with an angular velocity vector $\mathbf{\Omega}(t)$. Figure 1 shows a three-dimensional cylindrical container in motion. A Cartesian coordinate system, O-XYZ, is an inertial system. Z-axis is directed upward, namely, in the opposite direction to the gravity. Another Cartesian coordinate system, o-xyz, is fixed to the container in such a manner that x-axis is parallel to the undisturbed free surface and the z-axis is in coincidence with the center line of the container. The distance between the undisturbed free surface and the x-axis is denoted by e, which is taken positive when the free surface is above the x-axis. h is the depth of liquid. The origin o is taken as the center of rotation. $\alpha_x(t)$ and $\alpha_y(t)$ is the angular of inclination of container at the time t.

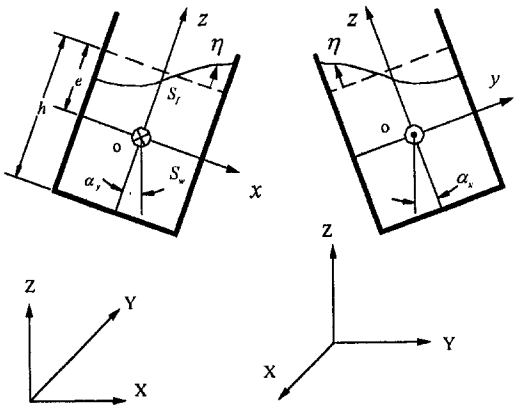


Fig. 1 A container under pitching and yawing excitation

It is assumed that the liquid is invisid and incompressible, and the flow is irrotational. The sloshing of liquid in container undergoing pitching and (or) yawing motion can be reduced to the following nonlinear, initial boundary value problem:

$$\nabla^2\Phi = 0 \quad \text{in } V \tag{1}$$

$$\frac{\partial\Phi}{\partial t} + \frac{1}{2}(\nabla\Phi)^2 - (\mathbf{\Omega}\times\mathbf{r})\cdot\nabla\Phi - \mathbf{g}\cdot\mathbf{r} = 0 \quad \text{on } S_f \tag{2}$$

$$\frac{\partial\eta}{\partial t} = (\nabla\Phi - \mathbf{\Omega}\times\mathbf{r})\cdot\nabla F \quad \text{on } S_f \tag{3}$$

$$\frac{\partial\Phi}{\partial n} = (\mathbf{\Omega}\times\mathbf{r})\cdot\mathbf{n} \quad \text{on } S_w \tag{4}$$

where V is the liquid region, $\mathbf{g}$ is the vector of gravity in the coordinate system o-xyz, $\mathbf{r}$ is the position vector of the liquid particle, $\mathbf{n}$ is the unit normal drawn outwardly on the wetted wall S_w, and $F = z - [\eta(x, y, t) + e]$ is the equation of the free surface. $\eta(x, y, t)$ is the height of the free surface measured from the undisturbed free surface. Up to now, the problem we are concerned with is expressed by Eqs. (1), (2), (3), and (4).

2.2 A Variational Principle. In the light of the ideas suggested by Luke, the expression of the pressure for a liquid in a container subjected to forced pitching and (or) yawing oscillation is used as the Lagrangian. Then, the variational principles is

$$\delta J = \delta\int_{t_1}^{t_2} L(\Phi, \eta)\cdot dt \tag{5}$$

where

$$L(\Phi, \eta) = -\iint\left\{\int_{-(h-e)}^{(\eta+e)}\left[\frac{\partial\Phi}{\partial t} + \frac{1}{2}(\nabla\Phi)^2 - (\mathbf{\Omega}\times\mathbf{r})\cdot\nabla\Phi - \mathbf{g}\cdot\mathbf{r}\right]dz\right\}dS \tag{6}$$

[1] Department of Astronautic and Mechanics, Harbin Institute of Technology, Harbin 150001, P. R. China.
[2] The Chinese Academy of Space Technology.

Contributed by the Applied Mechanics Division of THE AMERICAN SOCIETY OF MECHANICAL ENGINEERS for publication in the ASME JOURNAL OF APPLIED MECHANICS. Manuscript received by the ASME Applied Mechanics Division, July 9, 1998; final revision, July 8, 1999. Associate Technical Editor: D. A. Signier.

Downloaded 04 May 2010 to 171.66.16.27. Redistribution subject to ASME license or copyright; see http://www.asme.org/terms/Terms_Use.cfm

and where $\Phi(x, y, z, t)$ and $\eta(x, y, t)$ are allowed to vary, subject to the restriction $\delta\Phi = 0$, $\delta\eta = 0$ at t_1 and t_2.

According to the usual procedure in the calculus of variations, Eq. (5) becomes

$$\delta J = -\int_{t_1}^{t_2}\left\{\iint\left[[\Phi_t + \tfrac{1}{2}(\nabla\Phi)^2 - (\boldsymbol{\Omega}\times\mathbf{r})\cdot\nabla\Phi - \mathbf{g}\cdot\mathbf{r}\right]\delta\eta\right]_{z=\eta+e}dS_0 + \iint\left[\int_{-(h-e)}^{(\eta+e)}(\delta\Phi_t + \nabla\Phi\cdot\nabla\delta\Phi - (\boldsymbol{\Omega}\times\mathbf{r})\cdot\nabla\delta\Phi)dz\right]dS_0\right\}dt = 0 \quad (7)$$

where S_0 is the cross section of the container. Integrating the term $\delta\Phi_t$ in Eq. (7) with respect to z, and applying Green's first theorem, Eq. (7) can be rewritten as

$$\delta J = -\int_{t_1}^{t_2}\left\{\iint\left[\delta\eta\cdot\left[\frac{\partial\Phi}{\partial t} + \frac{1}{2}(\nabla\Phi)^2 - (\boldsymbol{\Omega}\times\mathbf{r})\cdot\nabla\Phi - \mathbf{g}\cdot\mathbf{r}\right]\right]_{z=\eta+e}dS_0 - \iiint\delta\Phi\nabla^2\Phi dV + \iint_{S_0}\left[\delta\Phi\cdot\left[-\frac{\partial\eta}{\partial t} + (\nabla\Phi - \boldsymbol{\Omega}\times\mathbf{r})\cdot\nabla F\right]\right]_{z=\eta+e}\times dS_0 + \iint_{S_w}[\delta\Phi\cdot[\nabla\Phi\cdot\mathbf{n} - (\boldsymbol{\Omega}\times\mathbf{r})\cdot\mathbf{n}]]dS\right\}dt = 0.$$

Considering that $\delta\eta$, $[\delta\Phi]_V$, $[\delta\Phi]_{S_f}$, $[\delta\Phi]_{S_w}$ may be given arbitrary independent values, we can also obtain Eqs. (1), (2), (3), and (4). Subsequently we will study the sloshing of liquid in a three-dimensional, circle cylindrical, rigid open tank without baffles, which is forced to oscillate harmonically with small and finite amplitude of pitching oscillation.

3 The Nonlinear Sloshing of Liquid in a Circle Cylindrical Container With Pitching

3.1 The Formation of Lagrangian. The tank model and coordinate system are shown in Fig. 2. It is assumed that the radius

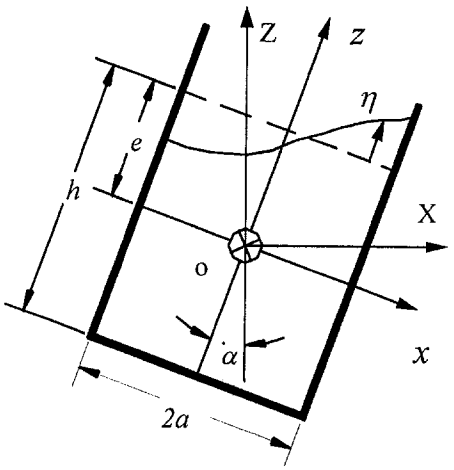


Fig. 2 Tank model and coordinate system ω is the angular frequency of pitching

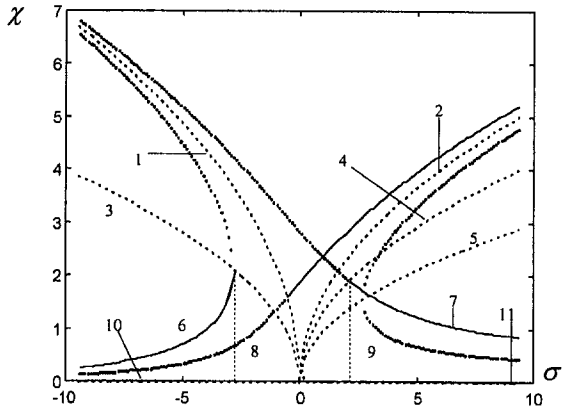


Fig. 3 Response curves of the liquid motion in a circle cylindrical tank under pitching excitation (a = 0.5 m, h = 0.5 m, e = 0.3 m, θ_0 = 0.08 rad)

of the tank a to be $O(1)$ and the depth of fluid h to be either $O(1)$ or infinite. The container is only forced to pitch around the y-axis with angular velocity Ω.

The motion of the tank is given as

$$\alpha = \theta_0 \sin\omega t$$

where α is the angular of inclination of the container and θ_0 is the peak amplitude of the tank pitching motion excitation.

Integrating Φ_t in Eq. (6) with respect to z, and expanding the other terms by the power series of η, and retaining the terms up to the fourth order, Eq. (6) becomes

$$L = \iint_{S_0}\left[\left(\Phi + \eta\cdot\Phi_z + \frac{\eta^2}{2}\Phi_{zz}\right)\eta_t - \frac{1}{2}\Phi\cdot\Phi_z - \frac{\eta}{2}(\nabla\Phi)^2 - \frac{\eta^2}{2}\left(\nabla\Phi\cdot\nabla\frac{\partial\Phi}{\partial z}\right) - \Phi r\cos\theta\Omega + \eta[(\boldsymbol{\Omega}\times\mathbf{r})\cdot\nabla\Phi] + \frac{\eta^2}{2}\left[\frac{\partial[(\boldsymbol{\Omega}\times\mathbf{r})\cdot\nabla\Phi]}{\partial z}\right] + g\eta r\cos\theta\sin\alpha - \frac{1}{2}g\cos\alpha\eta^2 - g\eta e\cos\alpha\right]dS + \frac{1}{2}\int[\Phi\Omega z\cos\theta]dS|_{r=a} + \frac{1}{2}\int(\Phi\Omega r\cos\theta)dS|_{z=e-h} \quad (8)$$

where S_0 is the cross section of container. As is seen, the integrals over the free surface S_f have been transformed into those over the still water surface S_0.

3.2 Solutions. The solution of $\Phi(r, \theta, z, t)$ and $\eta(r, \theta, t)$ is searched by the summation form of the eigenmodes as follows:

$$\Phi(r, \theta, z, t) = \Phi_0\Omega + \sum_n a_n\phi_n(r, \theta, z) \quad (9)$$

$$\eta(r, \theta, t) = \sum_n b_n\phi_n(r, \theta, e) \quad (10)$$

where $\Phi_0\Omega$ takes care of the inhomogeneous body boundary condition. We found Φ_0 when solving the linear problem and it is

Downloaded 04 May 2010 to 171.66.16.27. Redistribution subject to ASME license or copyright; see http://www.asme.org/terms/Terms_Use.cfm

Table 1 Explanations for curves and regions in Fig. 3

Curve or region	Explanation
(1)	backbone curve of planar motion
(2)	backbone curve of rotary motion
(6), (7)	response curve of planar motion
(8), (9)	response curve of rotary motion
(3)–(1)	unstable region for planar motion (jump phenomenon)
(1)–(4)	unstable region for planar motion (appearance of rotary motion)
(2)–(5)	unstable region for rotary motion (jump phenomenon)
(10)–(1), (4)–(11)	unstable region for rotary motion (decay)

$$\Phi_0 = a^2\left[\frac{z}{a}\cdot\frac{r}{a} - 2\sum_{n=1}^{\infty}\frac{ch[k_{1n}(z+h-e)]-2ch[k_{1n}(z-e)]}{\xi_{1n}(\xi_{1n}^2-1)sh(k_{1n}h)}\cdot\frac{J_1(k_{1n}r)}{J_1(\xi_{1n})}\right]\cos\theta \tag{11}$$

and $\phi_n(r, \theta, z)$ is the nth eigenmode of the liquid motion. Wave number $k_{nm} = \xi_{nm}/a$, ξ_{nm} is the eigenvalue for mode (n, m), representing the solution of $J_n'(\xi_{nm}) = 0$. J_n is the Bessel function of the first kind, order n, and the prime denotes differentiation with respect to r.

Substituting Eqs. (9) and (10) into Eq. (8) and carrying out integration, L can be expressed into the function of a_n, b_n, $\dot{b}_n$. Substituting the expression of L into variational equations, the set of two coupled nonlinear equations of system can be obtained. Then, the method of multiple scales is used to solve these equations.

Following the similar procedure in Komatsu's paper, the characteristic of liquid sloshing can be analyzed. Figure 3 shows the frequency-response curves and stable-unstable regions with the explanations in Table 1. Only the solid lines are stable for the planar and rotary motions.

4 Conclusions

A method is presented for analyzing finite amplitude sloshing of liquid in a tank undergoing pitching and yawing motion. As an example, the nonlinear sloshing of liquid in a circle cylindrical tank under pitching excitation is studied analytically for the first time. The present method can also be generalized to analyze the sloshing of liquid in another regular geometrical tank, such as a rectangular tank, which is forced to pitch. The effect of liquid viscosity and surface tension should be incorporated in an appropriate way in the present method in future studies.

References

Abramson, H. N., 1966, "The Dynamic Behavior of Liquids in Moving Containers," NASA Report No. SP-106.

Buseck, R., and Benaroya, H., "Mechanical Models for Slosh of Liquid Fuel," AIAA Paper 93-1093.

Faltinsen, O. M., 1974, "A Nonlinear Theory of Sloshing in Rectangular Tanks," *J. Ship Res.*, Vol. 18, pp. 224–241.

Hutton, R. E., 1963, "An Investigation of Resonant, Nonlinear, Nonplanar Free Surface Oscillations of a Fluid," NASA Report No. TN D-1870.

Komatsu, K., 1987, "Nonlinear Sloshing Analysis of Liquid in Tanks with Arbitrary Geometries," *Int. J. Non-linear Mechanics*, Vol. 22, No. 3, pp. 193–207.

Luke, J. C., 1967, "A Variational Principle for a Fluid with a Free Surface," *J. Fluid Mech.*, Vol. 27, No. 2, pp. 395–397.

Miles, J. W., 1976, "Nonlinear Surface Waves in Closed Basins," *J. Fluid Mech.*, Vol. 75, pp. 419–448.

Nakayama, T., and Washizu, K., 1980, "Nonlinear Analysis of Liquid Motion in a Container Subjected to Forced Pitching Oscillation," *Int. J. Num. Meth. Engng.*, Vol. 15, pp. 1207–1220.

A Generalization of Cattaneo-Mindlin for Thin Strips

J. Jäger[1]

In this paper, a generalization of the Cattaneo-Mindlin solution is derived for thin bonded layers with arbitrary surfaces. We assume that equal layers are in contact, and show that the normal and tangential stress displacement equations are uncoupled and of the same form. In this case the stick condition for tangential shift is identical with the contact condition in normal direction, and the tangential problem can be reduced to the normal problem. Finally, a recursive algorithm for general load cases is proposed. We believe that this model illustrates typical features of elastic bodies with friction. It can also serve as a model for memory effects, employing the elastic superposition technique.

Introduction

The problem of equal elastic spheres in contact with friction has been solved by Cattaneo (1938) and Mindlin (1949). It was shown that a circular stick area forms, and the tangential traction is the difference between the normal pressure for the actual contact area and the pressure for the stick area, multiplied with the coefficient of friction. This solution was generalized by Jäger (1995) for bodies of equal material with arbitrary axisymmetric surfaces in contact. It was later shown by Jäger (1997), that this generalization is always valid for plane contact of arbitrary surfaces. Some examples have been presented in Jäger (1998) and a general algorithm for arbitrary surfaces was proposed. Ciavarella (1998, 1999) published the special case of constant normal forces of Jäger's solutions, but Ciavarella did not relate it to the articles by Jäger (1995, 1997). In this article, we derive a generalization of the Cattaneo-Mindlin solution for thin elastic layers of equal material, which are bonded to a rigid base. The method of solution and the general algorithm are the same as in the earlier mentioned papers, but the mathematical model is much easier to understand.

Normal Contact

Following Bentall and Johnson (1968 Eq. (A.16)), the simplified expressions for the normal and tangential surface displacements w_k and u_k, respectively, of a very thin bonded strip are

$$w_k(x) = \frac{(1-2\nu_k)t_k}{(1-\nu_k)2G_k}p_k(x) + \frac{(1-4\nu_k)t_k^2}{(1-\nu_k)4G_k}\frac{\partial q_k}{\partial x}, \quad \nu_k \neq 0.5, \tag{1}$$

$$u_k(x) = \frac{(1-4\nu_k)t_k^2}{(1-\nu_k)4G_k}\frac{\partial p_k}{\partial x} + \frac{t_k}{G_k}q_k(x), \tag{2}$$

where the index k characterizes strip I or II, G_k the shear modulus, ν_k Poisson's ratio, p_k the normal pressure, q_k the tangential trac-

[1] IBAMA, Goerdelerstr. 8, D-91058 Erlangen, Germany. e-mail: j_jaeger@t-online.de.

Contributed by the Applied Mechanics Division of THE AMERICAN SOCIETY OF MECHANICAL ENGINEERS for publication in the ASME JOURNAL OF APPLIED MECHANICS. Manuscript received by the ASME Applied Mechanics Division, Oct. 15, 1998; final revision, July 9, 1999. Associate Technical Editor: R. C. Benson.

Downloaded 04 May 2010 to 171.66.16.27. Redistribution subject to ASME license or copyright; see http://www.asme.org/terms/Terms_Use.cfm

Table 1 Explanations for curves and regions in Fig. 3

Curve or region	Explanation
(1)	backbone curve of planar motion
(2)	backbone curve of rotary motion
(6), (7)	response curve of planar motion
(8), (9)	response curve of rotary motion
(3)–(1)	unstable region for planar motion (jump phenomenon)
(1)–(4)	unstable region for planar motion (appearance of rotary motion)
(2)–(5)	unstable region for rotary motion (jump phenomenon)
(10)–(1), (4)–(11)	unstable region for rotary motion (decay)

$$\Phi_0 = a^2\left[\frac{z}{a}\cdot\frac{r}{a} - 2\sum_{n=1}^{\infty}\frac{ch[k_{1n}(z+h-e)]-2ch[k_{1n}(z-e)]}{\xi_{1n}(\xi_{1n}^2-1)sh(k_{1n}h)}\cdot\frac{J_1(k_{1n}r)}{J_1(\xi_{1n})}\right]\cos\theta \tag{11}$$

and $\phi_n(r, \theta, z)$ is the nth eigenmode of the liquid motion. Wave number $k_{nm} = \xi_{nm}/a$, ξ_{nm} is the eigenvalue for mode (n, m), representing the solution of $J_n'(\xi_{nm}) = 0$. J_n is the Bessel function of the first kind, order n, and the prime denotes differentiation with respect to r.

Substituting Eqs. (9) and (10) into Eq. (8) and carrying out integration, L can be expressed into the function of a_n, b_n, $\dot{b}_n$. Substituting the expression of L into variational equations, the set of two coupled nonlinear equations of system can be obtained. Then, the method of multiple scales is used to solve these equations.

Following the similar procedure in Komatsu's paper, the characteristic of liquid sloshing can be analyzed. Figure 3 shows the frequency-response curves and stable-unstable regions with the explanations in Table 1. Only the solid lines are stable for the planar and rotary motions.

4 Conclusions

A method is presented for analyzing finite amplitude sloshing of liquid in a tank undergoing pitching and yawing motion. As an example, the nonlinear sloshing of liquid in a circle cylindrical tank under pitching excitation is studied analytically for the first time. The present method can also be generalized to analyze the sloshing of liquid in another regular geometrical tank, such as a rectangular tank, which is forced to pitch. The effect of liquid viscosity and surface tension should be incorporated in an appropriate way in the present method in future studies.

References

Abramson, H. N., 1966, "The Dynamic Behavior of Liquids in Moving Containers," NASA Report No. SP-106.

Buseck, R., and Benaroya, H., "Mechanical Models for Slosh of Liquid Fuel," AIAA Paper 93-1093.

Faltinsen, O. M., 1974, "A Nonlinear Theory of Sloshing in Rectangular Tanks," *J. Ship Res.*, Vol. 18, pp. 224–241.

Hutton, R. E., 1963, "An Investigation of Resonant, Nonlinear, Nonplanar Free Surface Oscillations of a Fluid," NASA Report No. TN D-1870.

Komatsu, K., 1987, "Nonlinear Sloshing Analysis of Liquid in Tanks with Arbitrary Geometries," *Int. J. Non-linear Mechanics*, Vol. 22, No. 3, pp. 193–207.

Luke, J. C., 1967, "A Variational Principle for a Fluid with a Free Surface," *J. Fluid Mech.*, Vol. 27, No. 2, pp. 395–397.

Miles, J. W., 1976, "Nonlinear Surface Waves in Closed Basins," *J. Fluid Mech.*, Vol. 75, pp. 419–448.

Nakayama, T., and Washizu, K., 1980, "Nonlinear Analysis of Liquid Motion in a Container Subjected to Forced Pitching Oscillation," *Int. J. Num. Meth. Engng.*, Vol. 15, pp. 1207–1220.

A Generalization of Cattaneo-Mindlin for Thin Strips

J. Jäger[1]

In this paper, a generalization of the Cattaneo-Mindlin solution is derived for thin bonded layers with arbitrary surfaces. We assume that equal layers are in contact, and show that the normal and tangential stress displacement equations are uncoupled and of the same form. In this case the stick condition for tangential shift is identical with the contact condition in normal direction, and the tangential problem can be reduced to the normal problem. Finally, a recursive algorithm for general load cases is proposed. We believe that this model illustrates typical features of elastic bodies with friction. It can also serve as a model for memory effects, employing the elastic superposition technique.

Introduction

The problem of equal elastic spheres in contact with friction has been solved by Cattaneo (1938) and Mindlin (1949). It was shown that a circular stick area forms, and the tangential traction is the difference between the normal pressure for the actual contact area and the pressure for the stick area, multiplied with the coefficient of friction. This solution was generalized by Jäger (1995) for bodies of equal material with arbitrary axisymmetric surfaces in contact. It was later shown by Jäger (1997), that this generalization is always valid for plane contact of arbitrary surfaces. Some examples have been presented in Jäger (1998) and a general algorithm for arbitrary surfaces was proposed. Ciavarella (1998, 1999) published the special case of constant normal forces of Jäger's solutions, but Ciavarella did not relate it to the articles by Jäger (1995, 1997). In this article, we derive a generalization of the Cattaneo-Mindlin solution for thin elastic layers of equal material, which are bonded to a rigid base. The method of solution and the general algorithm are the same as in the earlier mentioned papers, but the mathematical model is much easier to understand.

Normal Contact

Following Bentall and Johnson (1968 Eq. (A.16)), the simplified expressions for the normal and tangential surface displacements w_k and u_k, respectively, of a very thin bonded strip are

$$w_k(x) = \frac{(1-2\nu_k)t_k}{(1-\nu_k)2G_k}p_k(x) + \frac{(1-4\nu_k)t_k^2}{(1-\nu_k)4G_k}\frac{\partial q_k}{\partial x}, \quad \nu_k \neq 0.5, \tag{1}$$

$$u_k(x) = \frac{(1-4\nu_k)t_k^2}{(1-\nu_k)4G_k}\frac{\partial p_k}{\partial x} + \frac{t_k}{G_k}q_k(x), \tag{2}$$

where the index k characterizes strip I or II, G_k the shear modulus, ν_k Poisson's ratio, p_k the normal pressure, q_k the tangential trac-

[1] IBAMA, Goerdelerstr. 8, D-91058 Erlangen, Germany. e-mail: j_jaeger@t-online.de.

Contributed by the Applied Mechanics Division of THE AMERICAN SOCIETY OF MECHANICAL ENGINEERS for publication in the ASME JOURNAL OF APPLIED MECHANICS. Manuscript received by the ASME Applied Mechanics Division, Oct. 15, 1998; final revision, July 9, 1999. Associate Technical Editor: R. C. Benson.

Downloaded 04 May 2010 to 171.66.16.27. Redistribution subject to ASME license or copyright; see http://www.asme.org/terms/Terms_Use.cfm

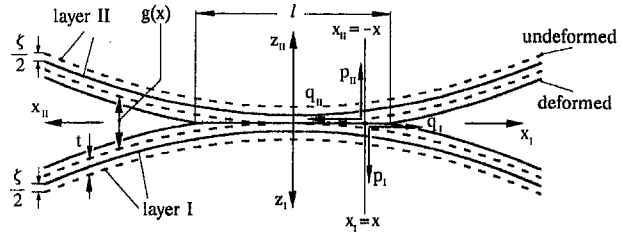


Fig. 1 Two equal layers in contact

tion, and t_k the layer thickness. Equations (1), (2) are not valid for the special case of incompressible material with $\nu_k = 0.5$.

When two *equal* elastic layers are in contact (Fig. 1), and the coordinates of layer I are opposite to the coordinates of layer II, a point x of layer I comes in contact with a point $-x$ of layer II. The stresses at the contact points are equal, and the combined displacements are

$$w(x) = w_I(x) + w_{II}(-x) = \frac{(1-2\nu)t}{(1-\nu)G}\, p(x), \tag{3}$$

$$u(x) = u_I(x) + u_{II}(-x) = \frac{2t}{G}\, q(x), \tag{4}$$

$$p(x) = p_I(x) = p_{II}(-x), \quad q(x) = q_I(x) = q_{II}(-x), \tag{5}$$

where t is the thickness and G the shear modulus of one layer. The surface stress at any point in Eqs. (3) and (4) depends only on the displacement at that point. This model was introduced as elastic foundation or wire-brush model, with Eqs. (4.52) and (8.63) in Johnson (1985).

The stress displacement relations (3), (4) in normal and tangential direction are uncoupled and of the same form. In the first step, the two layers are brought in contact on the interval $C_1 = [a, b]$. The displacement $w_1(x)$ is equal to the approach ζ_1 of the rigid foundations of both layers, reduced by the gap $g(x)$ between the layer surfaces in undeformed contact. Here and in the following equations, integer indices denote the numbers of a load increment. The pressure follows from (3):

$$p_1(x) = \frac{(1-\nu)G}{(1-2\nu)t}\, w_1(x), \quad w_1(x) = \zeta_1 - g(x). \tag{6}$$

For a continuous gap function $g(x)$ without edges, the displacement $w_1(x)$ and the pressure $p_1(x)$ fall to zero at the contact ends $x = a, b$ and the pressure vanishes outside of the contact interval. Only a contact edge with a vertical tangent can produce finite values for the pressure at the contact edge, where the pressure falls discontinuously to zero outside of the contact area. We have $w_1(x) = \zeta_1$ at the initial contact point, where the gap must be zero. For symmetric profiles, the initial contact point coincides with the origin $x = 0$.

In the next step, the normal force is increased, the contact region grows to $C_2 = [c, d]$, and the additional pressure p^* produces a constant displacement w^* of the old contact interval C_1

$$w^*(x) = \zeta_2 - \zeta_1, \quad \text{for } x \in C_1, \tag{7}$$

$$w^*(x) = \zeta_2 - \zeta_1 - g(x), \quad \text{for } x \in C_2 \backslash C_1, \tag{8}$$

$$w_2(x) = w_1(x) + w^*(x), \quad p_2(x) = p_1(x) + p^*(x), \tag{9}$$

with the new displacement w_2 and the pressure p_2. Again, the pressure disappears at the ends $x = c, d$ of C_2, when the surfaces have no edges.

Tangential Contact

When a tangential force is applied under constant normal forces in step 3, the stick condition requires a constant displacement $u_3(x) = \xi_3$ in the stick zone. For complete sticking of the entire contact region C_2, the tangential traction (4) is constant, and Coulomb's law is violated at the ends of C_2, i.e., a part of the contact region starts sliding. The boundary conditions are Coulomb's law in the slip zone S_3 and a constant displacement in the stick zone H_3

$$q_3 = fp_2(x), \quad \text{for } x \in S_3; \quad u_3(x) = \xi_3, \quad \text{for } x \in H_3. \tag{10}$$

Since the load displacement Eqs. (3) and (4) are of the same form, it is reasonable to assume a tangential traction distribution of the form p^* in (9), which produces a constant displacement of the previous contact region C_1. We also assume that the stick zone H_3 is identical with C_1. The traction distribution

$$q_3(x) = fp^*(x) = f[p_2(x) - p_1(x)], \quad H_3 = C_1, \quad S_3 = C_2 \backslash C_1, \tag{11}$$

satisfies Coulomb's law in the slip zone S_3, because p_1 vanishes outside of H_3. The stick condition is also satisfied, because p^* produces a constant displacement in H_3. The displacement $u_3(x)$ follows after insertion of (11) in (4), and (6) gives an expression for the tangential displacement as a function of the normal displacement

$$u_3(x) = \frac{2t}{G} f[p_2(x) - p_1(x)] = f\kappa[w_2(x) - w_1(x)],$$

$$\xi_3 = f\kappa(\zeta_2 - \zeta_1), \quad \kappa = \frac{2(1-\nu)}{(1-2\nu)}. \tag{12}$$

There are two side conditions for Coulomb's law in form of inequalities:

1 the tangential traction in the stick zone must be smaller than the value for sliding: $q < fp$, which we call the *traction inequality;*

2 the *displacement inequality* requires that the relative slip must be opposite to the tangential traction. When we assume a positive tangential traction in x-direction, the slip must be negative.

We will prove this conditions for convex surfaces under increasing forces.

1 The tangential traction is the difference between the pressure p_2 of the larger contact region C_2 and the pressure p_1: $q_3 = f(p_2 - p_1)$. Since $p_2 > p_1$, the inequality $q_3 = f(p_2 - p_1) < fp_2$ holds always. This inequality could only be violated for negative p_1, which would contradict the contact condition in C_1 of step 1. In other words, the traction inequality is identical with the contact condition.

2 The displacement $w_1(x)$ in (6) is zero outside of C_1 and $w_2 = \zeta_2 - g(x)$. The relative slip between both bodies follows from (12):

$$u_3(x) - \xi_3 = f\kappa[\zeta_1 - g(x)] < 0 \quad \text{for } x \in S_3. \tag{13}$$

In Eq. (13), the slip is the tangential displacement reduced by the rigid-body shift. Since the surfaces must not penetrate outside of C_1 in step 1, the gap $g(x) - \zeta_1$ must be positive for $x \in S_3$. It follows that the slip has everywhere the same sign, opposite to the traction, such that the displacement inequality is satisfied. Furthermore, the displacement inequality is identical with the condition of no overlapping of both surfaces in step 1.

The same proof can be performed for multiple contact regions $[a_i, b_i]$, when the intervals $[b_i, a_{i+1}]$ are free from stress. The total contact region C_1 is the set of C_{1i},

Downloaded 04 May 2010 to 171.66.16.27. Redistribution subject to ASME license or copyright; see http://www.asme.org/terms/Terms_Use.cfm

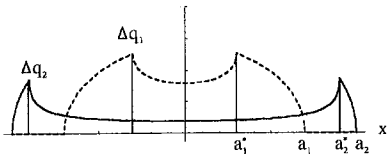


Fig. 2 No overlapping for $k = 2$, $s_1 = s_2 = f$, parabolic surfaces

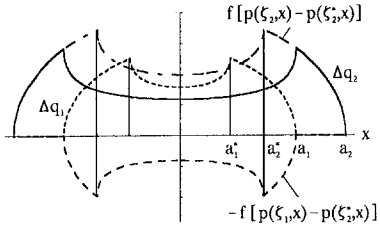


Fig. 3 Partial overlapping for $k = 2$, $s_1 = s_2 = f$, parabolic surfaces

$$C_1 = \bigcup_{i=1}^{N} C_{1i}, \quad C_{1i} = [a_i, b_i]. \tag{14}$$

The same summation must be performed for the total contact region in step 2. When we apply a tangential force, each stick zone is a combination of old contact intervals. We conclude that the stick zone decreases in the same way as the contact region decreases during unloading, and the number and size of the intervals are the same. When the tangential displacement is known, the stick zone follows from Eq. (12), where the pressure has to be summarized over all intervals. When the tangential force is given, the stick zone follows from (11).

The case of *proportional loading,* where an oblique force is increased in constant direction, can be solved similarly. We write the pressure as a function of the normal displacement ζ of a characteristic point in the contact region and the position x

$$dq(\zeta, x) = \tan \beta dp(\zeta, x). \tag{15}$$

Integration gives

$$\Delta q_2 = q(\zeta_2, \zeta_1, x) = \tan \beta[p(\zeta_2, x) - p(\zeta_1, x)] = \tan \beta \Delta p_2. \tag{16}$$

where loading starts at the normal displacement ζ_1 and ends at ζ_2, and β is the load angle.

The contact problem of rotating bodies is more complicated, and should be treated in a modified way, because the contact condition induces rotation and is not identical with the stick condition. The case of torsion of axisymmetric half-spaces in Jäger (1995) can serve as example for such problems. For thick layers in contact, the displacement-stress equations are also uncoupled but not of the same form. It is possible, however, to use the solution for the normal pressure and an appropriate stiffness factor κ as approximation for the tangential solution (Jäger, 1999).

General Load Histories

Finally, general load histories can be thought as a superposition of loading increments of type (11), but it has to be checked if the old and new slip zone overlap for two successive load increments. Each increment is applied in two steps, one in normal and another in tangential direction. When $\Delta\zeta_k$ increases, the normal increment is applied in the first step, and the tangential traction in step 2. In order to simplify the algorithm, the sequence is changed for decreasing $\Delta\zeta_k < 0$, where the tangential traction must be applied in the first step, and the normal traction in step 2. This procedure avoids that normal unloading reduces the previous stick region in the special case when the tangential load increment is opposite to the previous increment. Since the slip stress is reduced by a reverse tangential load increment, we expect that the old slip zone sticks at the beginning of such an increment. Normal unloading, on the other hand, decreases the normal pressure and increases the slip zone. To simplify matters, we consider only one increment of a load history in this paper. An example for positive load increments is illustrated in Figs. 2, 3 and more can be found in Jäger (1996, 1998). The general algorithm requires a distinction among three different contact regimes for each load increment: no overlapping (n.o.), partial overlapping (p.o.), and complete overlapping of the old and new slip zone. The mathematical formula for the tangential traction increment Δq_k can be written in the form

$$\Delta q_k = \begin{cases} s_k[p(\zeta_k, x) - p(\zeta_k^*, x)], & \text{for n.o.} \\ s_k[p(\zeta_k, x) - p(\zeta_k^*, x)] - s_{k-1}[p(\zeta_{k-1}, x) \\ \quad - p(\zeta_k^*, x)], & \text{for p.o.} \end{cases} \tag{17}$$

$$\Delta\xi_k = \begin{cases} s_k\kappa(\zeta_k - \zeta_k^*), & \text{for n.o.} \\ s_k\kappa(\zeta_k - \zeta_k^*) - s_{k-1}\kappa(\zeta_{k-1} - \zeta_k^*), & \text{for p.o.} \end{cases} \tag{18}$$

with $s_k = \pm f$ and the superscript * for values of the stick area. In the first line of (17), the contact regime of no overlapping (n.o.) takes place, where the old and new slip zone do not overlap, and we have $\zeta_k^* > \zeta_{k-1}$ ($a_2^* > a_1$ in Fig. 2). This solution was explained in the section on tangential contact above. For $\zeta_{k-1}^* < \zeta_k^* < \zeta_{k-1}$, partial overlapping (p.o.) takes place ($a_1^* < a_2^* < a_1$ in Fig. 3). Here, the overlapping part of the old and new slip zone must first be made traction free by the second expression in square brackets, before a traction distribution can be superposed, which satisfies Coulomb's law. Finally, for $\zeta_k^* < \zeta_{k-1}^*$, we have complete overlapping, and the old slip zone of step $k - 1$ is erased.

The general algorithm for displacement controlled loading begins with the test of the stick condition for a load increment k and consists of the following three steps:

1 Test the stick condition $|\Delta\xi_k| < f\kappa\Delta\zeta_k$. When it is satisfied, we have no overlapping and Eq. (17) gives the corresponding traction increment for no overlapping. The solution is found.

2 $|\Delta\xi_k| \geq f\kappa\Delta\zeta_k$. A new slip zone forms and we have either partial or complete overlapping of the old slip region. The virtual displacement ζ_k^* can be calculated from Eq. (18) for partial overlapping, when the displacement increments $\Delta\xi_k$ and $\Delta\zeta_k$ are given. For $\zeta_k^* > \zeta_{k-1}^*$, only a part of the old slip zone is erased by the new slip traction and the traction increments are given by Eqs. (17) for partial overlapping. The solution is found.

3 The stick condition $|\Delta\xi_k| < f\kappa\Delta\zeta_k$ and the condition for partial overlapping $\zeta_k^* > \zeta_{k-1}^*$ are violated and the new slip region overlaps the old slip zone completely. Apply the old and new increment $\Delta\xi_{k-1} + \Delta\xi_k$ in one step and repeat steps 1–3.

This algorithm must be successively repeated for all M steps of the load history, starting with the first step. An equivalent load history remains, where the contact regimes of complete overlapping have been eliminated. The force is the integral over the traction. A similar algorithm was published in Jäger (1996), for three-dimensional loading with oblique load increments.

References

Bentall, R. H., Johnson, K. L., 1968, "An Elastic Strip in Plane Rolling Contact," *Int. J. Mech. Sci.,* Vol. 10, pp. 637–663.

Cattaneo, C., 1938, "Sul contatto die due corpi elastici: Distributione locale degli sforzi," *Academia Nazionale dei Lincei, Rendiconti,* Serie 6, Vol. 27, pp. 342–348, 434–436, 474–478.

Ciavarella, M., 1998, "The Generalized Cattaneo Partial Slip Plane Contact Problem. I—Theory, II—Examples," *Int. J. Solids Structures,* Vol. 32, pp. 2349–2362, 2363–2378.

Ciavarella, M., 1999, "Indentation by Nominally Flat or Conical Indenters With Rounded Corners," *Int. J. Solids & Structures,* Vol. 36, pp. 4149–4181.

Jäger, J., 1995, "Axisymmetric Bodies of Equal Material in Contact Under Torsion or Shift," *Arch. Appl. Mech.,* Vol. 65, pp. 478–487.

Downloaded 04 May 2010 to 171.66.16.27. Redistribution subject to ASME license or copyright; see http://www.asme.org/terms/Terms_Use.cfm

Jäger, J., 1996, "Stepwise Loading of Half-Spaces in Elliptical Contact," ASME JOURNAL OF APPLIED MECHANICS, Vol. 63, pp. 766–773.
Jäger, J., 1997, "Ein neues Prinzip der Kontaktmechanik," *Z. Angew. Math. Mech.*, Vol. 77, pp. S143-S144, presented at the GAMM meeting, May 1996.
Jäger, J., 1998, "A New Principle in Contact Mechanics," ASME *Journal of Tribology*, Vol. 120, pp. 677–685.
Jäger, J., 1999, "Equal Layers in Contact With Friction," *Contact Mechanics IV*, L. Gaul and C. A. Brebbia, eds., WIT Press, Southampton, pp. 99–108.
Johnson, K. L., 1985, *Contact Mechanics*, Cambridge, CUP.
Mindlin, R. D., 1949, "Compliance of Elastic Bodies in Contact," ASME JOURNAL OF APPLIED MECHANICS, Vol. 16, pp. 259–268.

Interfacial Debonding of an Elliptical Inhomogeneity in Piezoelectric Solids

W. Deng[1] and S. A. Meguid[1,2]

1 Introduction

In view of their inherent electromechanical behavior, piezoelectric materials have been widely used as sensors and actuators. These sensors and actuators are taken as inhomogeneities, which are either bonded to or embedded in the structure to provide the necessary stimulus to meet the demands of the electromechanical loading environment. The presence of a weaker interface between the matrix and the inhomogeneity affects the performance of these sensors and actuators. The weaker interface may also lead to interfacial delamination or debonding. Recently, Zhong and Meguid (1997) developed a generalized model to treat the partially debonded circular inhomogeneity problem in piezoelectric materials using series expansion technique. More recently, Deng and Meguid (1999) reexamined this problem and derived closed-form expressions for the complex field potentials and electro-elastic field intensity factors by considering the behavior of the field components at origin and infinity.

It is the object of this study to extend the previous work of Zhong and Meguid (1997) and Deng and Meguid (1999) to deal with the more general interfacial debonding problem of an *elliptical* piezoelectric inhomogeneity in an infinite piezoelectric matrix. The original boundary value problem can be solved by means of the appropriate conformal mapping transformation and the Laurent series expansion. The formulae for evaluating the electro-elastic field intensity factors of the interfacial curvilinear crack are derived from the general solution.

2 Basic Equations and General Solutions

Consider an infinite piezoelectric medium containing a partially debonded elliptical piezoelectric inhomogeneity subject to remote antiplane mechanical and in-plane electric loads, as shown in Fig. 1. Both the inhomogeneity and the matrix are assumed to be transversely isotropic and the inhomogeneity is infinitely extended in a direction perpendicular to the xy-plane. The regions occupied by the matrix and the inhomogeneity are referred to as regions 1 and 2 and denoted by S^+ and S^-, respectively. The interface between S^+ and S^- is represented by $L\ (=L_c + L_b)$, where L_c is the cracked part which denotes an insulated and traction-free interfacial curvilinear crack, while L_b is the bonded part of L.

For the present problem, only the antiplane displacement w and the in-plane electric field E_x and E_y are assumed to exist. They are independent of the longitudinal coordinate, such that $w = w(x, y)$, $E_x = E_x(x, y)$ and $E_y = E_y(x, y)$. Note that $E_i = -\phi_{,i}$, where $\phi(x, y)$ is the electric potential. Let w and ϕ be the real parts of the analytic functions $\Psi(z)$ and $\Phi(z)$, such that

$$w = \frac{1}{2c_{44}}[\Psi(z) + \overline{\Psi(z)}], \quad \phi = \frac{1}{2\epsilon_{11}}[\Phi(z) + \overline{\Phi(z)}] \tag{1}$$

where $z = x + iy$ is the complex variable and the overbar refers to the complex conjugate. The electric field strength, the electric displacements, and the stresses can be expressed by $\Psi(z)$ and $\Phi(z)$ as follows (Deng and Meguid, 1999):

$$E_x - iE_y = -\frac{1}{\epsilon_{11}}\Phi'(z), \quad D_x - iD_y = \frac{e_{15}}{c_{44}}\Psi'(z) - \Phi'(z),$$

$$\sigma_{zx} - i\sigma_{zy} = \Psi'(z) + \frac{e_{15}}{\epsilon_{11}}\Phi'(z) \tag{2}$$

where the primed quantities denote the derivatives with respect to the arguments, σ_{zx} and σ_{zy} are the shear stresses, D_x and D_y are the electric displacements, and c_{44}, e_{15}, and ϵ_{11} are the longitudinal shear modulus, piezoelectric modulus, and dielectric modulus, respectively. Let us now introduce the following mapping function:

$$z = \Omega(\zeta) = \frac{c}{2}[R\zeta + (R\zeta)^{-1}], \quad R\zeta = \frac{1}{c}[z + (z^2 - c^2)^{1/2}] \tag{3}$$

with

$$\zeta = \zeta_1 + i\zeta_2 = \rho e^{i\psi}, \quad c = (a^2 - b^2)^{1/2} = a(1 - \epsilon^2)^{1/2}$$

$$R = \left(\frac{a+b}{a-b}\right)^{1/2} = \left(\frac{1+\epsilon}{1-\epsilon}\right)^{1/2}, \quad \epsilon = \frac{b}{a} \tag{4}$$

where $2a$ and $2b$ are the major and minor diameters of the elliptical inhomogeneity. This mapping function transforms region 1 (S^+) of the z-plane into the exterior region of the unit circle Γ_1 ($\zeta = \sigma = e^{i\psi}$) in the transformed ζ-plane and region 2 (S^-) into the annular region between the unit circle Γ_1 and a circle Γ_2 of radius $\rho = 1/R$ representing a cut from $-c$ to $+c$ in the z-plane (see Fig. 2). Γ_1 consists of two parts (Γ_c and Γ_b) which correspond to L_c and L_b in the z-plane, and the points $\sigma_1 = e^{i\psi_1}$ and $\sigma_2 = e^{i\psi_2}$ on Γ_1 correspond to the tips of the interfacial crack t_1 and t_2 on L in the z-plane. With the mapping function (3), Eqs. (1) and (2) can be rewritten in the ζ-plane as follows:

$$w = \frac{1}{2c_{44}}[\Psi(\zeta) + \overline{\Psi(\zeta)}], \quad \phi = \frac{1}{2\epsilon_{11}}[\Phi(\zeta) + \overline{\Phi(\zeta)}] \tag{5}$$

and

$$E_\rho - iE_\psi = -\frac{1}{\epsilon_{11}}\frac{\zeta}{|\zeta|}\frac{\Phi'(\zeta)}{|\Omega'(\zeta)|},$$

$$D_\rho - iD_\psi = \frac{\zeta}{|\zeta\Omega'(\zeta)|}\left[\frac{e_{15}}{c_{44}}\Psi'(\zeta) - \Phi'(\zeta)\right],$$

$$\sigma_{z\rho} - i\sigma_{z\psi} = \frac{\zeta}{|\zeta\Omega'(\zeta)|}\left[\Psi'(\zeta) + \frac{e_{15}}{\epsilon_{11}}\Phi'(\zeta)\right] \tag{6}$$

where $\Psi(\zeta)$ and $\Phi(\zeta)$ imply $\Psi[\Omega(\zeta)]$ and $\Phi[\Omega(\zeta)]$, respectively.

The assumption of no free charges and mechanical forces along the interface implies that both the traction and the normal components of the electric displacement can be taken as zero along the

[1] Engineering Mechanics and Design Laboratory, Department of Mechanical and Industrial Engineering, University of Toronto, Five King's College Road, Toronto, Ontario M5S 3G8, Canada.
[2] Mem. ASME.

Contributed by the Applied Mechanics Division of THE AMERICAN SOCIETY OF MECHANICAL ENGINEERS for publication in the ASME JOURNAL OF APPLIED MECHANICS. Manuscript received by the ASME Applied Mechanics Division, Apr. 16, 1999; final revision, July 1, 1999. Associate Technical Editor: M.-J. Pindera.

Downloaded 04 May 2010 to 171.66.16.27. Redistribution subject to ASME license or copyright; see http://www.asme.org/terms/Terms_Use.cfm

Jäger, J., 1996, "Stepwise Loading of Half-Spaces in Elliptical Contact," ASME JOURNAL OF APPLIED MECHANICS, Vol. 63, pp. 766–773.
Jäger, J., 1997, "Ein neues Prinzip der Kontaktmechanik," *Z. Angew. Math. Mech.*, Vol. 77, pp. S143-S144, presented at the GAMM meeting, May 1996.
Jäger, J., 1998, "A New Principle in Contact Mechanics," ASME *Journal of Tribology*, Vol. 120, pp. 677–685.
Jäger, J., 1999, "Equal Layers in Contact With Friction," *Contact Mechanics IV*, L. Gaul and C. A. Brebbia, eds., WIT Press, Southampton, pp. 99–108.
Johnson, K. L., 1985, *Contact Mechanics*, Cambridge, CUP.
Mindlin, R. D., 1949, "Compliance of Elastic Bodies in Contact," ASME JOURNAL OF APPLIED MECHANICS, Vol. 16, pp. 259–268.

Interfacial Debonding of an Elliptical Inhomogeneity in Piezoelectric Solids

W. Deng[1] and S. A. Meguid[1,2]

1 Introduction

In view of their inherent electromechanical behavior, piezoelectric materials have been widely used as sensors and actuators. These sensors and actuators are taken as inhomogeneities, which are either bonded to or embedded in the structure to provide the necessary stimulus to meet the demands of the electromechanical loading environment. The presence of a weaker interface between the matrix and the inhomogeneity affects the performance of these sensors and actuators. The weaker interface may also lead to interfacial delamination or debonding. Recently, Zhong and Meguid (1997) developed a generalized model to treat the partially debonded circular inhomogeneity problem in piezoelectric materials using series expansion technique. More recently, Deng and Meguid (1999) reexamined this problem and derived closed-form expressions for the complex field potentials and electro-elastic field intensity factors by considering the behavior of the field components at origin and infinity.

It is the object of this study to extend the previous work of Zhong and Meguid (1997) and Deng and Meguid (1999) to deal with the more general interfacial debonding problem of an *elliptical* piezoelectric inhomogeneity in an infinite piezoelectric matrix. The original boundary value problem can be solved by means of the appropriate conformal mapping transformation and the Laurent series expansion. The formulae for evaluating the electro-elastic field intensity factors of the interfacial curvilinear crack are derived from the general solution.

2 Basic Equations and General Solutions

Consider an infinite piezoelectric medium containing a partially debonded elliptical piezoelectric inhomogeneity subject to remote antiplane mechanical and in-plane electric loads, as shown in Fig. 1. Both the inhomogeneity and the matrix are assumed to be transversely isotropic and the inhomogeneity is infinitely extended in a direction perpendicular to the xy-plane. The regions occupied by the matrix and the inhomogeneity are referred to as regions 1 and 2 and denoted by S^+ and S^-, respectively. The interface between S^+ and S^- is represented by $L\ (=L_c + L_b)$, where L_c is the cracked part which denotes an insulated and traction-free interfacial curvilinear crack, while L_b is the bonded part of L.

For the present problem, only the antiplane displacement w and the in-plane electric field E_x and E_y are assumed to exist. They are independent of the longitudinal coordinate, such that $w = w(x, y)$, $E_x = E_x(x, y)$ and $E_y = E_y(x, y)$. Note that $E_i = -\phi_{,i}$, where $\phi(x, y)$ is the electric potential. Let w and ϕ be the real parts of the analytic functions $\Psi(z)$ and $\Phi(z)$, such that

$$w = \frac{1}{2c_{44}}[\Psi(z) + \overline{\Psi(z)}], \quad \phi = \frac{1}{2\epsilon_{11}}[\Phi(z) + \overline{\Phi(z)}] \tag{1}$$

where $z = x + iy$ is the complex variable and the overbar refers to the complex conjugate. The electric field strength, the electric displacements, and the stresses can be expressed by $\Psi(z)$ and $\Phi(z)$ as follows (Deng and Meguid, 1999):

$$E_x - iE_y = -\frac{1}{\epsilon_{11}}\Phi'(z), \quad D_x - iD_y = \frac{e_{15}}{c_{44}}\Psi'(z) - \Phi'(z),$$

$$\sigma_{zx} - i\sigma_{zy} = \Psi'(z) + \frac{e_{15}}{\epsilon_{11}}\Phi'(z) \tag{2}$$

where the primed quantities denote the derivatives with respect to the arguments, σ_{zx} and σ_{zy} are the shear stresses, D_x and D_y are the electric displacements, and c_{44}, e_{15}, and ϵ_{11} are the longitudinal shear modulus, piezoelectric modulus, and dielectric modulus, respectively. Let us now introduce the following mapping function:

$$z = \Omega(\zeta) = \frac{c}{2}[R\zeta + (R\zeta)^{-1}], \quad R\zeta = \frac{1}{c}[z + (z^2 - c^2)^{1/2}] \tag{3}$$

with

$$\zeta = \zeta_1 + i\zeta_2 = \rho e^{i\psi}, \quad c = (a^2 - b^2)^{1/2} = a(1 - \epsilon^2)^{1/2}$$

$$R = \left(\frac{a+b}{a-b}\right)^{1/2} = \left(\frac{1+\epsilon}{1-\epsilon}\right)^{1/2}, \quad \epsilon = \frac{b}{a} \tag{4}$$

where $2a$ and $2b$ are the major and minor diameters of the elliptical inhomogeneity. This mapping function transforms region 1 (S^+) of the z-plane into the exterior region of the unit circle Γ_1 ($\zeta = \sigma = e^{i\psi}$) in the transformed ζ-plane and region 2 (S^-) into the annular region between the unit circle Γ_1 and a circle Γ_2 of radius $\rho = 1/R$ representing a cut from $-c$ to $+c$ in the z-plane (see Fig. 2). Γ_1 consists of two parts (Γ_c and Γ_b) which correspond to L_c and L_b in the z-plane, and the points $\sigma_1 = e^{i\psi_1}$ and $\sigma_2 = e^{i\psi_2}$ on Γ_1 correspond to the tips of the interfacial crack t_1 and t_2 on L in the z-plane. With the mapping function (3), Eqs. (1) and (2) can be rewritten in the ζ-plane as follows:

$$w = \frac{1}{2c_{44}}[\Psi(\zeta) + \overline{\Psi(\zeta)}], \quad \phi = \frac{1}{2\epsilon_{11}}[\Phi(\zeta) + \overline{\Phi(\zeta)}] \tag{5}$$

and

$$E_\rho - iE_\psi = -\frac{1}{\epsilon_{11}}\frac{\zeta}{|\zeta|}\frac{\Phi'(\zeta)}{|\Omega'(\zeta)|},$$

$$D_\rho - iD_\psi = \frac{\zeta}{|\zeta\Omega'(\zeta)|}\left[\frac{e_{15}}{c_{44}}\Psi'(\zeta) - \Phi'(\zeta)\right],$$

$$\sigma_{z\rho} - i\sigma_{z\psi} = \frac{\zeta}{|\zeta\Omega'(\zeta)|}\left[\Psi'(\zeta) + \frac{e_{15}}{\epsilon_{11}}\Phi'(\zeta)\right] \tag{6}$$

where $\Psi(\zeta)$ and $\Phi(\zeta)$ imply $\Psi[\Omega(\zeta)]$ and $\Phi[\Omega(\zeta)]$, respectively.

The assumption of no free charges and mechanical forces along the interface implies that both the traction and the normal components of the electric displacement can be taken as zero along the

[1] Engineering Mechanics and Design Laboratory, Department of Mechanical and Industrial Engineering, University of Toronto, Five King's College Road, Toronto, Ontario M5S 3G8, Canada.
[2] Mem. ASME.

Contributed by the Applied Mechanics Division of THE AMERICAN SOCIETY OF MECHANICAL ENGINEERS for publication in the ASME JOURNAL OF APPLIED MECHANICS. Manuscript received by the ASME Applied Mechanics Division, Apr. 16, 1999; final revision, July 1, 1999. Associate Technical Editor: M.-J. Pindera.

Downloaded 04 May 2010 to 171.66.16.27. Redistribution subject to ASME license or copyright; see http://www.asme.org/terms/Terms_Use.cfm

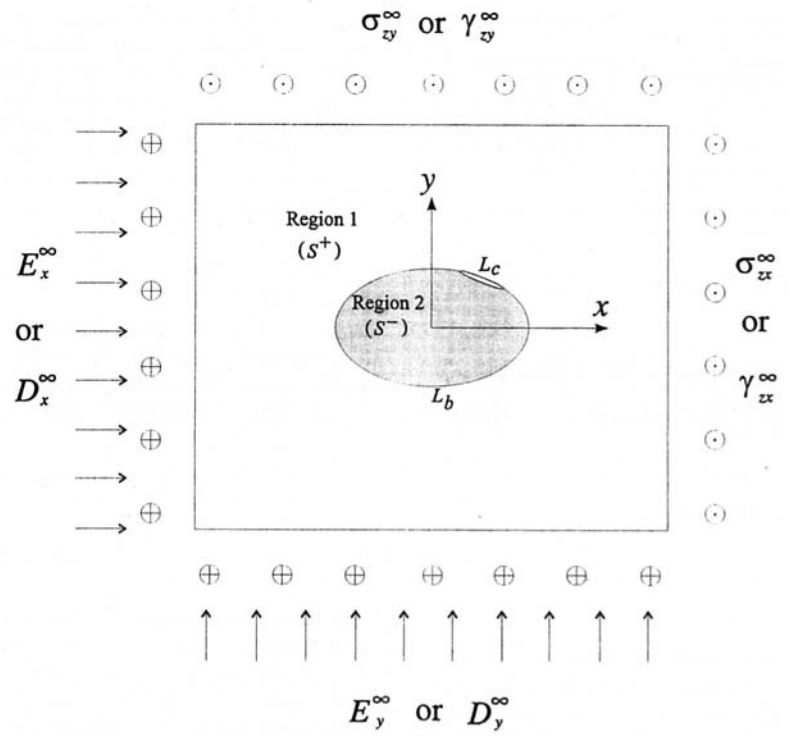


Fig. 1 Schematic of a partially debonded elliptical inhomogeneity in a piezoelectric matrix under antiplane shear and inplane electric field

cracked part L_c or Γ_c (Deeg, 1980; Pak, 1990), and that the displacement, electric potential, traction, and normal components of the electric displacement are continuous across the bonded part L_b or Γ_b. These conditions can be expressed in the transformed ζ-plane as

$$\sigma_{z\rho 1} = \sigma_{z\rho 2} = 0, \quad D_{\rho 1} = D_{\rho 2} = 0, \quad \sigma \in \Gamma_c$$

$$\sigma_{z\rho 1} = \sigma_{z\rho 2}, \quad D_{\rho 1} = D_{\rho 2}, \quad w_1 = w_2, \quad \phi_1 = \phi_2, \quad \sigma \in \Gamma_b. \tag{7}$$

In addition, the following conditions must be satisfied on Γ_2:

$$\Psi_2(\sigma/R) = \Psi_2(\bar{\sigma}/R), \quad \Phi_2(\sigma/R) = \Phi_2(\bar{\sigma}/R) \tag{8}$$

since the points σ/R and $\bar{\sigma}/R$ correspond to the same points of the cut from $-c$ to $+c$ in the z-plane.

Our task now is to determine the complex potentials Ψ_j and Φ_j $(j = 1, 2)$ for regions 1 and 2 which satisfy conditions (7) and (8).

The general solutions for the present problem can be obtained by using series expansion as described in Zhong and Meguid (1997). There are, however, a few critical differences between these two problems. For the elliptical inhomogeneity problem we are considering, all the complex potentials $\Psi_1(\zeta)$, $\Phi_1(\zeta)$, $\Psi_2(\zeta)$, and $\Phi_2(\zeta)$ should be expanded into the following Laurent series in the transformed ζ-plane:

$$\Psi_1(\zeta) = \sum_{k=0}^{\infty} (a_k^1 \zeta^{k+1} + b_k^1 \zeta^{-(k+1)}) \quad |\zeta| > 1 \tag{9}$$

$$\Phi_1(\zeta) = \sum_{k=0}^{\infty} (c_k^1 \zeta^{k+1} + d_k^1 \zeta^{-(k+1)}) \quad |\zeta| > 1 \tag{10}$$

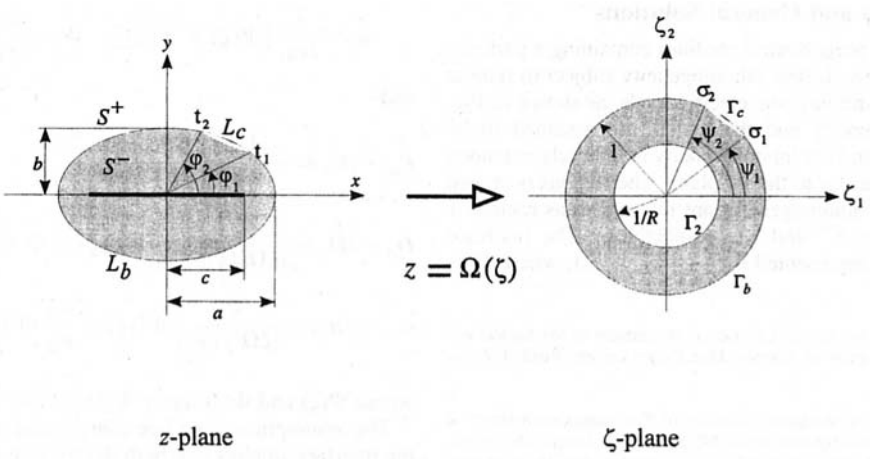


Fig. 2 Schematic of conformal mapping used

Downloaded 04 May 2010 to 171.66.16.27. Redistribution subject to ASME license or copyright; see http://www.asme.org/terms/Terms_Use.cfm

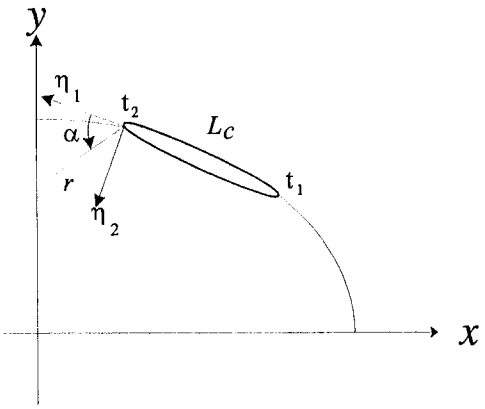


Fig. 3 Local coordinate system at a crack tip

$$\Psi_2(\zeta) = \sum_{k=0}^{\infty} (a_k^2 \zeta^{k+1} + b_k^2 \zeta^{-(k+1)}) \quad 1/R < |\zeta| < 1 \tag{11}$$

$$\Phi_2(\zeta) = \sum_{k=0}^{\infty} (c_k^2 \zeta^{k+1} + d_k^2 \zeta^{-(k+1)}) \quad 1/R < |\zeta| < 1 \tag{12}$$

where the constant terms correspond to rigid-body displacements and equi-potential body and have been omitted. The coefficients a_k^1 and c_k^1 can be determined from the remote boundary conditions, whereas the coefficients b_k^1, d_k^1, a_k^2, b_k^2, c_k^2, and d_k^2 are unknown and will be determined as part of the solution. The relations between a_k^2 and b_k^2, c_k^2, and d_k^2 can be obtained by substituting (11) and (12) into condition (8) as

$$a_k^2 = R^{2(k+1)} b_k^2, \quad c_k^2 = R^{2(k+1)} d_k^2. \tag{13}$$

Thus, once a_k^1 and c_k^1 are obtained from the remote boundary conditions, condition (13), together with Eqs. (93)–(102) given in Zhong and Meguid (1997), provides the relations needed for the determination of the remaining unknown coefficients, if the Eqs. (93) and (96) in their paper are replaced by

$$e_k = (k+1)\left(a_k^1 + \bar{b}_k^2 + \frac{e_{15}^1}{\epsilon_{11}^1} c_k^1 + \frac{e_{15}^2}{\epsilon_{11}^2} \bar{d}_k^2 \right) \tag{14}$$

and

$$g_k = (k+1)\left(\frac{e_{15}^1}{c_{44}^1} a_k^1 + \frac{e_{15}^2}{c_{44}^2} \bar{b}_k^2 - c_k^1 - \bar{d}_k^2 \right), \tag{15}$$

respectively, where e_k and g_k are also unknown coefficients defined in Eqs. (40) and (41) by Zhong and Meguid (1997).

3 Electro-elastic Field Intensity Factors

The electro-elastic field intensity factors, such as the stress intensity factor and the electric displacement intensity factor, are of major interest in the discussion of the fracture behavior of cracked piezoelectric media. For curvilinear cracks, it is convenient to introduce some local coordinate systems with origin at the crack tip. In our problem, we consider one of the crack tips, say the tip t_2. Let (η_1, η_2) be a local Cartesian system positioned at t_2 with the crack lying along the negative η_1-axis (Fig. 3). It can be shown (Gong and Meguid, 1994) that in the neighborhood of the crack tip

$$\zeta = \sigma_2 + \delta_2 \eta \tag{16}$$

where

$$\delta_2 = \frac{i\sigma_2}{|\Omega'(\sigma_2)|}, \quad \eta = \eta_1 + i\eta_2 = re^{i\alpha} \quad 0 \le \alpha \le 2\pi. \tag{17}$$

Substituting (16) into (9)–(12) and taking asymptotic expansions of the complex potentials with respect to η around the crack tip t_2, it can be shown that when $\eta = re^{i\alpha}$ tends to the bonded interface either from the matrix ($\alpha \to 2\pi$) or from the inhomogeneity ($\alpha \to 0$),

$$\Psi_1'^{+}(r) + \frac{e_{15}^1}{\epsilon_{11}^1} \Phi_1'^{+}(r) = \Psi_2'^{-}(r) + \frac{e_{15}^2}{\epsilon_{11}^2} \Phi_2'^{-}(r) = \frac{-\delta_2}{\sigma_2 \sqrt{(\sigma_2 - \sigma_1)\delta_2 r}} \left[A(\sigma_2) + \frac{e_{15}^1}{\epsilon_{11}^1} B(\sigma_2) \right] \tag{18}$$

$$\frac{e_{15}^1}{c_{44}^1} \Psi_1'^{+}(r) - \Phi_1'^{+}(r) = \frac{e_{15}^2}{c_{44}^2} \Psi_2'^{-}(r) - \Phi_2'^{-}(r) = \frac{-\delta_2}{\sigma_2 \sqrt{(\sigma_2 - \sigma_1)\delta_2 r}} \left[\frac{e_{15}^1}{c_{44}^1} A(\sigma_2) - B(\sigma_2) \right] \tag{19}$$

where the branch is cut along the bonded interface Γ_b, while $A(\sigma)$ and $B(\sigma)$ are functions given by

$$A(\sigma) = R(\sigma) - \tfrac{1}{2}[U_\infty(\sigma) + U_0(\sigma)], \quad B(\sigma) = \tilde{R}(\sigma) - \tfrac{1}{2}[V_\infty(\sigma) + V_0(\sigma)] \tag{20}$$

with $R(\zeta)$, $\tilde{R}(\zeta)$, $U_\infty(\zeta)$, $U_0(\zeta)$, $V_\infty(\zeta)$, and $V_0(\zeta)$ defined in Eqs. (77)–(82) of Zhong and Meguid (1997).

The stress intensity factor $K_T^{(2)}$ and the electric displacement intensity factor $K_D^{(2)}$ at the crack tip t_2 can thus be defined as

$$K_T^{(2)} = \lim_{r \to 0} \left\{ i\sqrt{2\pi r} \left[\Psi_1'^{+}(r) + \frac{e_{15}^1}{\epsilon_{11}^1} \Phi_1'^{+}(r) \right] \right\} = \frac{-i\sqrt{2\pi}\delta_2}{\sigma_2 \sqrt{(\sigma_2 - \sigma_1)\delta_2}} \left[A(\sigma_2) + \frac{e_{15}^1}{\epsilon_{11}^1} B(\sigma_2) \right] \tag{21}$$

and

$$K_D^{(2)} = \lim_{r \to 0} \left\{ i\sqrt{2\pi r} \left[\frac{e_{15}^1}{c_{44}^1} \Psi_1'^{+}(r) - \Phi_1'^{+}(r) \right] \right\} = \frac{-i\sqrt{2\pi}\delta_2}{\sigma_2 \sqrt{(\sigma_2 - \sigma_1)\delta_2}} \left[\frac{e_{15}^1}{c_{44}^1} A(\sigma_2) - B(\sigma_2) \right], \tag{22}$$

respectively. Accordingly, the crack-tip antiplane stress field and the in-plane electric displacement field can be expressed as

$$\sigma_{z\eta_1} - i\sigma_{z\eta_2} = \frac{iK_T^{(2)}}{\sqrt{2\pi r}} e^{-i\alpha/2} \quad (\pi \le \alpha \le 2\pi) \tag{23}$$

$$D_{\eta_1} - iD_{\eta_2} = \frac{iK_D^{(2)}}{\sqrt{2\pi r}} e^{-i\alpha/2} \quad (\pi \le \alpha \le 2\pi) \tag{24}$$

in the matrix, and

$$\sigma_{z\eta_1} - i\sigma_{z\eta_2} = \frac{-iK_T^{(2)}}{\sqrt{2\pi r}} e^{-i\alpha/2} \quad (0 \le \alpha \le \pi) \tag{25}$$

$$D_{\eta_1} - iD_{\eta_2} = \frac{-iK_D^{(2)}}{\sqrt{2\pi r}} e^{-i\alpha/2} \quad (0 \le \alpha \le \pi) \tag{26}$$

in the inhomogeneity.

The stress intensity factor $K_T^{(2)}$ and the electric displacement intensity factor $K_D^{(2)}$ are two constants that characterize the degree of the singularities of the mechanical and electric fields at the crack tip. They are related to the geometric and physical characteristics of both the matrix and the inhomogeneity and can be evaluated from the remote mechanical and electric loadings. Expressions

Downloaded 04 May 2010 to 171.66.16.27. Redistribution subject to ASME license or copyright; see http://www.asme.org/terms/Terms_Use.cfm

(21) and (22) reduce to those of Deng and Meguid (1999) when a partially debonded circular piezoelectric inhomogeneity is considered ($\epsilon = a/b = 1$, and $cR = 2a$).

Acknowledgments

The authors wish to acknowledge the financial support provided by NSERC, Materials and Manufacturing Ontario (MMO), Aluminum Company of America (ALCOA), and ALCOA Foundation of the USA.

References

Deeg, W. F., 1980, "The Analysis of Dislocation, Crack, and Inclusion Problems in Piezoelectric Solids," Ph.D. thesis, Stanford University, Stanford, CA.

Deng, W., and Meguid, S. A., 1999, "Closed Form Solutions for Partially Debonded Circular Inclusion in Piezoelectric Materials," *Acta. Mechanica,* in press.

Gong, S. X., and Meguid, S. A., 1994, "On the Debonding of an Elastic Elliptical Inhomogeneity Under Antiplane Shear," *Int. J. Fracture,* Vol. 67, pp. 37–52.

Pak, Y. E., 1990, "Crack Extension Force in a Piezoelectric Material," ASME JOURNAL OF APPLIED MECHANICS, Vol. 57, pp. 647–653.

Zhong, Z., and Meguid, S. A., 1997, "Interfacial Debonding of a Circular Inhomogeneity in Piezoelectric Materials," *Int. J. Solids Structures,* Vol. 34, pp. 1965–1984.

A Numerical Study on the Free Vibration of Symmetric Cross-Ply Laminated Cylindrical Helical Springs

V. Yıldırım[1]

The free-vibration problem of (0°/90°/90°/0°) laminated composite cylindrical helical springs is modeled theoretically as a continuous system. The first-order shear deformation theory is employed in the mathematical model. The free-vibration equations are solved by the transfer matrix method. A nondimensional parametric study is performed to investigate the effects of the number of active coils, the ratio of the diameter of the cylinder to the thickness of section, the helix pitch angle, and material types on the first six natural frequencies of helical springs with square section and fixed-fixed ends.

Introduction

Helical springs are used in various mechanisms to provide essential motions. The increasing usage of fiber composite materials encompasses applications in helical springs. In order to analyze dynamic behaviors of composite helical springs, an accurate formulation of the mathematical model is required. In this study, the cross-sectional rigidities on which the natural frequencies are closely depended are derived from the generalized Hooke's law in consideration of the classical beam theory. The rotary inertia, shear and axial deformation effects are included in the formulation. The free-vibration equations, which are 12 simultaneous first-order differential equations, are solved by the transfer matrix method.

Contributed by the Applied Mechanics Division of THE AMERICAN SOCIETY OF MECHANICAL ENGINEERS for publication in the ASME JOURNAL OF APPLIED MECHANICS. Manuscript received by the ASME Applied Mechanics Division, Apr. 28, 1999; final revision, Aug. 16, 1999. Associate Technical Editor: J. W. Ju.

[1] Associate Professor, Department of Mechanical Engineering, University of Çukurova, 01330 Balcalı-Adana, Turkey. e-mail: vebil@mail.cu.edu.tr.

Analysis

The governing equations of generally layered and pretwisted space rods made of an anisotropic material have been derived by Yıldırım (1999). The linear free-vibration equations of any symmetric cross-ply laminated space rod can be obtained referring to the Frenet reference frame, (**t**, **n**, **b**), as follows (Fig. 1(*a*)) (Yıldırım, 1999):

$$\frac{dU_t}{ds} = \chi U_n + A'_{11} T_t,$$

$$\frac{dU_n}{ds} = -\chi U_t + \tau U_b + \Omega_b + k' A'_{22} T_n,$$

$$\frac{dU_b}{ds} = -\tau U_n - \Omega_n + k' A'_{33} T_b,$$

$$\frac{d\Omega_t}{ds} = \chi \Omega_n + D'_{11} M_t,$$

$$\frac{d\Omega_n}{ds} = -\chi \Omega_t + \tau \Omega_b + D'_{22} M_n,$$

$$\frac{d\Omega_b}{ds} = -\tau \Omega_n + D'_{33} M_b,$$

$$\frac{dT_t}{ds} = \chi T_n - \bar{A}\omega^2 U_t,$$

$$\frac{dT_n}{ds} = \tau T_b - \chi T_t - \bar{A}\omega^2 U_n,$$

$$\frac{dT_b}{ds} = -\tau T_n - \bar{A}\omega^2 U_b,$$

$$\frac{dM_t}{ds} = \chi M_n - \bar{I}_1 \omega^2 \Omega_t,$$

$$\frac{dM_n}{ds} = \tau M_b - \chi M_t + T_b - \bar{I}_2 \omega^2 \Omega_n,$$

$$\frac{dM_b}{ds} = -\tau M_n - T_n - \bar{I}_3 \omega^2 \Omega_b \qquad (1)$$

where k' represents the shear correction factor, ω is the circular frequency (rad/s). χ and τ stand by the curvature and tortuosity of a curve in space. Denoting the helix pitch angle by α, and the radius of cylinder by R, the curvatures and the infinitesimal length of a cylindrical helical spring can be written as follows (Fig. 1(*b*)):

$$\chi = \cos^2 \alpha / R, \quad \tau = \sin \alpha \cos \alpha / R,$$

$$ds = R(1 + \tan^2 \alpha)^{1/2} d\theta. \qquad (2)$$

In Eqs. (1), T_t, T_n, T_b and M_t, M_n, M_b are the Frenet components of the internal force and internal moment vectors, respectively (Fig. 1(*a*)). The components of the displacement and rotation vectors for a point on the bar axis are represented by U_t, U_n, U_b and Ω_t, Ω_n, Ω_b, respectively. $\mathbf{A}' = 1/\mathbf{A}$ and $\mathbf{D}' = 1/\mathbf{D}$ matrices comprise the cross-sectional rigidities for symmetric cross-ply laminated composite bars. The elements of extensional and bending stiffness matrices, **A** and **D**, can be available in Yıldırım's (1999) study. The other quantities in Eqs. (1) are

$$\bar{A} = \sum_{k=1}^{N} \rho^{(k)} A^{(k)}, \quad \bar{I}_2 = \sum_{k=1}^{N} \rho^{(k)} I_n, \quad \bar{I}_3 = \sum_{k=1}^{N} \rho^{(k)} I_b,$$

Downloaded 04 May 2010 to 171.66.16.27. Redistribution subject to ASME license or copyright; see http://www.asme.org/terms/Terms_Use.cfm

(21) and (22) reduce to those of Deng and Meguid (1999) when a partially debonded circular piezoelectric inhomogeneity is considered ($\epsilon = a/b = 1$, and $cR = 2a$).

Acknowledgments

The authors wish to acknowledge the financial support provided by NSERC, Materials and Manufacturing Ontario (MMO), Aluminum Company of America (ALCOA), and ALCOA Foundation of the USA.

References

Deeg, W. F., 1980, "The Analysis of Dislocation, Crack, and Inclusion Problems in Piezoelectric Solids," Ph.D. thesis, Stanford University, Stanford, CA.

Deng, W., and Meguid, S. A., 1999, "Closed Form Solutions for Partially Debonded Circular Inclusion in Piezoelectric Materials," *Acta. Mechanica,* in press.

Gong, S. X., and Meguid, S. A., 1994, "On the Debonding of an Elastic Elliptical Inhomogeneity Under Antiplane Shear," *Int. J. Fracture,* Vol. 67, pp. 37–52.

Pak, Y. E., 1990, "Crack Extension Force in a Piezoelectric Material," ASME JOURNAL OF APPLIED MECHANICS, Vol. 57, pp. 647–653.

Zhong, Z., and Meguid, S. A., 1997, "Interfacial Debonding of a Circular Inhomogeneity in Piezoelectric Materials," *Int. J. Solids Structures,* Vol. 34, pp. 1965–1984.

A Numerical Study on the Free Vibration of Symmetric Cross-Ply Laminated Cylindrical Helical Springs

V. Yıldırım[1]

The free-vibration problem of (0°/90°/90°/0°) laminated composite cylindrical helical springs is modeled theoretically as a continuous system. The first-order shear deformation theory is employed in the mathematical model. The free-vibration equations are solved by the transfer matrix method. A nondimensional parametric study is performed to investigate the effects of the number of active coils, the ratio of the diameter of the cylinder to the thickness of section, the helix pitch angle, and material types on the first six natural frequencies of helical springs with square section and fixed-fixed ends.

Introduction

Helical springs are used in various mechanisms to provide essential motions. The increasing usage of fiber composite materials encompasses applications in helical springs. In order to analyze dynamic behaviors of composite helical springs, an accurate formulation of the mathematical model is required. In this study, the cross-sectional rigidities on which the natural frequencies are closely depended are derived from the generalized Hooke's law in consideration of the classical beam theory. The rotary inertia, shear and axial deformation effects are included in the formulation. The free-vibration equations, which are 12 simultaneous first-order differential equations, are solved by the transfer matrix method.

Contributed by the Applied Mechanics Division of THE AMERICAN SOCIETY OF MECHANICAL ENGINEERS for publication in the ASME JOURNAL OF APPLIED MECHANICS. Manuscript received by the ASME Applied Mechanics Division, Apr. 28, 1999; final revision, Aug. 16, 1999. Associate Technical Editor: J. W. Ju.

[1] Associate Professor, Department of Mechanical Engineering, University of Çukurova, 01330 Balcalı-Adana, Turkey. e-mail: vebil@mail.cu.edu.tr.

Analysis

The governing equations of generally layered and pretwisted space rods made of an anisotropic material have been derived by Yıldırım (1999). The linear free-vibration equations of any symmetric cross-ply laminated space rod can be obtained referring to the Frenet reference frame, (**t**, **n**, **b**), as follows (Fig. 1(*a*)) (Yıldırım, 1999):

$$\frac{dU_t}{ds} = \chi U_n + A'_{11} T_t,$$

$$\frac{dU_n}{ds} = -\chi U_t + \tau U_b + \Omega_b + k' A'_{22} T_n,$$

$$\frac{dU_b}{ds} = -\tau U_n - \Omega_n + k' A'_{33} T_b,$$

$$\frac{d\Omega_t}{ds} = \chi \Omega_n + D'_{11} M_t,$$

$$\frac{d\Omega_n}{ds} = -\chi \Omega_t + \tau \Omega_b + D'_{22} M_n,$$

$$\frac{d\Omega_b}{ds} = -\tau \Omega_n + D'_{33} M_b,$$

$$\frac{dT_t}{ds} = \chi T_n - \bar{A}\omega^2 U_t,$$

$$\frac{dT_n}{ds} = \tau T_b - \chi T_t - \bar{A}\omega^2 U_n,$$

$$\frac{dT_b}{ds} = -\tau T_n - \bar{A}\omega^2 U_b,$$

$$\frac{dM_t}{ds} = \chi M_n - \bar{I}_1 \omega^2 \Omega_t,$$

$$\frac{dM_n}{ds} = \tau M_b - \chi M_t + T_b - \bar{I}_2 \omega^2 \Omega_n,$$

$$\frac{dM_b}{ds} = -\tau M_n - T_n - \bar{I}_3 \omega^2 \Omega_b \qquad (1)$$

where k' represents the shear correction factor, ω is the circular frequency (rad/s). χ and τ stand by the curvature and tortuosity of a curve in space. Denoting the helix pitch angle by α, and the radius of cylinder by R, the curvatures and the infinitesimal length of a cylindrical helical spring can be written as follows (Fig. 1(*b*)):

$$\chi = \cos^2 \alpha / R, \quad \tau = \sin \alpha \cos \alpha / R,$$

$$ds = R(1 + \tan^2 \alpha)^{1/2} d\theta. \qquad (2)$$

In Eqs. (1), T_t, T_n, T_b and M_t, M_n, M_b are the Frenet components of the internal force and internal moment vectors, respectively (Fig. 1(*a*)). The components of the displacement and rotation vectors for a point on the bar axis are represented by U_t, U_n, U_b and Ω_t, Ω_n, Ω_b, respectively. $\mathbf{A}' = 1/\mathbf{A}$ and $\mathbf{D}' = 1/\mathbf{D}$ matrices comprise the cross-sectional rigidities for symmetric cross-ply laminated composite bars. The elements of extensional and bending stiffness matrices, **A** and **D**, can be available in Yıldırım's (1999) study. The other quantities in Eqs. (1) are

$$\bar{A} = \sum_{k=1}^{N} \rho^{(k)} A^{(k)}, \quad \bar{I}_2 = \sum_{k=1}^{N} \rho^{(k)} I_n, \quad \bar{I}_3 = \sum_{k=1}^{N} \rho^{(k)} I_b,$$

Downloaded 04 May 2010 to 171.66.16.27. Redistribution subject to ASME license or copyright; see http://www.asme.org/terms/Terms_Use.cfm

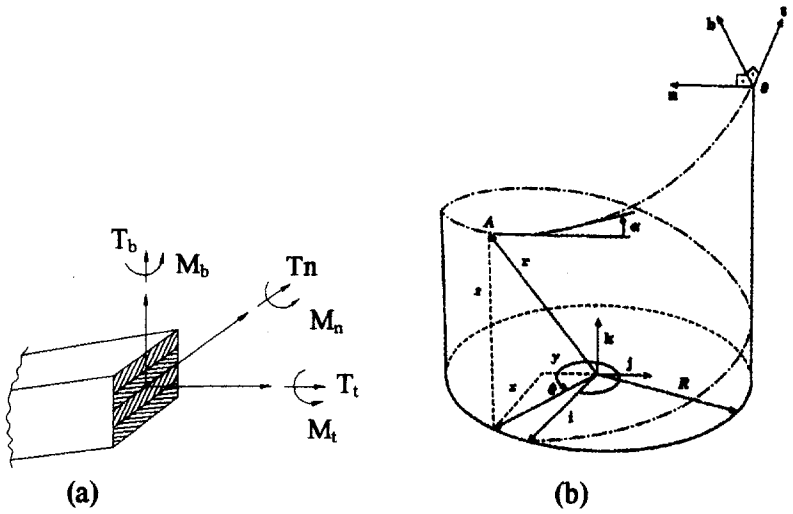


Fig. 1 (*a*) Stress resultants, (*b*) geometry of a cylindrical helical spring

$$\bar{I}_1 \cong \frac{1}{40}\sum_{k=1}^{N} \rho^{(k)} A^{4(k)}/(I_n^{(k)} + I_b^{(k)}) \quad \text{(for rectangular section)}. \quad (3)$$

Here ρ is the mass density, A is the undeformed cross-sectional area, N is the total number of plies, and I_n and I_b are the inertia moments about the normal and binormal axes, respectively.

Equations (1) can be expressed in a matrix notation as

$$d\mathbf{Z}(s)/ds = \mathbf{D}^o\mathbf{Z}(s) \quad (4)$$

where $\mathbf{D}^o$ is the dynamic differential matrix. In the transfer matrix method, the solution to Eq. (4) is given as (Pestel and Leckie, 1963)

$$\mathbf{Z}(s = 2\pi nR/\cos\alpha) = \mathbf{F}\mathbf{Z}(s = 0) \quad (5)$$

where n is the number of active turns. A series expression of the overall transfer matrix, $\mathbf{F}$, obtained by the Cayley-Hamilton theorem is as follows:

$$\mathbf{F}(s) = \sum_{k=0}^{11} \Phi_k(s)\mathbf{D}^{ok}. \quad (6)$$

As is well known, numerical computation of the overall transfer matrix in an accurate manner is a crucial step in the transfer matrix method. The numerical algorithm developed by Yıldırım (1996) allows utilization of Eq. (6) with a variable number of terms depending on the degree of required accuracy for large helix angles, the ratio of the cylinder diameter to the wire diameter, and the number of active turns. After computing $\mathbf{F}$, the frequency equation can be obtained from the boundary conditions given at both ends. In this study, free-vibration frequencies are obtained by the method of searching determinant.

Results

A composite straight beam is examined to check the accuracy of the present frequencies. The material and cross-sectional properties are given as follows: $G_{23} = 2.54$ GPa, $E_1 = 129$ GPa, $E_2 = E_3 = 9.39$ GPa, $G_{12} = G_{13} = 4.3$ GPa, $k' = 1.2$, $\nu_{12} = 0.3$, $\rho = 1551.47$ kg/m^3, width = 1.27 cm, d = thickness = 0.317 cm, length/thickness = 60. Here E_i, G_{ij}, ν_{ij} represent the Young's moduli, shear moduli, and Poisson's ratios for an orthotropic lamina. The results are given in Table 1. A good agreement is observed with the theoretical and experimental results reported in the literature.

After verifying the accuracy of the present results, a nondimensional parametric study of a symmetric cross-ply laminated cylindrical helical spring (0°/90°/90°/0°) with fixed-fixed ends and square section is performed to investigate the effects of vibrational parameters on the natural frequencies. It is assumed that each layer has the same thickness. Two different material types are examined in this section. The properties of these materials are given in Table 2. The nondimensional frequency is determined as

$$\varpi = \omega\sqrt{\rho A R^4/(E_1 I_n)}. \quad (7)$$

First, the effect of the D/d (diameter of the cylinder/thickness) ratios on the natural frequencies of the spring is investigated for $n = 3$ and $\alpha = 5$ deg. The results are presented in Fig. 2 for carbon-epoxy and Kevlar-epoxy materials. As observed from Fig. 2, the nondimensional natural frequencies increase slightly with increasing D/d ratios. The natural frequencies for carbon-epoxy

Table 1 Fundamental frequencies (in Hertz) of beam with rectangular section

	Fiber orientation	
	0 deg	90 deg
Abarcar and Cunniff (1972) (Experimental)	126.5	35.5
Hodges et al. (1991) (Finite element)	128.94	34.858
Present (Transfer matrix)	128.62	34.768

Table 2 The transversely isotropic material properties used in this study

	Carbon-Epoxy (T300/N5208)	Kevlar 49-Epoxy
E_1 (GPa)	181.0	76.0
$E_2 = E_3$ (GPa)	10.3	5.56
$G_{12} = G_{13}$ (GPa)	7.17	2.30
G_{23} (GPa)	3.433	1.618
ρ (kg/m^3)	1600.0	1460.0
ν_{12}	0.28	0.34

Downloaded 04 May 2010 to 171.66.16.27. Redistribution subject to ASME license or copyright; see http://www.asme.org/terms/Terms_Use.cfm

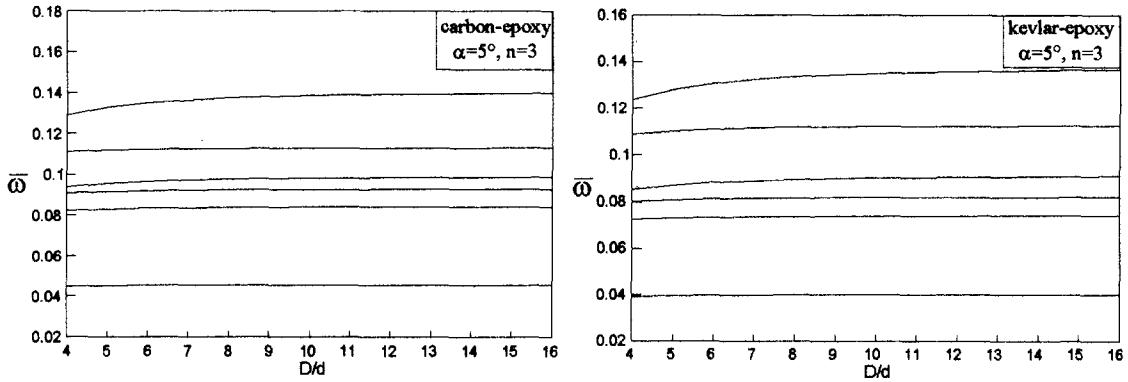


Fig. 2 Variational of the natural frequencies with *D/d* ratios and material types

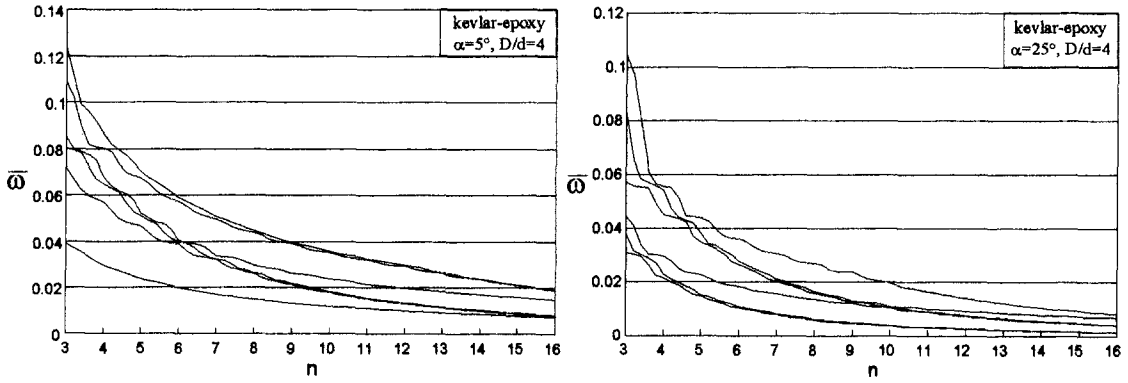


Fig. 3 Variation of the natural frequencies with *n* for Kevlar-epoxy material

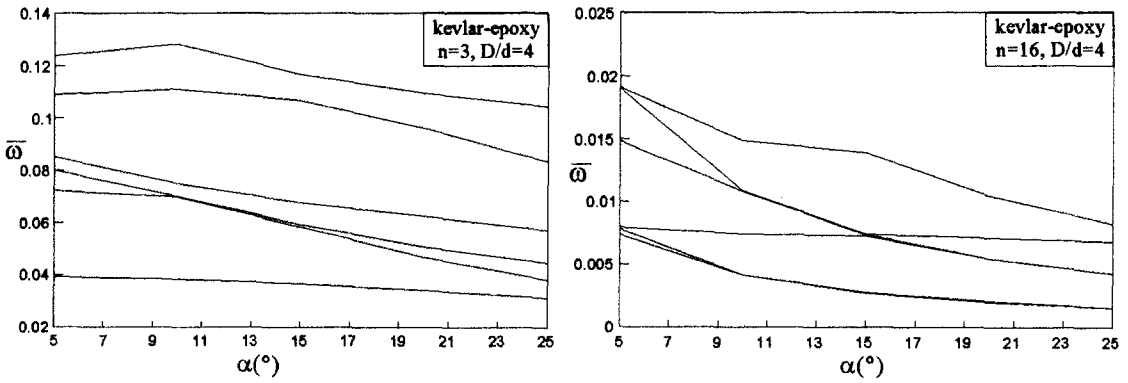


Fig. 4 Variation of the natural frequencies with helix pitch angle

material are higher than those frequencies of the spring made of a Kevlar-epoxy material.

Second, the effect of the number of active turns is investigated. Figure 3 shows the change of free-vibration frequencies of the Kevlar-epoxy spring with the number of active coils (n = 3–16) for D/d = 4 and α = 5 deg and α = 25 deg. The increase in the number of active coils results in a decrement in the natural frequencies for all values of the helix pitch angles. The change in the number of turns affects considerably the natural frequencies.

Finally, the influence of the helix pitch angle is studied. Figure 4 shows the variation of the first six natural frequencies of the Kevlar-epoxy spring for D/d = 4, and n = 3 and n = 16. These figures are obtained with increment of 5 degrees. When the helix pitch angle increases, the natural frequencies decrease. For the higher values of n, a fast decrement is observed in all the frequency values.

Conclusions

In this study, the free-vibration analysis of symmetric cross-ply laminated helical springs is reported. For the first six natural frequencies, the effects of the material types, helix pitch angle, number of active turns, and the ratio of the diameter of the cylinder to the thickness are investigated.

Acknowledgments

This study was sponsored by the Scientific and Technical Research Council of Turkey (TUBITAK).

References

Abarcar, R. B., and Cunniff, P. F., 1972, "The Vibration of Cantilever Beams of Fiber Reinforced Material," *J. Composite Materials,* Vol. 6, pp. 504–517.

Hodges, D. H., Atilgan, A. R., Fulton, M. V., and Rehfield, L. W., 1991, "Free-

Downloaded 04 May 2010 to 171.66.16.27. Redistribution subject to ASME license or copyright; see http://www.asme.org/terms/Terms_Use.cfm

Vibration Analysis of Composite Beams," *Journal of American Helicopter Society*, Vol. 36, No. 3, pp. 36–47.

Pestel, E. C., and Leckie, F. A., 1963, *Matrix Methods in Elastomechanics*, McGraw-Hill, New York.

Yıldırım, V., 1996, "Investigation of Parameters Affecting Free Vibration Frequency of Helical Springs," *Int. J. Numer. Meth. Engng.*, Vol. 39, No. 1, pp. 99–114.

Yıldırım, V., 1999, "Governing Equations of Initially Twisted Elastic Space Rods Made of Laminated Composite Materials," *International Journal of Engineering Sciences*, Vol. 37, No. 8, pp. 1007–1035.

Application of Laser Ultrasonics to Develop Dispersion Curves for Elastic Plates

C. Eisenhardt,[1] L. J. Jacobs,[2] and J. Qu[3]

Introduction

This technical note reports on a study that combines laser ultrasonic techniques with the two-dimensional Fourier transform to develop dispersion curves for Lamb waves propagating in an aluminum plate. This application demonstrates that by combing the high fidelity, broad bandwidth, point source/receiver, and noncontact nature of laser ultrasonics with the robustness and accuracy of the two-dimensional Fourier transform, it is possible to develop dispersion curves that contain more modes (through a broader bandwidth) than previously possible.

There has been extensive research into the numerical solution and application of the Rayleigh-Lamb frequency equations since the study by Mindlin (1960). Previous experimental studies have validated portions of the dispersion curves for Lamb waves propagating in a flat plate, but there has been limited success in developing a frequency spectrum that contains multiple modes through a broad frequency bandwidth. Alleyne and Cawley (1991) used the two-dimensional Fourier transform with piezoelectric (PZT) transducers to develop dispersion curves for the two lowest propagating Lamb wave modes, while Costley et al. (1994) combined laser generation and a (point) PZT receiver with the two-dimensional Fourier transform to develop dispersion curves through a limited frequency range. The PZT transducers used in each of these studies can introduce frequency biases that limit the fidelity of these measurements. Schumacher et al. (1993) integrated laser ultrasonics with a signal processing technique that extracted phase velocities from fast Fourier transforms of signals measured at two different points. Unfortunately, a requirement of this two-point phase velocity extraction method is that each propagating mode must be clearly discernible; each mode is identified and windowed (in the time domain) in a relatively arbitrary fashion. As a result, they could only identify three well-separated modes.

The motivation for the current research is to demonstrate the effectiveness of combining laser ultrasonic techniques with the two-dimensional Fourier transform to develop dispersion curves for Lamb waves propagating in an aluminum plate. The experimental procedure makes high-fidelity (resonance-free) measurements of ultrasonic waveforms over a wide frequency range (200 kHz to 10 MHz). The point source/receiver nature of laser ultrasonics enables a very fine spatial discretization, thus allowing for a wide wave number range (to 8000/m in this study). A final advantage is that the proposed technique is free from synthetic signal processing artifacts—there is no arbitrary identification and windowing of specific modes within a complicated waveform.

Experimental Procedure

The beam from a Nd:YAG laser (450 mJ, 4–6 ns pulse) is attenuated and focused before striking the specimen. The focusing lens and alignment mirror are mounted on a (micrometer-driven) translation stage that allows for precise movement of the optical source (see Fig. 1). This setup provides a laser source that generates exactly the same ultrasonic signal, at multiple, equally spaced locations, throughout each test. Laser detection of these waves is accomplished with a heterodyne interferometer (Bruttomesso et al., 1993) that uses the Doppler shift to measure out-of-plane surface velocity (particle velocity) at a point on the specimen's surface. The plate (203 mm by 153 mm) used in this study is 0.93-mm thick 3003 aluminum. Since all measurements are made prior to the arrival of any reflections from the edges, the specimen is treated as an infinite plate.

Experimental Results and Discussion

While the receiver is kept in a fixed position, the source is placed at 50 equally spaced locations (see Fig. 1); an incremental

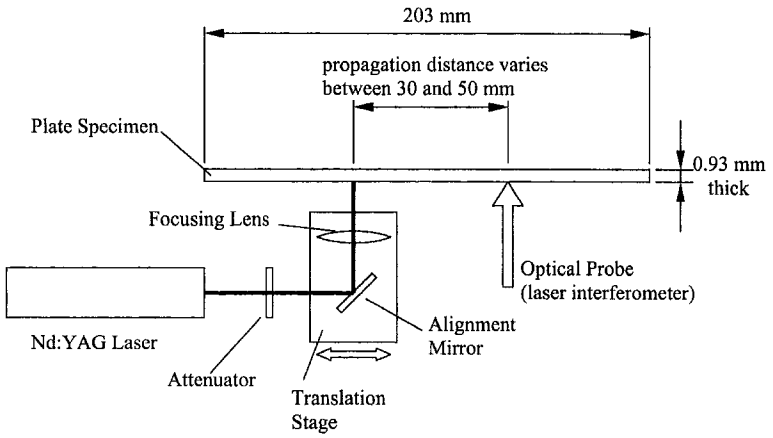


Fig. 1 Schematic of the experimental setup

[1] School of Civil and Environmental Engineering, Georgia Institute of Technology, Atlanta, GA 30332.

[2] To whom correspondence should be addressed. School of Civil and Environmental Engineering, Georgia Institute of Technology, Atlanta, GA 30332. Mem. ASME.

[3] G. W. Woodruff School of Mechanical Engineering, Georgia Institute of Technology, Atlanta, GA 30332. Mem. ASME.

Contributed by the Applied Mechanics Division of THE AMERICAN SOCIETY OF MECHANICAL ENGINEERS for publication in the ASME JOURNAL OF APPLIED MECHANICS. Manuscript received by the ASME Applied Mechanics Division, Mar. 24, 1999; final revision, Aug. 16, 1999. Associate Technical Editor: V. K. Kinra.

Downloaded 04 May 2010 to 171.66.16.27. Redistribution subject to ASME license or copyright; see http://www.asme.org/terms/Terms_Use.cfm

Vibration Analysis of Composite Beams," *Journal of American Helicopter Society*, Vol. 36, No. 3, pp. 36–47.

Pestel, E. C., and Leckie, F. A., 1963, *Matrix Methods in Elastomechanics*, McGraw-Hill, New York.

Yıldırım, V., 1996, "Investigation of Parameters Affecting Free Vibration Frequency of Helical Springs," *Int. J. Numer. Meth. Engng.*, Vol. 39, No. 1, pp. 99–114.

Yıldırım, V., 1999, "Governing Equations of Initially Twisted Elastic Space Rods Made of Laminated Composite Materials," *International Journal of Engineering Sciences*, Vol. 37, No. 8, pp. 1007–1035.

Application of Laser Ultrasonics to Develop Dispersion Curves for Elastic Plates

C. Eisenhardt,[1] L. J. Jacobs,[2] and J. Qu[3]

Introduction

This technical note reports on a study that combines laser ultrasonic techniques with the two-dimensional Fourier transform to develop dispersion curves for Lamb waves propagating in an aluminum plate. This application demonstrates that by combing the high fidelity, broad bandwidth, point source/receiver, and noncontact nature of laser ultrasonics with the robustness and accuracy of the two-dimensional Fourier transform, it is possible to develop dispersion curves that contain more modes (through a broader bandwidth) than previously possible.

There has been extensive research into the numerical solution and application of the Rayleigh-Lamb frequency equations since the study by Mindlin (1960). Previous experimental studies have validated portions of the dispersion curves for Lamb waves propagating in a flat plate, but there has been limited success in developing a frequency spectrum that contains multiple modes through a broad frequency bandwidth. Alleyne and Cawley (1991) used the two-dimensional Fourier transform with piezoelectric (PZT) transducers to develop dispersion curves for the two lowest propagating Lamb wave modes, while Costley et al. (1994) combined laser generation and a (point) PZT receiver with the two-dimensional Fourier transform to develop dispersion curves through a limited frequency range. The PZT transducers used in each of these studies can introduce frequency biases that limit the fidelity of these measurements. Schumacher et al. (1993) integrated laser ultrasonics with a signal processing technique that extracted phase velocities from fast Fourier transforms of signals measured at two different points. Unfortunately, a requirement of this two-point phase velocity extraction method is that each propagating mode must be clearly discernible; each mode is identified and windowed (in the time domain) in a relatively arbitrary fashion. As a result, they could only identify three well-separated modes.

The motivation for the current research is to demonstrate the effectiveness of combining laser ultrasonic techniques with the two-dimensional Fourier transform to develop dispersion curves for Lamb waves propagating in an aluminum plate. The experimental procedure makes high-fidelity (resonance-free) measurements of ultrasonic waveforms over a wide frequency range (200 kHz to 10 MHz). The point source/receiver nature of laser ultrasonics enables a very fine spatial discretization, thus allowing for a wide wave number range (to 8000/m in this study). A final advantage is that the proposed technique is free from synthetic signal processing artifacts—there is no arbitrary identification and windowing of specific modes within a complicated waveform.

Experimental Procedure

The beam from a Nd:YAG laser (450 mJ, 4–6 ns pulse) is attenuated and focused before striking the specimen. The focusing lens and alignment mirror are mounted on a (micrometer-driven) translation stage that allows for precise movement of the optical source (see Fig. 1). This setup provides a laser source that generates exactly the same ultrasonic signal, at multiple, equally spaced locations, throughout each test. Laser detection of these waves is accomplished with a heterodyne interferometer (Bruttomesso et al., 1993) that uses the Doppler shift to measure out-of-plane surface velocity (particle velocity) at a point on the specimen's surface. The plate (203 mm by 153 mm) used in this study is 0.93-mm thick 3003 aluminum. Since all measurements are made prior to the arrival of any reflections from the edges, the specimen is treated as an infinite plate.

Experimental Results and Discussion

While the receiver is kept in a fixed position, the source is placed at 50 equally spaced locations (see Fig. 1); an incremental

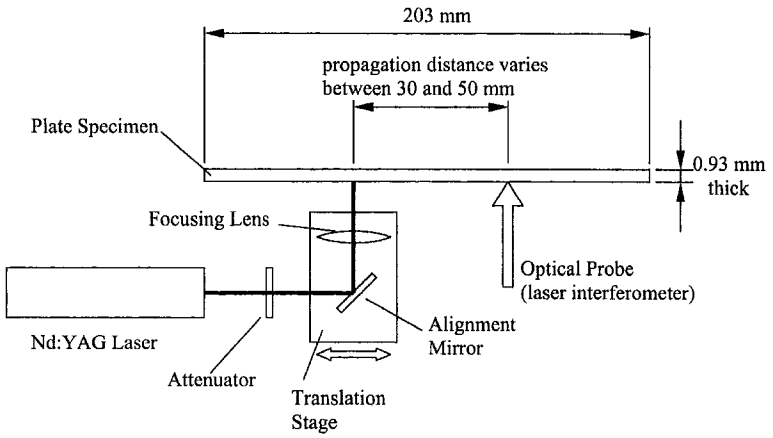


Fig. 1 Schematic of the experimental setup

[1] School of Civil and Environmental Engineering, Georgia Institute of Technology, Atlanta, GA 30332.

[2] To whom correspondence should be addressed. School of Civil and Environmental Engineering, Georgia Institute of Technology, Atlanta, GA 30332. Mem. ASME.

[3] G. W. Woodruff School of Mechanical Engineering, Georgia Institute of Technology, Atlanta, GA 30332. Mem. ASME.

Contributed by the Applied Mechanics Division of THE AMERICAN SOCIETY OF MECHANICAL ENGINEERS for publication in the ASME JOURNAL OF APPLIED MECHANICS. Manuscript received by the ASME Applied Mechanics Division, Mar. 24, 1999; final revision, Aug. 16, 1999. Associate Technical Editor: V. K. Kinra.

Downloaded 04 May 2010 to 171.66.16.27. Redistribution subject to ASME license or copyright; see http://www.asme.org/terms/Terms_Use.cfm

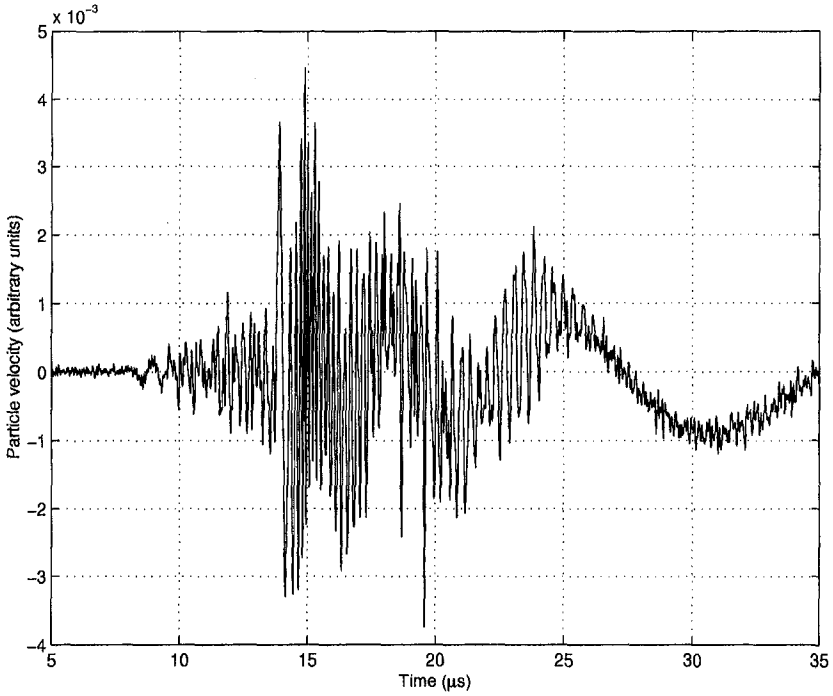


Fig. 2 Typical time-domain signal

(Δx) distance of 0.40 mm separates each source location. The closest source-to-receiver (propagation) distance is 30 mm while the farthest propagation distance is 50 mm; a typical time domain signal is shown in Fig. 2. This results in the (generation and) detection of 50 waveforms, each with a different propagation distance and each generated with exactly the same laser source. The two-dimensional Fourier transform routine operates on this set of (50) equally spaced, transient waveforms by computing a temporal Fourier transform (time to frequency domain) followed by a spatial Fourier transform (position to wave number domain). There is no windowing; the temporal fast Fourier transform operates on the entire transient waveform, and each of these 50 frequency domain signals (in their entirety) are used in the spatial fast Fourier transform. Note that the two-dimensional Fourier transform is most effective with a large number of broadband, transient signals, measured with a small spatial sampling distance.

The resulting frequency (f) versus wave number (k) spectrum indicates that certain k-f combinations have significant amplitudes (peaks), and these combinations are solutions to the plate's dispersion relationship (the plate's individual modes); a contour plot is shown in Fig. 3. The lowest (first from bottom to top) "mountain range" in Fig. 2 represents the first antisymmetric mode (a_0), while the next set of peaks is the first symmetric mode (s_0). There are more peaks (higher modes) that have definitive cutoff frequen-

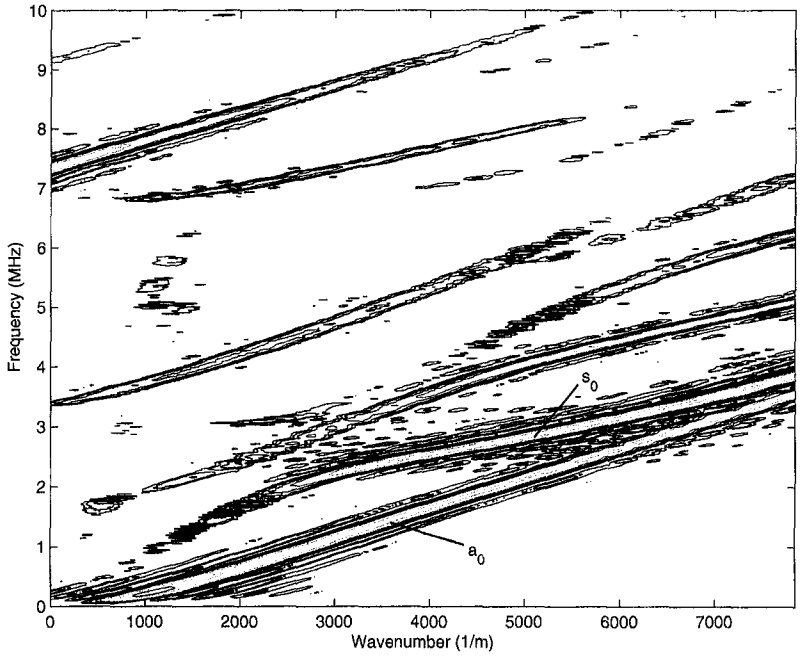


Fig. 3 Contour plot of the frequency versus wave number spectrum

Downloaded 04 May 2010 to 171.66.16.27. Redistribution subject to ASME license or copyright; see http://www.asme.org/terms/Terms_Use.cfm

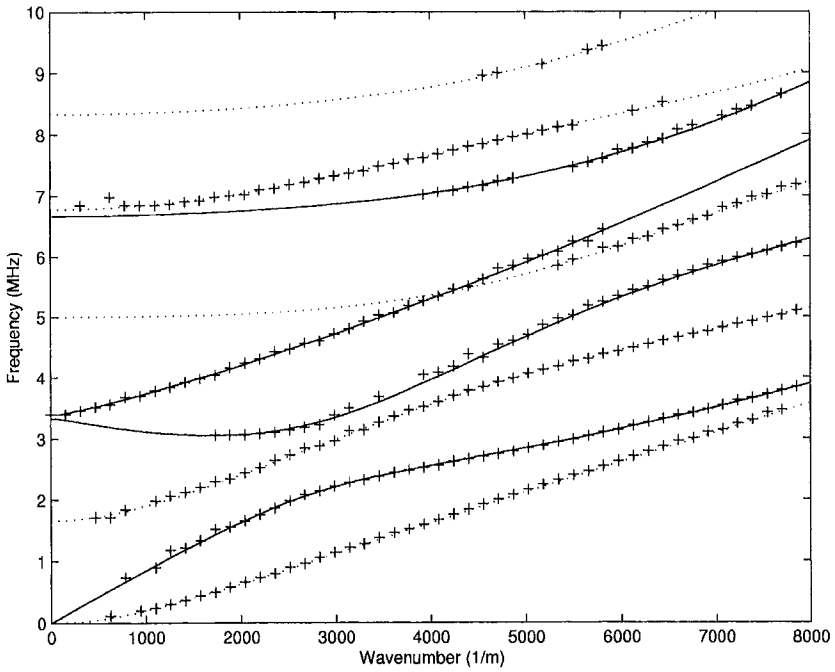


Fig. 4 Comparison of experimental and theoretical dispersion curves for the first nine modes: + experimental; solid line theoretical symmetric mode; and dotted line theoretical antisymmetric mode

cies; these higher modes only exist above a specific lower frequency value. Dispersion is clearly visible in all of the modes; they follow a curve in the beginning, and turn into straight lines at higher wave numbers (or frequencies). Finally, spatial aliasing (the spatial Nyquist "frequency" is 7854/m, $\pi/\Delta x$) is shown in the straight-line (nondispersive) peak that appears near 7 MHz (and to a lesser extent near 9 MHz). This peak is the spurious continuation of the intersection of the a_0 and s_0 modes at higher wave numbers; note that its slope is the Rayleigh phase velocity (and it is removed in Fig. 4).

The local maxima in the vicinity of each peak is plotted in Fig. 4 and compared to theoretically calculated dispersion curves (following Mindlin, 1960). The theoretical curves for the first nine modes are shown as solid (symmetric) and dotted (antisymmetric) curves, while the experimental peaks (maxima) are the crosses. There is excellent agreement between the experimental and theoretical dispersion curves through a wide frequency bandwidth (to 10 MHz). For example, the asymptotic behavior of the a_0 and s_0 modes tending towards the Rayleigh phase velocity is clearly visible. The two-dimensional Fourier transform provides accurate definition (for extended portions) of each of the first nine propagating Lamb modes; this level of experimental clarity has not been previously published.

Conclusion

This note clearly demonstrates the effectiveness of applying laser ultrasonic techniques and the two-dimensional Fourier transform to experimentally determine the dispersion curves of Lamb waves propagating in a flat plate. The experimental results presented here underscore the validity of the (well-accepted) theoretical dispersion curves through a broader bandwidth and for more modes than previously possible.

Acknowledgment

This work is supported by the Office of Naval Research M-URI Program "Integrated Diagnostics" (Contract number: N00014-95-1-0539). The Deutscher Akademischer Austausch Dienst (DAAD) provided partial support to Christoph Eisenhardt, and the authors wish to thank Mr. Kai Heller for his contributions.

References

Alleyne, D., and Cawley, P., 1991, "A Two-Dimensional Fourier Transform Method for Measurement of Propagating Multimode Signals," *J. Acoustic. Soc. Am.*, Vol. 89, No. 3, pp. 1159–1168.

Bruttomesso, D. A., Jacobs, L. J., and Costley, R. D., 1993, "Development of an Interferometer for Acoustic Emission Testing," *Journal of Engineering Mechanics*, Vol. 119, No. 11, pp. 2303–2316.

Costley, R. D., Berthelot, Y. H., and Jacobs, L. J., 1994, "Laser-Based Techniques to Resolve Mode Propagation of Lamb Waves in Plates," *Journal of Acoustic Emission*, Vol. 12, No. 1-2, pp. 27–38.

Mindlin, R. D., 1960, "Waves and Vibrations in Isotropic Elastic Plates," *Structural Mechanics*, J. N. Goodier and N. J. Hoff, eds. Pergamon Press, New York.

Schumacher, N. A., Burger, C. P., and Gien, P. H., 1993, "A Laser-Based Investigation of Higher-Order Modes in Transient Lamb Waves," *J. Acoustic. Soc. Am.*, Vol. 93, No. 5, pp. 2981–2984.

Downloaded 04 May 2010 to 171.66.16.27. Redistribution subject to ASME license or copyright; see http://www.asme.org/terms/Terms_Use.cfm

Journal of Applied Mechanics

Discussion

Dynamic Buckling and Post-buckling of Imperfect Cylindrical Shells Under Mechanical and Thermal Loads, Based on the Three-Dimensional Theory of Elasticity[1]

R. L. Citerley.[2] The analysis procedure for any method in applied mechanics requires five steps:

1 Develop the basic governing field equations and their boundary conditions.

2 Examine the possible employment of orthogonal functions to reduce the order of equations into a more manageable set, either by Fourier methods or modal (eigenvalue) methods—this may not be possible.

3 Use a specific numerical approximation for the derivatives of the reduced field equations to a specific numerical accuracy with a known error of approximation, both spatially and temporal. A further approximation may be introduced using finite element methods versus finite difference methods or direct numerical integration methods. In either case, errors are introduced with each method, but the finite element method is known to have more global effects than the local errors associated with the finite difference and integration methods.

4 The application of a solution procedure to the final governing numerical equations. One can apply over-relaxation or matrix inversion solution procedures. Relaxation methods are known to be less accurate with greater potential of error propagation than inversion methods. The latter, however, is much more resource-intensive and time-consuming.

5 Observation of the numerical results and correlate these with a definitive criterion. Being able to differentiate the true behavior of the proposed system of equations including possible nonlinear behavior or the proposed numerical error associated with the solution method becomes the focus.

The authors have made an excellent presentation on the governing equations of a cylindrical composite shell subjected to external loads that can create buckling (step 1). The fact that the authors use three-dimensional elastic theory with a brute force numerical approach raises some specific questions. The questions that the reviewer raises are a result of many years of practical analysis (linear, nonlinear, and dynamic) of composite shells. These questions have not been raised just because of the employment of three-dimensional elasticity, most of which have been presented by others for specific problems of a narrower focus such as vibration or static stress analysis of thick composite shells and not the all-encompassing approach taken by the authors.

The authors claim that the models employed for their examples are in the neighborhood of 150,000 grid points. This means that a banded matrix system of at least the order of 450,000 degrees-of-freedom would result. No mention has been given as to the difference operators used to develop the banded system when imposing specific boundary conditions (step 3). Some special considerations are necessary to eliminate fictitious boundary points in the finite difference grid. Further, the question of nonuniform difference grids needs to be addressed. The system of equations suggested by the authors would be full and not banded if a complete shell of revolution is analyzed. A suggestion has been inferred by the authors that a partial shell was considered by mentioning boundary conditions along a *longitudinal* edge, but no details are given on how the authors would handle nonsymmetric boundary conditions (encountering odd harmonic responses, for example). The reviewer also suspects that the general system of equations would be nonsymmetric, especially if the angle of the layer material composite no longer follows a consistent reference to the principal radii of curvature and/or the bending-membrane parameters of the constitutive equations are full and thus, the shell becomes anisotropic and the governing equations are no longer tridiagonal. With this high order of equations, stability of the solution procedure then comes into question.

For definitions of normal strains and shear strains through the thickness, the endpoints require an adjustment of the difference grid so that no external fictitious grid points would be introduced. Similar arguments are made when introducing the coupling of imperfection geometry (including the rotations about the normal) with the in-plane stress components. For the sake of argument, let us assume that at least five difference equation grid points are needed (and should be more) to adequately represent a smooth function and its derivative. Let us also assume that at least five difference stations are needed to adequately describe a waveform in each of the remaining orthogonal directions.

For many thin composite shells, the buckling waveform in the circumferential direction may be as high as 60. For the axial waveform, its magnitude will be around 20. 150,000 difference stations would be required on this basis. For the axial direction, a minimum of 100 difference stations would be needed to predict adequate bending boundary layer effects. Additional points are required for the zones away from any discontinuities. This raises the difference equations to 750,000 and a full matrix of the same order. The reviewer doubts very seriously that 10^{-12} accuracy could be attained, even with a 64-bit computer word length.

The question of establishing or recognizing a specific buckling mode comes into focus (step 5). Some buckling problems are denoted by a specific growth in a specific or adjacent buckling mode. This mode is usually identified by a specific Fourier harmonic, but can change in value due to coupling (the adding and subtracting of adjacent modes) (step 2). For two of the problems illustrated by the authors, using the procedure developed by Khot (1968) and Khot and Venkayya (1970) and a corresponding numerical procedure provided in the WRC Bulletin 313 (Citerley, 1986), the two axially loaded cases have participating Fourier harmonics that were rather widespread: For the four-ply problem, the critical wave numbers (axial (m), circumferential (n)) are predicted to be (22, 2), (15, 3), (15, 3), and (15, 3) for an

[1] by M. Shairyat and M. R. Eslami and published in the June 1999 issue of the ASME JOURNAL OF APPLIED MECHANICS, Vol. 66, pp. 476–484.

[2] 17901 Curtis Court, Pioneer, CA 95666. Mem. ASME.

 Copyright © 1999 by ASME

Downloaded 04 May 2010 to 171.66.16.27. Redistribution subject to ASME license or copyright; see http://www.asme.org/terms/Terms_Use.cfm

imperfection geometry of 0.0, 0.5T, T, and 2.0T, respectively. For the three-ply problem, the critical wave numbers were predicted to be (1, 11), (35, 6), (12, 25), and (23, 7) for $h = 2.54$ mm and (2, 3), (7, 2), (5, 3), and (2, 2) for $h = 25.4$ mm. Although the original theory employed to predict these results is based upon Donnell's shell theory, whose limits have been well categorized, one would not expect a major departure from those responses predicted using a three-dimensional theory. Similar results were obtained using the other numerical methods presented in Criterley (1986) and the nonlinear shell programs based on Sander's shell theory using the finite difference (Ball, 1968) and numerical integration (Criterley, 1987) methods. In addition, similar observations were made using the pseudo finite element method program STAGSC-1 (Almroth et al., 1979). Looking only at a w_{max} at a single point may not be easy to identify the buckling mode, especially if there are some 50 to 250 thousand displacements possible and one needs to recognize and identify a buckling pattern that changes with imperfection geometry. The reviewer finds that the reported results have an unusual regularity for the class of problems studied and notes that they differ in behavior from the results obtained from the three aforementioned numerical methods.

Another problem of the paper is that there is an inadequate description of the dynamic analysis methodology. How are the previous displacements of load step and iterations used? Are these quantities considered to be pseudo loads and are accounted for by shifting these to the right-hand side of the system of equations? Are the matrices being inverted and saved or are the system of equations being solved for each time step (step 4)? It is well known that using a Newmark or central difference time operator can produce an unstable solution. Runge-Kutta also falls into this category. Again, is the solution unstable or has the shell reached a bifurcation state? With a nonsymmetric system of equations, the eigenvalue associated with the time step and the matrix equation that represents the equations of motion can be such that a region of instability can be reached—similar to a Mathieu stability phenomenon. The solution could manifest itself with initially a very small error for a considerable length of time. Then, all of a sudden, a large growth in a displacement component is observed. If the solution steps are retraced, the displacement changes are found to exhibit a sign change for each time step. Numerical stability has therefore been encountered and not dynamic instability. One should be cautioned in using only a numerical method using a single observation without some sort of criterion-defining stability, such as applying a variation of energy or a Jacobian determinant. In the reviewer's opinion, this has not been adequately described.

Finally, the title suggest that post-buckling is being investigated. If the brute force method of the numerical solution was used by the authors for all of the classes of analyses presented, no mention has been made as to how the authors circumvent the ill-conditioning of the system of equations just beyond the critical point of bifurcation. Since there are at least two branch paths possible from a bifurcation point (whether static or dynamic), no mention has been made as to how the solution procedure accounts for this possibility.

References

Almroth, B. O., Brogan, F. A., and Stanley, G. M., 1979, "Structural Analysis of General Shells," Vol. II, *User Instructions for STAGSC-1*, LMSC-D633873, Applied Mechanics Laboratory, Lockheed Palo Alto Research Laboratory, Palo Alto, CA.

Ball, Robert E., 1968, "A Geometrically Nonlinear Analysis of Arbitrarily Loaded Shell of Revolution," NASA CR-909, Jan.

Criterley, Richard L., 1987, "The Inelastic Analysis of Shells of Revolution Subjected to Nonaxisymmetric Loads," *Recent Advances in Structural Dynamics*, H. Chung and H. D. Fisher, eds, ASME, New York.

Criterley, R. L., 1986, "Computer Programs for Imperfection Sensitivity Analysis of Stiffened Cylindrical Shells," WRC Bulletin 313, Apr.

Khot, N. S., 1968, "On the Influence of Initial Geometric Imperfections on the Buckling and Postbuckling Behavior of Fiber Reinforced Cylindrical Shells Under Uniform Axial Compression," AFFDL-TR-68-136, Oct.

Khot, N. S., and Venkayya, V. B., 1970, "Effect of Fiber Orientation on Initial Postbuckling Behavior and Imperfection Sensitivity of Composite Cylindrical Shells," AFFDL-TR-70-125, Dec.

Authors' Closure[3]

In the opinion of the authors, investigations of the reviewer are based on a conventional flexural matrix-based finite element analysis stand of view and a previous work by him. Thus, much of his claims are not hold for (does not contribute to) the full three-dimensional theory of elasticity and the proposed solution employed by the authors. He is familiar with a specific solution procedure, and has problems in relating the solution procedure proposed by the authors to what he has in mind.

Due to nonlinearity of the presented governing equations, no explicit stiffness matrix can be introduced unless these equations are linearized. For this reason, instead of using matrix procedures such as the Newton-Raphson method, Broyden-Fletcher-Goldfarb-Shanno method (Bathe, 1996) modal analysis, mode superposition, matrix reduction (Noor and McCom, 1981; Curnier, 1994) or subspace iteration methods, a modified Gauss-Siedel (SOR or successive over-relaxation method that is more rapidly convergent than the GS method) type of solution is used for each iteration within a time step. Thus, a solution vector refreshment is used rather than a matrix procedure. The results are presented for full cylindrical shells with arbitrary axial, radial, and tangential boundary conditions. Due to the variety of the presented examples (examples of static and dynamic buckling under mechanical and thermal loads with symmetric and antisymmetric ply sequences are considered) and due to limitation of the number of the paper pages, additional examples such as a cylindrical shell with asymmetric boundary conditions are not included. Due to the generality of the three-dimensional theory of elasticity, the proposed method is capable of investigating asymmetric and diamond-type buckling. In the presented examples, specifying the load cases was sufficient for understanding the required circumferential and radial boundary conditions. Concepts such as bending-membrane parameters are relevant to the conventional flexural theory that deals with the global behavior of the shell and cannot be defined for the three-dimensional theory of elasticity which is related to the elemental behaviors. On the other hand, it is well known that the prescription of the boundary conditions in the FDM is much simpler than that of FEM. In the paper, FDM is used for replacement of the spatial derivatives. Interlacing or noninterlacing grid points (Brush and Almroth, 1975) can be employed in this procedure and derivative values at the boundary points should be calculated based on the preceding points (Gerald, 1994).

Concepts such as in-plane stresses and rotations about the normals are relevant to global analysis and not to the three-dimensional theory of elasticity. The number of grid points in the axial and circumferential directions in the presented examples are predicted based on the deformed shapes and the number of axial and circumferential wave numbers reported in (Liaw and Yang, 1990; Reddy and Savoia, 1992) and previous works of the authors based on different theories proposed by them (Eslami and Shariyat, 1999; Eslami, Shariyat, and Shakeri, 1998; Shariyat and Eslami, 1999). Generally, grid point distances would be chosen in such a way that no remarkable difference is noticed by decreasing these distances so that effect on the higher modes can be incorporated. Based on this idea, various numbers of grid points are employed where the 150,000 grid points number was a mean value for the different examples. As pointed out earlier, since a vector refreshment scheme rather than a matrix procedure solves the equations, the required computer memory was notably lower. It was mentioned in the paper that the difference in the final results between two numbers of nodes was of the 10^{-12} order. This does not imply that the global error of the numerical procedure itself is of such order.

The authors are aware of interaction of the buckling modes and had confirmed this point in some of their works (Eslami and Shariyat, 1999; Eslami, Shariyat, and Shakeri, 1998; Shariyat and

[3] Amirkabir University of Technology, Mechanical Engineering Department, 424, Hafez Avenue, Teheran, Iran.

Downloaded 04 May 2010 to 171.66.16.27. Redistribution subject to ASME license or copyright; see http://www.asme.org/terms/Terms_Use.cfm

imperfection geometry of 0.0, 0.5T, T, and 2.0T, respectively. For the three-ply problem, the critical wave numbers were predicted to be (1, 11), (35, 6), (12, 25), and (23, 7) for $h = 2.54$ mm and (2, 3), (7, 2), (5, 3), and (2, 2) for $h = 25.4$ mm. Although the original theory employed to predict these results is based upon Donnell's shell theory, whose limits have been well categorized, one would not expect a major departure from those responses predicted using a three-dimensional theory. Similar results were obtained using the other numerical methods presented in Criterley (1986) and the nonlinear shell programs based on Sander's shell theory using the finite difference (Ball, 1968) and numerical integration (Criterley, 1987) methods. In addition, similar observations were made using the pseudo finite element method program STAGSC-1 (Almroth et al., 1979). Looking only at a w_{max} at a single point may not be easy to identify the buckling mode, especially if there are some 50 to 250 thousand displacements possible and one needs to recognize and identify a buckling pattern that changes with imperfection geometry. The reviewer finds that the reported results have an unusual regularity for the class of problems studied and notes that they differ in behavior from the results obtained from the three aforementioned numerical methods.

Another problem of the paper is that there is an inadequate description of the dynamic analysis methodology. How are the previous displacements of load step and iterations used? Are these quantities considered to be pseudo loads and are accounted for by shifting these to the right-hand side of the system of equations? Are the matrices being inverted and saved or are the system of equations being solved for each time step (step 4)? It is well known that using a Newmark or central difference time operator can produce an unstable solution. Runge-Kutta also falls into this category. Again, is the solution unstable or has the shell reached a bifurcation state? With a nonsymmetric system of equations, the eigenvalue associated with the time step and the matrix equation that represents the equations of motion can be such that a region of instability can be reached—similar to a Mathieu stability phenomenon. The solution could manifest itself with initially a very small error for a considerable length of time. Then, all of a sudden, a large growth in a displacement component is observed. If the solution steps are retraced, the displacement changes are found to exhibit a sign change for each time step. Numerical stability has therefore been encountered and not dynamic instability. One should be cautioned in using only a numerical method using a single observation without some sort of criterion-defining stability, such as applying a variation of energy or a Jacobian determinant. In the reviewer's opinion, this has not been adequately described.

Finally, the title suggest that post-buckling is being investigated. If the brute force method of the numerical solution was used by the authors for all of the classes of analyses presented, no mention has been made as to how the authors circumvent the ill-conditioning of the system of equations just beyond the critical point of bifurcation. Since there are at least two branch paths possible from a bifurcation point (whether static or dynamic), no mention has been made as to how the solution procedure accounts for this possibility.

References

Almroth, B. O., Brogan, F. A., and Stanley, G. M., 1979, "Structural Analysis of General Shells," Vol. II, *User Instructions for STAGSC-1*, LMSC-D633873, Applied Mechanics Laboratory, Lockheed Palo Alto Research Laboratory, Palo Alto, CA.

Ball, Robert E., 1968, "A Geometrically Nonlinear Analysis of Arbitrarily Loaded Shell of Revolution," NASA CR-909, Jan.

Criterley, Richard L., 1987, "The Inelastic Analysis of Shells of Revolution Subjected to Nonaxisymmetric Loads," *Recent Advances in Structural Dynamics*, H. Chung and H. D. Fisher, eds, ASME, New York.

Criterley, R. L., 1986, "Computer Programs for Imperfection Sensitivity Analysis of Stiffened Cylindrical Shells," WRC Bulletin 313, Apr.

Khot, N. S., 1968, "On the Influence of Initial Geometric Imperfections on the Buckling and Postbuckling Behavior of Fiber Reinforced Cylindrical Shells Under Uniform Axial Compression," AFFDL-TR-68-136, Oct.

Khot, N. S., and Venkayya, V. B., 1970, "Effect of Fiber Orientation on Initial Postbuckling Behavior and Imperfection Sensitivity of Composite Cylindrical Shells," AFFDL-TR-70-125, Dec.

Authors' Closure[3]

In the opinion of the authors, investigations of the reviewer are based on a conventional flexural matrix-based finite element analysis stand of view and a previous work by him. Thus, much of his claims are not hold for (does not contribute to) the full three-dimensional theory of elasticity and the proposed solution employed by the authors. He is familiar with a specific solution procedure, and has problems in relating the solution procedure proposed by the authors to what he has in mind.

Due to nonlinearity of the presented governing equations, no explicit stiffness matrix can be introduced unless these equations are linearized. For this reason, instead of using matrix procedures such as the Newton-Raphson method, Broyden-Fletcher-Goldfarb-Shanno method (Bathe, 1996) modal analysis, mode superposition, matrix reduction (Noor and McCom, 1981; Curnier, 1994) or subspace iteration methods, a modified Gauss-Siedel (SOR or successive over-relaxation method that is more rapidly convergent than the GS method) type of solution is used for each iteration within a time step. Thus, a solution vector refreshment is used rather than a matrix procedure. The results are presented for full cylindrical shells with arbitrary axial, radial, and tangential boundary conditions. Due to the variety of the presented examples (examples of static and dynamic buckling under mechanical and thermal loads with symmetric and antisymmetric ply sequences are considered) and due to limitation of the number of the paper pages, additional examples such as a cylindrical shell with asymmetric boundary conditions are not included. Due to the generality of the three-dimensional theory of elasticity, the proposed method is capable of investigating asymmetric and diamond-type buckling. In the presented examples, specifying the load cases was sufficient for understanding the required circumferential and radial boundary conditions. Concepts such as bending-membrane parameters are relevant to the conventional flexural theory that deals with the global behavior of the shell and cannot be defined for the three-dimensional theory of elasticity which is related to the elemental behaviors. On the other hand, it is well known that the prescription of the boundary conditions in the FDM is much simpler than that of FEM. In the paper, FDM is used for replacement of the spatial derivatives. Interlacing or noninterlacing grid points (Brush and Almroth, 1975) can be employed in this procedure and derivative values at the boundary points should be calculated based on the preceding points (Gerald, 1994).

Concepts such as in-plane stresses and rotations about the normals are relevant to global analysis and not to the three-dimensional theory of elasticity. The number of grid points in the axial and circumferential directions in the presented examples are predicted based on the deformed shapes and the number of axial and circumferential wave numbers reported in (Liaw and Yang, 1990; Reddy and Savoia, 1992) and previous works of the authors based on different theories proposed by them (Eslami and Shariyat, 1999; Eslami, Shariyat, and Shakeri, 1998; Shariyat and Eslami, 1999). Generally, grid point distances would be chosen in such a way that no remarkable difference is noticed by decreasing these distances so that effect on the higher modes can be incorporated. Based on this idea, various numbers of grid points are employed where the 150,000 grid points number was a mean value for the different examples. As pointed out earlier, since a vector refreshment scheme rather than a matrix procedure solves the equations, the required computer memory was notably lower. It was mentioned in the paper that the difference in the final results between two numbers of nodes was of the 10^{-12} order. This does not imply that the global error of the numerical procedure itself is of such order.

The authors are aware of interaction of the buckling modes and had confirmed this point in some of their works (Eslami and Shariyat, 1999; Eslami, Shariyat, and Shakeri, 1998; Shariyat and

[3] Amirkabir University of Technology, Mechanical Engineering Department, 424, Hafez Avenue, Teheran, Iran.

Downloaded 04 May 2010 to 171.66.16.27. Redistribution subject to ASME license or copyright; see http://www.asme.org/terms/Terms_Use.cfm

Eslami, 1999). The present results are not in contradiction with this point. However, the buckling modes presented by the reviewer are based on the conventional classic methods that have considerable errors in estimating the composite materials (Reddy and Savoia, 1992; Kardomatous and Philobas, 1995). As mentioned in the paper, the generalized concept of dynamic buckling proposed by Budiansky (1974) states that dynamic buckling of a structure occurs when small changes in the magnitude of the loading lead to large change in one of the displacement modes. Location of the buckling point does not alter the global concept of buckling and buckling will occur when the stated conditions are achieved. This criterion is employed widely (for example, Reddy and Savoia (1992) and Gillat et al. (1993)).

In the paper (steps 12 and 13 of the numerical solution scheme) it was emphasized that the results obtained at the end of each time step are added to the displacement or velocity components obtained at the end of the previous time interval (incremental nature of the results also implies this note). As mentioned before, since the governing equations are nonlinear, the idea of establishing any matrix equation is not justified. It seems that the reviewer was expecting a specific numerical procedure and had problems in relating the proposed procedure to what was expected. As may be noted from the proposed solution procedure, an implicit RK (Runge-Kutta) time integration scheme of the solution with iterative modifications is used within each time step. It is well known that the fourth-order RK method has a local error of $(\Delta t)^5$ order and a global error of $(\Delta t)^4$ order (Gerald, 1994). Therefore, for a Δt of 10^{-6} order chosen, the accumulated error in time integration for the whole range of application would be negligibly small. The iteration can actually be of the utmost importance, since any error admitted in the incremental solution at a particular time directly affects, in a path-dependent manner, the solution at any subsequent time. In contrast to explicit methods, implicit methods are unconditionally stable (Curnier, 1994). Time-step size is so chosen that no divergence, no numerical-induced oscillations, and no numerical damping may occur. As can be seen from Figs. 4 and 7 of the paper, the presented results are consistent and monotonous. Therefore, sign change in the results has not occurred. It has been mentioned that buckling is checked by means of the Budiansky criterion. Modal analysis and modal algorithm addressed by the reviewer are limited to smooth solutions of linear systems (Curnier, 1994). Instabilities similar to a Mathieu instability phenomenon that are relevant to influence of the parameters of the governing equations fall into a category of instability analysis known as the Hill-Hsu parametric resonance approach (Simitses, 1990), which is quite different from the proposed time marching approach.

The final paragraphs in the reviewer's note imply that he does not have complete knowledge of the buckling phenomenon and he reviewed the paper from a pure vibrational stand of view. It is well known that bifurcation sounds for perfect structures only (Simitses, 1990). In the presented examples, the studied shells either have initial imperfections or very negligible imperfections are incorporated to check the bifurcation point. Therefore, a buckling path is actually traced and the post-buckling behavior is investigated. Similar studies are done by some well-known references (Liaw and Yang (1990), Reddy and Savoia (1992), and Gillat et al. (1993) are examples).

References

Bathe, K. J., 1996, *Finite Element Procedures in Engineering Analysis,* Prentice-Hall, Englewood Cliffs, NJ.

Brush, O., and Almroth, B., 1975, *Buckling of Beams, Plates, and Shells,* McGraw-Hill, New York.

Budiansky, B., 1974, "Theory of Buckling and Postbuckling Behavior of Elastic Structures," *Advances in Applied Mechanics,* pp. 1–65.

Curnier, A., 1994, *Computational Methods in Solid Mechanics,* Kluwer Academic Publishers, Dordrecht, The Netherlands.

Eslami, M. R., and Shariyat, M., 1999, "A High-Order Theory for Dynamic Buckling and Postbuckling Analysis of Imperfect Laminated Cylindrical Shells," ASME *Journal of Pressure Vessel Technology,* Vol. 121, pp. 94–102.

Eslami, M. R., Shariyat, M., and Shakeri, M., 1998, "Layer-Wise Theory for Dynamic Buckling and Postbuckling of Laminated Composite Cylindrical Shells," *AIAA J.,* Vol. 36, No. 10, pp. 1874–1882.

Gerald, C. F., 1994, *Applied Numerical Analysis,* Addison-Wesley, Reading, MA.

Gillat, R., Feldman, E., and Aboudi, J., 1993, "Axisymmetric Response of Nonlinearly Elastic Cylindrical Shells to Dynamic Axial Loads," *Int. J. Impact Engineering,* Vol. 13, No. 4, pp. 545–554.

Kardomateas, G. A., and Philobos, M. S., 1995, "Buckling of Thick Orthotropic Cylindrical Shells Under Combined External Pressure and Axial Compression," *AIAA J.,* Vol. 33, No. 10, pp. 1946–1953.

Liaw, D. G., and Yang, T. Y., 1990, "Symmetric and Asymmetric Dynamic Buckling of Laminated Thin Shells With Effect of Imperfection and Damping," *J. Composite Materials,* Vol. 24, pp. 188–207.

Noor, A. K., and McCom, H. G., 1981, *Computational Methods in Nonlinear Structural and Solid Mechanics,* Pergamon Press, London.

Reddy, J. N., and Savoia, M., 1992, "Layer-Wise Shell Theory for Postbuckling of Laminated Circular Cylindrical Shells," *AIAA J.,* Vol. 30, No. 8, pp. 2148–2154.

Shariyat, M., and Eslami, M. R., 1999, "On Thermal Dynamic Buckling Analysis of Imperfect Laminated Cylindrical Shells," *ZAMM,* Vol. 79.

Simitses, G. J., 1990, *Dynamic Stability of Suddenly Loaded Structures,* Springer-Verlag, Berlin.

Tangential Loading of General Three-Dimensional Contacts[1]

J. Jäger.[2] Recently, Dr. Ciavarella published a paper in the *Journal of Applied Mechanics,* where he presented a generalization of the well-known Cattaneo-Mindlin solution for equal half-spaces with arbitrary contact areas and Poisson's ratio $\nu = 0$. We will shortly explain the background of this generalization, before we discuss some remarks. For vanishing Poisson's ratio, the normal and tangential stress-displacement relations are uncoupled and identical, with exception of a constant factor. Then, each normal solution is also a tangential solution. The two boundary conditions for unidirectional tangential shift are a constant displacement of the stick area and Coulomb's law $q = fp$ in the slip area, where q denotes the tangential traction, p the pressure, and f the coefficient of friction. When the normal pressure p_1 between two bodies in contact on the area C_1 is increased to a new value p_2, the additional pressure $\Delta p = p_2 - p_1$ causes a constant displacement of the old contact area C_1. The increment Δp satisfies the first boundary condition for the tangential problem, when we assume that the old contact area is identical with the stick area and Coulomb's law can be satisfied by setting $q = f\Delta p$. Thus, $q = f\Delta p$ is the solution for the tangential problem. The side conditions of Coulomb's law are also satisfied, as discussed in the article.

In the next paragraphs, we will discuss some points, which can mislead the reader. Some suggestions on future research are presented at the end.

1 The results for axisymmetric contact, summarized by Ciavarella in formulas (29)–(33), have already been published by Jäger (1995a), and presented at the ASME summer meeting (Jäger, 1995b). Table 1 shows a comparison of identical equations by Ciavarella (1998a) and Jäger (1995a). Equation (31) by Ciavarella was written in the form $Q^* = fP(a^*)$ by Jäger (1995a), with $c = a^*$ in Ciavarella's notation. The general solution for plane contact was also published by Jäger (1997a), and some examples have been presented in Jäger (1997b). Dr. Ciavarella requested and received Jäger's papers on April 30, 1998. Nevertheless, in a new publication from July 17, 1998 (Barber and Ciavarella, 1999), Dr. Ciavarella wrote: "A significant generalization of Cattaneo-Mindlin was discovered by Ciavarella . . . for any plane contact problem . . . ". Although this statement was corrected later, Ciavarella did not relate his axisymmetric solutions to Jäger (Jäger, 1995a).

2 "Flat regions are either entirely in full stick or are in full

[1] by M. Ciavarella and published in the Dec. 1998 issue of the ASME JOURNAL OF APPLIED MECHANICS, Vol. 65, pp. 998–1003.

[2] IBAMA, Goerdelestr. 8, 91058 Erlangen, Germany. e-mail: j_jaeger@t-online.de.

Downloaded 04 May 2010 to 171.66.16.27. Redistribution subject to ASME license or copyright; see http://www.asme.org/terms/Terms_Use.cfm

Eslami, 1999). The present results are not in contradiction with this point. However, the buckling modes presented by the reviewer are based on the conventional classic methods that have considerable errors in estimating the composite materials (Reddy and Savoia, 1992; Kardomatous and Philobas, 1995). As mentioned in the paper, the generalized concept of dynamic buckling proposed by Budiansky (1974) states that dynamic buckling of a structure occurs when small changes in the magnitude of the loading lead to large change in one of the displacement modes. Location of the buckling point does not alter the global concept of buckling and buckling will occur when the stated conditions are achieved. This criterion is employed widely (for example, Reddy and Savoia (1992) and Gillat et al. (1993)).

In the paper (steps 12 and 13 of the numerical solution scheme) it was emphasized that the results obtained at the end of each time step are added to the displacement or velocity components obtained at the end of the previous time interval (incremental nature of the results also implies this note). As mentioned before, since the governing equations are nonlinear, the idea of establishing any matrix equation is not justified. It seems that the reviewer was expecting a specific numerical procedure and had problems in relating the proposed procedure to what was expected. As may be noted from the proposed solution procedure, an implicit RK (Runge-Kutta) time integration scheme of the solution with iterative modifications is used within each time step. It is well known that the fourth-order RK method has a local error of $(\Delta t)^5$ order and a global error of $(\Delta t)^4$ order (Gerald, 1994). Therefore, for a Δt of 10^{-6} order chosen, the accumulated error in time integration for the whole range of application would be negligibly small. The iteration can actually be of the utmost importance, since any error admitted in the incremental solution at a particular time directly affects, in a path-dependent manner, the solution at any subsequent time. In contrast to explicit methods, implicit methods are unconditionally stable (Curnier, 1994). Time-step size is so chosen that no divergence, no numerical-induced oscillations, and no numerical damping may occur. As can be seen from Figs. 4 and 7 of the paper, the presented results are consistent and monotonous. Therefore, sign change in the results has not occurred. It has been mentioned that buckling is checked by means of the Budiansky criterion. Modal analysis and modal algorithm addressed by the reviewer are limited to smooth solutions of linear systems (Curnier, 1994). Instabilities similar to a Mathieu instability phenomenon that are relevant to influence of the parameters of the governing equations fall into a category of instability analysis known as the Hill-Hsu parametric resonance approach (Simitses, 1990), which is quite different from the proposed time marching approach.

The final paragraphs in the reviewer's note imply that he does not have complete knowledge of the buckling phenomenon and he reviewed the paper from a pure vibrational stand of view. It is well known that bifurcation sounds for perfect structures only (Simitses, 1990). In the presented examples, the studied shells either have initial imperfections or very negligible imperfections are incorporated to check the bifurcation point. Therefore, a buckling path is actually traced and the post-buckling behavior is investigated. Similar studies are done by some well-known references (Liaw and Yang (1990), Reddy and Savoia (1992), and Gillat et al. (1993) are examples).

References

Bathe, K. J., 1996, *Finite Element Procedures in Engineering Analysis,* Prentice-Hall, Englewood Cliffs, NJ.

Brush, O., and Almroth, B., 1975, *Buckling of Beams, Plates, and Shells,* McGraw-Hill, New York.

Budiansky, B., 1974, "Theory of Buckling and Postbuckling Behavior of Elastic Structures," *Advances in Applied Mechanics,* pp. 1–65.

Curnier, A., 1994, *Computational Methods in Solid Mechanics,* Kluwer Academic Publishers, Dordrecht, The Netherlands.

Eslami, M. R., and Shariyat, M., 1999, "A High-Order Theory for Dynamic Buckling and Postbuckling Analysis of Imperfect Laminated Cylindrical Shells," ASME *Journal of Pressure Vessel Technology,* Vol. 121, pp. 94–102.

Eslami, M. R., Shariyat, M., and Shakeri, M., 1998, "Layer-Wise Theory for Dynamic Buckling and Postbuckling of Laminated Composite Cylindrical Shells," *AIAA J.,* Vol. 36, No. 10, pp. 1874–1882.

Gerald, C. F., 1994, *Applied Numerical Analysis,* Addison-Wesley, Reading, MA.

Gillat, R., Feldman, E., and Aboudi, J., 1993, "Axisymmetric Response of Nonlinearly Elastic Cylindrical Shells to Dynamic Axial Loads," *Int. J. Impact Engineering,* Vol. 13, No. 4, pp. 545–554.

Kardomateas, G. A., and Philobos, M. S., 1995, "Buckling of Thick Orthotropic Cylindrical Shells Under Combined External Pressure and Axial Compression," *AIAA J.,* Vol. 33, No. 10, pp. 1946–1953.

Liaw, D. G., and Yang, T. Y., 1990, "Symmetric and Asymmetric Dynamic Buckling of Laminated Thin Shells With Effect of Imperfection and Damping," *J. Composite Materials,* Vol. 24, pp. 188–207.

Noor, A. K., and McCom, H. G., 1981, *Computational Methods in Nonlinear Structural and Solid Mechanics,* Pergamon Press, London.

Reddy, J. N., and Savoia, M., 1992, "Layer-Wise Shell Theory for Postbuckling of Laminated Circular Cylindrical Shells," *AIAA J.,* Vol. 30, No. 8, pp. 2148–2154.

Shariyat, M., and Eslami, M. R., 1999, "On Thermal Dynamic Buckling Analysis of Imperfect Laminated Cylindrical Shells," *ZAMM,* Vol. 79.

Simitses, G. J., 1990, *Dynamic Stability of Suddenly Loaded Structures,* Springer-Verlag, Berlin.

Tangential Loading of General Three-Dimensional Contacts[1]

J. Jäger.[2] Recently, Dr. Ciavarella published a paper in the *Journal of Applied Mechanics,* where he presented a generalization of the well-known Cattaneo-Mindlin solution for equal half-spaces with arbitrary contact areas and Poisson's ratio $\nu = 0$. We will shortly explain the background of this generalization, before we discuss some remarks. For vanishing Poisson's ratio, the normal and tangential stress-displacement relations are uncoupled and identical, with exception of a constant factor. Then, each normal solution is also a tangential solution. The two boundary conditions for unidirectional tangential shift are a constant displacement of the stick area and Coulomb's law $q = fp$ in the slip area, where q denotes the tangential traction, p the pressure, and f the coefficient of friction. When the normal pressure p_1 between two bodies in contact on the area C_1 is increased to a new value p_2, the additional pressure $\Delta p = p_2 - p_1$ causes a constant displacement of the old contact area C_1. The increment Δp satisfies the first boundary condition for the tangential problem, when we assume that the old contact area is identical with the stick area and Coulomb's law can be satisfied by setting $q = f\Delta p$. Thus, $q = f\Delta p$ is the solution for the tangential problem. The side conditions of Coulomb's law are also satisfied, as discussed in the article.

In the next paragraphs, we will discuss some points, which can mislead the reader. Some suggestions on future research are presented at the end.

1 The results for axisymmetric contact, summarized by Ciavarella in formulas (29)–(33), have already been published by Jäger (1995a), and presented at the ASME summer meeting (Jäger, 1995b). Table 1 shows a comparison of identical equations by Ciavarella (1998a) and Jäger (1995a). Equation (31) by Ciavarella was written in the form $Q^* = fP(a^*)$ by Jäger (1995a), with $c = a^*$ in Ciavarella's notation. The general solution for plane contact was also published by Jäger (1997a), and some examples have been presented in Jäger (1997b). Dr. Ciavarella requested and received Jäger's papers on April 30, 1998. Nevertheless, in a new publication from July 17, 1998 (Barber and Ciavarella, 1999), Dr. Ciavarella wrote: "A significant generalization of Cattaneo-Mindlin was discovered by Ciavarella . . . for any plane contact problem . . . ". Although this statement was corrected later, Ciavarella did not relate his axisymmetric solutions to Jäger (Jäger, 1995a).

2 "Flat regions are either entirely in full stick or are in full

[1] by M. Ciavarella and published in the Dec. 1998 issue of the ASME JOURNAL OF APPLIED MECHANICS, Vol. 65, pp. 998–1003.

[2] IBAMA, Goerdelestr. 8, 91058 Erlangen, Germany. e-mail: j_jaeger@t-online.de.

Downloaded 04 May 2010 to 171.66.16.27. Redistribution subject to ASME license or copyright; see http://www.asme.org/terms/Terms_Use.cfm

Table 1 Identical equations by Ciavarella (1998a) and Jäger (1995a)

Ciavarella	(29)	(30)	(31)	(32)	(33)
Jäger	(32) and (15a)	(33) and (14)	(34)	(32)	(33)

slip." This statement is only correct when all flat areas have the same height. Otherwise, only the lowest area is in initial contact. With increasing normal force, higher flat areas enter in contact, and the new contact areas change their form with the compression. When a tangential force is applied, the part of that area slides first, which was coming in contact latest, and the rest of that area sticks. Thus, partial slip of a flat area is possible.

3 For the direction of the slip traction, Ciavarella published the following formula (Eq. (18) in Ciavarella, 1998a):

$$\frac{\mathbf{q}_t}{|\mathbf{q}_t|} + \frac{\partial}{\partial t}\frac{\mathbf{u}_t}{|\mathbf{u}_t|} = 0. \tag{1}$$

In the case of rigid bodies, the displacement disappears, i.e., $\mathbf{u}_t = 0$ and the direction of the slip traction cannot be determined. To set this right, the slip traction must be opposite to the slip velocity, when the slip $\mathbf{s}$ denotes the difference between the rigid body shift $\boldsymbol{\delta}_t$ and the elastic displacement $\mathbf{u}_t$

$$\frac{\mathbf{q}_t}{|\mathbf{q}_t|} + \frac{\dot{\mathbf{s}}}{|\dot{\mathbf{s}}|} = 0, \quad \mathbf{s} = \mathbf{u}_t - \boldsymbol{\delta}_t. \tag{2}$$

When the slip velocity is unidirectional, which was the case investigated by Ciavarella, the derivation is unnecessary $\mathbf{q}_t/|\mathbf{q}_t| + \mathbf{s}/|\mathbf{s}| = 0$. The slip disappears in the stick region, thus: $\mathbf{u}_t = \boldsymbol{\delta}_t$ in the stick region.

4 Formula (23) seems not correct. The tangential force Q_x consists of two components: $Q_x = f(P - P^*)$. The first component fP is the resultant of the full slip traction in the actual contact area. The other component: $-fP^*$, is the resultant of the full slip traction in the stick area. With the distance d^* between fP and fP^*, the right formula for the distance d between Q_x and fP must be

$$d = \frac{fP \mp Q_x}{2fP - Q_x} d^*. \tag{3}$$

In contrast to Ciavarella's result, the distance for vanishing Q_x is $d = d^*/2$. It is not necessary to calculate the point of application of the tangential load. It is sufficient to restrict the rotation around the contact normal. In the experiment, the support mechanism must be constructed appropriately and the numerical solution requires the displacement increments anyway (Jäger, 1992). For most contacts, the contact area is very small compared with the dimensions of the body, and the local moments in the contact area can be neglected.

In this context, it should be noted that the generalization of the Cattaneo-Mindlin solution requires nonrotating bodies, because the stick condition is always a constant displacement, when the bodies do not roll. Therefore, it is consequent to suppress all rotations, especially the rotation around the tangential axes, which appeared in Ciavarella's Eqs. (5) and (6). It is worth remarking that a special case of transient rolling exists, where the Cattaneo-Mindlin solution can also be applied. General problems with transient rolling can only be solved numerically.

5 At the beginning of Section 3, Ciavarella classified the decreasing stick zone as a "receding" problem. This is in contrast to Dundurs' definition, who used the term for the case when the contact area decreases with increasing forces. In normal direction, the type of contact is "advancing," because the contact area increases with the force. The tangential traction is the superposition of two advancing solutions. The slip zone increases with the tangential force, while the stick area and the corresponding component Q_x^* decrease. It seems that the Cattaneo-Mindlin generalization cannot be used for receding contact problems. In fact, for a receding contact problem, the generalized Cattaneo-Mindlin theory would suggest that the slip area decreases with increasing tangential force, which contradicts gross slip.

6 There are also contradictions in Ciavarella's other publications. Formula (A9) in Ciavarella (1998b) for the pressure of surfaces $|x|^k$ has the wrong dimension and contains several typing errors. Furthermore, the hypergeometric function is singular for odd k. Jäger's formula (18), (1997b) should be used instead.

A possible field for future research are more general structures. The necessary condition for the generalization of the Cattaneo-Mindlin solution is that the stress displacement equations are equal, with the exception of a constant factor. This is the case for thin compressible layers in plane contact, and approximately for thick layers, too (Jäger, 1999c). For equal bodies with thin layers of equal material and geometry, the normal and tangential coupling disappears. When the coupling between the tangential components is also neglected, the Winkler model is obtained as limiting case for very thin layers. This model allows solutions for very complex contact surfaces (Jäger, 1999b). This generalization can also be used for impact calculations, where only the rigid friction model has been solved to date. For very thin, incompressible layers, the tangential displacement is much larger than the normal displacement and the rigid body assumption is wrong. A new application for granular material was also published (see Jäger, 1999a). The C&M generalization is always unique and can help to solve existence and uniqueness problems, as self-locking of brakes and machine elements. It is also possible to develop similar methods for uncoupled problems with different stress-displacement equations. Jäger's solution (1995a) for torsion can serve as example.

References

Barber, J. R., and Ciavarella, M., 1999, "Contact Mechanics," *Int. J. Solids Structures,* Vol. 37, pp. 29–43.

Ciavarella, M., 1998a, "Tangential Loading of General Three-Dimensional Contacts," ASME JOURNAL OF APPLIED MECHANICS, Vol. 65, pp. 998–1003.

Ciavarella, M., 1998b, "The Generalized Cattaneo Partial Slip Plane Contact Problem, II—Examples," *Int. J. Solids Structures,* Vol. 35, pp. 2363–2378.

Jäger, J., 1992, "Elastic Impact With Friction," thesis, Inst. Inf. and Maths., Delft, The Netherlands.

Jäger, J., 1995a, "Axi-symmetric Bodies of Equal Material in Contact Under Torsion or Shift," *Arch. Appl. Mech.,* Vol. 65, pp. 478–487.

Jäger, J., 1995b, "Contact With Friction of Elastically Similar Bodies," *Impact, Waves and Fracture,* R. C. Batra, A. K. Mal, and G. P. MacSithigh, eds., ASME, New York, pp. 125–152.

Jäger, J., 1997a, "Ein neues Prinzip der Kontakmechanik," *Z. angew. Math. Mech.,* Vol. 7, pp. S143–S144.

Jäger, J., 1997b, "Half-Planes Without Coupling Under Contact Loading," *Arch. Appl. Mech.,* Vol. 67, pp. 247–259.

Jäger, J., 1999a, "Uni-axial Deformation of a Random Packing of Particles," *Arch. Appl. Mech.,* Vol. 69, pp. 181–203.

Jäger, J., 1999b, "Conditions for the Generalization of Cattaneo-Mindlin," *ZAMM 2000,* to be published.

Jäger, J., 1999c, "Equal Layers in Contact With Friction," *Contact Mechanics IV,* L. Gaul and C. A. Brebbia, eds, WIT Press, pp. 99–108.

Author's Closure[3]

First of all, I thank Dr. Jäger for his interest in my paper "Tangential Loading of General Three-dimensional Contacts." I confess I don't understand very well the scope of Dr. Jäger's "discussion." At first I thought he was questioning the originality of my paper, but this is not the case as there is no previous paper where an extension to the Cattaneo's solution for isotropic materials but general three-dimensional geometry is given. Secondly, I thought Dr. Jäger was trying to improve the clarity of the presentation of my paper, by discussing what he calls the "background"

[3] M. Ciavarella, Primo Ricercatore, CNR-IRIS, str. Crocefisso 2B, 70126 Bari, Italy. e-mail: m.ciavarela@area.ba.cnr.it.

Downloaded 04 May 2010 to 171.66.16.27. Redistribution subject to ASME license or copyright; see http://www.asme.org/terms/Terms_Use.cfm

Table 1 Identical equations by Ciavarella (1998a) and Jäger (1995a)

Ciavarella	(29)	(30)	(31)	(32)	(33)
Jäger	(32) and (15a)	(33) and (14)	(34)	(32)	(33)

slip." This statement is only correct when all flat areas have the same height. Otherwise, only the lowest area is in initial contact. With increasing normal force, higher flat areas enter in contact, and the new contact areas change their form with the compression. When a tangential force is applied, the part of that area slides first, which was coming in contact latest, and the rest of that area sticks. Thus, partial slip of a flat area is possible.

3 For the direction of the slip traction, Ciavarella published the following formula (Eq. (18) in Ciavarella, 1998a):

$$\frac{\mathbf{q}_t}{|\mathbf{q}_t|} + \frac{\partial}{\partial t}\frac{\mathbf{u}_t}{|\mathbf{u}_t|} = 0. \tag{1}$$

In the case of rigid bodies, the displacement disappears, i.e., $\mathbf{u}_t = 0$ and the direction of the slip traction cannot be determined. To set this right, the slip traction must be opposite to the slip velocity, when the slip $\mathbf{s}$ denotes the difference between the rigid body shift $\boldsymbol{\delta}_t$ and the elastic displacement $\mathbf{u}_t$

$$\frac{\mathbf{q}_t}{|\mathbf{q}_t|} + \frac{\dot{\mathbf{s}}}{|\dot{\mathbf{s}}|} = 0, \quad \mathbf{s} = \mathbf{u}_t - \boldsymbol{\delta}_t. \tag{2}$$

When the slip velocity is unidirectional, which was the case investigated by Ciavarella, the derivation is unnecessary $\mathbf{q}_t/|\mathbf{q}_t| + \mathbf{s}/|\mathbf{s}| = 0$. The slip disappears in the stick region, thus: $\mathbf{u}_t = \boldsymbol{\delta}_t$ in the stick region.

4 Formula (23) seems not correct. The tangential force Q_x consists of two components: $Q_x = f(P - P^*)$. The first component fP is the resultant of the full slip traction in the actual contact area. The other component: $-fP^*$, is the resultant of the full slip traction in the stick area. With the distance d^* between fP and fP^*, the right formula for the distance d between Q_x and fP must be

$$d = \frac{fP \mp Q_x}{2fP - Q_x} d^*. \tag{3}$$

In contrast to Ciavarella's result, the distance for vanishing Q_x is $d = d^*/2$. It is not necessary to calculate the point of application of the tangential load. It is sufficient to restrict the rotation around the contact normal. In the experiment, the support mechanism must be constructed appropriately and the numerical solution requires the displacement increments anyway (Jäger, 1992). For most contacts, the contact area is very small compared with the dimensions of the body, and the local moments in the contact area can be neglected.

In this context, it should be noted that the generalization of the Cattaneo-Mindlin solution requires nonrotating bodies, because the stick condition is always a constant displacement, when the bodies do not roll. Therefore, it is consequent to suppress all rotations, especially the rotation around the tangential axes, which appeared in Ciavarella's Eqs. (5) and (6). It is worth remarking that a special case of transient rolling exists, where the Cattaneo-Mindlin solution can also be applied. General problems with transient rolling can only be solved numerically.

5 At the beginning of Section 3, Ciavarella classified the decreasing stick zone as a "receding" problem. This is in contrast to Dundurs' definition, who used the term for the case when the contact area decreases with increasing forces. In normal direction, the type of contact is "advancing," because the contact area increases with the force. The tangential traction is the superposition of two advancing solutions. The slip zone increases with the tangential force, while the stick area and the corresponding component Q_x^* decrease. It seems that the Cattaneo-Mindlin generalization cannot be used for receding contact problems. In fact, for a receding contact problem, the generalized Cattaneo-Mindlin theory would suggest that the slip area decreases with increasing tangential force, which contradicts gross slip.

6 There are also contradictions in Ciavarella's other publications. Formula (A9) in Ciavarella (1998b) for the pressure of surfaces $|x|^k$ has the wrong dimension and contains several typing errors. Furthermore, the hypergeometric function is singular for odd k. Jäger's formula (18), (1997b) should be used instead.

A possible field for future research are more general structures. The necessary condition for the generalization of the Cattaneo-Mindlin solution is that the stress displacement equations are equal, with the exception of a constant factor. This is the case for thin compressible layers in plane contact, and approximately for thick layers, too (Jäger, 1999c). For equal bodies with thin layers of equal material and geometry, the normal and tangential coupling disappears. When the coupling between the tangential components is also neglected, the Winkler model is obtained as limiting case for very thin layers. This model allows solutions for very complex contact surfaces (Jäger, 1999b). This generalization can also be used for impact calculations, where only the rigid friction model has been solved to date. For very thin, incompressible layers, the tangential displacement is much larger than the normal displacement and the rigid body assumption is wrong. A new application for granular material was also published (see Jäger, 1999a). The C&M generalization is always unique and can help to solve existence and uniqueness problems, as self-locking of brakes and machine elements. It is also possible to develop similar methods for uncoupled problems with different stress-displacement equations. Jäger's solution (1995a) for torsion can serve as example.

References

Barber, J. R., and Ciavarella, M., 1999, "Contact Mechanics," *Int. J. Solids Structures,* Vol. 37, pp. 29–43.

Ciavarella, M., 1998a, "Tangential Loading of General Three-Dimensional Contacts," ASME JOURNAL OF APPLIED MECHANICS, Vol. 65, pp. 998–1003.

Ciavarella, M., 1998b, "The Generalized Cattaneo Partial Slip Plane Contact Problem, II—Examples," *Int. J. Solids Structures,* Vol. 35, pp. 2363–2378.

Jäger, J., 1992, "Elastic Impact With Friction," thesis, Inst. Inf. and Maths., Delft, The Netherlands.

Jäger, J., 1995a, "Axi-symmetric Bodies of Equal Material in Contact Under Torsion or Shift," *Arch. Appl. Mech.,* Vol. 65, pp. 478–487.

Jäger, J., 1995b, "Contact With Friction of Elastically Similar Bodies," *Impact, Waves and Fracture,* R. C. Batra, A. K. Mal, and G. P. MacSithigh, eds., ASME, New York, pp. 125–152.

Jäger, J., 1997a, "Ein neues Prinzip der Kontakmechanik," *Z. angew. Math. Mech.,* Vol. 7, pp. S143–S144.

Jäger, J., 1997b, "Half-Planes Without Coupling Under Contact Loading," *Arch. Appl. Mech.,* Vol. 67, pp. 247–259.

Jäger, J., 1999a, "Uni-axial Deformation of a Random Packing of Particles," *Arch. Appl. Mech.,* Vol. 69, pp. 181–203.

Jäger, J., 1999b, "Conditions for the Generalization of Cattaneo-Mindlin," *ZAMM 2000,* to be published.

Jäger, J., 1999c, "Equal Layers in Contact With Friction," *Contact Mechanics IV,* L. Gaul and C. A. Brebbia, eds, WIT Press, pp. 99–108.

Author's Closure[3]

First of all, I thank Dr. Jäger for his interest in my paper "Tangential Loading of General Three-dimensional Contacts." I confess I don't understand very well the scope of Dr. Jäger's "discussion." At first I thought he was questioning the originality of my paper, but this is not the case as there is no previous paper where an extension to the Cattaneo's solution for isotropic materials but general three-dimensional geometry is given. Secondly, I thought Dr. Jäger was trying to improve the clarity of the presentation of my paper, by discussing what he calls the "background"

[3] M. Ciavarella, Primo Ricercatore, CNR-IRIS, str. Crocefisso 2B, 70126 Bari, Italy. e-mail: m.ciavarela@area.ba.cnr.it.

Downloaded 04 May 2010 to 171.66.16.27. Redistribution subject to ASME license or copyright; see http://www.asme.org/terms/Terms_Use.cfm

of my generalization. He writes literally

"For vanishing Poisson's ratio, the normal and the tangential stress-displacement relations are uncoupled and identical, . . . , each normal solution is also a tangential solution. The two boundary conditions for uni-directional tangential shift are a constant displacement of the stick area and Coulomb's law $q = fp$ in the slip area."

The point is that I do *not* agree with this oversimplification of the contact problem, for the reason that the two problems of normal contact and of tangential contact are governed also by *inequalities,* and there is no reason a priori to think that the inequalities in the normal contact (basically the condition for no overlap outside the contact area and positive pressure in the contact area) are connected at all with the inequalities of Coulomb's law, which Dr. Jäger seems to forget assuming a personal, reduced version of Coulomb's law "$q = fp$ in the slip area."

Therefore, also this scope is not reached, and I suggest the reader to refer to the original paper where the problem is approached with rigor.

Having said this, he then proceeds to "discuss some points, which can mislead the reader," to which I respond in order.

1 It may be true that some equations of his papers on axisymmetric contact and my paper where the axisymmetric case was just an example are similar, it remains the question on whether Dr. Jäger had proved them at all, given my remarks above about inequalities. As regarding my reading and referencing of his papers that I confirm I received from him in the course of a review paper written with Prof. J. R. Barber of University of Michigan, I invite Dr. Jäger to wait for when the review paper will be out in the press, not accusing me of omissions based on preliminary versions of the paper that I may have sent him in the course of this work, and which is largely different from the final version soon in print.[4]

2 For flat regions, I also assumed the same height. Other definitions of "flat" could be clearly used, and in the limit, every point is a flat region. I doubt this point was unclear in my text.

3 I agree his notation can be more general, but for the scopes of my paper, I was happy with my Eq. (18).

4 Dr. Jäger here is correct in pointing to a misprint, as in my Eq. (23) a denominator $(2 - Qx/fP)$ is missing as it can be obtained from elementary vector analysis. The results and the comments are not significantly altered. I don't follow Dr. Jäger when he says "a special case of transient rolling exists, where the C-M solution can also be applied," without further reference. But this is not important for the scope of this discussion.

5 I refer to Dundurs' reference obviously not in the section about receding contact areas, but receding stick areas in frictional problems.

6 This point is raised about my other publications and I will reply on the appropriate journals.

Finally, Dr. Jäger proposes his "suggestions for further research" which look to me more likely to be his further research than mine, and concludes with publicity on his work on other generalizations of the "C-M" theory, on which I don't have much to say, apart that I hope the proofs are rigorous, i.e., the inequalities are included.

In conclusion, it looks to me the whole of the "Discussion" comes down to the correction of the mispring in Eq. (23).

Reference

Barber, J. R., and Ciavarella, M., 1999, "Contact Mechanics," *Int. J. Solids Struct.,* Vol. 37, pp. 29–43.

[4] The paper is now in print. Please see Barber and Ciavarella (1999) in which Ciavarella wrote "A significant generalization of Cattaneo-Mindlin was discovered by Ciavarella . . . for any plane contact problem." Although this statement was corrected later, Ciavarella did not relate his axisymmetric solution to Jäger (1995a).

Downloaded 04 May 2010 to 171.66.16.27. Redistribution subject to ASME license or copyright; see http://www.asme.org/terms/Terms_Use.cfm